

AMMRC MS 80-4

LEVEL II

12

AD

4
ADA090684

**PROCEEDINGS OF THE ARMY SYMPOSIUM
ON SOLID MECHANICS, 1980 -
DESIGNING FOR EXTREMES:
ENVIRONMENT, LOADING, AND
STRUCTURAL BEHAVIOR**

September 1980

DTIC
ELECTE
OCT 22 1980

A

Approved for public release; distribution unlimited.

ARMY MATERIALS AND MECHANICS RESEARCH CENTER
Watertown, Massachusetts 02172

DDC FILE COPY

80 10 15 001

The findings in this report are not to be construed as an official Department of the Army position, unless so designated by other authorized documents.

Mention of any trade names or manufacturers in this report shall not be construed as advertising nor as an official indorsement or approval of such products or companies by the United States Government.

DISPOSITION INSTRUCTIONS

Destroy this report when it is no longer needed.
Do not return it to the originator.

UNCLASSIFIED

SECURITY CLASSIFICATION OF THIS PAGE (When Data Entered)

REPORT DOCUMENTATION PAGE		READ INSTRUCTIONS BEFORE COMPLETING FORM
1. REPORT NUMBER (14) AMMRC-MS-88-4	2. GOVT ACCESSION NO. AD-A090684	3. RECIPIENT'S CATALOG NUMBER
4. TITLE (and Subtitle) (6) Proceedings of the Army Symposium on Solid Mechanics, 1980 - Designing for Extremes: Environment, Loading, and Structural Behavior <i>Held at Cape Cod, Massachusetts</i>		5. TYPE OF REPORT & PERIOD COVERED (1) Final Report
7. AUTHOR(s) 39 ...		6. PERFORMING ORG. REPORT NUMBER
9. PERFORMING ORGANIZATION NAME AND ADDRESS Army Materials and Mechanics Research Center Watertown, Massachusetts 02172 DRXMR-T		8. CONTRACT OR GRANT NUMBER(s) (10) F71
11. CONTROLLING OFFICE NAME AND ADDRESS U. S. Army Materiel Development and Readiness Command, Alexandria, Virginia 22333		10. PROGRAM ELEMENT, PROJECT, TASK AREA & WORK UNIT NUMBERS
14. MONITORING AGENCY NAME & ADDRESS (if different from Controlling Office)		12. REPORT DATE (1) September 1980
		13. NUMBER OF PAGES 395
		15. SECURITY CLASS. (of this report) Unclassified
		15a. DECLASSIFICATION/DOWNGRADING SCHEDULE
16. DISTRIBUTION STATEMENT (of this Report) Approved for public release; distribution unlimited.		
17. DISTRIBUTION STATEMENT (of the abstract entered in Block 20, if different from Report)		
18. SUPPLEMENTARY NOTES		
19. KEY WORDS (Continue on reverse side if necessary and identify by block number) (See Reverse Side)		
20. ABSTRACT (Continue on reverse side if necessary and identify by block number) → Proceedings of the Army Symposium on Solid Mechanics, 1980 - Designing for Extremes: Environment, Loading, and Structural Behavior, held at Bass River (Cape Cod), Massachusetts, 30 September through 2 October 1980. ←		

DD FORM 1 JAN 73 1473

EDITION OF 1 NOV 65 IS OBSOLETE

UNCLASSIFIED

SECURITY CLASSIFICATION OF THIS PAGE (When Data Entered)

UNCLASSIFIED

SECURITY CLASSIFICATION OF THIS PAGE(When Data Entered)

Block No. 19

KEY WORDS

Aircraft	Fibers	Radiation
Aluminum Alloys	Fighter Aircraft	Reliability
Armor	Flow	Residual
Ballistics	Fluids	Rock
Biological Warfare	Fracture (Mechanics)	Rods
Blast Loads	Fragmentation	Shaped Charges
Bombs	Fragments	Shear Properties
Buckling	Gases	Shelters
Buildings	Gun Barrels	Shock (Mechanics)
Collapse	Gunfire	Shock Waves
Composite Materials	Guns	Spallation
Compression	Hardening	Specifications
Computerized Simulation	High Explosives	Spectra
Confidence Level	Howitzers	Stability
Corrosion	Hydrodynamics	Strain (Mechanics)
Cost Analysis	Impact	Strength (General)
Crack Propagation	Impingement	Stress Corrosion
Cracks	Instability	Stresses
Crash Resistance	Life (Durability)	Structural Properties
Cycles	Loads (Forces)	Structural Response
Damage	Materials	Structures
Debris	Mechanics	Super Alloys
Defects (Materials)	Mines (Ordnance)	Survival (General)
Deformation	Models	Tanks (Combat Vehicles)
Degradation	Non-Linear Systems	Temperature
Detonations	Ordnance	Thermal Radiation
Displacements	Panels	Threats
Dynamic Response	Plastic Properties	Trade Off Analysis
Dynamics	Plates	USSR
Electronic Warfare	Predictions	Velocity
Enemy	Pressure	Vibration
Environments	Probability	Vulnerability
Eutects	Projectiles	Warfare
Explosives	Protection	Weapon Systems
Failure	Pulses	Weight
Fatigue (Mechanics)	Radar Antennas	Wings

UNCLASSIFIED

SECURITY CLASSIFICATION OF THIS PAGE(When Data Entered)

PREFACE

The Army Symposium on Solid Mechanics, 1980 was the seventh in a series of biennial meetings sponsored by the Army Materials and Mechanics Research Center (AMMRC) in Watertown, Massachusetts. A Work-In-Progress Session(s) has been incorporated into these conferences since 1974 (called Ongoing Case Studies Session at the 1978 meeting). These sessions are comprised of a series of brief presentations and discussions of current, but not necessarily complete, research relating to the theme of the meeting. Abstracts of these presentations are published in a companion document to the regular proceedings; those presented at this 1980 symposium are published in AMMRC MS 80-5, dated September 1980. Addresses presented during the opening session of this symposium are published in another companion document: AMMRC MS 80-6 dated September 1980. The transactions of earlier symposia are listed on page ii of this document.

Participation in these symposia has broadened with time. Starting with the 1972 meeting, papers have been solicited from in-house and contract researchers and designers for the Navy, Air Force and other government agencies, in addition to those for the Army. The symposium committee has been expanded several times; its current membership is as shown on page iii. These expansions were made in recognition of the fact that many mechanics research and/or design problems are not unique to a single service or government agency.

Essentially, these symposia are a vehicle for enhancing the responsiveness of mechanics research efforts for the design of advanced military systems. They also facilitate communications and coordination between and among researchers and designers having common military theme interests, whether they work for a government service or agency, industry, or at some university or research institute.

No endeavor of the magnitude of this 1980 symposium could have been successfully conducted without the enthusiastic cooperation and support of many individuals and organizations. We greatly acknowledge:

The many authors, participants and session chairmen who made this conference such a success.

The manuscript reviewers from universities, industry and government organizations, for their diligence in carrying out a thankless task.

Max Williams, Dean of Engineering, University of Pittsburgh, who delivered a very interesting and relevant keynote address on "Coping With Extremes for Structural Performance."

And finally, the clerical staff of the Mechanics and Engineering Laboratory and the Technical Reports Office of AMMRC for their unflagging efforts in the preparation and printing of numerous symposium materials.

PREVIOUS DOCUMENTS IN THIS SYMPOSIA SERIES*

Proceedings of the Army Symposium on Solid Mechanics, 1968,
AMMRC MS 68-09, September 1968, AD 675 463

Proceedings of the Army Symposium on Solid Mechanics, 1970 -
Lightweight Structures,
AMMRC MS 70-5, December 1970, AD 883 455L

Proceedings of the Army Symposium on Solid Mechanics, 1972 -
The Role of Mechanics in Design - Ballistic Problems,
AMMRC MS 73-2, September 1973, AD 772 827

Proceedings of the Army Symposium on Solid Mechanics, 1974:
The Role of Mechanics in Design - Structural Joints,
AMMRC MS 74-8, September 1974, AD 786 543

Work-In-Progress Presented at the Army Symposium on Solid Mechanics, 1974:
The Role of Mechanics in Design - Structural Joints,
AMMRC MS 74-9, September 1974, AD 786 524

Stress Analysis of Structural Joints and Interfaces -
A Selective Annotated Bibliography
by M. M. Murphy and E. M. Lenee,
AMMRC MS 74-10, September 1974, AD 786 520

Proceedings of the Army Symposium on Solid Mechanics, 1976 -
Composite Materials: The Influence of Mechanics of Failure on Design,
AMMRC MS 76-2, September 1976, AD A029 735

Work-In-Progress Presented at the Army Symposium on Solid Mechanics, 1976 -
Composite Materials: The Influence of Mechanics of Failure on Design,
AMMRC MS 76-3, September 1976, AD A029 736

Proceedings of the Army Symposium on Solid Mechanics 1978 -
Case Studies on Structural Integrity and Reliability
AMMRC MS 78-3, September 1978, AD A059 834/261

Ongoing Case Studies Presented at the Army Symposium on Solid Mechanics, 1978 -
Case Studies on Structural Integrity and Reliability
AMMRC MS 78-4, September 1978, AD A059 605/661

* These documents may be ordered from the National Technical Information
Service, U. S. Department of Commerce, Springfield, VA 22161

SYMPOSIUM COMMITTEE

E. M. LENOE, Chairman, AMMRC
J. F. MESCALL, Vice Chairman, AMMRC
R. J. MORRISSEY, Coordinator, AMMRC

TECHNICAL PAPERS AND PROGRAM

J. ADACHI, Chairman, AMMRC
F. I. BARATTA, AMMRC
L. BERKE, NASA-Lewis Research Center
C. I. CHANG, Naval Research Laboratory
H. D. CURCHACK, Harry Diamond Laboratories
G. A. DARCY, JR., AMMRC
T. S. DESISTO, AMMRC
C. M. ELDRIDGE, Army Missile Command
J. FEROLI, Army Test and Evaluation Command
G. L. FILBEY, JR., Ballistic Research Laboratories
R. FOYE, Army Aviation R&D Command
C. E. FREESE, AMMRC
J. J. GASSNER, JR., AMMRC
A. J. GUSTAFSON, Army Aviation R&D Command
G. E. MADDUX, Air Force Flight Dynamics Laboratory
J. F. MESCALL, AMMRC
D. R. MULVILLE, Naval Research Laboratory
R. P. PAPIRNO, AMMRC
E. W. ROSS, JR., Army Natick R&D Command
E. SAIBEL, Army Research Office
T. SIMKINS, Army Armament R&D Command
J. H. SMITH, National Bureau of Standards
D. M. TRACEY, AMMRC
G. WILLIAMSON, Army Construction Engineering Research Laboratory

WORK IN PROGRESS SESSION

G. E. MADDUX, Co-Chairman, Air Force Flight Dynamics Laboratory
R. P. PAPIRNO, Co-Chairman, AMMRC

CONTENTS

SESSION I: HARDWARE SYSTEMS

THE F-16 AND DAMAGE TOLERANCE.	3
L. M. Smith, General Dynamics Corporation	
EVALUATION OF BLAST CAPACITIES OF A PRE-ENGINEERED AND STRENGTHENED STEEL BUILDING	21
N. Dobbs, F. E. Sock, and K. Shah, Ammann & Whitney, and P. Price and J. Caltagirone, Army Armament R&D Command	
C ³ SHELTER DESIGNS FOR THE TACTICAL BATTLEFIELD.	46
W. J. Schuman, Jr., Harry Diamond Laboratories, G. Zartarian and R. P. Yeghiayan, Kaman Avidyne, and W. D. Allison, Army Armament R&D Command	
COMPOSITE TANK FLOOR ARMOR	65
A. San Miguel, Systems, Science and Software	

SESSION II: DYNAMIC RESPONSE

DYNAMIC STABILITY OF STRUCTURAL ELEMENTS SUBJECTED TO STEP-LOADS	87
G. J. Simitses, Georgia Institute of Technology	
TRANSIENT ANALYSIS OF DOUBLE HULLS IMPINGED UPON BY INCIDENT UNDERWATER EXPLOSION WAVES	108
H. Huang, S. Halperson, and D. Curtis, Naval Research Laboratory	
DYNAMIC ELASTIC-PLASTIC RESPONSE OF UNSTIFFENED AND STIFFENED PANELS TO PRESSURE LOADINGS	126
L. J. Mento and W. N. Lee, Kaman Avidyne	

SESSION III. COMPOSITES

COMBAT DAMAGE TOLERANT WING STRUCTURAL DEVELOPMENT	159
J. G. Avery, S. J. Bradley, and K. M. King, Boeing Military Airplane Company	

THE RESPONSE OF ADVANCED COMPOSITE STRUCTURES TO HIGH EXPLOSIVE BLAST. .	187
--	-----

A. L. Dobyns and J. G. Avery, Boeing Military Airplane Company

STABILITY OF COMPOSITE PLATES SUBJECTED TO VARYING TANGENTIAL AND LATERAL LOADS.	204
--	-----

R. J. Stuart and S. Dharmarajan, San Diego State University

COMPRESSION STRENGTH DEGRADATION OF ADVANCED COMPOSITE STRUCTURES. . . .	219
--	-----

D. Y. Konishi, Rockwell International,
North American Aircraft Division

SESSION IV: PROJECTILE PHENOMENA-1

MODELING OF THE SHAPED-CHARGE JET FORMATION.	239
--	-----

W. P. Walters and J. T. Harrison, Army Armament R&D Command

EFFECT OF CASE MATERIAL PROPERTIES ON FRAGMENT VELOCITIES FROM BOMBS . .	255
--	-----

O. E. R. Heimdahl and W. J. Strongo, Naval Weapons Center

IN-BORE MOTION ANALYSIS OF THE 155mm XM712 PROJECTILE WHEN FIRED IN THE M198 HOWITZER.	270
--	-----

S. H. Chu, Army Armament R&D Command

IMPACT OF ROCK PROJECTILES ON A SIMPLY SUPPORTED BEAM.	289
--	-----

R. L. Mann, General Electric Company and
R. W. Perkins, Syracuse University

SESSION V: PROJECTILE PHENOMENA-2

DEFORMATION OF MAR-M200 (A NICKEL BASE SUPERALLOY) UNDER SHOCK LOADING TO 8.5 GPa AT ROOM TEMPERATURE	317
---	-----

D. P. Dandekar, A. G. Martin, and J. V. Kelley,
Army Materials and Mechanics Research Center

A FRACTURE INVESTIGATION OF A LAMELLAR EUTECTIC TWO-PHASE METAL ALLOY UNDER SHOCK LOADING.	330
--	-----

G. H. Brawley, Battelle Columbus Laboratories and
W. W. Predebon, Michigan Technological University

THE COMPRESSION TEST REVISITED	351
J. F. Mescall, R. P. Papirno, and J. McLaughlin, Army Materials and Mechanics Research Center	
BEYOND THE TAYLOR TEST TO FRACTURE	367
R. P. Papirno, J. F. Mescall, and A. M. Hansen, Army Materials and Mechanics Research Center	
AUTHOR INDEX	387

SESSION I: HARDWARE SYSTEMS

Chairman: R. M. Bader
Assistant Chief, Structures & Dynamics Division
Air Force Flight Dynamics Laboratory

THE F-16 AND DAMAGE TOLERANCE. 3

L. M. Smith
General Dynamics Corporation

EVALUATION OF BLAST CAPACITIES OF A PRE-ENGINEERED AND
STRENGTHENED STEEL BUILDING. 21

N. Dobbs,
F. E. Sock, and
K. Shah
Ammann & Whitney
P. Price
J. Caltagirone
Army Armament R&D Command

C³ SHELTER DESIGNS FOR THE TACTICAL BATTLEFIELD. 46

W. J. Schuman, Jr.
Harry Diamond Laboratories,
G. Zartarian
R. P. Yeghiayan
Kaman Avidyne, and
W. D. Allison
Army Armament R&D Command

COMPOSITE TANK FLOOR ARMOR 65

A. San Miguel
Systems, Science and Software

THE F-16 AND DAMAGE TOLERANCE

Larz M. Smith, Manager
Structures Technology

General Dynamics Corp.
Fort Worth Division
Fort Worth, Texas

ABSTRACT

The General Dynamics/USAF F-16 multirole fighter plane is one of the first military aircraft designed from its inception to the new damage tolerance specifications. The selection of materials and stress levels were affected by these requirements and are described. The selection of specific alloys of aluminum was predicated on a series of tests which are discussed. The importance of realistic cyclic loadings in crack growth testing along with environmental exposure is explained. This program demonstrated that fracture approach to design is not only feasible but practical and resulted in a durable, safe airframe.

INTRODUCTION

The General Dynamics/USAF F-16 multirole fighter is the newest and most maneuverable of the new generation warplanes. It is also one of the first to be designed to damage tolerance requirements from its inception and to be certified by successful structural testing.

The extreme maneuver factor coupled with a severe usage and prolonged service life requirement provided a challenging design task. This task was additionally complicated by weight and performance requirements as well as cost considerations.

Essentially, the F-16 is an aluminum alloy airplane. This material was selected for both its efficiency and its relatively low cost in comparison to other high strength materials. The particular alloy and temper of aluminum was selected by part size, toughness, crack growth characteristics, and corrosion resistance. Aluminum comprises about 80% of the airframe structural weight and is used for all primary structure except a few fittings.

The structure is conventional semi-monocoque design with simple straightforward arrangement. The fuselage has multiple bulkheads and frames with few longerons. The wing is multiple spar with few ribs or stiffeners. The arrangement and materials used are shown in Figure 1.

F-16 STRUCTURAL ARRANGEMENT AND MATERIALS

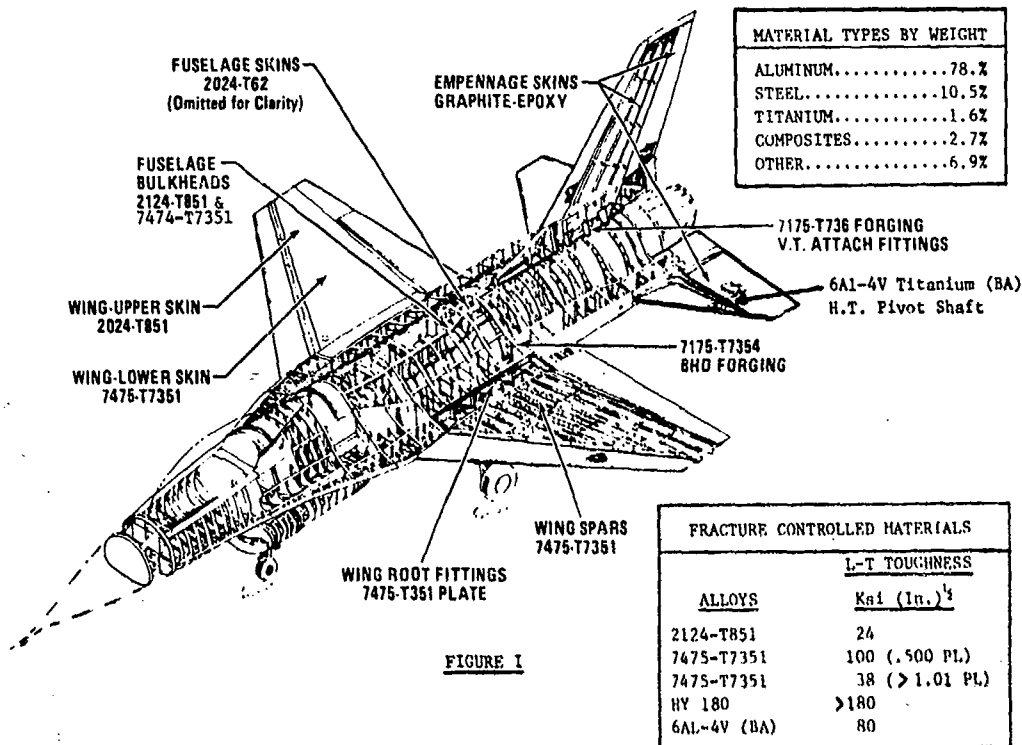


FIGURE 1

The requirements were based on MIL-STD-1530, MIL-A-83444 and MIL-A-008866A and were spelled out in detail in the F-16 Aircraft Structural Integrity Program Report, (ASIP document). The durability and damage tolerance analyses were required to be accomplished on a fracture or crack growth basis.

The damage tolerance requirement is to provide safety in flight. This requires (1) the assumption that critical parts contain a major initial (manufactured) flaw, assumed to be undetected; (2) then be cycled (or flown) for two complete design lifetimes with the flaw (crack) allowed to grow; and (3) after two lifetimes to withstand the maximum load ever expected in actual service to demonstrate that the crack had not reached critical length.

The durability (fatigue) requirement is to provide long life with minimized maintenance or repair. It requires critical parts to contain small, undetected manufacturing defects which are permitted to grow but must not cause functional impairment within one lifetime. This effectively requires that a crack shall not grow out from under the head of a fastener or through a skin, since a fuel leak is defined as "functional impairment."

Thus, it was necessary to determine the type, size, orientation, location and characteristics of flaws in F-16 structural parts. These were influenced by our nondestructive inspection methods and capabilities, the form of construction and operating stress levels.

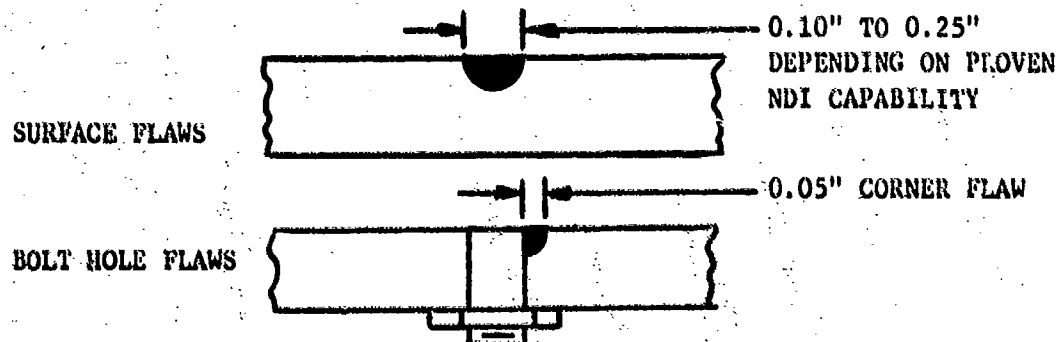
Basically, the F-16 flaw requirements are of two types; bolt hole corner flaws and surface flaws. The sizes are shown in Table I and requirements in Figure II.

TABLE I

TYPE FLAW	REQUIREMENT	
	DURABILITY	DAMAGE TOLERANCE
SURFACE	.01"	.10" TO .25"
BOLT HOLE	.005"	.05"

F-16 FATIGUE AND FRACTURE CRITERIA

- BASED ON MIL-STD-1530, MIL-A-008866A AND MIL-A-83444
- NO FUNCTIONAL IMPAIRMENT WITHIN ONE (1) SERVICE LIFETIME
- USEFUL ECONOMIC LIFE MUST EXCEED ONE (1) SERVICE LIFETIME
- DAMAGE TOLERANCE REQUIREMENTS:
- "ASSUMED FLAWS" WILL NOT GROW TO CRITICAL LENGTH IN TWO LIFETIMES



- RESIDUAL STRENGTH REQUIREMENT AFTER TWO LIFETIMES PER MIL-A-83444 EXCEPT LOADS NEED NOT EXCEED OPERATIONAL CAPABILITY OF AIRPLANE.

FIGURE II

One very significant requirement was the design life and type of usage. The great maneuverability of the F-16 resulted in a severe usage spectrum with regard to both the high "g" (load factor) levels and frequency of occurrence. The air-to-air combat mission was increased to five times as many occurrences as required by MIL Spec. This was further aggravated by the 15 year and 8,000 flight hour life designated for the F-16. The development of this spectrum was significant for both analysis and testing. For crack growth reasons it had to be as realistic as possible and was required for both small specimen testing as well as the full-scale testing. It should be noted that the fracture requirement dictates a randomized spectrum for high and low load occurrences. The old style block spectrum is not satisfactory for crack growth considerations. Details are shown in Table II.

TABLE II REPEATED LOADS SPECTRUM DEVELOPMENT

LOADS SPECTRUM ELEMENTS:

- 8000 FLIGHT HOURS - 15 YEARS
 - 5776 SORTIES
 - 12 MISSION TYPES
 - 10 MISSION SEGMENTS
 - 20 MACH-ALTITUDE COMBINATIONS
 - 7 GROSS WEIGHTS
 - 10 TYPES OF MANEUVERS
 - 1,059,188 FLIGHT MANEUVERS PRIOR TO FINAL TRUNCATION FOR TESTING
 - 782,096 Positive N_z Maneuvers
 - 277,092 Negative N_z Maneuvers
 - 6592 LANDINGS
 - MISSION CATEGORIES
 - 55.5% Air-Air, 20.0% Air-Ground, 24.5% General
- } 132 UNIQUE SORTIE LEGS

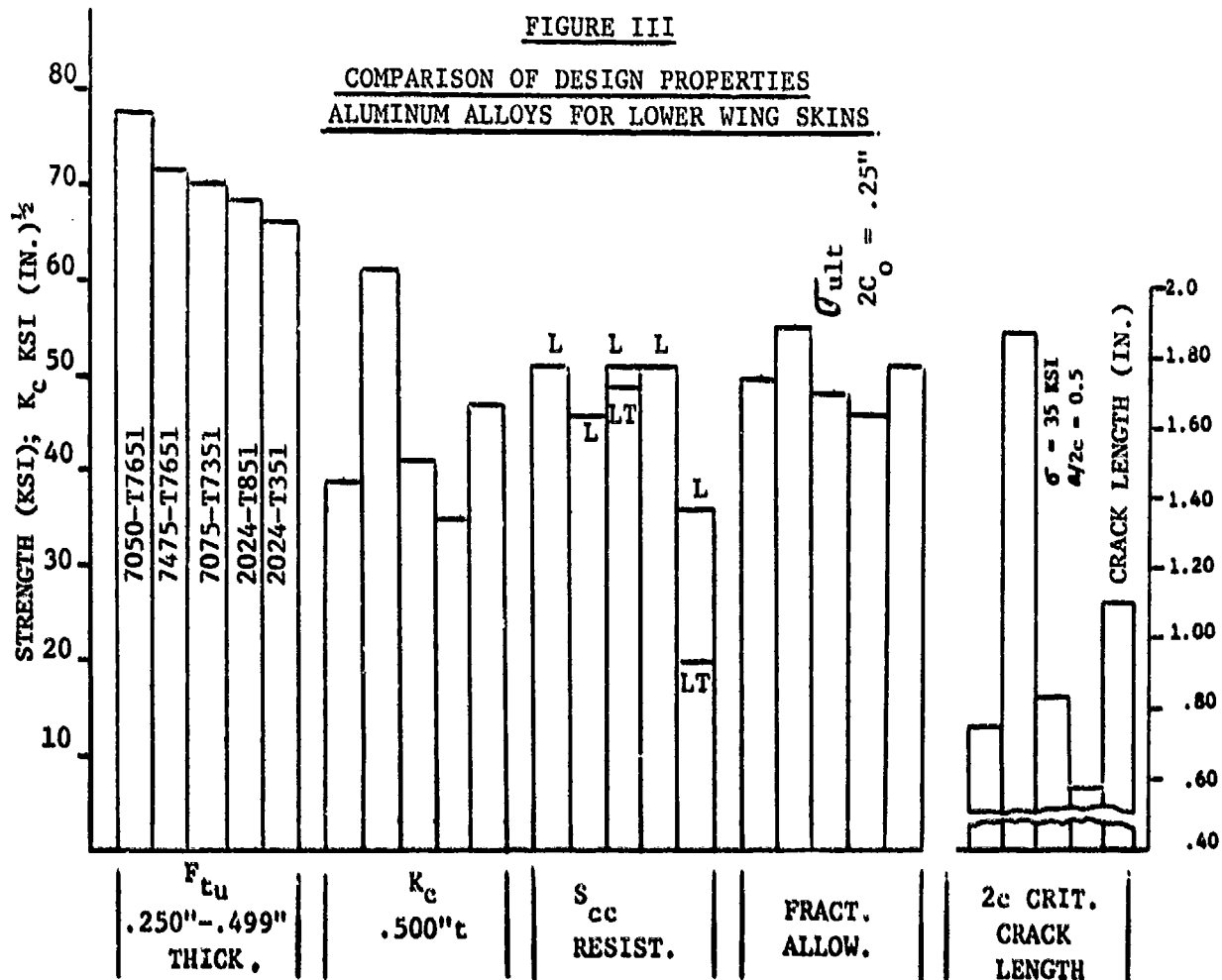
SPECTRUM CHARACTERISTICS:

- RANDOMIZED QUANTITIES
 - Sequence of 500-Hour-Segments
 - Sequence of Maneuvers Within a Sortie Leg
 - Sequence of Sortie Leg Maneuver Spectra Distributed to Each Sortie
- DETERMINISTIC QUANTITIES
 - Sequence of Flights Within a 500-Hour-Segment
 - Sequence of Mission Segments Within a Given Flight

Due to the limited scope of this discussion and the fact that the F-16 is essentially an "aluminum" airplane, the remainder of this presentation will deal with the fracture analysis and crack growth characteristics of the aluminum alloys used in the airframe structure.

The fracture requirements caused selection of materials having high toughness or slow crack growth, or both. An aluminum alloy screening program was established utilizing available data and candidate alloys were further screened in the General Dynamics Laboratory. The alloys were grouped by types and selection made for each application such as; (1) sheet, (2) plate, (3) thick plate, (4) extrusions, and (5) forgings.

Each alloy within each group was compared for both strength and toughness. Further, a critical crack length was calculated for the F-16 projected thickness and stress level. See Figure III for an example of comparisons.



Further testing was then conducted on one or two leading candidates in each group to evaluate the effects of various exposures. This was accomplished by da/dn testing (crack growth rate) using specimens as shown in Figure IV for exposure to high humidity and sump tank water. These two environments were selected after study of data available on aluminum.

It was found that one of the most aggressive fluids experienced was the water that collects in the bottom (sump) of the integral fuel tanks. This comes from condensation within the tanks as well as residue pumped from seagoing tankers and truck tankers. It is more aggressive because of the salts that collect. Chemists have characterized the "worst" of this water that has been experienced in other aircraft and have standardized a formula for test purposes as shown in Table III.

The effects of these exposures varied with the different alloys. The data used to analyze a given part depended on its location and thus the more critical environment it experiences. Many parts were critical for sump tank water or high humidity exposures. Examples are shown in Figures V and VI.

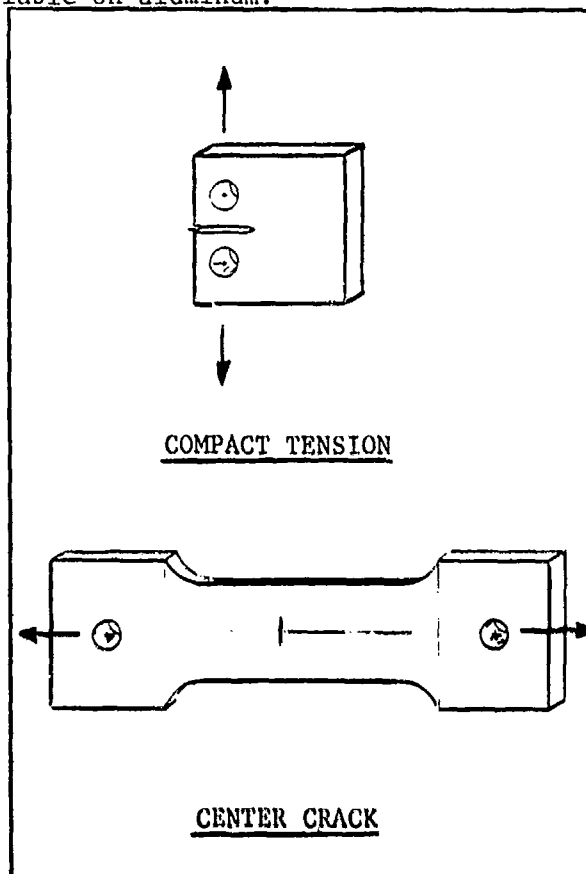


FIGURE IV

TABLE III

<u>SUMP TANK WATER</u> (CHEMICAL COMPOSITION)			
CaCl ₂	50 PPM	CrCl ₃ · 6H ₂ O	1 PPM
CdCl ₂	1000 PPM	CuCl ₃ · 2H ₂ O	1 PPM
MgCl ₂	50 PPM	FeCl ₃	5 PPM
NaCl	100 PPM	MnCl ₂ · 4H ₂ O	5 PPM
ZnCl ₂	10 PPM	NiCl ₂ · 6H ₂ O	1 PPM
PbCl ₂	1 PPM	Distilled Water	Balance

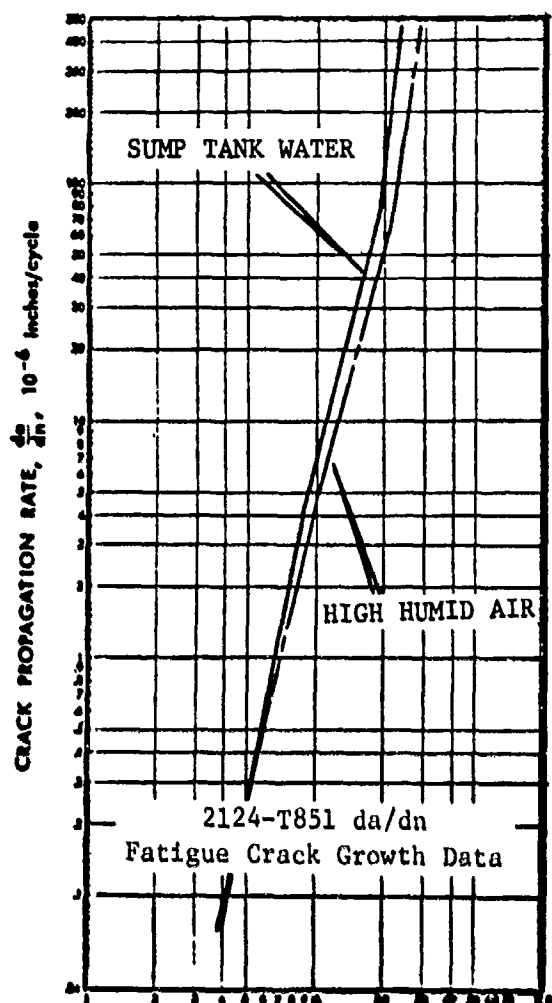


FIGURE V

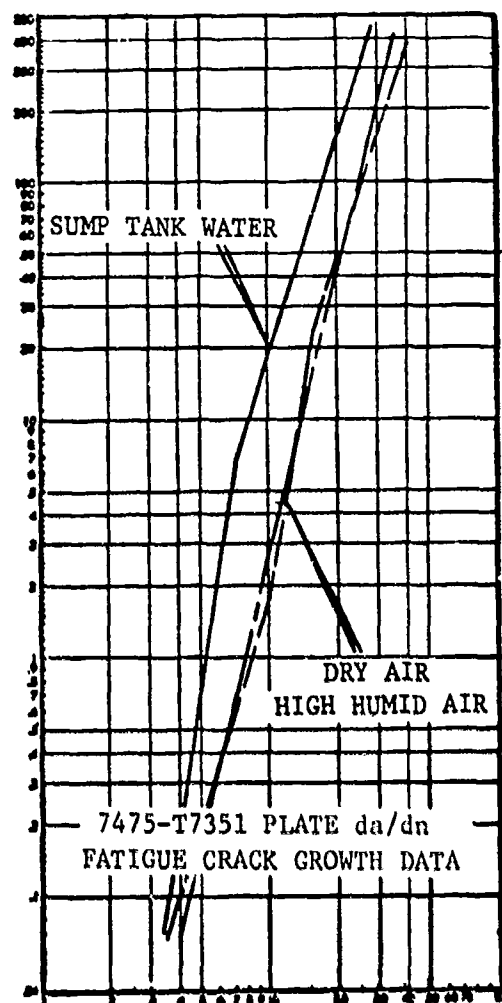


FIGURE VI

Based on the test data and cost studies, the materials shown in Table IV were selected. The larger fuselage bulkheads were machined from 2124 plate because 7475 alloy could not be obtained in the thickness required. Spectrum tests were then conducted on parts and special specimens.

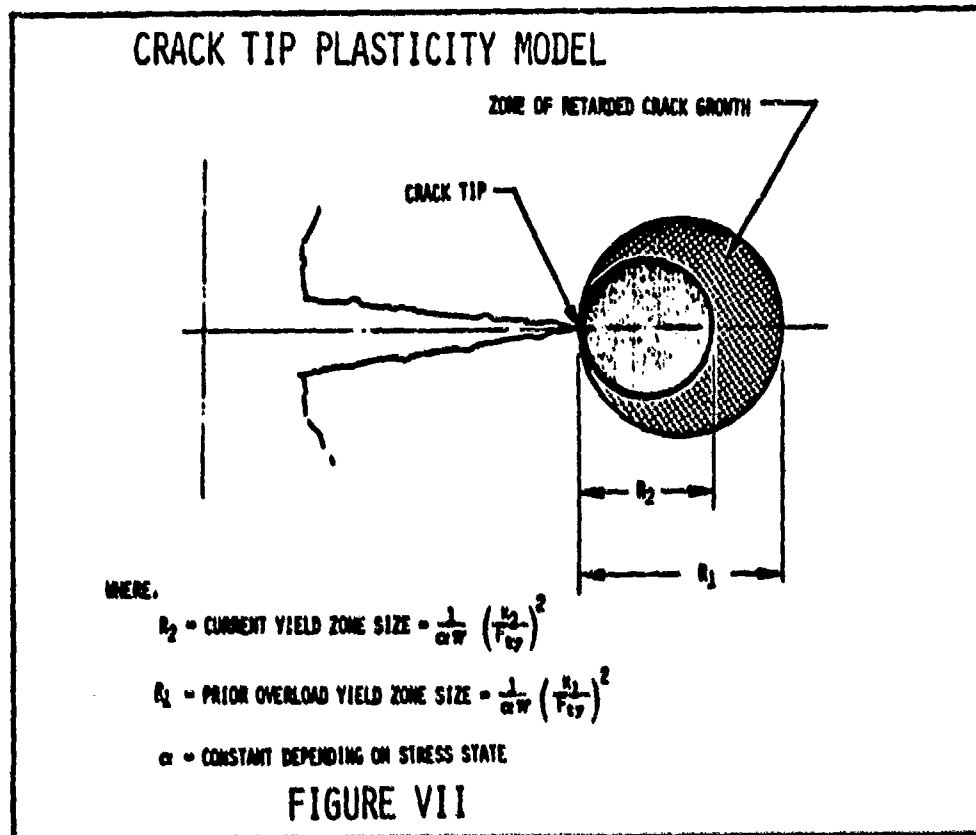
TABLE IV

TYPE PART	ALLOY/TEMPER	FORM
FUSE. SKIN/FRAMES	2024-T62	SHEET
FUSE. BULKHEADS (4"-6"t)	2124-T851	PLATE
WING LOWER SKIN (ORIGINAL)	7475-T7651	PLATE
WING UPPER SKIN	2024-T851	PLATE
WING FITTINGS (ORIGINAL)	7175-T736	FORGING

The first development of this testing was rapid crack growth in the 7475-T7651 aluminum alloy plate exposed to sump tank water. This was in spite of our screening and its excellent toughness.

It was known that the retardation effect under spectrum loading is often predicated on a plastic zone at the crack tip that results from high load applications. The larger the zone the greater the retardation effect (time to grow through the zone). See Figure VII.

This led to the idea that lowering the yield strength could increase the time to grow to critical crack length. This was feasible in static strength design since the allowable stress had been held considerably below F_{tu} for fatigue and fracture purposes. The 7475-T7651 material was overaged at 350° F to bring it to 7475-T7351. (yield lowered from 71 KSI nominal to 61 KSI nominal.) In addition to the effect on crack tip plasticity, the overaged condition was felt to have increased corrosion resistance in the aggressive sump tank water environment. The net effect of this somewhat unique "fix" was quite gratifying as shown in Figure VIII. All large plates in stock were overaged and new material ordered to this temper. This alloy and temper is used on all F-16 lower wing skins.



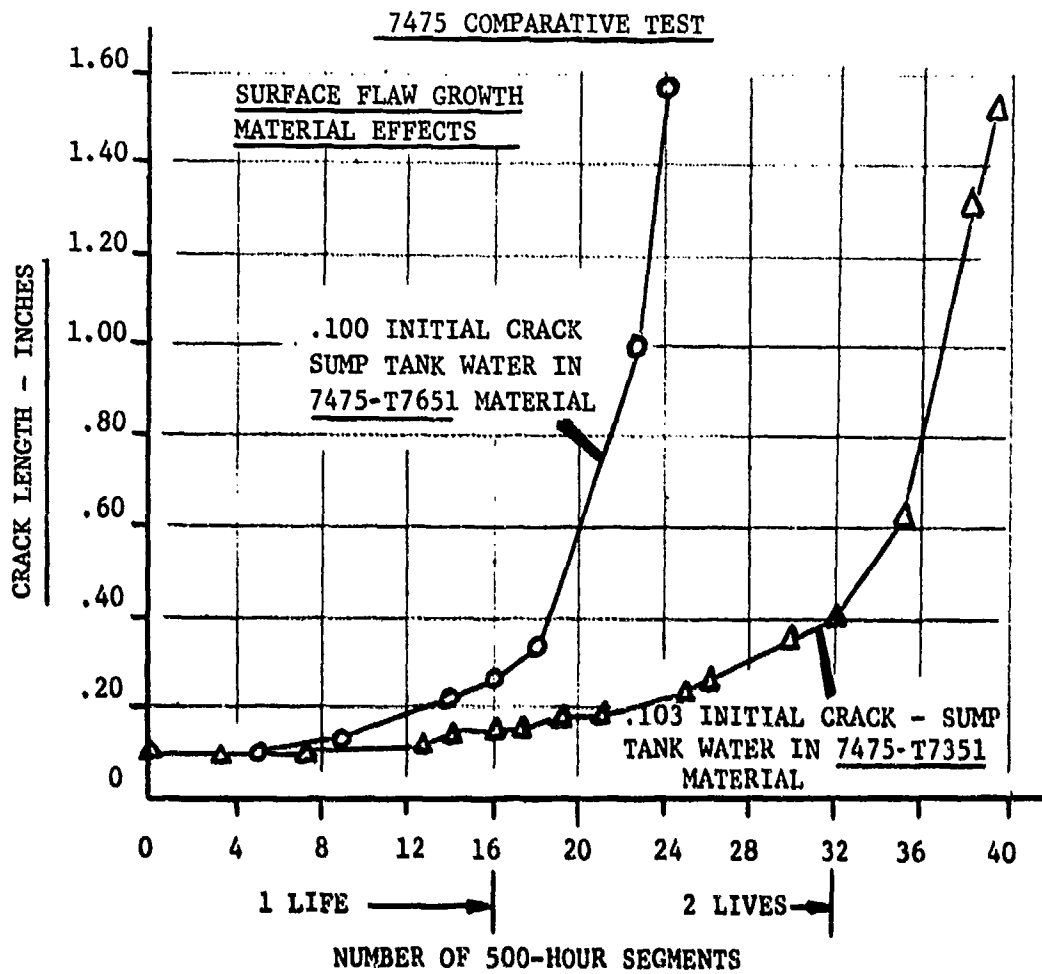
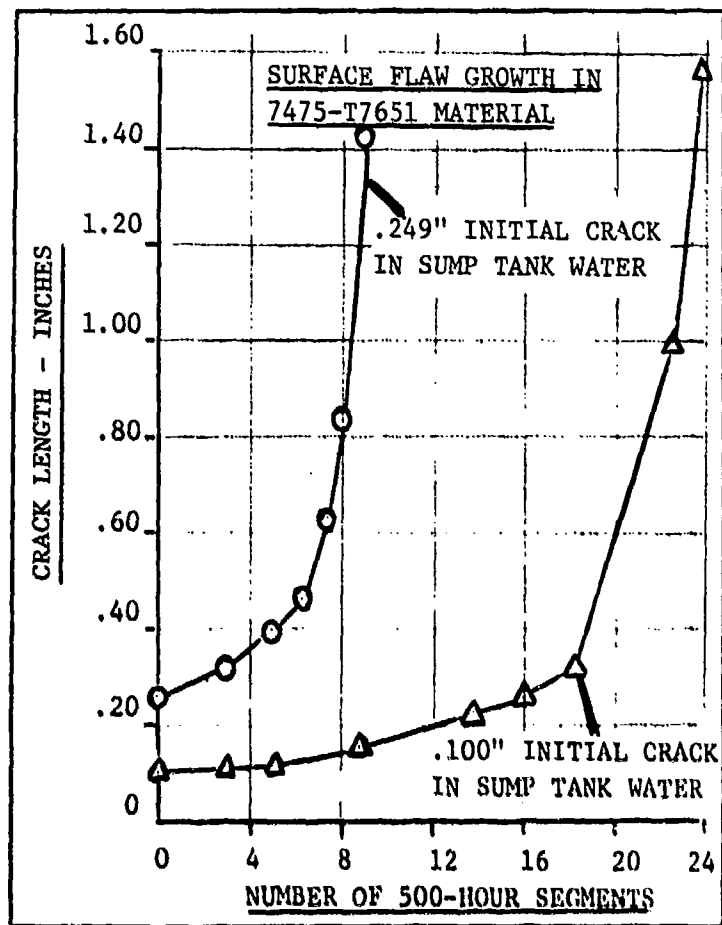


FIGURE VIII

The second development of the spectrum testing showed that the use of the specification required initial flaw size of .25 in. (surface flaw) length was unduly prohibitive in terms of lowered stress and the resulting increased weight. It was established that .10 inch was an achievable size to detect with fluorescent penetrant inspection. The experimental comparison is as shown in Figure IX. It resulted in a production shop demonstration program to prove the reliability of inspecting material for a .10 inch flaw (crack) with 90% reliability at a 95% confidence level. This demonstration was not only successfully conducted in our factory but in two others in Europe.

It should be noted that initial testing was on 7475-T7651 material. It took both the material yield decrease effect and the reduced initial flaw size to reach two (2) lives of our design spectrum. The result was to bring the .10" surface flaw and .05" bolt hole corner flaw into a comparable degree of criticality.

No attempt was made to reduce the bolt hole corner crack initial size by non-destructive test means. We felt that it was too expensive to inspect many hundreds of holes per airplane with the current NDI techniques. Therefore we accepted the specification value for design and require only visual inspection of holes.



SURFACE FLAW SIZE - FIGURE IX

Additional spectrum testing was conducted using both surface flawed and bolt hole flawed specimens (Figures X through XII) to study the sensitivity of numerous variables.

CENTER CRACK SPECIMEN

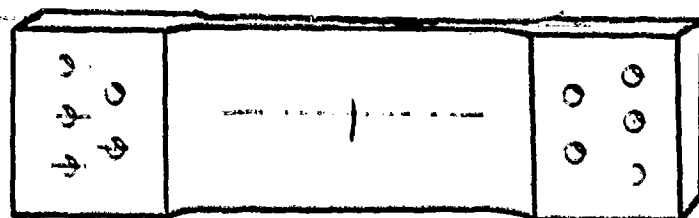


FIGURE X

The surface flawed specimen tests were conducted on various thickness and width plates similar to the design shown in Figure X.

The bolt hole specimen test included variables of bolt size, stress level and bolt load transfer in addition to plate thickness. The fixture shown in Figure XI was unique for this type testing but was extremely valuable in assuring correct bolt load parameters and in assessing their effects.

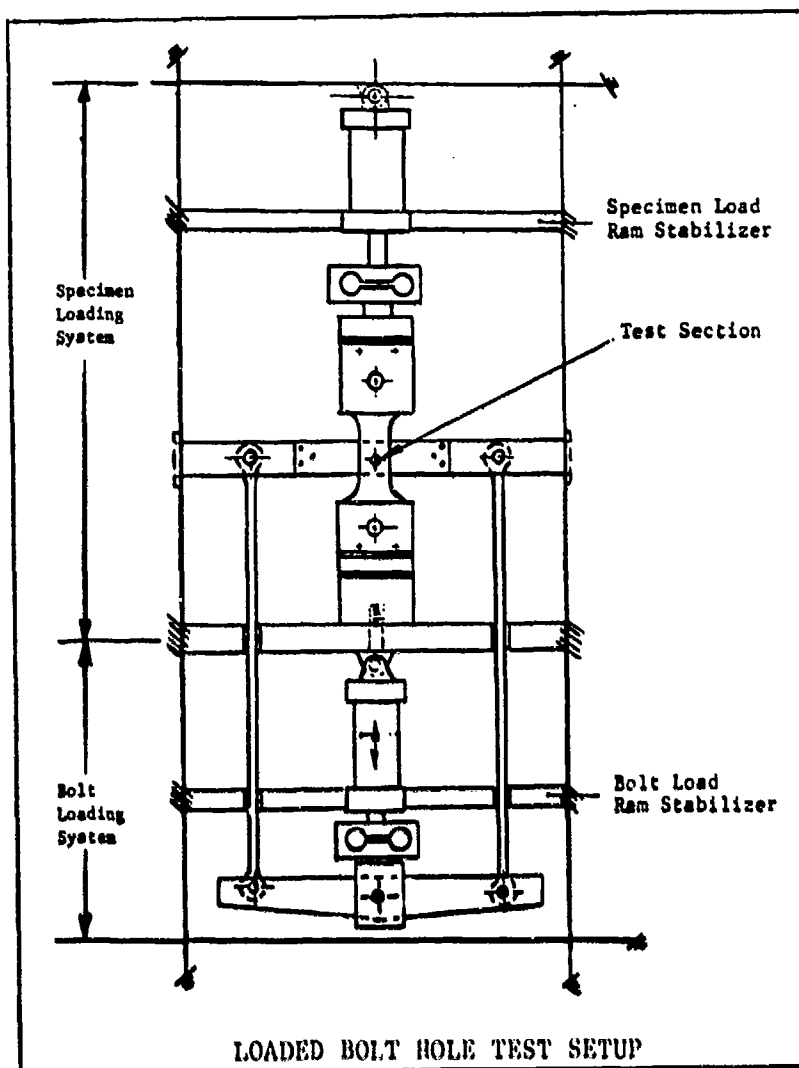


FIGURE XI

LOADED BOLT HOLE SPECIMEN

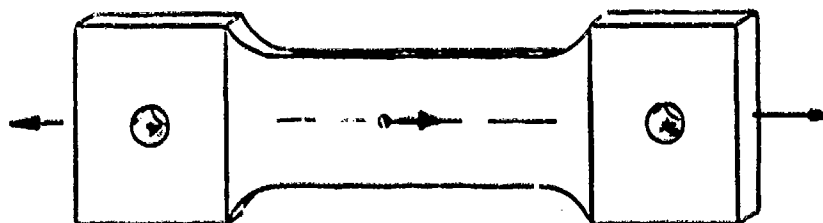


FIGURE XII

Table V summarizes much of the testing that shows comparison of the 2124 and 7475 alloys. The 7475 was preferred because of its toughness and long critical crack length. The 2124 alloy was used for machined bulkheads where thickness exceeded that obtainable in 7475. This was acceptable design even though the 2124 critical crack length is considerably shorter because the 2124 exhibited quite slow crack growth.

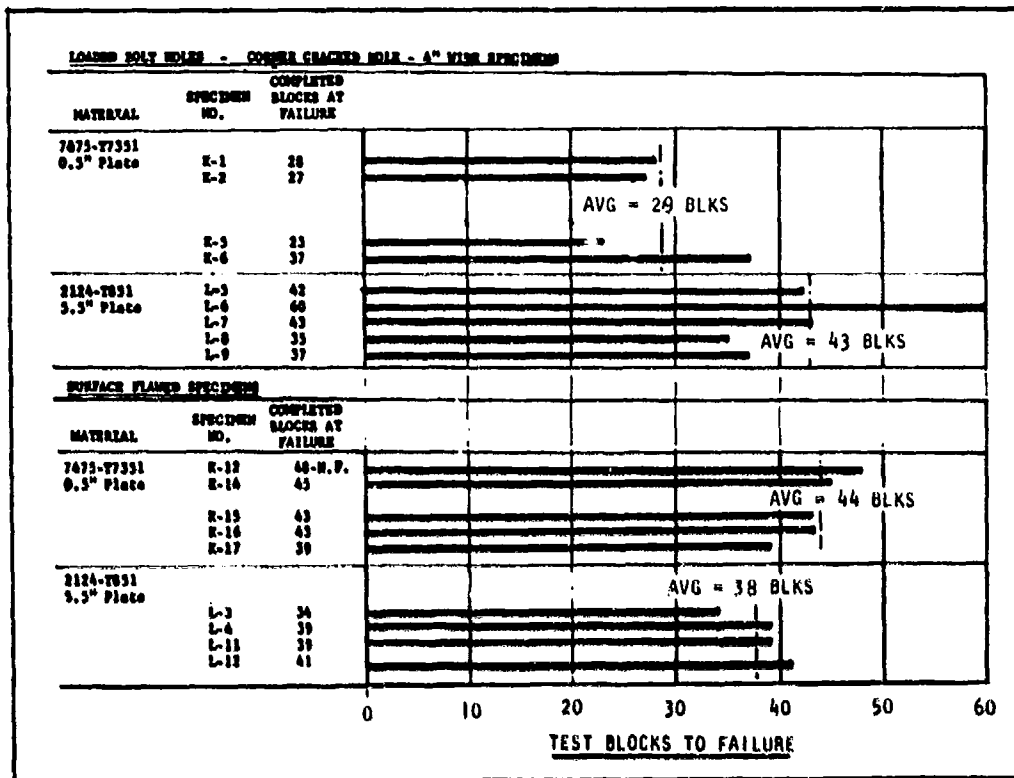
TABLE V
COMPARISON OF ALUMINUM ALLOYS

<u>SURFACE FLAWED SPECIMENS</u>									
MATERIAL	SPECIMEN NO.	INITIAL "2C" INCHES	DIR.	ENV.	MAX. STRESS psi	SPECTRUM WIDTH INCHES	COMPLETED BLOCKS AT FAILURE	FINAL "2C" INCHES	
7475-77451 0.3" Plate	K-9	.100	Long.	S.T.W.	31,000	1	6	27	4.09
	K-10	.250	Long.	S.T.W.	31,000	1	6	17	4.11
	K-11	.250	Long.	D.A.	31,000	1	6	55	4.05
7475-77351 0.3" Plate	K-12	.100	Long.	S.T.W.	31,000	1	6	48 N P	2.786
	K-14	.100	Long.	S.T.W.	31,000	1	6	45	3.54
	K-15	.100	Long.	S.T.W.	31,000	17	6	43	3.69
	K-16	.100	Long.	S.T.W.	31,000	17	6	43	3.84
	K-17	.250	Long.	H.N.A.	31,000	17	6	39	3.68
2124-7851 3.3" Plate	L-1	.250	Long.	S.T.W.	28,000	1	6	24	.750
	L-2	.250	Long.	D.A.	28,000	1	6	27	.414
	L-3	.250	Long.	S.T.W.	28,000	1	4	34	1.82
	L-4	.250	Long.	S.T.W.	28,000	1	4	39	2.56
	L-11	.250	Long.	S.T.W.	28,000	17	4	39	1.36
	L-12	.250	Long.	S.T.W.	28,000	17	4	41	1.86
	T-2	.250	Trans.	S.T.W.	42,000	1	4	6 N P	.350
	T-3	.250	Trans.	D.A.	28,000	1	4	29	1.30
	T-4	.250	Trans.	S.T.W.	28,000	1	4	13 N P	.345
	T-11	.250	Trans.	S.T.W.	28,000	1	4	22	1.36
	T-12	.250	Trans.	S.T.W.	28,000	17	4	31	1.24

<u>LOADING BOLT HOLES - CORNER CRACKED BOLT - 4" WIDE SPECIMENS</u>									
MATERIAL	SPECIMEN NO.	INITIAL "1C" INCHES	PASTURE DIAMETER INCHES	PASTURE LOAD POUNDS	100% SPECTRUM STRESS psi	DIR.	ENV.	COMPLETED BLOCKS AT FAILURE	FINAL CRACK LENGTH TOTAL "1C" INCHES (2)
7475-77351 0.3" Plate	K-1	.03	.250	2635	31,000	Long.	S.T.W.	28	2.33
	K-2	.03	.250	2635	31,000	Long.	S.T.W.	27	2.54
	K-3	.03	.250	2635	31,000	Long.	D.A.	19(1)N.P.	.895(1)
	K-4	.03	.250	2635	31,000	Long.	S.T.W.	20(1)N.P.	2.33 (1)
	K-5	.03	.250	2635	31,000	Long.	S.T.W.	23	2.33
	K-6	.03	.250	2635	31,000	Long.	D.A.	37	2.54
2124-7851 3.3" Plate	L-5	.03	.189	1415	28,000	Long.	S.T.W.	42	2.13
	L-6	.03	.189	1415	28,000	Long.	D.A.	60	.768
	L-7	.03	.189	1415	28,000	Long.	S.T.W.	43	1.92
	L-8	.03	.189	1415	28,000	Long.	S.T.W.	33	1.89
	L-9	.03	.250	1415	28,000	Long.	S.T.W.	37	2.03
	T-7	.03	.189	1415	28,000	Trans.	S.T.W.	33	1.56
	T-8	.03	.189	1415	28,000	Trans.	S.T.W.	31	1.07
	T-9	.03	.189	1415	28,000	Trans.	S.T.W.	33	1.30
	T-10	.03	.189	1415	28,000	Trans.	S.T.W.	33	1.30
2014-T61 .125" Sheet	V-4	.045	.189	746	18,400	Long.	S.T.W.	83(1)N.P.	.683
	V-5	.048	.189	870	18,400	Long.	S.T.W.	50(1)N.P.	1.035
	K-6	.037	.189	746	18,400	Trans.	H.N.A.	48 N P	.350
	K-5	.035	.189	870	18,400	Trans.	H.N.A.	76 N P	.627
2014-T62 Olycel Quench .125" Sheet	S-38	.058	.189	870	18,400	Trans.	S.T.W.	100 N P	.637
	S-48	.111	.189	870	18,400	Trans.	H.N.A.	52 N P	.510

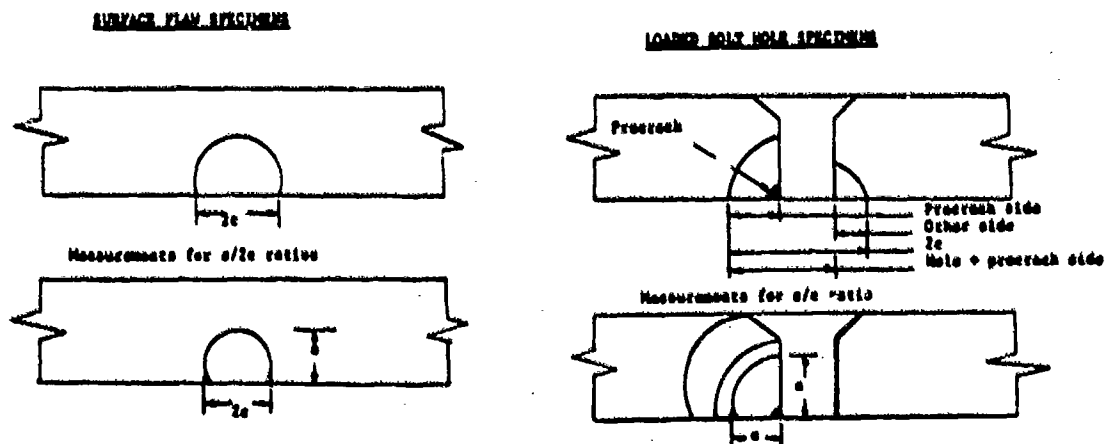
(1) Pasture Failure - Test Stopped
N.P. - No Failure - Test Stopped
(2) Includes Hole

Some of the other comparisons are shown in Figures XIII through XIX.



**COMPARISON OF FLAW SHAPES
FIGURE XIII**

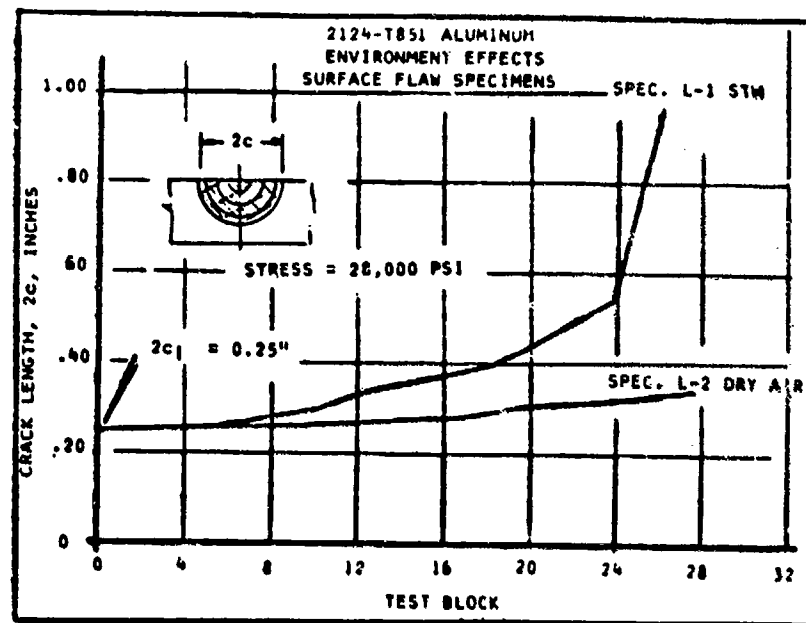
DETAILS OF FLAW SHAPES



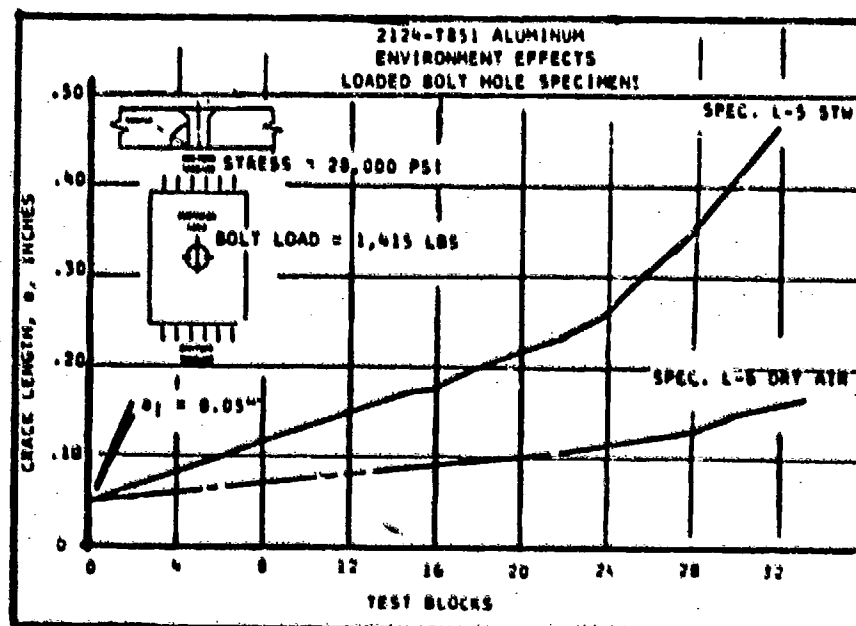
WHERE:

C or 2c = crack length
a = crack depth

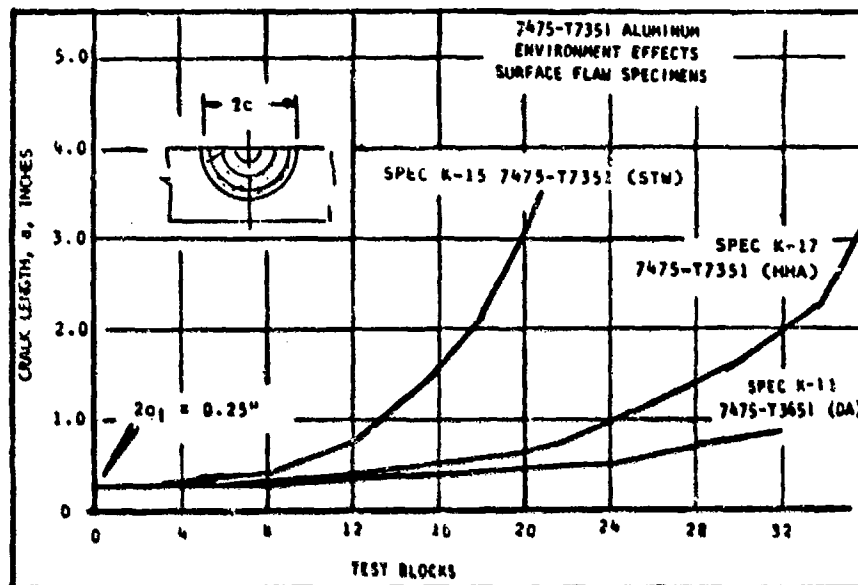
FIGURE XIV



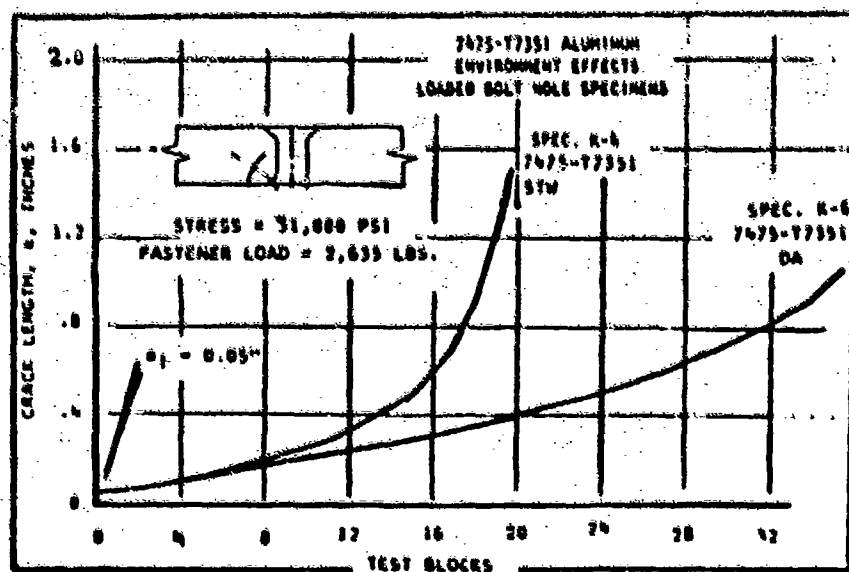
Comparison of Environmental Exposures
on 2124-T851 Aluminum
Figure XV



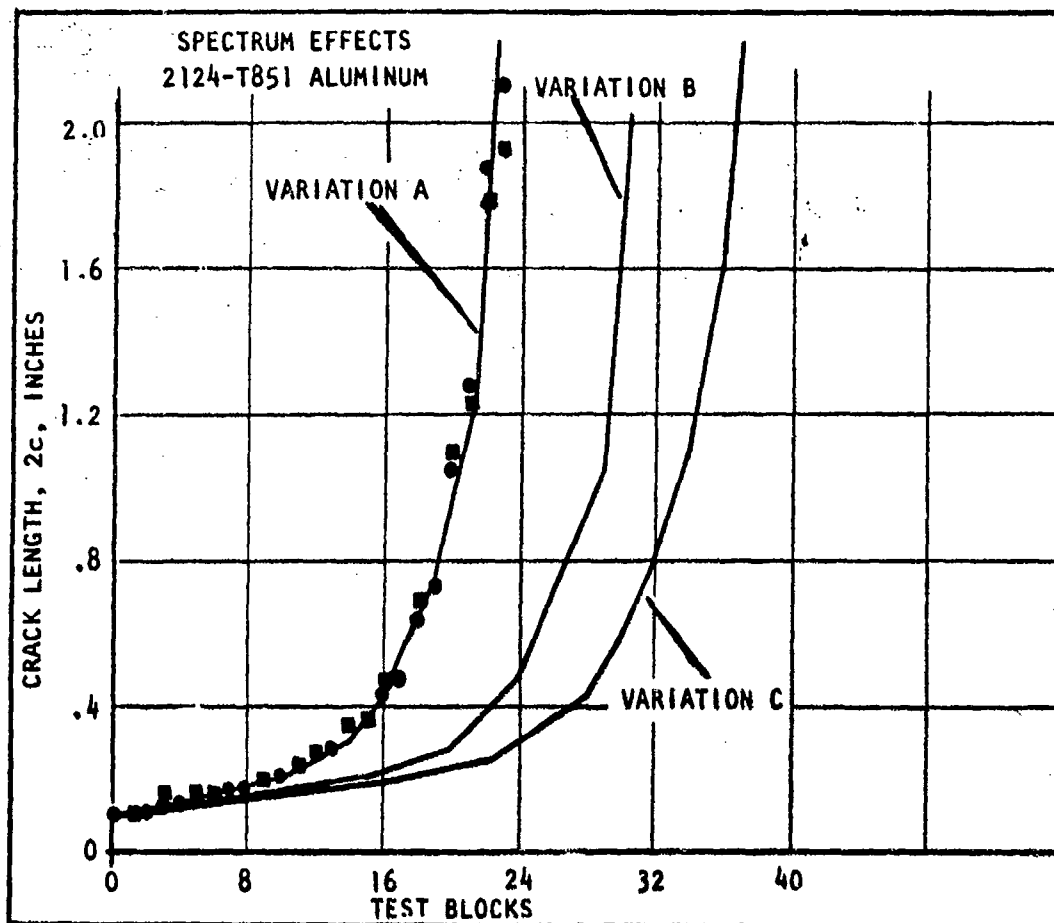
Comparison of Environmental Exposures
on 2121-T851 Aluminum
Figure XVI



Comparison of Environmental Exposures
on 7475-T7351 Aluminum
Figure XVII



Comparison of Environmental Exposures
on 7475-T7351 Aluminum
Figure XVIII



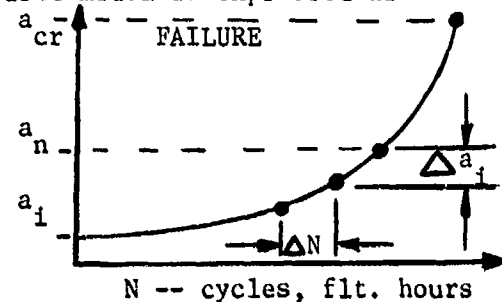
Comparison of Spectrum Effects
Figure XIX

The final analysis of each critical part required a theoretical analysis using a crack growth model since tests could not be conducted typical of every part. Also, design changes occasionally occurred after testing and the final part thickness and stress level changed.

The spectrum crack growth analysis was conducted on a cycle-by-cycle basis. Damage integration calculations were performed using a General Dynamics CDC 6600 computer procedure. The basic model is expressed as follows:

$$a_n = a_i + \sum_{n=1}^N [\Delta a_i = da/dn = f(\Delta k)]$$

WHERE



a_n = Crack Size After N Cycles of Spectrum Loading

a_i = Assumed Initial Crack Size

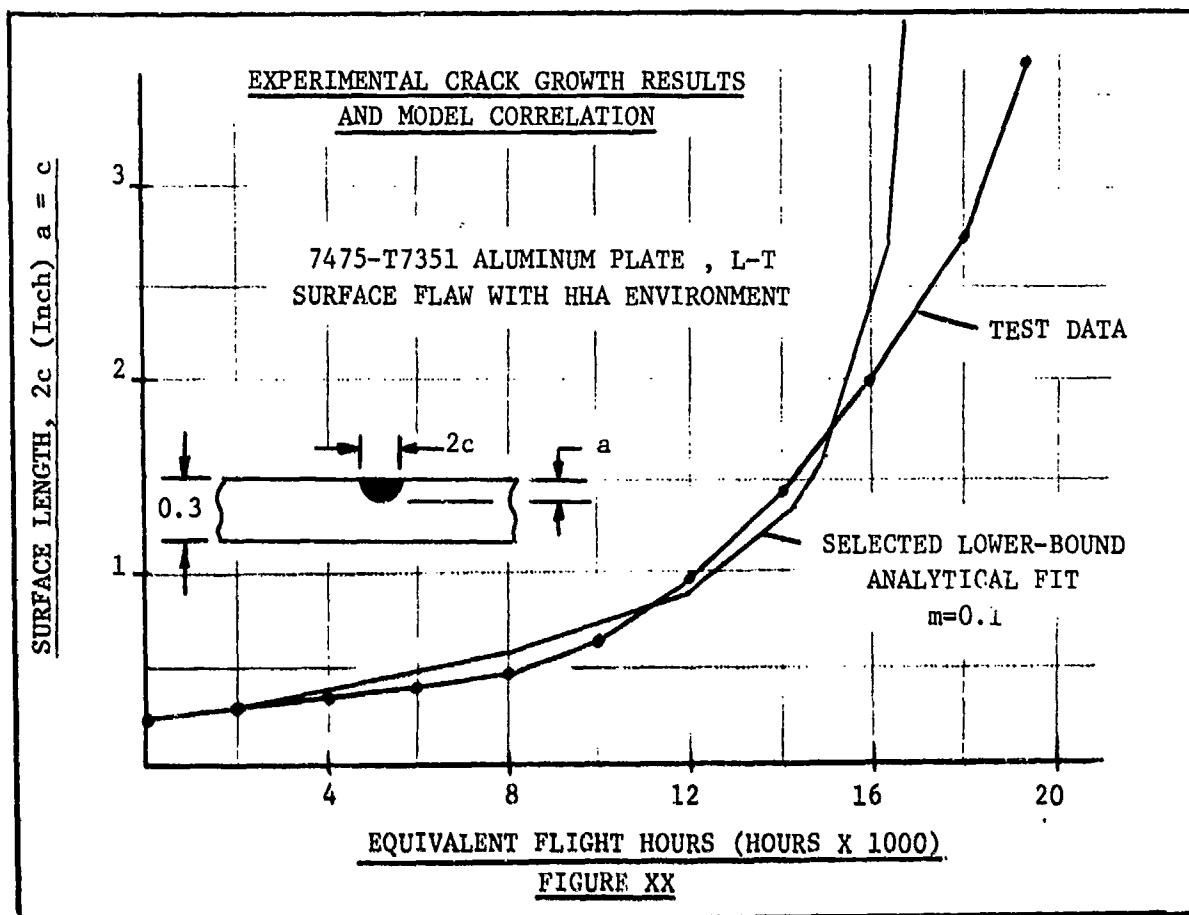
Δa_i = Growth Increment

da/dn = Crack Growth Per Load Cycle, n, Expressed as a Function of Δk . (Crack Growth Rate)

Δk = Stress Intensity Range Defined for Each Load Half Cycle (Minimum to Maximum) in The Spectrum

The basic da/dn rate is generally modified for spectrum retardation effects using The Wheeler Retardation Model. Retardation exponents must be established empirically through correlation of crack growth tests. The stress intensity factor (K) relates crack geometry, structural geometry, and applied loading to local crack tip stresses.

The stress intensity factor was selected in accordance with the type of flaw geometry. The da/dn rate was selected for the most severe assumed environmental exposure experienced by the particular part. An example of the correlation is shown in Figure XX. It should be noted that the main variable used in curve fitting was The Wheeler Model retardation exponent m . The final curve used for design was always kept to the left or conservative side as shown in Figure XX.



The F-16 damage tolerance analysis and test program showed that this approach is not only feasible but practical. It has resulted in a durable, rugged structure that is safe and economical to maintain. The impact on weight and cost was kept minimal by being selective of parts designated "fracture critical." They were required to be safety-of-flight structural parts designed by fracture allowables. In the F-16 design these were held to 82 parts per airplane.

In designing to these specifications we learned that the single most important item is to select fracture resistant materials. Secondly, we found it necessary to test with realistic spectrum loadings and environments on production material with typical processing and finish. Lastly, it is still necessary to use good design practice with reasonable stress levels. The cost differential for fracture requirements is not known precisely but is felt to be small. The weight penalty was less than 1% of the basic flight design gross weight which is used in establishing performance.

In summary, the fracture approach yields rugged, safe designs but requires engineering judgment and a good data base of material properties.

EVALUATION OF BLAST CAPACITIES OF A PRE-ENGINEERED

AND

STRENGTHENED STEEL BUILDING

Norval Dobbs
Senior Associate

Frederick E. Sock
Structural Engineer

Kirit Shah
Structural Engineer

Ammann & Whitney, Consulting Engineers
New York, N.Y. 10048

and

Paul Price
Structural Engineer

Joseph Caltagirone
Civil Engineer

Army Armament Research and Development Command
Dover, New Jersey 07801

ABSTRACT

This paper summarizes recent and ongoing Army Armament Research and Development Command (ARRADCOM) tests for the development of design criteria for acceptor structures subjected to low-to-intermediate range external blast pressures. Test procedures and results, and design criteria are presented for pre-engineered buildings (low pressure range) and for structural steel buildings subjected to blast loads up to 6-8 psi. The data presented in this paper, together with two of the referenced reports, should be implemented in the blast-resistant design of steel structures within facilities for manufacture and storage of explosive materials.

INTRODUCTION

Modern day Army Ammunition Plants require protection for facilities and personnel from the effects of an accidental explosion. Most previous work in this field has concentrated on the so-called "close-in" effects where protection was provided for facilities in the immediate proximity of a potential explosion. However, the majority of the affected personnel are located in adjacent process or office buildings separated at either intraline or inhabited building distances. Previous designs provided little or no protection for these personnel from the results of damage to their structure caused by an explosion in an adjacent building.

Therefore, in order to provide protection for personnel in "neighboring" buildings, ARRADCOM has undertaken a test program to develop criteria for structural steel buildings which will resist the effects of external blast loads. This program was performed in two phases. The first phase consisted of tests of pre-engineered structures to be used at low overpressure levels corresponding to inhabited building distances (ref. 1). Phase Two consisted of tests of strengthened structural steel buildings to be used in intraline distances. Both buildings were extensively instrumented to record applied blast loads as well as structural response to these loads.

This paper describes the series of blast tests performed on the pre-engineered and strengthened steel buildings at the U.S. Army Dugway Proving Ground, Utah, between February 1977 and June 1979. The behavior of each structure is described and the recorded damages are evaluated and compared with those predicted by the methods and criteria listed in References 2 and 3.

PRE-ENGINEERED AND STRENGTHENED STEEL BUILDINGS

GENERAL

In the design of steel buildings to withstand the effects of High Explosive (HE) and other types of explosions, standard structural members can be utilized for structures located in pressure ranges of 10 psi or less. Standard pre-engineered buildings which are normally designed to resist dead, wind, seismic and other conventional loads can, with some modifications (particularly when ultimate dynamic strength is considered and inelastic deformations are permitted), resist relatively large blast overpressures.

Significant factors in the evaluation of the blast capacity of conventionally designed structures include the difference in the relative proportions of lateral and vertical design loads for conventional structures, and the differences in the dynamic response of secondary members relative to that of the frames. Quite often, it has been found that for blast-resistant designs, the capacity of the frame members (in the case of the pre-engineered structure selected for conventional loads) greatly surpasses those of the supporting members (girts, purlins) and, therefore, modifications will be necessary.

Hence, in order to verify those modifications which will produce increased capacity in both structures and to identify unknown shortcomings of pre-engineered and strengthened steel buildings, a series of tests were performed at Dugway Proving Ground. Enough tests were performed on both structures such that a qualitative evaluation of the buildings' responses to blast loading could be made.

TEST DESCRIPTION

A total of thirteen tests, each utilizing approximately 2,000 pounds of nitro-carbo-nitrate, were performed on the structures - six tests on the pre-engineered building and seven on the specially designed steel building. The location of the charge during each test depended on the desired overpressure at the building. It was observed during the first few tests that the actual incident overpressure at the building was 10 percent lower than the anticipated value and, consequently, the distance was appropriately reduced.

Both the pre-engineered building (a modified version of the STR4 Series produced by the Star Corporation) and the strengthened steel building had the same overall dimensions; namely, 80 ft (24.4 m) long by 20 ft (6.1 m) wide by 12 ft (3.7 m) high. The pre-engineered building was oriented such that the long side of the structure faced the explosion. Its walls and roof consisted of 24-gage cold-formed metal panels having a static yield strength of approximately 80,000 psi (551,000 kPa). Certain modifications were made to the pre-engineered structure. These included increasing the number of Z-shaped girts to two per side. The sizes of both the panels and the girts were increased from 26- to 24-gage and from 8 in (0.20 m) by 3 in (0.08 m) by

0.0642 in (1.63 mm) to 9.75 in (0.25 m) by 4 in (0.10 m) by 0.13452 in (3.42 mm), respectively. The sizes of the purlins were also increased from 8 in (0.20 m) by 3 in (0.08 m) by 0.0642 in (1.63 mm) to 8 in (0.20 m) by 3 in (0.08 m) by 0.0842 in (2.13 mm). Modifications were also made to the foundation (made heavier and column footings tied together by floor slab) to insure that any resulting structural damage would occur within the structural steel portion.

The specially designed and fabricated columns, girts, beams, girders and purlins of the strengthened steel building were wide flanges with a minimum static yield stress of 36,000 psi (248,000 kPa). The walls and roof panels consisted of 18- and 20-gage cold-formed steel panels with a minimum static yield stress of approximately 33,000 psi (227,500 kPa).

Both structures were subdivided into four bays in the longitudinal direction, each of which was approximately 20 feet (6.1 m) wide. The primary structural framework in the transverse direction consisted of five rigid frames, except in the pre-engineered building where one of the end-frames was a "post and beam" setup. This type of frame obtains its strength to resist sidesway loads by its interaction with the wall panels, thereby producing diaphragm action.

The structures were extensively instrumented with accelerometers, deflection, pressure and strain gages, to record applied blast loads as well as structural response to the loads. Figures 1 and 2 show the location of the charges and instrumentation around the structures.

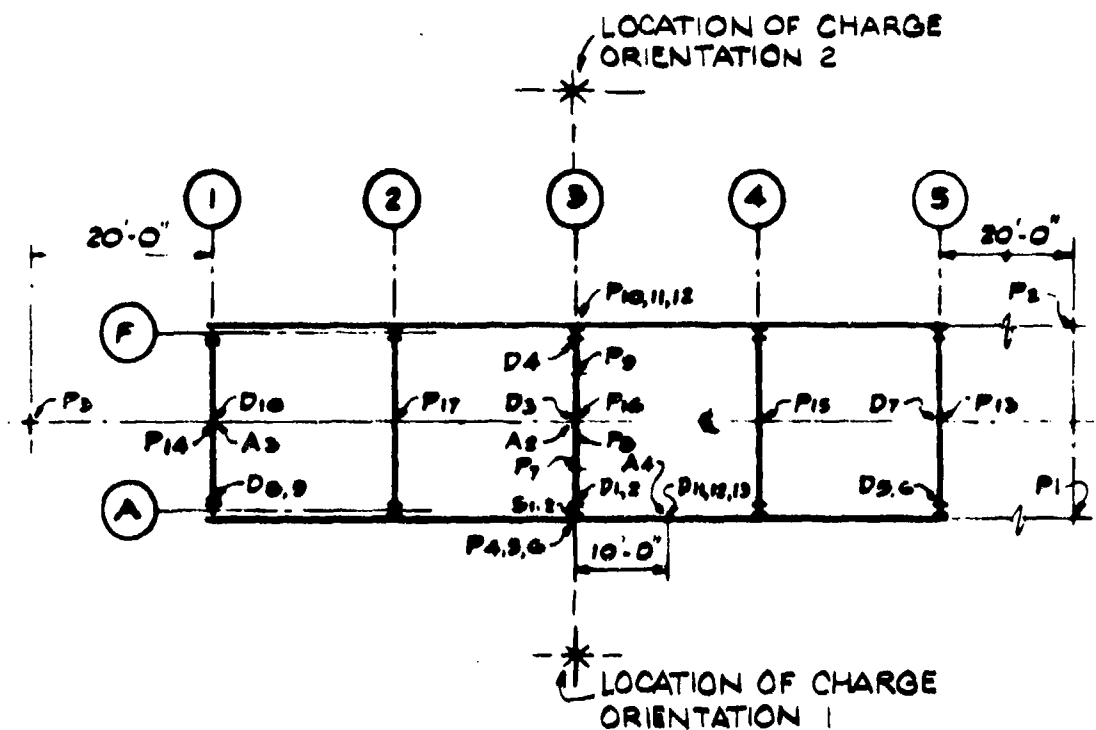
TEST RESULTS

(A) PRE-ENGINEERED BUILDINGS

Table I summarizes the pre-engineered building test results, including free-field pressures; frame, girt and panel displacements; and a brief description of typical damage for each test.

A minimal amount of damage was incurred in Test 1 (0.27 psi) which consisted primarily of the enlargement of the sidewall panel screw holes along the panel seams. This damage was attributed primarily to the interaction between sidewall frames and the panels which served as diaphragms in stiffening the frames against horizontal motion, thus reducing the sidesway motion. The repeated opening and closing of the panel seams during the test (as observed through motion pictures taken from the structure's interior) were the major source of the pressure buildup within the structure, as recorded by Gages P15 through 17.

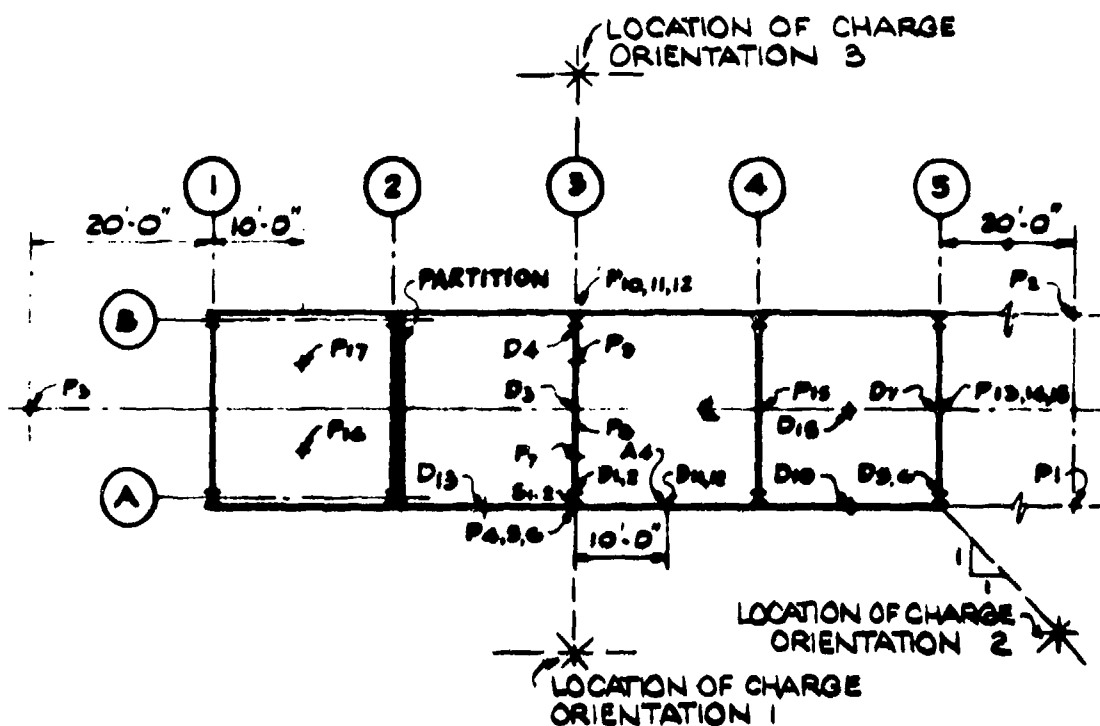
Similar damage was incurred in Test 2 (0.56 psi). In addition to the roof, small permanent gaps were formed at the panel seams of the rear wall. Screw hole enlargements formed in the first test were further enlarged. Although the locked door (resistance to opening provided solely by the hinges and striker) opened during Test 2, the pressure buildup in this test was not



TEST SCHEDULE				
TEST NO.	CHARGE SIZE (lbs)	PRESSURE (Psi)	CHARGE ORIENTATION (REFER TO SITE PLAN)	DISTANCE FROM FRONT WALL (FT)
1	2000	0.2	ORIENTATION 1	1577
2	"	0.3	"	797
3	"	0.5	"	600
4	"	0.7	"	472
5	"	1.0	"	402
6	"	TBD	ORIENTATION 2	355

Figure 1

SITE AND GAGE LOCATION PLAN
FOR PRE-ENGINEERING BUILDING



TEST SCHEDULE				
TEST NO.	CHARGE SIZE (lb)	PRESSURE (Psi)	CHARGE ORIENTATION (REFER TO SITE PLAN)	DISTANCE FROM FRONT WALL (FT)
1	2000	0.90	ORIENTATION 1	931
2	"	1.20	"	417
3	"	3.0	"	306
4	"	TBD	"	162
5	"	3.0	ORIENTATION 2	159
6	"	TBD	"	141
7	"	3.0	ORIENTATION 3	141

Figure 2

SITE AND GAGE LOCATION PLAN
FOR STRENGTHENED STEEL BUILDINGS

TABLE 1. SUMMARY OF PRE-ENGINEERED BUILDING TEST RESULTS

Test No.	FREE-FIELD PRESSURE		PEAK RELATIVE HORIZONTAL DISPLACEMENT						DAMAGE
			FRAME		GIRT ^a		PANEL		
	psi	(kPa)	in	(mm)	in	(mm)	in	(mm)	
1	0.27	(1.86)	1.7	(43.2)	0.8 1.0	(20.3) (25.4)	0.6	(15.2)	(1) Enlargement of side wall panel screw holes. (2) Small gaps between screws of roof panel seams.
2	0.55	(3.79)	2.1	(53.3)	b 2.4	b (61.0)	b	b	(1) Further enlargement of side wall panel screw holes. (2) Small gaps between screws of backwall panel seams. (3) Door opened outward.
3	0.74	(5.10)	3.1	(78.7)	2.5 3.0	(63.5) (76.2)	1.1	(27.9)	(1) Bent anchor bolt. (2) Front wall panel kinked along lower girt and pulled out at base of a few points. (3) Screw head pulled through front wall panel at columns. (4) Some twisting and tearing of girt clip angles. (5) Door opened outward.
4	1.0	(6.89)	3.8	(96.5)	4.7 4.1	(119.4) (104.1)	2.4	(61.0)	(1) Further twisting and tearing of girt clip angles. (2) Shearing of some girt connection bolts without collapse. (3) Twisting of girts. (4) Front wall panel anchorage pulled out. (5) Further kinking of front wall panel. (6) Plastic deformations of girts.
5	1.2	(8.27)	4.1	(104.1)	b 4.8	b (121.9)	3.8	(96.5)	(1) Further twisting of girts. (2) Kinking of front wall panel at each girt and between girts. (3) Front wall panel anchorage completely pulled out. (4) Panel screw holes pulled through at girts. (5) Plastic deformations of frame, girts and front wall panel.
6	1.3	(8.96)	4.9	(124.5)	4.9 ^c	(124.5) ^c	76.3	(195.4)	(1) Damage to front wall panel and girts similar to Test 5. (2) Buckling of roof purlin webs. (3) Some buckling of frame girder flange. (4) Plastic deformations of frame, girts and front wall panel.

^aValues are given for upper and lower girts.^bNo measurements were made.^cQuestionable value.

significantly greater than that of Test 1. The door did not open in the first test. This is a further indication that the primary source of pressure leakage into the building was through the gaps formed at the seams.

The structural damage in Test 3 (0.74 psi) was more extensive. The front panel buckled at points where it was supported on girts. In some places, the panel was slightly disengaged where it was fastened to the foundation. This damage was attributed to the inadequacy of the detail used for attaching the wall panels to the foundation slab. An improved detail using steel angles attached to the concrete by anchor straps is required for blast-resistant design.

The major structural damage which occurred in Test 3 consisted of the bending of one of the column anchor bolts and the twisting of several of the girt angle connections to the columns. The twisting is attributed to the panel attachment to the Z-shaped girts which produced eccentric loads on them.

The damage that occurred in Test 4 (1.04 psi) was similar to that of the previous test but somewhat more severe. The increased loading produced tearing of several of the girt angle connections to the columns as well as failure of several of the girt connection bolts. Damage to the blastwall panels was more severe, especially in those areas damaged in the previous test.

The resulting damage in Test 5 was somewhat similar to that in the previous tests. Further twisting of the girts occurred. Some enlargement of bolt holes at several girt/column connection occurred where high-strength bolts had been used. Permanent deformations of the main frames, girts and paneling were observed.

The damage incurred in Test 6 was essentially the same as that which occurred in Test 5. However, the major damage occurred to the rear side of the building which, in this test, was the blastward side. Permanent frame deflections produced in prior tests were reduced in this test.

(B) STRENGTHENED STEEL BUILDING

Table II summarizes the strengthened steel building test results, including the free-field pressures; center, end, longitudinal frames, girt and panel displacements; and a brief description of typical damage for each test.

Tests Nos. 1 and 2 were left out of Table II because of failure of the measuring instruments during both tests. However, the only damage observed during Test 2 was a crack that appeared at the concrete base around Column A3.

A minimal amount of damage was incurred in Test 3 (3.2 psi). The overlapping panel joints were opened approximately 3/8 inch half way between

TABLE II. SUMMARY OF STRENGTHENED STEEL BUILDING TEST RESULTS

Test No.	PEAK HORIZONTAL DISPLACEMENT								DAMAGE
	FREE-FIELD PRESSURE		CTR FRAME		GIRT*		PANEL		
	psi	(kPa)	in	(mm)	in	(mm)	in	(mm)	
3	3.20	(22.06)	1.29	(32.8)	2.01	(51.1)	1.65	(41.9)	(1) Overlapping panel joints on blastward wall were opened 3/8 in (0.95 cm) halfway between Frames 2 and 3. (2) Three foundation mounting screws at the panel joints at Frames 3 and 4 were pulled out. (3) Slight web crippling at the center girt near center frame.
4	3.5	(24.13)	1.57	(39.9)	0.79	(20.1)	2.96	(75.2)	(1) Panels were torn loose from foundation on blastward wall.
							2.55	(64.8)	(2) Roof panels buckled between two purlins. (3) The concrete at the 4-inch angle iron foundation connection showed movement at the angle.
5	5.31	(36.61)	0.97	(24.6)	2.34	(59.4)	6.60	(167.6)	(1) Web crippling in wall panels on Wall 5 by lower girt.
					2.32	(58.9)	(2) Panels on Wall A opened at seams. (3) Buckling of roof panels.		
6	6.79	(46.82)	1.13	(28.7)	2.55	(64.8)	7.58	(192.5)	(1) Web crippling in Wall 5 at foundation joint, and the lower and middle girts.
					2.41	(61.2)	(2) Minor web crippling at the girt connecting hat sections. (3) Column 2A showed three broken foundation bolts. Examination proved that two of these were improperly installed.		
7	4.21	(29.03)	1.29	(32.8)	2.05	(52.1)	1.81	(46.0)	(1) Wall B was ripped loose from foundation.
					3.69	(93.7)	(2) Web crippling in Wall B. (3) Roof flashing removed between Frames 2 and 4.		

*Absolute displacements of girts are listed here. Relative displacements are obtained by subtracting displacement of girt at column from displacement.

Frames 2 and 3. In some places, the panel was slightly disengaged where it was fastened to the foundation and girts. Gage D13 recorded a displacement of 1.78 inches which corresponded to a rotation of the supports of approximately 4 degrees. This value is greater than the reusable criteria of 0.9 degree for a cold-formed member. The damage is attributed to the connection detail at the foundation and its effect is to relieve the loading on the panel, thereby reducing its deflection. Slight web crippling was also observed at the center girt near the column.

More extensive damage was apparent in Test 4 (3.5 psi). The blastward panels were torn loose from points where they were supported at the foundation and girts. The roof panels buckled under the increased loading at points between purlins near the blastward wall (Wall A).

The resulting damage in Test 5 (5.31 psi) was similar to that in the previous test. However, damage was now incurred in one of the sidewalls (Wall 5). Some web crippling was also apparent in the wall panels in Wall 5 near the lower girt and the buckling in the roof panels between the first two purlins (observed in Test 4) increased.

Repairs, as in other tests, were done to the structure before Test 6 (6.79 psi). Damage to Wall 5 was more severe than the previous test; this included web crippling at the foundation joint, and the lower and middle girt for the full width. Some web crippling was also observed in the upper girt in Wall A.

The major structural damage which occurred in Test 6 consisted of failure of some of the foundation bolts. Examination of the connections showed that two bolts were properly installed, but two others on the easterly side were improperly installed (cut-off was essentially at the floor wall) and one of these failed.

The foundation bolts that failed during the previous test were repaired before Test 7 (4.21 psi). Almost all the panels in Wall B between Frames 2 and 5 were ripped loose from the lower girt and foundation, and some of the panel seams opened (Wall B was the blastward wall in this test). Web crippling was apparent on all girts and some of the purlins buckled under the blast load. Slight damage was observed in the wall and roof panels; this included missing foundation screws at the panel joints in Walls 1, 5 and A.

EVALUATION OF TEST RESULTS

This section discusses the test results on both structures in terms of the measured deflection responses and observed damage levels of the main frames, blastwall girts and panels. The evaluation of these results on the basis of dynamic analyses is also presented.

Several factors affected the frames' responses. The most significant of these factors was found to be the negative phase of the pressure loadings. Figures 3 and 4 present plots of the front wall pressure, backwall pressure

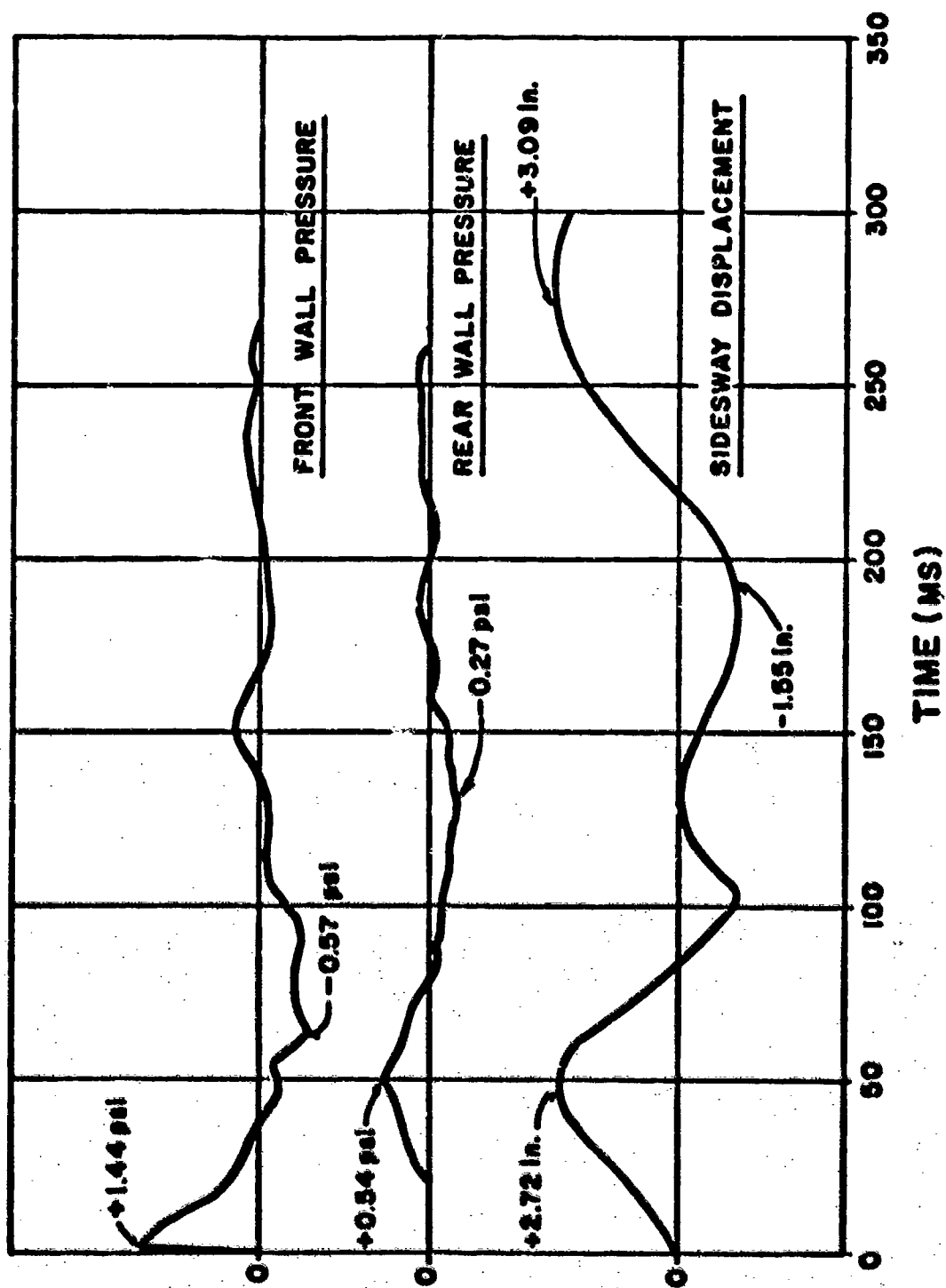


Figure 3 Pre-Engineered Building Pressures and Sidesway Displacement for Test 3

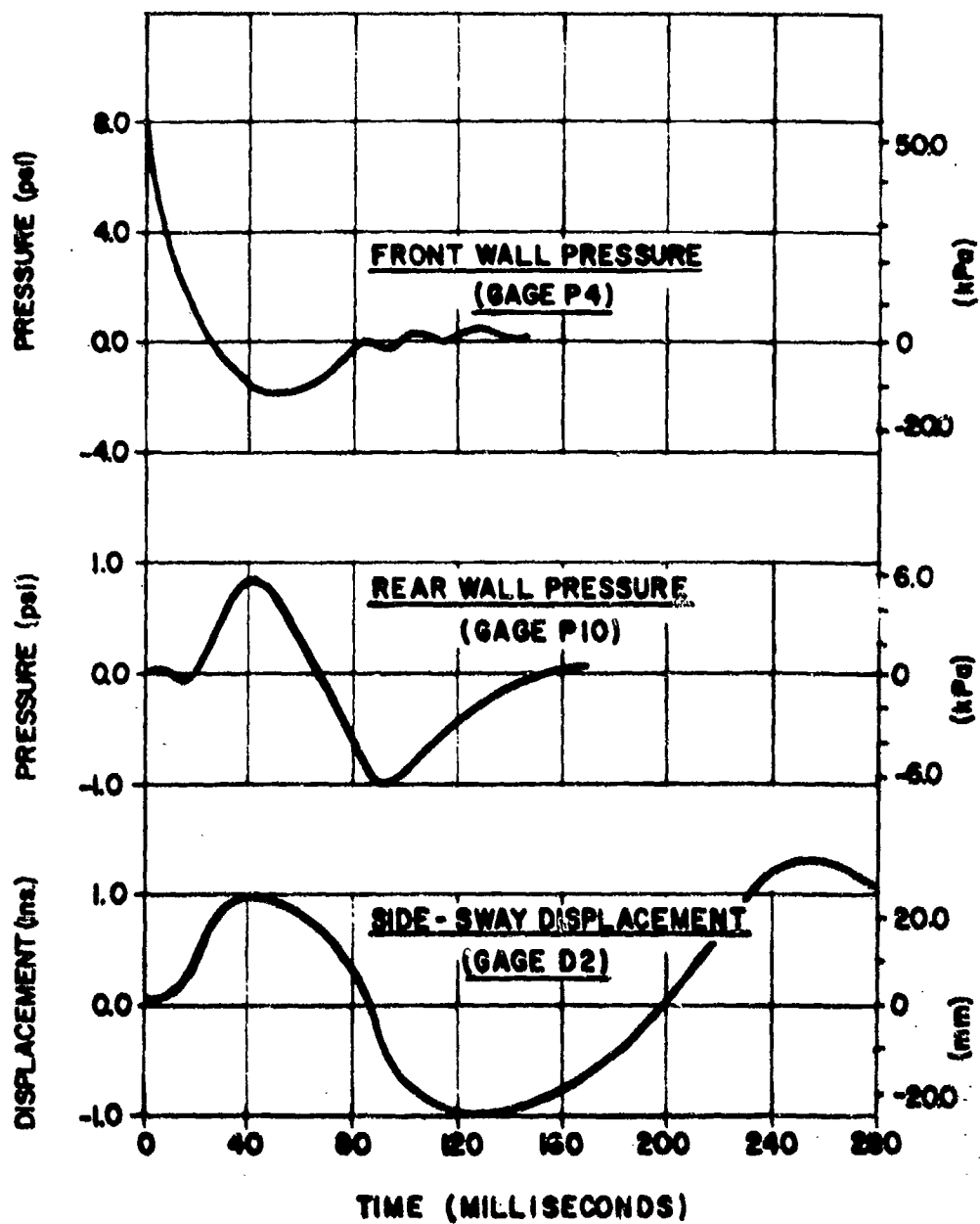


Figure 4 Strengthened Steel Building Pressures and Sidesway Displacement for Test 3

and sidesway displacement versus time for Test 3 (0.74 psi) of the pre-engineered building and for Test 3 (3.2 psi) of the strengthened steel structure. It is seen that the peak reflected pressure on the front walls of both structures is about twice the incident value, as expected. However, the peak backwall pressures range between 30 to 80 percent of the incident pressures, far less than expected.

The displacement curves for these tests show the sidesway buildup due to the loading, followed by a significant negative (rebound) displacement, and the peak positive displacement occurring in the second cycle after all the blast loading was off the structure. This behavior can be explained by the phasing of the blast loading as follows: the first peak is a result of the net positive loading on the building walls (front wall minus rear wall pressure). As the frame starts to rebound, the negative pressure on the front wall and the positive pressure on the rear are both acting in the same direction and in phase with the rebound. This combination of events produced a peak negative displacement which is greater than the positive displacement. A second positive displacement, which is greater than the first positive displacement, is produced by the rebound of the structure from the negative displacement combined with the negative phase of the loading on the rear walls. At higher pressures, the negative displacements were nearly equal to the positive displacement. This is due to the plastic deformation in the frame.

Other factors which affected the frame responses of both structures were:

- the buildup of internal pressure, resulting primarily from leakage through the seams of the panels, and
- the responses of the secondary members (purlins, girts, wall and roof panels) relative to those of the frames.

Through a series of dynamic analyses performed on the frames, using the computer program titled "Dynamic Non-Linear Frame Analysis" referred to as DYNFA (ref. 4), it was concluded that these factors had some impact on the frame responses in the plastic response range. In the case of the pre-engineered building, the interior pressures had a greater effect on the plastic deformations of the frame members than on the overall sidesway responses of the frames. This appears reasonable when one considers that the plastic deformations in the frame occur in local bending modes of the individual members. Since these modes have small periods of vibration, they are extremely sensitive to the peak pressure. On the other hand, the sidesway response of the frame is low frequency in nature and, therefore, is more dependent on the total impulse of the loading rather than on the peak pressure.

The pressure gages, located in the interior of the strengthened steel building, recorded insignificant pressure levels which were, on the average, only 16 percent of the incident pressures, compared to 40 percent for the

pre-engineered structure. Consequently, no analyses were done to determine the extent to which the responses of the frames of the strengthened steel building were affected.

The interaction between the secondary members and the main frames was considered in the dynamic analyses for Tests 3 and 4 of the pre-engineered and strengthened steel buildings, respectively. The results of these analyses are given in Figures 5 and 6 in terms of horizontal sidesway versus time curves for the center frames. The curves show that the responses of the secondary members did not significantly alter the first half-cycle of the sidesway response of the center frames. However, the rebound of both frames was significantly altered.

In the case of the pre-engineered structure, the rebound of the frame was significantly diminished and it was concluded that this occurred because of the large amount of energy absorbed by the plastic deformations of the girts. The remaining energy was transferred to the frame, thereby resulting in elastic rebound of the frame. However, the rebound of the frame of the strengthened steel building was increased due to the fact that a greater amount of energy was transferred to the main frame than was absorbed by the secondary members during deformations. The models used in the computer analyses are shown in Figures 7 and 8.

The ductility ratios and rotations associated with the girt displacements listed in Tables I and II have been compared to the design criteria presented in Reference 2 as follows:

1. The 2.5 in (0.064 m) of the upper girt of the strengthened steel building in Test 4 (3.5 in) corresponds to a rotation of 1.19 degrees, which is between the reusable criteria of 1 degree and non-reusable criteria of 3 degrees. The corresponding ductility ratio is 1.25 based on an elastic deflection of 2 in (0.051 m).
2. The 4.8-in (0.122-m) deflection for Test 5 (1.2-psi incident pressure) of the pre-engineered building corresponds to a ductility ratio of 1.4 which is between the reusable (1.25) and non-reusable (1.75) criteria values. Here, extensive twisting of the girts occurred, which would render the member non-reusable, which is consistent with the actual rotation of 2.3 degrees compared to the criteria value of 1.8 degrees.

To further evaluate the girt responses, single degree-of-freedom analyses were performed for the actual pressures on the blastward wall that were measured for Tests 3 and 4 of the pre-engineered and strengthened steel buildings. Comparisons of the analytical and measured girt responses for these tests are given in Figures 9 and 10. In the first case involving the pre-engineered building, the computed displacement was greater than the measured value; whereas for the strengthened steel building, the reverse was true. The discrepancies between the measured and computed girt responses result from:

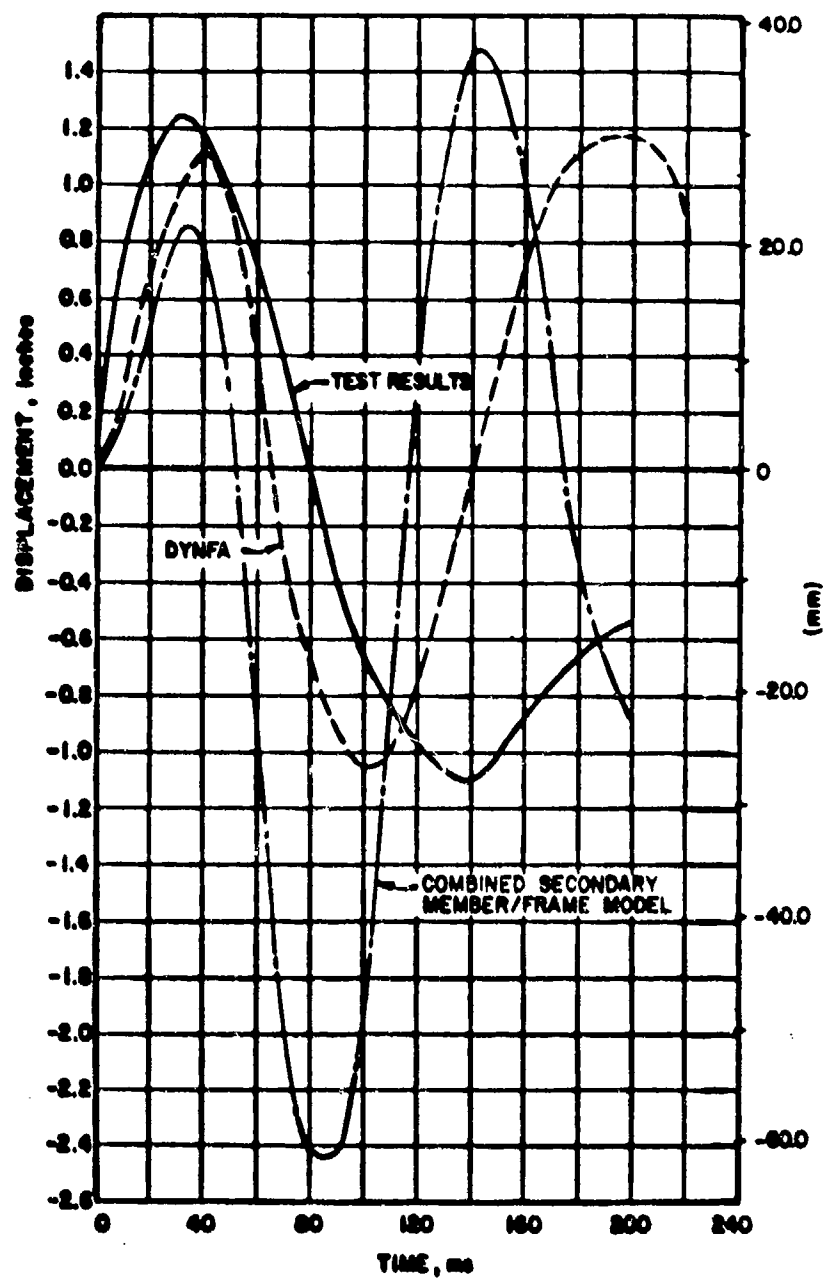


Figure 5 Strengthened Steel Building's Center: frame side-sway displacement - Test and Analytical results for Test 4

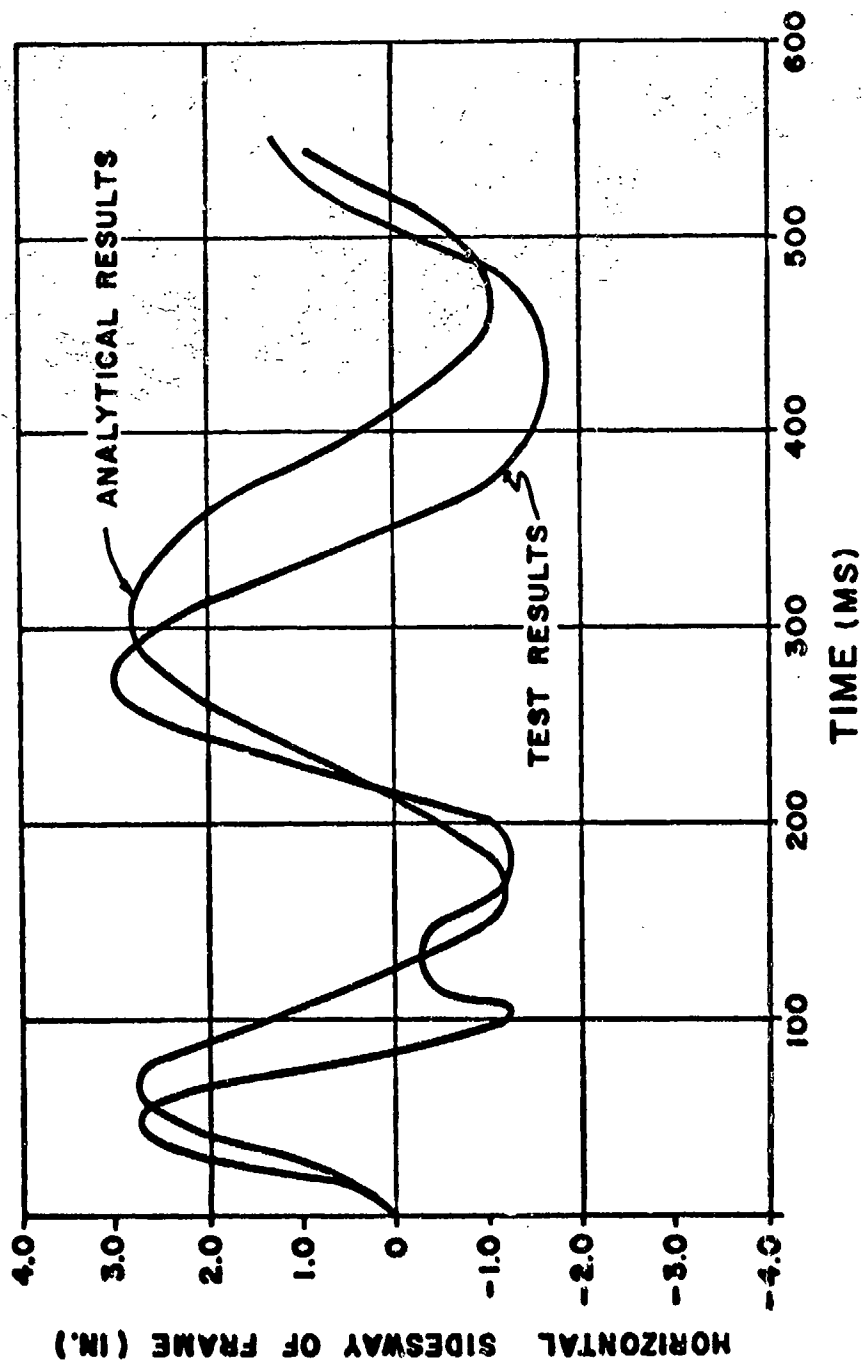
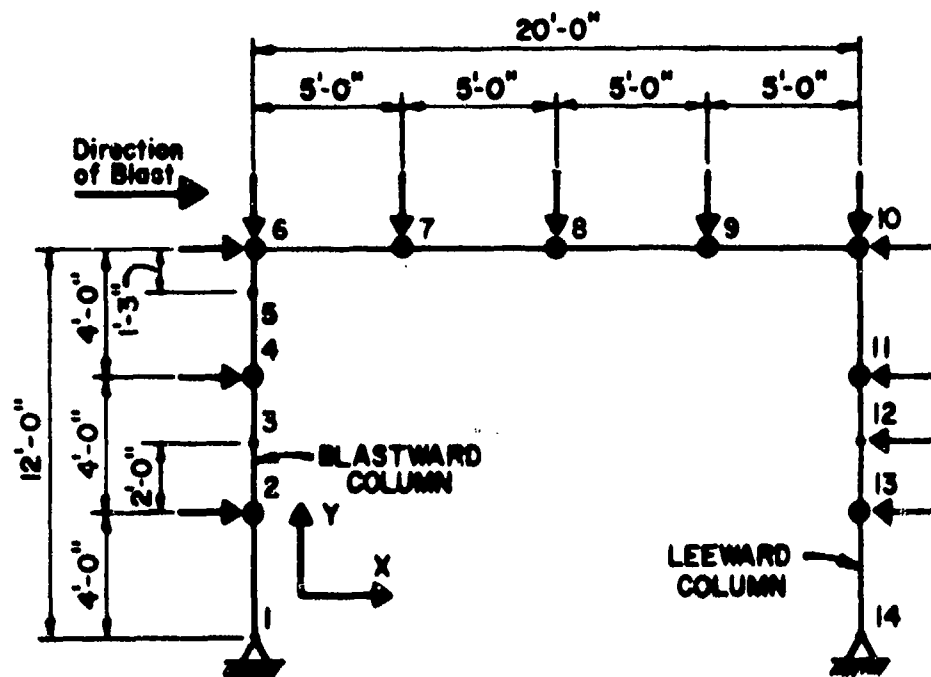


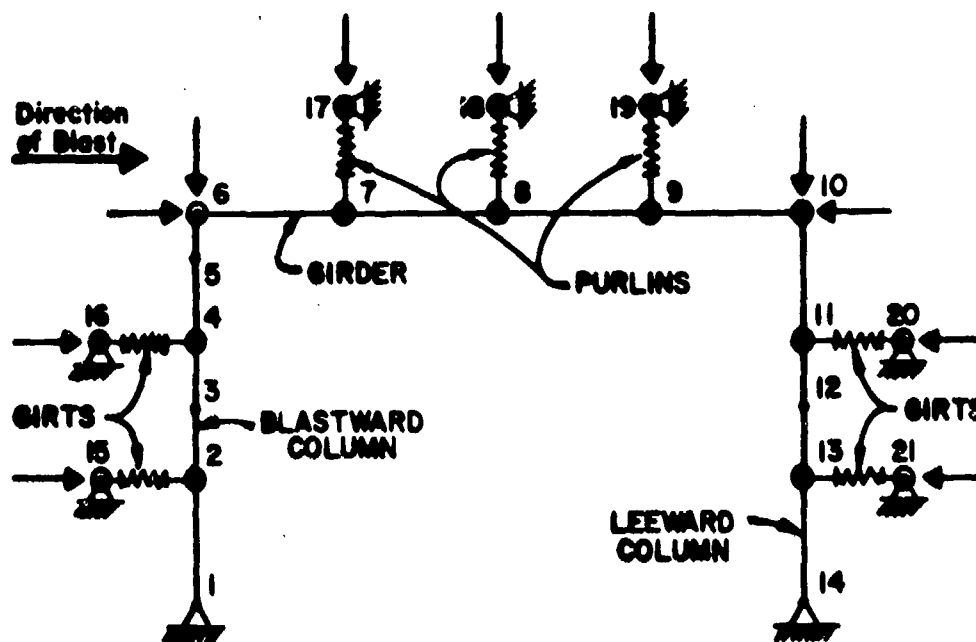
Figure 6 Pre-Engineered Building Center frame
sideway displacement - Test and
Analytical results for Test 3



LEGEND:

- NODE
- MASS POINT
- APPLIED LOAD

Figure 7 Basic Frame Model



NOTE:

FOR NODE DIMENSIONS & LEGEND,
SEE FIGURE 7

Figure 8 Basic Frame Model including Purlins
and Girts

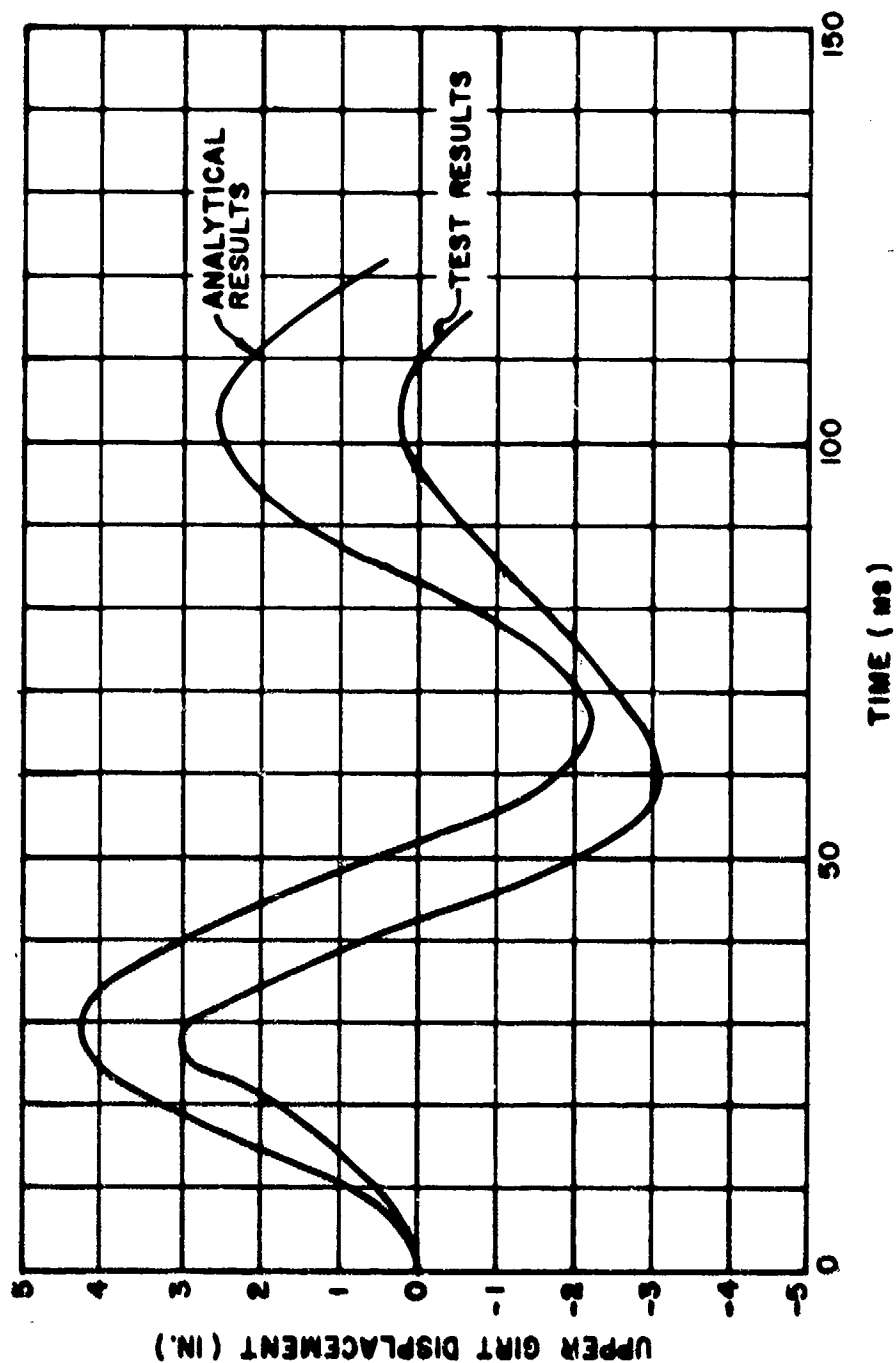


Figure 9 Upper Girt Displacement - Test and Analytical Results for Test 3 (Pre-Engineered Building)

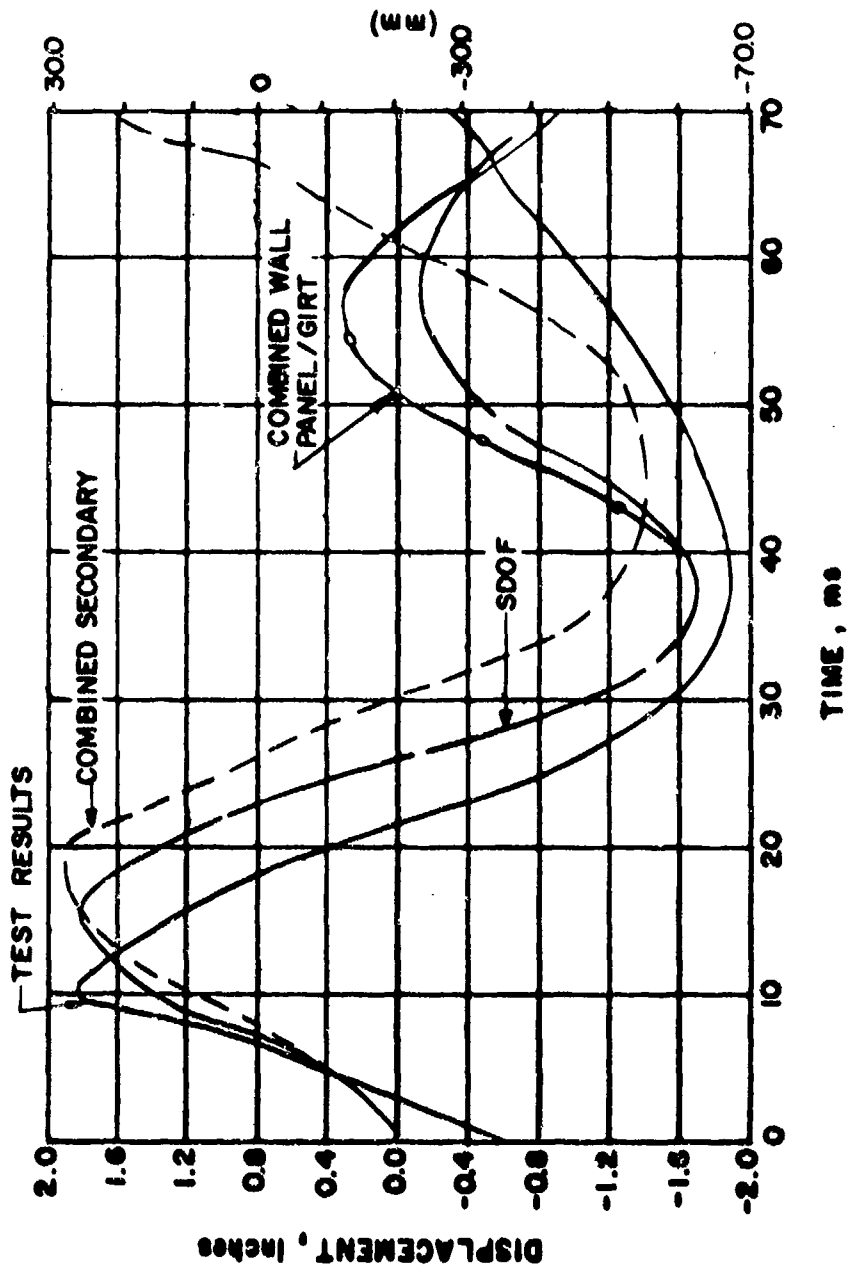


Figure 10 Lower Girt Displacement - Test and Analytical Results for Test 4 (Strengthened Steel Building)

1. The pressure buildup inside the pre-engineered building.
2. The interaction between the girt and frame responses and
3. The effect of the actual yield stress of the material used to fabricate the girts. The actual yield stress of the material used for the girts of the pre-engineered structure was not determined by tensile testing and, therefore, the analyses were based on the minimum specified yield stresses for the material used to fabricate these components of the building. In the case of the strengthened steel building, the actual yield stress of the material used to fabricate the girt was used in the single degree-of-freedom analyses.

The peak panel displacements of the pre-engineered building given in Table I were measured relative to the girts. The measurements are for a section of panel spanning between girts, which is assumed to behave more or less as a fixed-supported beam. On the basis of the measured response records for the panel and post-shot dynamic analyses, it was concluded that the panel measurements recorded was not accurate. This was attributed to the manner in which the panel displacements were measured (i.e., subtraction of absolute measurements of girt and panel deflections), the high frequency nature of the panel response and the excessive damage to the panels which made correlation between measurements and analysis possible.

For the strengthened steel structure, the recorded panel displacements already account for the displacements of the girts. Based upon past experience with the pre-engineered building, the deflection gages were mounted to frames which were attached to the members (purlins and girts) supporting the panel. Thus, a direct measurement of panel displacements were obtained. For Trial 6, the 4-foot long panel (distance between girts) showed a 7.6-inch displacement during rebound. This corresponds to a rotation of 18 degrees, which is far greater than the reusable criteria of 0.9 degree. The opening of the panel seams and the pull-out of several screws connecting the panels to the foundation are consistent with the criteria. The effect of this was to relieve the load of the panels. Test results also showed the inadequacy of the roof panels. Buckling of the panels was evident after all the tests. A displacement of 1.87 inches during Test 7 (which corresponds to a rotation of 3.6 degrees) and the raising of the panels at their seams are consistent with the reusable criteria of 0.9-degree rotation.

COMPARISON OF THE PRE-ENGINEERED AND STRENGTHENED STEEL BUILDINGS

The first section of this paper dealt with the test performed on the two steel buildings. The tests were described and evaluated for each structure, and the results were compared to the design criteria presented in References 2 and 3.

To further understand the behavior of the pre-engineered and strengthened steel buildings, and to pinpoint the similarities and differences in their responses to dynamic (blast) loads, the two structures are compared in this section.

The overall dimensions of the structures were identical; namely, 80 feet long by 20 feet wide by 12 feet high. Both structures were subjected to several tests involving the detonation of 2,000 pounds of nitro-carbonate of different locations around the buildings. The measuring gages were located at the same positions on the structures (except for the interior pressure gages and those gages monitoring the behavior of the longitudinal frames), thus allowing for a comparison of the responses of the two structures to blast loads.

MAIN FRAMES

A typical interior rigid frame of the pre-engineered building comprised of two columns and a girder which were fabricated of plate stock having a minimum static yield stress of 50,000 psi. The center (typical) frame of the strengthened steel building consisted of hot-rolled W-shaped members with a minimum static yield stress of 36,000 psi.

The responses of both structures to normal blast waves were very similar; namely, a positive peak displacement followed by a negative displacement, as the wave front travelled from one end of the frame to the other. Both structures showed a significant (maximum) sideways displacement after all the loading was off the structures. However, at higher pressure levels (peak side-on overpressures of approximately 1.3 psi), some plastic deformations were observed in the columns, girts and panels of the pre-engineered building. No plastic deformations were observed in the strengthened steel building, although buckling of the wall panels occurred in the latter tests.

The longitudinal frames could not be compared because no pressure gages were positioned to monitor the behavior of the longitudinal frame of the pre-engineered building.

SECONDARY MEMBERS

The blastward girts of the pre-engineered building consisted of Z-shaped members, 20 feet long and an ultimate flexural resistance of 16.6 kips. The outer flanges of these girts were securely fastened to the wall panels,

whereas the inner flanges were unbalanced. This resulted in greater deflections of the girts during rebound and, consequently, for peak side-on overpressures as low as 0.74 psi, the clip angles connecting the girts to the columns were twisted. As the peak side-on overpressure increased, the girt connection bolts failed, and in those members whose connections survived the blast loads, plastic deformation was apparent. The only damage to the girts of the strengthened steel building was slight web crippling observed after all the tests ($P_{SO} = 3.2$ through $P_{SO} = 6.79$).

Test results showed that the panels in both structures failed at higher pressure levels. Due to the inadequate connection details at the panel seams, the interior pressure levels were relatively higher in the pre-engineered building than in the steel building. Thus, the effects of these pressures (interior) were more significant in the analyses of the pre-engineered building.

In the evaluation of the effects of the secondary member displacements on the responses of the frames, it was observed that an excellent correlation of the first half cycle of the sidesway responses of both structures was obtained between analysis using the basic frame model and that using the refined model. However, during the rebound phase, analyses showed that the center frame sidesway displacement (in the pre-engineered building) was lower than shown in the test results. The opposite occurred in the case of the strengthened steel building. This is believed to have occurred because a larger amount of energy was absorbed during the plastic deformations of the girts in the pre-engineered building, thus reducing the effect on the rebound of the frame.

Since no gages were furnished to measure the responses of the purlins in the pre-engineered building, no comparison could be made for these secondary elements.

The ductility ratio for the columns and girders of the pre-engineered building approached the non-reusable design criteria of 6 for an incident pressure of 1.0 psi and exceeded it as the pressure increased to 1.25 psi. The girders of the strengthened steel building also approached the criteria at 3.5-psi side on overpressure and exceeded the limit as the pressure increased to 4.15 psi.

CONCLUSIONS AND RECOMMENDATIONS

Based upon the test evaluations presented in the preceding sections, the following comments are offered:

1. Use of pre-engineered and strengthened steel buildings to provide protection at overpressures ranging from 2.0 psi to about 6.79 psi are practical.

2. In the case of the pre-engineered building, some modifications will be needed to insure that the blast-resistant capacity of the individual structural components are consistent.
3. Other building revisions that may be required of both structures to fully develop the full capacity of the structure include:
 - a. Provide bigger washers or provide other means to prevent the heads of screws from pulling through the metal.
 - b. Strengthen the connection of wall panels at the foundation.
 - c. Use high-strength bolts and increase capacity of anchor bolts to be consistent with the blast capacities of the structures.
 - d. Increase the resistance of the wall panels by increasing the size of the cold-formed panels.
4. Dynamic analyses to evaluate the blast resistance of the main frames and secondary members (purlins and girts) should include the following effects:
 - a. The negative phase of the blast pressure.
 - b. The interaction between the responses of the secondary members and the frame responses.
5. The interaction between the sheet metal panels (siding and roofing) and their supporting members (girts and purlins) should be considered in evaluating the blast resistance of panels used on pre-engineered buildings.

REFERENCES

1. STEA, W., et al., "Blast Capacity Evaluation of Pre-Engineered Building", Technical Report prepared by Ammann & Whitney, Consulting Engineers, New York, N.Y., for Picatinny Arsenal, Dover, N.J., 1979.
2. Department of the Army, "Structures to Resist the Effects of Accidental Explosions (with Addenda), Technical Manual TM 5-1300, Washington, D.C., June 1969.
3. HEALEY, John J., et al, "Design of Steel Structures to Resist the Effects of HE Explosions", Technical Report 4837, prepared by Ammann & Whitney, Consulting Engineers, New York, N.Y., for Picatinny Arsenal, Dover, N.J., 1975.
4. STEA, W., et al., "Non-Linear Analysis of Frame Structures Subjected to Blast Overpressures", Report ARLCD-CR-77008, U.S. Army Armament Research and Development Command, Dover, N.J., May 1977.

C³ SHELTER DESIGNS FOR THE TACTICAL BATTLEFIELD

WILLIAM J. SCHUMAN, JR., U.S.A. Harry Diamond Laboratories
GARABED ZARTARIAN, Kaman AviDyne
RAFFI P. YEGHIAYAN, Kaman AviDyne
W. DON ALLISON, U.S.A. Ballistic Research Laboratory

ABSTRACT

Preliminary designs of two new Command, Control, and Communications (C³) shelters for the tactical battlefield have been formulated. The hostile threats accounted for in the designs include tactical nuclear weapons, fragmenting conventional munitions, and attacks by electronic warfare equipment and by chemical/biological agents. Inasmuch as the sequence in which these threats may be employed is unknown, various scenarios were considered. The conventional design requirements stemming from operational and ambient environmental conditions (e.g., deployment, temperature extremes, etc.) were also imposed. The designs were severely limited in weight and physical dimensions because of such requirements as transportability on standard DOD vehicles and efficient usability of inner space for crew and a variety of standardized equipment. This paper discusses the various expected environments and loadings and the predicted structural behavior. An extensive program of analysis and testing has been initiated to simulate loadings and responses. The planned validations include specimen tests, and model and full-scale simulated tests in shock tubes and in the field. Currently available results from this program and results from earlier efforts which form the basis of the preliminary designs are presented. Design trade-offs affecting weight and cost are briefly discussed. Present indications are that the novel wall design concepts provide a viable means for hardening shelters but at the expense of appreciable weight and cost penalties.

INTRODUCTION

Current DOD plans call for Hardened Tactical Shelters (HATS) to complement the currently operational and unhardened S-280 and S-250 versions (see Figures 1 and 2). These command, control, and communications shelters must survive under the "most severe situations" that can be associated with a number of hostile threats including nuclear weapons, fragmenting conventional munitions (hereafter referred to as conventional weapons), and attacks by chemical/biological (CB) agents and radiation from electronic warfare equipment. Thus, the new designs must strive towards a degree of hardening compatible with the military specifications reflecting the anticipated threat levels from various types of attack.

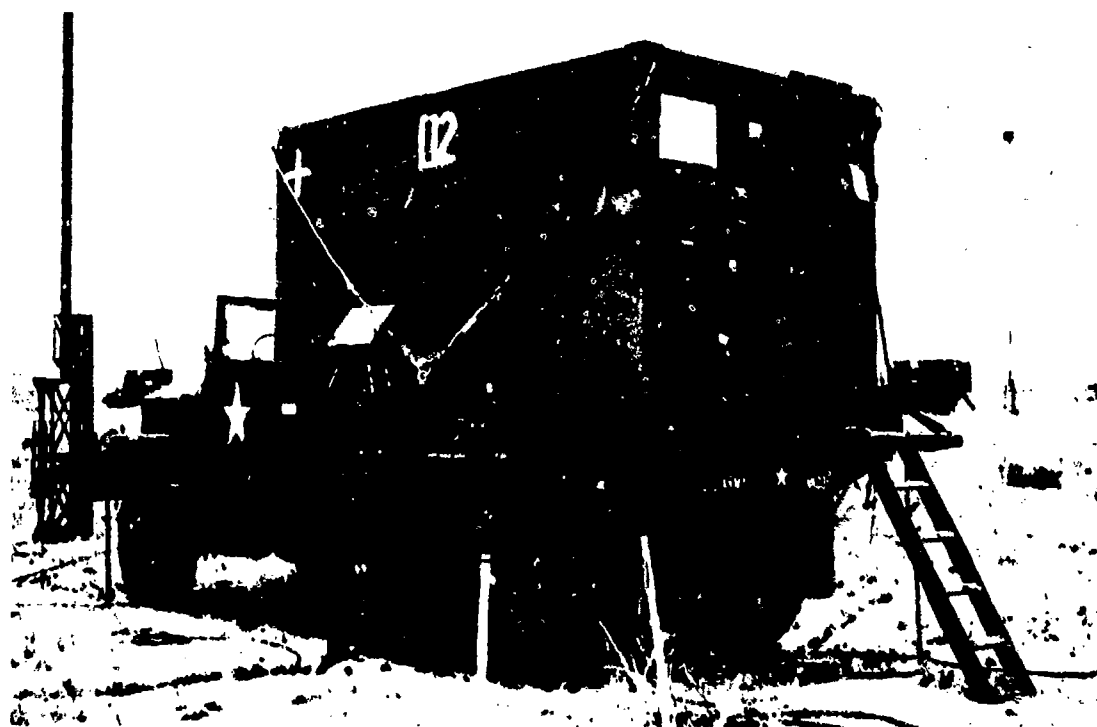


Figure 1. S-280 Shelter Mounted on M35A2 Truck

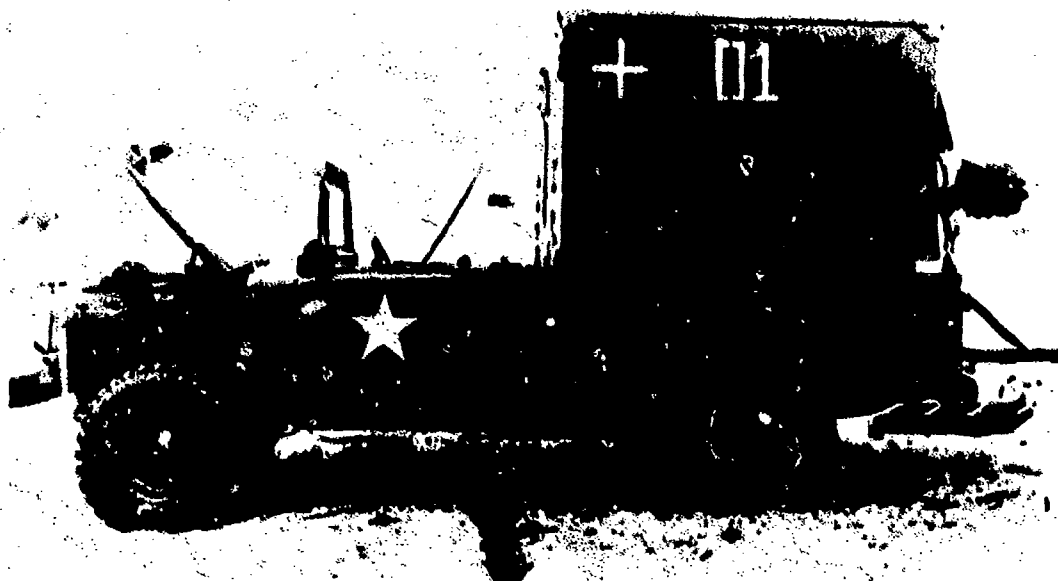


Figure 2. S-250 Shelter Mounted on Truck

Three important further stipulations need be stated to point out some major design implications. First, the most severe conditions should be considered in design. Two examples illustrating this point are: (i) the fragments impinge normally into the shelter walls, and (ii) the shock wave propagation is such that it results in the largest and most damaging loads. Thus, several shock directions need be considered, since different directions may be critical for different shelter structural components. Secondly, it should be assumed that the nuclear, conventional warfare, and CB threats can occur in all possible combinations and sequences, e.g., a CB attack preceding or following a nuclear attack, a conventional warfare prior to a nuclear attack, etc. (In these combinations, a single nuclear encounter may be assumed.) Two example implications raised by this point are: (i) the shelter skins may be allowed to yield but they shall not tear following a nuclear blast encounter, to preclude entry of contaminants from a subsequent CB attack, and (ii) the fragments from conventional warfare (of specified size and velocity) shall not pierce the conducting inner shield, to preclude severe degradation in shielding provided for protection against electromagnetic pulse (EMP), electromagnetic radiation (EMR) and electromagnetic interference (EMI). Thirdly, the requirement that the shelter shall survive to allow mission completion should be interpreted as follows: (i) the shelter structure shall have sufficient strength to protect the equipments inside so that they would remain fully operational after attack(s), and (ii) the shelter structure shall have sufficient rigidity to limit the maximum deflections at the centers of the wall panels to less than prespecified levels so as to avoid wall impacts with equipment racks placed nearby. Also, the permanent deformations, should they result, shall not impair the operation of equipment, doors, etc.

With the threat levels given in quantitative terms later, and in view of the brief discussion above, it should be apparent that the design conditions will be most severe. They will include large thermal inputs coupled with high dynamic stresses in the shelter structure (and the Total Environmental Control System (TECS) and Modular Collective Protection Equipment (MCPE) mounted on the shelter to provide CB protection), and penetration of fragments to cause structural damage, and component damage to TECS and MCPE. In addition, the protection against CB agents will require ducting, ducting valves, and special finishes; and the electrical loads induced by the EMP and EMR will be "large". As a result of these loadings one should expect the shelter structure and the TECS and MCPE to be deformed and partially penetrated, the shelter-truck combination to be rotated so as to require tie-downs to prevent overturning, and the EMP/EMR/EMI shield to be highly stressed.

Some of the needed preliminary work has been completed providing initial guidelines for the hardened designs. During the past several years, the U.S. Army Ballistic Research Laboratory has conducted analytical and experimental investigations to assess the survivability

of Electrical Equipment Shelters under simulated tactical combat conditions. They have utilized shelters such as the S-280 and S-250 with and without certain modifications. Unmodified, these shelters have walls of sandwich construction configured with aluminum skins and interior stiffeners, and with foam cores. The unhardened shelters have also been provided with protection from EMI by insuring electrical continuity in the aluminum skins, conductive sealants where needed, conductive gasketing around doors, and conductive honeycomb barriers on apertures.

In the analytical investigations referred to above, the shelter structural elements were modeled as beams, panels, and complete shelters when using a number of response codes such as NASTRAN, ADINA, DEPROP [1,2] and DEPROB [1,2]. In addition, the truck-shelter combination was modeled by the TRUCK code [3] to determine the overturning response and tie-down parameters. The complimentary test programs involved structural elements and shelter-truck combinations in testing machines, shock tubes, and in large scale high explosive (HE) field tests.

The full-scale field tests were conducted during the DIAL PACK [4,5,6], MIXED COMPANY [7], DICE THROW [8,9], and MISERS BLUFF [10] events. In all cases, the shelter was placed so as to receive the shock head-on to either its roadside or curbside wall. In DIAL PACK, some eight shelters were set on the ground, anchored, and subjected to different overpressure levels. Some of the shelters were empty, while the others had actual racks with weights simulating various equipment. In MIXED COMPANY, twelve empty S-280 shelters were placed on the ground and anchored. They were located at five different overpressure levels. Various types and degrees of hardening were tested, with some shelters having added inside and/or outside aluminum skins, and other with I-beams placed inside and backing the walls hit head-on by the shock. In the DICE THROW event, ten S-280 and S-250 shelters with operational equipment were mounted on trucks; and again they were exposed at different overpressure levels. Two of the S-280 shelters were retrofitted with Kevlar* skin/aluminum honeycomb on both the inner and outer skins. A different, hardened shelter built by Brunswick was also tested, at around the 6 psi (41.4 kPa) overpressure level. The wall panel of the latter was an aluminum skin/paper honeycomb sandwich with two internal vertical stiffeners. In the MISERS BLUFF event, four additional S-280's, fully equipped and mounted on trucks, were tested at higher but different overpressure levels. Of these, one standard shelter was first subjected to a thermal pulse (thus simulating for the first time the thermal pulse from a nuclear burst, a simulation lacking in other HE tests) followed by the blast wave from the HE burst. With another one of these shelters, a Kevlar layer was bonded to the outer skin; but this shelter was exposed to the blast only. One drawback in all the field tests was that the positive phase durations (and thus the total impulses) were less than one would get in nuclear blast encounters, resulting in less severe over-

*Kevlar is a registered trademark for an aramid fiber produced by E.I. DuPont de Nemours and Co. (Inc.).

turning conditions. Nevertheless, these tests have verified the computed responses from the TRUCK code, and thus provide some confidence for future analytical predictions.

Utilizing this background and results from tests conducted since (some of which will be commented on later), the preliminary designs of the hardened C³-shelters were effected. In what follows, the important design aspects are covered. Following a short section summarizing quantitatively the hardness-related design requirements, one of the two configurations is presented along with discussions related to the analytical methods and test results used, the choice of materials, the sizing, etc. The configuration covered here is the hardened version of the S-280 shelter. It will henceforth be designated as the A-Shelter. The design of the S-250 shelter (B-Shelter) is similar and the differences will be discussed briefly.

HARDENED SHELTER DESIGNS

Hardening-Related Design Requirements

The degree of hardening to be provided in the designs must be compatible with the anticipated threat levels which may be specified quantitatively as follows:

1. Nuclear Threat. The burst is of moderate yield and at low altitude. The shelter is located at sea level and at a range such that:
 - (i) The encounter is with the Mach stem of the reflected (and traveling) shock wave, with the shock plane perpendicular to the ground. Thus, the material (gust) velocities behind the shock are horizontal. Otherwise, the shock orientation is arbitrary, requiring consideration in design of all critical azimuthal directions.
 - (ii) At the location of the shelter the peak free-field over-pressure (just behind the Mach stem) is 7.3 psi (50.3 kPa) and the pressure positive phase duration is 1.0 second.
 - (iii) The thermal pulse has a fluence of 1.66 BTU/in² (65 cal/cm²) and is deposited in the 2 seconds before shock arrival.
 - (iv) The associated EMP is intensive with a broad frequency band requiring at least a 60 dB attenuation over the range 0.15 MHz to 18GHz, and even an 80 dB attenuation in the sub range 0.20 MHz to 1 MHz. These attenuation figures reflect the combination of EMP, EMR (electromagnetic radiation, see requirement under electronic warfare threat below), and the usual EMI shielding (specified also for unhardened shelters) requirements.

2. Conventional Warfare Threat. A fragment from a conventional weapon weighing 60 grains (3.9 g) and striking normally any shelter wall at a speed of 1640 ft/s (500 m/s) shall not perforate the wall, i.e., there shall be no puncture of the electromagnetic shield.
3. Electronic Warfare Threat. The shelter shall be shielded from the electromagnetic radiation from this type of attack. This requirement has been combined with that under item (iv) of "Nuclear Threat" above.
4. Chemical/Biological Threat. Hardened air conditioning and filter units, and decontamination vestibules (i.e., hardened TECS and MCPE units) are assumed to be available. Thus, the main shelter design tasks associated with this threat are to provide
 - (i) Proper mountings of all the equipment,
 - (ii) Suitable ducting and valves for proper operation of air filtration and of environmental control systems, even during the positive and negative phases of the nuclear blast field,
 - (iii) Sufficient air tightness to allow positive pressure method of collective protection for CB defense, and
 - (iv) Exterior surface finishes which can be easily decontaminated following a CB attack.

Other Design Requirements

In addition to the hardening-related requirements, the shelter designs must meet appropriate environmental and operational requirements which are always specified in the MIL SPECS for Electrical Equipment Shelters (and, whenever possible, including those requirements agreed upon by the Joint Committee on Tactical Shelters, JOCOTAS). Among them are those dealing with transportability, drop and railroad humping tests, operations in extreme climates, etc. Two specific items worthy of note here are (i) the solar load in a hot desert operation which results in outer skin temperatures of 200°F (93°C), and (ii) the requirement that the overall shelter heat transfer coefficient be kept below 0.35 BTU/hr ft²°F (0.171 cal/hr cm²°C) to minimize the needed air conditioning capacities.

Limitations

Because of air and truck transportability requirements, it is necessary to limit the exterior dimensions of the shelter; and in order to accommodate existing standard equipments and the crew, the inner dimensions have to be kept at specified values within close tolerances. Table I shows the dimension specifications for the A-Shelter. With these dimensions, it turns out that the maximum allowable wall panel thickness is 2.5 in (6.35 cm).

Table I - A-Shelter Dimension Specifications

	Interior in (cm)	Exterior Maximum in (cm)
Length	$138.0 \pm 1/8$ (350.5 \pm 0.3)	147.0 (373.4)
Width	$81.5 \pm 1/8$ (207.0 \pm 0.3)	87.0 (221.0)
Height	$77.0 \pm 1/8$ (195.6 \pm 0.3)	86.75 (220.3)

Meeting the hardening-related requirements imposed weight and cost penalties. Every effort was made to reduce the total shelter weight. The specified goal was to maintain it to within 2100 lbs (953 kg), i.e., some 700 lbs (318 kg) above that for the unhardened S-280 C. However, design and cost factors dictated acceptance of weight overruns which, according to the latest weight ledger, may amount to as much as 8 percent.

Wall Cross-Sectional Design

The wall cross-section shown in Figure 3 is the one eventually selected among several candidate configurations. It is of sandwich construction, with fairly thick inner and outer skins made of Kevlar laminates and spaced by a honeycomb core and Kevlar-based, box-like pultrusion stiffeners. The inner Kevlar skin is also faced with a thin aluminum sheet to provide the enclosure shielding for electromagnetic radiation protection. Besides providing thermal shielding and to some degree insulation, the Kevlar skins are the main contributors of strength and rigidity for carrying the blast-induced bending loads. Much lesser contributions in bending strength and rigidity are expected from the aluminum skin and the stiffeners. The combination of the honeycomb core and the periodically-spaced stiffeners (at the same longitudinal locations as in S-280) has the role of carrying the high shear loads predicted for the blast encounter period. Conservatively, one may assume that the total shear is carried by the core and the webs of the box-shaped stiffeners. (The B-Shelter has similar construction except that the wall and core thicknesses are 1.75 in (4.45 cm) and 1.41 in (3.58 cm), respectively.)

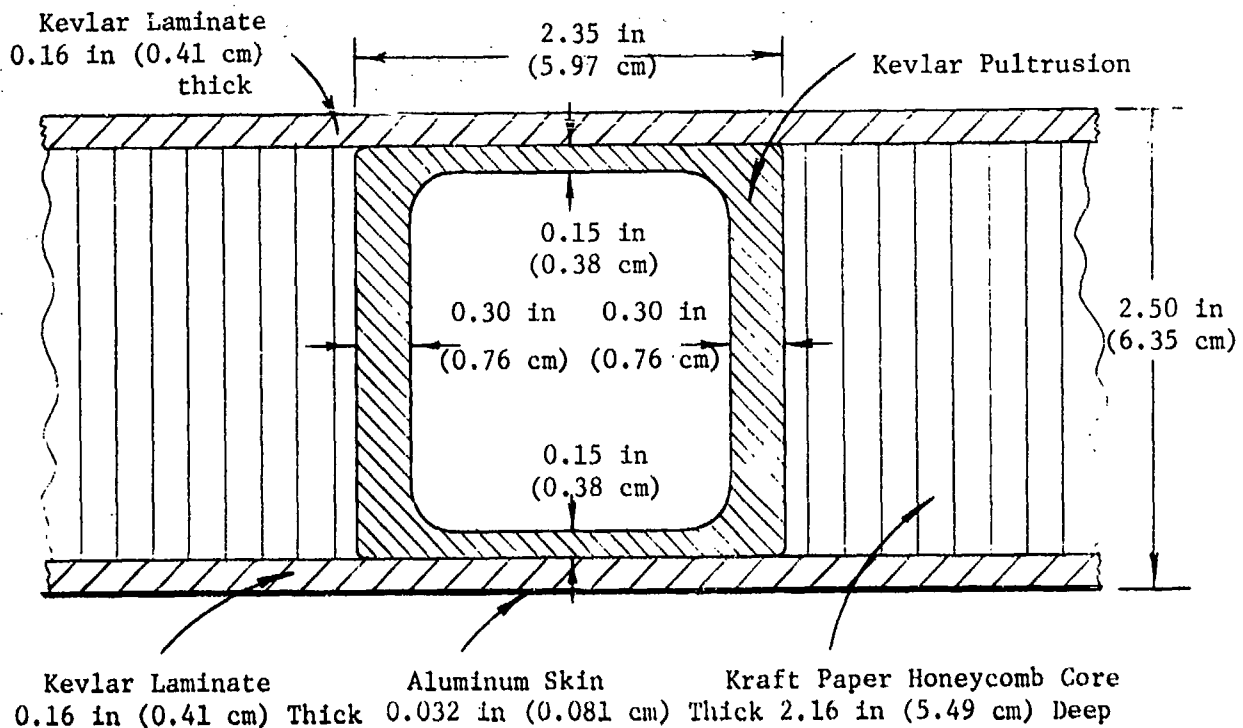


Figure 3. Wall Section at Box Stiffener Location for A-Shelter

The Kevlar cloth plies of the laminates are chosen for several reasons. First, they afford excellent protection against fragmentations. Secondly, they have higher strength to weight ratios and much lower thermal conductivity than aluminum. And finally, through charring of a small fraction of the outer skin thickness, they provide shielding against the high thermal pulse from the nuclear burst. Although Kevlar type 29 plies with low content vinylester or similar resins would have been preferable from the viewpoint of fragmentation protection, the choice in this design is to use Kevlar type 49, with moderate content (say 25-30 percent by weight) epoxy resin in order to achieve the strengths required by the high level blast loadings.

As to the core material, several alternatives were considered, including foams, polycarbonate forms such as Norcore and Quadricore, and aluminum and non-metallic honeycombs. Because of the high shear strengths needed, the expected maximum temperatures, and the heat conduction considerations, the only type of core deemed acceptable is the non-metallic honeycomb. With regards to the stiffeners, the Kevlar pultrusions are preferred (despite their high costs) over aluminum sections because of their low thermal conductivity (thus avoiding "hot spots" which occur

with aluminum stiffeners faced with thin wood thermal barriers) and their close matches in moduli and thermal expansions with the Kevlar skins. On the negative side, it is recognized that the shear strengths of the pultrusions (which is a critical factor in design) are only about one third of those of aluminum requiring thicker webs and thus weight penalties. As to the aluminum electromagnetic shield, a type with moderate to high strength and with at least 5 percent ultimate elongation is deemed adequate.

Each wall (including roof and floor) is made of a single panel, i.e., no seams are allowed. The six walls are assembled using edge and three-way corner treatments. At cross sections with no stiffeners, the arrangement is as shown in Figure 4. At locations with stiffeners, the "C" and mushroom-shaped edge pultrusions are interrupted to allow connection of stiffeners from adjacent panels using L-shaped aluminum inserts. The stiffeners thus connected form frame-like closed rings. The three-way corner fittings are special hefty aluminum castings which also serve as the mounting plates for the lifting and towing eye assemblies.

The wall cross-section design procedure involved essentially the following sequences of steps:

- (i) Determination of the required Kevlar skin thicknesses, based on fragmentation protection considerations.
- (ii) Determination of the type and density of the honeycomb core and the sizing of the stiffeners, based on considerations of required shear strengths.
- (iii) Determination of the required aluminum skin thickness, based on EMP/EMR/EMI protection considerations.
- (iv) Having thus established the sizings of the various components, checks for the strength and rigidity levels of the wall panels to insure structural integrity when subjected to the blast-induced bending loads.
- (v) Evaluation of the thermal characteristics of the cross-section, especially with regards to thermal conductivity to insure compliance with previously noted specifications.

In these assessments, the roadside (or the identical curbside) wall was isolated and treated as a single panel (or a segment of it as a beam) with clamped or simply-supported boundaries (with no translations at the boundaries). It was necessary of course to iterate these design steps in order to impose certain design trade-offs concerning weight, cost, strength, etc. In what follows, these design steps are discussed individually with more details, along with relevant "handbook data" and supporting analysis and test results.

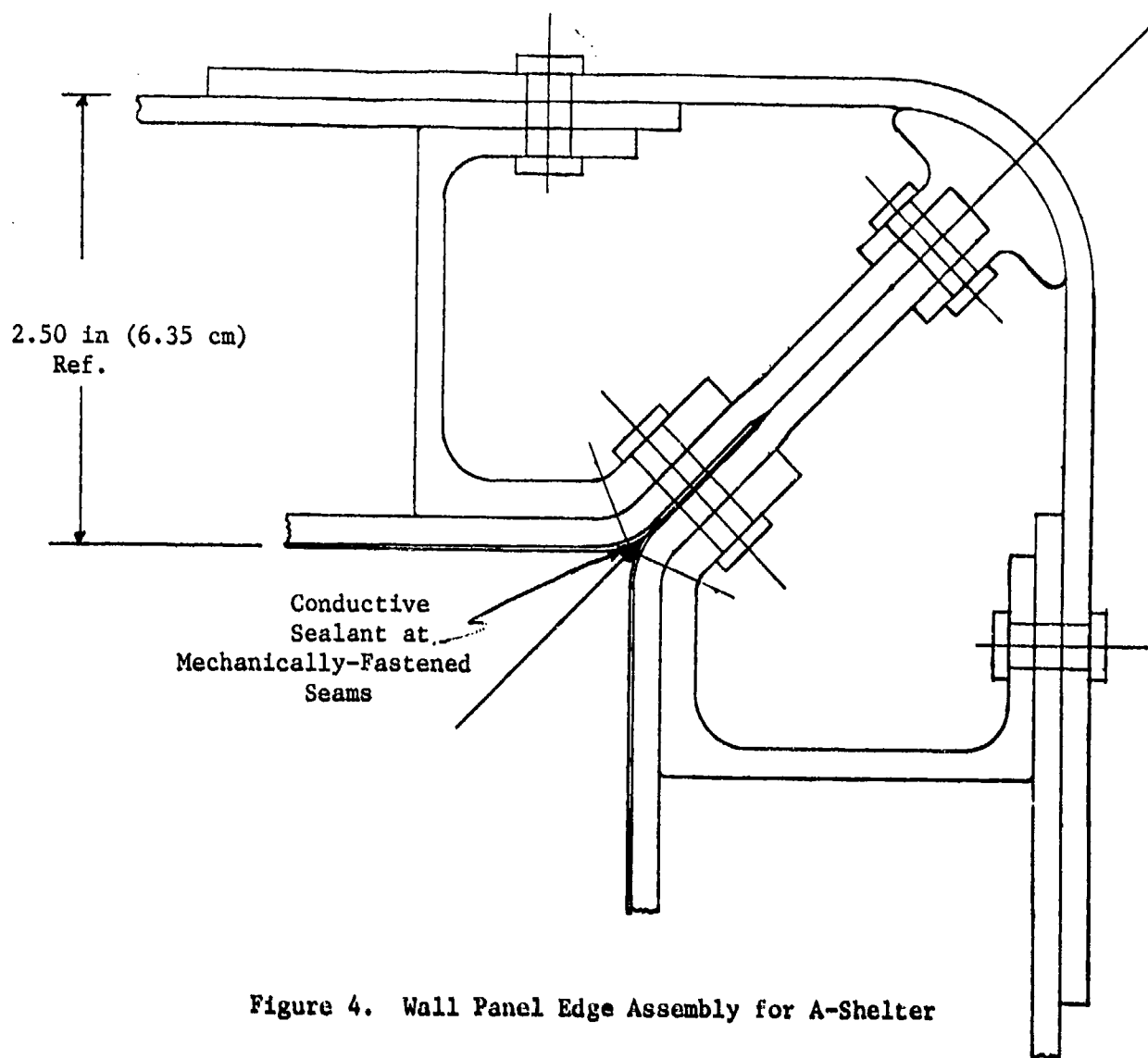


Figure 4. Wall Panel Edge Assembly for A-Shelter

1. Fragmentation Protection. Based on the simple method suggested by Reches [11], a set of curves was prepared which defines the critical (normal) impingement velocity versus fragment size for several values of the Kevlar skin areal density. These curves are according to the Johnson equation for cylindrical steel fragments with $L/D=1$, and use certain empirically derived constants for Kevlar protection which are tabulated by Reches. Assuming a skin density of 0.05 lbs/in^3 (1.38 g/cm^3), these curves indicate that a 0.32 in (0.81 cm) total Kevlar thickness should prove sufficient in providing the protection from the specified fragmentation threat (e.g., 60 grain (3.9 g) impinging normally at

1640 ft/s (500 m/s)). Unfortunately, it turned out that the Reches results apply only to low resin content, easily delaminated, low density (0.037 lbs/in³ (1.02 g/cm³)) "flexible" to "semi-flexible" Kevlar laminates. Additional experimental data from industrial sources indicated that the 0.32 in (0.81 cm) total thickness would be marginal if one uses "moderate" resin content, higher-density (0.048 to 0.050 lbs/in³ (1.32 to 1.38 g/cm³)) "rigid" Kevlar skins laminated under fairly high pressures. (These rigid Kevlar skins are needed for reasons of strength.) Some recent tests on two sandwich specimens (with two 0.16 in (0.41 cm) Kevlar skins and a total thickness of 2.5 in (6.35 cm)) conducted at BRL indicate this to be the case as shown by the results listed in Table II.

Table II - Shelter Panel Fragmentation Tests

Test No*	Impingement Velocity (m/s)	Impingement Yaw Angle (Deg) ^x	Perforated	Residual Velocity (m/s)
1)	542	1	Yes	234
2)	532	6	Yes	240
3) +	531	2	Yes	230
4)	484	0	Yes	60
5)	567	6	Yes	226
6)	473	3	No	-
7) ++	498	18	Yes	114
8)	529	0	Yes	152

* All tests with 60 grain steel cylinder, L/D=1, 0.5 in. gun launched.

+ Specimen 1, with aluminum skin as in Figure 3, with paper honeycomb core.

++ Specimen 2, with aluminum skin at mid thickness.

x From a direction normal to the panel, i.e., normal impingement angle = 0.

The specimens were not built specifically for these tests. They were about 4 in (10.2 cm) wide and 10 in (25.4 cm) long and cut from larger available panels. The resin type and content by weight are not known. From density measurements, it appears that the skins were "rigid", dense (0.05 lbs/in (1.38 g/cm³)) laminates. The guess is that the resin was epoxy with the resin content around 25-30 percent. Because of the narrowness of the specimens, the penetrations may have been enhanced by edge effects. Although most of these tests showed penetration at speeds near 500 m/s, those closer to the 500 m/sec condition showed low residual velocity. It appears possible to improve the situation by choosing a superior type resin and adjusting the resin content, without significant sacrifices in strength. With further tests to guide such trade-offs, it should be possible to meet the fragmentation protection requirement (i.e., no perforation by 50 grain fragments arriving at 500 m/s) with a total Kevlar skin thickness of 0.32 in (0.81 cm). A conservative alternative is to increase the total skin thickness; but this would result in weight and cost penalties which cannot be justified at this time, pending further tests.

2. Blast-Induced Shear Loads. Consider the roadside panel which has "unsupported" dimensions of roughly 77 in x 138 in (195 cm x 351 cm). To choose and size the honeycomb core and the stiffeners (which jointly sustain the shear loads), it is necessary to determine the maximum shear load during the specified blast encounter. The maximum shear occurs at the mid point of the longer side and next to the edges, and may be estimated in the following manner. With a 7.3 psi (50.3 kPa) head-on shock, the peak reflected overpressure is 17.5 psi (120.7 kPa). Assuming no attenuation and taking a dynamic magnification of 2.0, the equivalent uniform static loading for the entire panel is 35 psi (241.3 kPa). A vertical strip 22 in (55.9 cm) wide and 77 in (195 cm) long taken from the center of this panel is isolated and treated as a beam. (The beam contains one pultrusion stiffener centered as in Figure 3; and the 22 in width is chosen since it represents the separation between stiffeners.) On this basis, the maximum shear load amounts to about 29650 lbs (131.9 kN) and occurs near either end of the beam regardless of the edge fixity condition. For the cross-sectional dimensions indicated in Figure 3, and with due account to the difference in the moduli of the core and the stiffener, it is estimated through an approximate analysis that about 62 percent of this load is carried by the honeycomb and the remainder by the stiffener. Assuming uniform stresses over each of the two components, the required shear strengths turn out to be 431 psi (2.97 MPa) and 8670 psi (59.8 MPa) for the honeycomb and stiffener, respectively. The actual maximum shear stress values are expected to be lower than the above values for two reasons: (i) The Kevlar skins and the flanges of the stiffeners carry some of the shear loads, and they have been neglected in the analysis; (ii) By isolating the section as a beam, the load carrying capacity of the plate in a direction transverse to the beam is also neglected. Based on some charts obtained from classical theory of isotropic plates, it is estimated that the total shear load of 29650 lbs should be reduced by a factor of 0.85. (See Hexcel Design Handbook for Honeycomb Sandwich Structures [12].) If this 0.85 factor is applied to the above required shear strengths, the corresponding revised values would become 364 psi (2.52 MPa) and 7370 psi (50.8 MPa). Consider the use of a Kraftpaper honeycomb (Hexcel WRII) as the core material. With a proper resin, cell size, and paper thickness, it is possible to obtain the required shear strength with core densities of 6.8 lbs/ft³ (108.9 kg/m³) or more. From extrapolation of available data from Hexcel, it is estimated that the plate shear strengths of a 6.8 lbs/ft³ WRII honeycomb core, 2.16 in (5.49 cm) deep and at room temperature, are about 395 psi (2.72 MPa) and 272 psi (1.88 MPa) in the ribbon and "long" directions, respectively. With the core placed so that the ribbon direction is parallel to the stiffener (i.e., in the beam direction), this weight WRII core would be adequate provided no significant deteriorations in strength result from elevated temperatures. It is known that WRII strengths deteriorate severely when subjected to temperatures above 180°F (82°C) for "long" periods, i.e., several minutes or longer soak times. The maximum temperature in the core under the solar load of a hot desert operation is expected to be in the range of 150-175°F (66-79°C) for the roof but

lower for the side walls. With no thermal pulse from a nuclear pulse, the WRII core should prove acceptable. With the thermal pulse, the maximum core temperature is expected to increase by some 100°F (56°C), raising a doubt as to whether the WRII would fail in shear, even though the soak period is a few seconds. On the other hand, the blast-induced loads are also of short durations; and some recent data from shock tube tests on panels with WRII honeycomb cores indicate that the dynamic shear strengths of these cores are considerably higher than their static counterparts given earlier. Based on these discussions, and in view of its much lower cost (by nearly an order of magnitude) when compared with those for other non-metallic honeycombs, the WRII is accepted at this time but subject to further extensive tests.

As to the requirement that the pultrusion have a transverse shear strength of 7370 psi (50.8 MPa), no difficulty is foreseen in achieving this level if the pultrusion is reinforced with Kevlar and uses a suitable type and amount of resin, even at temperatures as high as 250°F (121°C).*

3. EMP/EMR/EMI Protection. The aluminum skins from all six wall panels are overlapped (as shown in the edge treatments, Figure 4) and form an "enclosed box" with no "gaps" in electrical continuity. With proper grounding, this provides levels of attenuation (for electric/magnetic fields and plane waves) which meet the specifications when tested according to MIL-STD 285 procedures. Note that this shield is purposely located as the innermost wall layer to avoid holes resulting from fragment penetrations. When properly bonded (and fastened mechanically with certain precautions, as needed) to the inner Kevlar skin, it also contributes, although to a much lesser degree than the Kevlar skins, to the bending strength and stiffness of the wall section. Utilizing the analysis technique and the data from Campi [13], it is estimated that a 0.032 in (0.081 cm) aluminum skin will prove sufficient for attaining the specified dB levels of enclosure shielding at all frequencies between 0.15 MHz and 18 GHz. Aperture shielding such as at exhaust ducts, RFI gasketing at doors, conductive sealants at mechanically-fastened seams to minimize long-term performance degradation, filtering at signal entry panels, etc. present other aspects of EMP/EMR/EMI shielding which were considered in the design.

The use of a single enclosure shield has been questioned and is under further study at this time. The main objection centers around the dissipation of the high currents resulting from the EMP. It is conceivable that these high currents may result in reradiations into the interior of the shelter from such areas as the seams of signal entry panels. With special procedures developed through extensive testing, it is very likely that such panels can be mounted so as to eliminate reradiations. An alternative is to provide dual shields by adding a second and electrically

*Based on discussions with one of the major pultrusion manufacturers.

separated aluminum enclosure, as in previous designs. However, this would impose considerable weight and cost penalties which cannot be justified at this time.

4. Structural States in Response to the Blast Loadings. Having thus established the wall cross-sectional design, the question remains whether the shelter would have sufficient strength and rigidity to withstand the blast-induced bending loads. For this purpose, somewhat simplified dynamic analyses were conducted to predict the maximum stresses and deflections for the largest panel, i.e., for the roadside or curbside wall. A head-on encounter was assumed since this is deemed the most critical shock orientation based on past experience. The time and spatial variations in the loadings were first calculated using the BLOCK code [14] (which is the aerodynamic subroutine in the updated TRUCK code). Rather than accounting for the spatial variations, it was deemed simpler and acceptable for present purposes to assume a uniform, averaged loading. The time variation of this uniform loading, shown in Figure 5, was then

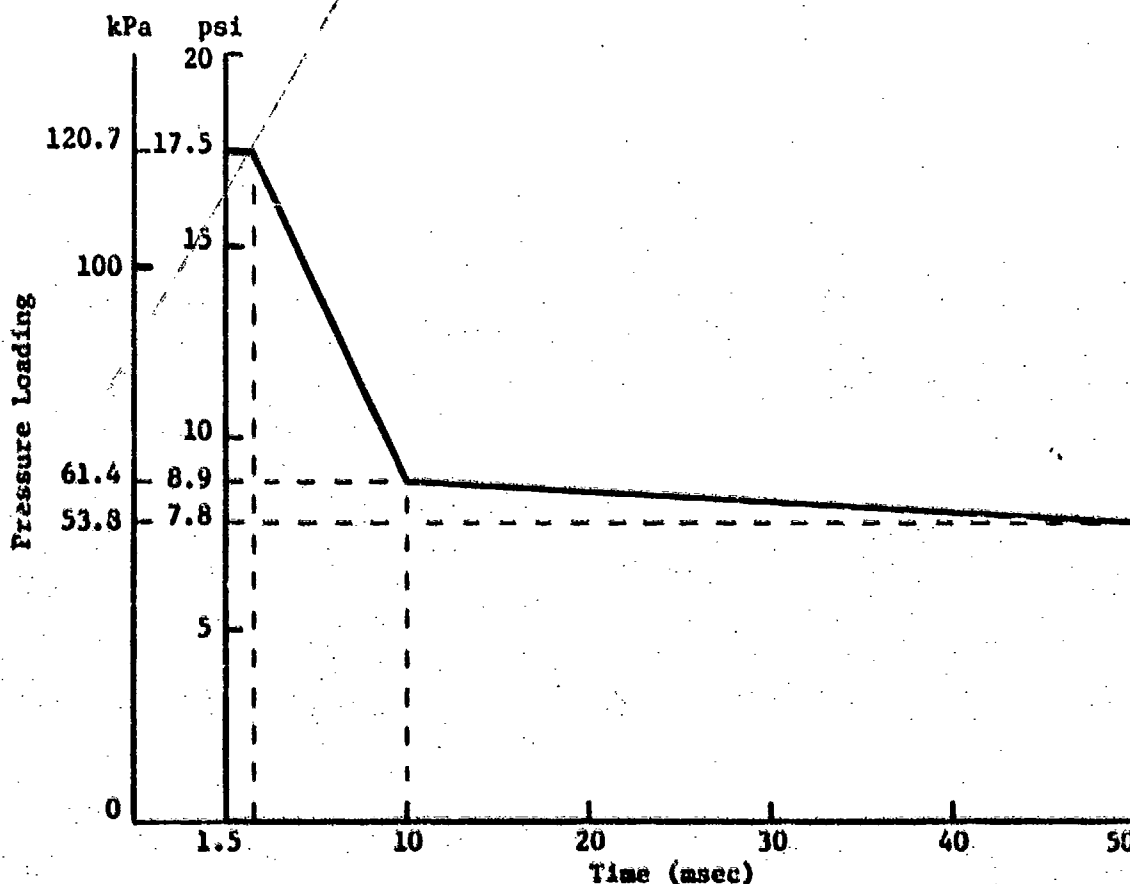


Figure 5. Time History for Uniform Pressure Loading of Wall Panel for 7.3 psi Head-on Shock Encounter

inputted in the structural response codes DEPROB and DEPROP. Both of these codes account for geometric and physical nonlinearities, i.e., membrane stresses, non-linear stress-strain relations, but omit strain rate effects. Two structural models were considered. With the much simpler DEPROB, a 22 in (56 cm) wide segment, 80 in (203 cm) long and backed centrally by a single pultrusion stiffener (see 2 above), was taken from the center of the whole panel and treated as an isolated beam. With DEPROP, the entire wall panel was modeled with some approximations which were required to include stiffeners along with the multi-layered skins. Most of the calculations for maximum stresses and deflections were effected with DEPROB. A few check calculations were made with DEPROP which is more accurate but which requires computation times an order of magnitude longer than those with DEPROB. Whenever checked, the results from the two sets of calculations showed reasonable agreement. Both simply-supported and clamped edge conditions were analyzed. The ends were assumed fixed, i.e., no longitudinal motions were allowed, and the compressive edge loads imposed by adjacent panels were neglected. Table III summarizes the results from the beam (DEPROB) analyses for the final configuration as shown in Figure 3.

Table III - Summary of Maximum Structural Responses From the Beam Analysis for the Final Wall Configuration

	Clamped Edges	Simply-Supported Edges
Peak Tensile Stress in Kevlar, kpsi (MPa)	43 (296)*	42 (290) [†]
Peak Compressive Stress in Kevlar, kpsi (MPa)	30 (207)**	11 (76) ^{††}
Peak Tensile Strain in Aluminum, %	0.46 ^x	0.95 ^x
Peak Compressive Strain in Aluminum, %	0.70 ^{xx}	Negligible
Peak Displacement, in (cm)	1.50 (3.81) ^x	3.22 (8.18) ^x
Time of Peak Displacement, msec	5.0	6.6

*At outer skin, clamped edge
[†]At inner skin, center span
^xAt center span

**At inner skin, clamped edge
^{††}At outer skin, center span
^{xx}At clamped edge

In these calculations, two linear segments approximated the elastic-plastic behavior of the aluminum skin with the maximum stress equal to 42 kpsi (290 MPa). Also, the Kevlar laminates were assumed to have a density of 0.05 lbs/in³ (1.38 g/cm³), and moduli $E=4.5 \times 10^6$ psi (31000 MPa) for the inner skin and 3.5×10^6 psi (24000 MPa) for the outer skin. (The reduced value of E was used for the outer skin because of the expected elevated temperatures there.)

Regardless of the edge conditions, the aluminum skin is expected to yield (since any strain beyond about 0.42% implies yielding) but not to fail since the ultimate strain for the chosen aluminum is over 10%, a value much higher than the values indicated in the table. The Kevlar tensile stresses (and also the pultruded stiffener tensile stresses) are below their allowables. The critical result is the peak compressive stress in the inner Kevlar skin which amounts to 30 kpsi (207 MPa) with clamped edges. Kevlar laminates have much lower compressive strengths than tensile strengths. Available test data indicate that the best one could attain with proper blend of Kevlar cloth and resin may yield compressive strengths of about 23 kpsi (159 MPa). Nevertheless, the wall cross-sectional design is tentatively (i.e., pending further developments) accepted for the following reasons. First and foremost is the fact that the edges are not ideally clamped. An edge fixity factor of about 0.8 was estimated. This depends, of course, on the edge treatments, and on the loadings of adjacent panels which are at lower levels. If this factor is applied to the 30 kpsi figure, the compressive stress requirement drops to about 24 kpsi (165 MPa), a value much closer to the available strength of 23 kpsi. Secondly, these maximum compressive stresses occur right at the panel edges, but drop sharply going away from the edges. At the edges, the C-shaped pultrusion stiffeners (see Figure 4) should contribute in carrying the loads, a condition which was omitted in the analysis documented in Table III. A test case accounting approximately for the thickness of the C-stiffeners indicates a reduction of some 25% in the Kevlar peak compressive stress. Thirdly, it is known that beam type analyses applied to low aspect ratio plates tend to yield somewhat higher stresses than those from more accurate plate type analyses. And finally, the unaccounted for strain rate effects may allow an allowable compressive stress for the Kevlar laminates higher than the 23 kpsi value quoted above for the static case. What this increase amounts to with the strain rates inferred from the times of peak displacements shown in Table III cannot be estimated without some basic tests on Kevlar laminates.

5. Thermal Considerations. Two specific specimen tests were conducted to determine certain thermal characteristics of the wall cross section. The first pertains to the thermal conductivity of a 24 in x 24 in (61 cm x 61 cm) panel with the same materials and cross-sectional geometry as in the present design, except that the panel had no pultruded stiffener. In the second test, a thin Kevlar laminate was subjected to a thermal pulse simulating that from a nuclear weapon to assess the thermal damage to the skin and the increases in the temperatures at the inner face of the outer skin where the honeycomb core is bonded to the skin.

The thermal conductivity test was done according to ASTM C518-76 using a heat flow meter. The heat was applied from the bottom of the horizontally placed specimen, maintaining a thermal difference across the thickness of about 72°F (40°C). The stabilized heat transfer

coefficient was found to be $0.28 \text{ BTU/hr-ft}^2\text{-}^\circ\text{F}$ ($0.137 \text{ cal/hr-cm}^2\text{-}^\circ\text{C}$). (Had the heat been applied from the top or the plate had been placed vertically, it is expected that the heat transfer coefficient would have been lower.) This result is acceptable for keeping the overall shelter heat transfer coefficient to below $0.35 \text{ BTU/hr-ft}^2\text{-}^\circ\text{F}$, although higher than that for earlier designs with foam cores which are excellent insulators. Also, in earlier designs the aluminum stiffeners, despite being faced with wood thermal barriers, created hot spots raising the overall heat transfer. In contrast, the pultruded stiffeners in the present design have much lower conductivity than aluminum thus preventing hot spots; and despite the presence of these pultruded stiffeners, it can be confidently stated that the overall shelter heat transfer coefficient can be kept below the 0.35 figure.

In the other test, conducted by Quigley at BRL [15], Kevlar 49-epoxy sheets, 0.091 in (0.23 cm) thick, were placed in a solar oven and exposed to two trapezoidal - and one nuclear-shaped thermal pulses. For the single data point with the nuclear pulse, the rise time was 0.9 sec, the total duration was 8.3 sec, and the fluence was 1.66 BTU/in^2 (65 cal/cm^2) (the same fluence value specified in this design). The recorded data was minimal. Before the thermal pulse, the skin temperature was 70°F (21°C). A "few mils" (say the thickness of the outer ply) was charred and the inner face temperature reached somewhere between 226°F and 252°F (108°C and 122°C). This is an increase of about 180°F (100°C) above the ambient. Extrapolating roughly this result to the present case of 0.16 in (0.41 cm) skin thickness, one would estimate a temperature rise of about 100°F (56°C) for the outer skin inner surface temperature. If the temperature at the same location and prior to the pulse is assumed to be say 150°F (66°C) (which is conceivable in a hot desert operation with the shelter air conditioned), the temperature at the core/outer skin bond could be as high as 250°F (121°C) at shock arrival time. This indicates that the temperature effects on the physical properties of the Kevlar outer skin, core, pultrusions, and the adhesives had to be considered in the design. Obviously, further and more controlled tests of this nature, with an actual panel cross section rather than with a thin Kevlar laminate, need be conducted for more realistic thermal assessments.

CONCLUSIONS

Preliminary designs of two new C³ shelters have been presented. They were designed for the extreme environment of the tactical battlefield. Some details of the threats and the resultant loadings and structural behavior were given. The designs are based on an extensive program of analyses and testing. Design trade-offs between weight and cost were considered.

A contract has been let to fabricate four each of these two shelters. An Integrated Test Plan includes specimen, model and full-scale tests to be conducted in the laboratory, shock-tube and field.

Although appreciable weight and cost penalties have been incurred, these shelter designs represent a significant increase in the survivability of the C³ systems that they will contain.

REFERENCES

1. Lee, W.N. and Mente, L.J., "NOVA-2 - A Digital Computer Program for Analyzing Nuclear Overpressure Effects on Aircraft," Air Force Weapons Laboratory Report, AFWL-TR-75-262, Pt. 1, August 1976.
2. Mente, L.J. and Lee, W.N., "NOVA-2S, A Stiffened Panel Extension of NOVA-2 Computer Program," Air Force Weapons Laboratory Report, AFWL-TR-78-182, December 1978.
3. Hobbs, N.P. and Lee, W.N., "TRUCK, Version 2.1 - Blast-Induced Response of Army Vehicles Equipped with Outriggers," Kaman Avidyne Technical Memorandum, KA-TM-113, Burlington, MA 01803, January 1979.
4. Ethridge, N.H., and Teel, G., "Blast Effects on Electrical Equipment Shelters (U)," DASA 2606-II, DASIAC SR 115, Event DIAL PACK Preliminary Report (U), Volume II, Published by DASA Information and Analysis Center, General Electric Company, TEMPO, Santa Barbara, CA 93102, May 1971, Secret.
5. Ethridge, N.H., and Teel, G., "Blast Effects on Electrical Equipment Shelters (U)," Project LN 112, Event DIAL PACK Symposium Report (U), Volume III, The Technical Cooperation Program, Panel N-2, DNA 2722T, Published by DASA Information and Analysis Center, General Electric Company, TEMPO, Santa Barbara, CA 93102, November 1971, Confidential.
6. Ethridge, N.H., "Acceleration Measurements Obtained in S-280 Shelters Containing Weighted Racks," BRL IMR No. 33, Ballistic Research Laboratories, Aberdeen Proving Ground, MD 21005, January 1972.
7. Freiberg, R.A., "Tactical Antenna and Shelter Response to Airblast Environment," Project LN118, Event MIXED COMPANY Report USAECOM, Fort Monmouth, NJ 07703.
8. Schuman, W.J. and Freiberg, R.A., "Command, Control and Communication Shelter Systems (U)," Proceedings of the DICE THROW Symposium, 21-23 June 1977 (U), Volume 4, Defense Nuclear Agency Report, DNA 4377P-4, July 1977, Secret Volume.
9. Calligeros, J.M. and Karlson, R.A., "Post-Test Analysis of the Brunswick MOD Shelter Tested in DICE THROW," Mitre Technical Report, MTR-3761, Bedford, MA 01731, 3 April 1979.

10. Schuman, W.J., Freiberg, R.A., and Mayerhofer, R.D., "Thermal-Blast and Blast Response of C³ Shelter and Antenna Systems - Event MISERS BLUFF," Project Officers' Report No ____, Defense Nuclear Agency. In Preparation.
11. Reches, M., "First Order Approximation of Ballistic Protection (U)," U.S. Army Materiel Systems Analysis Activity Technical Report, AMSAA TR-262, Aberdeen Proving Ground, MD 21005, March 1979, Confidential.
12. Anon., "Design Handbook for Honeycomb Sandwich Structures," Hexcel Publication TSB 123, Dublin, CA 94566, Second Edition, Reprinted 1978.
13. Campi, M., "Survey and Review of Building Shielding to Electromagnetic Waves from EMP," Harry Diamond Laboratories Report, HDL-TM-78-23, U.S. Army Electronics Research and Development Command, Harry Diamond Laboratories, Adelphi, MD 20783, November 1978.
14. Lee, W.N. and Zartarian, G., "BLOCK - A Digital Computer Program for Calculating the Blast Loadings on Box-Like Structures," Kaman Avidyne Technical Report, KA-TR-156, Burlington, MA 01803, January 1979.
15. Quigley, E., of U.S. Army Ballistic Research Laboratory, by Private Communication, July 1979.

COMPOSITE TANK FLOOR ARMOR

ANTHONY SAN MIGUEL
Staff Scientist
Systems, Science and Software
La Jolla, California 92038

ABSTRACT

A summary is given of previous related tests and theoretical approaches used to design tank floor armor. Survivable dynamic response requirements for a sitting crew member are identified. The methodology of scale testing is then reviewed. Scale tests using both steel and steel/polymer composite plates are next described. Finally measurements of the dynamic response of various composite plates are reported and discussed in the context of attenuation of dynamic load to the crew member. It is concluded that composite tank floor armor can attenuate blast loading better than monolithic steel armor plate of equal areal density.

INTRODUCTION

Combat experience has shown that tanks can readily be put out of action by blast from land mines. The blast defeat mechanisms are shock, deformation, fracture and overturn. Armor design of tank floors [1] apparently is based only on the criterion that the armor not fracture as a result of a nominal "belly" mine blast loading. It appears that the blast induced dynamic response of the floor upon crew members and other critical operational components has not received as much attention as perhaps it should. Without such information it is difficult to evaluate how to improve tank floor armor so as to improve the overall mission survivability of tanks.

Tank floor armor is made of class 2 rolled homogeneous armor plate intended for use where maximum resistance to structural failure under conditions of high rate of shock loading is required, and where resistance to armor piercing ammunition is of secondary importance [2]. Unfortunately, the history of design related analyses and tests has been such that the majority of design information generated is based on the response of a variety of steel plates tested with unclamped edge support. Design equations have been developed which predict permanent plate deformation and fracture as a function of thickness [3,4,5,6]. Recent studies have shown that transient plate response can now be predicted with the aid of computer codes [7,8].

In this paper the question entertained is whether or not composite tank floor armor should be considered as an alternative to monolithic steel armor. The answer is provided by first generating a baseline by reviewing tank floor armor technology. Next the required function of the tank floor armor is identified in the context of tank mission survivability from the point of view of dynamic response requirements for the crew members and other vital components. Model test methodology to be used as a tool for estimating the response of prototype armor plates is then reviewed. This is followed by a description of scale test apparatus. Then a family of composite armor designs using combinations of steel, balsa wood, Kevlar and high density steel honeycomb slabs is proposed. Test results from scale models of these plate designs are

reported and the answer to the question as to the feasibility of composite tank floor armor to defeat blast is given.

TANK FLOOR ARMOR TECHNOLOGY

It is beyond the scope of this particular discussion to review in detail the state-of-the-art of technologies and information that are identified in Figure 1. However, to understand why a composite tank floor armor should be considered to replace monolithic steel armor requires a brief synopsis of the genesis of tank floor design technology.

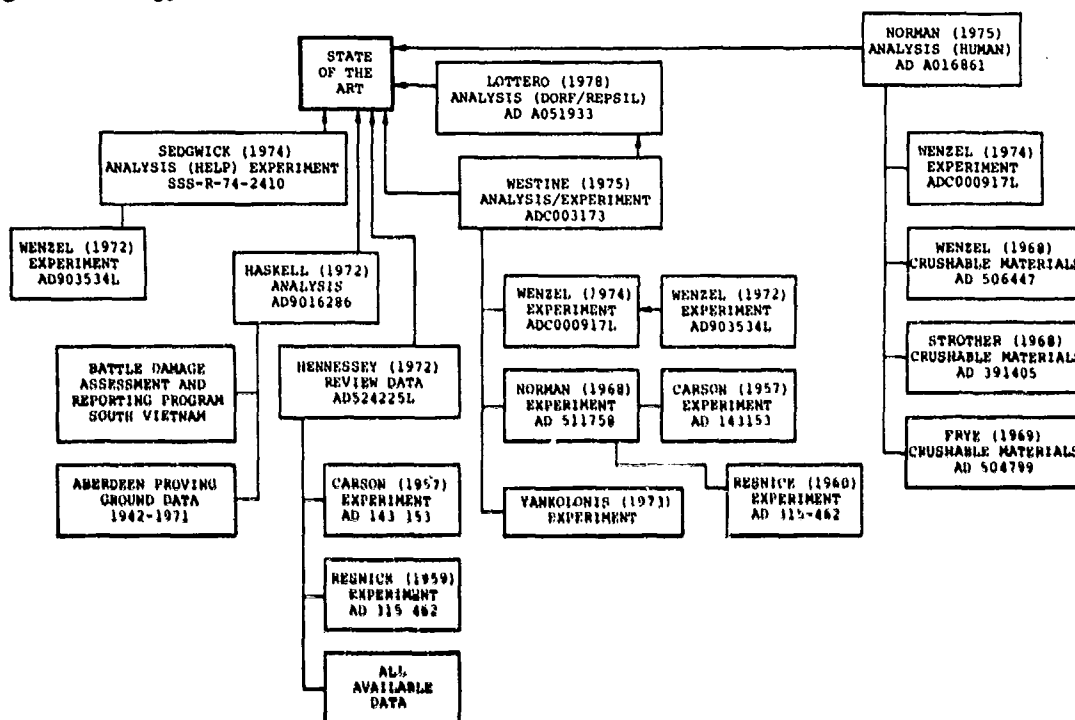


Figure 1. Methodologies used to predict the response of a tank floor subjected to blast loading.

Until the last few years, little regard was given to the relationship between tank floor design and tank mission effectiveness. With the advent of survivability/vulnerability methodology being imposed upon combat vehicle designs, new questions must now be answered related to component dynamic interactions within vehicles subjected to extreme loading environments.

In 1972, Hennessey [3] identified a simple empirical equation to predict the thickness of an armor plate required to withstand (i.e., not fracture) the blast of anti-tank mines. Furthermore he identified the significance of stress risers (attachments to plates), the increase of plate strength due to cross rolling, adverse effects caused by low temperature, and the observation that permanent plate deformation decreased linearly with increasing material hardness. Hennessey's work brought together the first systematic methodology for modern tank floor design.

Also in 1972, Haskell [4] suggested using Friedlander's equation to predict the reflective pressure induced on tank floor armor as a consequence of mine blast. Haskell pointed out that it was necessary to consider a plate hold down weight ratio of 28:1 and that the earth in which the mine was buried did not effect the intensity of the blast loading to the plate. Haskell used an approximate semi-inverse energy analysis approach in correlating design variables. The objective was to predict the thickness of the armor necessary to preclude failure.

In 1975 Norman [5] reiterated what was suspected for some time: that the dynamic response of tank armor plate was probably large enough to incapacitate the crew members even if the tank floor was not fractured. He showed that armor thickness was proportional to permanent plate deformation, thus indirectly suggesting that the thicker the steel plate, the better its capability to attenuate shock loads. Norman estimated that the step velocity response of the armor floor could be represented by a velocity step input of 340 ft/s (104 m/s). It is well known that this magnitude of velocity step would readily incapacitate an unprotected tank crew member. Norman proposed that crushable materials be identified to attenuate the velocity step.

The only pertinent data on crushable materials was that generated in 1969 by Frye [9]. Frye tested 12 lb/ft³ (0.19 g/cm³) aluminum honeycomb with no success, but data for 30 lb/ft³ (0.48 g/cm³) steel honeycomb suggested blast armor feasibility. It is noted that Frye was only concerned with floor fracture and not dynamic response.

In 1975 Westine [6] concluded an extensive study which used dimensional analysis to predict the permanent deformation of a tank floor as a function of anti-tank mine size and location. Westine assumed that plate data obtained from an assortment of tests had free fixity edge conditions. He also assumed that clamped fixity edge conditions could be accounted for by introducing a multiplication factor of 1.5. Westine emphasized the importance of the soil in which the mine was laid and used this assumption to correlate data.

Sedgwick [7] showed in 1974 that the computer code HELP could be used to characterize the blast loading of an anti-tank mine. Sedgwick reported that it appeared that dry soil was not an important variable in characterizing blast loading for pancake charges similar in aspect ratio to land mines.

Finally, Lottero [8] extended the analysis of the tank floor response to a land mine by using the computer codes DORF and REPSIL. DORF characterized the blast loading whereas REPSIL predicted the tank floor response. The example that Lottero used to illustrate computer applicability was based on an experiment performed in 1975.

In overview, current tank armor floor design analysis has developed to the point of being able to predict the transient phenomena of an anti-tank mine blast and to then predict the consequential residual deformation of the tank floor armor, assuming a priori that the armor will not first fracture. Potential vital component kill mechanisms, caused by the violent deformation of steel tank floors due to blast, have not been positively determined. An approximate experimental data base has not yet

been generated. Interest in the use of composite armor to attenuate the response of tank floors to mine blast(s) has historically been low key.

SURVIVABLE DYNAMIC RESPONSE REQUIREMENTS

There is speculation that a tank crew member will not survive the dynamic response represented by a step velocity change of 15 ft/s (4.6 m/s) over a duration of one millisecond. Since the dynamic response of a tank floor subject to a mine blast is quite violent, current practice is to suspend the crew member above the tank floor. This solution to the problem of crew member survivability is now being re-examined.

Crew member survivability studies directly pertinent to tanks subjected to blast have been made by Strother [10] and Wenzel [11]. Closely related studies are also reported by Hirsch [12,13]. Shock isolation requirements that the tank crew member seat must meet if injury is to be avoided are given in any of a number of crash design handbooks [14]. The data reported in these references has been generated from volunteers, accident reports, and human simulators such as animals, anthropomorphic dummies, and cadavers. As might be expected, the wide variation in the physiological and psychological structure of humans precludes a simple prediction of injury that will occur as a function of shock loading. Further insight into the uncertainties associated with predicting/measuring crew member survivability is given by King [15]. The point being made is that suspending the crew member above the floor does not ensure that he will not be incapacitated as a consequence of a mine blast.

It is proposed that survivable dynamic response requirements be based on the mission survivability of a tank. In this manner the survivability of the crew member is prominent since he is the most critical system component. Intrinsic to this approach is that the survivability of a crew member is dependent upon other critical components functioning after a land mine blast. The degradation of tank mission effectiveness can range from significant fracture of structure (such as optics) to the generation of noise in electronic circuitry. Such degradation probably results in greater vulnerability to enemy attack and hence lowering of crewman survivability.

If it is assumed that all critical components within a tank are of equal importance for crew member survival of a mine blast, then the survivable dynamic response design requirements are that the tank floor armor absorb and redistribute the blast load in a relatively mild manner. In principle this goal should be achieved if space is made available to use shock isolation materials in composite structural configurations. One way to generate the data needed to design such structure is next proposed.

MODEL TEST METHODOLOGY

Sealed model test data represents a significant portion of all the data identified in Figure 1. Care must be taken whenever such data is used to predict prototype response. To begin with, it is important to recognize that scale testing is at best only an approximation of prototype testing. This is because all model testing requires the use of assumptions to simplify the complexity of the real world problem. Sealed tests by definition assume that locations, times and forces are homologous [16,17] in

corresponding systems. It is because of this assumption that the response of a model system can rationally be used to predict prototype response.

Scaled model tests have been the bases for tank-floor studies because of both safety considerations and the complexity of blast-structure interaction phenomena. The objective for tank floor armor scale testing is to obtain quantitative data for prototype design, to identify significant design variables, to estimate the extreme performance potential of an existing prototype system, and to investigate new phenomena when there are no other alternatives.

In this paper the results from quarter scale tests are reported, i.e., $\lambda = 1/4$. The well known scaling relationships [16,17] between model, m, and prototype, p, are as follows:

$$\text{length; } x_m = \lambda x_p$$

$$\text{time; } t_m = \lambda t_p$$

$$\text{velocity; } \dot{x}_m = \dot{x}_p$$

$$\text{acceleration; } \ddot{x}_m = \lambda^{-1} \ddot{x}_p$$

$$\text{mass; } m_m = \lambda^3 m_p$$

$$\text{force; } f_m = \lambda^2 f_p$$

$$\text{strain; } [\epsilon_{ij}]_m = [\epsilon_{ij}]_p$$

$$\text{stress (or pressure); } [\sigma_{ij}]_m = [\sigma_{ij}]_p$$

$$\text{energy; } E_m = \lambda^3 E_p$$

Unfortunately, gravity effects do not scale. This is because the scaling laws would require the acceleration due to gravity to be changed by the ratio λ^{-1} . Scaling of model plastic deformation response can only be representative of prototype plastic deformation response if the real life plastic failure criteria is invariant, and such is not the case for materials in general. Strain rate effects and related yield phenomena cannot be scaled. The general design rule of thumb is that model tests be interpreted in terms of deformation and that prototype tests be used to obtain failure criteria. Therefore, displacement is the important measurement in a tank floor armor/mine blast test in which a tank floor plate response is characterized by a step increase in force, undergoes a pulsed increase in acceleration, resulting in a continuous time history of velocity, and an even smoother time displacement.

A concluding note on the scale testing of a tank floor subjected to blast is that most types of transducers designed to sense velocity and displacement are not suitable for use in dynamic models. This is because these transducers require the attachment of relatively large masses to the model, therefore seriously affecting the inertial properties of the armor system being tested.

Physical dimensions used for armor blast scale testing are given in Figure 2 and 3. In essence, an explosive of disk geometry characterized by dimensions d and a is placed a distance R from the bottom of the tank hull. Upon detonation a time dependent pressure is applied to the plate at t_0 , resulting in a positive impulse, I , which is bounded by t . Using the Hopkinson blast wave scaling law [18], where $k = \lambda = 1/4$, the scaled model parameters are obtained. The mass of a 22 lb (10 kg) prototype explosive is scaled to a 0.34 lb (154 g) model explosive. Observe from Figure 2 that the maximum pressure is the same for both prototype and model (since $[\sigma_{ij}]_m = [\sigma_{ij}]_p$). However, the time scale and impulse have been altered and must be interpreted in a homologous manner. Another uncertainty consideration is that the use of the Hopkinson blast law at close standoff distances could lead to misleading results since the expansion and shock waves decay at different rates which are not subject to scaling.

NEGLECTING VISCOSITY, STRAIN-RATE, GRAVITY, NON-LINEAR, ETC.

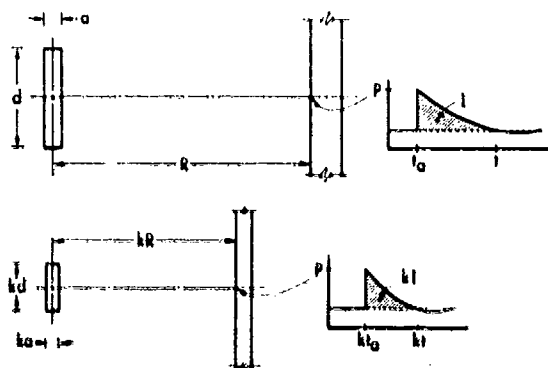


Figure 2. Hopkinson blast wave scaling of tank floor armor.

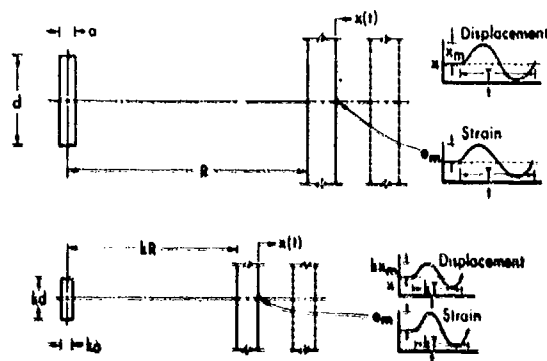


Figure 3. Dynamic response scaling of tank floor armor to blast loading.

However, experimental evidence exists [19] to show that the law is a reasonable approximation. The assumed response of the prototype and model tank floors are shown in Figure 3. Note that the maximum displacement of the inner surface of the model tank floor is scaled ($k = \lambda = 1/4$) from that of the prototype. However, the maximum strains are the same. Again the time scale and the plate response must be interpreted in a homologous manner. It is noted that such scaling assumes that viscosity, strain rate, gravity and other non-linear thermo-viscoelastic phenomena can be neglected.

SCALE TEST

A review of all the test data reported in the literature identified in Figure 1 showed that scaled model response data exhibited wide scatter. One reason for significant data scatter was due to the manner in which the various sized model

plate specimens were held along their edges. For structural analysis considerations, as well as to physically approximate a prototype tank floor, the fixity of the model test plate should approach classical clamped edge conditions. This means that the boundaries should be relatively fixed in space and that both shear and moments must be readily reacted by the holding fixture. Another consideration was that the holding fixture should be representative of a scaled tank mass and mass distribution. The attempt made to achieve these goals is illustrated in Figure 4.

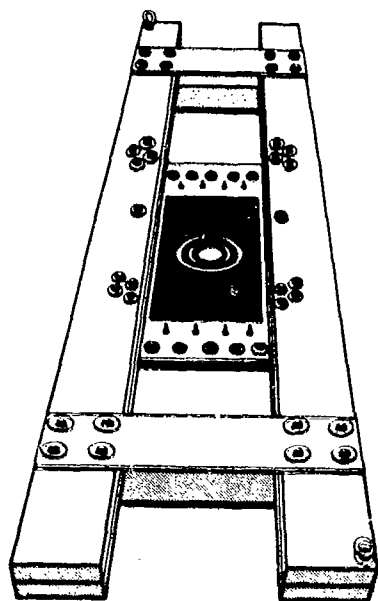


Figure 4. Tank scaled test fixture attached to tank floor.

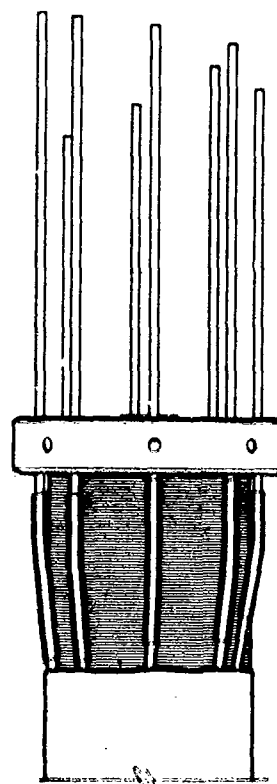


Figure 5. Copper pin probe transducer to measure time-of-arrival, average velocity and instantaneous velocity (hence average acceleration) of tank floor surface

The total weight of the test fixture is 1620 lbs (735.5 kg) scaled from a 51 ton (46308 kg) tank. The model test plate is attached on four sides to the framing fixture by means of rows of 1/4 inch (0.65 cm) and 3/4 inch (1.91 cm) brass bolts equally spaced. The framing fixture is attached to the test fixture on two sides by means of 16-3/4 inch (1.91 cm) steel bolts. The hold down ratio of the test fixture to framing fixture is about 28:1. The overall length of the test fixture is 6 feet (183 cm) and its width is 31 inches (78.7 cm). The model tank floor plate is 2 ft (61 cm) by 2 ft (61 cm), with 15 inches (38 cm) x 15 inches (38 cm) being exposed from the framing fixture and available to react against the blast load.

Transient plate deformation data is obtained using eight pure copper pin probes that were housed in a collar fixture as shown in Figure 5. In this manner electrically measured time of arrival of the tank floor surface is obtained. Since the relative position of the end of each pin is measured, average velocity data can be obtained. In addition, a novel measurement of instantaneous velocity can be obtained by measuring the plastic radial strain induced along the end region of the pin. By assuming incompressible flow for the copper pin, the instantaneous velocity at the time of pin to plate contact can be obtained by measuring the pin diameter after the test, and using the velocity-longitudinal strain relationship developed by White [20,21]. Knowing each time of arrival enables the computation of average acceleration of the tank floor surface.

The pin holding collar was rigidly attached to the test fixture as shown in Figure 6. Also shown in Figure 6 is a stainless steel rod painted with alternating white and black markings. The rod is loosely placed in a hole within the center of the collar holding the copper pins. The purpose of the rod was to measure plate-rod interaction response so that additional characterization of plate deformation due to blast could be obtained [22-31].

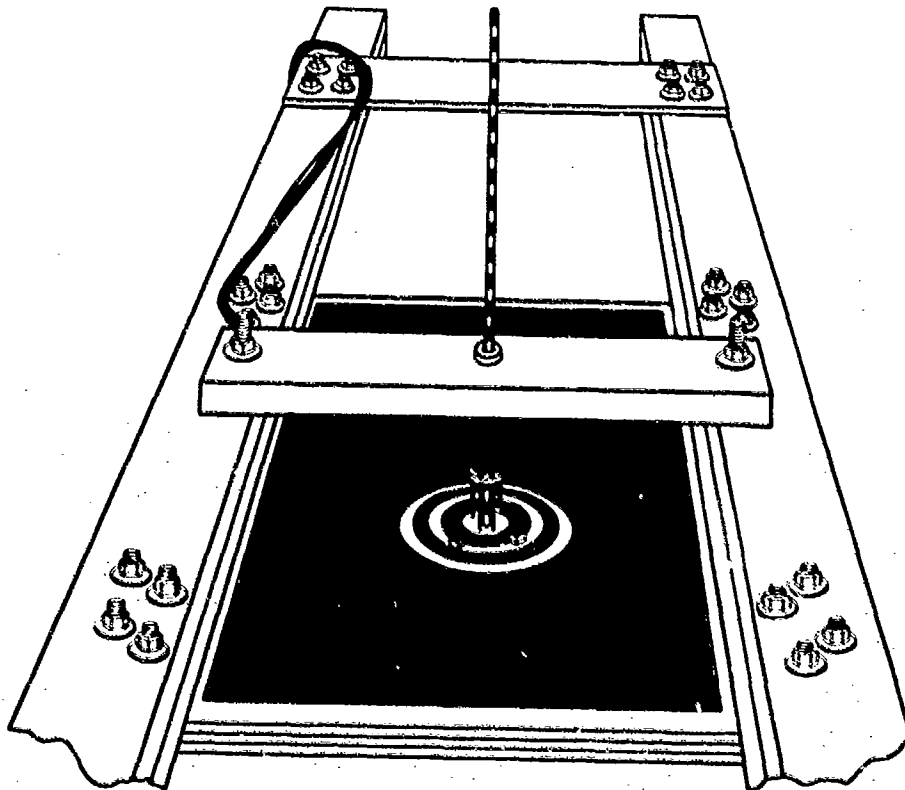


Figure 6. Stainless steel rod used to measure plate-component interaction located in collar holding concentric copper pins.

CANDIDATE COMPOSITE ARMOR DESIGN

Composite armor materials appeared in World War II as flak suits (nylon-steel) which weighed about 4.5 lb/ft² (2.2 g/cm²). A summary of lightweight armor materials through 1959 is given by Mascianica [32]. Although significant work has been performed since the Korean War with lightweight non-metallic materials (ballistic nylon, fiberglass reinforced plastic), little has been done in the realm of blast protection [33]. Eichelberger [34] has recently discussed tank armor evolution and concludes that although composites offer much more efficient protection than steel against HEAT warheads, with little or no loss in efficiency against kinetic energy rounds, the combination of weight and thickness are still deemed impractical. He further stated that many of the composite designs lacked the structural strength to survive multiple-shot attacks.

As a consequence of a review of the material literature, three materials were identified as candidates for use in hybrid composite armor designs which would defeat land mine blast loading. These materials are steel honeycomb, balsa wood and nylon (Kevlar).

Interest in the use of steel honeycomb as a blast isolator was stimulated by the test results of Frye [9]. His tests showed that steel plate sandwiched steel honeycomb of density greater than 30 lb/ft³ (0.48 g/cm³) could survive mine blast without structural fracture. A second stimulus was that David [35] reported that steel plate sandwiched stainless steel honeycomb, when subjected to initial velocity changes of the order of 650 ft/sec, exhibited an increase in ability to dissipate energy by a factor of 2 to 3 over that observed for static loading crushing tests such as reported by McFarland [36].

Balsa wood was considered a candidate because its specific energy absorption was nearly equivalent to that of steel honeycomb for static loading conditions [37]. Furthermore, the spring back of Balsa wood is negligible when the grain is parallel to the load. This property could serve to provide the space necessary for other materials to absorb blast energy.

No study of composite armor would be complete without considering Kevlar. The energy potential to absorb blast loading is significant if a design is chosen which allows the material to stretch and not fracture.

As longitudinal and shear waves traverse a composite material, stresses are transmitted and reflected at each material interface. For design purposes, an estimate of attenuation or amplification to be expected from a given composite layered design is given by Kinslow [38]. The method is based on assumptions which predict stress wave transmissions and reflections on the basis of impedance mismatch relations and criteria.

Based upon the above considerations, the baseline composite armor design that was chosen is shown in Figure 7. The actual materials and layer thicknesses investigated in this study are listed in Table 1. The numbers listed in the table

correspond to the layer numbers shown in Figure 7. Table 1 lists the test number, the material layer and corresponding thickness, the order in which the materials were layered, the total composite plate thickness tested, the total weight of the two foot by two foot plate tested (excluding test frame and bolts), and the areal density of each composite plate. Constraints placed on the composite armor were that it not exceed a 3 inch (7.6 cm) prototype thickness, that its prototype areal density not exceed 65 lb/ft² (320 kg/m²) which is equivalent to about 1.5 inch thick steel, that the prototype cover plate be steel armor and not exceed a 3/4 inch (1.9 cm) thickness, and, finally, that the prototype hull plate be steel armor and not exceed a 1/2 inch (1.27 cm) thickness.

GOALS		
Material	Thickness Inches	Areal Density #/ft. ²
1	0.125	5.10
2	0.125	0.13
3	0.010	0.41
4	0.125	0.94
5	0.010	0.41
6	0.150	0.55
7	0.188	7.69
Total	0.733	16.01
Full Scale	2.93	64

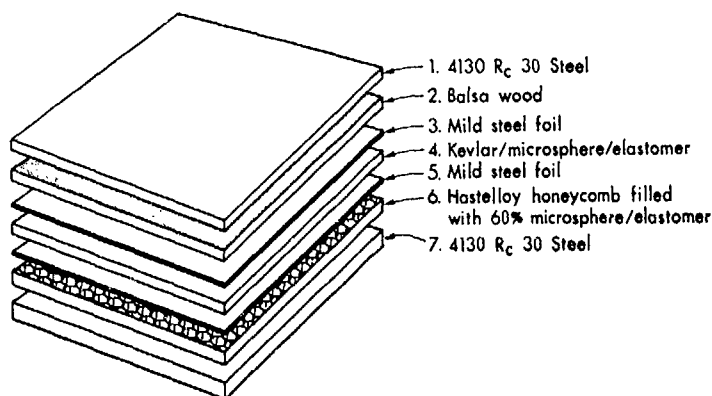


Figure 7. Candidate composite tank floor armor.

The armor design shown in Figure 7 was chosen on the assumption that the steel cover plate would transmit the reflected impulse into the tank in a uniform homogeneous manner. The functions of the steel honeycomb (filled or unfilled with crushable microspheres/elastomer) was to slow down the motion of the cover plate and to attenuate the transmitted shock waves and associated reflected waves by means of crushing, refraction, reflection and viscoelastic phenomena. The steel unbonded membrane cushions the motion of the honeycomb against the Kevlar (woven roving weave impregnated with 20% microspheres/elastomer) via membrane action. The crushable, viscoelastic behavior of the Kevlar adhesive was expected to further attenuate the transmitted stress waves. Since the Kevlar as shown is not bonded at either boundary to the steel membrane separators, the Kevlar is free to move and absorb/slow down the stress waves and honeycomb loading. The second steel membrane encourages a uniform load to be transmitted to the balsa wood. The balsa wood serves to allow the Kevlar to strain and to further absorb the attenuated residual energy to the hull plate. The expectation was for the steel hull plate to react to a

TABLE 1
CANDIDATE MATERIAL COMBINATIONS FOR COMPOSITE BLAST ARMOR

Test Number	Composite Plate Materials							Total Plate Thickness (inch)	Total Plate Weight (pounds)	Plate Area Density Pounds/ft ²
	1	2	3	4	5	6	7			
P1	--	--	--	--	--	--	S-0.25	0.25	40.4	10.1
P2	--	--	--	--	--	--	S-0.313	0.313	50.6	12.7
P3	S-0.125	B-0.156	S-0.010	--	--	HF-0.160	S-0.188	0.69	60.8	15.2
P4	S-0.125	HF-0.160	S-0.010	--	S-0.010	HF-0.140	S-0.188	0.72	65.2	16.3
P5	S-0.125	HU-0.160	S-0.010	--	S-0.010	HU-0.160	S-0.188	0.73	59.2	14.8
P6	--	--	--	--	--	--	S-0.375	0.375	60.6	15.2
P7	S-0.125	B-0.156	S-0.010	B-0.156	S-0.010	B-0.156	S-0.188	0.801	57.0	14.3
P8	S-0.125	A-0.5	--	--	--	--	S-0.188	0.813	50.6	12.7
P9	S-0.125	B-0.156	S-0.010	K-0.165	S-0.010	HF-0.140	S-0.188	0.794	61.75	15.4
P10	S-0.125	B-0.156	S-0.010	K-0.192	S-0.010	HU-0.160	S-0.188	0.841	61.5	15.4
P11	--	--	--	--	--	--	S-0.25	0.25	40.4	10.1
P12	S-0.125	--	--	A-0.25	S-0.010	HU-0.160	S-0.188	0.733	55	13.8
P13	S-0.125	K-0.192	S-0.010	K-0.192	--	--	S-0.188	0.707	57.5	14.4
P14	S-0.125	B-0.159	S-0.010	A-0.25	S-0.010	K-0.146	S-0.188	0.886	55	13.8
P15	S-0.125	B-0.159	S-0.010	B-0.159	S-0.010	K-0.170	S-0.188	0.821	57	14.3

S = steel

B = balsa wood

K = Kevlar

A = air

HF = honeycomb-filled with Stycast CFC-41 containing 60% by volume microspheres

HU = honeycomb-unfilled consists of 1/16 hexagon cell - Hastelloy steel (43.9 #ft³).

nominal load of longer duration (as compared to the initial impulse loading history). Furthermore, it is expected that much of the blast loading will be diffused into the test fixture structure in a manner representative of the prototype.

TRANSIENT PLATE DISPLACEMENT DATA

Two sets of transient plate/rod displacement data were obtained for both quarter scaled monolithic steel and composite armor plates. Transient plate surface displacement data were obtained from the electric shorting of copper pins shown in Figure 5. Transient displacement of the stainless steel rod's center of gravity was obtained from film (Figure 6). Resulting velocities for both the plate and rod were graphically generated from the displacement data. The instantaneous plate velocity was obtained by measurement of the radial plastic strain for each copper pin as described above. Typical data from fifteen quarter scale tests are shown in Figures 8-10.

Data in Figure 8 is from a 0.25 inch (0.64 cm) thick monolithic steel plate model representative of a one-inch thick prototype tank floor. Data in Figure 9 is from a 0.79 inch (1.9 cm) thick composite floor model (Figure 7) representative of a 3.1 inch (7.9 cm) thick prototype tank floor. Finally, data in Figure 10 is from a 0.375 inch (0.95 cm) thick monolithic steel plate model which is equivalent in areal density to that of the composite plate. Also shown in Figures 8-10 are the permanent rod plastic deformation (a), the estimated time of plate-rod separation (b), the permanent deformation of the plate (c), and the maximum elastic deflection of the rod (d). In each figure, circles (○) represent plate surface displacement, squares (◻) represent rod center of gravity displacement, triangles (Δ) represent plate lateral velocity, stars (☆) represent rod center of gravity velocity, and diamonds (◇) represent instantaneous velocity measurements.

The basic characteristics of the steel plate responses are similar to those predicted by Lottero [8] and measured by Wenzel [11], Jones [23], Bodner [26] and Florence [28]. The basic characteristics of the steel rods are identical to those reported by Valentine [29], Abrahamson [30], and Wright [31]. Similarly, the plastic deformation and buckling of the copper pins were identical to that reported by Holloway [25], and White [21].

Close agreement is found between theory based on test data [6] and tests performed in this study if the soil Rayleigh wave velocity is correctly assumed. Design equations proposed by Westine [6] and those measured in this study for 0.25 in (0.64 cm), 0.31 inch (0.79 cm) and 0.38 inch (0.95 cm) thick plates are compared. Westine's design equations predict (using a soil Rayleigh wave velocity of 846 ft/s) maximum residual plate deflections for fixed edge-clamped steel plates of 0.95 inch (2.4 cm), 0.72 inch (1.8 cm) and 0.56 inch (1.4 cm), respectively. In this study, the deflections measured were 0.94 inch (2.4 cm), 0.66 inch (1.7 cm), and 0.55 inch (1.4 cm), respectively. These agreements are excellent. The ratios of maximum deflection to permanent deflection for the scaled monolithic plates were within the range of the ratios obtained by Wenzel [19].

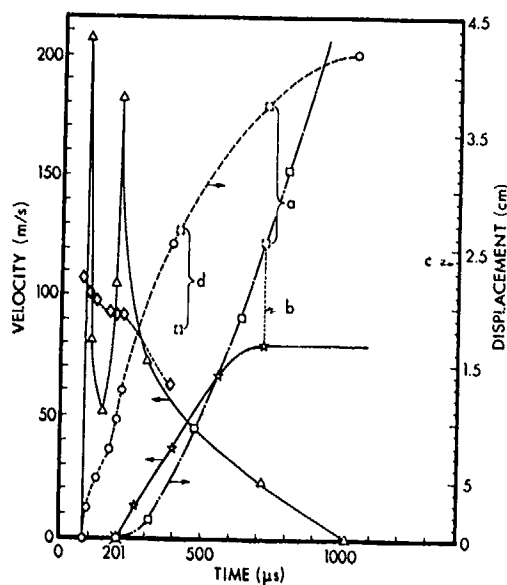


Figure 8. Displacement and Velocity measurements of a 0.25 in. (0.64 cm) baseline steel plate clamped on four edges and a 0.25 in. (0.64 cm) diameter by 16 in. (40.6 cm) length stainless steel rod placed vertically on the center of the plate.

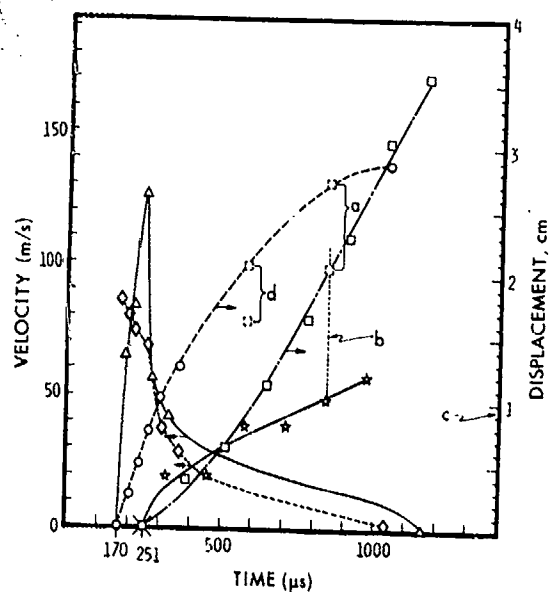


Figure 9. Displacement and Velocity measurements of a composite plate (see Fig. 7) clamped on four edges and a 0.25 in. (0.64 cm) diameter by 18 in. (45.7 cm) length stainless steel rod placed vertically on the center of the plate.

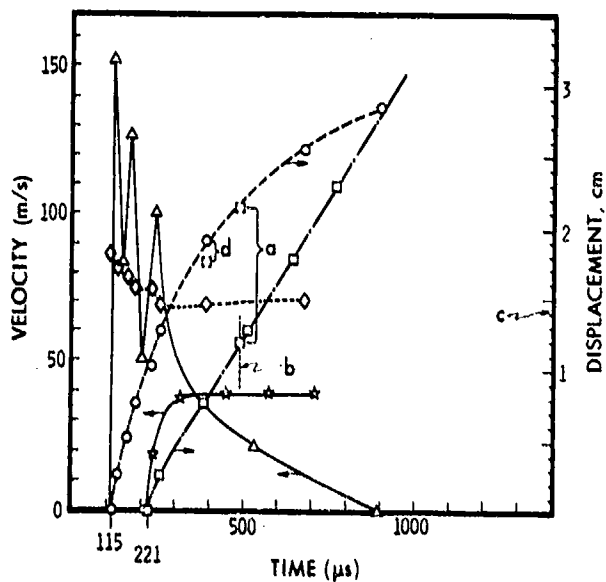


Figure 10. Displacement and velocity measurements of a 0.375 in. (0.95 cm) steel plate clamped on four edges and a 0.25 in. (0.64 cm) diameter by 18 in. (45.7 cm) length stainless steel rod placed vertically on the center of the plate.

LEGEND	
a -	Permanent rod plastic deformation
b -	Estimated time of plate rod separation
c -	Permanent deformation of plate
d -	Maximum elastic deflection of rod
o -	Plate surface displacement
□ -	Rod center of gravity displacement
Δ -	Plate lateral velocity
* -	Rod center of gravity velocity
◇ -	Instantaneous velocity measurements

Quantitative and qualitative data obtained from the rod related to plastic deformation and buckling as a function of impact velocity was also in agreement with that reported elsewhere [29-31].

In the context that only three monolithic steel plates were tested, it is concluded that the data obtained using the specified test apparatus is valid and representative of quarter scaled tank floor response to blast. For the purposes of this paper, steel plate data is considered as a baseline from which to compare the responses obtained from composite floor armor.

DISCUSSION

It is not the purpose of this paper to discuss the theoretical and experimental phenomena of plate, plate/rod and rod deformation induced by blast loading. The purpose is to present reasonably valid data that can be used to estimate the potential advantages and disadvantages of hybrid composite tank floor armor as compared with monolithic steel armor.

Table 2 lists an overview of the data. Various relative ratings were obtained based on six different types of measurements. The six measurements used to rate the composite plates were velocity/force measurements obtained from the copper pins, longitudinal permanent deformation of the stainless steel rod, permanent plate deflection, average maximum velocity of the plate surface, average plate decelerations, and maximum initial acceleration.

Data given in Figure 9 shows the greatest blast loading attenuation of the various combinations of balsa wood, honeycomb (filled and unfilled) and Kevlar composite plates tested, based only on permanent plate deformation. Comparison of Figure 9 with Figure 8 shows that the composite plate (Figure 7) significantly attenuates the blast loading with respect to the baseline for monolithic steel tank floor armor (one-inch thick prototype). Comparison of Figure 9 with Figure 10 shows that the structural response of the composite armor is more or less equivalent to that of a monolithic steel armor of equivalent areal density. However, the shock isolation of the composite armor is significantly greater than that of the equivalent areal density steel armor. This is evidenced by the residual permanent deformation of the steel surface plate (1.42 cm versus 0.94 cm) and the stainless steel rods (0.95 cm versus 0.71 cm) and the G load attenuation given in Table 2.

Model data given in Figures 8-10 must be interpreted, as discussed above, whenever prototype behavior is being estimated. Recall from Figures 2 and 3 that the time scale, impulse and displacements in Figures 8-10 must be adjusted by a factor of four. The model plate accelerations are four times those expected for the prototype plate. But, the forces transmitted by the model plate to the test fixture representative of the adjacent tank structure are one-sixteenth times those expected for the prototype model. Therefore, in the context of shock isolation to critical items within a prototype tank, the shock isolation improvement expected is an order of magnitude greater than that observed from the scaled model tests. Improvement in shock isolation over that

TABLE 2
SIX RELATIVE RATINGS OF BLAST COMPOSITE ARMOR PLATES

Copper Pin Velocity and Force	Stainless Steel Rod Maximum Strain	Permanent Plate Deformation (cm)	Average Maximum Velocity (m/s)	Average Plate Deceleration (G's)	Average Plate Acceleration (G's)	G Attenuation With Respect to P1 & P11
P14	P5 (0.668)	P9 (0.94)	P7 (88)	P13 (84700)	P12 (1,758,000)	.21
P7	P9 (0.671)	P15 (1.19)	P10 (100)	P3 (37800)	P10 (1,878,000)	.22
P9	P8 (0.671)	P5 (1.22)	P5 (105)	P12 (33700)	P9 (2,335,000)	.26
P10	P15 (0.673)	P3 (1.27)	P9 (127)	P4 (29600)	P7 (2,861,000)	.33
P15	P10 (0.673)	P4 (1.28)	P3 (129)	P9 (28600)	P8 (2,425,000)	.34
P12	P14 (0.676)	P14 (1.38)	P14 (132)	P5 (26500)	P5 (3,291,000)	.39
P5	P13 (0.676)	P6 (1.42)	P6 (152)	P10 (26500)	P4 (3,712,000)	.43
P3	P7 (0.676)	P7 (1.46)	P2 (153)	P8 (23500)	P3 (3,936,000)	.46
P8	P8 (0.678)	P10 (1.55)	P8 (168)	P2 (22400)	P14 (3,936,000)	.46
P6	P12 (0.681)	P8 (1.77)	P12 (182)	P11 (16900)	P6 (5,265,000)	.61
P4	P2 (0.683)	P8 (1.77)	P12 (182)	P11 (16900)	P2 (6,123,000)	.72
P2	P3 (0.686)	P12 (1.83)	P1 (208)	P1 (13400)	P15 (8,265,000)	.98
P13	P4 (0.688)	P13 (2.05)	P11 (227)	P6 (12600)	P11 (8,189,000)	1
P1	P1 (0.699)	P1 (2.40)	P15 (228)	P15 (12200)	P1 (8,933,000)	1
P11	P11 (0.704)	P11 (2.56)	P13 (240)	P14 (10200)	P13 (14,825,000)	1.74

inherent to the one-inch baseline floor armor is obviously even greater. Those predicted improvements in shock isolation must, of course, be verified by prototype tests.

It is obvious from Figure 8 that the crew member of a conventional tank must be suspended from the floor if he is to survive the blast effects from a land mine. It is not known if and how the shock loading can indirectly incapacitate the crew member or other critical components within a tank. Speculation made in 1968 by Wenzel [11] is confirmed. Velocity data in Figure 8 confirms the floor velocity estimates made by Norman in 1970 [39] and updated in 1975 [5] which predicted that average tank floor velocity changes could be at least 340 ft/s (104 m/s). Hence, it is apparent that significant shock isolation improvement is needed if tank mission survivability against mine blasts is to be realized.

CONCLUSION AND RECOMMENDATIONS

Data was presented to confirm that the shock isolation of monolithic steel floor armor to mine blast is unacceptable for the survivability of critical items within a tank. Scaled tests showed that a composite armor consisting of balsa wood, Kevlar and steel honeycomb offers a significant improvement in shock attenuation over that of monolithic steel armor plate of equivalent areal density. Prototype tests should be performed to evaluate the predicted improvement in shock isolation of the given composite design. Other hybrid composite designs should also be evaluated.

ACKNOWLEDGEMENT

The study presented in this paper was performed under contract no. DAAK30-79-R-0023. The author acknowledges the guidance, advice and information provided to him by Dr. John Jellinek and Mr. Victor Pagano of the U.S. Army Tank-Automotive Research and Development Command.

REFERENCES

1. Engineering Design Handbook: Armor and Its Applications, Army Materials Command Pamphlet, AMCP 706-170, Alexandria, Virginia, November 1973 (Classified).
2. MIL-A-12560D (MR) ARMOR PLATE, STEEL, WROUGHT, HOMOGENEOUS.
3. Hennessy, J. M., "Compilation and Evaluation of Steel Armor Plate Performance Against Mine Blast," Army Tank-Automotive Command, TACOM TR 11494, June 1972 (Classified).
4. Haskell, D. F., "Deformation and Fracture of Tank Bottom Hull Plates Subjected to Mine Blast," BRL TR-1587, May 1972.
5. Norman, R. M., "Rupture as a Function of Deformation in Flat Plates Exposed to HE Mine Blast," Army Material Systems Analysis Activity, AMSAA TR-127, May 1975.

6. Westine, P. S., and Hokanson, J. C., "Procedures to Predict Plate Deformations from Land Mine Explosions," Army Tank-Automotive Command, TR-12049, August 1975.
7. Sedgwick, R. T., Gaffney, E. S., Wilkins, E. E., and Walsh, L. J., Numerical Techniques for Predicting the Effects of Buried Explosive Charges," Systems, Science and Software Final Report SSS-R-73-1968, La Jolla, California, December 1973.
8. Lottero, R. E., and Kimsey, K. D., "A Comparison of Computed Versus Experimental Loading and Response of a Flat Plate Subjected to Mine Blast," Ballistic Research Laboratory, ARBRL-MR-02807, January 1978.
9. Frye, W. B., "Engineer Design Test of Carrier, M113, Double Bottom Hull," Aberdeen Proving Grounds, Report no. APG-MT-3331, October 1969 (Classified).
10. Strother, C. E., "An Exploratory Investigation of the Threat to Armored Vehicle Personnel from Mine-Induced Shock Motion," Naval Ship Research and Development Center, TR C-2711, April 1968 (Classified).
11. Wenzel, A. B., Young, R. C., and Russell, C. R., "Structural Response and Human Protection from Land Mines," Army Material Command Sheridan Project Office, TR-3481, June 1968.
12. Hirsch, A. E., "Effects of Underwater Shock on Personnel," David Taylor Model Basin, DTMB-C-1871, August 1965 (Classified).
13. Hirsch, A. R., "Man's Response to Shock Motions," David Taylor Model Basin, DTMB - 1797, January 1964 (Classified).
14. Crash Survival Design Guide, Army Air Mobility Research and Development Laboratory, USAAMRDL TR-71-22, October 1971.
15. King, W. F. and Mertz, H. J., "Human Impact Response," Plenum Press, New York, 1973.
16. Schuring, D. J., "Scale Models in Engineering," Pergamon Press, New York, 1977.
17. Baker, W. E., Westine, P. S., and Dodge, F. T., "Similarity Methods in Engineering Dynamics, Theory and Practice of Scale Modeling," Hayden, Rochelle Park, New Jersey, 1973.
18. Baker, W. E., "Explosions in Air," University of Texas Press, Austin, Texas, 1973.
19. Wenzel, A. B., and Esparza, E. D., "Measurements of Pressures and Impulses at Close Distances from Explosive Charges Buried and in Air," Army Mobility Equipment Research and Development Center, TR SwRI02-31231, August 1972.

20. White, M. P., and Griffis, L., "The Permanent Strain in a Uniform Bar Due to Longitudinal Impact," Journal of Applied Physics, s. A, December 1947, 337-343.
21. White, M. P., and Griffis, L., "The Propagation of Plasticity in Uniaxial Compression," Journal of Applied Mechanics, v. 15, September 1948, 256-260.
22. Von Karman, T., and Deevey, P., "The Propagation of Plastic Deformation in Solids," Journal of Applied Physics, v. 21, October 1950, 987-994.
23. Jones, N., Uran, T. O., and Tekin, S. A., "The Dynamic Plastic Behavior of Fully Clamped Rectangular Plates," International Journal of Solids Structures, v. 6, 1970, 1499-1512.
24. Perrone, N., and Bhadra, P., "A Simplified Method to Account for Plastic Rate Sensitivity with Large Deformations," Journal of Applied Mechanics, v. 46, December 1979, 811-816.
25. Holloway, G., and Shelton, A., "The Plastic Behavior of Annealed OFHC Copper," Journal Mechanical Engineering Science, v. 21, no. 4, 1979, 221-233.
26. Bodner, S. R., and Symonds, P. S., "Experiments on Viscoplastic Response of Circular Plates to Impulsive Loading," Brown University Report N00014-0860/4, July 1977.
27. Jones, N., "Recent Progress in the Dynamic Plastic Behavior of Structures," Massachusetts Institute of Technology Report 78-1, January 1978.
28. Florence, A. L., "Circular Plate Under a Uniformly Distributed Impulse," International Journal Solids Structures, v. 2, 1966, 37-47.
29. Valentine, M. B., and Whitehouse, G. D., "Transient Deformation of Slender Rods Impacting Rigid Plates," American Society of Mechanical Engineers, paper number 171-Vibr-93, June 1971.
30. Abrahamson, G. R., and Goodier, J. N., "Dynamic Flexural Buckling of Rods Within an Axial Plastic Compression Wave," Journal of Applied Mechanics, June 1966, 241-247.
31. Wright, T. W., "Buckling of Long Rod Penetrators," Ballistic Research Laboratories memorandum report no. 2296, May 1973.
32. Mascianica, F. S., "Lightweight Armor Materials," Watertown Arsenal Laboratories, June, 1959.
33. Ballistic Technology of Lightweight Armor - 1979, AMMRC TR 79-10, February 1979 (Classified).

34. Eichelberger, R. J., "Tank Armor Evolution," Journal of Defense Research Armored Fighting Vehicles Special Issue 79-1, January 1980, 115-123
35. David, C. V., "Energy Absorption by Dynamic Crushing," General Atomic report GA-6625, August 1965.
36. McFarland, R. K., "Hexagonal Cell Structure Under Post-Buckling Axial Load," AIAA Journal, v. 1, no. 6, June 1963, 1380-1385.
37. Daigle, D. L., and Lonborg, J. O., "Evaluation of Certain Crushable Materials," Jet Propulsion Laboratory, Technical Report no. 32-10, January 1961.
38. Kinslow, R., "Stress Waves in Laminated Materials," AIAA Paper no. 67-140, AIAA 5th Aerospace Sciences Meeting, January 1967.
39. Norman, R. M., "Deformation in Flat Plates Exposed to HE Mine Blast," Army Material Systems Analysis Agency, Technical Memo 74, May 1970.

SESSION II: DYNAMIC RESPONSE

Chairman: M. S. Hirschbein
Aerospace Engineer
NASA-Lewis Research Center

DYNAMIC STABILITY OF STRUCTURAL ELEMENTS SUBJECTED TO STEP-LOADS 87

G. J. Simitzes
Georgia Institute of Technology

TRANSIENT ANALYSIS OF DOUBLE HULLS IMPINGED UPON BY INCIDENT
UNDERWATER EXPLOSION WAVES 108

H. Huang,
S. Halperson, and
D. Curtis
Naval Research Laboratory

DYNAMIC ELASTIC-PLASTIC RESPONSE OF UNSTIFFENED AND STIFFENED
PANELS TO PRESSURE LOADINGS. 126

L. J. Mente
W. N. Lee
Kaman Avidyne

DYNAMIC STABILITY OF STRUCTURAL ELEMENTS SUBJECTED TO STEP-LOADS

GEORGE J. SIMITSES
Professor
Georgia Institute of Technology
Atlanta, Georgia 30332

ABSTRACT

The dynamic stability of two mechanical models, subjected to suddenly applied loads of finite duration, is presented. These models are characteristic of structural elements and configurations, which (a) have initial geometric imperfections, (Model A) and (b) are subject to unstable bifurcation (Model B). The emphasis is placed on presenting a clear definition of the concept of dynamic stability and clear criteria and related estimates. For each model a complete stability analysis is presented for quasistatic application of the load as well as for dynamic application (suddenly applied loads with finite duration, including the extreme cases of infinite duration and ideal impulse).

I. INTRODUCTION

Dynamic stability of elastic structures has drawn considerable attention in the past thirty years. The importance of the subject lies primarily in the constant demand for lightweight efficient structures, which requires a good understanding of how structures respond to loads that induce dynamic effects.

The term "Dynamic Stability" encompasses many classes of problems and it has been used, by the various investigators, in connection with a particular study. Therefore, it is not surprising that there are various interpretations of the meaning of the term.

The class of problems falling in the category of parametric excitation are the best defined, conceived and understood problems of dynamic stability. An excellent treatment and bibliography can be found in the book by V.V. Bolotin [1].

Moreover, many authors refer to problems of the "follower force" type as problems of dynamic stability [2-3]. The primary reason for this is that critical conditions can be obtained (in many cases) only through the use of the "kinetic" or "dynamic" approach to static stability problems (flutter instead of divergence type of instability).

In addition, problems of aeroelastic instability and flow-induced instability (fluid flowing through pipes) also fall under the general heading of dynamic stability.

A large class of structural problems that has received attention recently and does qualify as a category of dynamic stability is that of impulsively loaded configurations and configurations which are suddenly loaded with loads

of constant magnitude and infinite duration. These two types of loads may be thought of as mathematical idealizations of blast loads of (a) large decay rates and small decay times and (b) small decay rates and large decay times respectively. For these loads, the concept of dynamic stability is related with the observation that for sufficiently small values of the loading the system simply oscillates about the near static equilibrium point and the corresponding amplitudes of oscillation are sufficiently small. If the loading is increased, some systems will experience large amplitude oscillations or in general divergent type of motion. For this phenomenon to happen the configuration (turns out) must possess two or more static equilibrium positions and "tunneling-through" [4] occurs by having trajectories that can pass through an unstable static equilibrium point. Consequently, the methodologies developed by the various investigators are for structural configurations that exhibit snap-through buckling when loaded quasistatically.

Solutions to such problems started appearing in the open literature in the early 1950's. Hoff and Bruce [5] considered the dynamic stability of a pinned half-sine arch under a half-sine distributed load. The ideal impulse problem as well as the case of a suddenly applied load with constant magnitude and infinite duration were considered in this paper. Budiansky and Roth [6] in studying the axisymmetric behavior of a shallow spherical cap under suddenly applied loads defined the load to be critical, when the transient response increases suddenly with very little increase in the magnitude of the load. This concept was adopted by numerous investigators [7] in the subsequent years because it is tractable to computer solutions. Conceptually, one of the best efforts in the area of dynamic buckling, under impulsive and suddenly applied loads, is the work of Hsu and his collaborators [8-11]. In his studies, he defined sufficiency conditions for stability and sufficiency conditions for instability, thus finding upper and lower bounds for the critical impulse or critical sudden load. Independently, the present author [12] in dealing with the dynamic buckling of shallow arches and spherical caps termed the lower bound as a minimum possible critical load (MPCL) and the upper bound as a minimum guaranteed critical load (MGCL).

The purpose of the present paper is twofold. First, it is intended to clearly demonstrate the concept of dynamic instability, including criteria and estimates, for impulsive and suddenly applied loads of infinite duration through some simple mechanical models (one- and two-degrees of freedom). Second, to extend the concept to the case of suddenly applied loads of finite duration. These models are representative of imperfection sensitive structures, and of systems that exhibit unstable bifurcation (shallow arch and spherical cap).

II. MODEL A. GEOMETRICALLY IMPERFECT MODEL

Consider the model shown on Fig. 1. This model consists of two rigid bars of equal length, L , pinned together. The left bar is pinned on an immovable support, A, while the right end of the second bar is pinned on a movable support, C, and loaded by a horizontal constant-directional force P . A linear spring of stiffness k connects the bar common pin, B, to an immovable

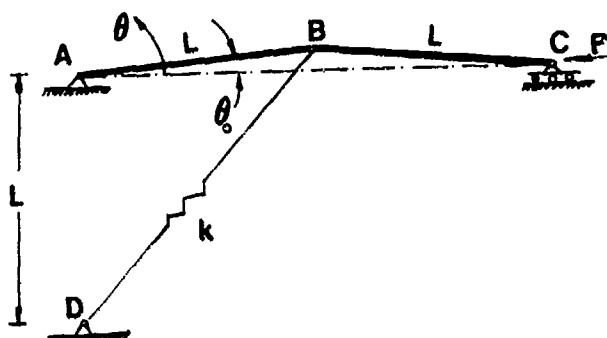


Figure 1. Geometry and Sign Convention (Model A).

support, D, which is L units directly below support A. The initial geometric imperfection, θ_0 , is an angle between the horizontal line, joining supports A and C, and bar AB (or BC). The deformed position is characterized by angle θ , as shown (in its positive direction).

II - 1. Static Analysis

The stability analysis of this model under quasi-static application of the load P is performed by employing the energy approach. Through this approach, equilibrium is characterized by

$$dU_T/d\theta = 0 \quad (1)$$

where U_T is the total potential, and the character of equilibrium (stable or unstable) by the sign of the second derivative.

The total potential is:

$$\bar{U}_T^P = U_T/kL^2 = [\sqrt{1 + \sin \theta} - \sqrt{1 + \sin \theta_0}]^2 - p (\cos \theta_0 - \cos \theta) \quad (2)$$

where $p = 2P/kL$, and U_T^P denotes the nondimensionalized total potential. The superscript p implies "under load p."

The static equilibrium points are characterized by

$$p = [\sqrt{1 + \sin \theta} - \sqrt{1 + \sin \theta_0}] \cot \theta / \sqrt{1 + \sin \theta} \text{ for } \theta \neq 0 \quad (3)$$

Note that, for $\theta_0 = 0$ equilibrium is characterized by

$$\text{either } \theta = 0 \text{ or } p = \cot \theta (1 - 1/\sqrt{1 + \sin \theta}) \quad (4)$$

Equilibrium positions are plotted on Fig. 2 as p versus $\theta - \theta_0$ for various values of the geometric imperfection θ_0 . The stability test reveals that the dashed line positions are stable, while the solid line positions are unstable and snapping (violent buckling) takes place through the existence of a limit point. Also note that positions characterized by negative values for $\theta - \theta_0$ (not shown herein) are stable and there is no possibility of buckling. Therefore, our interest lies in the area of $\theta_0 > 0$ and $\theta - \theta_0 > 0$.

II - 2. Ideal Impulse

Assume that the load is suddenly applied with very short time, so that the impulse, (Pt_0) , can be imparted instantaneously into the system as initial kinetic energy. Through impulse-momentum, one can easily derive the following relation

$$(Pt_0) = \left(\frac{8}{24} + \sin^2 \theta_0 \right) \frac{ml}{\sin \theta_0} (\dot{\theta}_0) \quad (5)$$

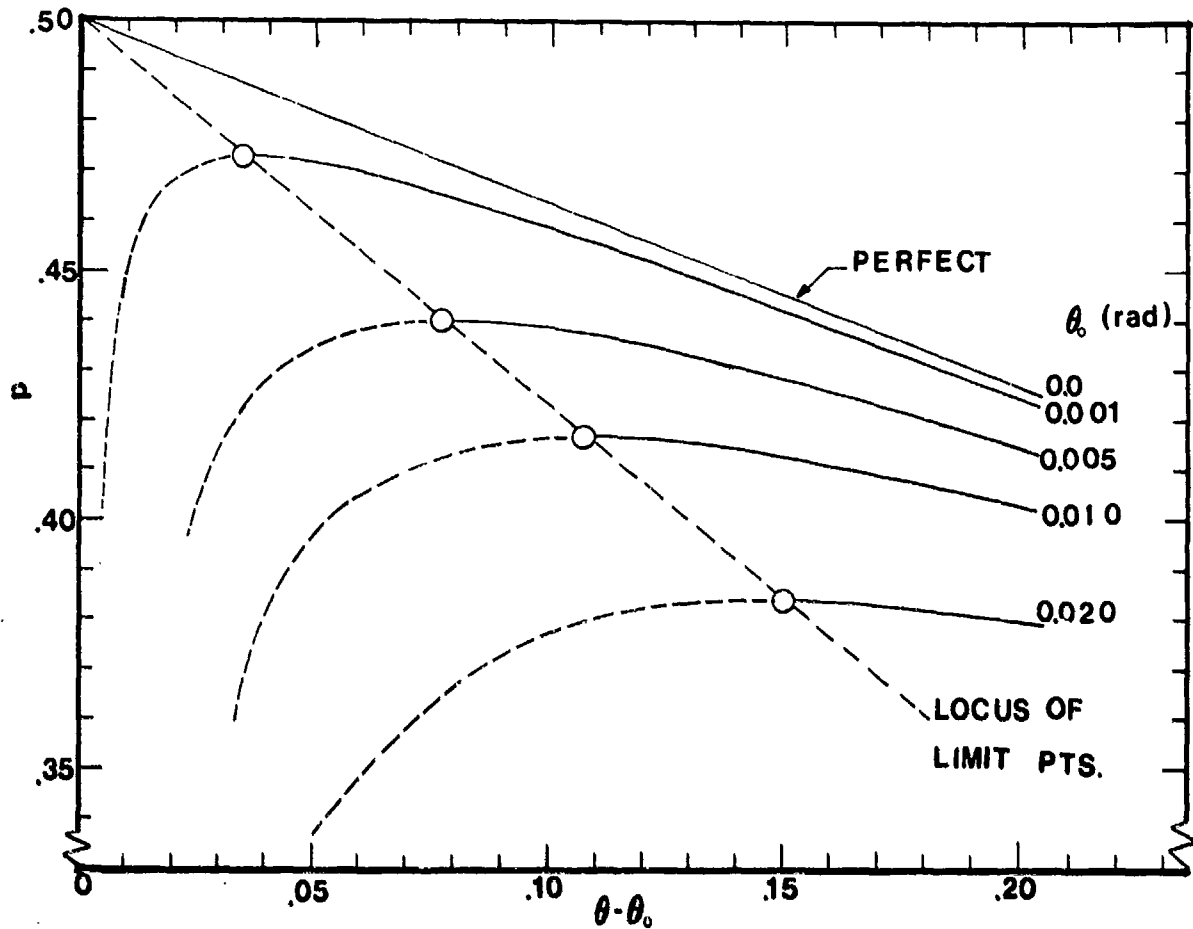


Figure 2. Load-Displacement Curves (Model A).

where m is the mass of each rigid bar, $\dot{\theta}_0 = \frac{d\theta}{dt}$ at $\theta = \theta_0$, and t_0 the duration time. Since the system is conservative, then

$$U_T^0 + T^0 = \text{const. } T_1^0 \quad (6)$$

where U_T^0 denotes the total potential for $p = 0$ [see Eq. (2)], T^0 is the kinetic energy, given by

$$T^0 = mL^2 (1 + 3 \sin^2 \theta) (\dot{\theta})^2 / 3 \quad (7)$$

and T_1^0 is the initial kinetic energy, imparted by the impulsive load. Note that the constant in Eq. (6) is T_1^0 because $U_T^0(\theta = \theta_0) = 0$. Also, by Eqs. (7) and (5)

$$T_1^0 = \frac{mL^2}{3} (1 + 3 \sin^2 \theta_0) \frac{\sin^2 \theta_0}{m^2 L^2 \left(\frac{8}{24} + \sin^2 \theta_0 \right)^2} (pt_0)^2 \quad (8)$$

In order to understand the "concept" of stability or instability under an impulsive load for this one-degree-of-freedom model, let us consider Fig. 3, which is a plot of \bar{U}_T^0 versus $\theta - \theta_0$.

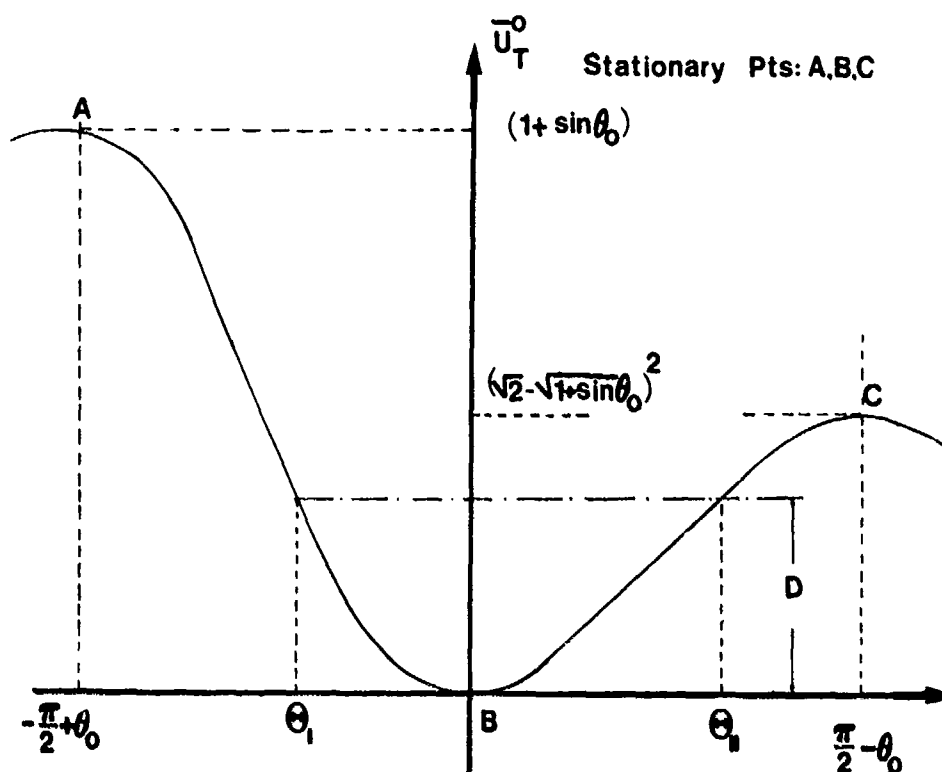


Figure 3. "Zero-Load" Total Potential Curve (Model A).

According to Eq. (6), and since T^0 is positive definite, motion is possible if and only if

$$T_i^0 - U_T^0 \geq 0 \quad (9)$$

This implies that, for a given initial kinetic energy, and consequently a given impulse, Eq. (8), say $T_i^0 = D$ (see Fig. 3), motion is confined in the region $\theta_I < \theta - \theta_0 < \theta_{II}$. It is clearly seen then that, as long as $T_i^0 = D < kL^2 \times (\sqrt{2} - \sqrt{1 + \sin \theta_0})^2$, the motion of the system is bounded and it contains only the stable "zero load" static equilibrium point, B. Such a motion is termed "unbuckled." For the motion to cease to be "unbuckled," i.e. to become unbounded, D must be, at least, equal to the value of U_T^0 at the unstable point C. Then that point (C) can be reached with zero velocity and the motion can become unbounded. Clearly if D is even slightly higher than the U_T^0 - value at point C, the motion does become unbounded and it can contain other static equilibrium points, such as point C. Such a motion is called "buckled" and a critical condition exists when the impulse is large enough to satisfy the relation

$$T_i^0 = U_T^0(C) \quad (10)$$

Introducing nondimensionalized time and load parameters

$$\tau_0 = \tau_0 (k/m)^{1/2} \quad p = 2P/kL \quad (11)$$

and making use of Eqs. (10) and (8), one obtains

$$(p\tau_o)_{cr} = 2\sqrt{3} \frac{(\frac{8}{24} + \sin^2\theta_o)(\sqrt{2} - \sqrt{1+\sin\theta_o})}{\sin\theta_o \sqrt{1+3\sin^2\theta_o}} \quad (12)$$

Two observations are worth mentioning at this point: (a) Because this is a one-degree-of-freedom model, the critical impulse $(p\tau_o)$ given by Eq. (12) represents both the minimum possible (MPCL) and minimum guaranteed (MGCL) values as defined in [12]; (b) Although, the concept presented so far is clear and it leads to a criterion and estimate of the critical condition, it might be impractical when applied to real structures. In the particular example shown so far, it is clear that, according to the presented concept of dynamic instability, "buckled" motion is possible if the system is allowed to reach the position $\theta = \pi/2$. In many cases such positions may be considered excessive, especially in deflection-limited designs. In such cases, if θ cannot be larger than a specified value, then the allowable impulse is smaller and its value can be found from Eq. (10), if C is replaced by the maximum allowable value of θ , say θ_L . In this case

$$(p\tau_o)_{allowable} = 2\sqrt{3} \frac{(\frac{8}{24} + \sin^2\theta_o)(\sqrt{1+\sin\theta_L} - \sqrt{1+\sin\theta_o})}{\sin\theta_o \sqrt{1+3\sin^2\theta_o}} \quad (13)$$

II - 3. Constant Load of Infinite Duration

The concept of stability, for this case, is also based on the definition of "buckled" or "unbuckled" motion. For this case, the sum of the total potential and kinetic energy is zero

$$U_T^p + T^p = 0 \quad (14)$$

Fig. 4 shows plots of \tilde{U}_T^p versus $\theta - \theta_o$ for various values of the applied load, p . It is seen from this figure that for $p < 0.632$ motion is confined between the origin and $\theta - \theta_o = \Lambda$. A critical condition exists when the motion can become unbounded by including position A (buckled motion). Thus the critical load is found by solving the following equations, simultaneously

$$\begin{aligned} \tilde{U}_T^p &= 0 \text{ and } p = [\sqrt{1+\sin\theta} - \sqrt{1+\sin\theta_o}] \frac{\cot\theta}{\sqrt{1+\sin\theta}} \\ \text{with } \frac{d^2\tilde{U}_T^p}{d\theta^2} &< 0 \end{aligned} \quad (15)$$

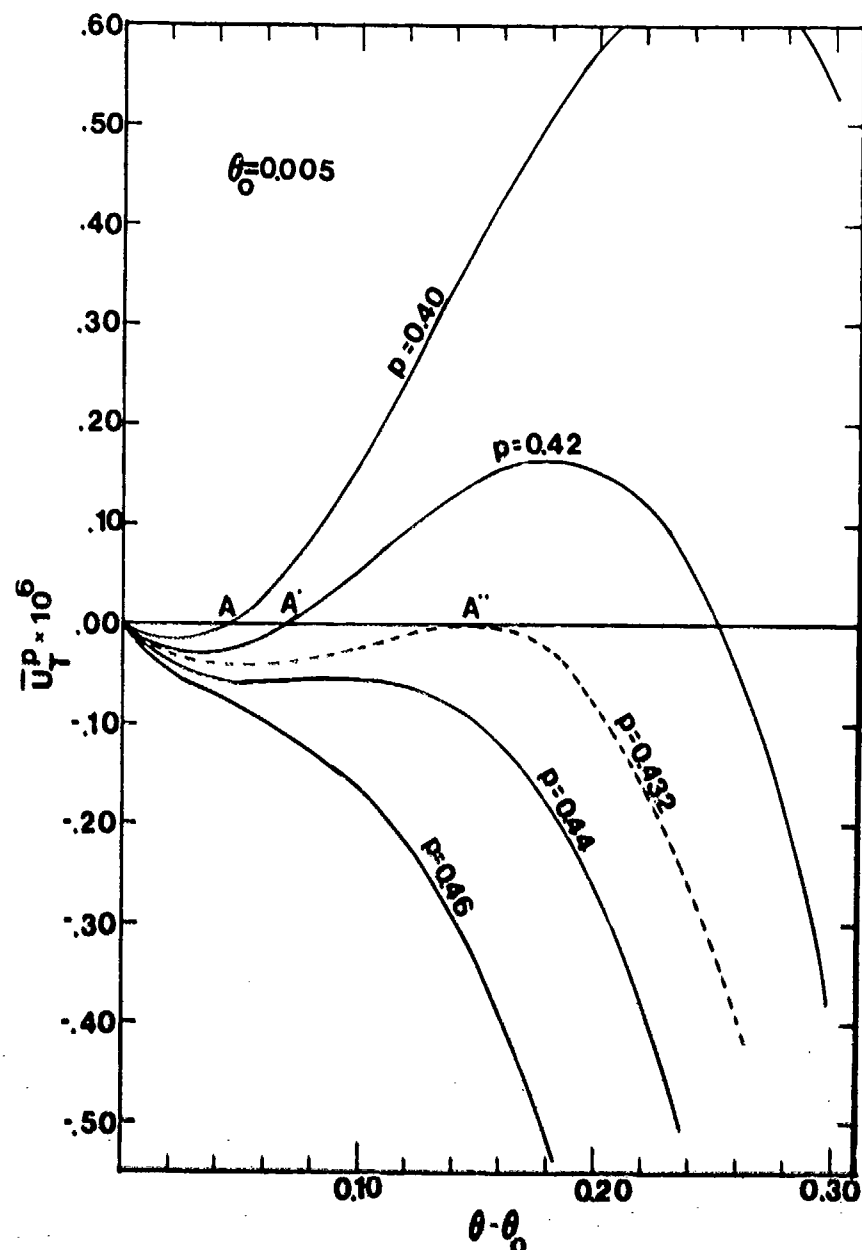


Figure 4. Total Potential Curves (Model A; $\theta_0 = 0.005$).

The inequality condition ensures that $\bar{U}_T^p = 0$ at an unstable equilibrium point. The results, for this model, are presented graphically on Fig. 5. For this load case also, (NPCL) and (MGCL) are the same.

II - 4. Constant Load of Finite Duration

The concept of dynamic stability and the related criterion and estimate for this load case, are extensions of those used in the previous two dynamic cases. Moreover, these previous cases are limiting cases of the present one.

Since the system is conservative, one can write

$$\bar{U}_T^P + \bar{T}^P = 0 \quad 0 \leq \tau \leq \tau_0 \quad (16)$$

where τ_0 is a time parameter characterizing the load duration time.

Similarly,

$$\bar{U}_T^0 + \bar{T}^0 = \bar{U}_T^0(\tau_0) + \bar{T}^0(\tau_0); \tau \geq \tau_0 \quad (17)$$

The following observations are made concerning the boundedness of motion for load p applied for τ_0 units. First, it is recognized that if the applied load is smaller than the critical load for the case of constant load and infinite duration (see Fig. 4), then the system will simply oscillate about the near stable static equilibrium position and there is no possibility of "buckled" motion, regardless of the duration time. Therefore, dynamic instability can exist, if at all, only for loads greater than the critical load of case II-3. The question, then, is for how long, τ_0 , must such a load be applied in order for the motion to become unbounded (buckled). This question and its answer are best understood by referring to Fig. 6.

In Fig. 6 the total potential for zero load, \bar{U}_T^0 , and for load, p , greater than the case II-3 critical load, \bar{U}_T^P , are plotted versus $\theta - \theta_0$. Let θ denote the position θ reached by the system at the end of the duration time, τ_0 . A critical condition can exist (buckled motion is possible), if the load p , applied for τ_0 units, has imparted sufficient energy into the system, so that it can reach position $A[\bar{U}_T^0(\frac{\pi}{2} - \theta_0)]$ with zero kinetic energy. Note that position A corresponds to the unstable static equilibrium position under zero load.

On the basis of these observations, one is interested in estimating the critical condition (the combination of p and τ_0 for this dynamic instability to exist). This is accomplished through the following steps: (a) at the instant the load p is released, τ_0 , there exists continuity in kinetic energy,

$$T^P(\tau_0) = T^0(\tau_0) \quad \text{or} \quad T^P(\theta) = T^0(\theta) \quad (18)$$

$$(b) \text{ from Eq. (16)} \quad T^P(\theta) = -\bar{U}_T^P(\theta) \quad (19)$$

(c) use of Eqs. (19) and (18) in Eq. (17) yields

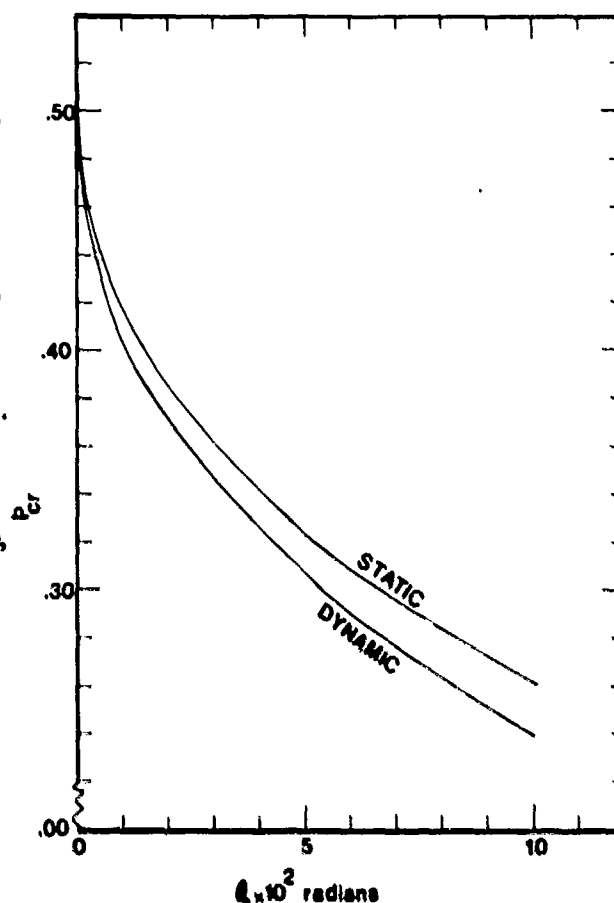


Figure 5. Static and Dynamic Critical Loads (Model A).

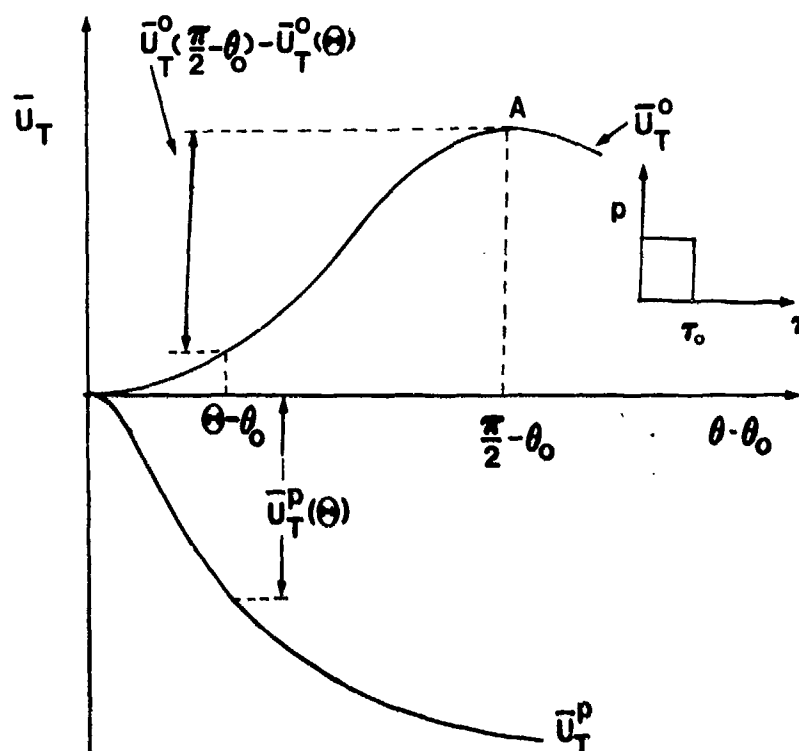


Figure 6. Total Potential Curves (Model A).

$$\bar{U}_T^0\left(\frac{\pi}{2} - \theta_0\right) = \bar{U}_T^0(\theta) - \bar{U}_T^p(\theta); \quad (20)$$

$$\text{which for this model becomes } (\sqrt{2} - \sqrt{1 + \sin \theta_0})^2 = p (\cos \theta_0 - \cos \theta) \quad (21)$$

(d) From Eq. (16), through Eqs. (2) and (7), one may find the expression for $d\theta/d\tau$ and consequently

$$\tau_0 = \int_{\theta_0}^{\theta} \frac{(1/3 + \sin^2 \theta) d\theta}{[p(\cos \theta_0 - \cos \theta) - (\sqrt{1 + \sin \theta} - \sqrt{1 + \sin \theta_0})^2]^{\frac{1}{2}}} \quad (22)$$

Thus, for a given p , calculate θ from Eq. (21), and the corresponding, τ_0 from Eq. (22). Note, that computationally, it is easier to assign values of θ (from θ_0 to $\frac{\pi}{2}$) and compute the corresponding values of p , from Eq. (21) and τ_0 , from Eq. (22).

The results for this model are presented graphically on Fig. 7, as plots of p_{cr} versus τ_0 for various values of θ_0 . Note that, as $\tau_0 \rightarrow \infty$, p_{cr} approaches the value of p_{cr} for constant load and infinite duration. The results also show that for extremely small $(\theta - \theta_0)$ -values, $(p_{cr})_{cr}$ is the same as the ideal impulse. For this case also, the (MPCL) and (MGCL) are the same.

Note, from Fig. 7, that for small duration times ($\tau_0 \lesssim 0.1$), the critical loads are extremely high. This suggests that, in real structures, there might be a critical condition in material behavior, rather than in system response.

Finally, in this case also, if one deals with a deflection-limited

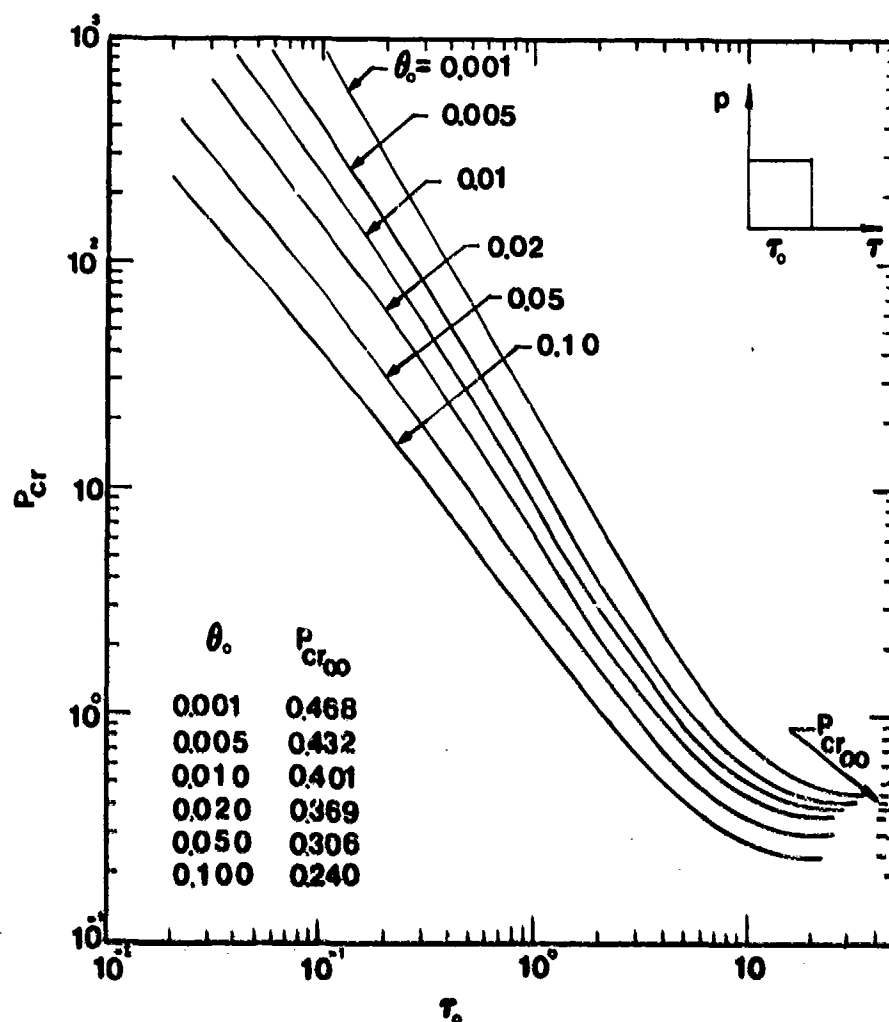


Figure 7. Critical Conditions for Step-Loads
(P_{cr} vs τ_0 or p vs τ_0 ; Model A).

design, say $0 \leq A$, $U_T^0(\frac{\pi}{2} - 0)$ must be replaced by $U_T^0(A - \theta_0)$ in Eq. (21).

III. MODEL B. A SNAP-THROUGH MODEL

Consider the model shown on Fig. 8, which consists of three equal length rigid bars. The three bars are pinned to each other, and they are connected with rotational springs of stiffness β (linear). The left bar is pinned onto an immovable support, while the right bar is pinned onto a movable support, which in turn is connected to a wall through a linear extensional spring (horizontal) of stiffness k (linear). The middle bar is originally horizontal and the loading consists of two equal concentrated forces, P , applied at the ends of the middle bar and remaining vertical. The original angle between the horizontal line, joining the supports and the end bars is α . The angle between the horizontal and the left bar in a deformed state is θ , while the angle between the horizontal and the right bar is φ .

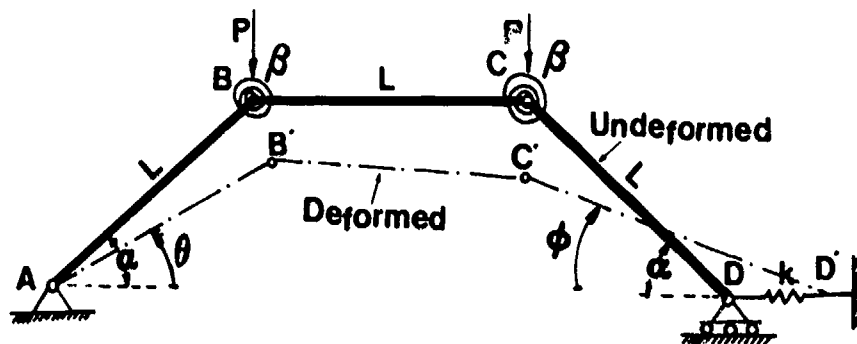


Figure 8. Geometry and Sign Convention (Model B).

This is a two-degree-of-freedom model, and as it will be seen, from the ensuing discussion, certain new features enter into the solution.

Assuming that α , θ , and ϕ are small angles such that their sine can be well approximated by the angle itself and the cosine by one minus half of the angle squared, then the expression for the total potential is given by

$$U_T = \frac{1}{2} \beta [5\theta^2 + 5\phi^2 - 8\phi\theta - 2\theta\alpha - 2\phi\alpha] + \frac{KL^2}{2} (\alpha^2 - \theta^2 - \phi^2 + \phi\theta)^2 - PL(2\alpha - \theta - \phi) \quad (23)$$

The independent variables are ϕ and θ and the symmetric response mode is characterized by $\theta = \phi$.

New variables r & s , are introduced such that the symmetric response is characterized by $s = 0$.

These are

$$\theta = \sqrt{\beta} (r - s) \quad \phi = \sqrt{\beta} (r + s) \quad (24)$$

$$\text{or } r = (\theta + \phi)/2\sqrt{\beta} \quad s = (\phi - \theta)/2\sqrt{\beta} \quad (25)$$

where $\tilde{\beta} = \beta/kL^2$ is a nondimensionalized rotational spring stiffness parameter. Through introduction of additional nondimensionalized parameters

$$\bar{U}_T = \frac{U_T}{\beta^2 kL^2} \quad p = \frac{P}{kL \tilde{\beta}^{3/2}} \quad (26)$$

$$\text{and by letting } \alpha^2 = \tilde{\beta}\Lambda \quad (27)$$

the following expression for the total potential is obtained.

$$\bar{U}_T = (r^2 + 9s^2 - 2\sqrt{\Lambda} r + \Lambda) + \frac{1}{2} (\Lambda - r^2 - 3s^2)^2 - 2p(\sqrt{\Lambda} - r) \quad (28)$$

IV - 1. Static Analysis

It can easily be shown that, if $\tilde{\beta} = 0$ (no rotational springs), the system is unstable for zero load, $P = 0$, and thus the $\tilde{\beta} = 0$ case is excluded from the present discussion, which also allows the nondimensionalization given by Eqs. (27) and (28) (division by a nonzero number).

The static analysis is performed by employing the energy approach.

For equilibrium $\frac{d\bar{U}_T}{dr} = 0 = 2(r - \sqrt{\Lambda}) - (\Lambda - r^2 - 3s^2) 2r + 2p$ (29)

and

$$\frac{d\bar{U}_T}{ds} = 0 = 18s - (\Lambda - r^2 - 3s^2) 6s \quad (30)$$

By introducing a new load parameter, $Q = p - \sqrt{\Lambda}$ (31)

the equilibrium equations, Eqs. (29) and (30) become

$$(\Lambda - 1 - r^2 - 3s^2) r = Q; \quad s(\Lambda - 3 - r^2 - 3s^2) = 0 \quad (32)$$

There are two possible solution to Eqs. (32)

(i) Symmetric response $s \equiv 0$, and

$$(\Lambda - 1 - r^2) r = Q \quad (33)$$

(ii) Existence of asymmetric response, $s \neq 0$

$$\Lambda - 3 = r^2 + 3s^2; \quad 2r = Q \quad (34)$$

The equilibrium positions, Eqs. (32), are plotted on Fig. 9 as a load-deflection, Q - r , curve.

On the basis of the results and by performing the stability test (second derivatives), the following conclusions are drawn.

(a) For $\Lambda < 1$ there is no possibility of buckling

(b) For $1 \leq \Lambda \leq 3$ the response is symmetric ($s \equiv 0$) and buckling occurs through the limit point (pt. C on Fig. 9). Positions between A and C are stable, and the critical load is given by

$$Q_{cr} = \frac{2\sqrt{\Lambda-1}}{3} \quad \text{or} \quad P_{cr} = \sqrt{\Lambda} + \frac{2\sqrt{\Lambda-1}}{3} \quad (35)$$

(c) For $3 < \Lambda < 4$ there is a possibility of asymmetric modes, but for this range of Λ -values, point B is to the left of point C (Fig. 9), i.e.

$$\frac{\sqrt{\Lambda-1}}{3} < \sqrt{\Lambda-3} \quad (36)$$

and buckling still occurs through the limit point. Therefore, P_{cr} is given by Eq. (35).

(d) For $\Lambda > 4$, buckling occurs through the existence of unstable bifurcation (Pt. B). Positions A to B are stable, positions BCO and BO are unstable, and the critical load is given by

$$Q_{cr} = 2\sqrt{\Lambda-3}, \quad \text{or} \quad P_{cr} = \sqrt{\Lambda} + 2\sqrt{\Lambda-3}. \quad (37)$$

Critical (buckling) loads are plotted on Fig. 10.

III - 2. Ideal Impulse

In order to simplify matters, it is assumed that the three bars are weightless and that the impulse is imparted into the system through two masses, m , at points B and C. This is also used in determining the initial T_1^0 , kinetic

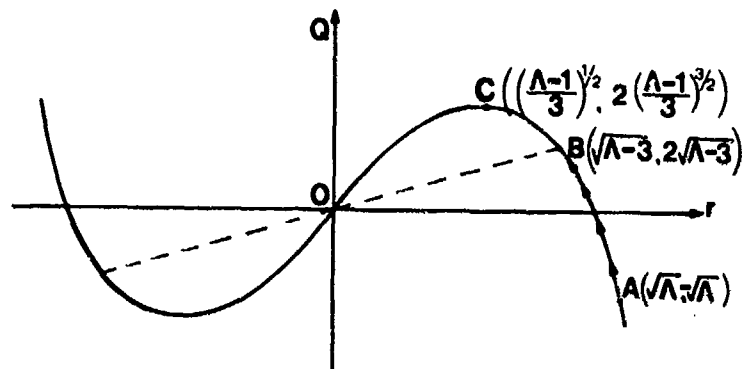


Figure 9. Load-Displacement Curves (Model B).

energy of the system. Thus

$$(PT_0) = 2mL \sqrt{\beta} \left(\frac{dr}{dt} \right) \Big|_{r=\sqrt{\Lambda}} \quad \text{and} \quad T_1^0 = mL^2 \beta \left(\frac{dr}{dt} \right)^2 \Big|_{r=\sqrt{\Lambda}} \quad (38)$$

where T_0 is the duration time.

Introduction of the new nondimensionalized parameters

$$\tau = t \left(\frac{\beta k}{2m} \right)^{1/2} \quad \text{and} \quad \bar{T}_1 = T_1 / \beta^2 k L^2, \quad (39)$$

yields

$$(pr)_0 = \left(\frac{dr}{d\tau} \right) \Big|_{r=\sqrt{K}} \quad \bar{T}_1^0 = \frac{1}{2} \left(\frac{dr}{d\tau} \right)^2 \Big|_{r=\sqrt{K}} \quad (40)$$

The concept of dynamic stability is similar to the one used in case II-2.

$$\bar{U}_T^0 + \bar{T}^0 = \bar{T}_1^0 \quad (41)$$

A critical condition exists, if the impulse, $(pr)_0$, imparts sufficient kinetic energy into the system so it can reach, with zero velocity, an unstable static equilibrium point on the "zero-load" total potential, \bar{U}_T^0 .

Clearly, then from Eqs. (4) and (41)

$$(pr_0)_{cr} = \sqrt{2} (\bar{T}_1^0)^{1/2} = \sqrt{2} \bar{U}_T^0 \text{ (unst. st. pt.)} \quad (42)$$

Thus, before $(pr)_{cr}$ can be found, one must have knowledge of all stationary points and of their character (stable, unstable etc.). Starting with the expression for \bar{U}_T^0 [Eq. (28) with $p = 0$], requiring equilibrium, and performing a stability analysis the following results are obtained.

Stationary points and Their character

Pt. 1 at $(\sqrt{\Lambda}, 0)$ Stable (Relative Minimum)

Pt. 2 at $[-(\sqrt{\Lambda} - \sqrt{\Lambda-4})/2, 0]$	Unstable (Relative Maximum)
Pt. 3 at $[-(\sqrt{\Lambda} + \sqrt{\Lambda-4})/2, 0]$	Stable (Relative Minimum)
Pt. 4 at $[-\sqrt{\Lambda}/2, \sqrt{\Lambda-2}/2]$	Unstable (Saddle Point)
Pt. 5 at $[-\sqrt{\Lambda}/2, -\sqrt{\Lambda-2}/2]$	Unstable (Saddle Point)

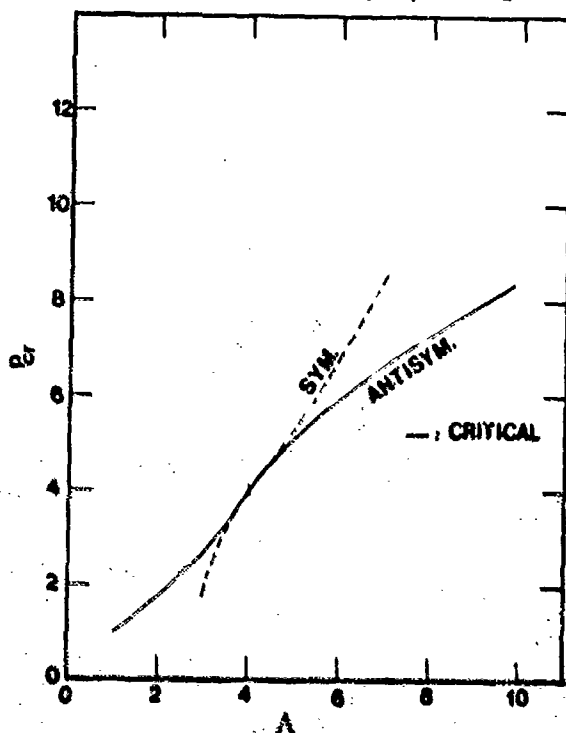


Figure 10. Static Critical Loads (Model B).

By Eq. (42),
(MPCL)

$$(p_{r_0})_{cr} = 3\sqrt{\Lambda-1}$$

(MGCL)

$$(p_{r_0})_{cr} = [5\Lambda - 2 + 3\sqrt{\Lambda^2 - 4\Lambda} + \frac{1}{4}(\Lambda + 2\sqrt{\Lambda^2 - 4\Lambda})^2]^{1/2} \quad (43)$$

Note that critical conditions exist only for $\Lambda \geq 4$. If $\Lambda < 4$, there is no far stable static equilibrium point on the "zero-load" total potential. The results are plotted on Fig. 11.

III - 3. Constant Load of Infinite Duration

The concept of dynamic stability is similar to the one used for one-degree-of-freedom models. The only difference is that, in this case, there is a lower bound (MPCL) and an upper bound (MGCL). The lower bound corresponds to loads for which there is a possibility of "buckled" motion, while the upper bound corresponds to loads for which the motion will definitely be "buckled." Because the existence of bounds is dependent upon the value of Λ the discussion will be based on the range of Λ -values.

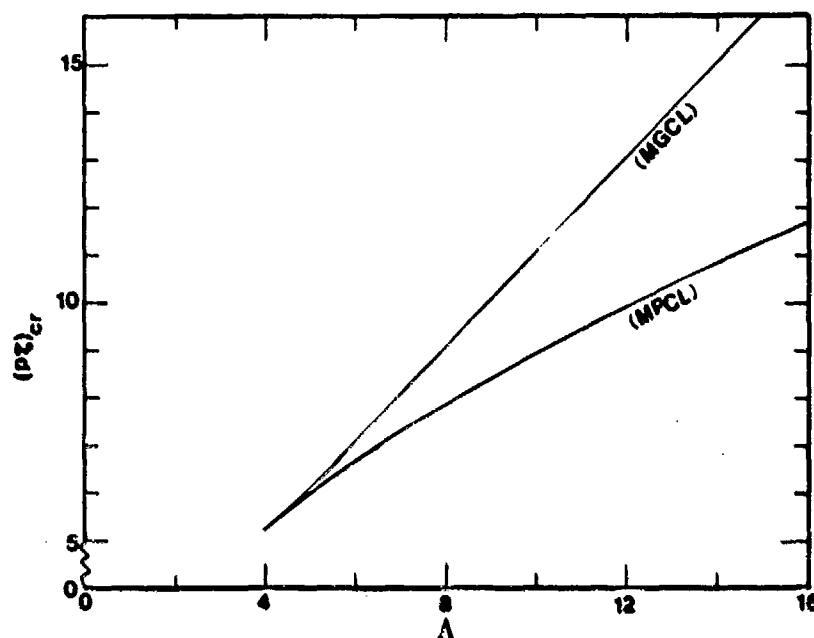


Figure 11. Critical Ideal Impulse (Model B)

(a) For $\lambda < 3$ there are no saddle points and the system behaves as a one-degree-of-freedom system. Therefore, for this case the governing equations are

$$\ddot{U}_T^p = 0 ; (\lambda - 1 - r^2) r = Q;$$

$$\text{and } \frac{2\ddot{U}_T^p}{dr^2} < 0 \text{ at the solution} \quad (44)$$

Note that for this case "buckled" motion is both possible and guaranteed. Thus the upper and lower bounds are coincident.

(b) For $\lambda > 3$, there exist "saddle" points on the total potential, in addition to the relative maximum point. All three are unstable static equilibrium points. Therefore, the motion can become "buckled" either through a saddle point or through the relative maximum point. It will next be shown that, in certain instances, "buckled" motion is possible and in others guaranteed. Before proceeding with the analysis the following observations are made:

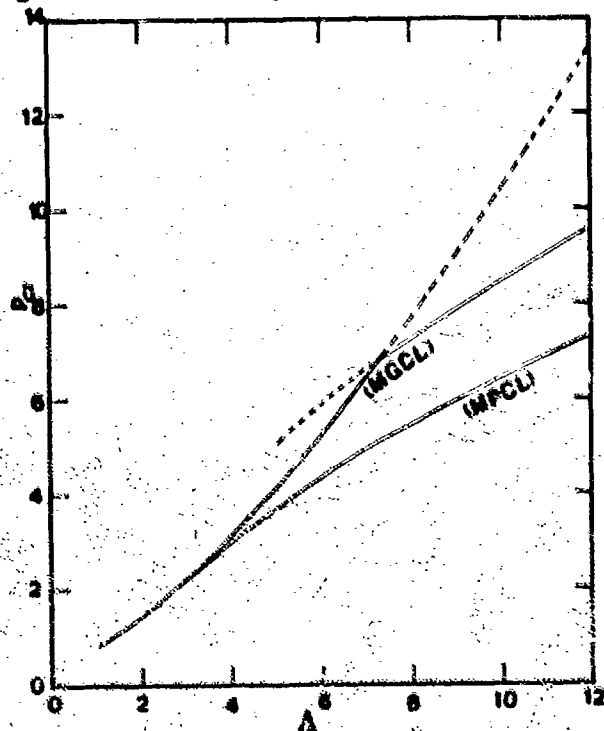


Figure 12. Critical Dynamic Load (Infinite Duration; Model B)

Parenthesis 1: For a specified load the total potential has a lower value

at a "saddle" point than at a relative maximum point. This can be proven through computation of \bar{U}_T^P at the corresponding points.

Parenthesis 2: Regardless of the value of p and Λ (for $\Lambda > 3$), the total potential at any s position, but a fixed r -position ($r = \bar{r} < \sqrt{\Lambda-3}$), has a higher potential than that of a position characterized by $r = \bar{r}$ and an s -position on the ellipse

$$r^2 + 3s^2 = \Lambda - 3 \quad (45)$$

Note that the ellipse, Eq. (45), defines the locus of static equilibrium points ("saddle" points).

Proof: Let $\Delta \bar{U}_T^P$ denote the difference in total potential, between the any s -position and that of an s -position on the ellipse ($r = \bar{r}$). Then, from Eqs.

$$\begin{aligned} (28) \text{ and } (45) \quad \Delta \bar{U}_T^P &= [\bar{r}^2 + 9s^2 - 2\sqrt{\Lambda} \bar{r} + \Lambda + \frac{1}{2}(\Lambda - \bar{r}^2 - 3s^2)^2 - 2p(\sqrt{\Lambda} - \bar{r})] \\ &\quad - [4\Lambda - \frac{9}{2} - 2\bar{r}^2 - 2\sqrt{\Lambda} \bar{r} - 2p(\sqrt{\Lambda} - \bar{r})] \\ &= 3(\bar{r}^2 + 3s^2 - \Lambda) + \frac{9}{2} + \frac{1}{2}(\Lambda - \bar{r}^2 - 3s^2)^2 \\ &= \frac{1}{2}(\Lambda - 3 - \bar{r}^2 - 3s^2)^2 \geq 0 \quad \text{Q.E.D.} \end{aligned} \quad (46)$$

Clearly the difference is zero when s is on the ellipse and positive for all other s .

Parenthesis 3: For $p \geq \sqrt{\Lambda} + 2\sqrt{\Lambda-3}$ [loads higher than the static critical load - see Eq. (37)], if $r_1 < r_2 \leq \sqrt{\Lambda-3}$, then the total potential on the ellipse, Eq. (45), is higher at r_2 than at r_1 .

Proof: By Eqs. (42) and (59)

$$\Delta \bar{U}_T^P = \bar{U}_T^P(r_2) - \bar{U}_T^P(r_1) = 2(r_2 - r_1) [p - \sqrt{\Lambda} - (\bar{r}_2 + \bar{r}_1)] \quad (47)$$

Since $r_2 - r_1$ is positive, $\Delta \bar{U}_T^P$ is positive if $p > \sqrt{\Lambda} + (\bar{r}_2 + \bar{r}_1)$. But $p \geq \sqrt{\Lambda} + 2\sqrt{\Lambda-3}$, thus if $\sqrt{\Lambda} + 2\sqrt{\Lambda-3} > \sqrt{\Lambda} + (\bar{r}_2 + \bar{r}_1)$ then definitely $p > \sqrt{\Lambda} + (\bar{r}_2 + \bar{r}_1)$. Clearly from the statement of the parenthesis $2\sqrt{\Lambda-3} > \bar{r}_2 + \bar{r}_1$, which concludes the proof.

As the load is increased from zero, at low values of p the zero potential lines in the rs -space enclose only the near static equilibrium point and the motion is "unbuckled". At same value of the load, the first unstable point(s) at which the total potential can become zero is (are) the "saddle" point(s) according to Parenthesis 1. At this load there is a possibility of "buckled" motion through the saddle point. This load, then, is called (MPCL). The governing equations for finding this critical load, as well as the corresponding position (sr coordinates) of the saddle point are:

$$\begin{aligned} \bar{U}_T^P &= (r^2 + ps^2 - 2\sqrt{\Lambda} r + \Lambda) + \frac{1}{2}(\Lambda - r^2 - 3s^2)^2 - 2p(\sqrt{\Lambda} - r) = 0 \\ (\Lambda - 1 - r^2 - 3s^2)r &= p - \sqrt{\Lambda} \\ \Lambda - 3 - r^2 - 3s^2 &= 0 \end{aligned} \quad (48)$$

Note that "saddle" points are unstable, thus, there is no need for applying the stability requirements. The solution to Eqs. (45) yields (MPCL): $p_{cr} = 3(\sqrt{\Lambda}-1)$ and "saddle" point at $r = \sqrt{\Lambda}-3/2$; $s = \pm (\sqrt{\Lambda}-7/4)^{1/2}$. (49)

The solutions to Eqs. (43) and (48) are plotted on Fig. 12.

As far as the case of the upper bound is concerned (MGCL), there are two ways through which a guaranteed "buckled" motion can be achieved. One way is to require \dot{U}_T^0 at the relative maximum unstable static point to be zero. In this case the motion is definitely buckled and the critical load can be obtained from the solution of Eqs. (43). The second way is for loads which are equal to the static critical load for asymmetric buckling ($\sqrt{\Lambda} + 2\sqrt{\Lambda-3}$). In this case, although the total potential at the relative maximum point is higher than zero, guaranteed "buckled" motion can be achieved because of Parentheses 2 and 3. In this latter case, p_{cr} (MGCL) is given by the expression for the static load. Both results are shown graphically on Fig. 12.

Note, that the upper bound is the smallest load computed, either by the solutions of Eqs. (43) (for $\sqrt{7/4} \leq \Lambda \leq 5.3$), or by the static critical load (for $\Lambda \geq 5.3$). Moreover, for very large Λ -values the upper and lower bounds approach each other, ($3/\Lambda$).

III - 4. Constant Load of Finite Duration

In this particular load case, the critical load is bounded between an upper bound (MGCL) and a lower bound (MPCL). In either case the question to be resolved is as follows: For a specified duration time, τ_0 , what is the value of the load such that the subsequent motion can definitely become unbounded for the former case, (MGCL), or can possibly become unbounded for the latter case, (MPCL). Since the load is released after τ_0 time, the motion becomes unbounded through either the relative maximum point on the "zero-load" total potential or the "saddle" point on the same potential. Therefore, the solution is sought by requiring the load for duration time τ_0 to impart sufficient kinetic energy into the system in order to reach the unstable static equilibrium points (stationary points) with zero velocity.

On the basis of the above discussion one may proceed as follows (in a similar manner as in II-4):

$$\begin{aligned} \text{and} \quad \ddot{U}_T^0 + \ddot{T}^0 &= \ddot{U}_T^0(\tau_0) + \ddot{T}^0(\tau_0); \quad \tau > \tau_0 \\ \ddot{U}_T^p + \ddot{T}^p &= 0; \quad 0 \leq \tau \leq \tau_0 \end{aligned} \quad (50)$$

Note that at τ_0 the system is at some position (\bar{r}, \bar{s}) , which implies that the path associated with the motion during $0 \leq \tau \leq \tau_0$ can play a significant role.

Requiring continuity in kinetic energy at $\tau = \tau_0$, one may write

$$\dot{T}^0(\tau_0) = \dot{T}^p(\tau_0) = -\dot{U}_T^p(\tau_0) \quad (51)$$

Consequently, requiring the system to reach an unstable static equilibrium point with zero velocity yields

$$\ddot{U}_T^0(\text{unst. st. pt.}) = \ddot{U}_T^0(\tau_0) - \ddot{U}_T^p(\tau_0) \quad (52)$$

This last equation, when the expressions for \ddot{U}_T^0 and \ddot{U}_T^p are substituted on the right-hand-side, becomes

$$\ddot{U}_T^0(\text{unst. st. pt.}) = 2p(\sqrt{\Lambda} - \bar{r}) \quad (53)$$

From this equation it is clearly seen that for a fixed \bar{r} -value, there is only one p -value. Therefore, a better question to ask is "out of all possible paths in the rs -space, which one must be followed in order that the system reaches position \bar{r} with minimum time (τ_0)?" Thus, the problem in reality falls in the category of the "brachistochrone" problem.

The left hand side of Eq. (53) is given by either

$$\bar{U}_T^0 \text{ (Pt. 4 or 5)} = \frac{9}{2} (\Lambda - 1) \quad (54)$$

$$\text{or } \bar{U}_T^0 \text{ (Pt. 2)} = \frac{5\Lambda}{2} - 1 - \frac{3}{2} \sqrt{\Lambda^2 - 4\Lambda} + \frac{1}{8} (\Lambda + 2 + \sqrt{\Lambda^2 - 4\Lambda})^2$$

The kinetic energy expression is given by

$$\bar{T} = \frac{1}{2} \left[\left(\frac{dr}{d\tau} \right)^2 + \left(\frac{ds}{dt} \right)^2 \right] \quad (55)$$

It is clear, so far, that the (MPCL) case corresponds to using the first of Eqs. (54) into Eq. (53). The (MGCL) case corresponds to using the second of Eqs. (54) into Eq. (53). Only the lower bound (MPCL) is found in this paper, and the following reasoning is employed. When very high loads are used in Eq. (53), the corresponding position \bar{r} is very close to the initial position $r = \sqrt{\Lambda}$. Because of this, the probable and logical path is a symmetric path, $s \equiv 0$.

Then, from the second of Eqs. (50) one may solve for $\left(\frac{dr}{dt} \right)$ and consequently through integration for τ_0 , or

$$\tau_0 = \int_{\sqrt{\Lambda}}^{\bar{r}} \frac{dr}{\sqrt{\Lambda} [8p(\sqrt{\Lambda} - r) - 4\sqrt{\Lambda} - r)^2 - 2(\Lambda - r^2)^2]^{\frac{1}{2}}} \quad (56)$$

Then, for a given high load p , one can solve for \bar{r} from Eq. (53) and for τ_0 from Eq. (56). Computationally, the problem is easier solved as follows: Assign values of \bar{r} , ($\sqrt{\Lambda - 3} \leq \bar{r} < \sqrt{\Lambda}$) and solve for p and τ_0 from Eqs. (53) and (58).

If the combination of p , τ_0 is such that $r < \sqrt{\Lambda - 3}$, then the best candidate for a path of motion, during $0 < \tau < \tau_0$, seems to be symmetric, $s \equiv 0$, for $\sqrt{\Lambda - 3} \leq r < \sqrt{\Lambda}$ and asymmetric, see Eq. (45), for $r < \sqrt{\Lambda - 3}$ primarily because of Parentheses 2 and 3 of Art. III-3. For this condition, the governing equations consist of Eqs. (53) in combination with the first of Eqs. (57) (equation of motion), which leads to the time τ_0 -equation (here the equation of the path is employed as well as continuity in the speed, dr/dt).

The equations of motion are:

$$\frac{d^2 r}{d\tau^2} - 4[r(\Lambda - 1 - r^2 - 3s^2) - p + \sqrt{\Lambda}] = 0; \quad \frac{d^2 s}{d\tau^2} - 12s(\Lambda - 3 - r^2 - 3s^2) = 0 \quad (57)$$

The total time, τ_0 is given by

$$\tau_o = \tau_1 + \tau_2 \quad (58)$$

where τ_1 is given by

$$\tau_1 = \int_{\sqrt{\Lambda}}^{\sqrt{\Lambda-3}} \frac{dr}{[8p(\sqrt{\Lambda-r}) - 4(\sqrt{\Lambda-r})^2 - 2(\Lambda-r^2)^2]^{\frac{1}{2}}} \quad (59)$$

$$\tau_2 = \int_{\sqrt{\Lambda-3}}^{\bar{r}} \frac{dr}{\sqrt{\Lambda-3} [8r^2 + 8p(\sqrt{\Lambda-r} + 8\sqrt{\Lambda}r - 16\Lambda + 18)]^{\frac{1}{2}}} \quad (60)$$

Computationally, values of \bar{r} are assigned ($-\frac{\sqrt{\Lambda}}{2} < r < \sqrt{\Lambda-3}$) and p and τ_o are obtained from Eqs. (53) and (58).

The results are shown graphically in Fig. 13. Note that as $\tau_o \rightarrow \infty$, p_{cr} approaches the value corresponding to the critical condition of constant load of indefinite duration. As $\tau_o \rightarrow 0$, ($p\tau_o$) approaches half of the value obtained for the ideal impulse case, Eqs. (43), because there are two loads p .

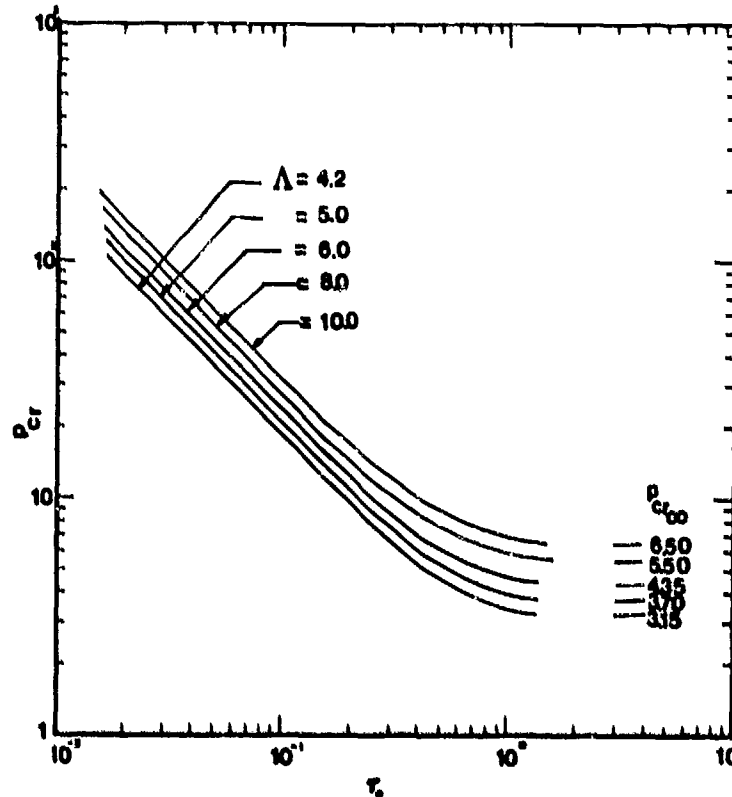


Figure 13. Critical Conditions for Step-Loads (Lower Bound; Model B).

V. CONCLUSIONS

Two models are completely analyzed for quasistatically applied loads as well as suddenly applied loads of constant magnitude and finite duration, τ_0 , including the extreme cases of $\tau_0 \rightarrow 0$ and $\tau_0 \rightarrow \infty$. These models are representative of (a) imperfection sensitive structures and (b) of structures that tend to snap-through because of unstable bifurcational paths such as shallow arches and shallow spherical caps.

The detailed analysis for the dynamic load cases leads to clear definition of the concept of instability under dynamic conditions, as well as clear criteria and related estimates for this class of problems.

Moreover, on the basis of this presentation, criteria and estimates may be formulated for more general dynamic loads, such as time-dependent loads. In addition it is the belief of the author, that the analyses of the one- and two-degree-of-freedom models are also applicable to a large class of structural elements and configurations, because many of them do behave as a one- or two-degree-of-freedom systems. Examples of these include the two bar frame loaded in a direction parallel to one of the bars with or without eccentricity [13] (one-degree-of-freedom), and the shallow arch [5,9,12] (two degree of freedom). This contention should not be confused with vibration modes or how many terms in a series are needed to represent the static or dynamic response of the system.

Finally, it should be stressed again, that in the case of suddenly applied loads of finite but small duration, the level of the critical load is very high, which suggests that the structure is critical because of material behavior, rather than kinematic response.

ACKNOWLEDGEMENTS

This work is supported by the United States Air Force, Aeronautical Systems Divisions (AFSC) under contract No. F33615-79-C-3221. This support is gratefully acknowledged. The author wishes to thank Professor G. M. Rentzepis for his suggestions and his students, C. Lazopoulos and A. Vlahinos for doing the figures and some of the computations.

REFERENCES

1. Bolotin, V. V., The Dynamic Stability of Elastic Systems, (Translated by V. I. Weingarter, et al.) Holden-Day, San Francisco, 1964.
2. Bolotin, V. V., Nonconservative Problems of the Theory of Elastic Stability, Moscow 1961; English Translation published by Pergamon Press, New York, 1963.
3. Herrmann, G., "Stability of Equilibrium of Elastic Systems Subjected to Nonconservative Forces, Applied Mechanics Reviews, Vol. 20, 1967, 103-108.
4. Hsu, C. S., "Stability of Shallow Arches Against Snap-Through Under Tunewise Step Loads", J. Appl. Mech., Vol. 35, No. 1, 1968, 31-39.

5. Hoff, N. J. and Bruce, V. G., "Dynamic Analysis of the Buckling of Laterally Loaded Falt Arches", J. Math and Phys., Vol. 32, 1954, 276-388.
6. Budiansky, B. and Roth, R. S., "Axisymmetric Dynamic Buckling of Clamped Shallow Spherical Shells", Collected Papers on Instability of Shell Structures, NASA TN D-1510, 1962.
7. Simites, G. J., "On the Dynamic Buckling of Shallow Spherical Caps", J. Appl. Mech., Vol. 41, No. 1, 1974, 299-300.
8. Hsu, C. S., "On Dynamic Stability of Elastic Bodies with Prescribed Initial Conditions", International J. of Eng. Sciences, Vol. 4, 1966, 1-21.
9. Hsu, C. S., "The Effects of Various Parameters on the Dynamic Stability of a Shallow Arch," J. Appl. Mech., Vol. 34, No. 2, 1967, 349-356.
10. Hsu, C. S., "Equilibrium Conifigurations of a Shallow Arch of Arbitrary Shape and Their Dynamic Stability Character", International J. Nonlinear Mechanics, Vol. 3, June 1968, 113-136.
11. Hsu, C. S., Kuo, C. T. and Lee, S. S., "On the Final States of Shallow Arches on Elastic Foundations Subjected to Dynamic Loads", J. Appl. Mech., Vol. 35, No. 4, 1968, 713-723.
12. Simites, G. J., "Dynamic Snap-Through Buckling of Low Arches and Shallow Spherical Caps", Ph.D. Dissertation, Department of Aeronautics and Astronautics, Stanford University, June 1965.
13. Kounadis, A. N., Giri, J., and Simites, G. J., "Nonlinear Stability Analysis of an Eccentrically Loaded Two-Bar Frame", J. Appl. Mech., Vol. 44, No. 4, December 1977, 701-706.

TRANSIENT ANALYSIS OF DOUBLE HULLS IMPINGED UPON BY INCIDENT UNDERWATER EXPLOSION WAVES

HANSON HUANG
Research Physicist

STANLEY HALPERSON
Mechanical Engineer

DANIEL CURTIS
Mechanical Engineer
Naval Research Laboratory
Washington, D. C. 20375

ABSTRACT

A practical scheme for the transient response analysis of submerged double hulls impinged upon by incident pressure pulse is described. Its validity is demonstrated by comparing results to analytical solutions for two elementary double hull configurations. An approximate treatment of the shielding effect of the outer hull is also suggested.

INTRODUCTION

The transient response of submerged fluid-coupled double hull structures impinged upon by incident pressure waves has been studied for two elementary configurations which lend themselves to be analyzed by the classical partial differential equation techniques such that the transient scattering and radiation problems in the fluids and the dynamic response problem of the elastic shells are solved simultaneously. These cases are the axisymmetric response of two initially concentrated spherical shells [1] and the plane strain response of two co-axial cylindrical shells [2]. It has been learned that a thin outer shell tends to be transparent to short incident pulses and that the primary shielding effect of the outer shell against long incident pulses can be estimated by asymptotic formulae.

In practical situations, however, the double hull configurations are much more complex than the cases mentioned above. Moreover, for damage predictions, the response analysis is often required to be carried into the nonlinear elasto-plastic regime including possible dynamic instabilities. For such analyses, the use of numerical and/or approximate methods is inevitable.

A PRACTICAL ANALYSIS SCHEME

An analysis scheme which is practical within the current computation technology has been proposed in reference [3]. It is briefly summarized here and will later be tested vis-a-vis the

two analytical solutions mentioned in the preceding section.

For general double hull configurations, the solid structural members as well as the entrained fluid will be treated by the finite element method which has recently made great strides in computing the nonlinear dynamic elasto-plastic response of metallic structures. There already exist various generalized computer programs (codes) for linear and nonlinear analyses, e.g., NASTRAN, ADINA, PETROS, SKAGS, etc. [4]. Here the entrained fluid is considered to be compressible and inviscid. Finite elements for such an ideal fluid have long been formulated for transient analyses of fluid-structure systems, e.g. [5,6,7]. In parallel to solid finite element practices, there are elements based on displacement and force (pressure) formulations and their relative advantages have been discussed in references [8,9]. The "pressure" elements have the least number of degrees of freedom per element since each node has only one unknown. When they are used for the fluid-structure interaction problems, however, the resultant system matrix is nonsymmetric with the associated numerical difficulties. Since many finite element computer programs are structured for only symmetric matrices, it would be impossible to use the "pressure" elements in such programs without major reprogramming. Even for programs with nonsymmetric matrix operation capabilities, the use of the "pressure" elements still requires some additional programming for satisfying the boundary conditions imposed by such elements. The "displacement" elements have more degrees of freedom per element since each nodal displacement has n components for an n -dimensional element. Nonetheless, the use of such elements for fluid-structure interaction analyses ends up with a symmetric system matrix and the associated numerical efficiencies. Moreover, by appropriately modifying their material property matrices, many "displacement" solid elements can be "mocked" as fluid-elements and therefore many existing structural finite element programs can immediately be used without any reprogramming [8,9]. For both types of elements, the use of suitable constitutive relations (equations of state) in the formulation could also take into account the effect of possible cavitation [10,11]. The effectiveness of the fluid finite elements for this type of problems, however, is not previously known and will also be examined here.

The treatment of the interaction of the incident pressure wave with the finite element structural system requires some consideration. It is neither necessary nor practical to use the finite element or finite difference method to analyze the wave field in the external fluid. Firstly, for any realistic configuration the finite element representation of the structural system already requires a substantial portion of the capacity of a modern computer. To do the same for the external wave field which is in general 3-dimensional would require even much larger computer capacity albeit there exist many finite difference and

finite element hydrodynamic computer codes. Moreover, the propagation and accumulation of numerical truncation and round-off errors often render the accuracy of such large scale computations uncertain. Secondly, for many practical situations, the strengths of the incident underwater shock waves are such that the problem does not require the full set of hydrodynamic equations. For instance, if the strength of the underwater incident wave is below $4 \times 10^7 \text{ Pa}$, it behaves practically as an acoustic pulse propagating in an acoustic medium [12]. This linearized "acoustic" treatment is used in the present analysis scheme for analyzing the transient scattering and radiation wave fields and determining the interaction loading on the structure. Here, the exact solution is represented by Kirchhoff's Retarded Potential Integral which reduces the 3-dimensional wave field problem to a 2-dimensional problem at the fluid-structure interface [13]. Even for this 2-dimensional problem, a full-fledged solution of the interaction problem is still being considered to be too demanding on the current computing capability and further simplifications can still be used to advantage. The currently most widely used approximation for this type of problem is the Doubly Asymptotic Approximation (DAA) [14,15] which greatly reduces the computation for the wave field in the external fluid. It is therefore adopted here. Its range of application has been discussed in references [15,16] and its mathematical expression is briefly described in the following paragraph.

For the analysis of a submerged complex structure impinged upon by an incident pressure pulse, it is well known that for the early part of the interaction or in the high-frequency limit the scattered and radiated wave forces can be simply given as

$$\{F_s\} = \rho^e c^e [A] \{\dot{u}_s\} \quad (1)$$

The above equation has been written in matrix form for convenient interfacing with finite element structural analyses and therein $\{\dot{u}_s\}$ is the vector for scattered and radiated wave fluid particle velocities normal to the structure's surface in contact with the external fluid, $[A]$ is the finite element area matrix for that surface, and ρ^e and c^e are respectively the mass density and the sound speed of the fluid. It is also well known that for long time interaction (or in the low-frequency limit) the wave forces are simply

$$\{F_s\} = [M_v] \{\ddot{u}_s\} \quad (2)$$

where $\{\ddot{u}_s\}$ denotes the fluid particle acceleration vector and where $[M_v]$ is the added mass matrix which may be readily determined by an analysis of incompressible fluid motion appropriate

to a distribution of elemental source on the structure's external surface [17]. Equations (7) and (2) are actually two asymptotic relations, therefrom Geers [14,15] formulated an approximate expression for the scattered and radiated forces

$$(\rho^e c^e)^{-1} [A]^{-1} \{\dot{F}_s\} + [M_v]^{-1} \{F_s\} = \{\dot{u}_s\} \quad (3)$$

where the dot denotes time differentiation and $[A]^{-1}$ and $[M_v]^{-1}$ are the inverse of $[A]$ and $[M_v]$ respectively. This expression is asymptotically exact for both early-time (high-frequency) and late-time (low-frequency) fluid motion, effecting a smooth transition in the intermediate range. It is therefore termed Doubly Asymptotic Approximation. Equation (3) is to be solved simultaneously with the equation of motion (linear or nonlinear) of the finite element structural system subjected also to forces due to the incident wave and the boundary condition at the interface between the structure and the external fluid

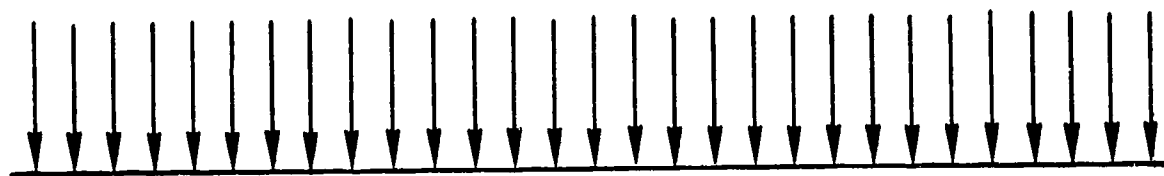
$$\{\dot{w}\} = \{\dot{u}_i\} + \{\dot{u}_s\} \quad (4)$$

where $\{\dot{w}\}$ is the normal velocity vector of the structure elements at the fluid-structure interface and \dot{u}_i represents the incident wave fluid particle velocity in the same direction. Various computational strategies for such a simultaneous solution have been formulated and several computer codes have been disseminated [18,19]. Equation (3) is a system of first order differential equations. If the external fluid-structure interface of an N -degrees-of-freedom structure has N' ($N' \leq N$) degrees of freedom normal to the interface, by this approximation the entire fluid-structure interaction problem has $N + N'/2$ degrees of freedom.

An appraisal of the effectiveness of this analysis scheme is made here by means of comparisons with the presently available analytical solutions.

THE TEST PROBLEMS

Figure 1 sketches a submerged fluid-coupled cylindrical or spherical shell system impinged upon by an incident plane pressure wave. The fluid surrounding the outer shell and that between the two shells are considered to be ideal compressible fluids in linear wave motions and can be characterized by their unperturbed mass densities and sound speeds (ρ^e, c^e) and (ρ, c) respectively. The external fluid is of infinite extent. The shells are initially concentric. In this study, the strength of the incident wave is sufficiently weak such that the shell deflections are elastic and small and the deviation from the concentricity remains negligible for the time duration of



INCIDENT PLANE WAVE

ρ^e, c^e

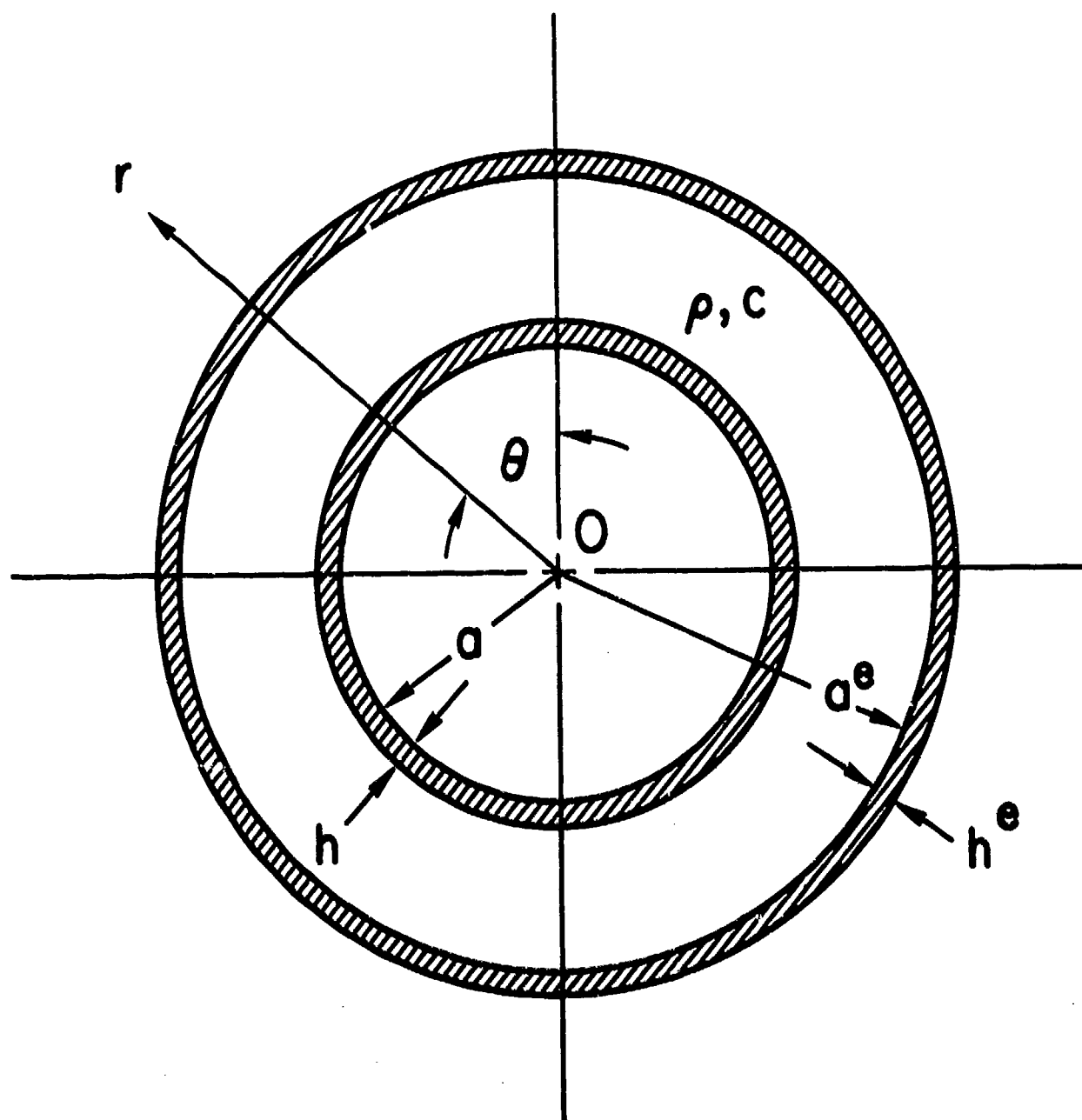


Fig. 1: Sketch of the Test Problem.

interest. The middle surface radii, thickness, mass densities, Young's moduli and Poisson's ratios of the outer and inner shells are $(a^e, h^e, \rho^e, E^e, \nu^e)$ and (a, h, ρ_s, E, ν) , respectively. For the case of two coaxial cylindrical shells, it is a plane strain problem, while for the two spherical shells the problem is axisymmetric.

The deflections of the inner shell in the r - and θ -direction normalized with respect to the outer shell radius a^e are denoted by w and v respectively and those of the outer shell by w^e and v^e respectively. Since this is a linear problem, it suffices to only consider the case for which the incident wave is a step wave. The numerical results here are for two steel shells with water in both the exterior and the inter-shell regions. The incident pressure normalized with respect to $\rho(c)^2$ is equal to unity. The material properties and dimensions are:

$$\begin{aligned} c^e &= c = 1524 \text{ m/sec} \\ \rho^e &= \rho = 100 \text{ kg/m}^3 \\ \rho_s^e &= \rho_s = 7785 \text{ kg/m}^3 \\ E^e &= E = 0.206844 \times 10^{12} \text{ PA} \\ \nu^e &= \nu = 0.3 \end{aligned} \tag{5}$$

$$\left. \begin{aligned} h/a &= 1/69 \\ h^e/a^e &= 1/345 \end{aligned} \right\} \text{ for the cylindrical system}$$

$$\left. \begin{aligned} h/a &= 1/50 \\ h^e/a^e &= 1/250 \end{aligned} \right\} \text{ for the spherical system}$$

$$a/a^e = 0.8$$

$$h/h^e = 4$$

COMPUTATIONS AND RESULTS

For the cylindrical plane strain problem, the simultaneous solution of the Doubly Asymptotic Approximation equation of wave

motion in the external fluid and the equation of motion of the double-walled shell system is carried out by an Underwater Shock Analysis (USA) code [19] interfacing with NASA's general purpose structural analysis code NASTRAN [20]. The Doubly-Asymptotic-Approximation-NASTRAN computation has been demonstrated to be highly effective for the cylindrical plane strain configuration since it reproduces the results of an exact analysis of the transient response of a single cylindrical shell to an incident step wave [21].

Due to the symmetry of the present problem it is only necessary to use a finite element model for the region, $0 < \theta < \pi$. In the plane strain fashion, each half shell is represented by 28 plate bending elements, and the entrained fluid by NASTRAN "displacement" hexahedron solid elements, each composed of five tetrahedrons "mocked" as fluid elements [9]. The finite element gridworks used for the computations are depicted in Figure 2 with 56 fluid elements and Figure 3 with 112 fluid elements. The lumped mass matrices for the systems are used. It is also decided that the first, instead of higher, order hexahedron elements are used for the maintenance of completeness and interelement continuity. The complete NASTRAN finite element models are then interfaced with the USA code for computing the transient responses using an unconditionally stable staggered time integration technique [22].

The finite element solutions are carried out by first using an integration time step equal to 1/50 of the transit time for the incident wave front to traverse the distance of one outer shell diameter. This time step size is based on the experience in obtaining the analytical solution. Results are computed for 100 time steps. Later, half of this time step is also used and produces results which merely change the 5th or 6th digits of the coarser time step results.

Figure 4 compares the analytical and the NASTRAN-USA finite element solutions for the time histories of the hoop stress resultant

$$N_{\theta}(\theta, T) = \frac{Eh}{1-\nu^2} \left(w + \frac{\partial v}{\partial \theta} \right) \quad (6)$$

at various locations of the interior shell using the gridwork of Figure 2. In Figure 4,

$$\begin{aligned} T &= c^e t / a^e \\ T' &= (T - n) / \xi, \\ \xi &= a / a^e \end{aligned} \quad (7)$$

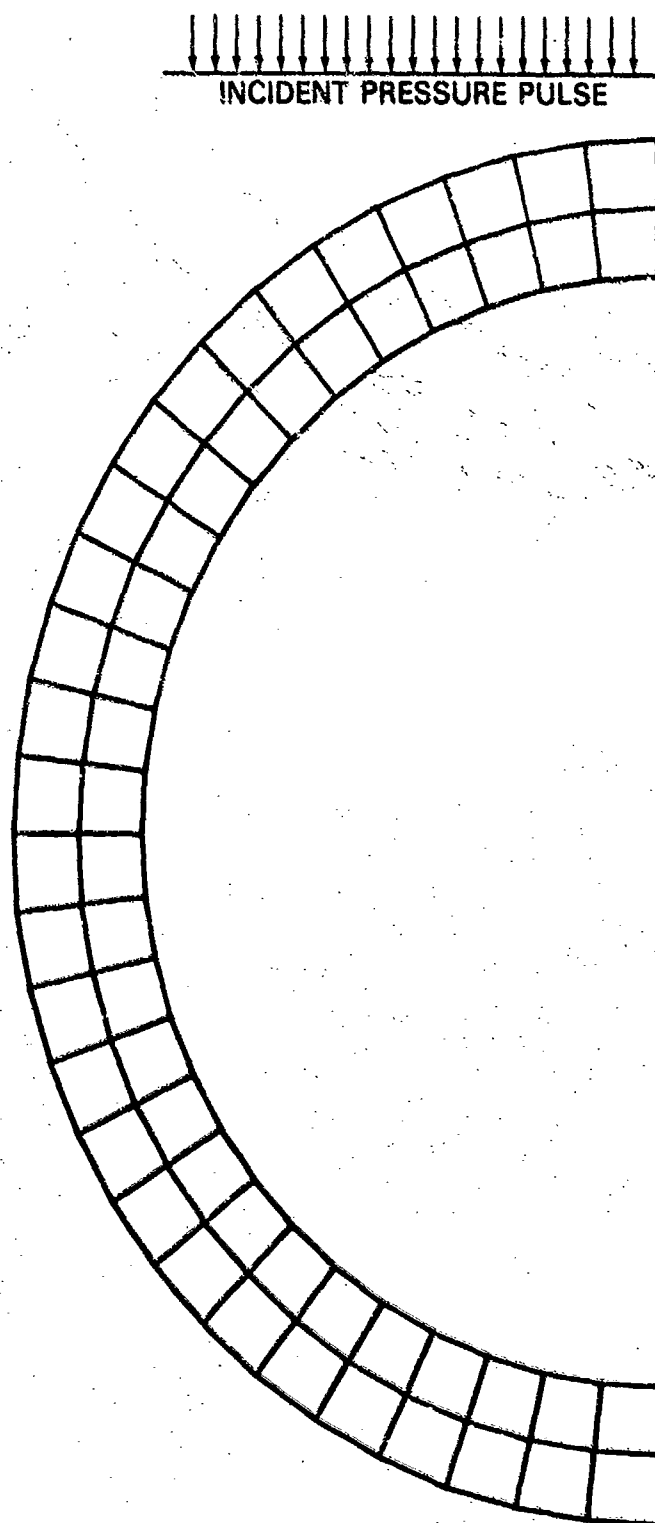


Fig. 2: Finite Element Gridwork with Two Layers of Fluid Elements.

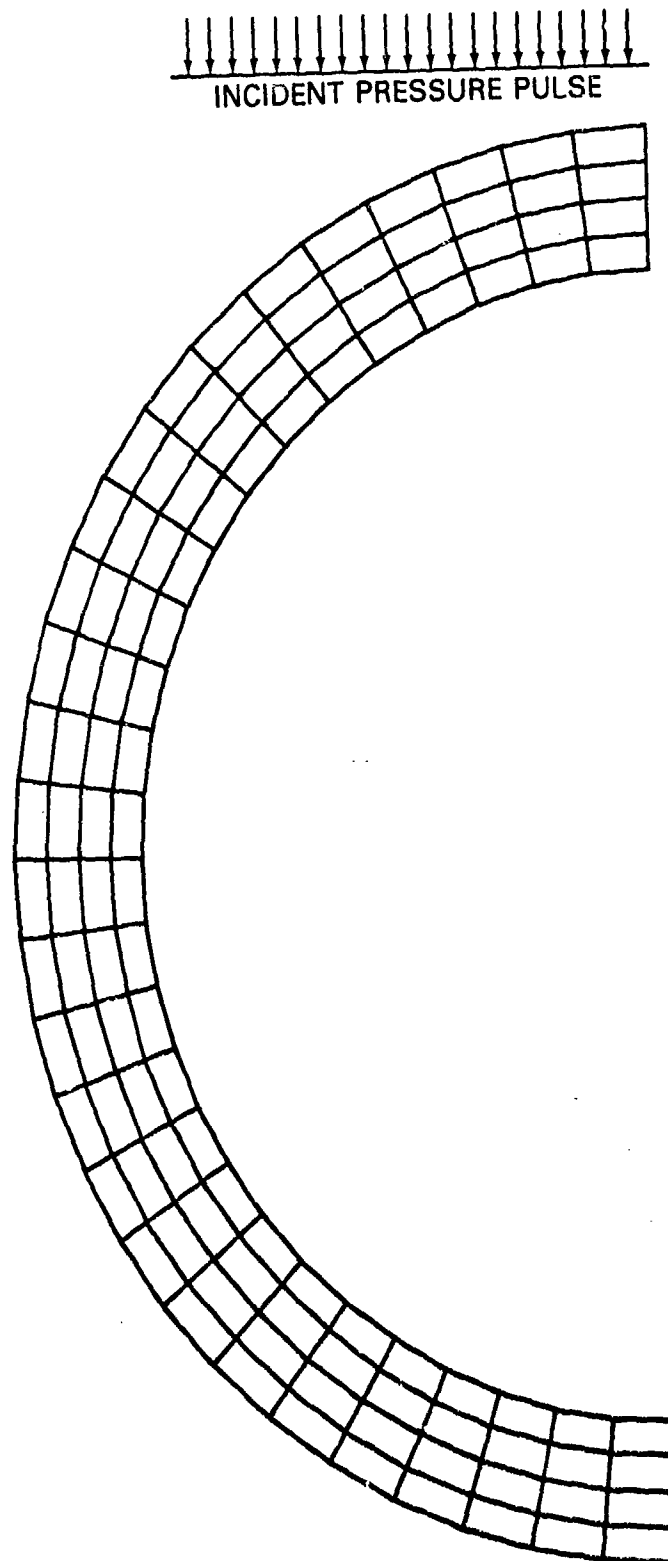


Fig. 3: Finite Element Gridwork with Four Layers of Fluid Elements.

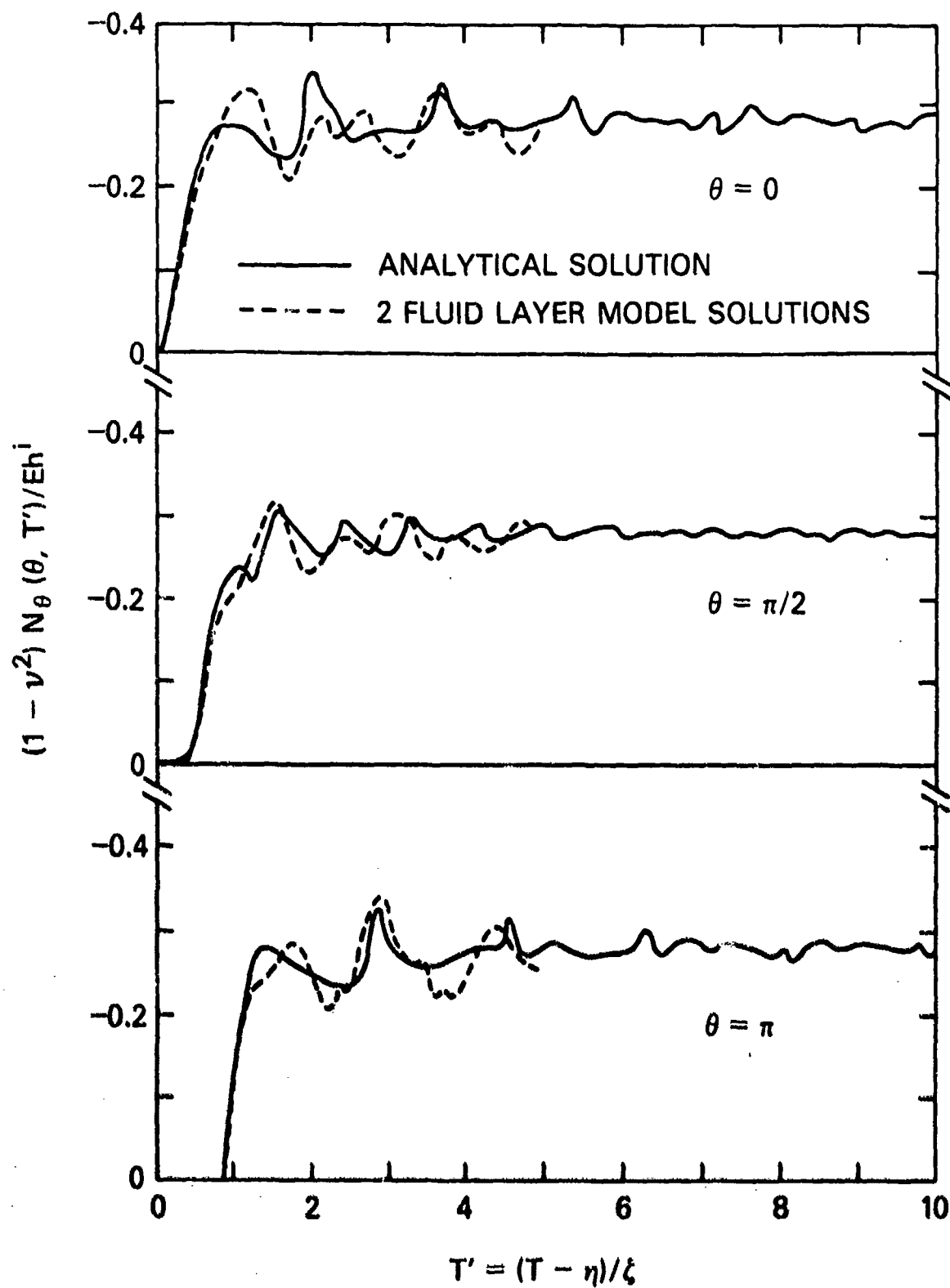


Fig. 4: Time Histories of Hoop Stress at the Inner Cylindrical Shell Middle Surface, Using Gridwork of Figure 2.

and

$$\eta = (1 - \xi)c^e/c$$

where t is the time. It can be seen that there is a very good agreement for the arrival times and magnitudes of $N_\theta(\theta, T')$ between the analytical and finite element solutions.

Figure 5 compares the same hoop stress time histories of the finite element solution using the refined gridwork of Figure 3. There, it can be seen that doubling the number of fluid elements further improves the finite element results in that the peaks and valleys of the stress-time curves rise and fall following more closely with those of the analytical solution. These peaks and valleys represent the circumferential stress waves encircling the shell with the dilatational wave speed [2,21] - a distinct response feature of this problem.

The time histories of the hoop stress resultant at various locations of the outer shell computed based on the gridworks of Figures 2 and 3 are plotted in Figure 6. It would be interesting to note that in the absence of the entrained fluid the stress in the outer shell, based upon the solution in [21], would be approximately 3.5 times higher than the present results.

For the axisymmetric response of the spherical shell system, the simultaneous solution is carried out by the DAA computation procedure developed in [18,23]. Figures 2 and 3 now represent the cross-sections of the axisymmetric finite element gridworks. Now the outer and inner shells are discretized by NASTRAN's CONEAX axisymmetric conical shell elements and the entrained fluid is modeled by "pressure" fluid finite element formulated in the fashion of NASTRAN's TRIAAX axisymmetric ring elements. The transient solution is integrated using a Newmark-Beta direct integration subroutine in NASTRAN [23]. Since this is intrinsically a 3-dimensional problem and therefore numerically more difficult than the preceding plane strain problem. A sample result from reference [23] is compared to the analytical solution [1] in Figure 7 where the time histories of the normalized relative radial deflection of the two apexes ($\theta = 0$ and $\theta = \pi$) of the inner shell are juxtaposed. This NASTRAN-DAA solution is obtained using three layers of fluid ring elements for the entrained fluid and an integration time step equal to $1/25$ of the transit time of the incident wave front to traverse one outer shell diameter. The agreement is obviously quite good.

DISCUSSIONS

The above comparison study has demonstrated the viability of this analysis scheme. In particular, the good agreement of the response data for the inner shell indicates that the

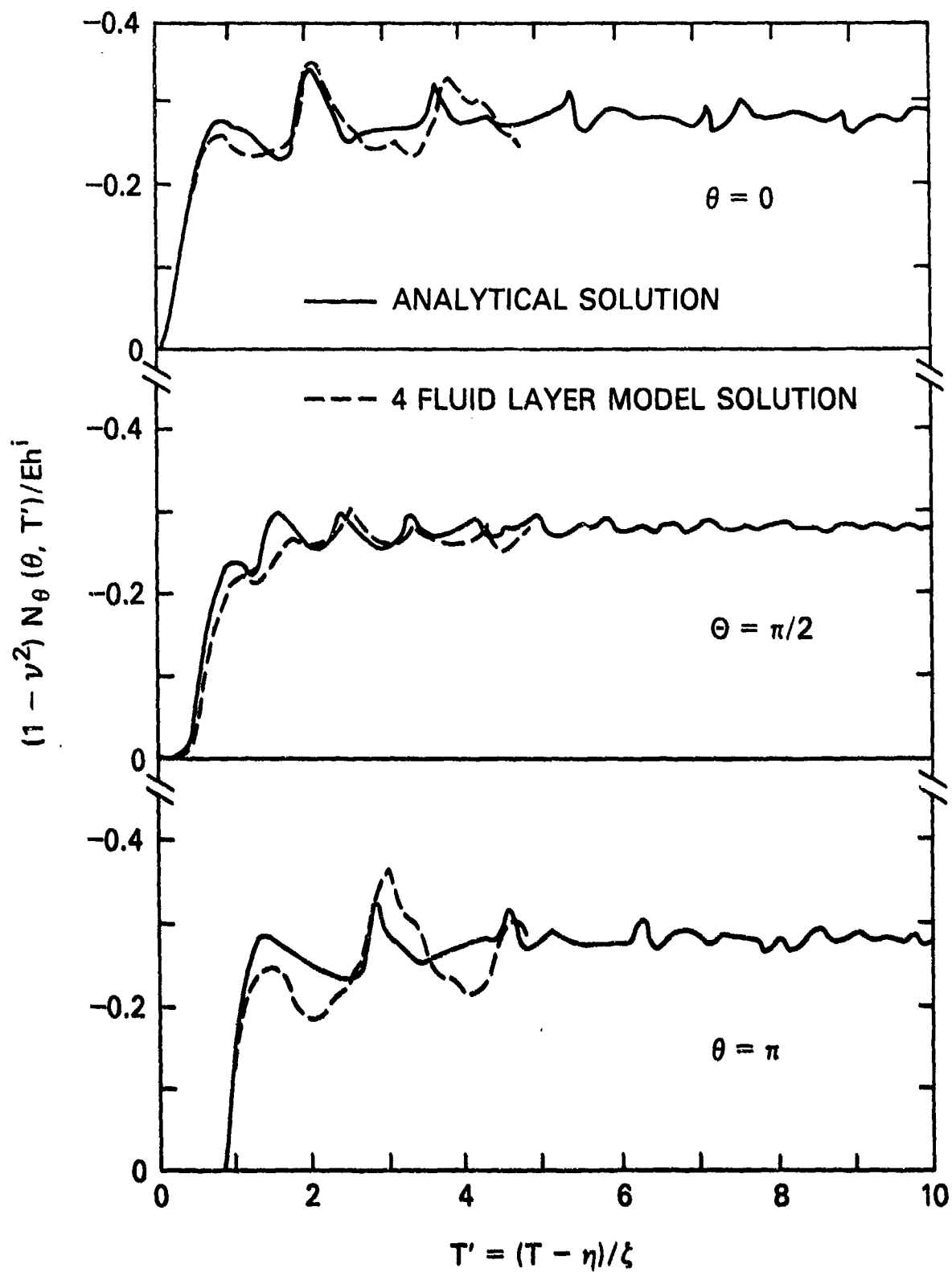


Fig. 5: Time Histories of Hoop Stress at the Inner Cylindrical Shell Middle Surface, Using Gridwork of Figure 3.

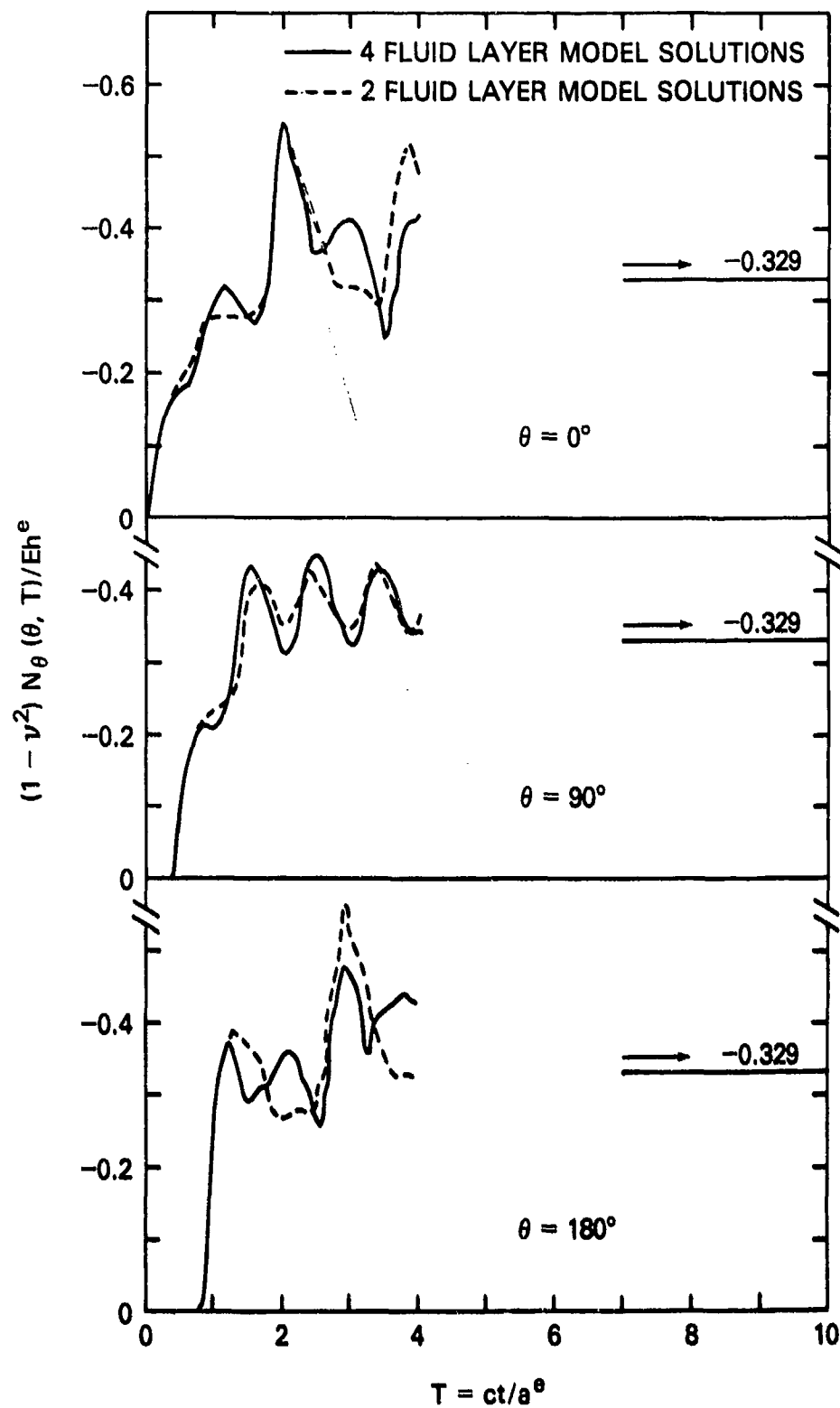


Fig. 6: Time Histories of Hoop Stress at the Outer Cylindrical Shell Middle Surface, Using Gridwork of Figure 3.

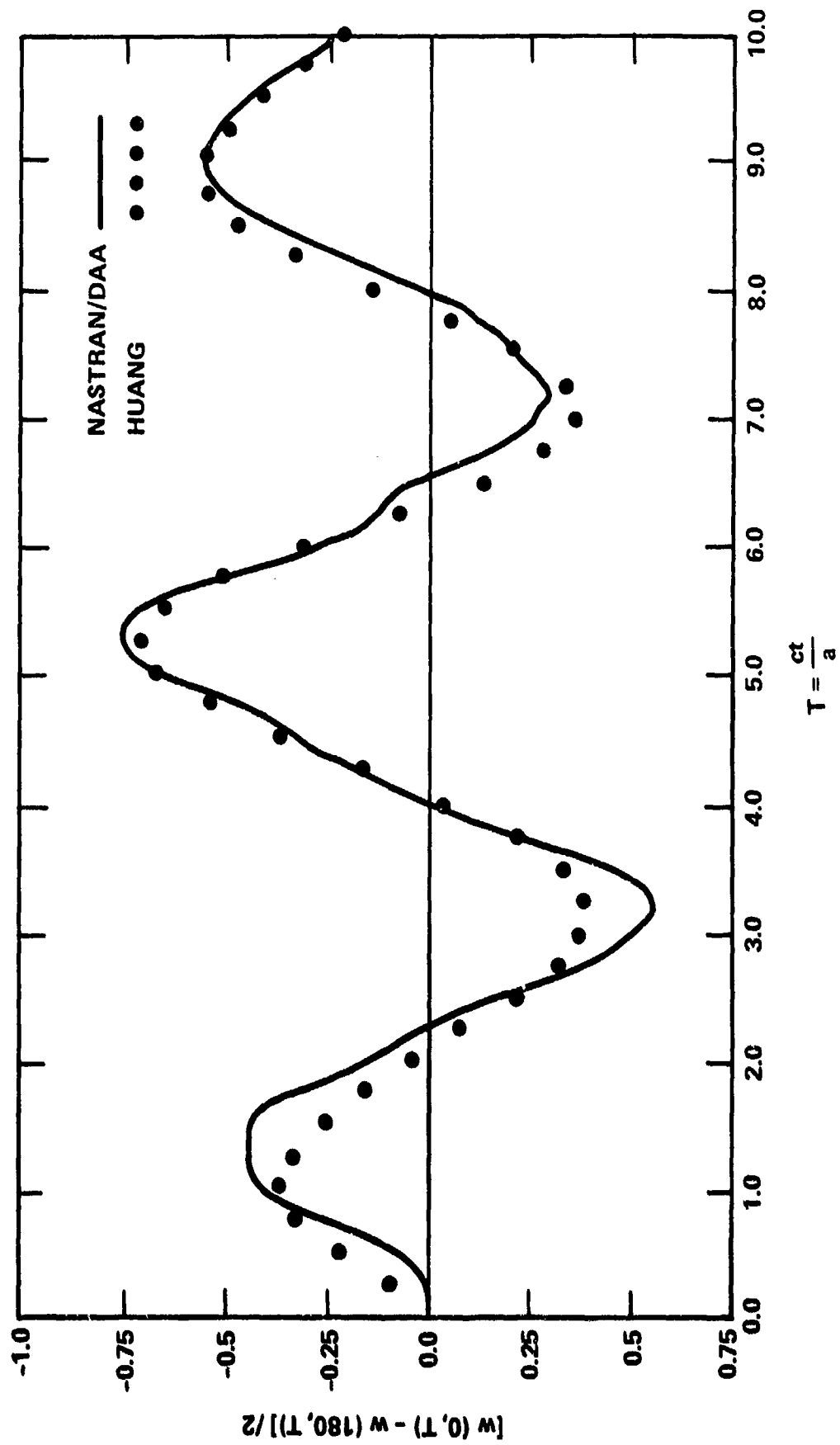


Fig. 7 - Relative Radial Displacement Between Positive and Negative Poles of the Inner Spherical Shell.

dynamics pressure loading is correctly transmitted through the outer shell and the entrained fluid. Although the test problems are for linear and elastic responses, it could be expected that the same would also be true when this scheme is used for non-linear elasto-plastic response analyses.

For practical problems, the fluid finite elements for the entrained fluid are in general 3-dimensional and the number of degrees-of-freedom for the finite element system increases very rapidly with the number of such elements. In view of the prospective numerical and computational difficulties to be encountered, it might be more advantageous to approximately represent the shielding effect of the outer hull without including it and the entrained fluid in the nonlinear elasto-plastic damage analysis of the inner hull. Based on the analytical study of [1,2], such an approximation can be suggested for the analysis of stiffened or unstiffened cylindrical double hulls with thin outer hull and finite length. For exponentially decaying type of incident plane pressure pulses

$$p^{inc} = p_0 \exp[(x - c_e t)/c_e \tau] \quad (8)$$

where p_0 is the wave front pressure and τ the decay constant, this approximation would modify equation (8) and the new incident wave formula to be used for analyzing the interaction of the modified incident wave and the inner hull is

$$p^{inc} = \kappa p_0 \exp[(x - c_e t)/c_e \tau] \quad (9)$$

where the coefficient κ depends on the duration of the incident wave and is a function of the fluid properties and the elastic properties and dimensions of the inner and outer hulls. It approximately takes into account of the transmissibility and dynamic response effects of the outer hull, the response effects of the inner hull, the added mass, the compressibility and the reverberating effects of the entrained fluid. This coefficient is given by

$$\begin{aligned} \kappa &= 1, \text{ if } \tau \ll a^e/c_e \\ &= \frac{\rho_r M^e (2 + M)}{(1 - \xi^2)(2 + M^e) + \rho_r (1 + \xi^2)(M + M^e) + 0.5 \rho_r M M^e [1 + \xi^2 + c_r (1 - \xi^2)]} \\ &\text{if } \tau \approx 2a^e/c_e \\ &= \frac{2M^e c^2}{c^2 c_e^2 (1 - \xi^2) + 2\rho_r M^e c^2 + 2\rho_r \xi^2 M c_e^2} \end{aligned} \quad (10)$$

$$\text{if } \tau > 2a^e/c_e$$

where

$$\rho_r = \rho/\rho^e$$

$$c_r = c^e/c$$

$$M = \rho^e a / (\rho_s h)$$

(11)

$$M^e = \rho^e a^e / (\rho_s^e h^e)$$

$$c^2 = E / [\rho_s (1 - \nu^2) (c^e)^2]$$

$$c_e^2 = E^e / \{ \rho_s^e [1 - (\nu^e)^2] (c^e)^2 \}$$

In equation (77), h and/or h^e are the average or the smeared thicknesses of the stiffened hulls. It should be noted that equations (9) - (11) are primarily meant for the calculation of the elasto-plastic strain of the inner hull.

ACKNOWLEDGEMENT

The work was supported by the Defense Nuclear Agency under DNA Subtask Y99QAXSF502, Work Unit 17, Title: Double Hull Damage Prediction. The author also wishes to express his appreciation to Dr. I. M. Blatstein and Mr. M. Giltrude of the Naval Surface Weapons Center, White Oak Laboratory, for their helpful discussions.

REFERENCES

1. Huang, H., "Transient Response of Two Fluid-Coupled Spherical Elastic Shells to an Incident Pressure Pulse," J. Acoust. Soc. Am., Vol. 65, No. 4, April 1979, 881-887.
2. Huang, H., "Transient Response of Two Fluid-Coupled Cylindrical Elastic Shells to an Incident Pressure Pulse," J. Appl. Mech. Vol. 46, 1979, 513-518.
3. Huang, H., "Transient Response of Two Fluid-Coupled Spherical Elastic Shells to an Incident Pressure Pulse," NRL Report 8185, December 1977.
4. Ball, R. E., "Dynamic Buckling of Structures," Shock and Vibration Computer Programs, edited by W. Pilkey and B. Pilkey, The Shock and Vibration Information Center, SVM-10, 1975, 299-321.

5. Gladwell, E.M.L. and Zimmerman, E., "On Energy and Complementary Energy Formulations of Acoustic and Structural Vibration Problems," J. Sound Vib., Vol. 3, No. 3, 1966, 233-241.
6. Zienkiewicz, O. C. and Newton, R. E., "Coupled Vibration of a Structure Submerged in a Compressible Fluid," Finite Element Techniques, edited by M. Sorensen, University of Stuttgart, Germany, 1969, 359-369.
7. Bathe, K. J. and Hahn, W. F., "On Transient Analysis of Fluid-Structure Systems," Int. J. Comput Structures, Vol. 10, No. 1/2, 1979, 383-391.
8. Kalinowski, A. J., "Fluid Structure Interaction," Shock and Vibration Computer Programs, edited by W. Pilkey and B. Pilkey, The Shock and Vibration Information Center, SVM-10, 1975, 504-552.
9. Everstine, G., Schroeder, E. A. and Marcus, M. S., "The Dynamic Analysis of Submerged Structures," NASTRAN: User's Experiences, NASA TMX-3278, 1975, 419-429.
10. Newton, R. E., "Finite Element Study of Shock Induced Cavitation," Preprint 80-110, ASCE Convention & Exposition, Portland, Oregon, April 14-18, 1980.
11. Bleich, H. H. and Sandler, I. S., "Interaction Between Structures and Bilinear Fluids," Int. J. Solids Structures, Vol. 6, 1970, 617-639.
12. Cole, R. H., Underwater Explosion, Dover Publications, Inc., New York, New York, 1965.
13. Huang, H., Everstine, G. C. and Wang, Y. F., "Retarded Potential Techniques for the Analysis of Submerged Structures Impinged by Weak Shock Waves," Computational Methods for Fluid-Structure Interaction Problems, edited by T. Belytschko and T. L. Geers, ASME AMD-26, 1977, 83-93.
14. Geers, T. L., "Transient Response Analysis of Submerged Structures," Finite Element Analysis of Transient Nonlinear Structural Behavior, Belytschko, T., Oslas, J. R. and Marcel, P. V., eds, AMD Vol. 14, ASME, New York, New York, 1975, 59-84.
15. Geers, T. L., "Doubly Asymptotic Approximations for Transient Motions of Submerged Structures," J. Acoust. Soc. Am. Vol. 64, No. 5, 1978, 1500-1508.

16. Huang, H., "A Qualitative Appraisal of the Doubly Asymptotic Approximation for Transient Analysis of Submerged Structures Excited by Weak Shock Waves," NRL Memo Report 3125, September 1975.
17. DeRuntz, J. A. and Geers, T. L., "Added Mass Computation by the Boundary Integral Method," Int. J. Num. Meth. Eng. Vol. 12, 1977, 531-549.
18. Everstine, G. C., "A NASTRAN Implementation of the Doubly Asymptotic Approximation for Underwater Shock Response," NASTRAN User's Experiences, NASA TMX-3428, October 1976, 207-228.
19. DeRuntz, J. A., Geers, T. L. and Felippa, C. A., "The Underwater Shock Analysis (USA) Code, A Reference Manual," DNA Report 4524F, February 1978.
20. Butler, T. G. and Michel, D., "NASTRAN: A Summary of Functions and Capabilities of the NASA Structural Analysis Computer System," NASA SP-260, Washington, D. C., 1971.
21. Huang, H., "An Exact Analysis of the Transient Interaction of Acoustic Plane Waves with a Cylindrical Elastic Shell," J. Appl Mech. Vol. 37, 1970, 1097-1099.
22. Park, K. C., Felippa, C. A. and DeRuntz, J. A., "Stabilization of Staggered Solution Procedures for Fluid-Structure Analysis," Computational Methods for Fluid-Structure Interaction Problems, Geers, T. L. and Belytschko, T., eds., AMD Vol. 26, ASME, New York, New York, 1977, 95-124.
23. Neilson, H., Everstine, G. and Wang, Y. F., "Transient Response of a Submerged Fluid-Coupled Double-Walled Shell Structure to a Pressure Pulse," ASME Paper No. 80-C2/PVP-136 Fluid-Structure Interaction Session of the 1980 ASME Pressure Vessel and Piping Conference, August 1980.

DYNAMIC ELASTIC-PLASTIC RESPONSE OF UNSTIFFENED AND
STIFFENED PANELS TO PRESSURE LOADINGS

LAWRENCE J. MENTE
Senior Research Engineer

WILLIAM N. LEE
Senior Engineer

Kaman Avidyne
Burlington, Massachusetts 01803

ABSTRACT

The DEPROP computer program determines the dynamic elastic-plastic large displacement response of cylindrical and flat panels to arbitrary blast loadings. The analysis is capable of analyzing unstiffened or discretely stiffened panels in which the stiffeners in both coordinate directions are allowed various eccentric positions relative to the single layered, multilayered and sandwich panel skin configurations. The inelastic formulation is based on the extension of the plasticity constitutive relations from deformation theory to regions of elastic unloading and reyielding. A confidence level is established for DEPROP by comparing the analytical solutions with experimental results from various panel blast tests and with other nonlinear computer codes.

NOMENCLATURE

a = radius of cylindrical panel
 \bar{A} = undeformed surface area
 A_s = area of stiffener
 \bar{b} = width of stiffener segment
 E = modulus of elasticity
 E_s = secant modulus
 E_t = strain hardening slope
 $\bar{G}_\gamma, \bar{G}_\beta$ = shear moduli of γ and β stiffeners
 h, h_η = total thickness of panel
 h_i = distance from inner panel skin surface to the furthest edge of the i th stiffener segment
 \bar{H} = distance from the inner panel skin surface to the coordinate surface
 H_i = weighting values for Legendre-Gauss quadrature formula
 H_j, H_k = weighting values for Simpson's quadrature formula in γ and β directions
 $J = \pi/\theta_0$
 J_γ, J_β = torsional constants for the γ and β stiffeners

$K = \kappa a$
 $k_\gamma, k_\beta = \sqrt{2}$ for C-C or C-S opposite boundaries for w-equations
 $= 1/\sqrt{2}$ for S-S opposite boundaries for w-equations
 $= 1/\sqrt{2}$ for u and v-equations
 $k_b^\gamma = \sqrt{2}k_\gamma, k_b^\beta = \sqrt{2}k_\beta$
 l = length of panel
 $L = \frac{l}{\pi a}$
 \bar{M}, \bar{N} = number of spatial integration points in the γ and β directions
NSG, NSB = number of γ and β stiffeners
NSEG = total number of segments for a stiffener
 p = pressure
 $R = a/h$
 T = kinetic energy
 u, v, w = axial, tangential and radial displacement components
 U, V, W = displacement components divided by a
 x, θ, z = cylindrical coordinates
 $\beta = \frac{\pi \theta}{\theta_0}$
 $\beta_k = \left(\frac{k-1}{\bar{N}-1} \right) \pi$
 $\gamma = \frac{\pi x}{l}$
 $\gamma_j = \left(\frac{j-1}{\bar{M}-1} \right) \pi$
 $\delta_{ij}, \delta_{mr}, \delta_{ns}$ = Kronecker delta
 $\tilde{\epsilon}_{ij}$ = components of total strain
 ϵ_{ij} = components of strain
 η = total number of layers
 θ_0 = subtended angle of cylindrical panel
 κ_{ij} = components of change of curvature
 ν = Poisson's ratio
 ξ_1 = zeros of the Legendre polynomial
 $\rho, \bar{\rho}, \rho_s$ = composite, skin and stiffener mass densities
 σ_{ij} = components of stress
 ϕ_m, ϕ_n = spatial functions for displacements

INTRODUCTION

A digital computer program DEPROP, has been developed as a special purpose code to calculate the linear elastic and elastic-plastic structural response of aircraft panels to blast overpressure loads [1], [2]. The analysis is formulated for cylindrical or flat panels with clamped or simply supported edges. The panels can have discrete stiffeners in two perpendicular directions. The modal method of solution is used with numerical spatial integration techniques employed to obtain the discretization of the structure required to incorporate the physical nonlinear behavior.

The panel analysis is an extension of the DEPICS computerized analysis [3] for the dynamic response of linear elastic cylindrical shells which included geometrical nonlinearities. The DEPROP analysis employs the Novozhilov nonlinear strain-displacement relations for large displacement response of thin panels based on the assumption of undeformable normals. The inelastic formulation is based on the Mises-Hencky yield surface, a kinematic hardening model and the Hencky stress-strain relations from the deformation theory of plasticity with modifications for regions of elastic unloading and reyielding. Material behavior of the skin and stiffeners is represented by a bilinear stress-strain curve. Displacement, strain, and stress time histories are calculated at selected positions on the panel.

The geometry of the unstiffened or stiffened, cylindrical or flat panel is illustrated in Figure 1. The cylindrical coordinates (x, θ, z) and the axial, tangential, and radial displacement components (u, v, w) are shown in Figure 1 on the coordinate surface of the panel. In DEPROP the skin of the panel can be single or multi-layered for elastic materials, while for elastic-plastic material behavior the skin is limited to single layered and sandwich (honeycomb) construction. Figure 1 depicts discrete stiffeners located along various integration grid lines in both of the dimensionless γ and β coordinate directions. The stiffeners must be oriented parallel to either or both spatial coordinate directions of the flat or cylindrical panel, and stiffener locations are restricted to coincide with spatial integration grid lines. The stiffeners in the circumferential coordinate direction can have variable cross sections.

The eccentricity of the stiffeners either above or below the panel skin is taken into account in the analysis. Both bending and membrane deformations causing normal strains and stresses in the stiffener's coordinate direction are included, but lateral bending of the stiffener is ignored. Thus, in the analysis the stiffener is assumed symmetrical about the plane of bending. The torsional stiffnesses of the stiffeners are included in a limited manner by assuming that the twisting is always elastic. Therefore, the shear stress associated with torsion of the stiffener is assumed small compared to the normal stresses and is neglected in the elastic-plastic formulation.

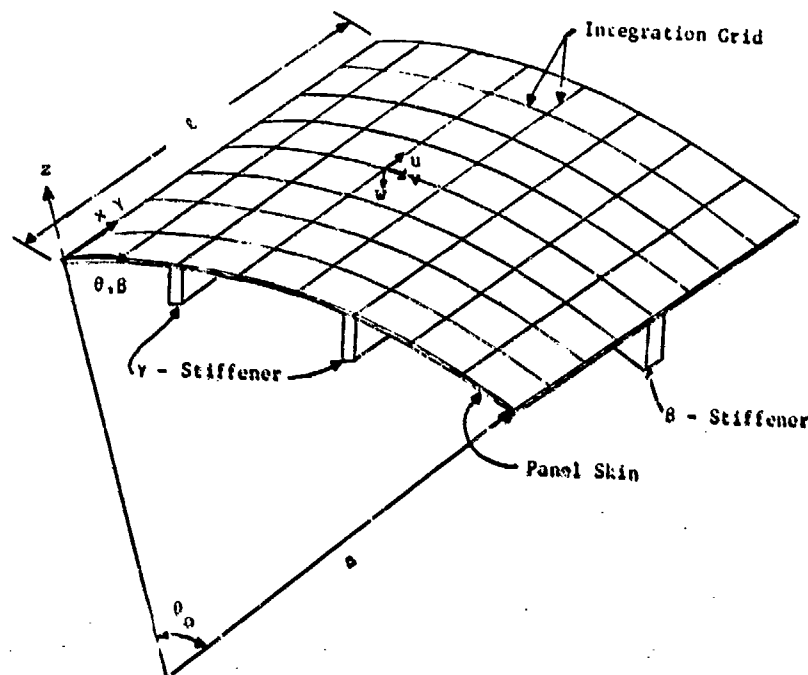


Figure 1. Stiffened Panel Geometry

The analysis accommodates stiffeners with any shape whose cross section can be represented as a series of connected rectangular segments. Since lateral bending of the stiffeners is ignored, stiffeners such as channels and z-sections are treated symmetrically as I-sections. Figure 2 illustrates the stiffener configurations included in DEPROP. Configurations A and B of Figure 2 show the stiffener attached to the outer and inner surfaces, respectively, of any panel skin construction i.e., single-layered, multilayered and sandwich (honeycomb). Configuration C shows the stiffener located in the interior of a sandwich panel and configuration D shows the stiffener attached to the inner surface of a sandwich panel that has been crimped for connection purposes.

ANALYTICAL FORMULATION

The governing equations of motion for the panel are obtained from the principle of virtual work for a dynamic structural system in which the material behavior and the force system are nonconservative. The displacement components are represented by truncated series of the

products of undetermined time-dependent coefficients and orthogonal spatial functions which satisfy the boundary conditions in the form

$$u_i(x, \theta, t) = \sum_{m=1}^M \sum_{n=1}^N u_{mn}^i(t) \phi_m^{u_i}(x) \phi_n^{u_i}(\theta) \quad (i=1,2,3) \quad (1)$$

where for notation convenience u_1, u_2, u_3 correspond to u, v, w , respectively.

With these functions introduced into the virtual work equations, a set of $3MN$ coupled modal equations of motion are generated and are given by

$$\frac{d}{dt} \frac{\partial T}{\partial \dot{u}_{mn}^i} + \iiint_V \sigma_{ij} \frac{\partial \varepsilon_{ij}}{\partial u_{mn}^i} dV - \iint_A \bar{Q}_{mn}^{u_i} d\bar{A} = 0 \quad (2)$$

(m=1,2,3...M) (n=1,2,3...N)

where the integrands of the generalized forces are

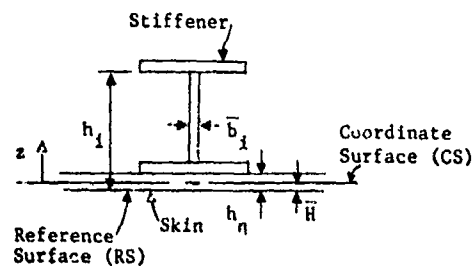
$$\bar{Q}_{mn}^{u_1} = p N_u \frac{\partial u}{\partial u_{mn}}, \quad \bar{Q}_{mn}^{u_2} = p N_v \frac{\partial v}{\partial v_{mn}}, \quad \bar{Q}_{mn}^{u_3} = p N_w \frac{\partial w}{\partial w_{mn}} \quad (3)$$

where

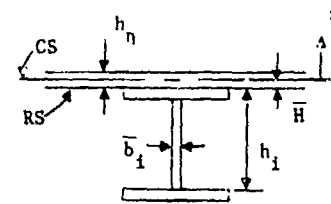
$$\begin{aligned} N_u &= -w_x \\ N_v &= -(w_\theta + v)/a \\ N_w &= 1 - (w - v_\theta)/a + u_x \\ \bar{A} &= \text{undeformed surface area} \\ T &= \frac{1}{2} \iiint_V \rho(x, \theta, z) (\dot{u}^2 + \dot{v}^2 + \dot{w}^2) dV \end{aligned}$$

Dots denote differentiation with respect to time.

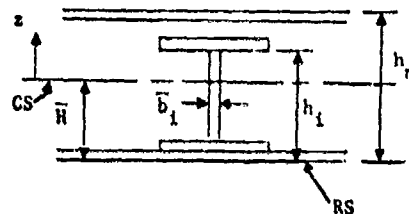
It is assumed that the blast pressure, $p(x, \theta, t)$, acts on the coordinate surface of the cylindrical or flat panel. As the panel surface deforms, the elemental pressure force vector remains normal to the coordinate surface so that it changes direction during deformation. The magnitude of this force vector also changes as the element surface area of the deformed panel changes. The rotary inertia contributions to the kinetic energy have been neglected. The volume and surface integrations contained in these equations are performed numerically by various techniques, except for integration of the kinetic energy which is performed analytically. This set of simultaneous second-order differential equations are solved numerically in time by use of the central difference method.



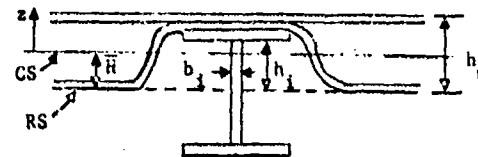
A. Outer Stiffener



B. Inner Stiffener



C. Internal Stiffener with Sandwich Panel



D. Stiffener with Crimped Sandwich Panel

Figure 2. Stiffener Configurations

Strain-Displacement Relations

The strain-displacement relations used in this analysis are based on the assumptions: (1) strains are small compared with unity, (2) the thickness of the shell is small compared with the radius and (3) the Kirchhoff-Love hypothesis that straight fibers which are normal to the undeformed coordinate surface remain straight and normal to the deformed coordinate surface and are not elongated, thus neglecting transverse shear and normal strains. The basic formulation of the following set of nonlinear strain-displacement relations is attributed to Novozhilov [4]. The total strain consists of membrane and bending components expressed by the form $\epsilon = \epsilon + z\kappa$. The membrane elongation and shear strains

(ϵ_{xx} , $\epsilon_{\theta\theta}$, $\epsilon_{x\theta}$) on the coordinate surface are expressed in terms of the displacement components and their spatial derivatives:

$$\begin{aligned}
\epsilon_{xx} &= u_x + \frac{1}{2} [w_x^2 + u_x^2 + v_x^2] \\
\epsilon_{\theta\theta} &= \frac{1}{a} v_\theta - \frac{1}{a} \lambda w + \frac{1}{2a^2} [(w_\theta + \lambda v)^2 + (v_\theta - \lambda w)^2 + u_\theta^2] \\
\epsilon_{x\theta} &= v_x + \frac{1}{a} u_\theta + \frac{1}{a} w_x (w_\theta + \lambda v) + \frac{1}{a} v_x (v_\theta - \lambda w) + \frac{1}{a} u_\theta u_x
\end{aligned} \tag{4}$$

Similarly, the change of curvature quantities (κ_{xx} , $\kappa_{\theta\theta}$, $\kappa_{x\theta}$) of the coordinate surface which characterize the bending and torsional deformations of the panel are given by

$$\begin{aligned}
\kappa_{xx} &= w_{xx} (1 + v_\theta/a - \lambda w/a + u_x) \\
\kappa_{\theta\theta} &= \frac{1}{a^2} w_{\theta\theta} + \frac{\lambda}{a^2} v_\theta + \frac{\lambda}{a^2} (-w + v_\theta) + \frac{\lambda}{a} u_x \\
&\quad + \frac{1}{a^3} (w_{\theta\theta} + \lambda v_\theta) (v_\theta - \lambda w) + \frac{1}{a^2} w_{\theta\theta} u_x \\
&\quad + \frac{\lambda}{a^3} (v_\theta - w)^2 + \frac{\lambda}{a^3} (w_\theta + v)^2 + \frac{\lambda}{a^3} w_\theta (w_\theta + v) \\
\kappa_{x\theta} &= \frac{2}{a} w_{x\theta} + \frac{\lambda}{a} v_x + \frac{2}{a^2} w_{x\theta} (v_\theta + a u_x - \lambda w) \\
&\quad + \frac{2\lambda}{a^2} w_x (w_\theta + v)
\end{aligned} \tag{5}$$

Only those nonlinear terms which primarily involve the radial displacement and its derivatives are included in Equation 5. The subscripts on the displacement components in Equations 4 and 5 denote partial spatial derivatives. The parameter λ is introduced in the strain-displacement relations so that they apply to both curved and flat panels. Thus, $\lambda = 1$ for curved panels. For flat panels, $\lambda = 0$, $a = 1$, θ is replaced by y , and θ_0 is replaced by b , the width of the flat panel.

Constitutive Relations

In DEPROP, the behavior of the panel material is treated as elastic-plastic for isotropic single-layered and sandwich panels and elastic for isotropic and orthotropic multilayered panels. The elastic-plastic analysis for the single-layered panel has been established as the basic formulation in the DEPROP program. The elastic multilayered analysis is established as an alternate option based on appropriate modifications of the elastic-plastic formulation. In the DEPROP analysis the solution

involves total strains and stresses; therefore, for response in the inelastic region, it was convenient to use the deformation theory of plasticity instead of flow theory which involves incremental strains and stresses. Plastic deformation theory is based on an averaging process that permits a total strain solution dependent upon only the final stress state at the end of a loading path. In general, deformation theory is an approximation of the more rigorous flow (incremental) theory, except for proportional loading. However, since the dynamic response solution is solved incrementally in time by numerical methods in DEPROP, the strain increments are small over each time step for which the equations of motion are solved. Thus, the plastic deformation theory provides a much more accurate solution when the averaging process takes place separately over each small time increment as the response solution is obtained by a step-by-step timewise procedure.

It is assumed that the material's uniaxial stress-strain curve is modeled by the bilinear representation shown in Figure 3 in which the strain hardening is defined by slope E_t . This stress-strain representation is interpreted for the biaxial state of stress through the use of the effective stress ($\bar{\sigma}$)-effective strain ($\bar{\epsilon}$) concept in which the secant modulus (E_s) indicated in Figure 3 is defined by

$$E_s = \frac{\bar{\sigma}}{\bar{\epsilon}} = \frac{\sigma_0 + E_t (\bar{\epsilon} - \epsilon_0)}{\bar{\epsilon}} \quad (6)$$

where σ_0 , ϵ_0 are the yield stress and strain, respectively, from the material's uniaxial bilinear representation. Thus, the effective stress, effective strain and secant modulus quantities are used to relate the biaxial stress-strain condition to the assumed uniaxial bilinear stress-strain representation for the isotropic material. A kinematic hardening model is employed in conjunction with the Mises-Hencky yield surface which accounts for the Bauschinger effect when reyielding occurs due to the strain reversals during unloading. The kinematic hardening models discussed in [5] assume that during plastic deformation the yield surface translates as a rigid body in stress space with the size, shape and orientation of the elliptical yield surface being invariant. The kinematic hardening model to be used in this analysis is illustrated in Figure 4 for the Mises-Hencky yield surface in the plane of the principal stresses σ_1 and σ_2 . Corresponding to the initial yielding position (i) and the unloading position (f) indicated in Figure 3, the rigid translation of the yield surface for a shift of the stress state from position (i) to position (f) is shown in Figure 4. The change in total stress components from position (i) to position (f) are defined by α_{1j} and, similarly, the corresponding change in the total strain components are defined by β_{1j} , so that

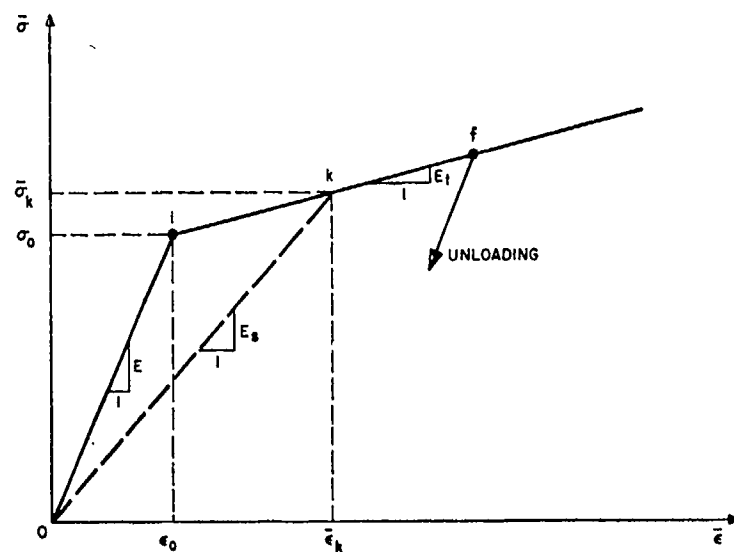


Figure 3. Effective Stress-Strain Bilinear Representation

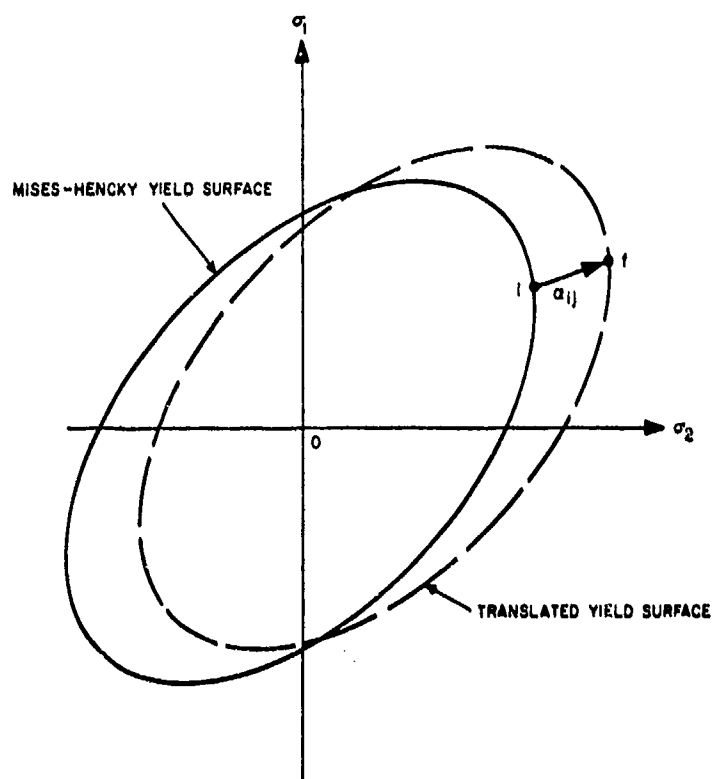


Figure 4. Kinematic Hardening Model

$$\alpha_{ij}^r = \alpha_{ij}^{r-1} + \sigma_{ij(f)}^{r-1} - \sigma_{ij(i)}^{r-1} \quad (7)$$

$$\beta_{ij}^r = \beta_{ij}^{r-1} + \epsilon_{ij(f)}^{r-1} - \epsilon_{ij(i)}^{r-1}$$

where

r = the number of elastic unloadings from yielded conditions
($r=1,2,\dots$)

$$\alpha_{ij}^0 = \beta_{ij}^0 = 0$$

(i) indicates initiation of yielding or reyielding

(f) indicates final position prior to unloading

The Mises-Hencky yield criterion for the translated yield surface is based on the effective stress given as

$$\bar{\sigma} = [(\sigma_{11} - \alpha_{11}^r)^2 - (\sigma_{11} - \alpha_{11}^r)(\sigma_{22} - \alpha_{22}^r) + (\sigma_{22} - \alpha_{22}^r)^2 + 3(\sigma_{12} - \alpha_{12}^r)^2]^{1/2} \quad (8)$$

Furthermore, it is advantageous in this analysis to relocate the origin on the $\bar{\epsilon}$ axis after each unloading such that the extended elastic unloading curve passes through the zero position. This is accomplished by defining the effective strain as follows:

$$\begin{aligned} \bar{\epsilon} = & \left\{ \frac{1}{(1-\nu_s^2)^2} \left[(1-\nu_s + \nu_s^2) \left((\bar{\epsilon}_{11} - \beta_{11}^r)^2 + (\bar{\epsilon}_{22} - \beta_{22}^r)^2 \right) \right. \right. \\ & \left. \left. - (1-4\nu_s + \nu_s^2) (\bar{\epsilon}_{11} - \beta_{11}^r) (\bar{\epsilon}_{22} - \beta_{22}^r) \right] \right. \\ & \left. + \frac{3}{(1+\nu_s)^2} (\bar{\epsilon}_{12} - \beta_{12}^r)^2 \right\}^{1/2} \quad (9) \end{aligned}$$

$$\text{where } \nu_s = \frac{1}{2} - E_s/E \left(\frac{1}{2} - \nu \right)$$

Thus, the elastic-plastic behavior of the material for subsequent yieldings after an unloading has occurred is always based on the same σ versus $\bar{\epsilon}$ curve which originates at position (0,0). This approach requires that the stress-strain relations be modified by the α_{ij} and

β_{ij} quantities for unloading and reyielding conditions to account for

the past stress-strain history. The general form of the inverted Hencky

stress-strain relations for the elastic, elastic-plastic, elastic unloading and plastic reyielding regions are identical, so that the general stress-strain relations is given by

$$\sigma_{ij} = \alpha_{ij}^r + \frac{E_s}{1-\nu_s} \left[(1-\nu_s) (\epsilon_{ij}^r - \beta_{ij}^r) + \nu_s (\epsilon_{kk}^r - \beta_{kk}^r) \delta_{ij} \right] \quad (10)$$

(i, j, k = 1, 2)

where for the following regions of response,

- a) initial elastic loading $E_s = E, \alpha_{ij}^r = \beta_{ij}^r = 0$
- b) initial plastic loading $E_s = E_s, \alpha_{ij}^r = \beta_{ij}^r = 0$
- c) qth elastic unloading $E_s = E, \alpha_{ij}^r = \alpha_{ij}^q, \beta_{ij}^r = \beta_{ij}^q$
- d) qth reyielding $E_s = E_s, \alpha_{ij}^r = \alpha_{ij}^q, \beta_{ij}^r = \beta_{ij}^q$

Thus, there are four basic regions of response for which the stress-strain relations have been established by Equation 10. For an elastic-perfectly plastic material, $E_t = 0$ and α_{ij}^r are set equal to zero in Equations 8 and 10. It should be noted that for a strain hardening material, a stress path which may move along the yield surface (neutral loading) would not be properly represented in the analysis, since, upon unloading, the yield surface would be rigidly translated.

The constitutive relations for the stiffener's material are based on those used for the skin, except they reduce to the uniaxial case. The stiffeners may be of material different from each other and different from that of the panel skin to which they are attached. For elastic-plastic solutions the stiffeners are segmented by a sufficient number of layers so as to represent the stress distribution across the cross-section.

For elastic, isotropic or orthotropic multilayered panels, the stress-strain relation formulation follows the approach presented in [6]. In orthotropic layers, the geometric cylindrical coordinate axes and principal orthotropic direction are assumed parallel. For the elastic solution, additional membrane, bending and cross coupling stiffness coefficients are computed at all integration points at which stiffeners are located. In computing these stiffness coefficients, the segmented stiffener is treated as a multilayered configuration with variable widths.

Displacement Component Functions

In Equation 1 the displacement components are expressed in series form as a product of time-dependent coefficients and independent spatial functions $\phi_m(x)$ and $\phi_n(\theta)$. These spatial functions are selected so as to satisfy the geometric boundary conditions of the panels. The boundaries of the panel are assumed to be either clamped or simply supported and held from inplane movement. The spatial functions for the u and v displacements are assumed to be the same whether the edges are clamped or simply supported and are given by

$$\begin{aligned}\phi_m^u(\gamma) &= \sin(m+1)\gamma, & \phi_m^u(\beta) &= \sin(n)\beta \\ \phi_m^v(\gamma) &= \sin(m)\gamma, & \phi_n^v(\beta) &= \sin(n+1)\beta\end{aligned}\quad (11)$$

The boundary combinations for the γ and β directions are based on opposite edges being both clamped, both simply supported or one clamped and one simply supported. The w-displacement functions for the γ and β directions are based on the natural vibratory mode shapes of a uniform beam and are given as follows for the three boundary combinations:

For clamped/clamped or clamped/simply supported

$$\begin{aligned}\phi_m^w &= \cosh \frac{\lambda_m \gamma}{\pi} - \cos \frac{\lambda_m \gamma}{\pi} - \alpha_m \left(\sinh \frac{\lambda_m \gamma}{\pi} - \sin \frac{\lambda_m \gamma}{\pi} \right) \\ \phi_n^w &= \cosh \frac{\lambda_n \beta}{\pi} - \cos \frac{\lambda_n \beta}{\pi} - \alpha_n \left(\sinh \frac{\lambda_n \beta}{\pi} - \sin \frac{\lambda_n \beta}{\pi} \right)\end{aligned}\quad (12)$$

where

λ_m or λ_n are the roots of $\cos \lambda_i \cosh \lambda_i = 1$ for the clamped/clamped boundary condition

λ_m or λ_n are the roots of $\tan \lambda_i = \tanh \lambda_i$ for the clamped/simply supported boundary condition

$$\alpha_i = \frac{\cosh \lambda_i - \cos \lambda_i}{\sinh \lambda_i - \sin \lambda_i} \quad (i = n \text{ or } m)$$

For simply supported/simply supported

$$\begin{aligned}\phi_m^w &= \sin(m)\gamma \\ \phi_n^w &= \sin(n)\beta\end{aligned}\quad (13)$$

Governing Equations of Motion

The spatial integrations in Equation 2 are to be accomplished numerically thus providing a mechanism for discretization through the spatial points selected to compute the representative elastic-plastic behavior throughout the panel. For integration through the thickness of the panel in the z direction, it is convenient to separate the integrand into parts which either are or are not explicitly dependent on the z variable, that is involving membrane strains and bending strains. The total strain quantities ϵ_{ij} for an arbitrary position in the panel consist of the membrane and bending components given by

$$\epsilon_{ij} = \epsilon_{ij} + z\kappa_{ij} \quad (14)$$

Therefore, the integrand can be given by $f^m + zf^b$ where

$$\begin{aligned} f^m &= \sigma_{xx} \frac{\partial \epsilon_{xx}}{\partial W_{mn}} + \sigma_{\theta\theta} \frac{\partial \epsilon_{\theta\theta}}{\partial W_{mn}} + \sigma_{x\theta} \frac{\partial \epsilon_{x\theta}}{\partial W_{mn}} \\ f^b &= \sigma_{xx} \frac{\partial \kappa_{xx}}{\partial W_{mn}} + \sigma_{\theta\theta} \frac{\partial \kappa_{\theta\theta}}{\partial W_{mn}} + \sigma_{x\theta} \frac{\partial \kappa_{x\theta}}{\partial W_{mn}} \end{aligned} \quad (15)$$

and the total stress components are obtained from Equations 10 and 7 in which $i,j=1$ denotes x and $i,j=2$ denotes θ . The Legendre-Gauss quadrature formula [7] was chosen for the numerical integration in the z direction where \bar{L} is the number of points selected through the thickness of the panel. In the γ and β directions it is convenient to have even spacing and it is advantageous to have spatial points on the clamped edges and at the center of the panel. Simpson's quadrature formula [7] satisfies these desirable features and therefore was selected over various Gaussian quadrature formulas. The number of spatial points selected in the γ and β directions are given by \bar{M} and \bar{N} , respectively, where \bar{M} and \bar{N} must be odd numbers. The integrand quantities for the stiffener are given by

$$\begin{aligned} f^\gamma &= \sigma_{xx} \frac{\partial \epsilon_{xx}}{\partial W_{mn}} + \frac{\bar{z}_i}{a} \sigma_{xx} \frac{\partial \kappa_{xx}}{\partial W_{mn}} \quad (\text{for } \gamma\text{-stiffeners}) \\ f^\beta &= \sigma_{\theta\theta} \frac{\partial \epsilon_{\theta\theta}}{\partial W_{mn}} + \frac{\bar{z}_i}{a} \sigma_{\theta\theta} \frac{\partial \kappa_{\theta\theta}}{\partial W_{mn}} \quad (\text{for } \beta\text{-stiffeners}) \end{aligned} \quad (16)$$

where \bar{z}_i is the distance from the coordinate surface to the center of the i^{th} stiffener segment and is expressed as $\bar{z}_i = \pm \frac{1}{2} (h_i + h_{i-1}) - \bar{h}$

where the plus sign is used for "outer" stiffeners and the minus sign for "inner" stiffeners. The trapezoidal rule is used for the numerical integration through the depth of a stiffener in the equation of motion.

In the spatial surface integration of the kinetic energy the addition of the line integrals in the γ and β directions to include the mass of the stiffeners leads to inertial coupling of the modes. The M_{pq} coefficients associated with the w-equations of motion of the inertial coupling matrix [M] are determined from

$$M_{pq} = k_{\gamma} k_{\beta} \bar{\rho} \delta_{mr} \delta_{ns} + \frac{k_{\gamma} \delta_{mr}}{a \theta_o h_{\eta}} \sum_{i=1}^{NSG} \rho_s^i A_s^i \phi_n^w(\beta_k) \phi_s^w(\beta_k) \quad (17)$$

$$+ \frac{k_{\beta} \delta_{ns}}{b h_{\eta}} \sum_{i=1}^{NSB} \rho_s^i A_s^i \phi_m^w(\gamma_j) \phi_r^w(\gamma_j)$$

where

p, q extends over all the modal combinations selected for the solution.
 r, s are particular values of m and n , respectively

In general matrix form the w-equations of motion are given by

$$\ell^2 [M] \{\ddot{w}_{rs}\} = -\{f_{rs}\} \quad (18)$$

For the solution of these equations in DEPROP, Equation 18 is placed in the form

$$\{\ddot{w}_{rs}\} = -\frac{1}{\ell^2} [M]^{-1} \{f_{rs}\} \quad (19)$$

It should be noted from Equation 19 that the inertial coupling matrix has been inverted. In order to accomplish this operation, a matrix inversion subroutine is used in the DEPROP program. Although the above derivation is only demonstrated for the normal motion of the stiffened panel, similar inertial coupling matrices have been established in the program for the inplane motions of the panel (u and v-equations of motion).

For the elastic-plastic solution of a stiffened single-layered panel the equations of motion are given by

$$k_{\gamma} k_{\beta} [M] \ell^2 \ddot{w}_{mn} + \frac{\pi^2}{9(\bar{M}-1)(\bar{N}-1)} \sum_{j=1}^{\bar{M}} \sum_{k=1}^{\bar{N}} H_j H_k \left\{ L^2 \sum_{i=1}^{\bar{L}} H_i \left[f_i^m(\gamma_j, \beta_k) \right] \right\}$$

$$\begin{aligned}
& + \frac{1}{2R} \xi_i f_i^b (\gamma_j, \beta_k) \left| + \frac{6L^2}{h} \left[\frac{(\bar{N}-1)}{H_k a \theta_o} \sum_{i=1}^{NSEG} \bar{b}_i (h_i - h_{i-1}) f_i^\gamma (\gamma_j, \beta_k) \right. \right. \\
& + \left. \left. \frac{(\bar{M}-1)}{H_j \ell} \sum_{i=1}^{NSEG} \bar{b}_i (h_i - h_{i-1}) f_i^\beta (\gamma_j, \beta_k) \right] \right. \\
& + \left. \frac{L^2 R}{2a^3} \left[\frac{3(\bar{N}-1)}{a \theta_o H_k} \bar{G}_\gamma J_\gamma + \frac{3(\bar{M}-1)}{\ell H_j} \bar{G}_\beta J_\beta \right] K_{x\theta} \frac{\partial K_{x\theta}}{\partial W_{mn}} - \tilde{Q}_w (\gamma_j, \beta_k) \right\} = 0 \quad (20)
\end{aligned}$$

where

$$\tilde{Q}_w = 2L^2 R p (1 - \lambda W - + J V_\beta + \frac{1}{L} U_\gamma) \frac{\partial W}{\partial W_{mn}}$$

$$\tilde{Q}_v = -2L^2 R p (J W_\beta + + \lambda V) \frac{\partial V}{\partial V_{mn}}$$

$$\tilde{Q}_u = -2L R p W_\gamma \frac{\partial U}{\partial U_{mn}}$$

Although Equation 20 is given in terms of W_{mn} , the equations of motion for the tangential and axial displacement directions are obtained by omitting the torsion term and using the appropriate k_γ , k_β and \tilde{Q} expressions.

For elastic solutions the equations of motion are simpler since the stiffness coefficients of the stiffeners are integrated directly with the stiffness coefficients of the panel skin (see [1] and [2]).

For sandwich panels, it is assumed that the core of the sandwich or honeycomb always remains undamaged and the normal stresses are carried just by the face sheets. It is further assumed that the stress across each face sheet is constant. In the equations of motion given by Equation 20, the single layered expression in the first brackets (associated with the first summation over i) is replaced for the sandwich panel by

$$\frac{2L^2}{h_3} \sum_{i=1}^{1\&3} (h_i - h_{i-1}) \left| f_i^m (\gamma_j, \beta_k) + \frac{z_i}{a} f_i^b (\gamma_j, \beta_k) \right| \quad (21)$$

where

$$\begin{aligned} z_1 &= \frac{1}{2}h_1 - \bar{H} \\ z_3 &= \frac{1}{2}(h_3 + h_2) - \bar{H} \end{aligned}$$

In stiffened honeycomb panels the honeycomb core is often crimped where the panel skin intersects the various stiffeners for attachment purposes (see configuration D of figure 2). It is assumed that the core is fully removed over the stiffener, so that the bending resistance of the panel along the stiffener line is negligible compared with that of the uncrimped honeycomb panel. Thus, only membrane stresses in both coordinate directions are assumed to be transmitted through the honeycomb face sheets at positions along the stiffener lines for this type of construction.

The second-order differential equations given by Equation 20 and corresponding equations for V_{mn} and U_{mn} are to be solved numerically in time. The integration method used to obtain an approximate timewise step-by-step solution is based on the central difference formula given by

$$X_{k+1} = \ddot{X}_k (\Delta t)^2 + 2X_k - X_{k-1} \quad (22)$$

where

X represents the normalized undetermined time-dependent displacement coefficients, W_{mn} , V_{mn} and U_{mn} .

In solving the set of simultaneous second-order differential equations, spatial integrations must be performed in the γ and β directions and in the z direction for the elastic-plastic solution during the stepwise time integration. The required integrations are performed numerically during each time step using the values of the displacement coefficients W_{mn} , V_{mn} and U_{mn} for the particular time step to compute the displacements and their derivatives, the strain quantities and the stress quantities used in Equation 20.

Special numerical schemes [1] are used to treat the overshoot during the time increment in which yielding occurs, to establish the criteria for determining elastic unloading and to obtain a consistent determination of $\bar{\epsilon}$, E_s , v_s and σ_{ij} during each time step.

DEPROP Comparisons with Experiments and Other Analyses

Comparisons are made between experiment results from various tests performed on unstiffened and stiffened panels subjected to blast loading and those predicted by the DEPROP analysis. In Figure 5 the permanent center displacements of 18 in. by 18 in. clamped unstiffened aluminum

plates of 0.063 in. and 0.071 in. thicknesses, which were blast tested at Eglin Air Force Base [8], are compared with corresponding DEPROP predictions. It should be noted that these plates were close to the point of rupture along the clamped edges.

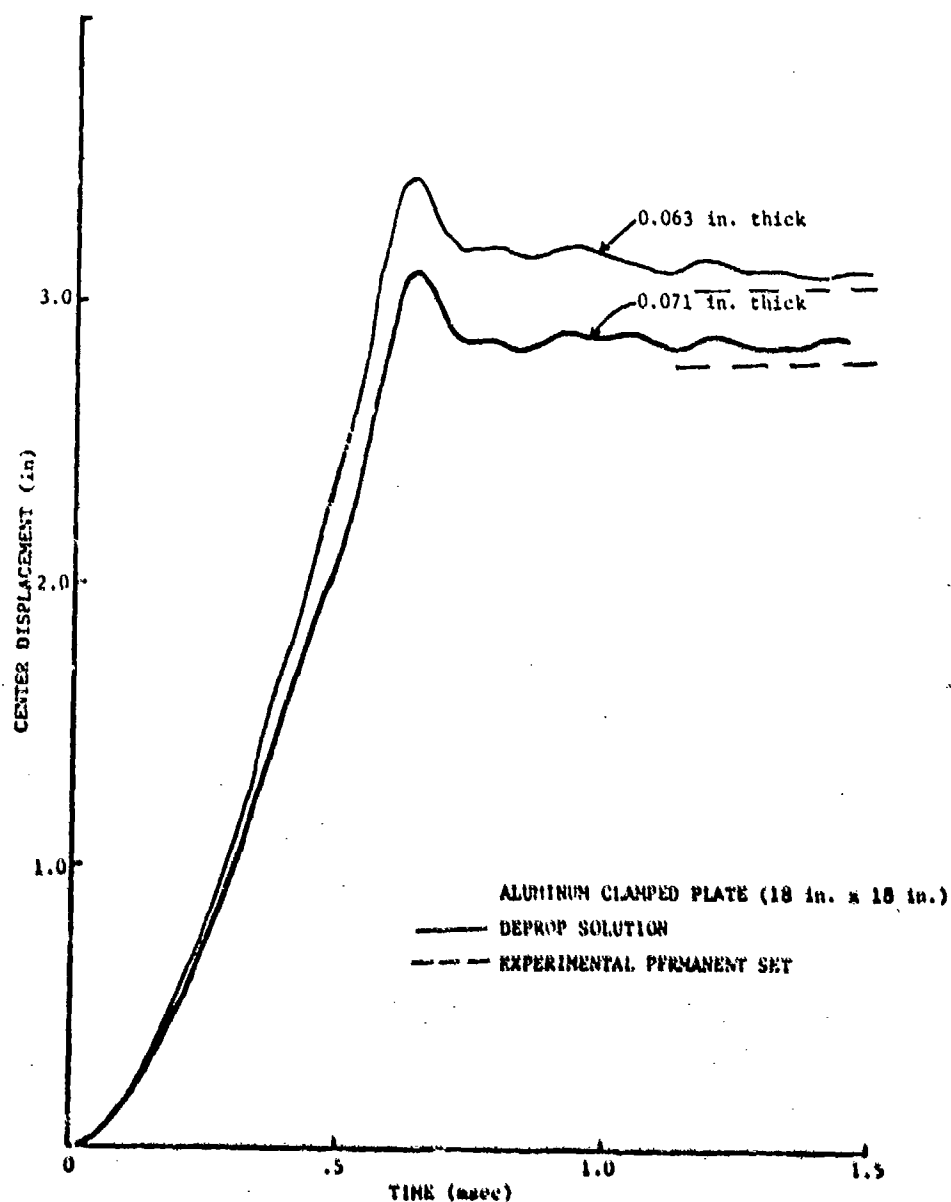


Figure 5. Center Displacement Response of the Eglin Test Plates

Comparisons of DEPROP predictions with strain and displacement measurements made on an unstiffened 15 in. by 15 in. aluminum plate of .05 in. thickness, which was tested in the shock tube at the Naval Surface Weapons Center (NSWC) [9], are presented in Figures 6, 7, and 8. The response of this plate was in the elastic region and the assumed uniform pressure loading was generated from measured pressure time history data taken near the edge of the plate.

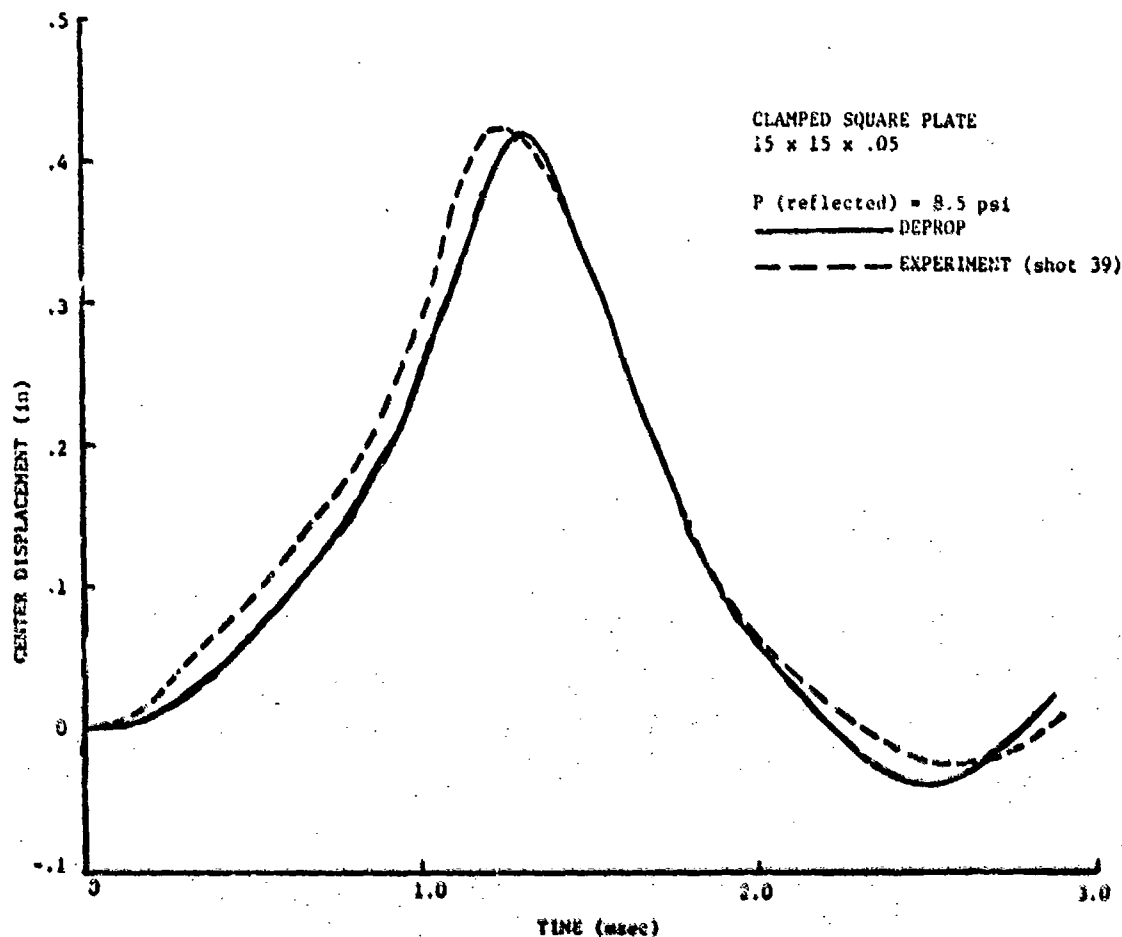


FIGURE 6. CENTER DISPLACEMENT OF A .05 in CLAMPED SQUARE PLATE AT NSWC

Well-defined response tests were performed on stiffened cylindrical panels with clamped edges in [10]. To assure reliable structural geometry and clamped-edge boundary conditions, the test specimens were machined from solid blocks of 6061-T6 aluminum. The test specimen is nominally a 60-degree cylindrical panel, 0.1 inch thick, 6.0 inches long and 6.0 inches in radius. The integral inner stiffener in the circumferential direction is located in the center of the panel and is nominally 0.1 inch thick and 0.4 inch deep. An impulsive loading was obtained by placing a high explosive (HE) sheet with a foam buffer over a prescribed area of the panel. The magnitude, I , of the impulsive loading applied to the panel is 0.162067 psi-sec.

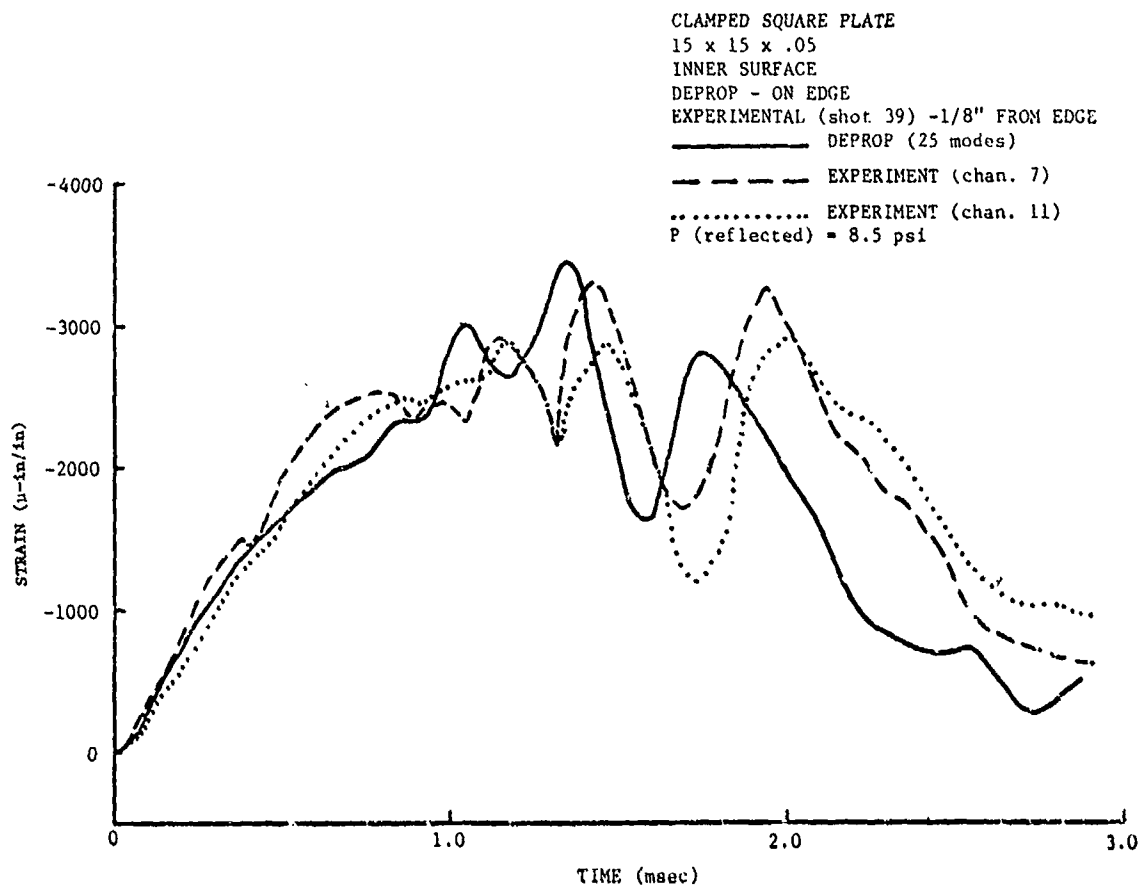


FIGURE 7. EDGE STRAINS FOR .05" CLAMPED SQUARE PLATE AT NSWC

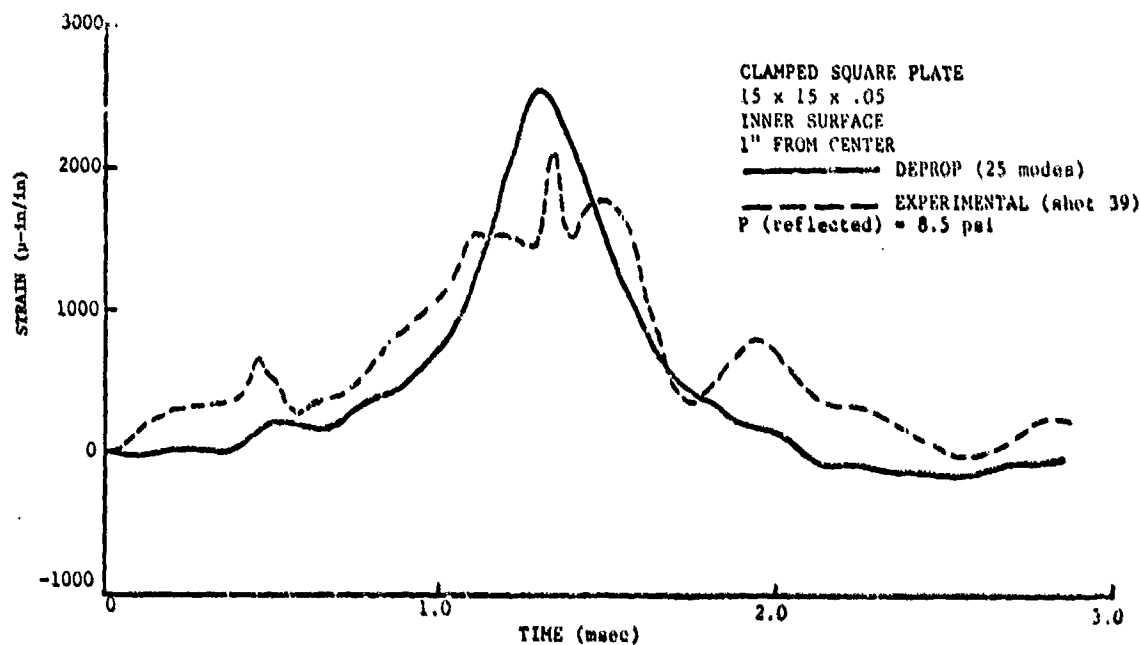


FIGURE 8. NEAR CENTER STRAINS FOR A .05 in CLAMPED SQUARE PLATE AT NSWC

This clamped cylindrical stiffened panel subjected to an impulsive loading was modeled using the DEPROP program to predict the analytical response for comparison with the experimental results. Figure 9 illustrates the geometry of the analytical model for the stiffened panel. The circumferential stiffener located midway along the length of the panel is rectangular in cross section and has 1/8 inch filets where it intersects the panel skin. The shaded area indicates the portion of the panel that was impulsively loaded by the HE sheet. As shown in Figure 9 the stiffener is divided evenly into five segments for the elastic-plastic solution. The width of the first segment is increased to account for the area of the filets.

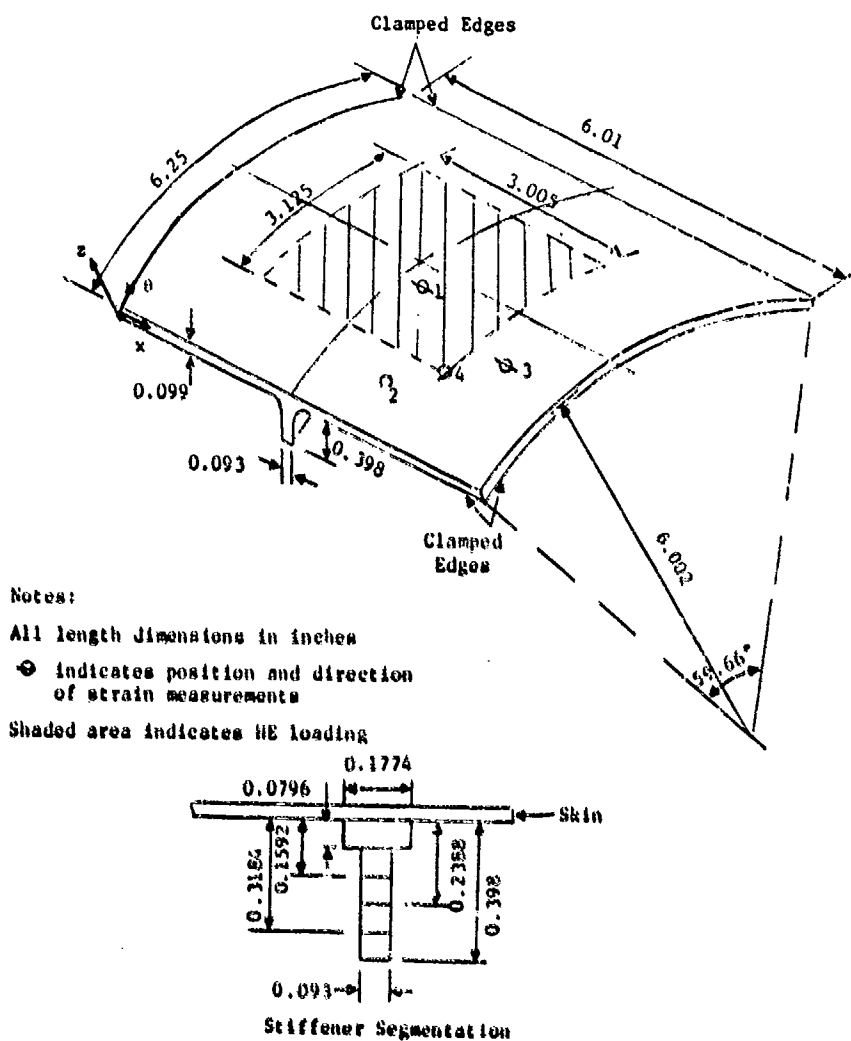


Figure 9. MIT Cylindrical Stiffened Panel Model

Comparisons between analytical and experimental results for the MIT stiffened cylindrical panel are made for the four measured inner surface strain time histories and two permanent-set displacement measurements. Figures 10 and 11 show the comparisons for the four measured strain positions where the solid lines are analytically determined from DEPROP and the dashed lines are experimentally measured. At position 1 the experimental strain trace terminated just after reaching the peak and at position 3 the strain trace briefly went out of recording range during the peak portion of the response. This stiffened panel underwent large plastic deformations throughout the panel skin and the stiffener. Figure 12 illustrates the analytically determined displacement time histories at two positions on the panel. The measured permanent set values at these positions are compared to the level of oscillation near the end of the analytical time histories. The projected analytical permanent sets are slightly lower than the measured values. This might be expected since the stiffener exhibited plastic lateral buckling over a small region near the ends of the stiffener which can not be represented in the analytical model.

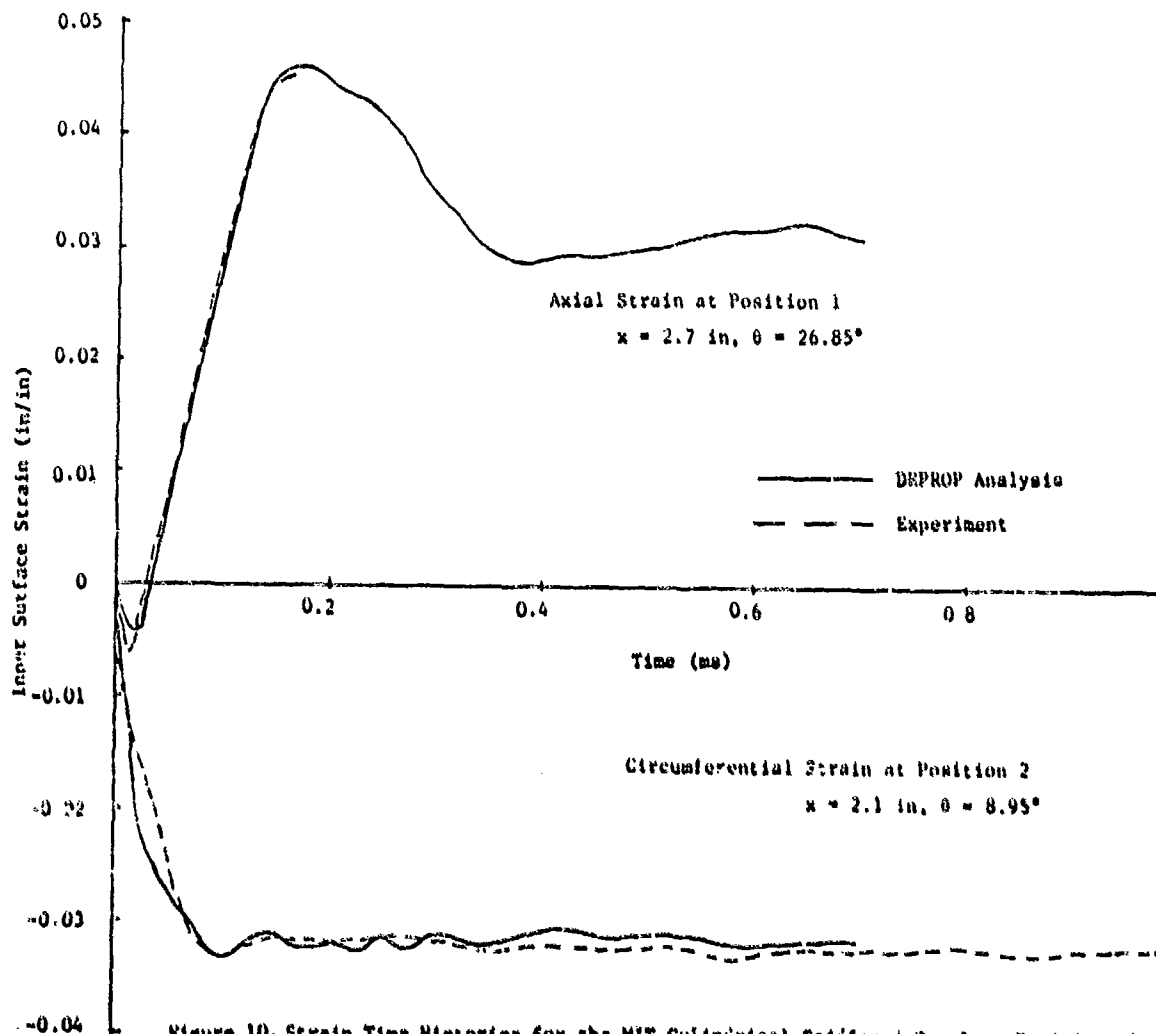


Figure 10. Strain Time Histories for the MIT Cylindrical Stiffened Panel at Positions 1 and 2

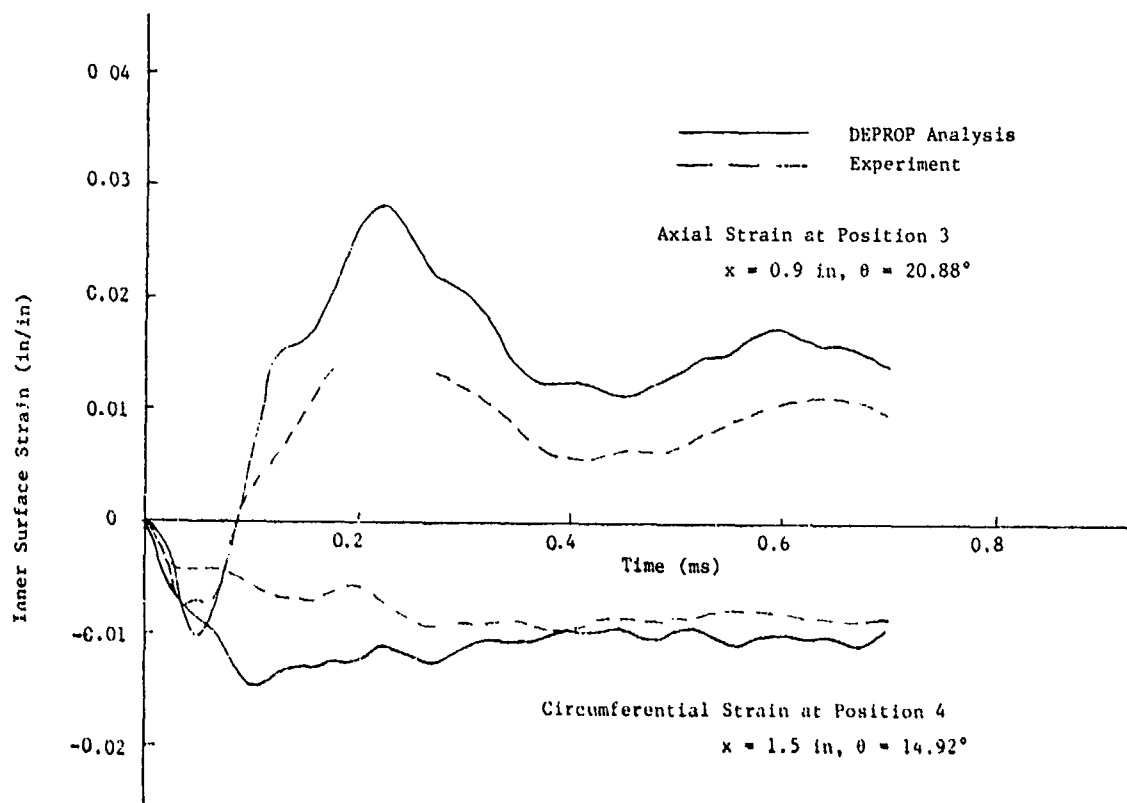


Figure 11. Strain Time Histories for the MIT Cylindrical Stiffened Panel at Positions 3 and 4

The STRESNO test program [11] tested a variety of unstiffened and stiffened panels in the Sandia Thunderpipe shock tube. From the stiffened panels tested, specimen number 10 was selected for the comparison with the stiffened panel analysis. Specimen 10 is a flat 36-by 36-inch skin panel stiffened by three z-shaped inner stiffeners spaced 9 inches apart. The ends of the stiffeners are pinned to the support frame. The skin panel boundaries parallel to the stiffeners are hinged while the skin panel boundaries perpendicular to the stiffeners are unattached except for being riveted to the stiffeners at their three locations. Figure 13 illustrates the geometry of the stiffened panel and the locations of the strain and pressure measurements. The dimensions of the cross section of the stiffeners are also given on Figure 13. The material of the 0.0625-inch panel skin is 2024-T3 aluminum while the material of the stiffeners is 2024-T3511 aluminum.

Analytical and experimental comparison were made for shot 4 on specimen number 10 in which the response remained elastic. The spatial distribution of the pressure measured at P10-1 is assumed uniform over the panel. Strain responses at the center of the stiffener are compared at the lower surface of the lower flange (S10-6) and at the upper skin surface in the β -direction (S10-2a). Figures 14 and 15 show these comparisons for shot 4 where the solid trace is the analytical results

and the dashed trace is the measured results. The largest strains occurred on the lower flange of the stiffener and this strain comparison is shown in Figure 14. Figure 15 shows the comparison of the edge strains at the upper skin surface of the local panel between stiffeners.

Comparisons are also made between DEPROP response results and the nonlinear solutions generated from the finite difference code PETROS-3 [12] and the finite element code ADINA [13]. Figures 16 and 17 show the comparisons for square unstiffened and stiffened flat plates, respectively, subjected to a triangular pressure pulse which produce significant elastic-plastic behavior in the panels.

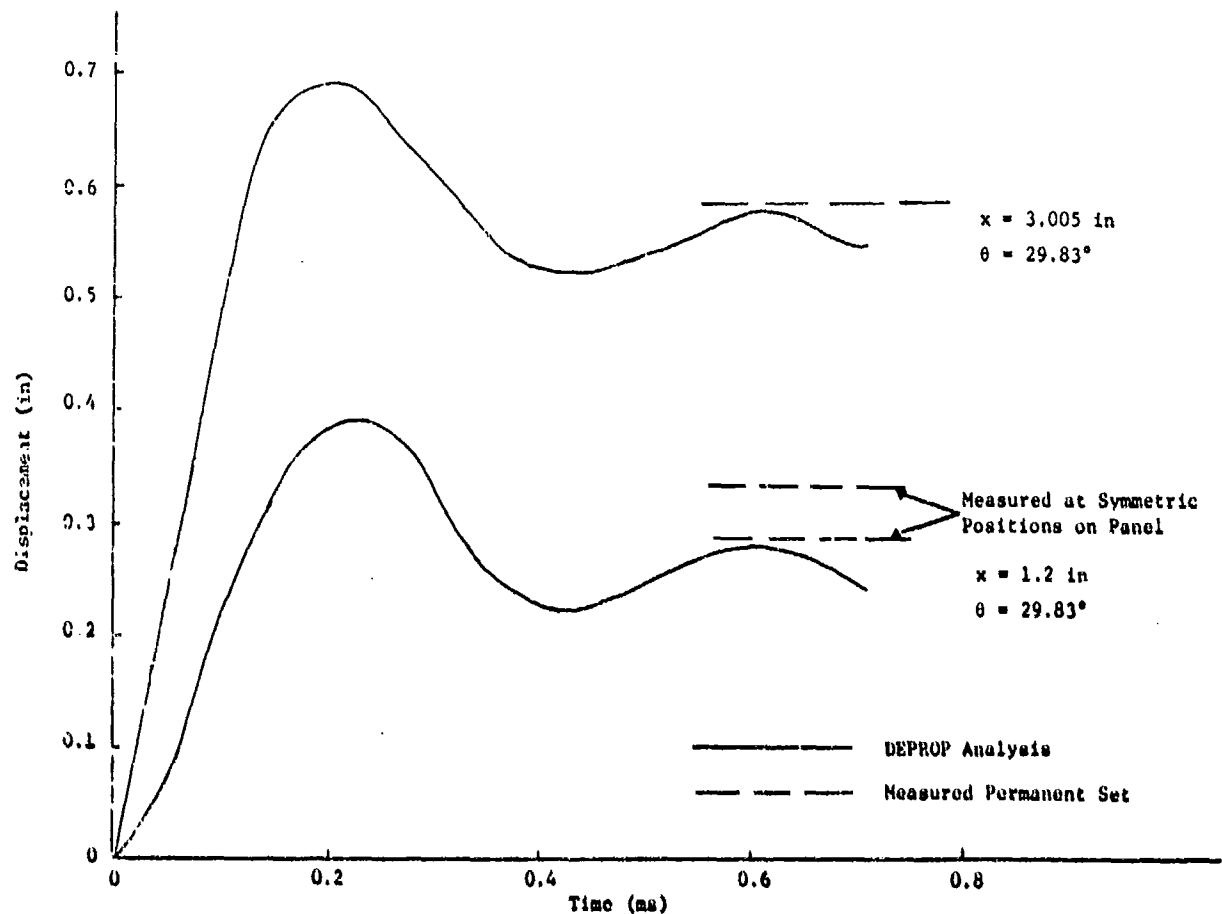


Figure 12. Displacement Time Histories for the MIT Cylindrical Stiffened Panel

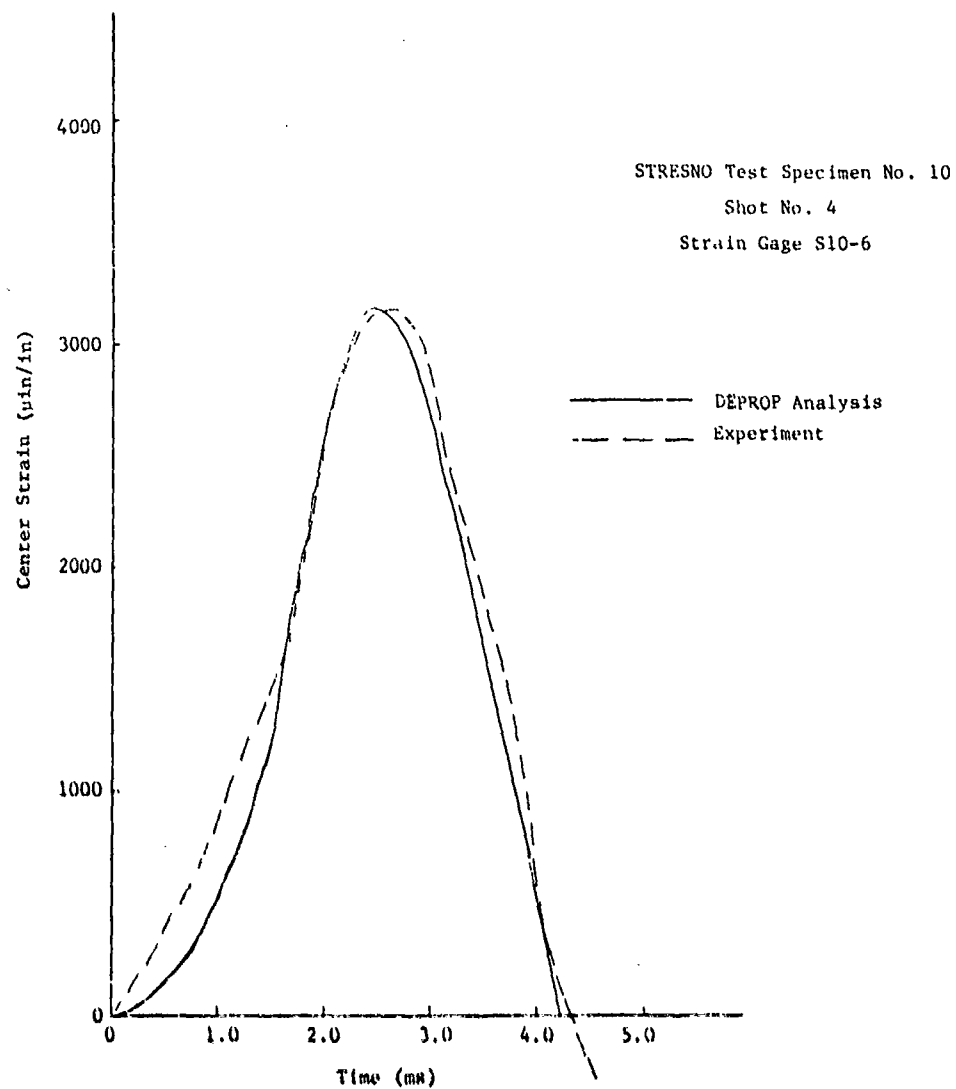


Figure 14. Center Strain Time Histories on Lower Flange of Stiffener for Shot No. 4

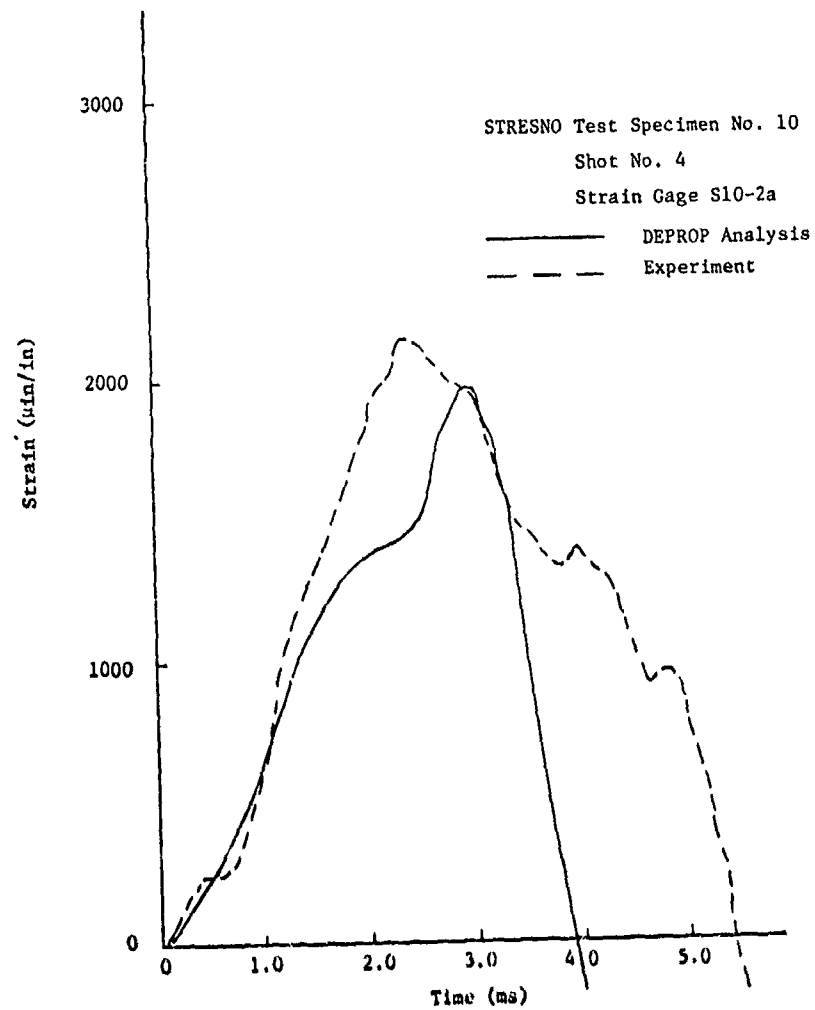


Figure 15. Center Strain Time Histories on Edge of Panel Skin for Shot No. 4

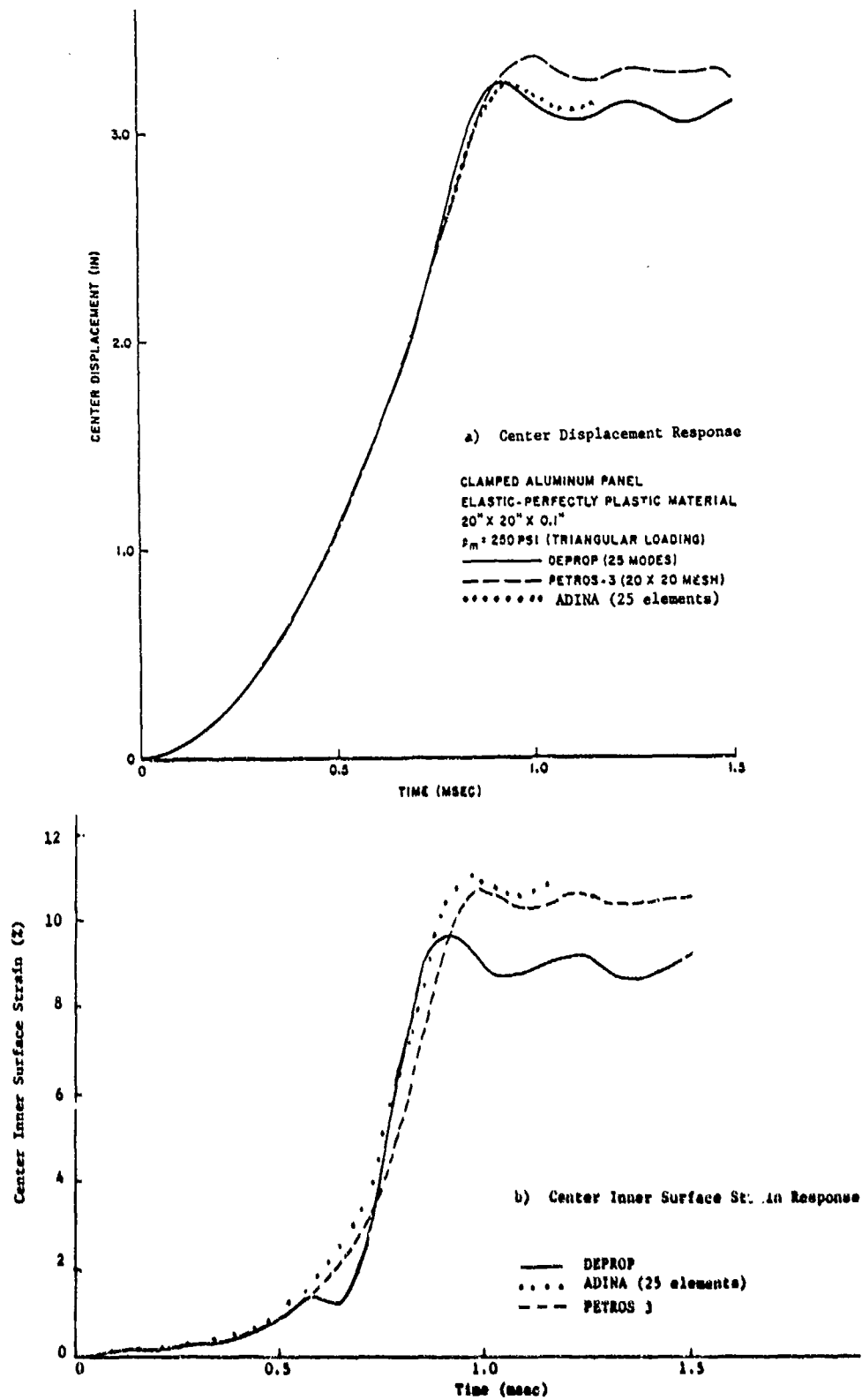


Figure 16. Comparison of DEPROP with PETROS-3 and ADINA Responses for a Clamped Unstiffened Panel

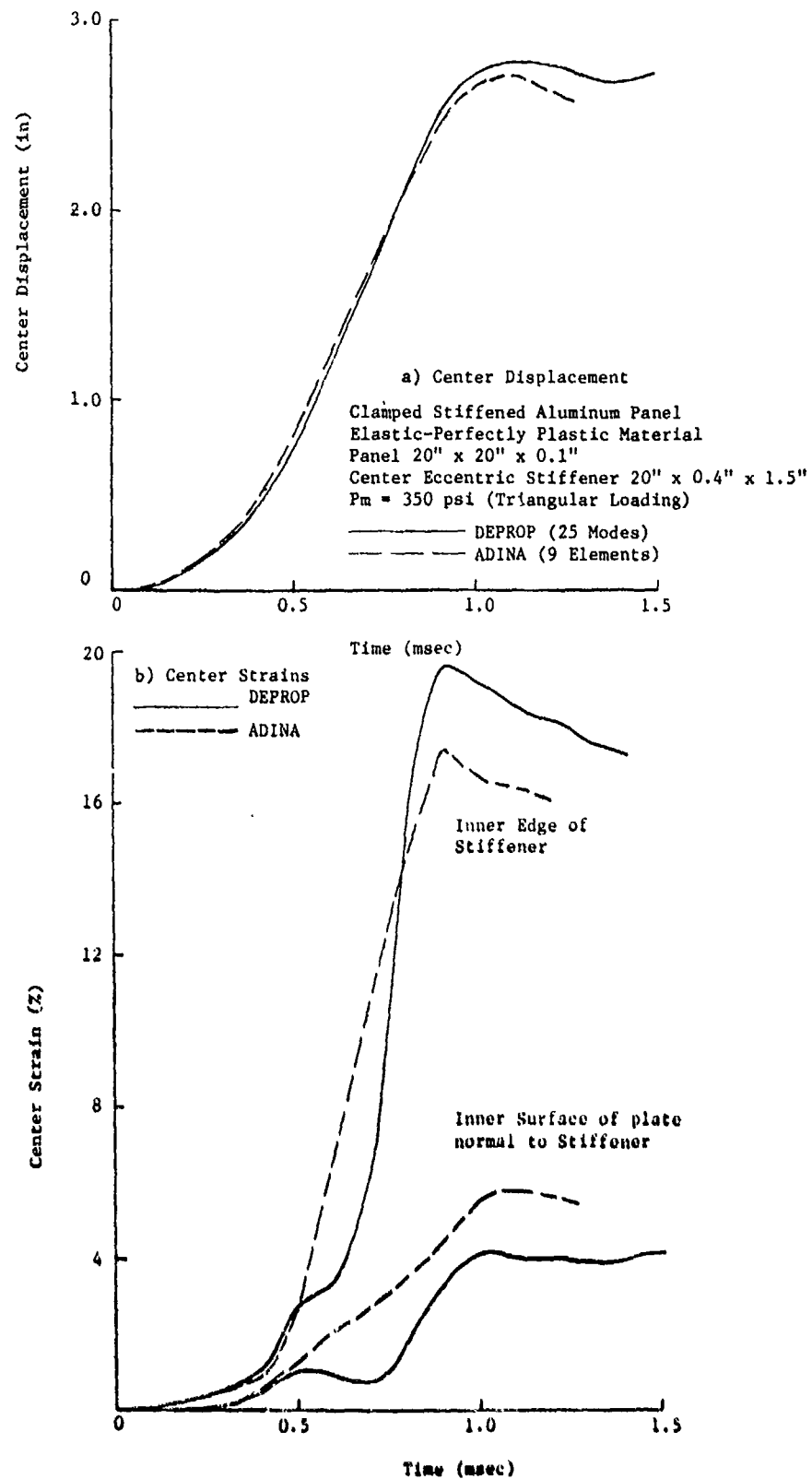


Figure 17. Comparison of DEPROP with ADINA
Response for a Clamped Stiffened Panel

CONCLUSIONS

DEPROP has the capability predicting dynamic response for various unstiffened and stiffened cylindrical or flat panels undergoing deformations which are both geometrically and physically nonlinear. DEPROP was developed specifically to study the vulnerability of aircraft-type panels to overpressure effects from nuclear blast loadings. With its limitations on the initial geometry of the panel, DEPROP was not intended to be a general purpose structural computer code. For elastic solutions DEPROP can handle orthotropic multilayered skin panels, while for inelastic solutions the skin panels are restricted to isotropic single layered and sandwich configurations. For both elastic and inelastic solutions, discrete stiffeners of various cross-sections can be analyzed in both coordinate directions at various eccentricities relative to the panel skin. Comparisons with available experimental results from blast tests on panels and comparisons with other nonlinear structural computer codes has built up confidence in the ability of DEPROP to predict the elastic-plastic response of unstiffened and stiffened panels with well-defined clamped or simply supported boundary conditions.

ACKNOWLEDGEMENT

The development of DEPROP was supported by the Air Force Weapons Laboratory, Kirtland Air Force Base, NM under Contracts F29601-75-C-0032 and F29601-78-C-0019.

REFERENCES

1. Lee, W.N. and Mente, L.J., "NOVA-2 - A Digital Computer Program for Analyzing Nuclear Overpressure Effects of Aircraft," Air Force Weapons Laboratory Report, AFWL-TR-75-262, Pt. 1, August 1976.
2. Mente, L.J. and Lee, W.N., "NOVA-2S, A Stiffened Panel Extension of NOVA-2 Computer Program," Air Force Weapons Laboratory Report, AFWL-TR-78-182, December 1978.
3. Mente, L.J., "Dynamic Nonlinear Response of Cylindrical Shells to Asymmetric Pressure Loading", AIAA Journal, Vol. 11, No. 6, June 1973.
4. Novozhilov, V.V., Foundations of the Nonlinear Theory of Elasticity, Graylock Press, Rochester, N.Y., 1953.
5. Arman, H., Jr., Levine, H.S., and Pifko, A.B., "Plasticity-Theory and Finite Element Applications", Advances in Computational Methods in Structural Mechanics and Design, UAI Press, Huntsville, Alabama, 1972.

6. Ambartsumayan, S.A., "Theory of Anisotropic Shells," NASA TT F-118, May 1964.
7. Hildebrand, F.B., Introduction to Numerical Analysis, McGraw-Hill, New York, 1956.
8. Strickland, W.S., and Ross, C.A., "The Plastic Response of Rectangular Membrane Plates to Mild Explosive Loading Functions," Air Force Armament Laboratory, Eglin AFB, AFATL-TR-74-181, November 1974.
9. Yeghiayan, R.P., "Analytical Predictions and Correlation with Experiments for Thermal/Blast Exposure of Aircraft Panels," Defense Nuclear Agency Report, DNA4446F, July 1977.
10. Witmer, E.A., Wu, R.W-H. and Merlis, F., "Experimental Transient and Permanent Deformation Studies of Impulsively-Loaded Rings and Cylindrical Panels, Both Stiffened and Unstiffened," Aero-elastic and Structures Research Laboratory, Mass. Inst. of Tech., ASRL TR171-3 (AMMRC CTR 74-29), April 1974.
11. Syring, R.P. and Pierson, W.D., "Structural Response to Simulated Nuclear Overpressure (STRESNO): A Test Program Establishing a Data Base for Evaluating Present and Future Analytical Techniques," Defense Nuclear Agency, DNA4278F-1 & 2, March 1977.
12. Atluri, S., Witmer, E.A., Leech, J.W., and Morino, L., "PETROS 3: A Finite-Difference Method and Program for the Calculation of Large Elastic-Plastic Dynamically-Induced Deformations of Multi-layer Variable-Thickness Shells", BRL CR 60 (MIT-ASRL TR 152-2), November 1971.
13. Bathe, K.J., "ADINA, A Finite Element Program for Automatic Dynamic Incremental Nonlinear Analysis," Report 82448-1, Acoustics and Vibration Lab., Mechanical Engineering Dept. MIT, May 1977.

SESSION III: COMPOSITES

Chairman: R. Foye
Aerospace Technologist
Army Research & Technology Laboratory, AVRADCOM

COMBAT DAMAGE TOLERANT WING STRUCTURAL DEVELOPMENT 159

J. G. Avery,
S. J. Bradley, and
K. M. King
Boeing Military Airplane Company

THE RESPONSE OF ADVANCED COMPOSITE STRUCTURES TO HIGH EXPLOSIVE BLAST. . 187

A. L. Dobyms
J. G. Avery
Boeing Military Airplane Company

STABILITY OF COMPOSITE PLATES SUBJECTED TO VARYING TANGENTIAL AND
LATERAL LOADS. 204

R. J. Stuart
S. Dharmarajan
San Diego State University

COMPRESSION STRENGTH DEGRADATION OF ADVANCED COMPOSITE STRUCTURES. . . . 219

D. Y. Konishi
Rockwell International,
North American Aircraft Division

SESSION III: COMPOSITES

Chairman: R. Foye
Aerospace Technologist
Army Research & Technology Laboratory, AVRADCOM

COMBAT DAMAGE TOLERANT WING STRUCTURAL DEVELOPMENT 159

J. G. Avery,
S. J. Bradley, and
K. M. King
Boeing Military Airplane Company

THE RESPONSE OF ADVANCED COMPOSITE STRUCTURES TO HIGH EXPLOSIVE BLAST. . 187

A. L. Dobyns
J. G. Avery
Boeing Military Airplane Company

STABILITY OF COMPOSITE PLATES SUBJECTED TO VARYING TANGENTIAL AND
LATERAL LOADS. 204

R. J. Stuart
S. Dharmarajan
San Diego State University

COMPRESSION STRENGTH DEGRADATION OF ADVANCED COMPOSITE STRUCTURES. . . . 219

D. Y. Konishi
Rockwell International,
North American Aircraft Division

COMBAT DAMAGE TOLERANT WING STRUCTURAL DEVELOPMENT

JOHN G. AVERY
Engineering Manager

SUSAN J. BRADLEY
Technical Analyst

KENNETH M. KING
Design Engineer

Boeing Military Airplane Company
Advanced Airplane Branch
Seattle, Washington 98124

ABSTRACT

This paper describes the development of a graphite/epoxy fighter wing-box capable of sustaining limit load and cyclic loading following worst-case damage from a 23-mm HEI (superquick fused) projectile impact. This work was done under the Battle Damage Tolerant Wing Structural Development Program (N00019-75-C-0178) sponsored by the Naval Air Systems Command. The objective was to develop and demonstrate the technology needed to design battle damage tolerant aircraft structure using advanced fiber composites. It was felt that the high strength-to-weight ratio of advanced composites combined with their flexibility in design applications could result in structure which was lighter than metal configurations while providing superior battle damage tolerance. Program results have confirmed this belief, including a successful 23-mm HEI ballistic testing of full-scale structure under load.

1.0 INTRODUCTION

Military aircraft must be capable of performing successfully in hostile environments created by small-arms automatic weapons, anti-aircraft artillery, and surface-to-air and air-to-air missiles. Consequently, designing for resistance and tolerance to combat damage is an important consideration facing structural designers. In this context, damage "resistance" is a measure of the amount of damage inflicted by a threat exposure, and damage "tolerance" is a measure of the ability of the structure to endure the inflicted damage.

Although the vulnerability analyst has always been concerned with the effects of ballistic weapons on aircraft, this is unfamiliar ground for the structural designer. The potential effects of this unfamiliarity became especially evident in the early 1970's as a result of increasing consideration of using graphite/epoxy in the primary structure of combat airplanes. Graphite/epoxy laminates configured in a quasi-isotropic 0_{+45}_{-90} layup are very damage sensitive, comparable in damage sensitivity to 7075-T6 aluminum. To obtain useful levels of battle damage tolerance in these materials, the required design technology must be formulated and integrated within the structural design process. The Battle Damage Tolerant Wing Structural Development Program, sponsored by the Naval Air Systems Command (Ref. 1), was initiated in 1974 to develop and demonstrate the technology needed to design fiber composite structure having good survivability to

ballistic weapon threats, particularly high-explosive anti-aircraft artillery rounds such as the 23-mm HEI projectile.

The technology developed under this program resulted from the combined efforts of weapons effects experts, vulnerability specialists, structural analysts, and structural designers. The goal was to develop and demonstrate a graphite/epoxy wing-box capable of meeting a worst-case battle damage tolerance criteria, while at the same time obtaining a weight savings relative to a baseline metallic wing-box patterned after the F-14 titanium configuration.

The final wing-box design meets all these requirements. A significant advancement in composite design technology was a new skin/spar concept that can sustain limit loads in the presence of massive structural damage. This concept makes effective use of hybrid laminates combining graphite/epoxy with fiberglass. As final verification a full-scale test component was built and tested by firing a 23-mm HEI projectile directly into a spar while the box was loaded to 4-g's in combined bending and torsion. After damage, limit load in bending and torsion was successfully applied, followed by ten cycles of two-thirds limit load to verify full flight capability.

2.0 PROGRAM DEFINITION

The first major program decision was the selection of the F-14 wing as the baseline configuration. Design attention was directed at the mid-span section shown in Figure 1. The external geometry, applied load conditions, and general design criteria of the F-14 wing were retained throughout the development.

Specific design requirements and criteria, summarized in Figure 2, were mutually agreed upon by Boeing and Navy personnel early in the program. The General Design Criteria incorporate the design requirements of the F-14. The Structural Weight Criteria requires that the battle damage tolerant fiber composite wing-box weigh 25-percent less than the titanium F-14 baseline wing-box.

The Battle Damage Tolerance Criteria require the wing-box to survive a worst-case hit by a 23-mm HEI projectile while undergoing a 4-g maneuver and be capable of limit load after the hit. Cruise home and landing capability after damage is also required. The limit load conditions consisted of 7.5-g maximum positive bending and 3.0-g maximum negative bending. The worst-case hit was defined as a direct hit into a spar. In effect, these criteria mean virtual invulnerability of the structure to the 23-mm HEI projectile. This is a very stringent design objective, especially in conjunction with the weight savings objective.

Design development of the battle damage tolerant wing-box was started in 1972 under Contract N00019-72-C-0433 as indicated in Figure 3. This initial work (Ref. 1) defined the impact of the battle damage tolerance design criteria on weight and cost for many types of structural configurations, including metal designs. In addition, a preliminary wing design concept using graphite/epoxy was developed that met all requirements. A second contractual effort in 1973, N00019-73-C-0501 (Ref. 2), verified the flutter performance of the damaged wing-box. The work reported herein was done under the

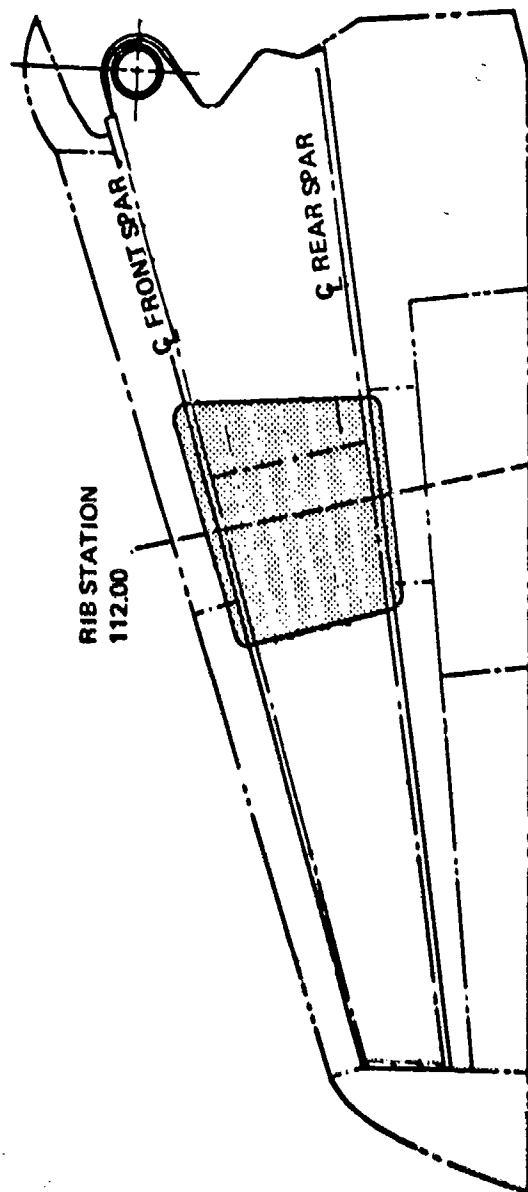
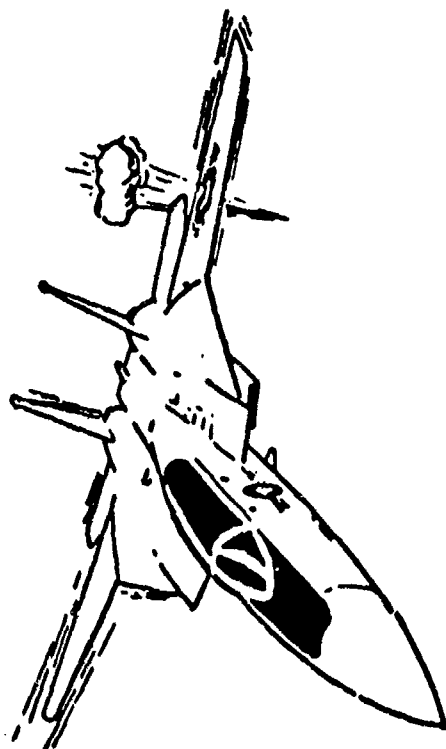


Figure 1. Design Development Was Directed at the Midspan Section of an F-14 Fighter Aircraft



I. GENERAL DESIGN CRITERIA

1. Maximum speed on $M = 2.0$ at altitude and $M = 1.0$ at sea level
2. Critical design load cases are at $M = 0.66$ at sea level (25-deg sweep angle, $+7.5g$, $-3.0g$)
3. Carrier landing design sink speed of 23 ft/s
4. Ultimate internal pressure of 30 lb/in²
5. Fatigue life shall be 12,000 hr for the applicable maneuver spectrum of MIL-A-8886 for the undamaged or repaired structure
6. Corrosion resistance in salt air environment, and fracture resistance will be primary factors

II. STRUCTURAL WEIGHT CRITERIA

Wing must achieve battle damage tolerance with a 25% weight savings over the baseline two-spar titanium wing

III. BATTLE DAMAGE TOLERANCE CRITERIA

1. Wing contains no fuel or fuel vapor at time of projectile impact
2. Structure must sustain a single 23-mm HE impact while undergoing a 4g symmetrical maneuver
3. After damage, structure must not fail from one occurrence of limit load
4. After damage, structure must not fail from:
 - a. 5-hr cruise with maximum 2g load
 - b. A carrier landing at design sink speed of 23 ft/s
5. Design shall stress economic and efficient repair

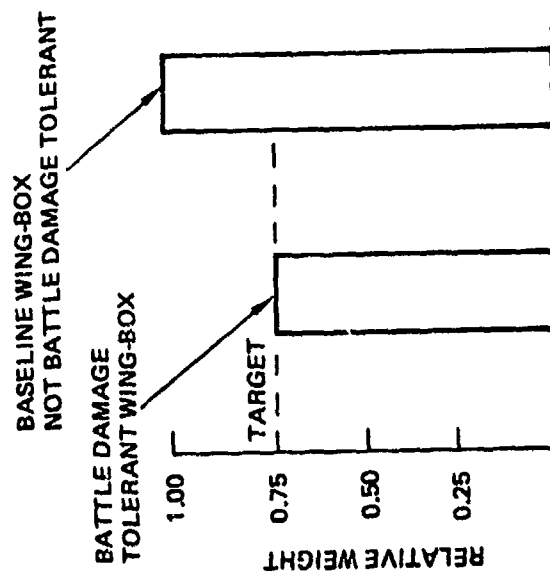


Figure 2. Criteria for Battle Damage Tolerant Wing Structural Development

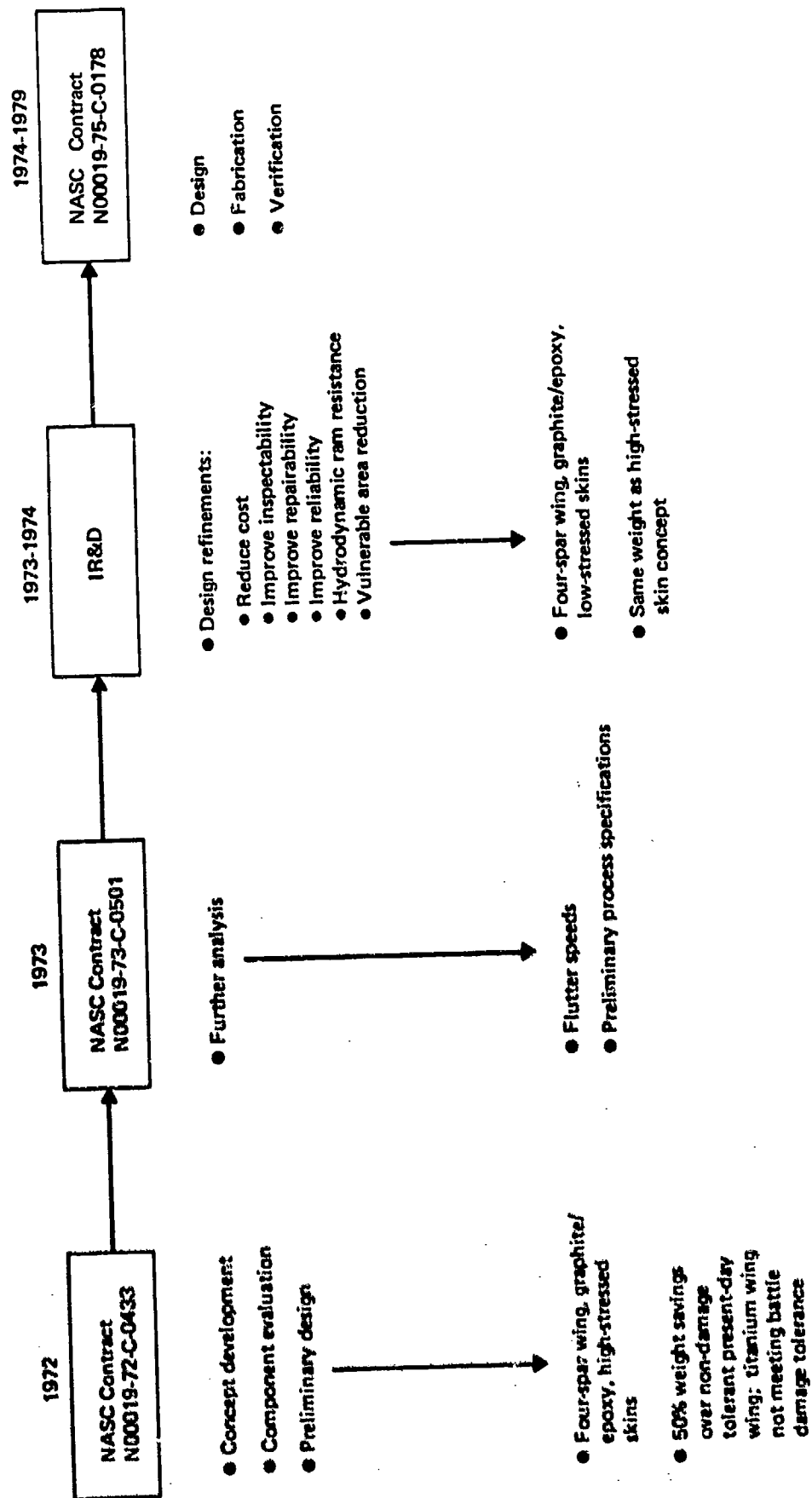


Figure 3. Programs Leading to Development of Battle Damage Tolerant Wing

third contract of the series (Ref. 3), and includes final development, fabrication, and demonstration by ballistic testing of a full-scale graphite/epoxy wing-box component.

The design problems associated with developing wing structure that meets the battle damage tolerance requirements include overcoming the effects of:

- o Extensive fragment and blast damage to skin and substructure;
- o Dynamic internal load redistribution resulting from severed elements;
- o Pronounced notch-sensitivity of graphite/epoxy.

Figure 4 illustrates the high damage sensitivity of graphite/epoxy laminates. The figure compares the residual tensile strengths of ballistic damaged graphite/epoxy and 7075-T6 aluminum alloy, one of the more damage sensitive aircraft structural materials. The graphite/epoxy shown is even more damage sensitive than the 7075-T6, losing 50-percent of its tensile strength when containing ballistic damage one inch in diameter.

Innovative design approaches were developed to circumvent this damage sensitivity, by taking advantage of the considerable design flexibility afforded by graphite/epoxy.

3.0 PRELIMINARY WING-BOX DESIGN

Based on an assessment of the design problems relative to the capabilities of composites, the preliminary wing-box concept shown in Figure 5 was developed. This was a four spar graphite/epoxy configuration with stiffeners between spars. A feature for battle damage tolerance was the use of a skin laminate that contains no 0-degree graphite/epoxy. Because of the resulting low spanwise stiffness, the skins carry virtually none of the spanwise bending loads. These loads are carried in the spar caps by high stiffness chords of 0-degree graphite/epoxy.

The effectiveness of this approach in improving battle damage tolerance stems from the fact that 0-degree graphite/epoxy in the skin laminate causes the high notch sensitivity mentioned above. Taking the 0-degree graphite/epoxy out of the skins and putting it in the chords results in a more ductile and forgiving skin. The fracture toughness of the ± 45 graphite/epoxy skin laminate was further enhanced by adding 0° S-glass, forming an interply hybrid laminate.

The four spars provide multiple paths for the wing loads and are sized so that limit load can be sustained with any three surviving spars. During the concept design study (Ref. 1), an assessment was made of the efficiency of two, three, and four spar configurations in meeting the battle damage tolerance criteria. As Figure 6 shows, four spars provided the smallest weight penalty for this configuration and threat.

4.0 DESIGN DEVELOPMENT

With the design concept described above as a starting point, the development activity was organized into the three phases shown in Figure 7. Material selection, design analysis, and ballistic damage assessment were accomplished in Phase I. Phase II included detail design, subcomponent verification testing, and further ballistic damage assessment. In Phase III, a full-scale wing-box incorporating all final design features was

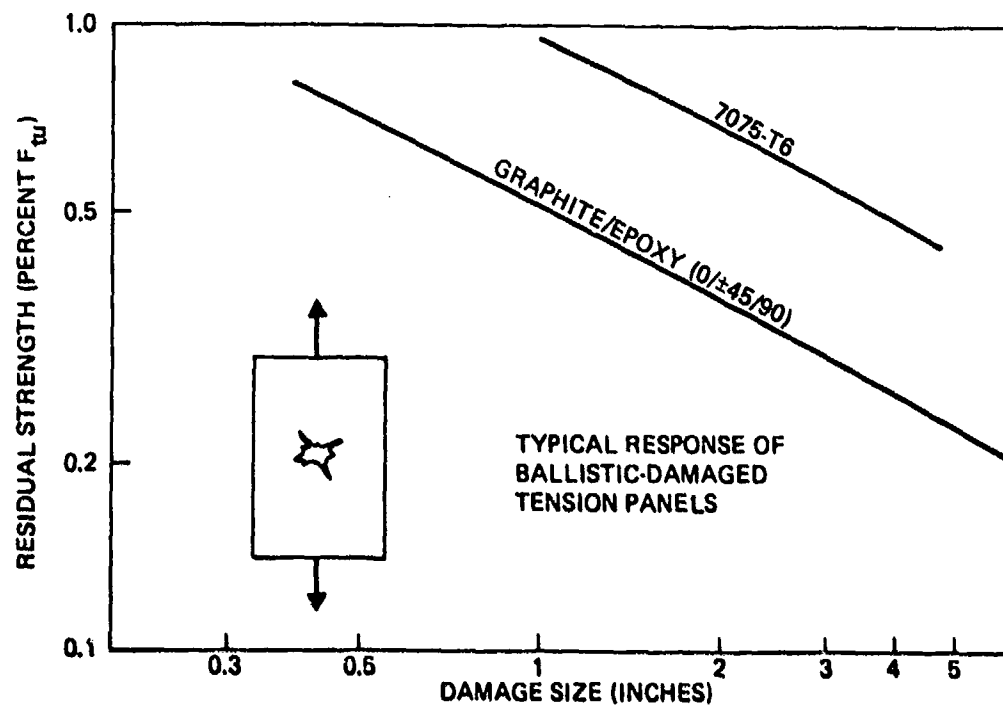


Figure 4. Graphite/Epoxy Laminates Can Be Highly Damage Sensitive

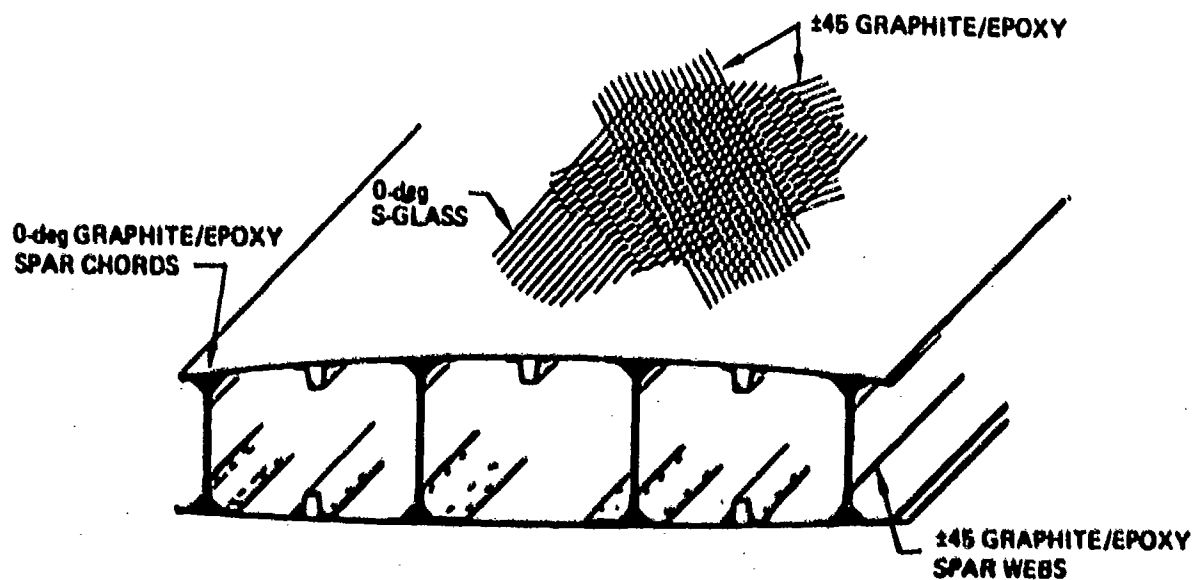


Figure 5. Preliminary Battle Damage Tolerant Wing Box Design

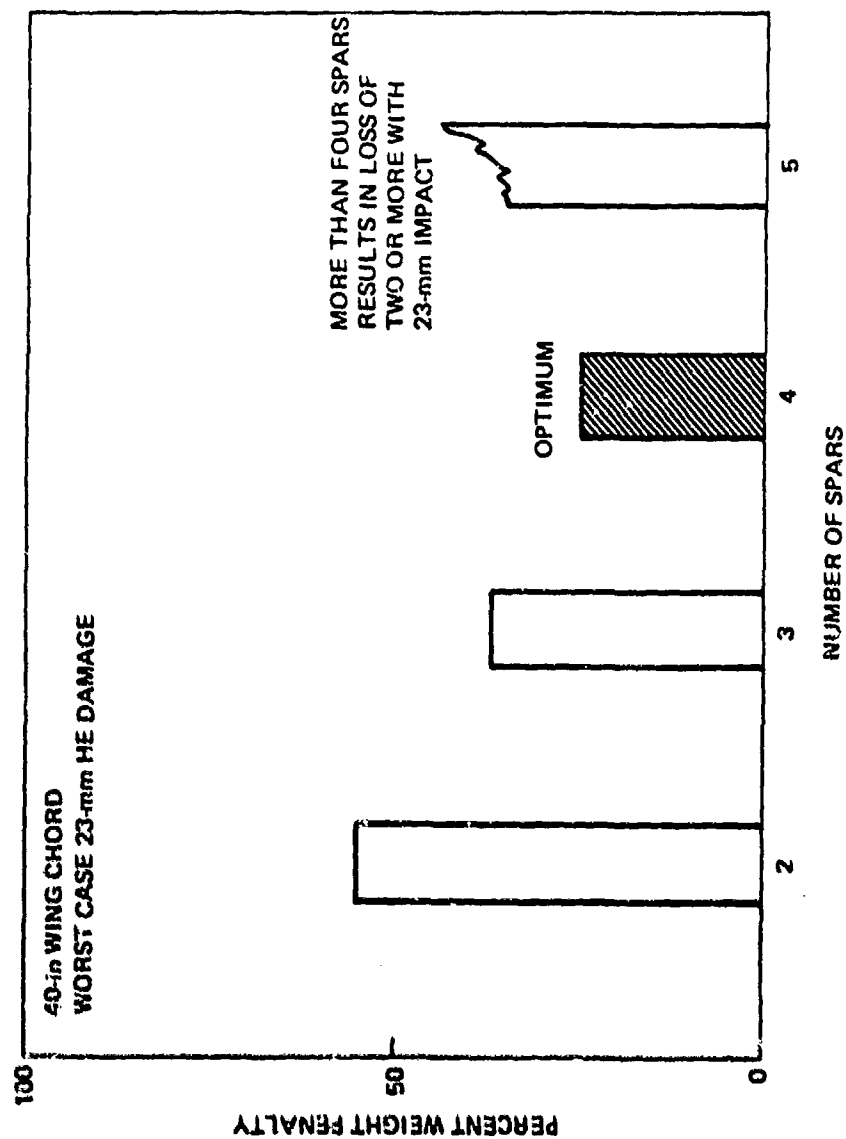


Figure 6. Effect of Number of Spars on Weight Penalties for Battle Damage Tolerance

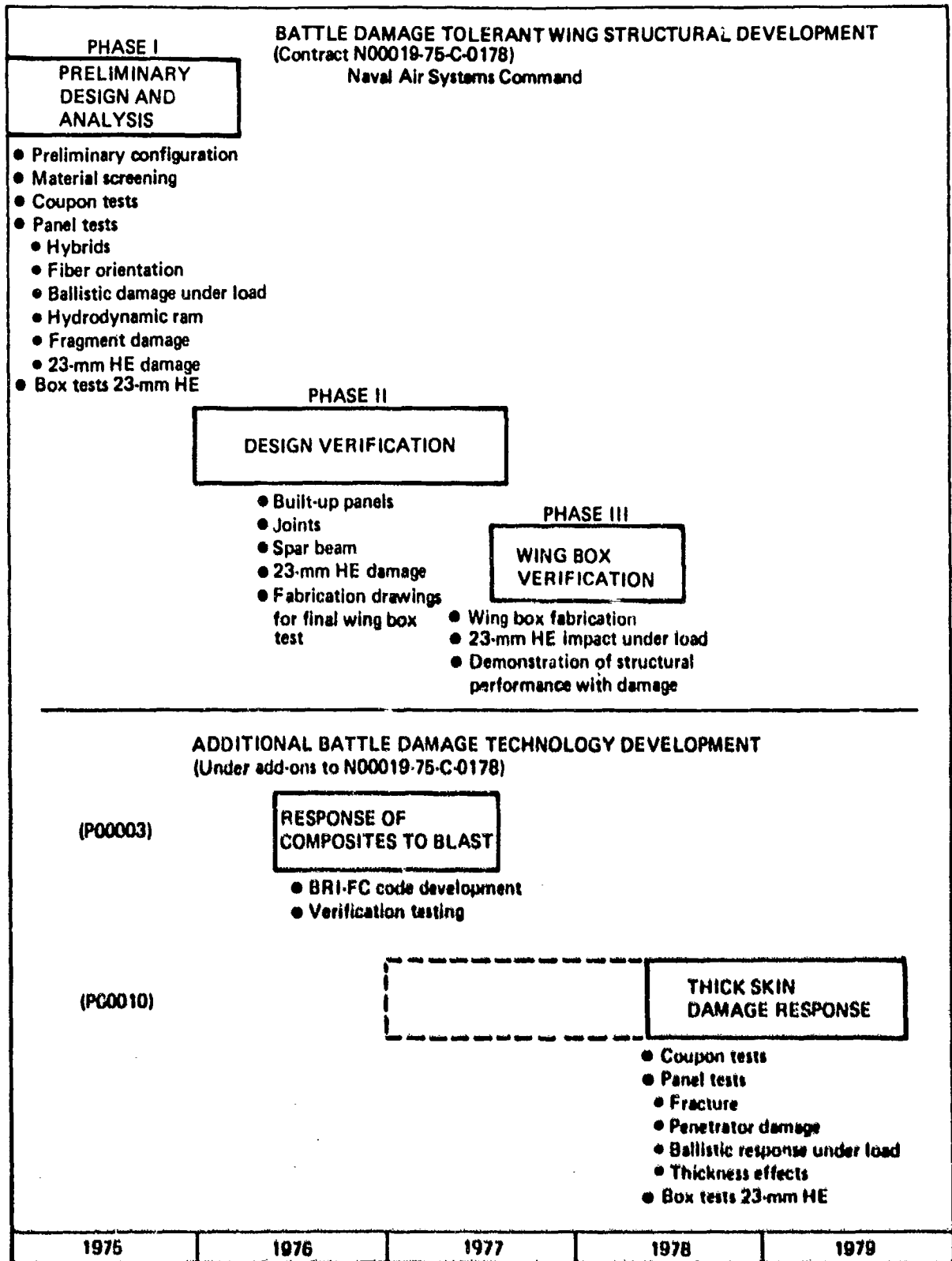


Figure 7. Battle Damage Tolerant Wing Program Summary

fabricated and successfully tested under load against the 23-mm HEI projectile. Figures 8 through 12 illustrate key activities and tests performed during the phases and add-ons.

In addition to configuration development, two further technology developments were made under contract extensions. Under Contract Modification P00003, a finite element analysis program (BR-IFC) was developed that predicts the response of fiber composite structure to blast pressures. Under Contract Modification P00010, ballistic damage response models were developed for thick 0, ± 45 , 90 graphite/epoxy laminates.

The design of the wing-box was developed using the battle damage tolerance design approach shown in Figure 13. The final structural design, shown in Figures 14 through 17, includes all the general configuration details employed in the preliminary concept: graphite/epoxy construction, four spars with integral chords of 0-degree graphite/epoxy, stiffeners between spars, and bolted attachments.

The containment of large ballistic damages in graphite/epoxy tension surfaces was achieved by developing a damage tolerant skin combining ± 45 graphite/epoxy with 0-degree glass/epoxy thus forming an interply hybrid laminate. Figure 18, gives an indication of the improvement in fracture toughness obtained by combining ± 45 T300/934 graphite/epoxy with 0-degree S-GL/1002 glass/epoxy.

Ballistic testing using 23-mm HEI projectiles showed that the optimum method of using the hybrid laminate was constructing the skins in a "waffle" configuration, placing the hybrid laminate only at the spar, rib and stiffener interfaces. The laminate within the waffle cell is ± 45 graphite/epoxy.

The high fracture toughness of the hybrid pads prevents crack propagation across the skin. The pads also resist and control damage imposed by the severe internal blast pressures generated by the threat. With this concept, skin failure under blast or hydrodynamic ram pressures occurs by local bending within the cell as shown in Figure 19. The thinner skin segment between pads "blows out," confining the damage to the single cell, and prevents splitting and detachment at the fasteners.

The large cross-section, 0-degree graphite/epoxy spar chords, integral to the spar web, are an important program design development. This design provides a highly desirable "soft" load path between the spars and the skin for redistributing spar chord loads following severance of a spar due to ballistic impact. Test and analysis demonstrated that bolting the spars to the skin through a ± 45 graphite/epoxy shear flange induces bearing failures along the flange, thus redistributing the severed spar loads away from the damaged region and reducing the tensile stresses contributing to propagation of damage across the skin.

The final wing-box design meets the target weight saving of 25-percent relative to the titanium baseline wing. Figure 20 shows weight summaries prepared at several stages of design development. The March 1976 wing-box configuration met all design requirements, and was substantially lighter than criteria. This margin was used to increase the 0-degree graphite/epoxy in the compression spar chords, to improve resistance to delamination caused by direct fragment impacts.


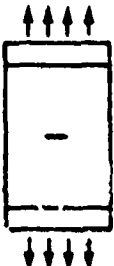
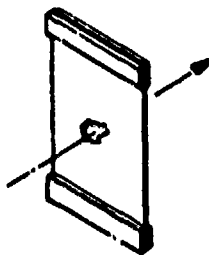
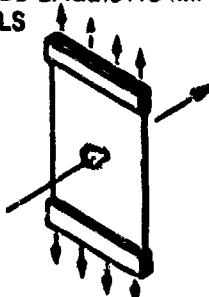

<p>TENSILE COUPONS</p> 	<ul style="list-style-type: none"> • Provided material property information including ultimate strength, strain-to-failure, and stress/strain curves • Verified quality and consistency of material and processing
<p>SAWCUT FRACTURE PANELS</p> 	<ul style="list-style-type: none"> • Established relative fracture performance of various ± 45 deg graphite/epoxy systems including effects of hybridization with 0-deg S-glass epoxy and comparisons with other fiber orientations
<p>BALLISTIC IMPACT PANELS</p> 	<ul style="list-style-type: none"> • Established relative ballistic response of various ± 45-deg graphite/epoxy systems including obliquity effects, damage characterization, and ultrasonic scan
<p>LOADED BALLISTIC IMPACT PANELS</p> 	<ul style="list-style-type: none"> • Determined strength degradation due to load at impact for candidate fiber/resin layups including panel residual strength with ballistic damage and effect of load on damage extent
<p>SPAR/SKIN INTEGRATION FRACTURE PANELS</p> 	<ul style="list-style-type: none"> • Provided comparison of fracture performance of various spar/skin integration concepts with one spar chord severed

Figure 8. Battle-Damage-Tolerant Wing Structural Development— Phase I Tests

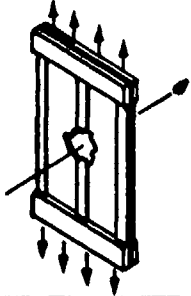

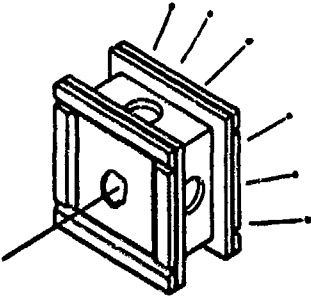
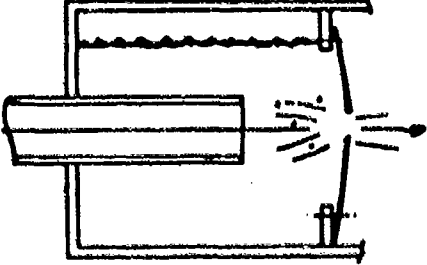
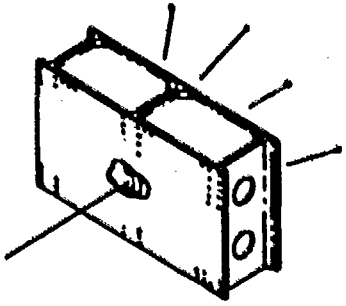
<p>SPAR/SKIN INTEGRATION BALLISTIC PANELS</p> 	<ul style="list-style-type: none"> • Provided comparison of various spar/skin integration concepts when impacted at a spar chord while under load
<p>BOLT BEARING</p> 	<ul style="list-style-type: none"> • Established bearing strength for various candidate skin/flare laminates
<p>23-mm REPLICA BOX PANELS</p> 	<ul style="list-style-type: none"> • Provided 23-mm HEI entry and exit damage information for various candidate skin laminates in replica wing cell • Included the effects of internal blast • Provided comparison with aluminum
<p>HYDRODYNAMIC RAM PANELS</p> 	<ul style="list-style-type: none"> • Determined structural response of various skin materials to intense fluid pressures (similar to blast pressures)
<p>THREE-SPAR, ONE BAY BOXES (2)</p> 	<ul style="list-style-type: none"> • Provided information on 23-mm HE damage type and extent for the candidate wing configuration

Figure 5. Battle-Damage-Tolerant Wing Structural Development-- Phase I Tests


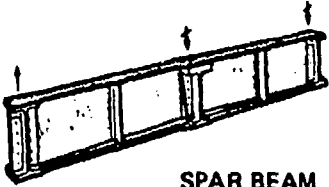


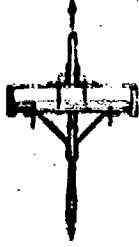

 <p>SPAR CAP MANUFACTURING DEVELOPMENT</p>	<ul style="list-style-type: none"> • Developed a spar cap design that can be fabricated easily and readily
 <p>SPAR BEAM STRENGTH TEST</p>	<ul style="list-style-type: none"> • Verified the fabrication approach and structural integrity of the spar beam design
 <p>SKIN BENDING TEST</p>	<ul style="list-style-type: none"> • Established the bending moment at failure for the hybrid pads for attachment design to resist internal blast
 <p>SKIN DETACHMENT TEST</p>	<ul style="list-style-type: none"> • Established the tension load at skin detachment for attachment design to resist internal blast
 <p>SPAR/SKIN INTERFACE TENSION TEST</p>	<ul style="list-style-type: none"> • Verified the spar/skin attachment for tension loads from blast pressures
 <p>RIB/SKIN INTERFACE TENSION TEST</p>	<ul style="list-style-type: none"> • Verified the rib/skin attachment for tension loads from blast pressures

Figure 10. Battle-Damage-Tolerant Wing Structural Development—Phase II Tests


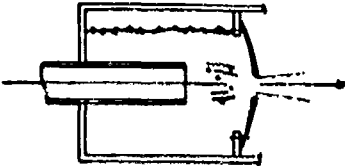
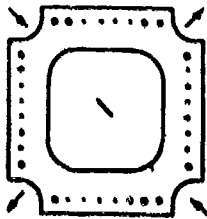
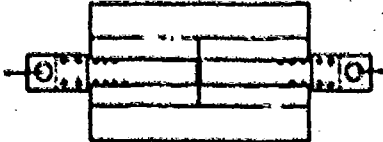
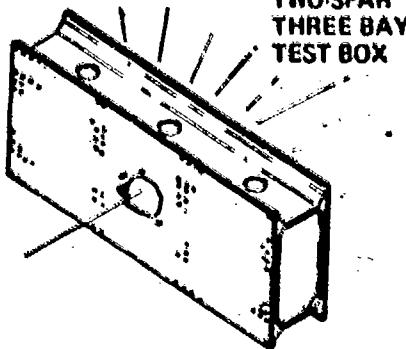
<p>SPAR/SKIN ATTACHMENT STRENGTH VERIFICATION</p> 	<ul style="list-style-type: none"> • Verified the spar/skin attachment for shear strength
<p>HYDRODYNAMIC RAM PANEL TEST</p> 	<ul style="list-style-type: none"> • Determined structural response of graphite/glass hybrids to fluid pressures and verified hybrid pad concept
<p>SHEAR FRACTURE PANEL TESTS</p> 	<ul style="list-style-type: none"> • Verified skins for shear • Established shear fracture failure stress
<p>SEVERED SPAR LOAD REDISTRIBUTION TESTS</p> 	<ul style="list-style-type: none"> • Demonstrated load redistribution from severed spar through bolted spar/skin attachments • Established influence length for bolts transmitting severed spar chord loads
<p>TWO-SPAR THREE BAY TEST BOX</p> 	<ul style="list-style-type: none"> • Verified "waffle" skin design with hybrid pads to predetermine damage from 23-mm HE

Figure 11. Battle-Damage-Tolerant Wing Structural Development—Phase II Tests

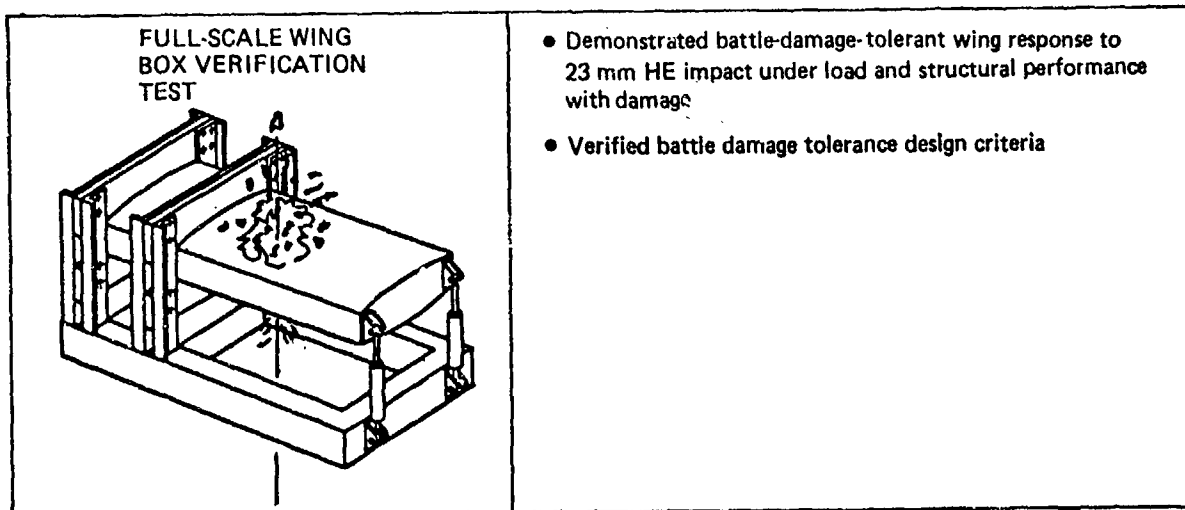


Figure 12. Battle-Damage-Tolerant Wing Structural Test—Phase III Test

Develop damage resistant/tolerant load paths



- Develop damage-size model
- Define load path geometry
- Develop finite-element model
- Model damage
- Find internal loads (with damage)
- Resize for damage capability

Develop damage containment



- Improve fracture toughness of skin
- Predetermine damage modes
- Provide crack arrestment
- Reduce dynamic effects
- Design details for damage resistance and tolerance

Figure 13. Battle Damage Tolerant Design Approach

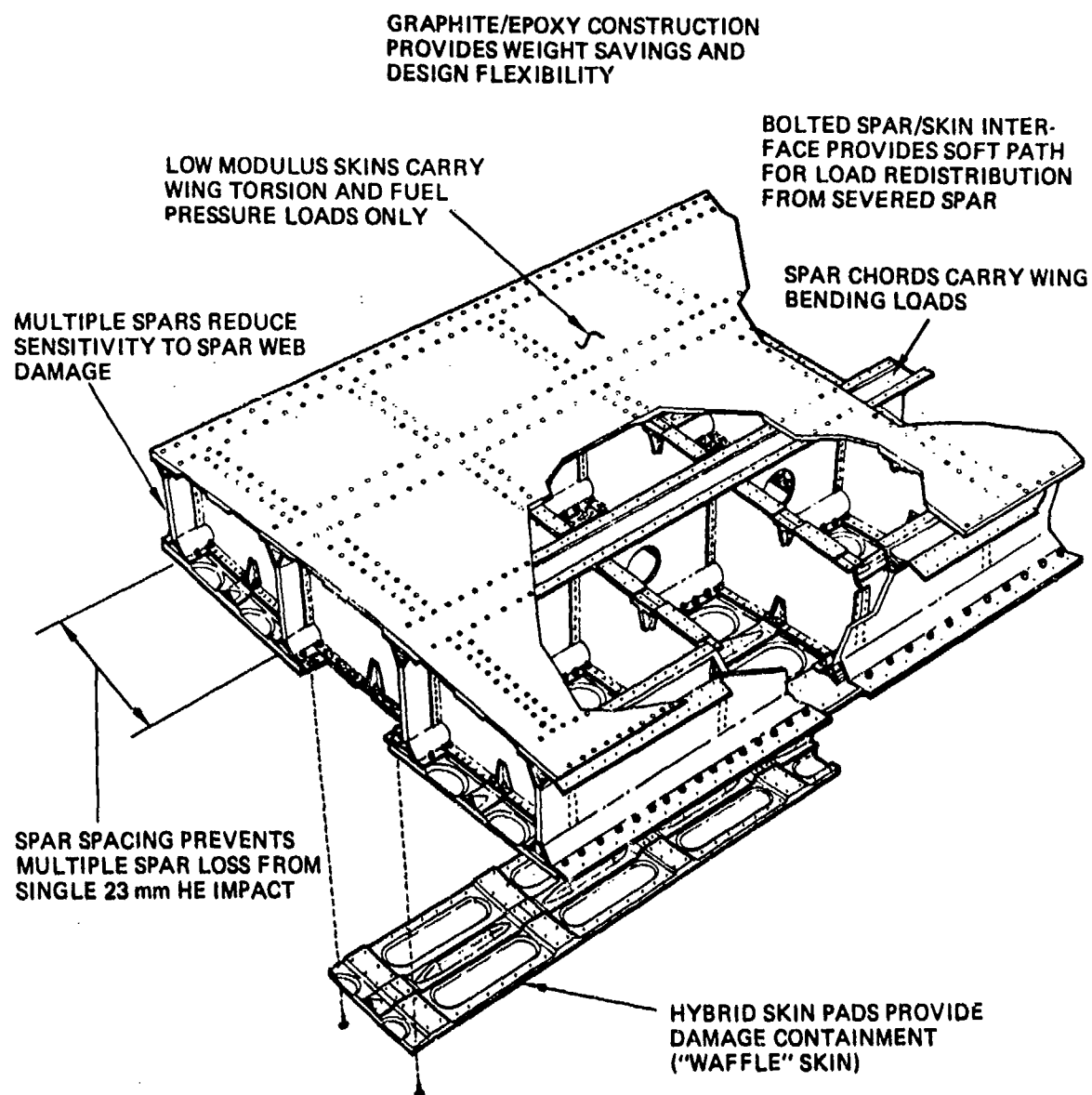


Figure 14. Battle-Damage-Tolerant Wing Final Design—Design Summary

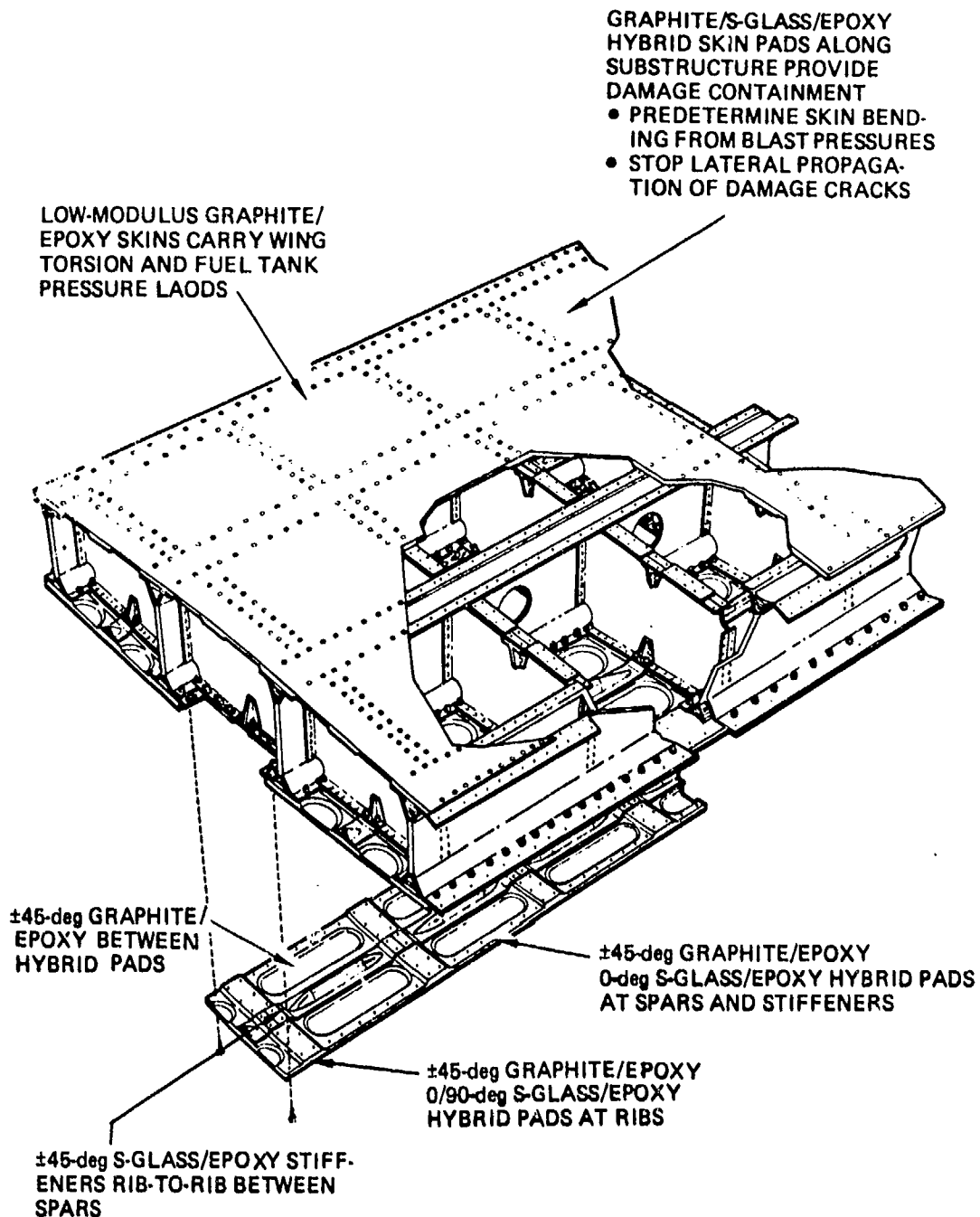


Figure 15. Battle-Damage-Tolerant Wing Final Design—Skins

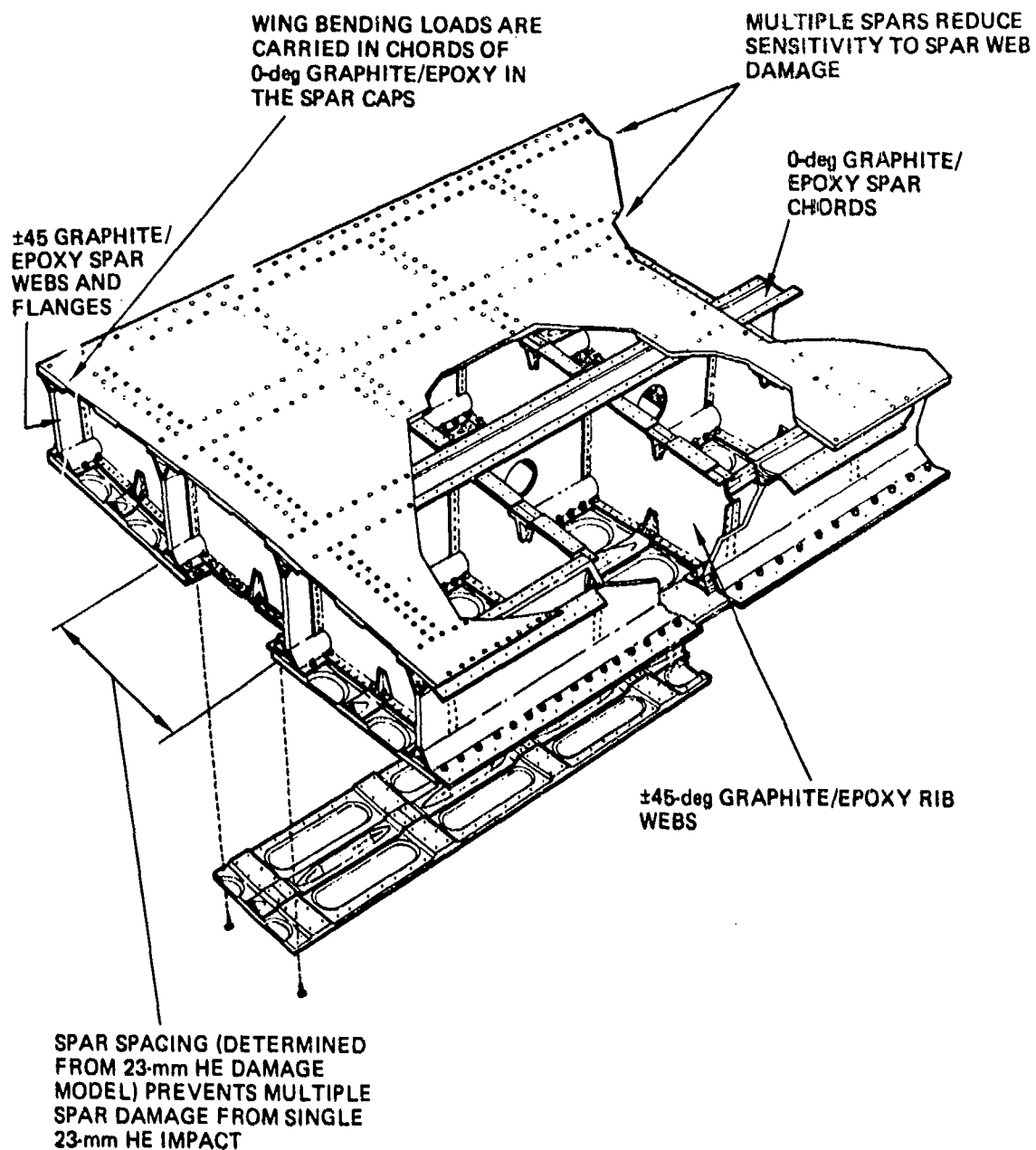


Figure 16. Battle-Damage-Tolerant Wing Final Design—Spars and Ribs

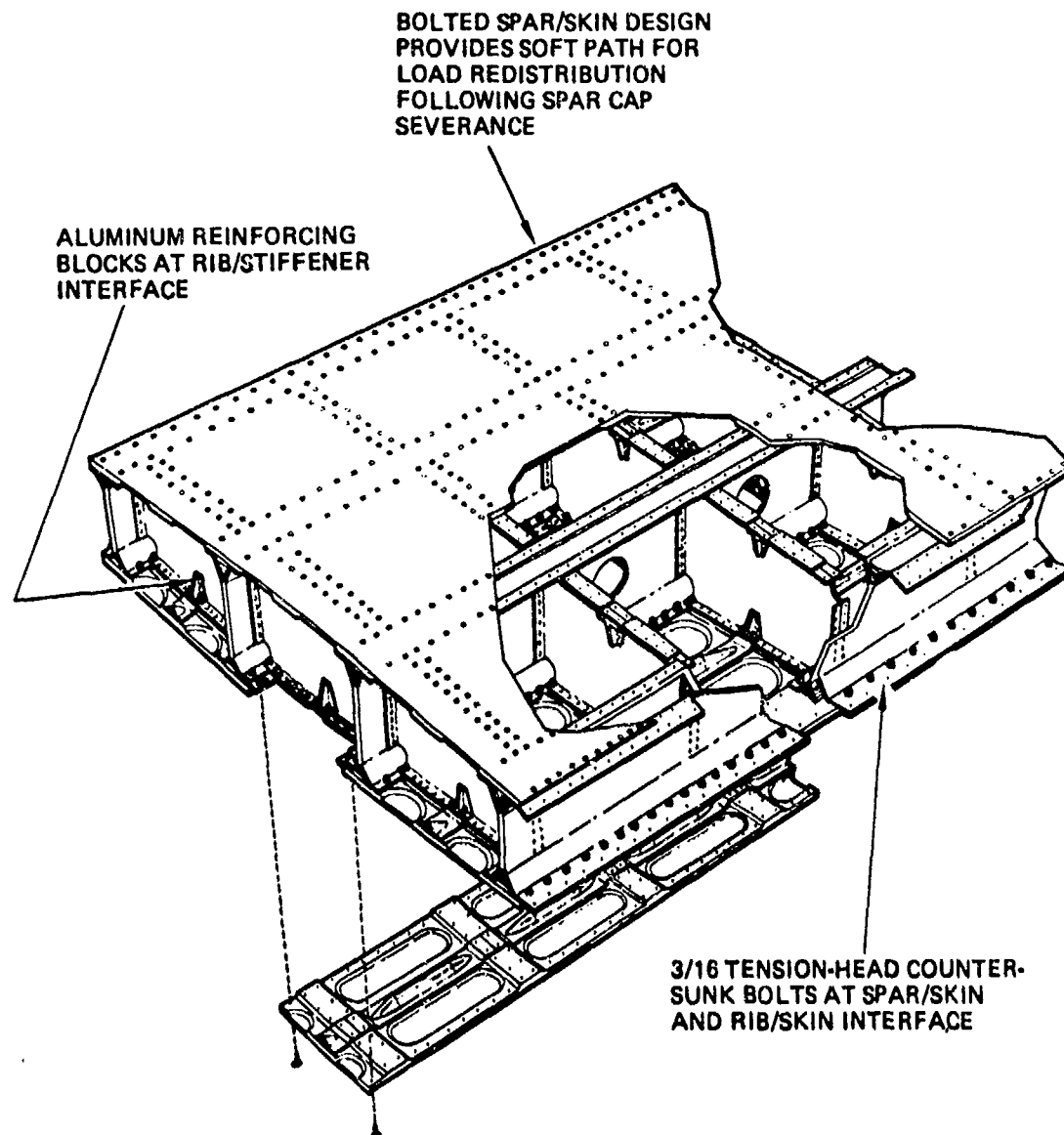


Figure 17. Battle-Damage-Tolerant Wing Final Design—Attachments

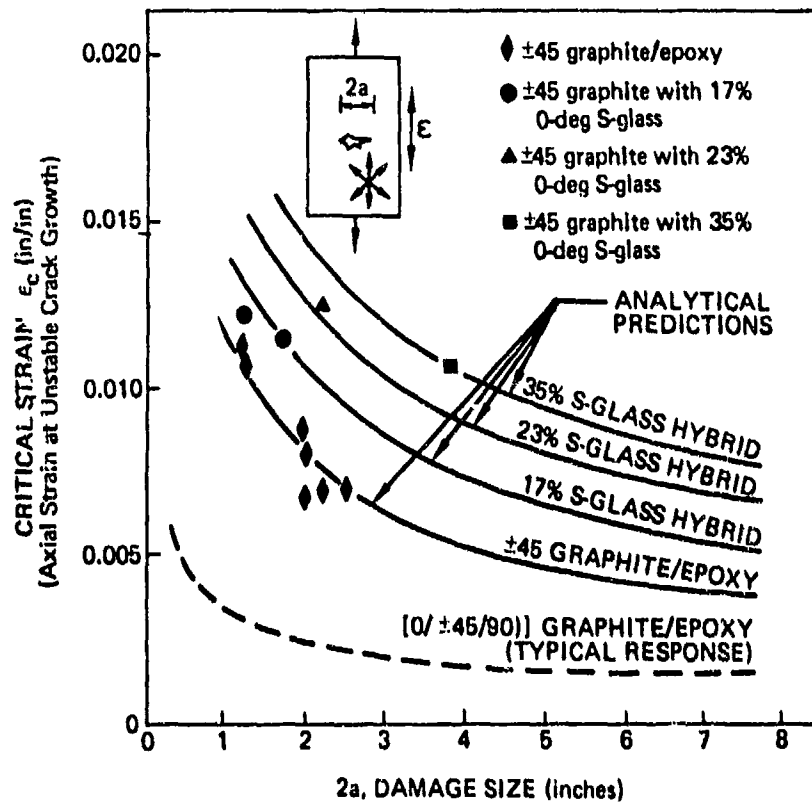
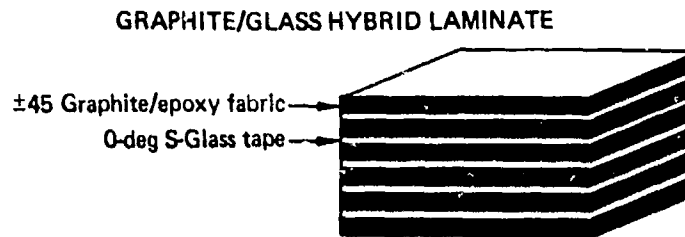


Figure 18. Damage Containment Improvement From Adding 0-deg S-Glass to ±45 Graphite/Epoxy

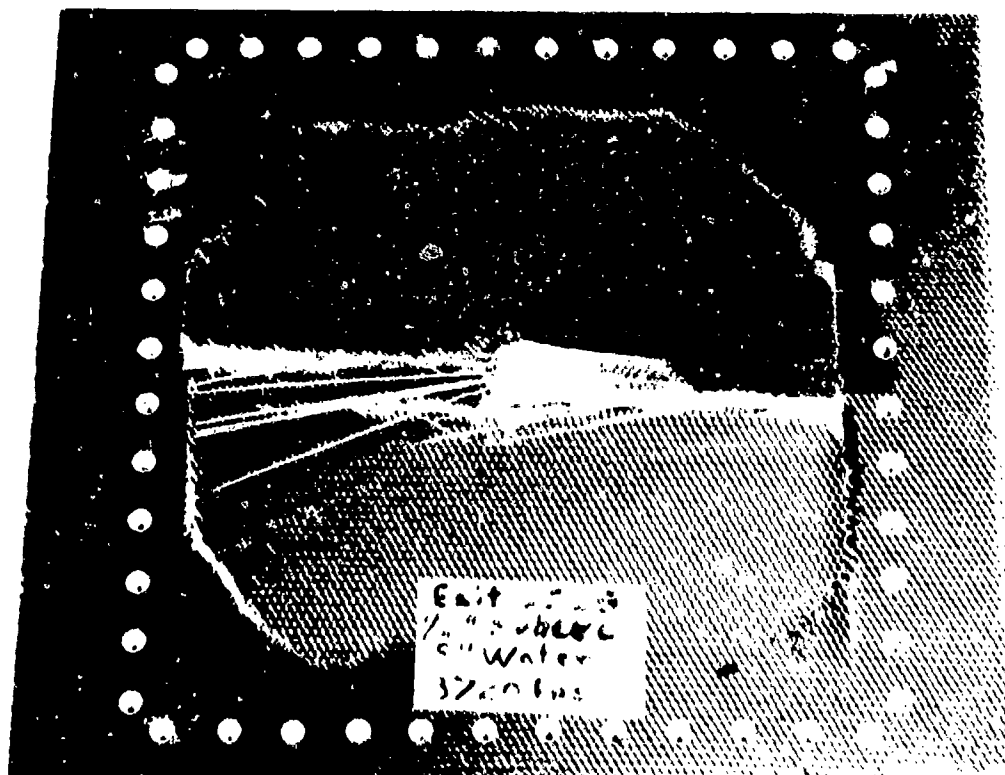
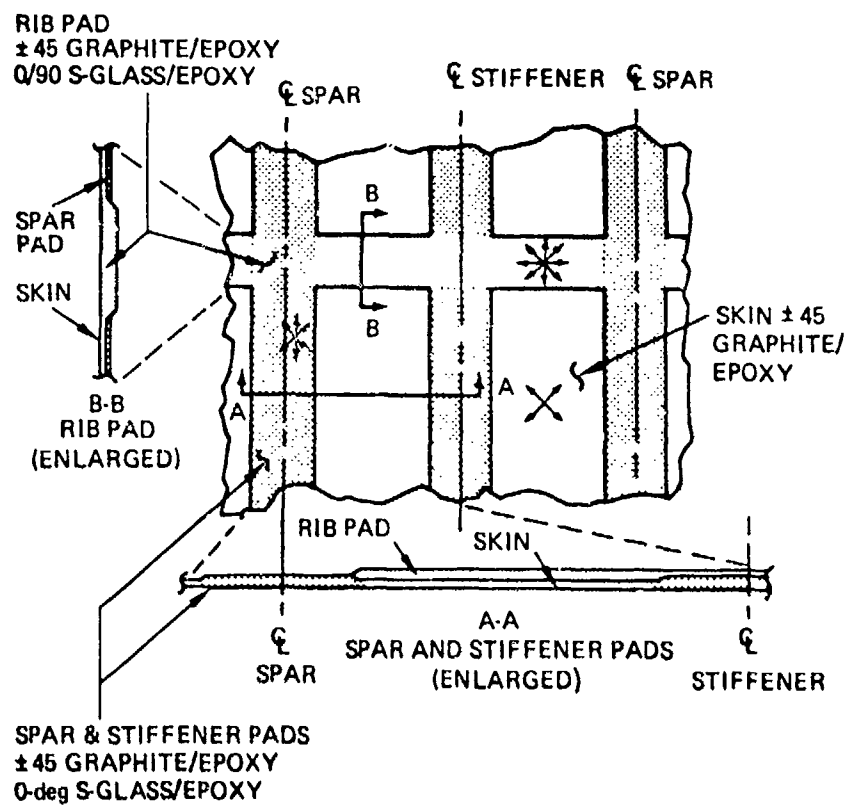


Figure 19. Battle Damage Tolerant Skin Configuration for Crack Arrest and Ballistic Damage Control

	Titanium baseline (two-spar box)	Battle damage tolerant wing (graphite/epoxy four-spar box)		
		October 1974	March 1976	June 1977
Maximum strain for sizing	—	0.0060	0.0053	0.0047
Skins				
Upper skin and pads	44.0	23.4	21.8	21.8
Upper stiffeners	12.9	4.4	1.6	1.6
Lower skin and pads	37.0	20.8	22.6	22.6
Lower stiffeners	9.6	3.5	1.6	1.6
Spars				
Upper chord	9.9	7.2	7.9	16.25
Lower chord	15.0	5.9	13.8	16.25
Webs	14.1	21.4	27.5	27.5
Web stiffeners	3.1	—	—	—
Radius blocks	—	—	3.1	3.1
Ribs				
Webs	6.5	3.8	11.1	11.1
Radius blocks	—	—	1.8	1.8
Skin attachment fittings	—	—	5.3	5.3
Miscellaneous fasteners, bonds, etc.	25.9	15.0	4.6	4.6
Totals	178.0	105.4	122.7	133.5
Percent	100%	59%	69%	75%

↑
TARGET
WEIGHT

Figure 20. Battle Damage Tolerant Wing Weight Summary

5.0 DESIGN VERIFICATION

The contractual effort was directed at developing a wing structural configuration that is virtually invulnerable to a 23-mm HEI impact, with a 25-percent weight savings over the titanium baseline. The program culminated in the fabrication and testing of a full-scale three-spar wing-box component incorporating the battle damage tolerant design features developed during the program. The box was fabricated using methods developed during subcomponent verification, then tested according to the criteria defined at the beginning of the program.

As indicated in Figure 21, the test box was loaded in combined bending and torsion to the 4-g condition, and a 23-mm HEI round was fired into the center spar cap at the tension surface. The component survived the impact with no indication of structural failure. After the impact, the bending and torsion loads were increased to the 7.5-g limit load. The damaged box successfully sustained these loads. Ten cycles of two-thirds limit load were then applied, demonstrating the 2-hour cruise capability after damage. The component was then loaded to failure, which occurred in a compression spar cap at 8.6-g's.

These tests demonstrated that the structural design meets all residual strength and stiffness requirements after damage from a worst-case 23-mm HEI hit. The battle damage tolerant design features that were verified include:

- o The structural integrity and damage tolerance capability of +45 graphite/epoxy skins combined with highly loaded spar chords of 0-degree graphite/epoxy.
- o The effectiveness of the multi-spar configuration and bolted attachment design in surviving dynamic load redistribution after 23-mm HEI ballistic impact.
- o The effectiveness of the "blow-out" skin panel design in controlling damage caused by the internal blast pressures and fragments of the 23-mm HEI projectile.
- o The effectiveness of the graphite/glass hybrid pad crack arresting design for containing large ballistic damage in tension surfaces, including the case in which a spar chord is severed.

In addition to battle damage tolerance, the weight criteria for the wing-box was easily met.

Figure 22 shows full scale wing-box test component in final stages of fabrication. In Figure 23, it has been mounted in the load fixture at Boeing's Tulalip Test Range. The hydraulic actuators used to apply bending and torsion loads are visible in the photograph, as is the target marker for impacting the spar beam with the 23-mm HEI projectile under the 4-g load condition. Figure 24 is a photograph of the damage to the tension skin following impact by the 23-mm HEI. The severed spar cap and rib web required for the worst-case damage criterion are clearly visible. The undamaged spars successfully picked up the extra loads from the severed spar cap.

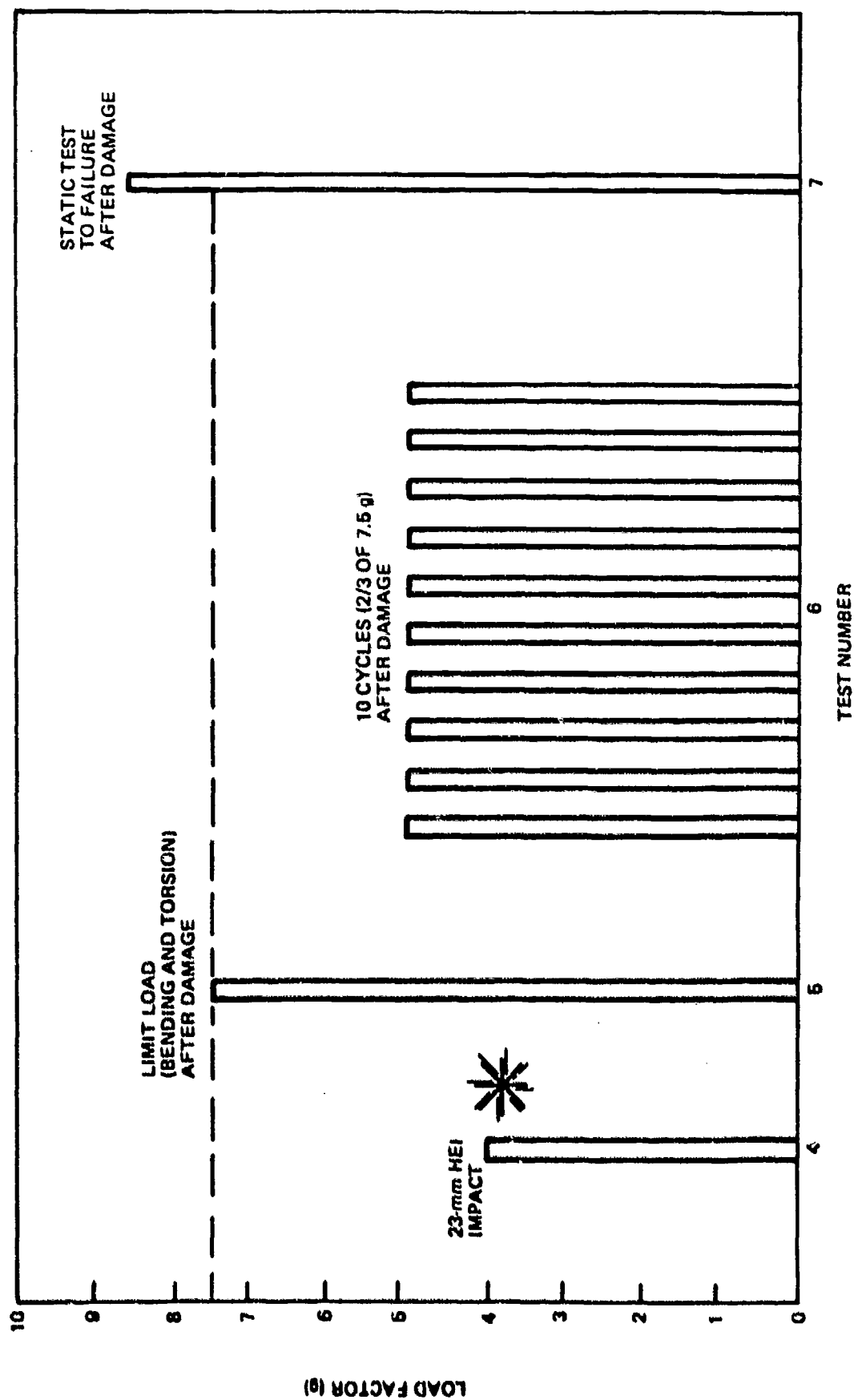


Figure 21. Test Conditions for the Damaged Wing Box Test Component

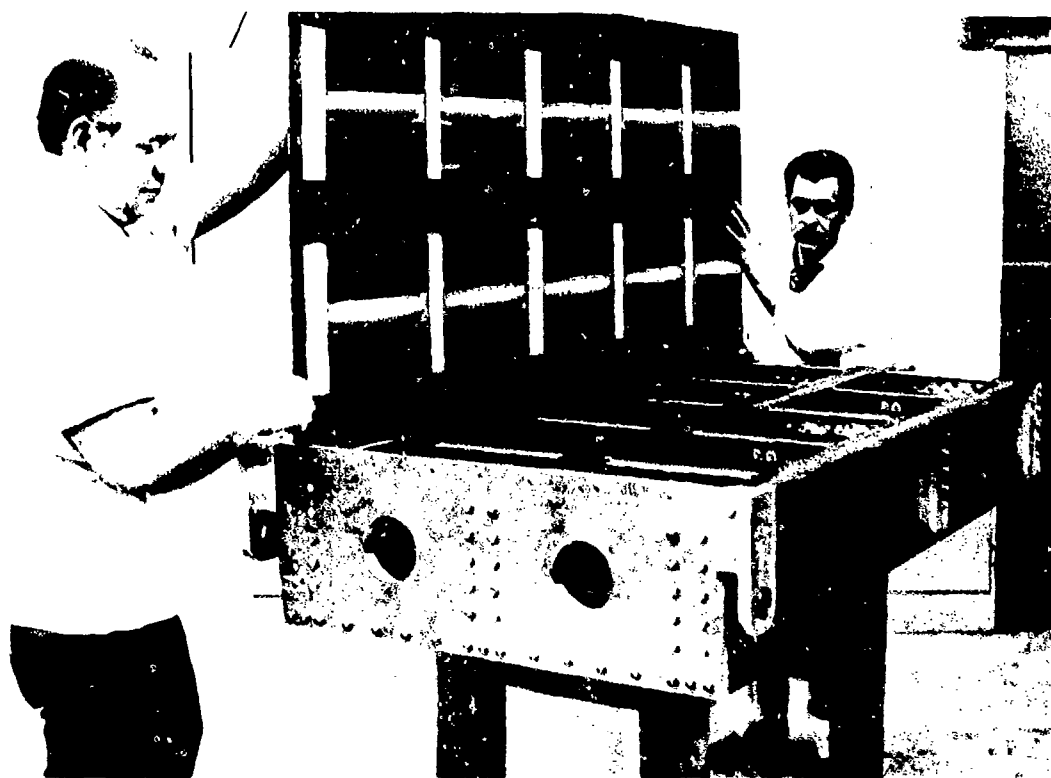


Figure 22. Full-Scale Wing-Box Component Assembly

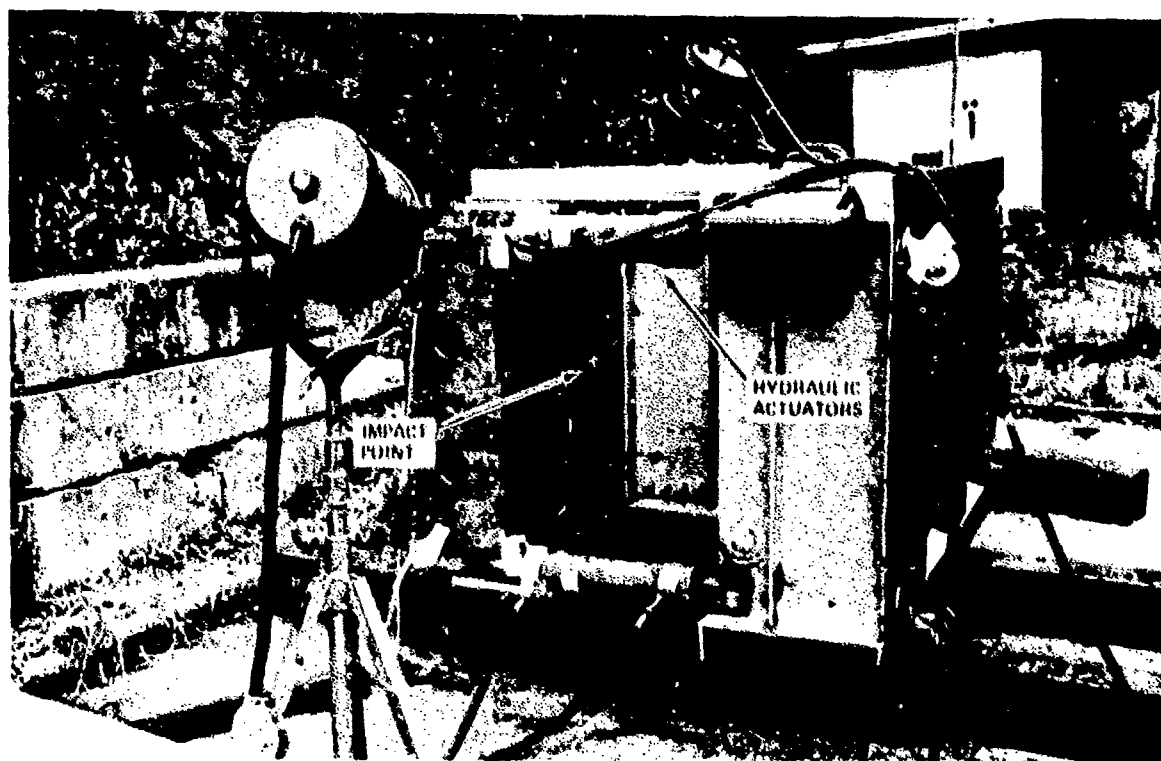


Figure 23. Full-Scale Wing-Box Component Ready for 23-mm HEI Impact

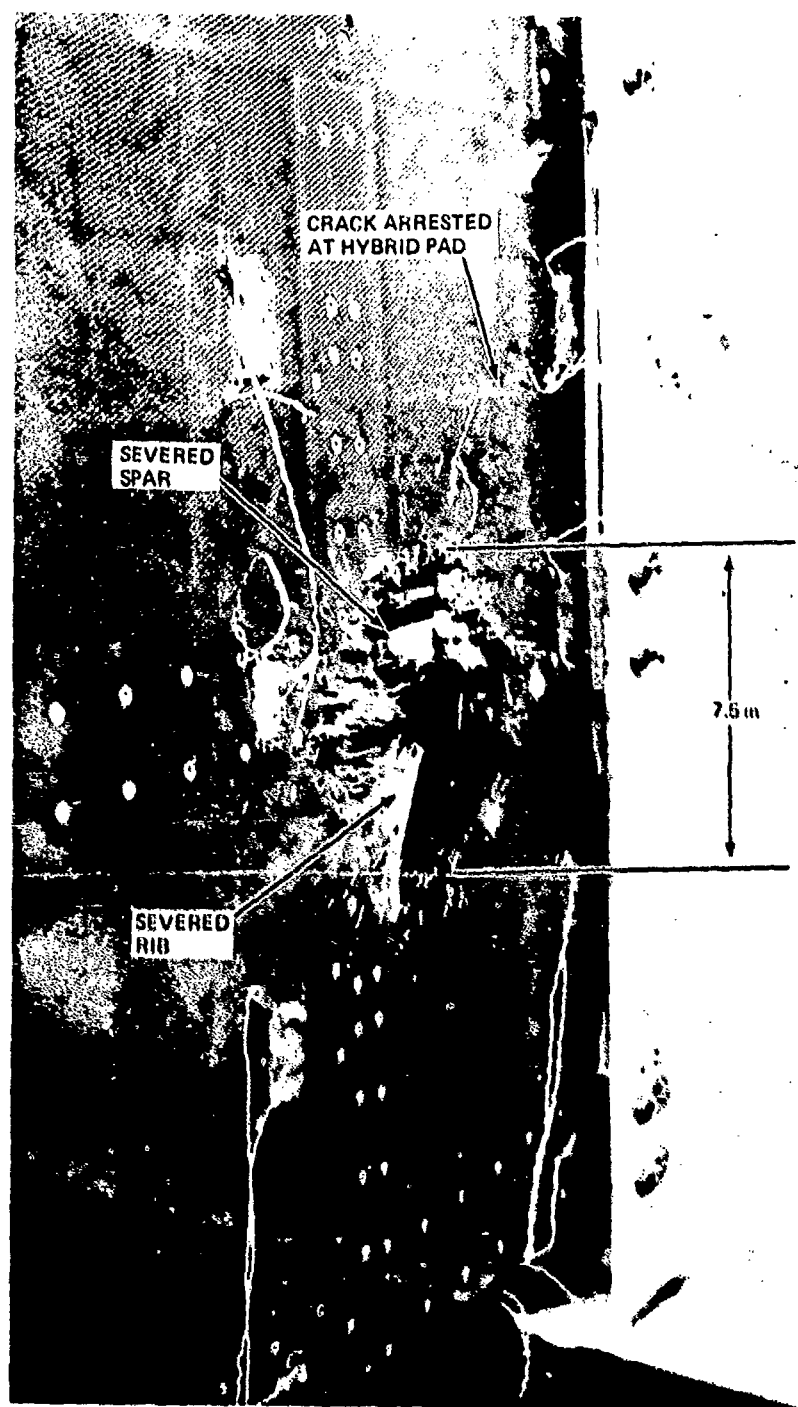


Figure 24. 23-mm HEI Entry Damage in Tension Skin – Full-Scale Wing-Box Component

The photograph of the tension skin in Figure 24 was taken following successful application of limit loads to the damaged wing-box. A crack can be seen in the upper right of the damage which propagated to the nearest hybrid pad and was successfully arrested by the pad. This verified the crack arresting capability of the pads, and the analysis methods developed for predicting the fracture characteristics of fiber composite materials.

The damage to the compression skin is shown in Figure 25. The raised segment of skin resulting from "blow-out" between the hybrid pads is quite evident. This occurred under blast pressures, thus venting the pressures and preventing attachment failure and extension of damage beyond the impacted cell. This response verified the "waffle" skin configuration using graphite/glass hybrid laminates.

Evidence of the final failure is also visible in Figure 25, which occurred at the compression spar cap at 8.6-g's. The skin buckled along the lower spar and above the central spar, with some skin detachment. The tension skin never failed.

CONCLUSIONS

The successful results of this development demonstrate the versatility of fiber composite materials. This versatility provided the design alternatives needed to configure structure that is both lighter and more battle damage tolerant than current metallic configurations. Combat aircraft incorporating this capability can have a significantly higher probability of mission completion and safe return. In addition, the high level of battle damage tolerance provides the option for repair deferral which can be a great advantage in short war scenarios.

ACKNOWLEDGMENT

The authors acknowledge the support of the Naval Air Systems Command for the work reported herein, conducted under Contract N00019-75-C-0178, with special expressions of appreciation to D. R. Mulville, A. Somoroff, and A. Cowles.

REFERENCES

1. McKinney, M. E., Porter, T. R., and Sedlacek, C. J., "Battle Damage Tolerant Wing Study," Final Report, NASC Contract N00019-72-C-0433, Boeing Document D180-15150-1, 1972.
2. Beaupain, H. E., Herlin, W., Krupnick, M. N., "Battle Damage Tolerant Wing Study -Flutter Analysis and Materials/Processes Specifications," Final Report, NASC Contract N00019-73-C-0501, Boeing Document D180-18205-1, 1974.
3. Avery, J. G., Bradley, S. J., King, K. M., "Battle Damage Tolerant Wing Structural Development Program," Final Report, NASC Contract N00019-75-C-0178, Boeing Document D180-26069-1, 1979.

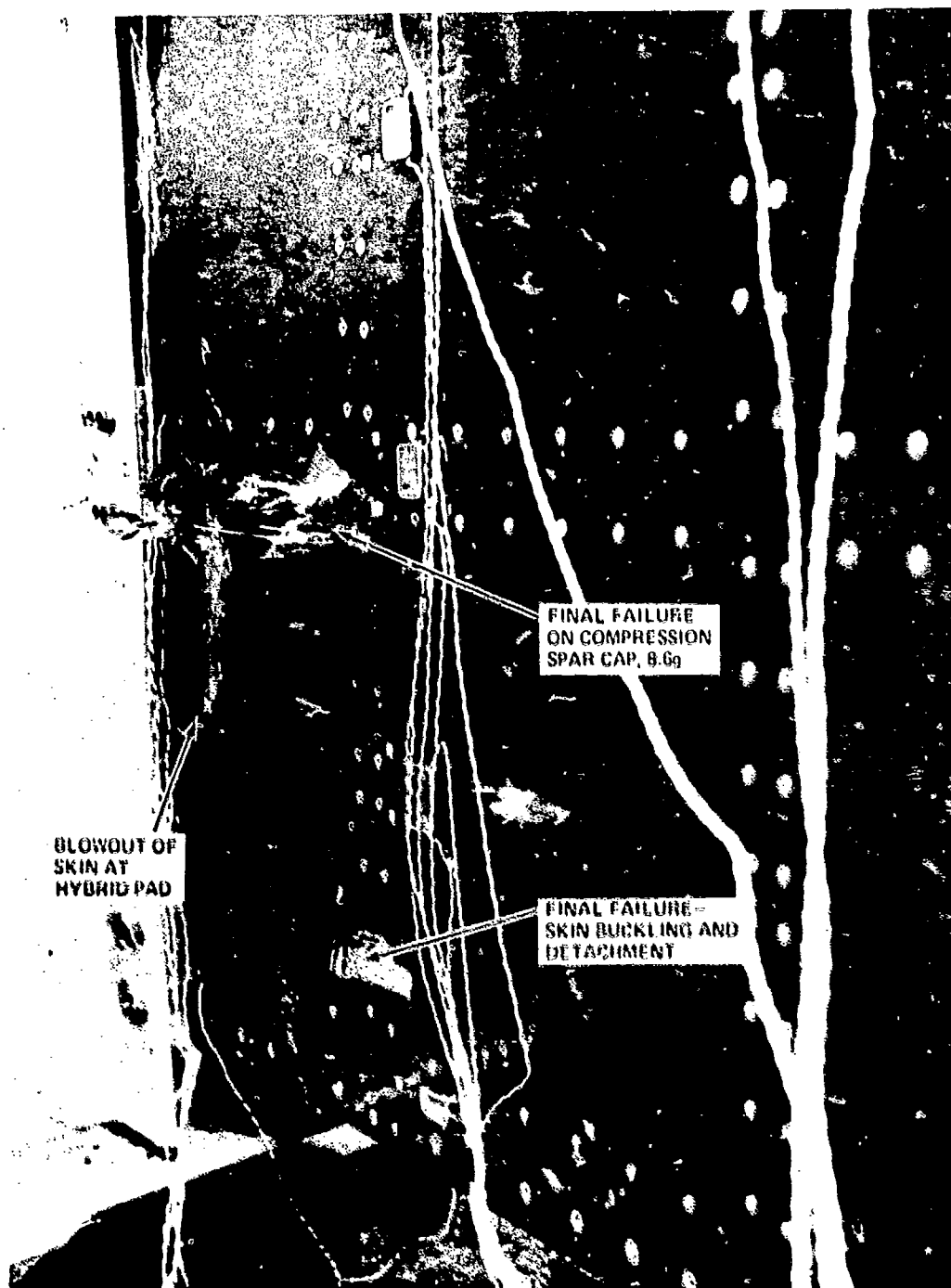


Figure 25. 23-mm HEI Exit Damage in Compression Skin (Photographed After Final Box Failure)

THE RESPONSE OF ADVANCED COMPOSITE STRUCTURES TO HIGH EXPLOSIVE BLAST

ALAN L. DOBYNS
Research Engineer

JOHN G. AVERY
Engineering Manager
Boeing Military Airplane Company
Seattle, Washington 98124

ABSTRACT

This paper describes the modification of an existing finite-element blast response program (the BR-1) to allow it to use laminated composite rectangular and triangular plate elements and a test program in which thirteen graphite/epoxy panels and six aluminum panels were subjected to blast loadings. Good correlation was obtained between the test results and analytical predictions.

INTRODUCTION

The effects of high explosive blast damage on composite aircraft structures consist of fragment damage and blast pressure damage. In fragment damage numerous holes are produced in the structure, each of which acts as a stress concentration. Blast pressure damage is produced by the reflected and confined gas overpressures and is a transient dynamic process in which the pressure is applied for a relatively short time, imparting a high velocity to the affected sections. Deflections of over an inch can be produced in typical aircraft panels, producing high stresses and strains in the process. In order to evaluate the effect of fragment damage on strength, it is necessary to determine if the fragment damage will extend and link up under this stress. Thus, a transient structural analysis capability is needed to attempt an analysis of blast damage in composites.

There are several elastic-plastic dynamic computer codes available, as shown in Table I. BR-1A, ANSYS, MARC, and STAGS-C are dynamic response analysis codes using isotropic elastic-plastic stress-strain laws. ANSYS and STAGS-C have elastic laminated orthotropic capability. However, the BR-1FC is the only program with laminated orthotropic elastic-plastic capability. In addition, the BR-1A and BR-1FC use the blast routines developed by NOL (1) to compute the blast pressure and fragment dispersion on each element as a function of time for several popular high-explosive shells, while MARC, ANSYS and STAGS-C require hand input of pressures and times to simulate a blast.

*Table I. Finite Element Programs for Blast Response Analysis
(All Programs Have Large Displacement Transient Analysis Capability)*

Programs	Capabilities				
	Isotropic	Orthotropic	Laminated orthotropic	Elastic plastic	Computes blast pressure for each time increment
BR1-FC	X	X	X	X	X
MARC	X			X	
		X		X	
ANSYS	X			X	
			X	Elastic only	
BR-1A	X			X	X
STAGS-C (Finite difference)	X			X	
			X	Elastic only	

The BR-1 (Blast Response) computer code (2) developed by J. Brass, M.J. Jacobson and J.R. Yamane of the Northrop Corporation predicts the response-to-failure of metallic aircraft structural panels and compartments exposed to the blast fragments of internally detonating high explosive projectiles.

The BR-1 code uses the equations of dynamic equilibrium, developed originally by Salus, IP and Valderlinden (3) and extended by Witmer and Wu (4) to determine the transient response of a finite-element model subject to time varying loads. The equations of dynamic equilibrium of the form:

$$[M]\{\ddot{q}^*\} - \{F\} \cdot \{P\} - [H]\{q^*\} = \{C\} \quad (1)$$

Where $\{F\}$ consists of a vector of internal loads and body forces, $\{P\}$ and $[H]\{q^*\}$ are the nodal forces resulting from member internal stresses, $[M]$ is the structure mass matrix and $\{q^*\}$ is the vector of nodal displacements.

Equation 1 is integrated numerically using a finite difference method, as described in Reference 2, to find the incremental and total displacements at each time step. The incremental and total strains and

stresses are then determined using the element strain-displacement relations and the material constitutive equations. The $\{P\}$ and $[H]\{q^*\}$ forces are then used to determine the vector of nodal forces $\{C\}$ and the acceleration $\{\ddot{q}^*\}$. The incremental deflection vector for time increment $i+1$ is then:

$$\{\Delta q^*\}_{t_{i+1}} = \{\Delta q^*\}_{t_i} + \Delta t^2 \{\ddot{q}^*\}_{t_i} \quad (2)$$

This process is repeated for each time step until a failure occurs or the specified number of steps are completed.

MODIFICATION OF BR-1 PROGRAM

A similar capability was needed for fiber composite structure because of the increased usage of orthotropic materials such as graphite/epoxy for combat aircraft. Consequently, work was initiated to extend the structural analysis portion of the of the BR-1 code to include fiber composite analysis capability. The BR-1A version of the code, which contains triangular plate elements, rectangular plate elements, and beam elements, was selected for the modification.

The modified code has been designated BR-1FC (Fiber Composite). The modification is an additional capability, i.e., full BR-1A capability is retained. The modification to enable the BR-1A code to analyze laminated composites consisted of replacing the isotropic elastic-plastic stress-strain relations with nonlinear orthotropic laminated plate equations of the type developed by Sandhu (5). In the Sandhu method, stresses and strains are computed in each layer of the laminate at a given load level and used to determine the moduli in the layer coordinate system. The moduli are then used to calculate the laminate stiffnesses for use in determining the incremental stresses and strains due to the next load increment.

A spline fit method was used to interpolate between input points in the stress-strain curves to determine the stresses and moduli. A layer is defined as having failed in a given direction (fiber direction, transverse to fiber direction or shear) when the strain in that direction is greater than the maximum value input for its stress-strain curves. The BR-1FC program requires tension and compression stress-strain curves to define the stress-strain behavior of a laminate.

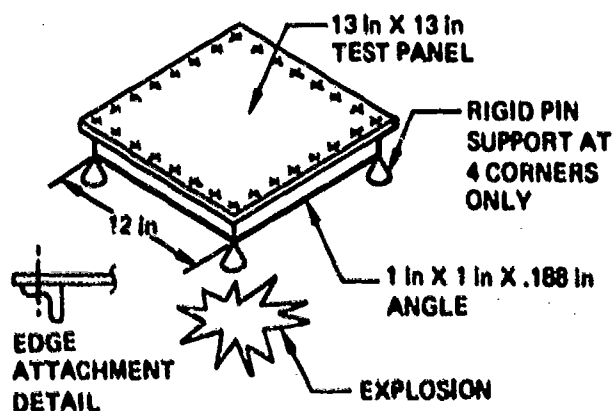
The BR-1FC code was compared with the STAGS-C finite difference transient analysis code using a fixed ended beam model idealized with plate elements and subjected to loadings by a step function pressure load. Several thicknesses and loadings were modeled with good correlation obtained between the two codes, as given in Reference 6.

BLAST TESTS

A test program consisting of blast testing of several panels was conducted to provide a check on the predictions of the BR-1FC. Each 13" X 13" test panel was mounted in a fixture with edge attachments simulating aircraft wing type joints, as shown in Figure 1. A small spherical charge of C-4 explosive (equivalent to the Russian 23MM HE) was detonated at varying distances from the panels. Blast pressure versus time plots were produced at two points on each panel. Panel deflection versus time plots were produced for the panel center and two other points on the panel.

The test setup consisted of a charge suspended in the center of a spherical blast chamber, with the panel positioned at the required standoff distance and supported by an aluminum angle frame mounted on four steel support beams. A second frame on the opposite side of the charge supported the pressure gage assembly.

Panel displacement was measured by photographing a silhouette along the rear surface of the panel with a Barr and Stroud high-rate framing camera. The maximum frame rate obtainable with this camera is one frame per microsecond (1,000frames/sec) although it was slowed down to between 7 and 14 frames/microsecond for this test program.



PANEL	LAMINATE	THICKNESS
BR1-1	± 45	.143
BR1-2	0/±45/90	.119
BR1-3	0/±45/90	.145
BR1-4	0/90	.098
BR1-5	7075-T6	.100
BR1-6	7075-T6	.083
BR1-7	0/±45/90	.082
BR1-8	0/±45/90	.077
BR1-9	7075-T6	.040

Figure 1. Panel Blast Testing

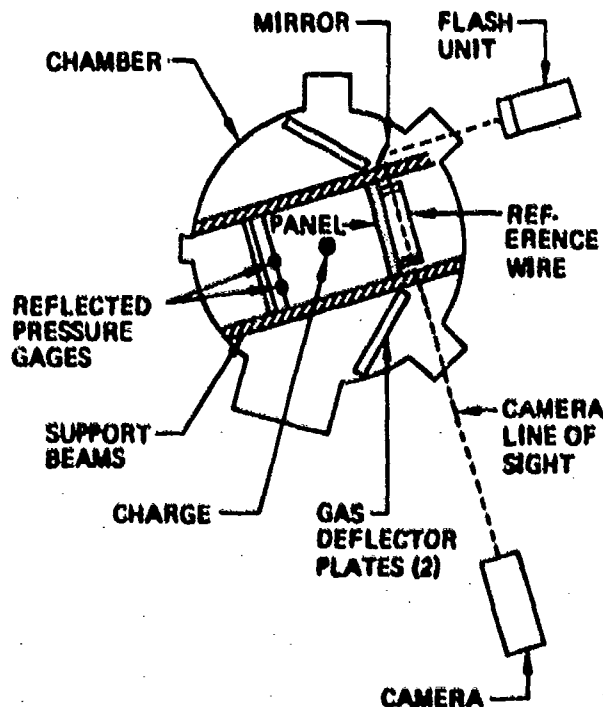


Figure 2. Blast Test Arrangement

This was done to get the maximum time span recorded on the 28 frames in the camera. A flash tube was used to provide a back light to silhouette the panel. A diagram of the test setup is shown in Figure 2, showing the 3-foot diameter spherical blast chamber, test panel, pressure gages and camera. Figure 3 is a photograph of the test setup with the camera on the left and the blast chamber on the right. The camera is directed through the viewport in the center of the sphere. Figure 4 is a photograph of the interior of the blast chamber showing the panel, gages, charge, and support fixtures.

The reflected-pressure gages were carbon elements bonded to the face of a 2-inch thick Plexiglass plate. The Plexiglass was then fastened to an aluminum frame similar to the panel support. The Plexiglass provides the mass to reflect the air shock, and the two-inch thickness delays the rear surface reflection for approximately 37 microseconds. Although the finite thickness of the carbon elements cause some internal reflections and resulting fluctuations in the signal, the overall peak and decay of the pressure pulse are considered to be valid.

The detonator was fired by discharging a .5 μ fd capacitor charged to 2 KV. This mode of firing provides a firing delay of less than 5 microseconds, allowing accurate timing of the event relative to the camera and gage recording. The charge consisted of a measured quantity of Composition C-4 molded around a U.S. Flare NND-211 detonator. The charge assembly was taped to a net of lock stitch tied to the support beams providing a stable location at the center of the chamber, as shown in Figure 4.

The panels were 13-inch square and were fastened to the 1" X 1" X 13/16" angles of the frame using 10-32 bolts on 1-inch centers. This provided an open exposed surface 11-inches square and a 12-inch support span. A reference wire was also attached to the aluminum frame to provide a fixed line and scale for displacement measurements.

The actual firing sequence was controlled by the camera. When the camera reached the preset speed a timing pulse was generated that started delays for the detonator, flash unit, and the scope sweeps. The timing of these events was recorded on a raster scope along with a marker pulse. A camera pulse every half revolution of the mirror was recorded on the raster scope to provide an accurate measurement of camera speed. On the later shots the camera tachometer was also recorded since the regular timing pulse had failed to appear on some of the shots. The tachometer speed measurement was less accurate than the normal timing pulse but did provide a usable speed measurement.

Figure 5 is an enlargement of the film taken by the Barr and Stroud camera for shot 16. In the picture the panel is seen in silhouette at the bottom of the frame with a reference wire shown above. The reference

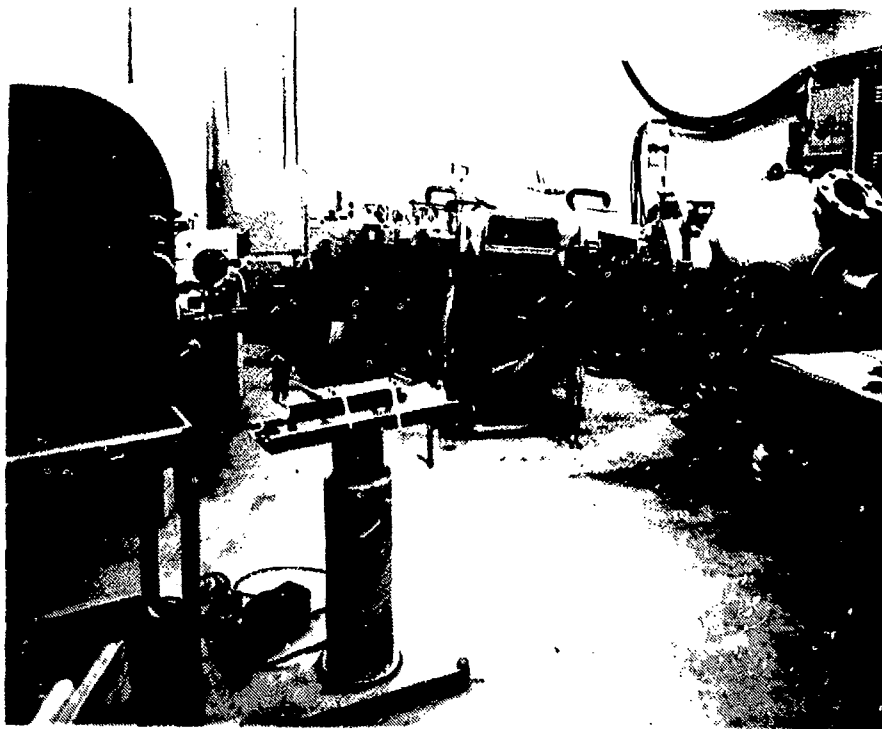


Figure 3. Test Arrangement Showing Camera and Blast Chamber

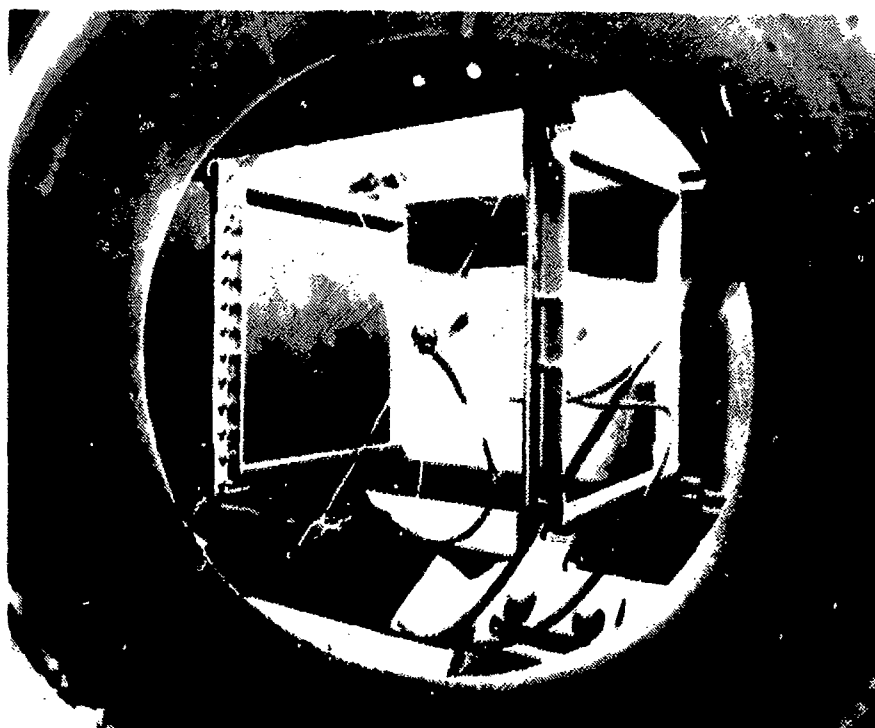


Figure 4. Interior View of Blast Chamber

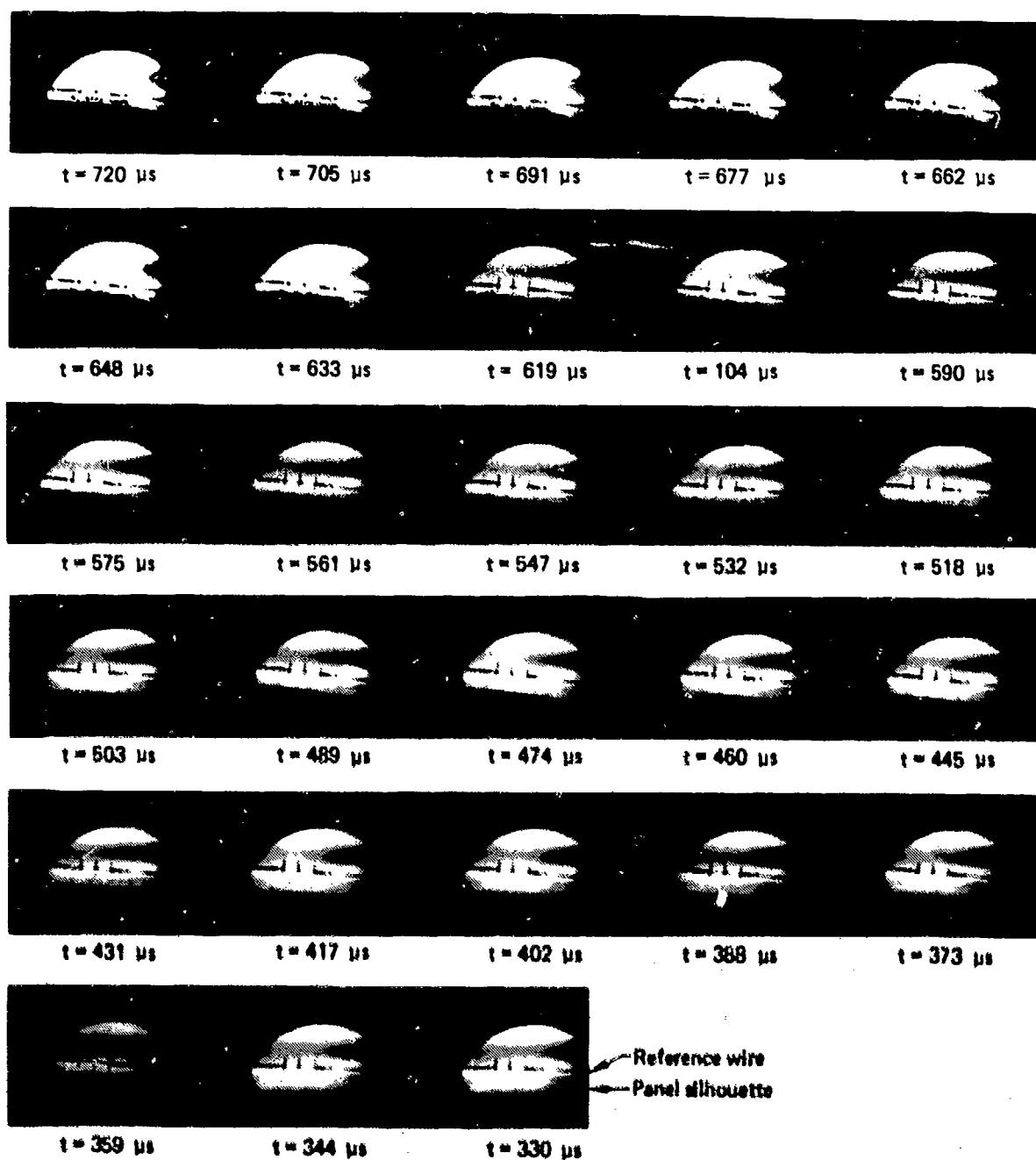


Figure 5. Film Strip From Shot 16 BR1-4-1 Panel - .098 Inches (0/90) Laminate

wire has three vertical posts attached to it with the center post indicating the center of the panel. The time after detonation (in microseconds) is given for each frame. The figure shows a BR1-4 composite panel in which particles of epoxy are seen leaving the panel. The point at which the first fragments are seen is near the peak deflection reached by the panel, indicating that considerable damage has occurred, which can also be seen in the post shot photos. Post shot photographs of several panels are shown in Figure 6.

COMPARISON OF TEST RESULTS WITH BR-1 ANALYSIS

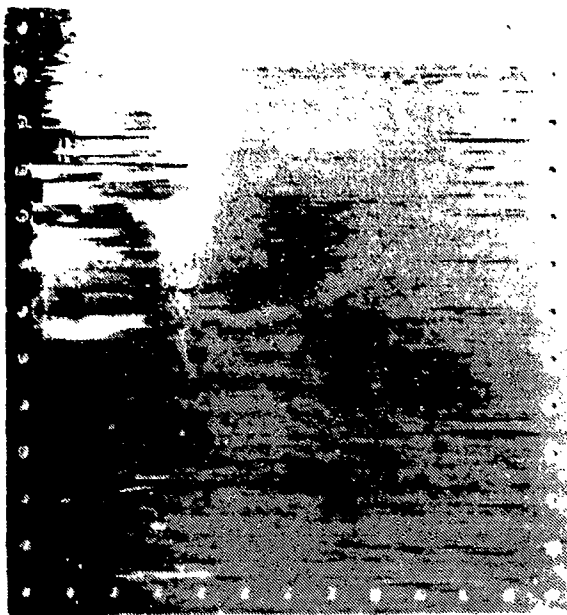
A list of the panel designs used in the blast test program is given in Table II. Three panels of each design were constructed. T300/934 graphite/epoxy was used for the laminates, with 7075-T6 bare aluminum sheet used for the aluminum panels. Aluminum angles were bolted to the panels to simulate the edge conditions normally found in aircraft wing structures.

The finite-element model used in the BR-1 runs is shown in Figure 7. The edge beams were modeled as tees in the program since angles are not available in the BR-1.

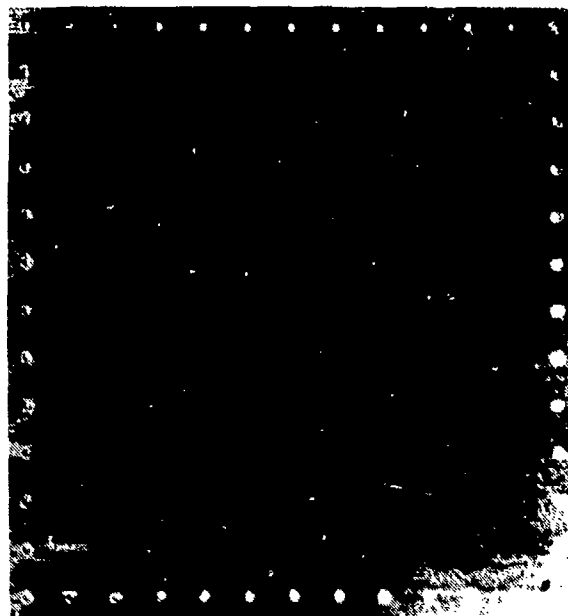
Table II shows the blast distance and charge weight for each test as well as the time interval which was captured on film and the maximum deflection recorded. The initial shots were filmed at a frame speed of about 7 microseconds/frame, starting at 100 microsecond after detonation, so that the peak deflection occurred after the last frame had been exposed. The camera was then slowed down to the 12-14 microsecond/frame region and the first frame was delayed to about 300-400 microsecond after detonation in order to capture the maximum deflection within the 28 frames in the camera.

Figures 8 and 9 give a comparison of the predicted center deflection vs time for the aluminum and laminated composite panels with the results of several test shots. The aluminum panel tests given in Figure 8 show good correlation with the predicted deflections. The predicted peak deflection is consistently slightly lower than the test peak deflection and occurs before the test peak deflection. A model with more node points would probably have produced better correlation, both due to the better modeling of the structure and due to the better modeling of the blast loads, which are applied as nodal loads.

Predicted failures are indicated on the plots by X's with a letter showing the type of failure predicted. "M" indicates the first matrix failure which occurred in the panel, which is usually due to a transverse tension failure. "F" indicates a fiber failure in which the fibers have failed in some layer. Each time step during which at least one fiber failure for the composite panels, has occurred is indicated with an "F" while only the first matrix failure is shown since every time step after



BR1-4-3



BR 1-7-2



BR 1-8-1



BR 1-9-3

Figure 6. Photographs of Rear Surface of Blast Test Panels After Testing

Table II. Blast Test Summary

Panel	Laminate	Thickness in (mm)	Blast distance in (mm)	Charge (gm)	Shot no.	Time interval filmed (μ s)	Max deflection measured in (mm)
BR1-1-1	(+45)	.143 (3.63)					
-2	(+45)	.143 (3.63)					
-3	(+45)	.143 (3.63)					
BR1-2-1	(0/+45/90)	.119 (3.02)					
-2	(0/+45/90)	.119 (3.02)	6 (152)	13g	10	412-800	.82 (20.83) A
-3	(0/+45/90)	.119 (3.02)	6 (152)	13g	7	106-435	.62 (15.74)
BR1-3-1	(0/+45/0/90)	.145 (3.63)	6 (152)	13g	3	100-290	.23 (5.84)
-2	(0/+45/0/90)	.145 (3.63)	6 (152)	13g	17	410-740	.80 (20.32) A
-3	(0/+45/0/90)	.145 (3.63)					
BR1-4-1	(0/90)	.098 (2.49)	6 (152)	13g	16	330-720	1.20 (30.48) A
-2	(0/90)	.098 (2.49)					
-3	(0/90)	.098 (2.49)	6 (152)	13g	4	106-295	.46 (11.68) C
BR1-5-1	7075-T6	.100 (2.54)					
-2	7075-T6	.100 (2.54)					
-3	7075-T6	.100 (2.54)	6 (152)	13g	2	100-225	.2 (5.08)
BR1-6-1	7075-T6	.083 (1.60)	6 (152)	13g	8	108-400	.68 (16.76)
-2	7075-T6	.083 (1.60)	6 (152)	13g	9	320-690	1.09 (27.68) A
-3	7075-T6	.083 (1.60)					
BR1-7-1	(0 ₂ /+44/90)	.082 (1.57)	6 (152)	13g	6	93-270	.68 (17.27) B
-2	(0 ₂ /+45/90)	.082 (1.57)	10 (254)	13g	13	LAMP FAILURE	
-3	(0 ₂ /+45/90)	.082 (1.57)	6 (152)	13g	18	370-690	1.97 (50.04) B
BR1-8-1	(0/+45 ₂ /90)	.077 (1.98)	6 (152)	13g	6	148-486	.91 (23.11) B
-2	(0/+45 ₂ /90)	.077 (1.98)	10 (254)	13g	14	LAMP FAILURE	
-3	(0/+45 ₂ /90)	.077 (1.98)	6 (152)	13g	19	360-720	1.18 (29.97) A
BR1-9-1	7075-T6	.040 (1.02)	6 (152)	13g	11	402-745	1.48 (37.59) A
-2	7075-T6	.040 (1.02)	10 (254)	13g	12	200-540	.88 (22.35)
-3	7075-T6	.040 (1.02)	10 (254)	25g	15	210-570	1.30 (33.02)

- A Passed peak deflection
 B Panel fractured
 C Panel cracked

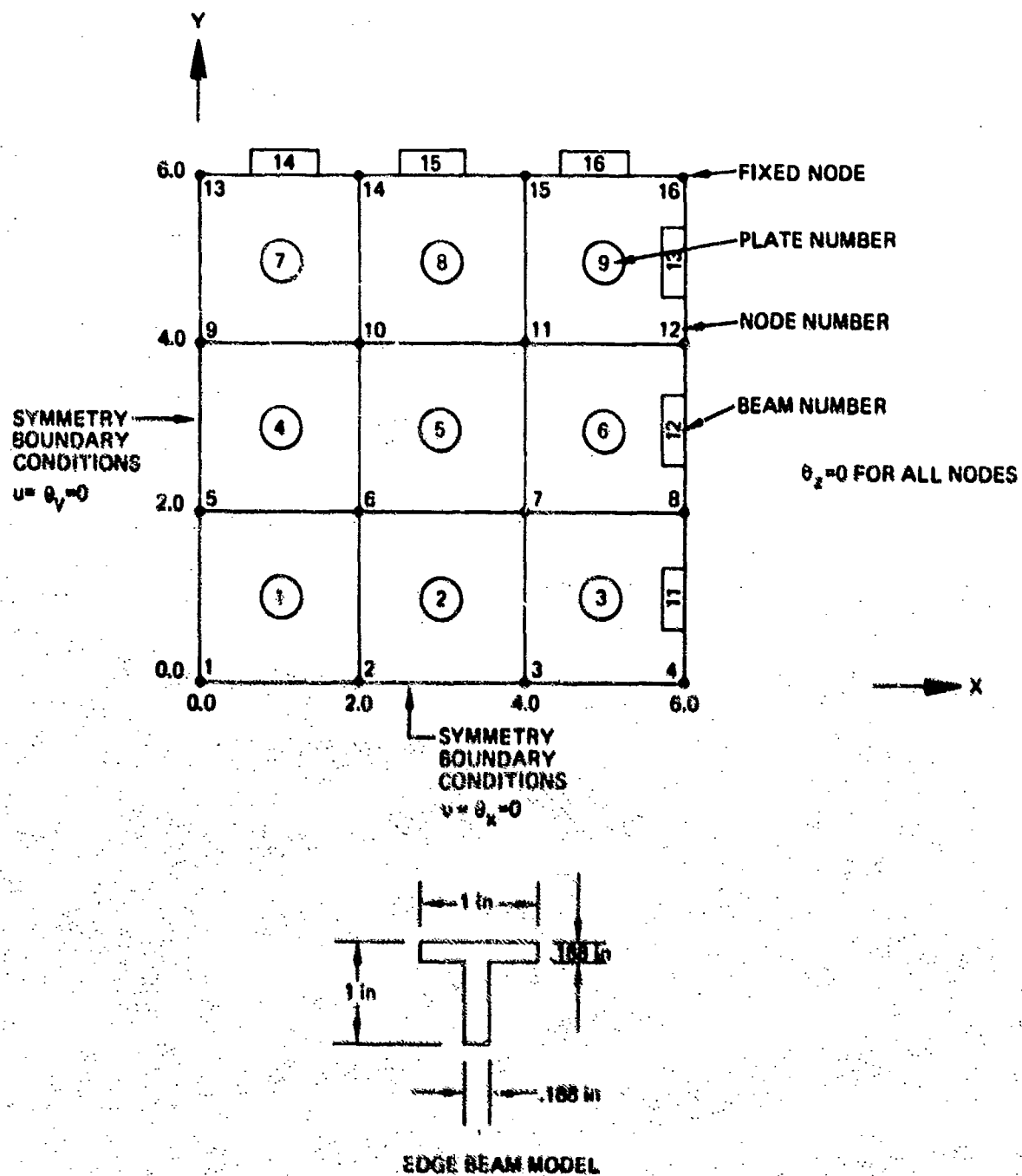
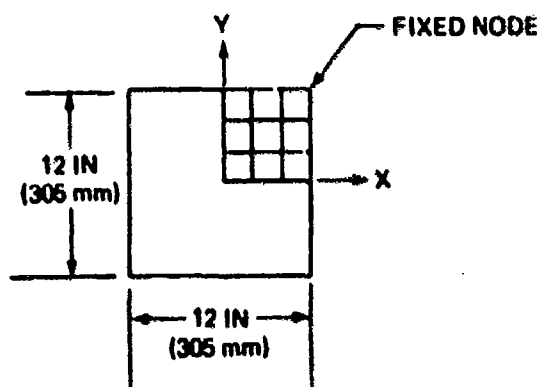


Figure 7. BR-1 Finite-Element Model of Blast Panel



0.03 LB (0.014 KG) EXT NO. 4 (PENTOLITE)

— Predicted panel center deflection

- - - Blast test center deflection

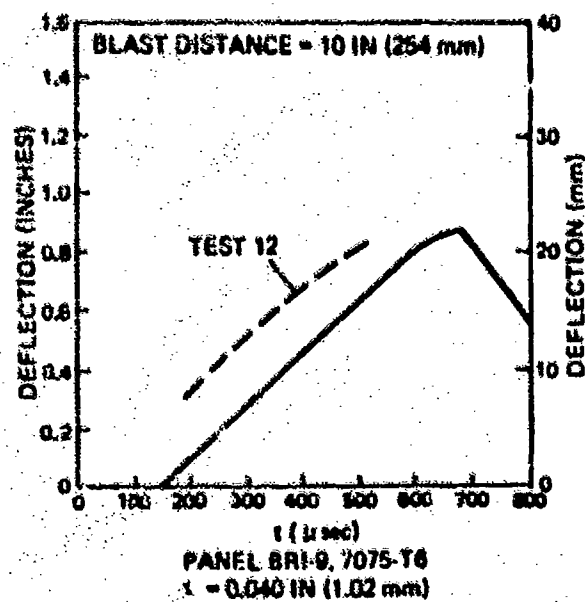
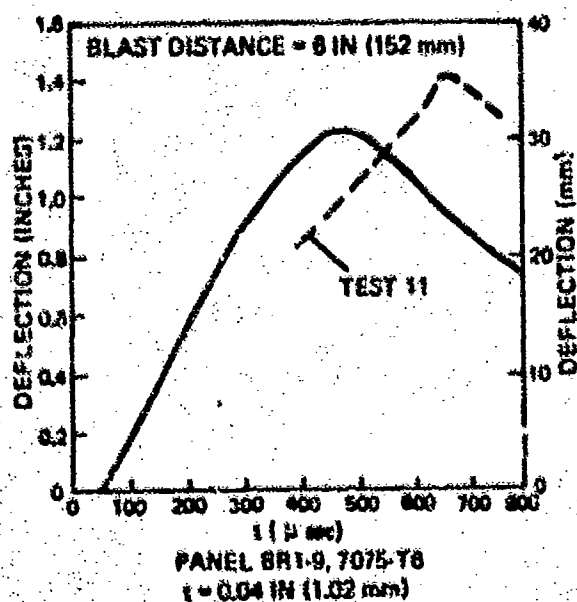
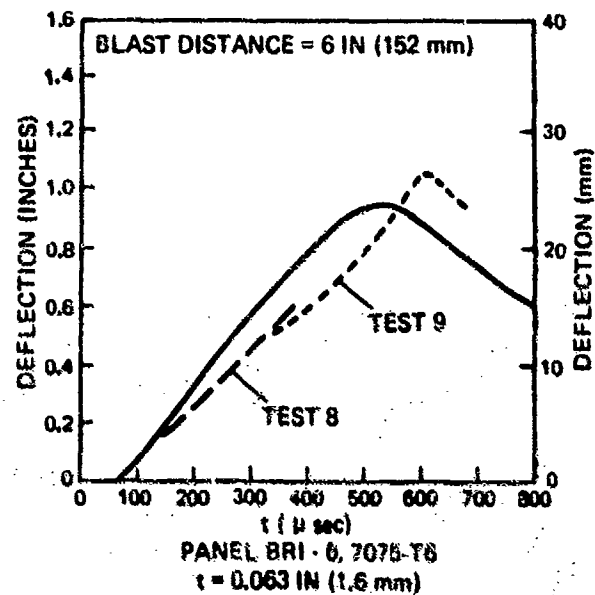
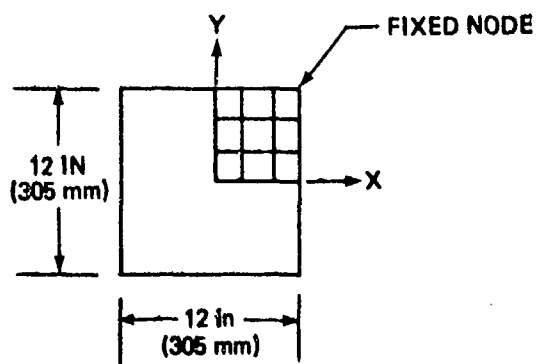


Figure 8. Aluminum Panel Blast Response



Blast distance = 6 in (152 mm)
 0.03 lb (0.014 kg) EXP No. 4 (pentollite)
 Failure codes

M = First matrix failure
 F = Fiber failure

— Predicted panel center deflection
 - - - Blast test center deflection

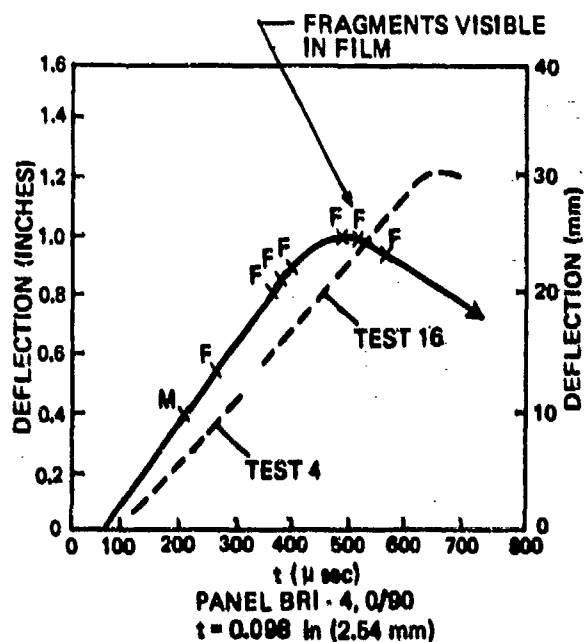
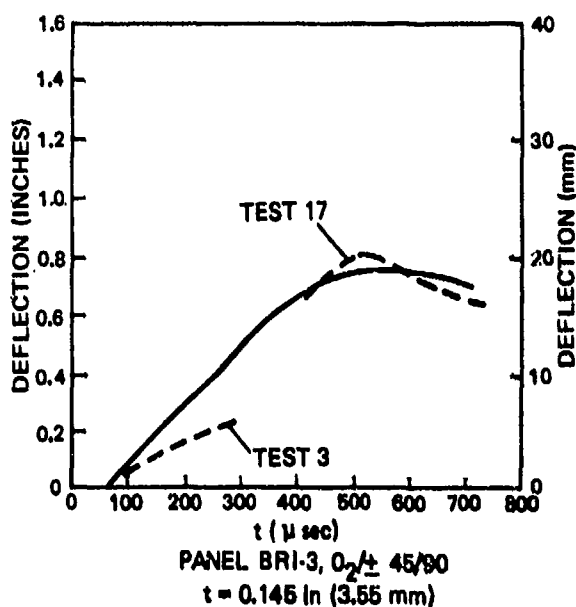
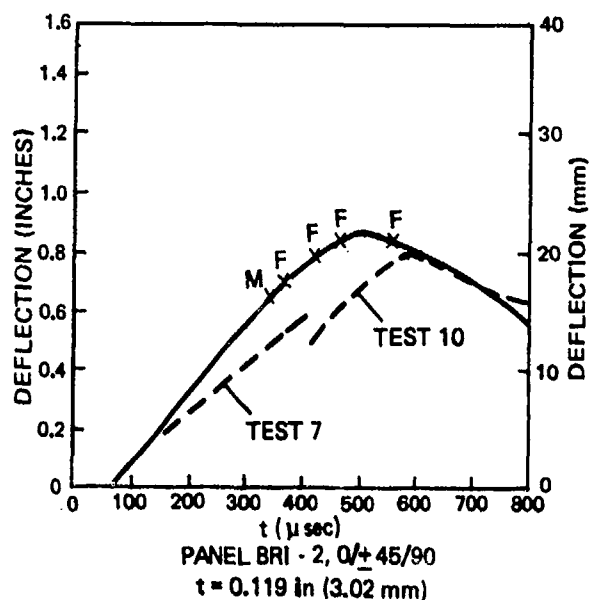


Figure 9. Composite Panel Blast Response

the initial failure would usually have several matrix failures. Station failures are indicated with an "S", while node failures are indicated by an "N". A station failure is indicated whenever at least three stations in each element connecting to a node have failed, indicating massive damage.

For the composite panels, the predicted maximum deflections were generally close to those seen in the tests although the time at which the peak occurred was usually underestimated by 100-200 microseconds. Panel BR1-2 has a lower test peak than predicted while panel BR-4 has a higher test peak than predicted. Test shot 3 for panel BR1-3 shows poor correlation while test shot 17 shows good correlation. A possible explanation is that the explosive failed to detonate properly in shot 3. Another possible explanation is the camera, which tends to run erratically when forced to run at the low speeds used in this program. The deflection-time plots might have shown better correlation if a more refined model had been used, although the correlation obtained seems acceptable.

Table III gives a comparison between the damage observed in the blast tests and the damage predicted by the BR-1FC program. It can be seen that good correlation was obtained in that a prediction of fiber

Table III. Correlation of Blast Panel Condition with Prediction

Panel	Test Result	BR-1FC Prediction
BR1-2	No visible damage	Small number of matrix failures predicted
BR1-3	No visible damage	No failures predicted
BR1-4,1,2	Cracks, some fibers broken	Many matrix failures, small number of fiber failure
BR1-7-1,3	Blown out of frame	Many station failures, node failure
BR1-8-1,3	Many fibers broken	Many fiber failures, 2 station failures

Matrix failure = Transverse or shear failure in a layer

Fiber failure = Fiber fracture in a layer

Station failure = Inability of laminate to carry load at one of the nine stations in the plate

Node failure = At least 3 station failures in all elements connecting to a node

fractures correlated with broken fibers in the test, while a prediction of station failures correlated with a severely damaged panel and the prediction of a node failure correlated with a panel blown out of the frame. Also, the prediction of no failure corresponds to test panels in which little damage could be seen.

BALLISTIC TESTING

A section of the Battle Damage Tolerant Wing three-spar test box was modeled using the BR-1FC code. This box was loaded to 53% limit bending load and shot with a quick fused 23mm high explosive projectile during the Damage Tolerant Wing program. The box design consisted of +45 fabric skin with spar caps consisting of bundles of 0 graphite tape encapsulated in +45 fabric. Glass fabric stiffeners were used between spars to support the skin and feed the blast pressure loads into the ribs. Figure 10 shows the BR1-FC model of the box, which consisted of 72 nodes, 60 plates and 36 beams. Only the exit skin was modeled, since the entrance skin was expected to be almost entirely removed due to fragment effects, based on our experience with this projectile. Figure 11 is a plot of the Z deflections vs time for the three nodes on the exit skin with the highest predicted deflections, with matrix, fiber, station and node failures noted on the node closest to the given failure. Figure 11 shows that the deflection at the three nodes reached a peak and then started to decline without any catastrophic failure. Experience with the panel tests previously done led us to conclude that the test box would survive intact, although with several areas of delamination and fiber fracture. The test box was not instrumented to determine the panel deflections during the shot so the predicted deflections could not be checked. Several fragment penetrations were observed on the exit skin, but the skin was still capable of carrying loads, as predicted by the analysis. The box test is discussed further in another paper at this conference.

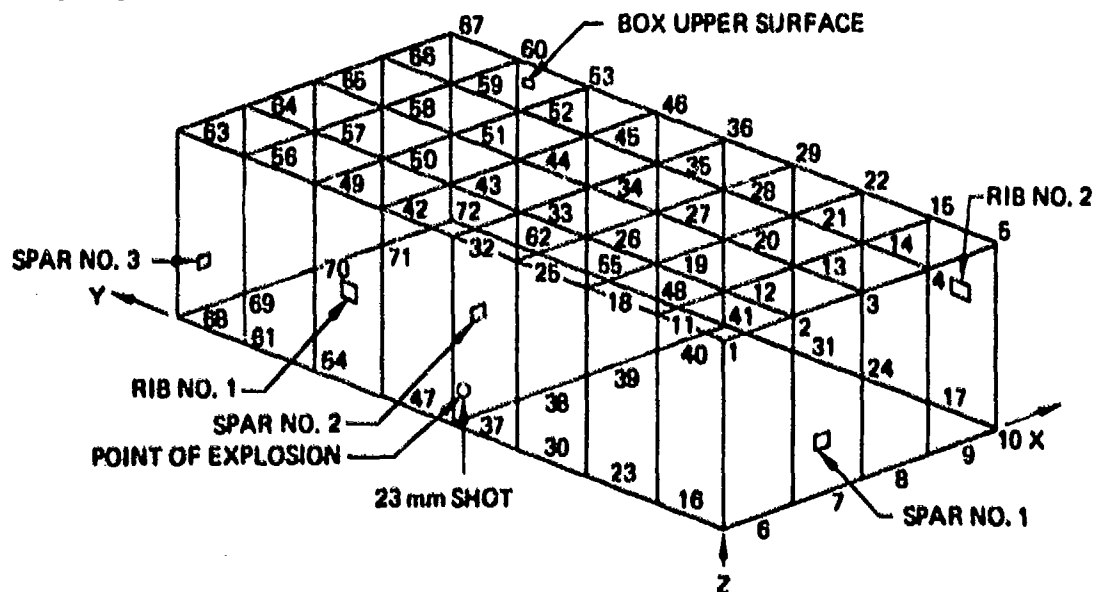


Figure 10. DT Wing Box Model

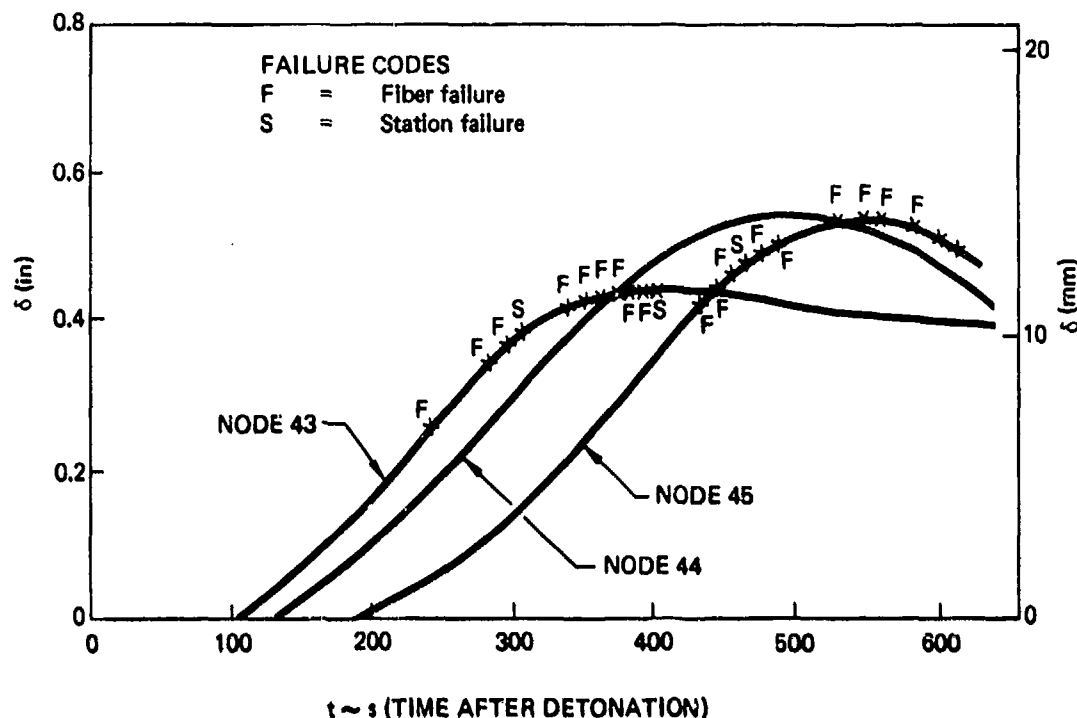


Figure 11. Damage Tolerant Wing Box Model—Predicted Nodal Deflection Versus Time Plot

CONCLUSIONS

The BR-1FC produced good correlation with test data for the panel tests consisting of an explosive with no fragments. It was also satisfactory in predicting the results of a box test with a 23-mm HEI explosive in that it predicted that the box would survive the explosion, which was borne out by the test.

Due to the combined effects of blast pressure and fragment penetrations, a fracture mechanics approach would probably be required in the general case. The stresses predicted by the finite-element analysis would be used to determine if crack extension and panel removal would occur.

The BR-1FC finite-element computer program could be improved by the inclusion of plate elements which include the effects of normal shear stiffness, which can be important in laminated composites.

An instrumented test of a wing box with stiffeners should be done to obtain correlation with common aircraft structural elements.

Reference 6 provides a user's manual for the BR-1FC computer program and gives further details on the panel blast test program.

ACKNOWLEDGMENT

The authors acknowledge the support of Andre Holten of the Air Force Flight Dynamics Laboratory for the work reported herein, conducted under contract N000-19-75-C-0718 (MODP0003)

REFERENCES

1. PROCTER, J.F., "Internal Blast Damage Mechanisms Computer Program", NOLTR 72-231, Naval Ordnance Laboratory, White Oaks, Silver Springs, Maryland, August 1972.
2. BRASS, J., JACOBSON, M.J., "Effects of Internal Blast on Combat aircraft Structures, Volume 1, Engineers Manual"., AFFDL-TR-73-136, Volume I, Jan. 1974.
3. SALUS, W.L., IP, C., "Design Considerations of Elastic-Plastic Structures Subjected to Dynamic Loads; AIAA/ASME 11th Structures Structural Dynamics and Materials conference, New York, 1970, pp 145-153.
4. WU, R.W., WITMER, E.A., "Finite-Element Analysis of Large Elastic-Plastic Transient Deformations of Simple Structures", AIAA J., Vol. 9, No. 9, September 1971, pp 1719-1724.
5. SANDHU, R.S., "Fiber Composite Blast Response Computer Program (BR1-FC) Br-1 Code Modification and Test Program", AFFDL-TR-78-29, JTCG/AS-76-T-008, October 1977.
6. DOBYNS, A. L. , "Fiber Composite Blast Response Computer Program (BR-1FC) BR-1 Code Modification and Test Program", AFFDL-TR-78-29, JTCG/AS-76-T-008, October 1977.

STABILITY OF COMPOSITE PLATES SUBJECTED TO VARYING TANGENTIAL AND LATERAL LOADS

ROBERT J. STUART
Associate Professor of Electrical
and Computer Engineering

SANGIAHNADAR DHARMARAJAN
Professor of Aerospace Engineering
College of Engineering
San Diego State University
San Diego, California 92182

ABSTRACT

The stability of a flat rectangular composite plate with either clamped or simply supported boundary conditions and subjected to tangential and lateral loads which vary exponentially with one space coordinate is considered. By using Liapunov's direct method, extended to continuous systems by Movchan, three conditions sufficient to guarantee stability under extreme loading are derived. The three stability conditions relate material properties, geometry and loading conditions and may be used for design purposes. The paper extends to orthotropic materials the work done by Leipholz and Bhalla for isotropic materials.

INTRODUCTION

Leipholz and Bhalla (1) considered the stability of a flat plate under combined normal and tangential loading. The loading that they considered was motivated by the storage of grain in silos. Some of the weight of the stored material is transferred to the walls by friction, thus subjecting the walls to vertical compression and hence buckling. It is apparent that the silo wall undergoes a combined load composed of normal forces exerted on the wall by the stored material and frictional forces acting along the wall. Both these types of loads vary exponentially with depth. When the silo is emptied, the friction may cause vibrations which can become very large.

In this paper, the exponential loading used by Leipholz and Bhalla (1) is postulated and could come from aerodynamic loading or other sources as well as storage of grain in a silo. The work in Leipholz and Bhalla (1) is extended from isotropic to orthotropic material. If the material is isotropic, the results in this paper reduce to those of Leipholz and Bhalla (1).

The stability of the plate is analyzed by the second or direct method of Liapunov as extended to continuous systems by Movchan (2,3). A description of the method together with several examples of its application to elastic systems is given in Knops and Wilkes (4). Liapunov's direct method is an extension of the energy methods used by structural engineers. The advantage of this method is that it is not necessary to solve the equations of motion in order to determine the stability of a system, i.e., stability may be determined directly from the equations of motion.

The results of the stability analysis take the form of three conditions which are sufficient to guarantee stability even under the influence of extreme loading. The conditions relate material properties, geometry and loads and may be used for design criteria. A convenient plot may be made which displays the stable region in terms of system parameters.

PROBLEM STATEMENT

In this paper a flat rectangular composite plate will be considered. The coordinates of the plate are $0 \leq x \leq a$, $0 \leq y \leq b$. The boundaries of the plate are either clamped or simply supported. The plate is subjected to a normal load

$$P_n = P[1 - e^{-(a-x)/r}] \quad (1)$$

where P and r are positive constants. The plate is also subjected to a frictional follower load acting along the wall in the negative x direction.

$$P_f = \mu P_n = \mu P[1 - e^{-(a-x)/r}] \quad (2)$$

Here μ is the coefficient of friction at the surface of the plate. The problem is to determine relationships among the parameters describing the plate and its loading which will suffice to guarantee stability of the plate under extreme loading.

LIAPUNOV STABILITY

Let Q be a vector whose components define the state of the plate, i.e., the components of Q are the deflection and a certain number of its derivatives with respect to space and time. Let \underline{Q} denote the Q vector whose components are all zero. Let t be the time variable. Following Knops and Wilkes (4), the point \underline{Q} is said to be stable with respect to the norms $\rho_0(Q, t)$, $\rho_1(Q, t)$ if the following conditions are met:

$$\rho_1 \text{ is a continuous function of } t \quad (3)$$

$$\rho_1 \text{ is continuous with respect to } \rho_0 \quad (4)$$

$$\text{Given an } \epsilon > 0, \delta(\epsilon) > 0 \text{ can be found such that} \quad (5)$$

$$\rho_0(Q_0, t_0) < \delta \text{ implies } \rho_1(Q, t) < \epsilon \text{ for } t \geq t_0$$

Movchan (2,3) has generalized to continuous systems the stability theorem of Liapunov for discrete systems. The following theorem follows Knops and Wilkes (4).

The state (\underline{Q}, t) is stable with respect to the norms ρ_0 and ρ_1 if there exists a Liapunov functional M with the following properties:

$$M \geq 0 \quad (6)$$

$$\dot{M} \leq 0 \quad (7)$$

Given $\varepsilon > 0$, $\delta(\varepsilon) > 0$ can be found such that $\rho_1 > \varepsilon$ implies $M > \delta$ (8)

Given $\varepsilon > 0$, $\delta(\varepsilon) > 0$ can be found such that $\rho_0 < \delta$ implies $M < \varepsilon$ (9)

Conditions (6) and (8) designate a functional which is called "positive definite." To some authors this term implies only (6). The distinction is important in the discussion of stability.

In the work that follows, pseudo-norms ρ_0^* and ρ_1^* will be used in place of the norms ρ_0 and ρ_1 , i.e., the norms used will not involve all the components of Q . The use of the pseudo-norms means that the stability statements do not exclude instability with respect to the omitted components.

DERIVATION OF STABILITY CONDITIONS

Fundamental Equations

For notational simplicity it is convenient to define the operator $L(W)$.

$$L(W) = D_{11} W_{xxxx} + 2(D_{12} + 2D_{66}) W_{xxyy} + D_{22} W_{yyyy} \quad (10)$$

The differential equation of motion of the plate, subjected to a normal load given by (1) and a tangential follower compressive frictional load given by (2) is

$$\begin{aligned} L(W) + \mu P \left\{ (a-x) - r[1 - e^{-(a-x)/r}] \right\} W_{xx} + \rho \ddot{W} + \beta \dot{W} \\ = P[1 - e^{-(a-x)/r}] \end{aligned} \quad (11)$$

where D_{ij} is the flexural rigidity of the plate

W is the lateral deflection of the plate

β is the damping coefficient of the plate

ρ is the mass per unit area of the plate

The subscripts x and y denote differentiation with respect to those variables. Dots represent differentiation with respect to time.

The deflection W may be decomposed into its static and dynamic parts, W_0 and w respectively. By substituting

$$W = W_0 + w \quad (12)$$

into (11) and separating the static and dynamic parts, there results two equations

$$L(W_0) + \mu P \left\{ (a-x) - r[1 - e^{-(a-x)/r}] \right\} W_{0xx} = P[1 - e^{-(a-x)/r}] \quad (13)$$

and

$$L(w) + \mu P \left[(a-x) - r[1 - \epsilon^{-(a-x)/r}] \right] w_{xx} + \rho \ddot{w} + \beta \dot{w} = 0 \quad (14)$$

It is apparent that the static deflection w_0 will be bounded, however, the solution of (14) could be unstable.

The Liapunov Functional

In order to investigate the stability of the plate, the following Liapunov functional is chosen

$$M = \int_A \left[U(w) + \rho \dot{w}^2 + \frac{\beta^2 w^2}{2\rho} + \beta w \dot{w} - \mu P(a-x) w_x^2 + \mu P r [1 - \epsilon^{-(a-x)/r}] w_x^2 \right] dA \quad (15)$$

where

$$U(w) = D_{11} w_{xx}^2 + 2D_{12} w_{xx} w_{yy} + D_{22} w_{yy}^2 + 4D_{66} w_{xy}^2 \quad (16)$$

The first step is to show that the Liapunov functional is positive definite. Note that

$$\rho \dot{w}^2 + \beta w \dot{w} + \frac{\beta^2 w^2}{2\rho} = \rho \left(\dot{w} + \frac{\beta w}{2\rho} \right)^2 + \frac{\beta^2 w^2}{4\rho} \geq 0 \quad (17)$$

$$\text{and that } \mu P r [1 - \epsilon^{-(a-x)/r}] w_x^2 \geq 0 \quad (18)$$

Substituting (17) and (18) into (15) yields

$$M \geq \int_A \left[U(w) - \mu P (a-x) w_x^2 \right] dA \quad (19)$$

In Appendix B it is shown that if λ_1 is the lowest eigenvalue of the equation

$$L(w) + \lambda [(a-x) w_x]_x = 0 \quad (20)$$

subject to the same clamped or simply supported boundary conditions as the plate, then

$$\int_A U(w) dA \geq \lambda_1 \int_A (a-x) w_x^2 dA \quad (21)$$

Using (21) in (19) gives

$$M \geq \int_A (\lambda_1 - \mu P) (a-x) w_x^2 dA \quad (22)$$

From (22) it is apparent that M will be positive definite if

$$\mu P \leq \lambda_1 \quad (23)$$

This is the first stability condition. It relates the flexural rigidity parameters D_{ij} which affect λ_1 to the maximum load P which may be affected by geometry.

The next step is to show that the time derivative of M is negative definite

$$\begin{aligned} \dot{M} = \int_A \left\{ 2D_{11} w_{xx} \dot{w}_{xx} + 2D_{12} (\dot{w}_{xx} w_{yy} + w_{xx} \dot{w}_{yy}) \right. \\ + 2D_{22} w_{yy} \dot{w}_{yy} + 8D_{66} w_{xy} \dot{w}_{xy} + 2\rho \dot{w} \ddot{w} + \frac{\beta \dot{w}^2}{\rho} + \beta \dot{w}^2 \\ \left. + \beta w \ddot{w} - 2\mu P(a-x) w_x \dot{w}_x + 2\mu P r [1 - e^{-(a-x)/r}] w_x \dot{w}_x \right\} dA \end{aligned} \quad (24)$$

By making use of the relationships given in Appendix A and the clamped or simply supported boundary conditions, there results

$$\begin{aligned} \int_A [2D_{11} w_{xx} \dot{w}_{xx} + 2D_{12} (\dot{w}_{xx} w_{yy} + w_{xx} \dot{w}_{yy}) \\ + 2D_{22} w_{yy} \dot{w}_{yy} + 8D_{66} w_{xy} \dot{w}_{xy}] dA = \int_A 2\dot{w} L(w) dA \end{aligned} \quad (25)$$

and also

$$\begin{aligned} \int_A 2\mu P \left\{ -(a-x) + r [1 - e^{-(a-x)/r}] \right\} w_x \dot{w}_x dA \\ = \int_A \left\{ 2\mu P [(a-x) - r [1 - e^{-(a-x)/r}]] w_{xx} \right. \\ \left. + 2\mu P [-1 + e^{-(a-x)/r}] w_x \right\} dA \end{aligned} \quad (26)$$

When these two equations are substituted into (24), the result is

$$\begin{aligned} \dot{M} = \int_A \left\{ 2\dot{w} [L(w) + \rho \ddot{w} + \mu P [(a-x) - r (1 - e^{-(a-x)/r})] w_{xx}] \right. \\ \left. + \frac{\beta w}{\rho} (\beta \dot{w} + \rho \ddot{w}) + \beta \dot{w}^2 - 2\mu P [1 - e^{-(a-x)/r}] w_x \dot{w}_x \right\} dA \end{aligned} \quad (27)$$

The equation of motion of the plate (14) may be substituted into (27) in two places to yield

$$\begin{aligned} \dot{M} = \int_A \left\{ -\beta \dot{w}^2 + \frac{\beta w}{\rho} [-L(w) - \mu P [(a-x) - r (1 - e^{-(a-x)/r})]] w_{xx} \right. \\ \left. - 2\mu P [1 - e^{-(a-x)/r}] w_x \dot{w}_x \right\} dA \end{aligned} \quad (28)$$

Now, again applying the results of Appendix A

$$\int_A \left(-\frac{\beta}{\rho} \right) w L(w) dA = \int_A \left(-\frac{\beta}{\rho} \right) U(w) dA \quad (29)$$

where $U(w)$ has been defined in (16). Also

$$\begin{aligned} \int_A \left(-\frac{\beta \mu P}{\rho} \right) \left\{ (a-x) - r[1 - \epsilon^{-(a-x)/r}] \right\} w w_{xx} dA \\ = \int_A \left(\frac{\beta \mu P}{\rho} \right) \left\{ [(a-x) - r[1 - \epsilon^{-(a-x)/r}]] w_x^2 \right. \\ \left. + [-1 + \epsilon^{-(a-x)/r}] w w_x \right\} dA \end{aligned} \quad (30)$$

Furthermore

$$\begin{aligned} \int_A \left(\frac{\beta \mu P}{\rho} \right) [-1 + \epsilon^{-(a-x)/r}] w w_x dA \\ = \int_A \left(\frac{\beta \mu P}{\rho r} \right) [-\epsilon^{-(a-x)/r}] w^2 dA \\ - \int_A \left(\frac{\beta \mu P}{\rho} \right) [-1 + \epsilon^{-(a-x)/r}] w w_x dA \end{aligned} \quad (31)$$

By combining terms in (31) there results

$$\begin{aligned} \int_A \left(\frac{\beta \mu P}{\rho} \right) [-1 + \epsilon^{-(a-x)/r}] w w_x dA \\ = \int_A \left(\frac{\beta \mu P}{2r\rho} \right) [-\epsilon^{-(a-x)/r}] w^2 dA \end{aligned} \quad (32)$$

Substituting (32) into (30) and then substituting (29) and (30) into (28) yields

$$\begin{aligned} \dot{M} = \int_A \left\{ -\beta \dot{w}^2 - \frac{\beta}{\rho} U(w) + \frac{\beta \mu P}{\rho} [(a-x) - r[1 - \epsilon^{-(a-x)/r}]] w_x^2 \right. \\ \left. - \left(\frac{\beta \mu P}{2r\rho} \right) \epsilon^{-(a-x)/r} w^2 - 2\mu P [1 - \epsilon^{-(a-x)/r}] w_x \dot{w} \right\} dA \end{aligned} \quad (33)$$

$$\text{Now } \frac{\beta \mu P r}{\rho} [1 - \epsilon^{-(a-x)/r}] w_x^2 \geq 0 \quad (34)$$

$$\text{and } \frac{\beta \mu P}{2r\rho} \epsilon^{-(a-x)/r} w^2 \geq 0 \quad (35)$$

Hence using (21), (34) and (35) in (33) yields

$$\begin{aligned} \dot{M} \leq \int_A \left\{ -\beta \dot{w}^2 - \frac{\beta}{\rho} [\lambda_1 - \mu P] (a-x) w_x^2 \right. \\ \left. - 2\mu P [1 - \epsilon^{-(a-x)/r}] w_x \dot{w} \right\} dA \end{aligned} \quad (36)$$

By the mean value theorem

$$\int_A (a-x) w_x^2 dA = m \int_A w_x^2 dA \quad (37)$$

where $0 \leq m \leq a$ (38)

Hence $\dot{M} \leq - \int_A \left[\beta \dot{w}^2 + \frac{\beta}{\rho} (\lambda_1 - \mu P) m w_x^2 + 2\mu P [1 - \epsilon^{-(a-x)/r}] w_x \dot{w} \right] dA$ (39)

Since $\beta \dot{w}^2 + 2\mu P [1 - \epsilon^{-(a-x)/r}] w_x \dot{w} + \frac{\beta}{\rho} (\lambda_1 - \mu P) m w_x^2$
 $= \beta \left[\dot{w}^2 + \frac{2\mu P}{\beta} [1 - \epsilon^{-(a-x)/r}] w_x \dot{w} + \left(\frac{\mu P}{\beta} \right)^2 [1 - \epsilon^{-(a-x)/r}]^2 w_x^2 \right]$
 $+ \left\{ \frac{\beta m}{\rho} (\lambda_1 - \mu P) - \frac{\mu^2 P^2}{\beta} [1 - \epsilon^{-(a-x)/r}]^2 \right\} w_x^2$ (40)

will be positive definite if

$$\beta \geq \frac{\mu P [1 - \epsilon^{-(a-x)/r}] \sqrt{\rho}}{\sqrt{m(\lambda_1 - \mu P)}} \quad (41)$$

choosing

$$\beta \geq \frac{\mu P \sqrt{\rho}}{\sqrt{m(\lambda_1 - \mu P)}} \quad (42)$$

will guarantee that \dot{M} is negative definite. (42) is the second stability condition and may be used to establish a lower bound for required material damping.

Boundedness of the Liapunov Functional

Define the norms

$$\rho_0^* = \left[\sup |\dot{w}|^2 + \sup |U(w)| + \sup |w|^2 + \sup |w_x|^2 \right]^{1/2} \quad (43)$$

and

$$\rho_1^* = \sup |w| \quad (44)$$

In order to show that the Liapunov functional has an upper bound, the negative terms in M can be dropped.

$$M \leq \int_A \left\{ U(w) + \rho \dot{w}^2 + \frac{\beta^2 w^2}{2\rho} + \beta w \dot{w} + \mu P w_x^2 \right\} dA \quad (45)$$

Using the inequality

$$\rho \dot{w}^2 + \frac{\beta^2 w^2}{2\rho} + \beta w \dot{w} \leq \frac{3}{2} \rho \dot{w}^2 + \frac{\beta^2 w^2}{\rho} \quad (46)$$

in (45) yields

$$M \leq \int_A \left[U(w) + \frac{3}{2} \rho w^2 + \frac{\beta^2 w^2}{\rho} + \mu P w_x^2 \right] dA \quad (47)$$

$$\text{Defining } k_0 = \text{Max} \left[A, \frac{3}{2} \rho A, \frac{\beta^2 A}{\rho}, \mu P A \right] \quad (48)$$

and using (43) in (47) yields

$$M \leq k_0 \rho_0 w^2 \quad (49)$$

Hence M has an upper bound.

In order to show that the Liapunov functional is bounded below, some positive terms in M can be dropped.

$$M \geq \int_A \left\{ U(w) - \mu P (a-x) w_x^2 \right\} dA \quad (50)$$

Since it is shown in Leipholz (5) that for the boundary conditions of the plate

$$\int_A w_{xx} w_{yy} dA = \int_A w_{xy}^2 dA \quad (51)$$

the first term on the right hand side of (50) may be written in expanded form as

$$\int_A U(w) dA = \int_A \left[D_{11} w_{xx}^2 + 2(D_{12} + 2D_{66}) w_{xy}^2 + D_{22} w_{yy}^2 \right] dA \quad (52)$$

If D is defined as

$$D = \text{Min} [D_{11}, D_{12} + 2D_{66}, D_{22}] \quad (53)$$

$$\text{then } M \geq \int_A \left\{ D [w_{xx}^2 + 2w_{xy}^2 + w_{yy}^2] - \mu P (a-x) w_x^2 \right\} dA \quad (54)$$

If (37) is applied to (54) and the positive term $\int_A \mu P m w_y^2 dA$ is subtracted, the result is

$$M \geq \int_A \left\{ D [w_{xx}^2 + 2w_{xy}^2 + w_{yy}^2] - \mu P m (w_x^2 + w_y^2) \right\} dA \quad (55)$$

By using Poincaré's inequality from Appendix C, (55) may be transformed into

$$M \geq \int_A [D - \mu P m l^2] [w_{xx}^2 + 2w_{xy}^2 + w_{yy}^2] dA \quad (56)$$

$$\text{where } l^2 = \text{Max}[a^2, b^2] \quad (57)$$

By using Sobolev's inequality from Appendix C, the above inequality may be written as

$$M \geq \frac{D - \mu P m l^2}{c^2} \sup |w|^2 \quad (58)$$

$$\text{Defining } k_1 = \frac{D - \mu P m \lambda^2}{c^2} \quad (59)$$

and using (44) in (58) yields

$$M \geq k_1 \rho_1^{*2} \quad (60)$$

M will be bounded from below if k_1 is positive. This gives the third stability condition

$$\mu P \leq \frac{D}{m \lambda^2} = \lambda^* \quad (61)$$

Condition (61) may be avoided by using the norm

$$\bar{\rho}_1 = \left[\int_A w^2 dA \right]^{1/2} \quad (62)$$

instead of (44). By substituting (21) and (37) into (50), the result is

$$M \geq \int_A m(\lambda_1 - \mu P) w_x^2 dA \quad (63)$$

By Friedrich's inequality (C1) of Appendix C

$$M \geq \frac{m(\lambda_1 - \mu P)}{a^2} \int_A w^2 dA \quad (64)$$

$$\text{Hence } M \geq k_2 \bar{\rho}_1^2 \quad (65)$$

$$\text{where } k_2 = \frac{m(\lambda_1 - \mu P)}{a^2} \quad (66)$$

Condition (23) is sufficient to guarantee that k_2 will be positive.

Stability Considerations

Let the initial disturbance of the system in terms of the norm ρ_0^* be

$$\rho_0^* = \epsilon \quad \text{for } t = t_0 \quad (67)$$

$$\text{Then by (49) } M \leq k_0 \rho^{*2} = k_0 \epsilon^2 \quad \text{for } t = t_0 \quad (68)$$

However, \dot{M} is negative definite and therefore M does not increase with time. Hence

$$M \leq k_0 \epsilon^2 \quad \text{for } t \geq t_0 \quad (69)$$

(60) together with (69) implies

$$k_1 \rho_1^{*2} \leq k_0 \varepsilon^2 \quad \text{for } t \geq t_0 \quad (70)$$

$$\text{or} \quad \sup |w| = \rho_1^* \leq \sqrt{\frac{k_0}{k_1}} \varepsilon \quad \text{for } t \geq t_0 \quad (71)$$

This implies that if the initial deflections of the plate are small in the sense of ρ_0^* , then the deflections of the plate will be small for all time in the sense of ρ_1^* if the stability conditions (23), (42) and (61) are met.

If instead, the norm $\bar{\rho}_1$ is used, then (65) and (69) imply

$$k_2 \bar{\rho}_1^2 \leq k_0 \varepsilon^2 \quad \text{for } t \geq t_0 \quad (72)$$

$$\text{or} \quad \int_A w^2 dA = \bar{\rho}_1^2 \leq \frac{k_0}{k_2} \varepsilon^2 \quad \text{for } t \geq t_0 \quad (73)$$

As pointed out by Leipholz and Bhalla (1), the stability criterion based on $\bar{\rho}_1$ is weaker than that based on ρ_1^* . (71) guarantees that deflections will be small everywhere, whereas (73) only ensures the smallness of deflections in the mean square sense. This means that deflections may be large in a localized area and that buckling may occur in that small area. Thus there is a trade-off in the omission of condition (61) and the weakening of the stability criterion.

SUMMARY

In this paper three stability conditions are derived which are sufficient to guarantee the stability of a flat rectangular composite plate with loading in the normal direction given by (1) and in the tangential direction by (2). The stability conditions are repeated below.

$$\mu P \leq \lambda_1 \quad (23)$$

$$\beta \geq \frac{\mu P \sqrt{\rho}}{\sqrt{m(\lambda_1 - \mu P)}} \quad (42)$$

$$\mu P < \frac{D}{m\ell^2} = \lambda^* \quad (61)$$

These relations relate material properties, geometry, and loadings and may be used for design criterion. The relationships are displayed in Figure 1.

The curve in Figure 1 comes from (42). Points falling in region I will be stable in the sense of ρ_1^* while points falling in region II will be stable in the sense of $\bar{\rho}_1$.

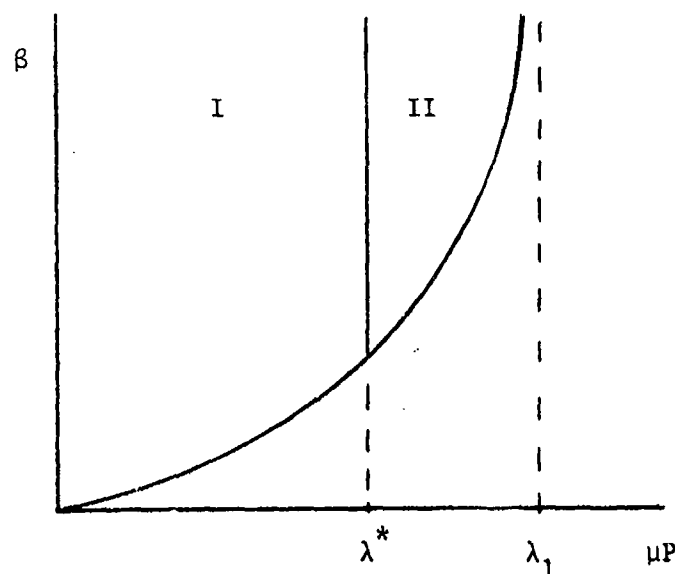


Figure 1. Stability Region

ACKNOWLEDGEMENT

The authors are grateful to Prof. H. H. E. Leipholz for the comments that he has made and for providing copies of several of his papers relating to Liapunov's second method applied to continuous systems.

APPENDICES

A. GREEN'S THEOREM

The form in which Green's Theorem usually appears is

$$\int_A \left(\frac{\partial P}{\partial x} + \frac{\partial Q}{\partial y} \right) dA = \int_C (Pdy - Qdx) \quad (A1)$$

Here C is the boundary of the surface A. Since Green's Theorem is used several times in this paper, it is helpful to make some substitutions into (A1) in order to make it easier to use. By writing $P = fg$, $Q = 0$ in (A1), the two-dimensional analog of integration by parts results

$$\int_A f_x g dA = - \int_A f g_x dA + \int_C f g dy \quad (A2)$$

By setting $P = f_x g - f g_x$, $Q = 0$ in (A1), the result obtained is

$$\int_A f_{xx} g dA = \int_A f g_{xx} dA + \int_C (f_x g - f g_x) dy \quad (A3)$$

The use of $P = 0$, $Q = f_y g - f g_y$ in (A1) yields

$$\int_A f_{yy} g dA = \int_A f g_{yy} dA - \int_C (f_y g - f g_y) dx \quad (A4)$$

Finally, setting $P = \frac{1}{2}(f_y g - f g_y)$, $Q = \frac{1}{2}(f_x g - f g_x)$

provides

$$\begin{aligned} \int_A f_{xy} g dA &= \int_A f g_{xy} dA + \frac{1}{2} \int_C (f_y g - f g_y) dy \\ &\quad - \frac{1}{2} \int_C (f_x g - f g_x) dx \end{aligned} \quad (A5)$$

In this paper all integrals on the boundary C will vanish due to the boundary conditions. This fact is obvious for clamped boundary conditions while a proof for simply supported boundary conditions may be found in Leipholz (5).

B. GENERALIZED STEKLOV'S INEQUALITY

Let λ_1 be the lowest eigenvalue of the equation

$$L(w) + \lambda [(a-x)w_x]_x = 0 \quad (B1)$$

where w meets either clamped or simply supported boundary conditions. Then for any w which meets the boundary conditions

$$\int_A U(w) dA \geq \lambda_1 \int_A (a-x) w_x^2 dA \quad (B2)$$

$L(w)$ and $U(w)$ have been defined previously in (10) and (16) respectively.

In order to prove this result, let ϕ_1 be the eigenfunction corresponding to the eigenvalue λ_1 , i.e.,

$$L(\phi_1) + \lambda_1 [(a-x) \phi_{1x}]_x = 0 \quad (B3)$$

By applying the results of Appendix A, there results

$$\int_A \phi_j [(a-x) \phi_{1x}]_x dA = - \int_A (a-x) \phi_{jx} \phi_{1x} dA \quad (B4)$$

and

$$\begin{aligned} \int_A \phi_j L(\phi_1) dA &= \int_A \{ D_{11} \phi_{1xx} \phi_{jxx} + 2(D_{12} + 2D_{66}) \phi_{1xy} \phi_{jxy} \\ &\quad + D_{22} \phi_{1yy} \phi_{jyy} \} dA \end{aligned} \quad (B5)$$

If (B3) is multiplied by ϕ_1 and integrated, use of (B4) and (B5) yields

$$\int_A \{ D_{11} \phi_{1xx} \phi_{1xx} + 2(D_{12} + 2D_{66}) \phi_{1xy} \phi_{1xy} + D_{22} \phi_{1yy} \phi_{1yy} \} dA \quad (B6)$$

$$-\lambda_i \int_A (a-x) \phi_{ix} \phi_{jx} dA = 0 \quad (B6)$$

Subtracting a result similar to (B6) with i and j interchanged from (B6) gives

$$(\lambda_i - \lambda_j) \int_A (a-x) \phi_{ix} \phi_{jx} dA = 0 \quad (B7)$$

If $\lambda_i \neq \lambda_j$, this implies the orthogonality relationship

$$\int_A (a-x) \phi_{ix} \phi_{jx} dA = 0 \quad \text{for } i \neq j \quad (B8)$$

Since $a-x$ is positive in A and since the vanishing of ϕ_{ix} in A would imply ϕ_i vanishes identically in A due to the boundary condition $\phi_i = 0$, it may be assumed that the eigenfunctions are normalized by

$$\int_A (a-x) \phi_{ix}^2 dA = 1 \quad (B9)$$

To show that the eigenvalues are positive, let $i = j$ in (B6). Then

$$\lambda_i = \int_A U(\phi_i) dA > 0 \quad (B10)$$

Assume that the eigenvalues are arranged in ascending order

$$0 < \lambda_1 \leq \lambda_2 \leq \lambda_3 \leq \dots \quad (B11)$$

To do an eigenfunction expansion, let

$$w = \sum_{j=1}^{\infty} C_j \phi_j \quad (B12)$$

Note that

$$w_x = \sum_{j=1}^{\infty} C_j \phi_{jx} \quad (B13)$$

Multiplying (B13) by $(a-x) \phi_{ix}$, integrating and using (B8) and (B9) yields

$$\int_A (a-x) \phi_{ix} w_x dA = C_i \quad (B14)$$

Also note that

$$\int_A (a-x) w_x^2 dA = \int_A (a-x) w_x \sum_{i=1}^{\infty} C_i \phi_{ix} dA = \sum_{i=1}^{\infty} C_i^2 \quad (B15)$$

By making use of Appendix A and the previous results of this Appendix, the desired result may be shown.

$$\int_A U(w) dA = \int_A w L(w) dA = \int_A w L\left(\sum_{i=1}^{\infty} C_i \phi_i\right) dA$$

$$\begin{aligned}
&= \sum_{i=1}^{\infty} C_i \int_A w L(\phi_i) dA = - \sum_{i=1}^{\infty} C_i \lambda_i \int_A w [(a-x)\phi_{ix}]_x dA \\
&= \sum_{i=1}^{\infty} C_i \lambda_i \int_A (a-x) \phi_{ix} w_x dA = \sum_{i=1}^{\infty} C_i^2 \lambda_i^2 \\
&\geq \lambda_1 \sum_{i=1}^{\infty} C_i^2 = \lambda_1 \int_A (a-x) w_x^2 dA
\end{aligned} \tag{B16}$$

C. INEQUALITIES

Friedrich's Inequality

The vanishing of w on the boundary is sufficient to guarantee that

$$\int_A w^2 dA \leq a^2 \int_A w_x^2 dA \tag{C1}$$

The proof may be found in Mikhlin (6).

Poincaré's Inequality

Poincaré's inequality reads

$$\int_A u^2 dA \leq \ell^2 \int_A (u_x^2 + u_y^2) dA + \frac{1}{A} \left(\int_A u dA \right)^2 \tag{C2}$$

$$\text{where} \quad \ell^2 = \text{Max}(a^2, b^2) \tag{C3}$$

The proof may be found in Mikhlin (6).

Letting first $u = w_x$ and then $u = w_y$ and adding yields

$$\begin{aligned}
\int_A (w_x^2 + w_y^2) dA &\leq \ell^2 \int_A (w_{xx}^2 + 2w_{xy}^2 + w_{yy}^2) dA \\
&+ \frac{1}{A} \left(\int_A w_x dA \right)^2 + \frac{1}{A} \left(\int_A w_y dA \right)^2
\end{aligned} \tag{C4}$$

The last two terms vanish when w vanishes on the boundary since, by Appendix A

$$\int_A w_x dA = \int_C w dy = 0 \tag{C5}$$

$$\text{and} \quad \int_A w_y dA = - \int_A w dx = 0 \tag{C6}$$

$$\text{Hence} \quad \int_A (w_x^2 + w_y^2) dA \leq \ell^2 \int_A (w_{xx}^2 + 2w_{xy}^2 + w_{yy}^2) dA \tag{C7}$$

Sobolev's Inequality

If w vanishes on the boundary, then

$$\sup |w|^2 \leq C^2 \int_A (w_{xx}^2 + 2w_{xy}^2 + w_{yy}^2) dA \quad (C8)$$

where C is an appropriately chosen constant.

This result may be found in Knops and Wilkes (4).

REFERENCES

1. Leipholz, H. H. E. and Bhalla, K. D., "Stability of a Simply Supported or Clamped Silo Wall Subjected to Frictional Tangential Follower Loads," Trans. of the CSME, V. 5, No. 2, 1978-79, 69-78.
2. Movchan, A. A., "The Direct Method of Liapunov in Stability Problems of Elastic Systems," J. Appl. Math. Mech., 23: 686-700, 1959.
3. Movchan, A. A., "Stability of Processes with Respect to Two Metrics," J. Appl. Math. Mech., 24: 1506-1524, 1960.
4. Knops, R. J. and Wilkes, E. W., "On Movchan's Theorems for Stability of Continuous Systems," Int. J. Engng. Sci., 4: 303-329, 1966.
5. Leipholz, H. H. E., "Liapunov's Second Method and Its Application to Continuous Systems," SM Archives, 1: 367-444, 1976.
6. Mikhlin, S. G., Variational Methods in Mathematical Physics, Macmillan, New York, 1964.

COMPRESSION STRENGTH DEGRADATION OF ADVANCED COMPOSITE STRUCTURES

DON Y. KONISHI

Member Technical Staff

Rockwell International/North American Aircraft Division (NAAD)

ABSTRACT

The ability to predict the serviceability of advanced composite structures on an aircraft undergoing a service loading/temperature/environmental spectrum is discussed. One of the critical factors is the degradation of the residual compressive strength of the structure after spectrum loading. There are two causes for this strength reduction. The primary cause is the degradation of the matrix, resulting from the moisture/temperature environment. A secondary cause is the propagation of delamination-type flaws emanating from flaw nuclei, causing loss of strength due to local instabilities. Test results are presented for graphite/epoxy (Gr/Ep) coupons undergoing a fully reversed loading/moisture/temperature spectrum enhanced so that maximum spectrum loading represents design limit load. Flaw growth rate was determined by using a pulse-echo ultrasonic inspection technique at prescribed intervals of the spectrum loading.

INTRODUCTION

It is now apparent that under conventional use advanced composite structures are indeed durable. However, the question remains as to whether composites tailored to meet unusual requirements are still durable. In order to predict durability under such conditions, it is necessary to understand the physics of failure. Once this is accomplished, such questions as the validity of accelerated testing schemes, adequacy of flaw detectability devices, adequacy of geometric complexity simplification, etc, can be answered with some degree of certainty.

The Advanced Composite Serviceability Program [1] systematically explored many of these questions. The approach used is shown in Table I. The degradation of the residual compressive strength of the structure after spectrum loading apparently has two primary causes. One cause is the degradation of the matrix, resulting from the moisture/temperature environment. This phenomenon has been extensively studied, and it has been found that, although no serious degradation occurs below the glass transition temperature T_g , temperature excursions above T_g cause irreversible matrix damage. This damage is characterized by crazing and the presence of "free" moisture which invalidates moisture content experiments based on "Fickian" diffusion. Another cause of strength degradation is the propagation of delamination-type flaws emanating from flaw nuclei generated during the manufacturing

Table I Advanced Composite Serviceability Program Tasks

Phase	Title	Task	Title	Subtasks	Reference
I	Defect/Damage Detection and Degradation Assessment	1	Flaw/NDE Assessment	Flaw Characterization	2
				Flaw Detectability	3
		2	Analytic Methods Development		5
		3	Experimental Data Base Development	Accelerated Test Techniques	4
				Tension Coupon Tests	6, 7
				Compression Coupon Tests	
				Bolted Joint Coupon Tests	
		4	Inspection/Acceptance Criteria Development		
II	Structural Element Manufacturing	1	Fabrication Plan Development	Manufacturing	
				NDE	
				Cost Tracking	
		2	Normal Element Production	Element (27) Production	
				Production Rate	
				Production Technique	
		3	Induced Flaw Element Production	Element (72) Production	
				Manufacturing Flaws	
				Service-Induced Flaws	
III	Element Serviceability Evaluation	1	Mechanical Testing	Baseline Property	
				Effect of Defects	
		2	Coupon Data Correlation		

NOTE: The work was part of the Advanced Composites Serviceability Program, contract F33615-76-C-5344, monitored by Mr. Robert Neff of the United States Air Force Materials Laboratory and jointly sponsored with the United States Air Force Flight Dynamics Laboratory. Rockwell International, North American Aircraft Division (NAAD), is the prime contractor, and the Science Center is a subcontractor engaged to study flaw detectability. ITT Research Institute is a subcontractor engaged to perform all the coupon testing, and Washington University, St. Louis, is a subcontractor engaged to develop analytic techniques.

process or in service. Since these flaws are random by nature, a strictly analytic treatment is impractical. An engineering approach relating initial flaw size, damage propagation rate, and spectrum loading to residual compressive strength must be used to provide insight to the phenomenon. This paper will focus on this study. Data are presented from tests run during the Air Force Advanced Composite Serviceability Program. Since the strength degradation is predominantly associated with unstable localized regions, the analytic treatment is limited to determination of stresses in the region of a flaw to predict flaw growth trajectory. An empirical approach to determine the growth rate is then used to obtain the final delamination extent from which residual strength can be obtained. The treatment is based on a simplified model [8], the physics of which is the "billowing" of a localized delaminated area caused by loading of an initially deformed plate. This produces moment resultants due to eccentric loading, which results in delamination-propagating stresses at the boundaries of the original delaminated region. Eventually, the delaminated region becomes unstable and thus cannot carry more loading. This causes residual strength degradation.

COMPRESSION COUPONS

This paper discusses the compression coupon test data within the framework of the determination of its durability under a service environment. The coupon geometries are shown in Figure 1. This figure also contains a description of the flaw types.

The selection criteria of the compression coupon stacking sequences was to enhance the probability of delamination-type flaw growth. By contrast, the earlier selection of tension coupon stacking sequences was guided by a need to represent realistic design stacking sequences. Since the likelihood of inducing delamination propagation is heightened as the elastic coefficient A_{11}^u increases while D_{11}^u decreases, the compression stacking sequences chosen were those in which the short transverse axial stresses σ_z are maximized. The selected stacking sequences (those most delamination prone) are:

<u>Stacking Sequence</u>	<u>Ply Orientation</u>
1	$[(90/0/\mp 45)_2]_s$
2	$[(0_2/\mp 45)_2]_s$

Flaw location, with respect to layer number, was determined using earlier studies of the effects of defects and anticipating the location of the highest likelihood of defect propagation. These studies incorporated a fatigue test program in which 12.7-millimeter-diameter delaminations were

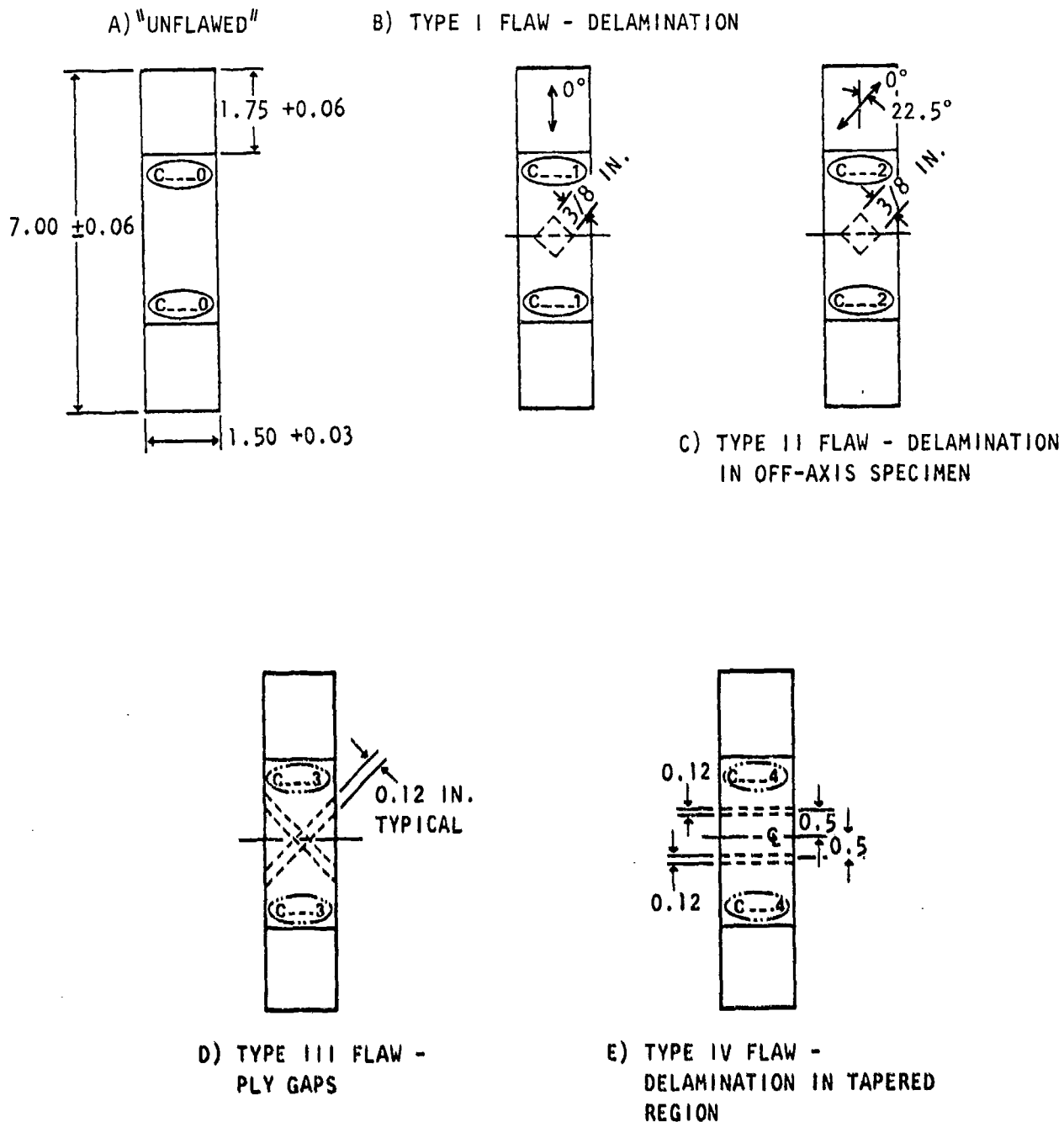


Figure 1 Compression Coupon Configuration - Flaw Size A

investigated. The analyses indicated that peeling moments at the edge of the delamination became largest when the flaw was between layers where sequence repetition (not symmetry) occurred, usually at the quarter-depth plane. Accordingly, the flaw in the compression coupons was between the fourth and fifth ply in flaw types I and II and as close to the fourth ply as possible in flaw types III and IV. The geometry of flaw types I and II was designed to represent the shape of the most common internal delaminations and the size anticipated for a critical borderline flaw. Type III flaw geometry resulted from extensive discussions with subcontractors, and type IV flaw geometry represents a purposeful ply interruption situation required in tapered sections.

The real-life environment for the 16-ply section would include not only the degrading effects of loading and temperature but the absorption and desorption of water. In order to simulate an environment for the Serviceability Coupon Test Program, loading and temperature histories were defined and applied to the coupons by initially moisturizing to a predetermined moisture content level. Although moisture content and distribution are random quantities, the procedure described in reference 4 was used to make testing feasible.

The objective of the flaw screening program was to determine the critical flaw for laminates undergoing an $R = -1$ loading/temperature/humidity spectrum. Two types of spectra were applied. The room temperature dry (RTD) spectrum considers only the effect of loading, while the real temperature/wet (ETW) spectrum considers the coupled effects of loading, temperatures, and moisture. In the former case, the residual strength was taken at room temperature; in the latter, it was taken at the expected failure temperature of 260° F.

The scatter of test data results was significant, but trends of damage propagation are based on these data. The two most critical flaw types were found to be types 1 and 4. The next estimate for the critical flaw, size B, are shown in the following:

<u>Flaw Orientation</u>	<u>Flaw Type</u>	<u>Size</u>
1, 2	1	5/16-inch delamination
1, 2	4	Drop -45-degree ply closest bag side, instead of second one down

Because the test program was not completed, a statistical analysis was not conducted. Instead, a presentation based on the mean of the test data is given. The presentation will, however, be related to the physics of failure. For an "unflawed" coupon in tension, the failure generally

initiates at a point of fiber breakage; thus, the presence of a small hole (radius equal to fiber spacing) does not degrade the strength. Two types of thermal residual stresses are formed in a laminate since it sets at around 260° F. The first is formed to maintain compatibility at the fiber/matrix interface in a lamina. This stress is accounted for in unidirectional laminate tests. The second is to maintain compatibility between laminae in forming a cross-plyed laminate. In both cases, the 0°-degree fiber tends to be in compression at room temperature. These thermal residual stresses are relieved by matrix crazing and moisture absorption. In the presence of a far-field tension loading, the 90-degree plies fail in matrix crazing, followed by the +45-degree plies. If unloading is not allowed to occur, local load concentrations remain and through-the-thickness stress redistribution occurs. If the coupon is allowed to unload, such as in a fatigue coupon, the reduced stiffness in the region of the flaw mollifies the load concentration, thus increasing the load capacity from that for a monotonically increasing load. The failure process for types I and II flaws is similar, except that delamination growth occurs during compression loading since the region above the delamination is not flat [8]. For the type III flaw, delaminations in the region of the gap occur due to unloading of the terminated ply. Otherwise, unless membrane/flexural coupling is significant, the primary strength reduction is due only to the ply loss. This effect is small for the geometry selected. For the type IV flaw, the process is identical to that for types I and II, flaws except that delamination growth is enhanced by changes in curvature resulting from the nonuniformity of the taper.

Table II shows the mean of the test data. The following contains a list of the nomenclature.

NOMENCLATURE

F_o^u = Unflawed coupon strength at RTD

F_f^u = Flawed coupon strength at RTD

$K_f = F_f^u / F_o^u$

F_T^u = Coupon strength at designated temperature dry

$K_T^f = F_T^u / F_f^u$

F_M^u = Coupon strength with designated moisture at room temperature

$K_M^f = F_M^u / F_f^u$

Table II Compression Coupon Test Results

Laminate	Flaw		Static Strength										Fatigue Strength				
	Type	Size (in.)	F_T^{cu} (ksi)	K_f	F_M^{cu} (ksi)	K_M^f	Temp ($^{\circ}$ F)	F_T^{cu} (ksi)	K_T^f	F_{TM}^{cu} (ksi)	K_{TM}^f	Environ-ment	No. Specs	Life-times	F_{TMF}^{cu} (ksi)	K_{TMF}^f	
¹ (90/0/-45) ₂ /S	0-.016" flaw		89.5	1	63.6	0.711	Room	56.4	0.630	54.3	0.607	Dry	3	2	76.2	0.851	
							260					Wet	3	2	53.7	.600	
	1-delamination	3/8	68.1	.761			Room			56.8	.834	Dry	3	2	63.6	.934	
							260					Wet	1	2	52.6	.691	
													1	1-1/2	a		
													1	1	a		
^{1 2} ([-67.5/-42.5/-67.5] ₂ /S	2-delamination	3/8	50.3	.562			Room			45.4	.903	Dry	3	2	53.7	1.068	
							260					Wet	3	2	36.9	.734	
			63.8	.713			Room			45.3	.710	Dry	3	2	59.8	.937	
							260					Wet	1	1-1/2	48.8	.765	
													2	2	49.3	.773	
¹	3-ply gap	1/8	70.2	.784			Room					Dry	3	2	68.7	.979	
							260			48.1	.685	Wet	1	1-1/2	48.0	.684	
												2	2	54.2	.772		
^{1 b} (90/0/-45) ₂ /S	4-ply drop	"A"	64.5	.721			Room					Dry	3	2	60.2	.933	
							260			47.5	.736	Wet	1	1/6	a		
												2	1/2	50.5	.783		
													3	2	74.3	.872	
			81.7	.946			Room			40.5	.478	Wet	3	2	33.3	.393	
							260										

Table II Compression Coupon Test Results (Concl)

Laminate	Flare		Static Strength										Fatigue Strength			
	Type	Slc (in.)	F_{cu}^w (ksi)	R_f	F_{cu} (ksi)	F_u	Temp (° F)	F_T (ksi)	K_T	F_{TM} (ksi)	K_{TM}	Environ- ment	No. Specs	Life- times	F_{TM}^{cu} (ksi)	K_{TM}^f
z^a [(0 ₂ /-45) ₂] _s	0		92.6	1			Room					Dry	3	3	78.7	0.950
							260			79.9	0.863	Wet	1	1/6	a	
	1-dominant						Room					Dry	2	2	57.7	.623
		3/8	79.1	.854			Room			64.5	.815	Wet	1	1	72.1	.912
z^a [(22.5/67.5) -22.5] _{2s}							Room					Dry	2	2	75.0	.948
		5/16	75.2	.812			Room			58.4	.777	Wet	3	2	62.2	.768
	2						Room					Dry	1	1	64.1	.934
		3/8	68.6	.741			Room			43.6	.636	Wet	2	2	72.8	1.061
2	3						Room					Dry	1	1/6	a	
		1/8	83.2	.499			Room			50.5	.607	Wet	1	1-1/2	81.8	.983
	4						Room					Dry	2	2	68.9	.828
		"A"	66.4	.717			Room					Wet	2	2	75.0	.901
z^b [(0 ₂ /-45) ₂] _s							Room					Dry	1	1	64.9	.977
		"B"					Room			52.5	.788	Wet	1	2	64.1	.965
	4						Room					Dry	3	1/2	49.4	.744
		"B"	74.6	.806			Room			45.6	.611	Wet	3	2	79.4	1.064
							Room					Wet	5	2	55.4	.475

^a Failed during fatigue spectrum loading

F_F^u = Coupon strength after designed lifetimes of a spectrum loading consistent with the strength temperature

$$K_F^f = F_F^u / F_f^u$$

NOTE: As subscripts are added, coupled effects must be considered.

F_{TM}^u = Coupon strength at designated temperature and moisture

F_{TMF}^u = Coupon strength after designated lifetimes of a quasi-real-time spectrum loading and at a designated temperature, etc

Figures 2 through 11 are plots of the test data. The same nomenclature is used.

BASELINE DATA - "NO-FLAW" COUPONS (FIGURES 2 AND 3)

For the type I [(90/0/+45)₂]_s laminate, the RTD static baseline strength was 89.5 ksi. This is 108 percent of the design strength and 86 percent of the expected strength. The 260° F dry value was 63 percent of this baseline. The room temperature and 260° F wet values were 71 and 61 percent, respectively. The residual strengths after two lifetimes of ambient environment and quasi-real-time loading spectra taken at room temperature and 260° F, respectively, were 85 and 60 percent of this value, respectively.

For the type II [(0₂/+45)₂]_s laminate, the RTD static 16-ply baseline strength was 92.6 ksi. This was low due to some bending in the coupons even though they were supported on all four edges. The 260° F wet static strength was 85 percent of this baseline value. The residual strengths after two lifetimes of ambient environment and quasi-real-time loading spectra taken at room temperature and 260° F, respectively, were 85 and 62 percent of this basepoint value, respectively.

TYPE I FLAW - DELAMINATION (FIGURES 4 AND 5)

The type I flaw is a delamination. This was a potential critical flaw. Two sizes were tested; namely, 3/8 and 5/16 inch. No critical flaw size was found because the 5/16-inch delamination data unexpectedly were smaller than the 3/8-inch data. The reason for this is probably material property variation, although there is the possibility that the increased curvatures resulting from the formation of the fabricated delaminations could have contributed.

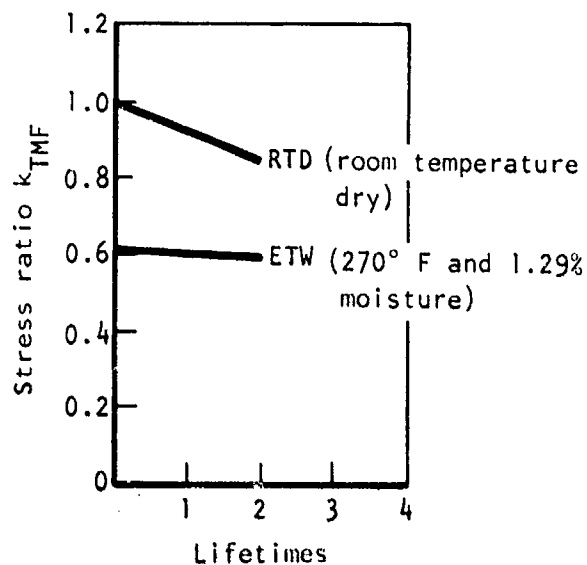
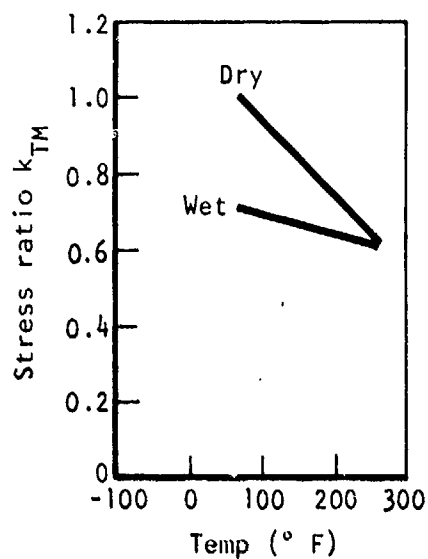


Figure 2 Compression Coupon Test Data: Stress Ratio Versus Temperature and Lifetimes: Laminate Type 1, Flaw Type 0

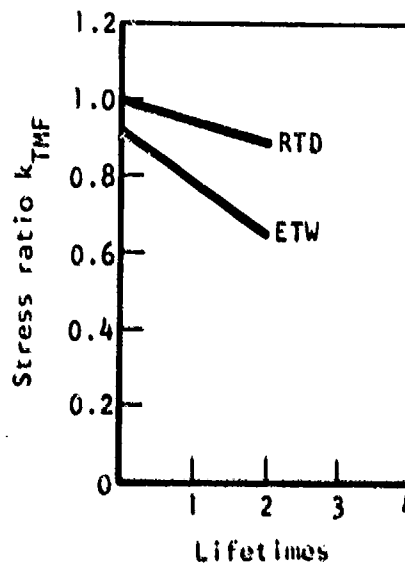
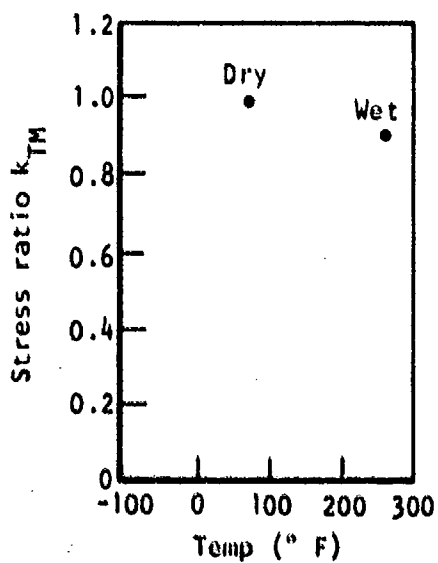


Figure 3 Compression Coupon Test Data: Stress Ratio Versus Temperature and Lifetime: Laminate Type 2, Flaw Type 0

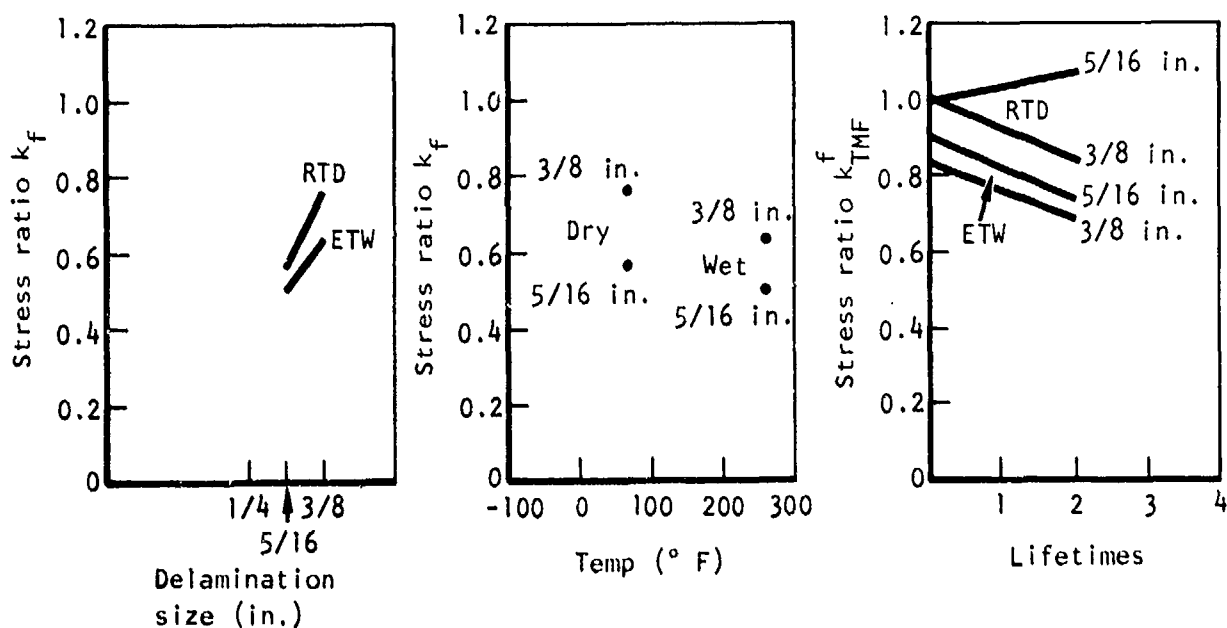


Figure 4 Compression Coupon Test Data - Stress Ratio Versus Delamination Size, Temperature, and Lifetimes (Laminate Type 1, Flaw Type 1)

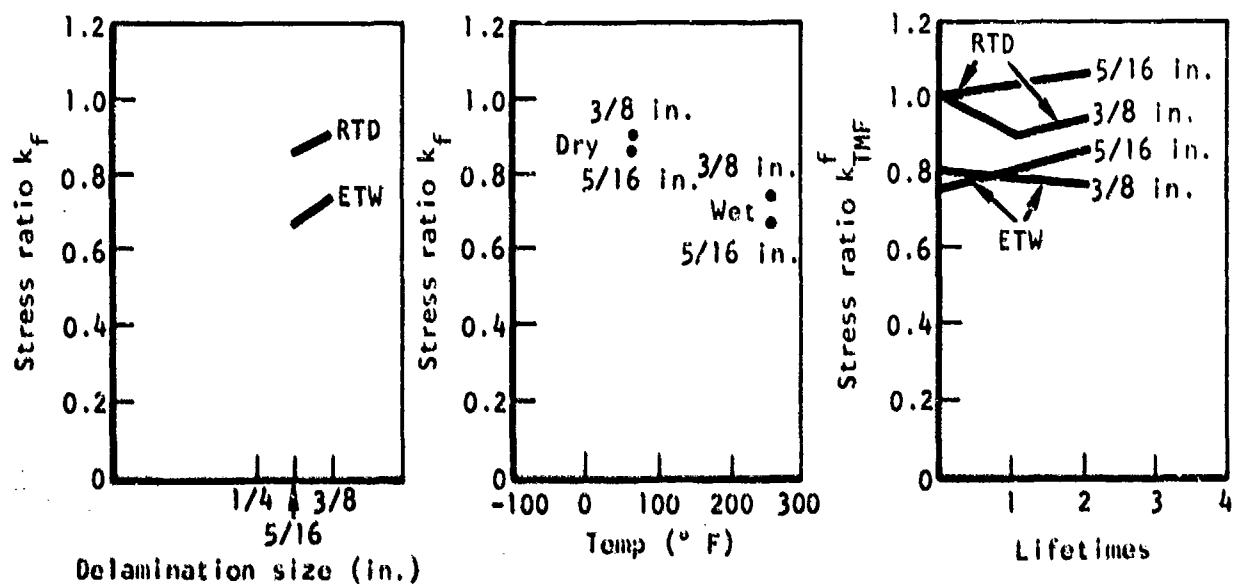


Figure 5 Compression Coupon Test Data - Stress Ratio Versus Delamination Size, Temperature, and Lifetimes (Laminate Type 2, Flaw Type 1)

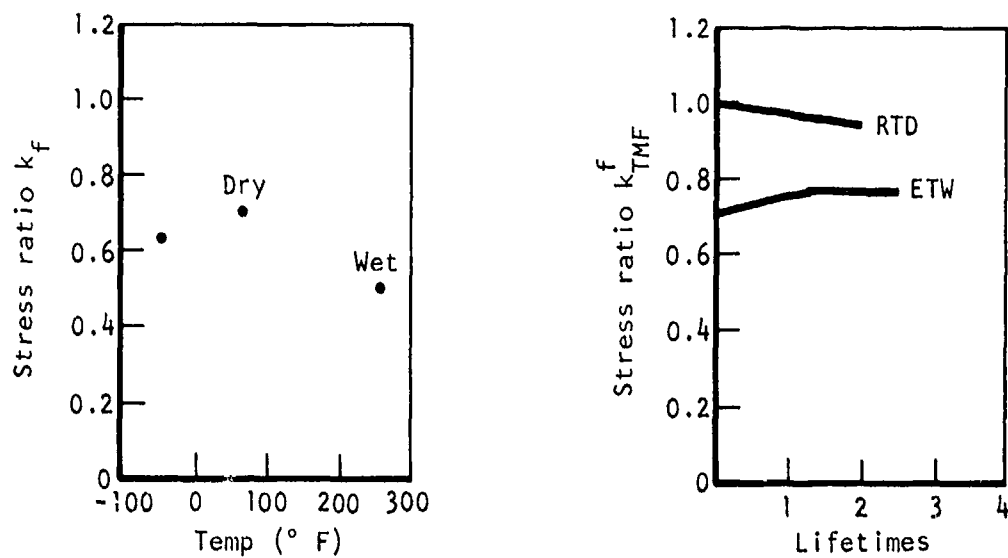


Figure 6 Compression Coupon Test Data - Stress Ratio Versus Temperature and Lifetime (Laminate Type 1, Flaw Type II)

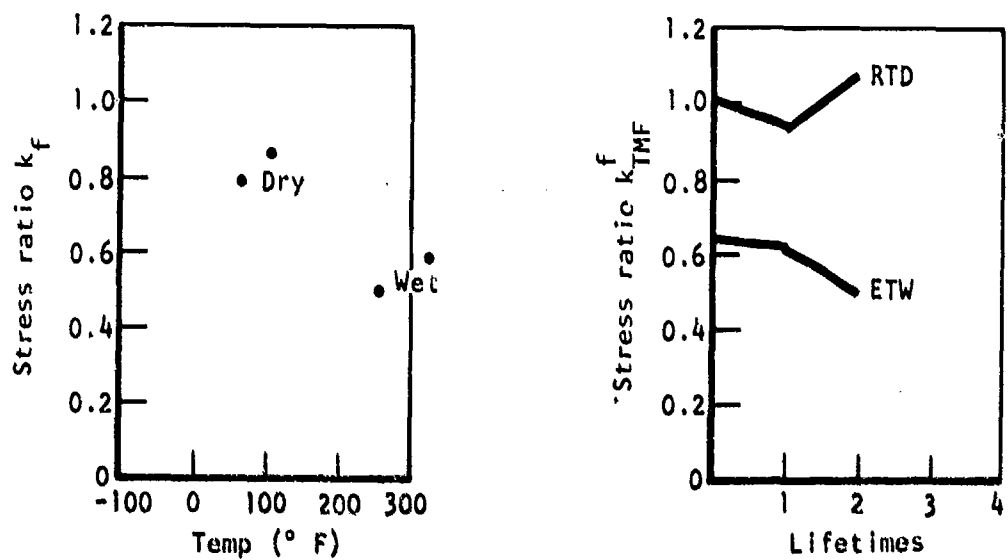


Figure 7 Compression Coupon Test Data - Stress Ratio Versus Temperature and Lifetimes (Laminate Type 2, Flaw Type II)

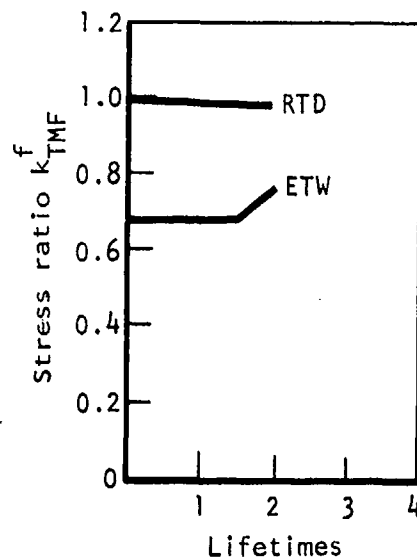
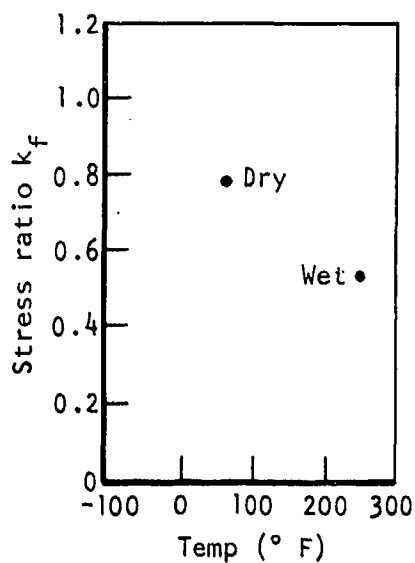


Figure 8 Compression Coupon Test Data - Stress Ratio Versus Temperature and Lifetimes (Laminate Type 1, Flaw Type III)

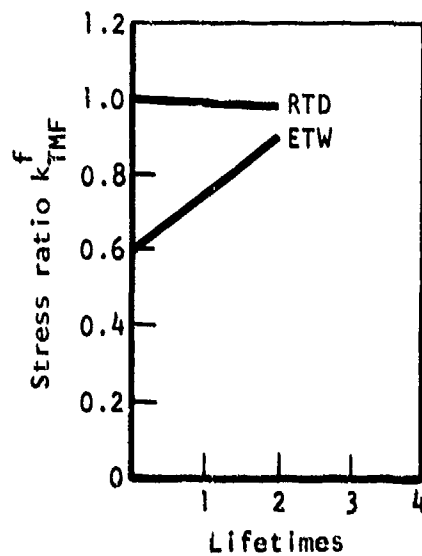
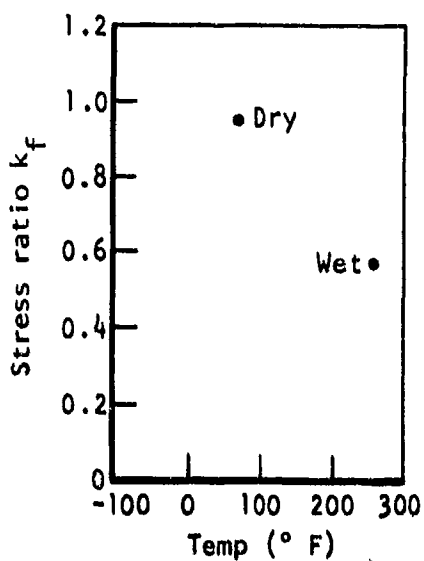


Figure 9 Compression Coupon Test Data - Stress Ratio Versus Temperature and Lifetimes (Laminate Type 2, Flaw Type III)

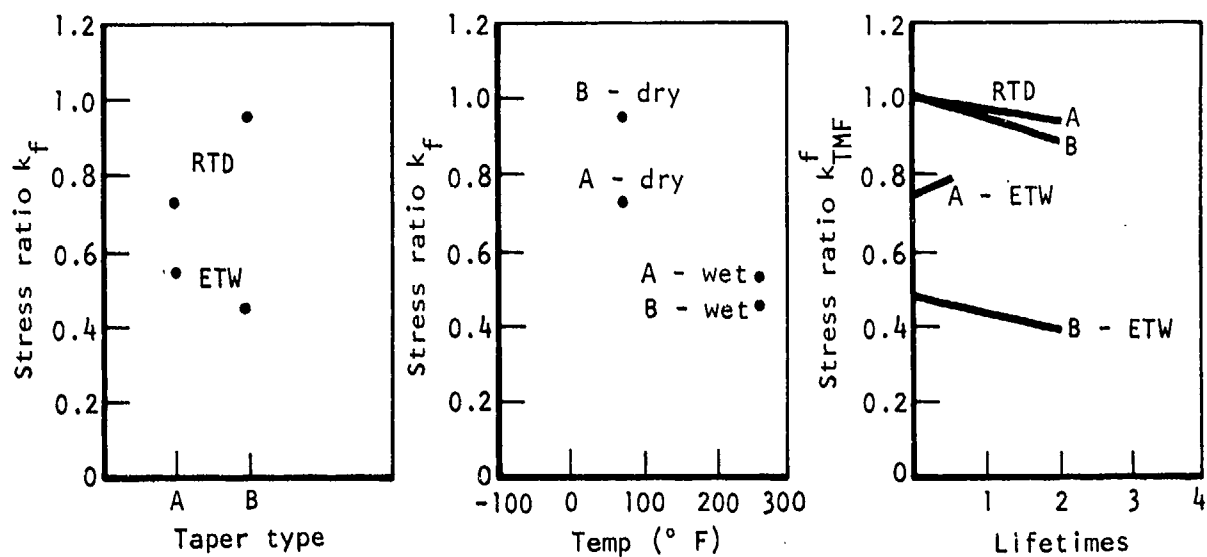


Figure 10 Compression Coupon Test Data - Stress Ratio Versus Taper Type, Temperature, and Lifetimes (Laminate Type 1, Flaw Type IV)

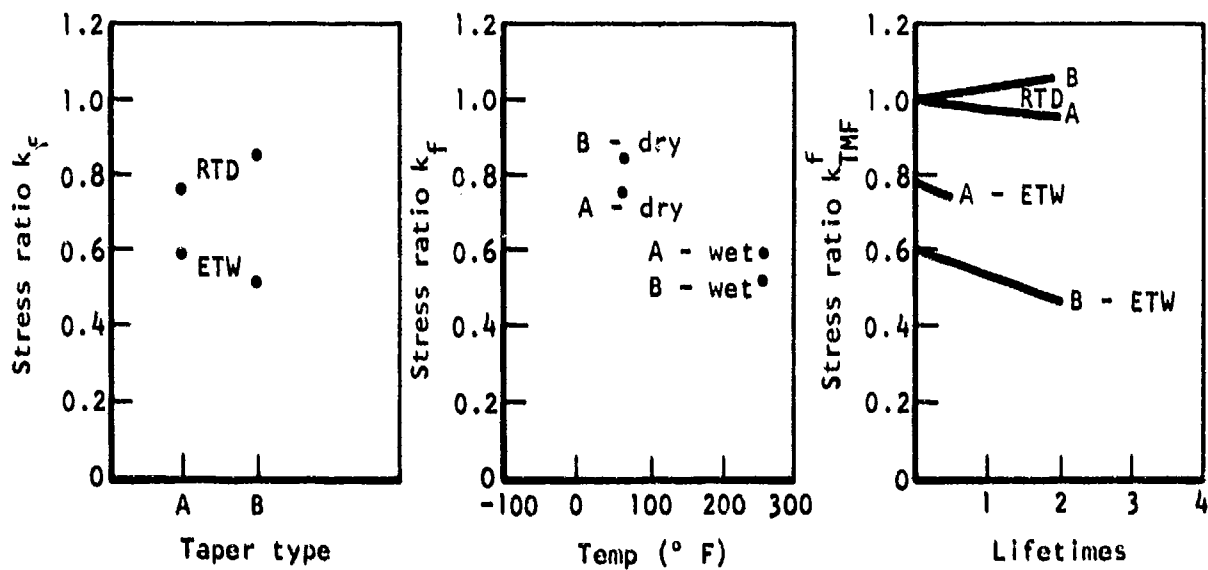


Figure 11 Compression Coupon Test Data - Stress Ratio Versus Taper Type, Temperature, and Lifetimes (Laminate Type 2, Flaw Type IV)

For the type I laminate, the RTD static strengths for the 3/8- and 5/16-inch delaminations were 68.1 and 50.3 ksi. These values are used as the basepoints for the fatigue tests and were 76 and 56 percent of the baseline values, respectively. The 260° F wet tests were 83 and 90 percent of the basepoint values, respectively.

The ambient environment residual strength tests after two lifetimes of an ambient environment spectrum loading were 93 and 107 percent of the basepoints, respectively. The 260° F residual strength tests after two lifetimes of a quasi-real-time spectrum loading were 69 and 73 percent of the basepoints, respectively.

For the type II laminate, the RTD basepoint static tests were 79.1 and 75.2 ksi, which are 85 and 81 percent of the respective baselines. The 260° F wet tests were 82 and 78 percent of the basepoints, respectively. The ambient environment residual strength tests for the 3/8-inch delamination after one and two lifetimes of an ambient environment spectrum loading were 91 and 95 percent of the basepoints, respectively. For the 5/16-inch delamination after two lifetimes, the tests were 106 percent of the basepoint value. The 260° F residual strength tests after two lifetimes of a quasi-real-time spectrum loading were 77 and 86 percent of the basepoints, respectively.

TYPE II FLAW - DELAMINATION UNDER COMBINED LOAD (FIGURES 6 AND 7)

The type II flaw is a 3/8-inch delamination in a coupon whose laminate reference axis is oriented 22.5 degrees to the coupon centerline. This was done to simulate a combined load condition. The ambient temperature dry static strength for types I and II laminates was 63.8 and 68.6 ksi, respectively. This was 71 and 74 percent of the unflawed specimen baseline values. The 260° F wet tests were 71 and 64 percent of the RTD basepoint values, respectively.

TYPE III FLAW - PLY GAP (FIGURES 8 AND 9)

The type III flaw, a set of 1/8-inch-ply gaps, had RTD static strengths of 70.2 and 83.2 ksi for types I and II laminates, respectively. They served as basepoint values for the fatigue tests and are 78 and 90 percent of the unflawed coupon baseline strengths, respectively. The 260° F wet tests were 69 and 61 percent of the basepoint values, respectively. The room temperature residual strength tests after two lifetimes of an ambient environment spectrum loading were both 98 percent of the basepoint values, respectively. The 260° F residual strength tests for the type I laminates after 1-1/2 and

two lifetimes of a quasi-real-time spectrum loading were 68 and 77 percent of the basepoint values, respectively; while for the type II laminates, the tests were 83 and 90 percent.

TYPE IV FLAW - DELAMINATION IN TAPERED REGION (FIGURE 10 AND 11)

The type IV flaw is a delamination in the tapered region of a tapered laminate coupon. This was the second potential critical flaw candidate. The two flaw sizes were actually not size differences but rather delamination/ply-drop location differences. The size B flaw comprises regions of 1/8-inch delaminations in regions of taper where the taper is formed by two dropped consecutive plies 1-inch apart. The size A flaw on the other hand dropped plies which were three layers apart. The size B flaw comes very close to satisfying the requirements for a critical flaw, as can be seen from the following analyses. One minor reservation for the test coupon configuration is that the delamination traverses the width of the coupon, thus the local instability failure mode is a column-type rather than a plate-type. However, because most of the peel stresses result from the curvature in the region above the delamination, the results should be representative.

The RTD static strengths for the type I laminate and sizes A and B flaws were 64.5 and 84.7 ksi, respectively. They are 72 and 95 percent of the baseline unflawed specimen RTD static strengths, respectively, and serve as basepoints for the remaining tests. The 260° F wet tests were 74 and 48 percent of the basepoint values, respectively. The room temperature residual strengths after two lifetimes of an ambient environment loading spectrum were 93 and 88 percent of the basepoint values, while the 260° F residual strength test results after one-half and two lifetimes of quasi-real-time spectrum loading were 78 and 39 percent of the basepoint values, respectively. An interesting point is that the 260° F residual strength test for the size B delamination was 33.3 ksi, which is 143 percent of the maximum spectrum load.

For the type II laminate, the RTD static strength for the size A and B flaws were 66.4 and 74.6 ksi, respectively. These are 72 and 81 percent of the baseline values, respectively. The 260° F wet tests were 79 and 61 percent of the basepoint values. The room temperature residual strength tests for the flaws after one and two lifetimes of an ambient environment loading spectrum were 98 and 97 percent of the basepoint values, respectively. For the size B flaw after two lifetimes, the tests were 106 percent of the basepoint value. The 260° F tests after one-half and two lifetimes of a quasi-real-time spectrum loading were 74 and 48 percent, respectively. For the size B flaw, this was 35.4 ksi or 109 percent of the maximum spectrum load. Of the three fatigue tests of this type, all survived, and the results

ranged from 99 to 115 percent of the maximum spectrum loadings. Were more specimens tested, these results would have substantiated a critical flaw size. Because an analytic stress distribution technique for this flaw type was not developed, however, extrapolation to other laminate configurations cannot be made yet.

CONCLUSIONS

The durability of advanced composite structures designed to encounter large compression loads must be considered. The results herein showed that one means of strength degradation is the loss of strength in portions of a laminate due to local instability failures such as occur in regions adjacent to a delamination. This can be minimized by proper design considerations pertaining to the selection of the stacking sequence. The occurrence of delaminations in tapered laminate regions appears to be one of the most critical flaws because the delamination growth mechanism is enhanced by the presence of changes of curvature.

The statistical aspects of the test program; i.e., relationship between duration of spectrum loading and flaw growth, were not carried out because these tests were not conducted. Future completion of this task would lend credence to a tractable failure model for durability of the advanced composite structures containing delaminations or matrix crazed under a service (moisture/temperature/loading) spectrum.

REFERENCES

1. Altman, J., et al, "Advanced Composite Serviceability Quarterly Progress Reports," Rockwell International Report NA-76-783-N, Air Force Material Laboratory contract F33615-76-C-5344.
2. Hoffman, G. A., and Konishi, D. Y., "Characterizations of Manufacturing Flaws in Graphite/Epoxy," Army Materials and Mechanics Research Center Report AMMRC MS 77-5, Watertown, Mass., June 1977.
3. Liber, T., et al, "Ultrasonic Techniques for Inspecting Flat and Cylindrical Composite Specimens, "ASTM STP 696, proceedings of the Symposium on Nondestructive Evaluation and Flaw Criticality for Composite Materials, Philadelphia, PA, October 1978.
4. Parmley, P.A., et al, "On the Accelerated Testing of Graphite/Epoxy Coupons," proceedings of the Second International Conference on Composite Materials, Toronto, Canada, April 1978.

5. Konishi, D.Y., and Lo, K. H., "Flaw Criticality of Graphite/Epoxy Structures," ASTM STP 696, proceedings of the Symposium on Nondestructive Evaluation and Flaw Criticality for Composite Materials, Philadelphia, PA, October 1978.
6. Hofer, K. E., and Waring, G., "Fatigue and Residual Strength and Flaw Growth of Graphite/Epoxy Composites under Simulated Aerospace Environment," proceedings of the Second International Conference on Composite Materials, Toronto, Canada, April 1978.
7. Konishi, D. Y., "Effects of Defects on Tension Coupons Undergoing an Accelerated Environmental Spectrum," to be published in the Proceedings of the Fourth Conference on Fibrous Composites in Structural Design, San Diego, CA, November 1978.
8. Konishi, D. Y., and Johnston, W.R., "Fatigue Effects on Delaminations and Strength Degradation in Graphite/Epoxy Laminates," ASTM STP 674, proceedings of the Conference on Composite Materials: Testing and Design, New Orleans, LA, March 1978.

SESSION IV: PROJECTILE PHENOMENA-1

Chairman: G. L. Filbey, Jr.
Research Physicist - Armor Team Leader
Ballistics Research Laboratory, ARRADCOM

MODELING OF THE SHAPED-CHARGE JET FORMATION. 239

W. P. Walters
J. T. Harrison
Army Armament R&D Command

EFFECT OF CASE MATERIAL PROPERTIES ON FRAGMENT VELOCITIES FROM BOMBS . . 255

O. E. R. Heimdahl
W. J. Stronge
Naval Weapons Center

IN-BORE MOTION ANALYSIS OF THE 155mm XM712 PROJECTILE WHEN FIRED IN
THE M198 HOWITZER. 270

S. H. Chu
Army Armament R&D Command

IMPACT OF ROCK PROJECTILES ON A SIMPLY SUPPORTED BEAM. 289

R. L. Mann
General Electric Company
R. W. Perkins
Syracuse University

MODELING OF THE SHAPED-CHARGE JET FORMATION

WILLIAM P. WALTERS
Mechanical Engineer

JOHN T. HARRISON
Mathematician
U.S. Army Armament Research and
Development Command
Ballistic Research Laboratory
Aberdeen Proving Ground, Maryland 21005

ABSTRACT

The USSR model for determining the shaped-charge jet velocity is discussed along with the USSR criterion for coherent jet formation. The USSR model for shaped-charge jet formation differs from the US models in that a visco-plastic behavior, i.e., a strain rate dependence, is postulated for the explosively driven shaped-charge liner. Thus, a viscous dissipation term is employed to retard the shaped-charge jet formation and to establish a critical liner flow velocity and Reynolds number for jet formation. Detailed comparisons are made between the US and USSR models for both steady state and transient collapse processes. Both models are compared with US experimental data. A survey of the USSR open literature on shaped-charge and wedge collapse and formation is presented.

INTRODUCTION

Numerous open literature publications have originated in the USSR related to the collapse and formation of high explosive charges containing cavities with metal liners, i.e., shaped charge devices. The USSR models [1-7] are analogous to those employed by the Ballistic Research Laboratory (BRL) [8-11], but the USSR has extended their models to include the impact of asymmetric plates [3] and visco-plastic material behavior [2,3]. The basic BRL models employ a one-dimensional, incompressible, inviscid flow model for the shaped-charge or wedge collapse process based on principles formulated by Birkhoff, et al. [8], Pugh, et al. [9] and Defourneaux [10]. These results [8-10] were incorporated into a computer code by Harrison, et al. [11] where transient effects, i.e., the collapse velocity variation for each liner element [9], and the acceleration of each liner element to the axis-of-symmetry, were included.

The USSR models are based on the formulation of Birkhoff, et al. [8] or Lavrent'ev [1] and extended to include visco-plastic effects by Godunov [2]. A detailed derivation and discussion of the USSR model is given by Walters [12]. This model does not include transient effects. Typically, in the axisymmetric hydrocode models used at the BRL, compressible flow is assumed and the material constitutive relationships are based on elastic-perfectly plastic or work hardening models. The USSR models typically assume an incompressible flow, but use a rate-dependent, visco-plastic material

constitutive equation [2,3,12].

Thus, the USSR visco-plastic models require a knowledge of the dynamic viscosity coefficient and many USSR investigators have deduced viscosity coefficients from experimental measurements under shock loading conditions. Walters [12] summarizes many of the USSR experimentally deduced viscosity values. Additional data related to viscosity measurements and the collapse of metallic bodies by high explosives are given by [13-36]. Material viscosity values have also been experimentally determined in the US [12,37] under shock loading conditions. The viscosity values deduced from various experimental measurements depend on many parameters, primarily strain rate, pressure, and temperature. However, the US measured viscosity values under shock loading conditions are typically two orders-of-magnitude lower than the viscosity values measured in the USSR [12-37].

The USSR shaped-charge liner collapse model, due to the incompressible but viscid flow assumption, establishes a critical Reynolds number, and analogously a critical flow velocity, to determine a jet-no jet criterion [2,3]. In the US models, the criterion used for predicting a jet-no jet or coherent jet condition is based on the analysis of Chou, et al. [40], where a subsonic flow condition is required for the formation of a coherent jet. Reliable models of the shaped-charge liner collapse and accurate criteria to predict the transition from the jet regime to a jetless regime would be a valuable aid to the shaped-charge designer. Thus, detailed comparisons between the BRL and USSR collapse models are warranted.

ANALYSIS

The USSR shaped-charge jet collapse model derived by Godunov [2] relaxes to the classical US model [8-10] when the dynamic viscosity is zero. Basically, the USSR model yields a lower jet velocity and a lower flow velocity than the US models. However, the USSR predicts a higher slug velocity than the US models.

The USSR criterion to form a coherent jet is that the Reynolds number,

$$Re = \frac{t u \sin^2 \beta}{\nu (1 - \sin \beta)} \quad (1)$$

be greater than two. The wall thickness is denoted by t , ν is the kinematic viscosity, 2β is the collision angle, and u is the inviscid flow velocity as given by Defourneaux [10], for example. The Reynolds number greater than two criterion is based on experimental observations [2,12]. Detailed USSR formulae for the jet strain rate, jet velocity, viscid flow velocity, and slug velocity, are given in [2,12]. Also, by setting $Re=2$ in Equation (1), an expression for the critical flow velocity as a function of β , t and ν can be obtained. If the critical flow velocity is greater than the flow velocity, a coherent jet will not form. Simonov [6] and others [14-17, 19, 21-23, 25, 26, 29, 30, 33, 34] define collapse angles for the transition from the jet regime to the jetless regime for explosive bonding applications.

These USSR investigators define collapse angles below which only incoherent jets will form and collapse angles below which no jet at all will form. Walsh, et al. [38] served as the basis for many of the USSR studies.

For both the BRL and USSR models, plane wave detonation was assumed although spherical detonation waves were studied to determine the influence of the wave shape on the shaped-charge jet collapse. Also, transient flow was assumed in both models based on the analyses of [10, 11] even though the basic USSR model assumes steady flow [2]. Transient calculations provide more realistic collision angle calculations. The overall validity of the model is not the issue of this report, only the relative comparison between the BRL model and the USSR model.

For the transient flow case, the stagnation point velocity (V_c) is given by

$$V_c = D_a \left[\frac{\sin(\beta-\alpha) - \sin(\beta-\alpha-\phi)}{\sin\beta} \right] \quad (2)$$

where D_a is the speed of the detonation wave, 2α is the conical liner apex angle and ϕ is the plate bending angle. Equation (2) is used in both the US and USSR models. Its derivation is given in [8-10]. The inviscid flow velocity is given by

$$U = D_a \left[\frac{\sin(\alpha+\phi) - \sin\alpha}{\sin\beta} \right] \quad (3)$$

in the US model [8-11]. The viscid flow velocity is

$$U_2 = U (1 - 2/Re)^{1/2} \quad (4)$$

in the USSR model [2] for $Re > 2$. Also, $U_2 = U$ when the dynamic viscosity is zero.

In the US model, the jet velocity and slug velocity are, respectively,

$$V_j = V_c + U, \quad (5)$$

and

$$V_s = V_c - U. \quad (6)$$

In the USSR model, the jet and slug velocities are

$$V_j = V_c + U_2, \quad (7)$$

and
$$V_s = V_c - U_2. \quad (8)$$

For a steady state collapse, analogous formulae are available [2, 8-10].

RESULTS

Steady state collapse models such as [1, 8-10] are conceptually simple, but typically overestimate the jet-tip velocity. For example, Figures 1 and 2 present the jet velocity distribution along the shaped charge liner axis-of-symmetry normalized by the liner altitude (Z/H), for steady state and transient flow, respectively. The resultant jet-tip velocities are recorded in Table I. This steady flow-transient flow comparison is given for the BRL 105mm charge which consists of a copper conical liner with a 42° apex angle, a 86.4mm cone diameter and a wall thickness of 2.69mm. In Figure 2, the experimental data obtained by Allison and Vitali [42] are also plotted. Both the US and USSR transient models exhibit the same amount of agreement with the experimental data. Note that the USSR steady state jet-tip velocity closely approximates the BRL transient jet-tip velocity and the BRL steady state model overestimates the experimental jet-tip velocity. The experimental jet-tip velocity is associated with the liner and not with a specific shape of the detonation wave.

The USSR model reduces to the BRL model for low values of the dynamic viscosity, i.e., when US measured values [37] of the dynamic viscosity are used in the USSR model, the two models are indistinguishable. Also, for wide angle conical liners, or when the collapse angle is large, the BRL and USSR models yield approximately the same results for either the USSR or US viscosity values. In order to amplify the difference between the BRL and USSR collapse models, the dynamic viscosity was taken to be $10^4 \text{ Pa}\cdot\text{s}$, which is somewhat higher than the quoted USSR values for copper [2, 12] and two orders-of-magnitude higher than the US measured values [37]. This value of the viscosity ($10^4 \text{ Pa}\cdot\text{s}$) was fixed in all test cases even though the viscosity is dependent upon the strain rate, detonation velocity, etc.

Figure 3 shows the jet velocity distribution for the BRL 81mm - liner diameter precision shaped charge. The liner was fabricated from copper, the high explosive was Composition B, the liner wall thickness was 1.9mm and the liner apex angle was 42° [43,47]. The jet-tip velocities are listed in Table I. The measured slug velocity was 0.61 km/s [47]. The BRL and USSR models predicted 0.53 and 0.93 km/s, respectively. The USSR model predicts a high slug velocity since the sum of equations (5) and (6) or (7) and (8) yield

$$V_j + V_s = 2V_c, \quad (9)$$

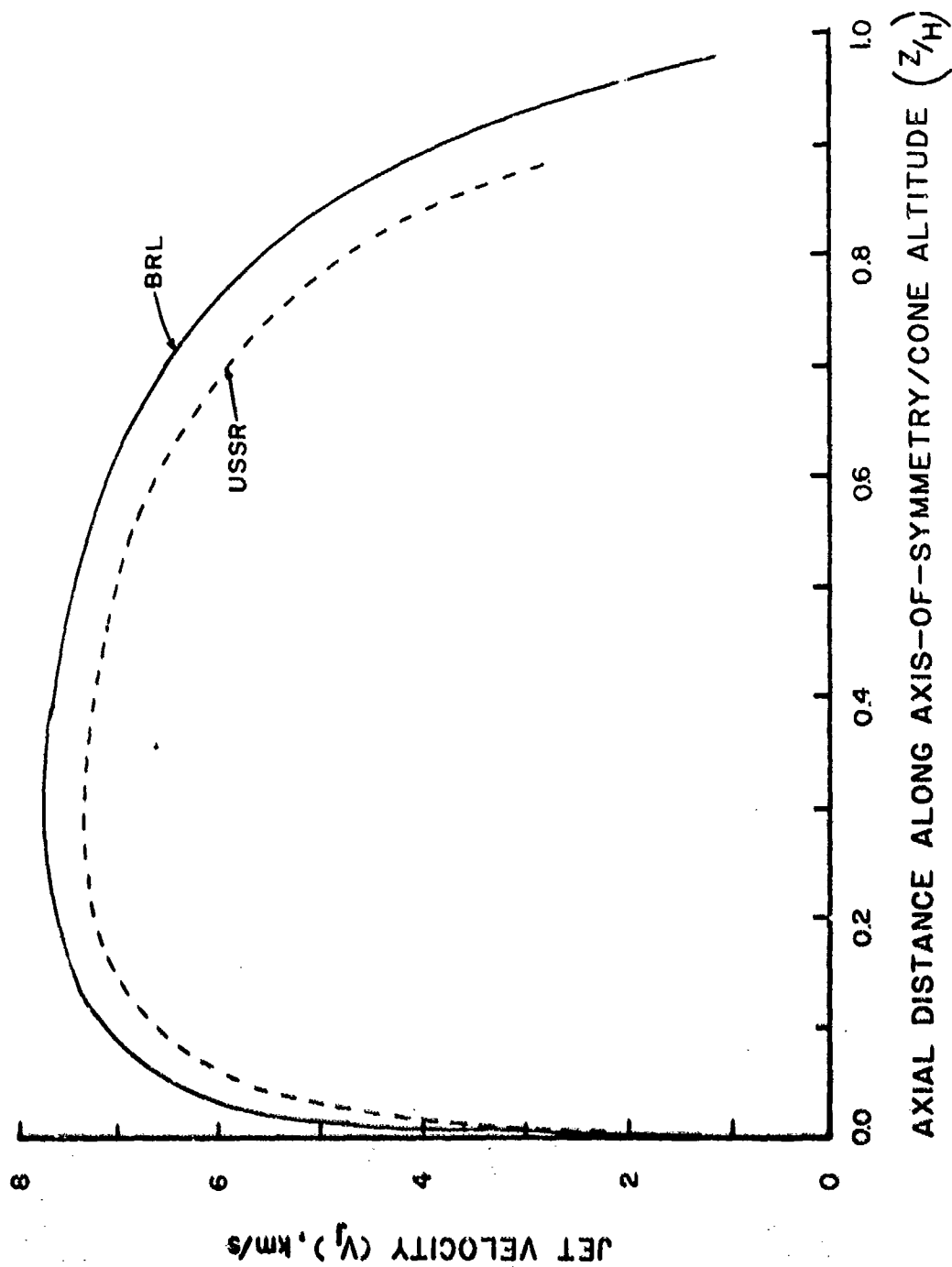


Figure 1 Jet Velocity Distribution for a Conical Copper Liner With a 42° Apex Angle, a Plane Wave Detonation Velocity of 8km/s, a Wall Thickness of 2.69mm, and Steady Flow.

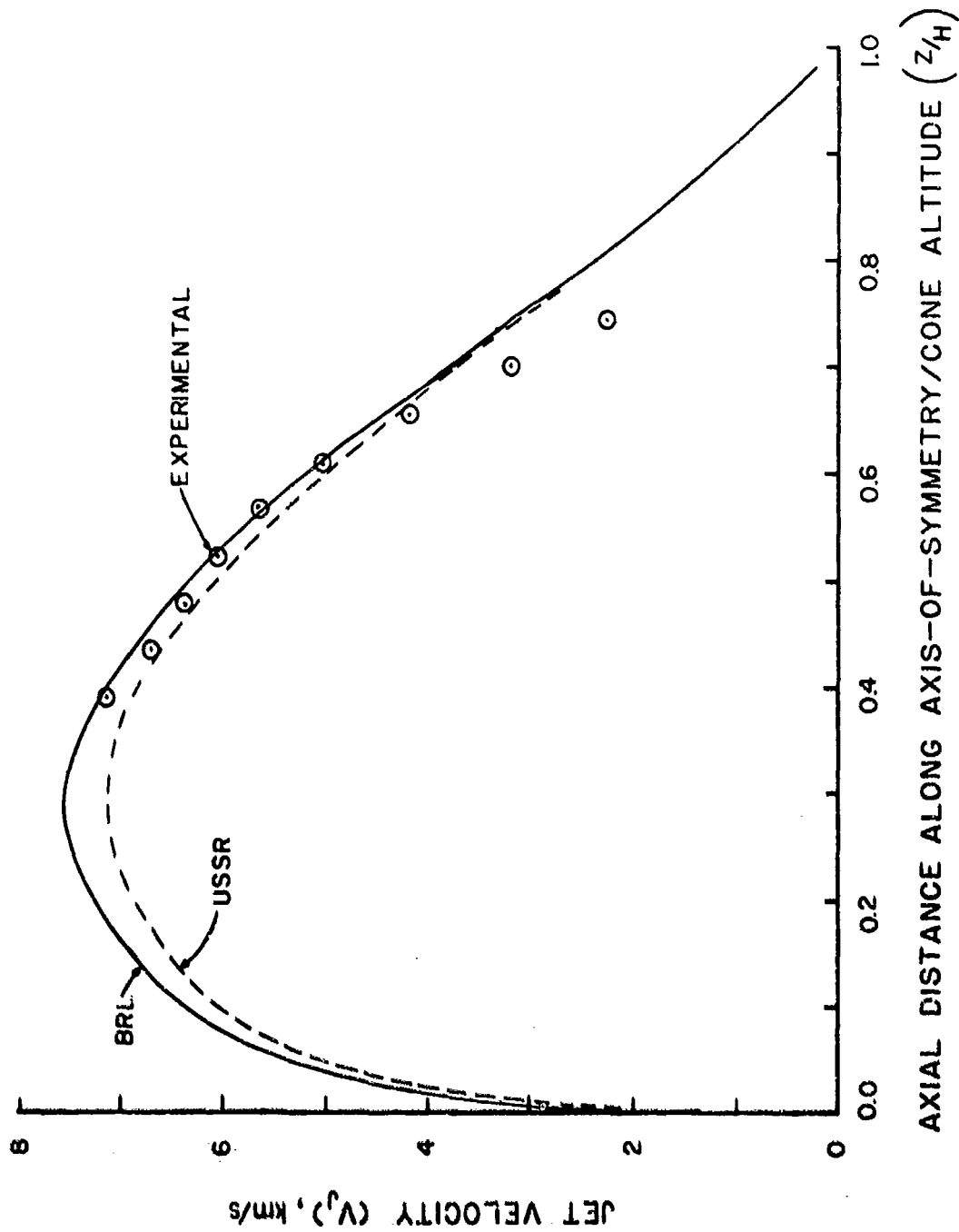


Figure 2 Jet Velocity Distribution for a Conical Copper Liner With a 42° Apex Angle, a Plane Wave Detonation Velocity of 8km/s, a Wall Thickness of 2.69mm, and Transient Flow.

Table I Jet-Tip Velocities for Several Shaped-Charge Liner Designs

<u>Liner Description</u>	<u>Cone Apex Angle (Degrees)</u>	<u>Wall Thickness (mm)</u>	<u>Detonation Velocity (km/s)</u>	<u>JET-TIP VELOCITIES (km/s) BRL/USSR/Experimental</u>
BRL-105mm Charge	42	2.69	0.8, plane wave, steady	7.605/7.18/7.01
BRL-105mm Charge	42	2.69	0.8, plane wave, transient	7.23/6.87/7.01
BRL-105mm Charge	42	2.69	0.8, spherical wave, transient	6.95/6.58/7.01
BRL-81mm Precision Charge	42	1.9	0.8, plane wave, transient	8.02/7.62/7.62 \pm .2
BRL-81mm Precision Charge	42	1.9	0.8, spherical wave, transient	7.8/7.39/7.62 \pm .2
Parametric Study	42	1.0	0.8, plane wave, transient	9.58/9.14/----
Parametric Study	42	4.0	0.8, plane wave, transient	5.95/5.62/----
Parametric Study	42	2.69	0.6, plane wave, transient	5.62/5.28/----
Parametric Study	42	2.69	0.4, plane wave, transient	3.92/3.60/----
Parametric Study	14	2.69	0.8, plane wave, transient	11.01/9.23/----
Parametric Study	120	2.69	0.8, plane wave, transient	3.985/3.891/----
BRL Small Caliber Charge [48]	20	1.17	0.8, plane wave, transient	10.43/8.03/9.9

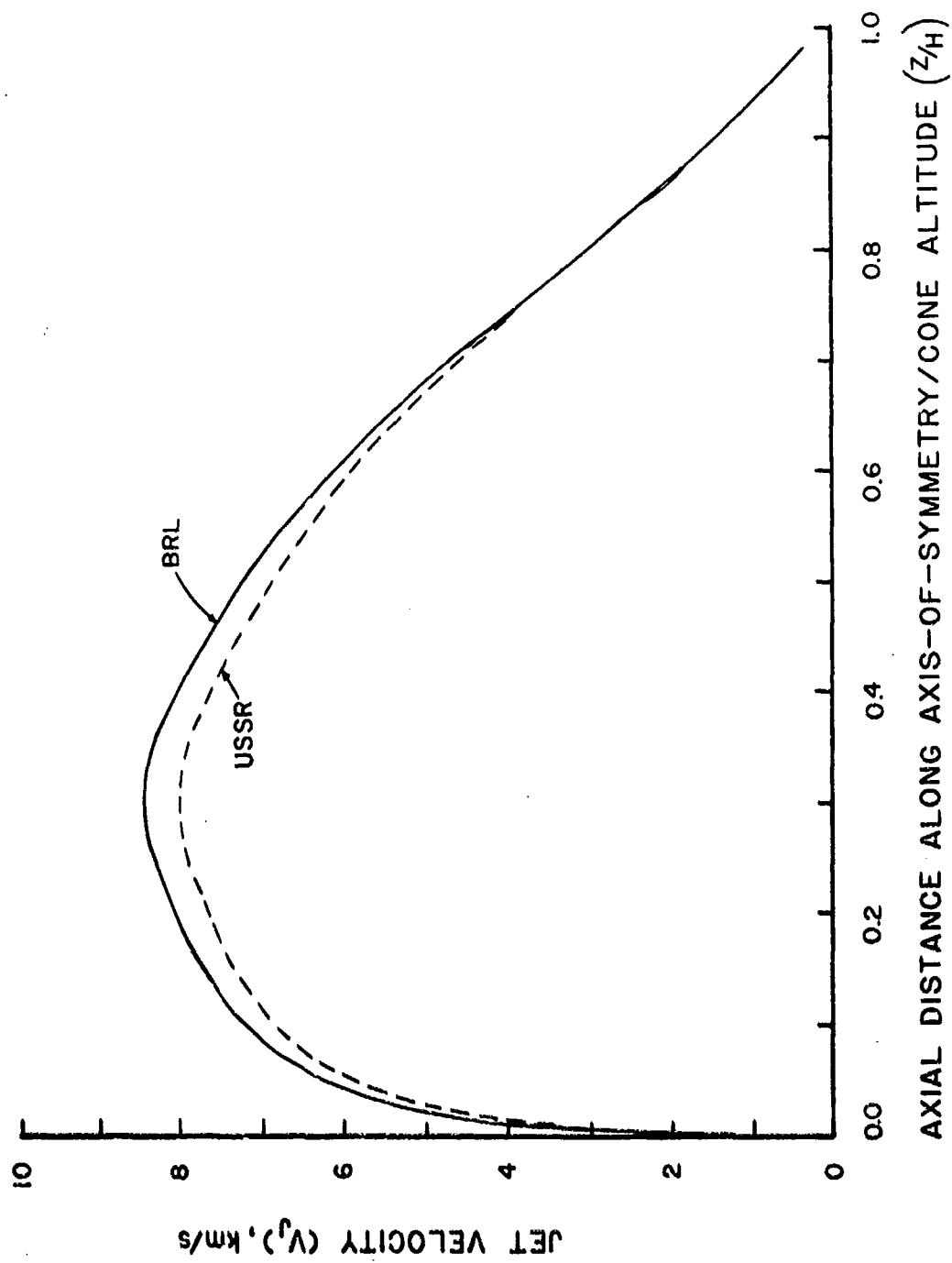


Figure 3 Jet Velocity Distribution for a Precision Conical Copper Liner With a 42° Apex Angle, a Plane Wave Detonation Velocity of 8km/s, a Wall Thickness of 1.9mm, and Transient Flow.

and V_c is the same for both the US and USSR models. Thus, since the USSR value of V_j is lower than the US value, the USSR value of V_s must be higher than the US value. In other words, the sum of the US jet and slug velocities are equal to the sum of the USSR jet and slug velocities.

Also, the strain rates calculated by the USSR models [2] are of the order of $10^6/s$ and show little variation with liner element position. Carleone, et al. [41, 44] calculated strain rates for the 81mm-diameter precision charge and found a larger variation of strain rate with liner element position including liner elements in both compression and tension. The peak strain rate was $10^5/s$. Experimental measurements of the strain rate of collapsing liners are not available, but Bauer and Bless [45] measured the strain rate of exploding copper tubes to be about $10^4/s$ and Walters [46] deduced the strain rates of stretching jets to be of the order of $10^4/s$.

Next, parametric studies were performed on the BRL 105mm-charge [42]. The liner apex angle, the liner wall thickness, and the high explosive detonation velocity were all varied independently. The jet-tip velocities are listed in Table I. Space limitations prohibit inclusion of the plots of the jet and flow velocities. However, the parametric studies indicated that some of the liner designs considered may fail to form coherent jets, i.e., in the BRL model by a supersonic flow velocity, or in the USSR model by a Reynolds number less than two (as indicated by the absence of plotted data). In order to investigate the validity of any semi-empirical coherent jet formation criterion, an actual jet which was shown experimentally to have an incoherent tip was analyzed. Figure 4 presents this analysis for a copper cone with a 20° apex angle, a 38.1mm liner diameter with a 1.17mm wall thickness and heavily confined in a steel body [48]. Both the USSR and the US models indicate a region of what could be incoherent jet formation. The USSR model predicts a Reynolds number less than two for the initial jet elements, Z/H from 0 to 0.07. The BRL flow velocity is supersonic over the central range of the liner, Z/H from 0.03 to 0.7. In the BRL model, the initial liner elements (near the apex) proceed along the axis with a subsonic flow velocity. Liner elements formed later have a higher velocity (supersonic) and compress the slower, preceding elements forming a bifurcated, or nearly incoherent, jet tip. The USSR model indicates that the initial liner elements will not produce a coherent jet and the inverse velocity gradient is smaller, and always subsonic. The BRL model is in closer agreement with the experimental jet-tip velocity than the USSR model and for this reason, is deemed to be more accurate. Note that a firm criterion to predict the transition from a jet to jetless regime does not exist. Hence, both the simple US and USSR models use semi-empirical criteria to predict this transition.

For all the liner designs considered in this study, neither the BRL nor the USSR model appears to yield a consistently accurate criterion for the transition from a jet regime to a jetless regime. However, a critical

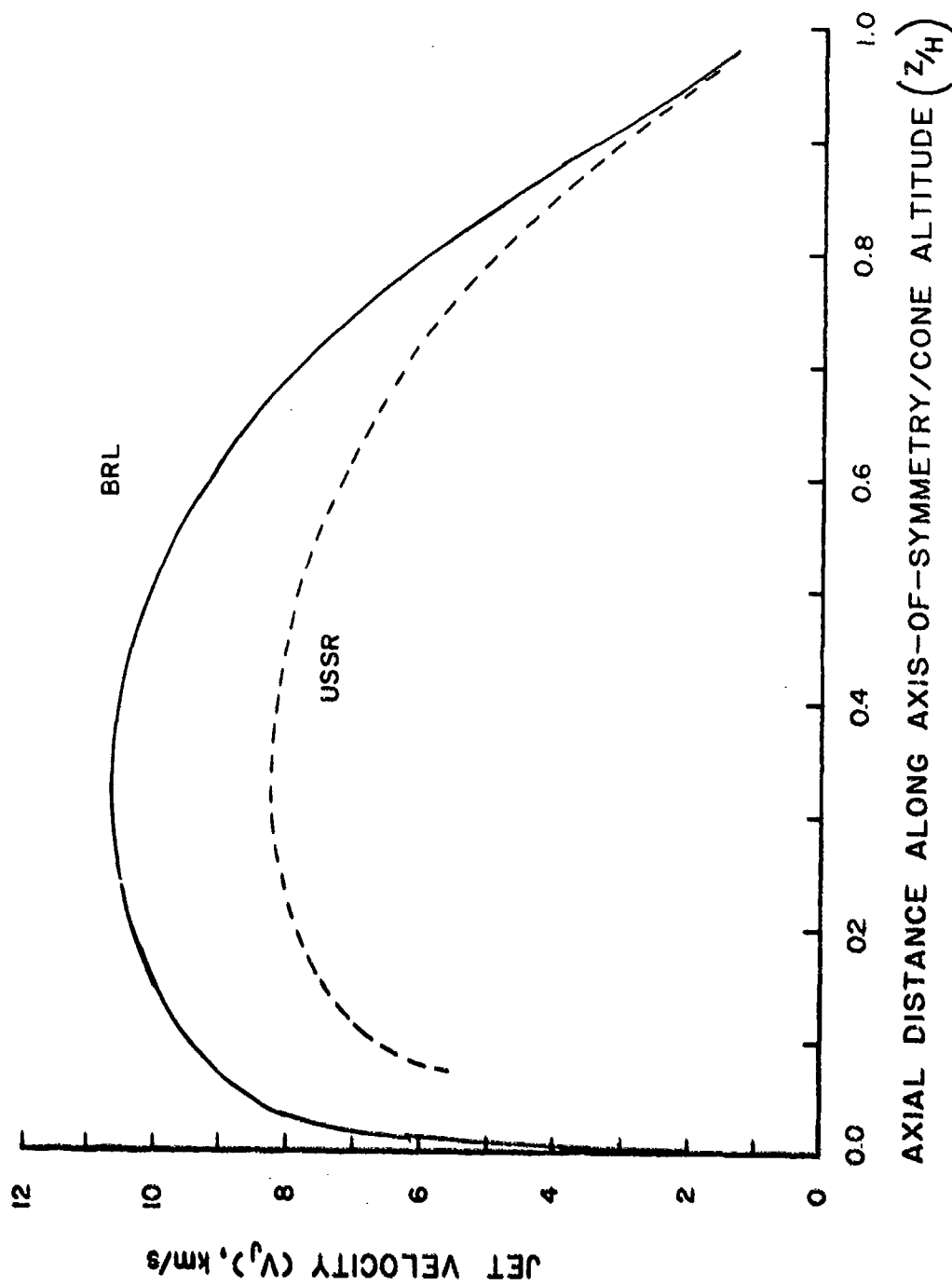


Figure 4 Jet Velocity Distribution for a Conical Copper Liner With a 20° Apex Angle, a Plane Wave Detonation Velocity of 8km/s, a Wall Thickness of 1.17mm, and Transient Flow.

collision angle (β) may be calculated from Equation (1) by setting the Reynolds number equal to two and calculating the critical β . Any β greater than this critical β will imply a jet regime. To investigate any coincidence between a Reynolds number equal to two and a sonic flow velocity, Equation (1) can be solved for a Reynolds number of two and u equal to the liner material bulk speed of sound (c). The collision angles calculated as outlined above are given in Table II along with the code calculated collision angles corresponding to flow velocities near 3.9km/s (the speed of sound of copper), 4.8km/s (1.23 times the speed of sound of copper), and a Reynolds number of two. A flow velocity of 4.8km/sec is the calculated flow velocity above which 20° copper liners have been observed to have incoherent jet tips [11]. The criteria for coherent jet formation based on a Reynolds number of two, or a flow velocity of 1.23 times the speed of sound of the liner material are both based on experimental observations.

Table II Comparison of Critical Collision Angles for Transition Into a Jetless Regime With Calculated Collision Angles Based on a Flow Velocity of 3.9km/s, 4.8km/s, and a Reynolds Number of 2

Shaped-Charge Liner	β Critical For Re=2*	β Critical For Re=2 and $u=3.9$ km/s	Computer Results		
			Reynolds Number	Flow Veloc- ity (km/s)	β (degrees)
14° apex angle, 2.69mm wall	22.1	21.6	1.55	3.8	19.6
			2.0	4.42	21.2
			2.75	4.8	22.5
42° apex angle, 1mm wall	37.7	31.6	9	3.9	49.5
20° apex angle, 1.17mm wall	35.5	29.8	1.47	3.86	26.5
			2.09	4.48	28.6
			2.54	4.83	29.9

*Assume the plate bending angle [10] to be 10°.

From Table II, the 14° apex angle liner would probably not jet completely since the calculated β values are less than, or nearly equal to, the critical β values. The 42° apex angle liner should jet coherently since the calculated β is well above the critical β value. The 20° apex angle liner should not jet completely. It is noteworthy that the β value occurring at a Reynolds number of two is always within a few degrees of the

β value at a flow velocity of 4.8km/s. The calculated flow velocity depends on the plate being angle (ϕ) which was assumed to be 10° . Of course, this angle is not constant, and increasing ϕ will decrease β . Also, a critical Reynolds number of two is not a firm criterion and may in fact be higher, as discussed by Mali, et al. [39].

Thus, the critical collision angles for $Re=2$ and $u=c$ appear to represent approximate values of the collision angle which must be exceeded to remain in the jet regime. Within the limited amount of experimental data available, this value would appear to be accurate to within a few degrees. However, since the β versus Z/H curve can exhibit a plateau for liner elements associated with the central region of the liner, a error in β of over a few degrees could be critical in determining the correct transition from a jet regime to a jetless regime.

CONCLUSIONS

The BRL and USSR models both provide a satisfactory prediction of the shaped-charge jet velocity distributions. Agreement between the USSR steady state visco-plastic model and the BRL transient flow model is good. The USSR visco-plastic model, modified to include transient effects, predicts lower jet and flow velocities than the BRL model. For large values of the collision angle, such as experienced with wide angle cones, the USSR models (transient or steady) agree closely with the BRL model. Also, US determined viscosity values (up to two orders-of-magnitude lower than the USSR measured values) when used with the USSR shaped-charge jet collapse model cause the USSR models to agree closely with the BRL model. In fact, the models coincide for a zero value of the viscosity coefficient. The trends exhibited by the USSR and BRL models coincide. The jet-tip velocity increases as the high explosive detonation velocity increases, or as the conical apex angle decreases, or as the wall thickness decreases.

Both the BRL and the USSR models appear to have the same capability and suffer the same limitations. Neither model is capable of providing a universal criterion regarding the transition between the jet regime and the jetless (i.e., incoherent jet) regime.

However, the BRL has observed that the maximum obtainable jet velocity for a copper conical liner corresponds to a calculated flow velocity of about 4.8km/sec, where the maximum jet velocity is defined as the velocity just before a bifurcation or incoherency of the jet tip occurs [11]. The β corresponding to a flow velocity of 4.8km/s is nearly the same as the β for $Re=2$ in the USSR model. Only further experimental studies involving incoherent (or bifurcated) shaped-charge jets will clarify this point.

REFERENCES

1. Lavrent'ev, M.A., "A Cumulative Charge and the Principle of its Work," Usp. Mat. Nauk., v. 12, no. 4, 1957.
2. Godunov, S. K. Deribas, A. A. and Mali, V. I., "Influence of Material Viscosity on the Jet Formation Process During Collisions of Metal Plates," Fizika Goreniya i Vzryva, v. 11, no. 1, Jan-Feb 1975.
3. Godunov, S. K. and Deribas, A. A., "Jet Formation Upon Collision of Metals," Doklady Akademii Nauk. SSSR, v. 202, no. 5, Feb 1972.
4. Deribas, A. A., Kudinov, V. M., Matveenkov, F. I., and Simonov, V. A., "Determination of the Impact Parameters of Flat Plates in Explosive Welding," Fizika Goreniya i Vzryva, v. 3, no. 2, 1967.
5. Novikov, N. P., "Certain Properties of High-Speed Cumulative Jets," Zh. Prikladnoy Mekhaniki i Tekhnicheskvy Fiziki, no. 1, 1963.
6. Simonov, V. A., "Flows Due to an Incident Impact Wave on a Wedge-Shaped Cavity," Fizika Goreniya i Vzryva, v. 7, no. 2, April-June 1971.
7. Godunov, S. K., Deribas, A. A., Zabrodin, A. V. and Kozin, N. S., "Hydrodynamic Effects in Colliding Solids," J. of Comp. Phys., v. 5, 1970.
8. Birkhoff, G., MacDougall, D. P., Pugh, E. M. and Taylor, G., "Explosives with Lined Cavities," J. Appl. Phys., v. 19, no. 6, June 1948.
9. Pugh, E. M., Eichelberger, R. J. and Rostoker, N., "Theory of Jet Formation by Charges with Lined Conical Cavities," J. Appl. Phys., v. 23, no. 5, May 1952.
10. Defourneaux, M., "Hydrodynamic Theory of Shaped Charges and of Jet Penetration," Memorial De L'art Ille'rie Francasise-T, 44, 1970.
11. Harrison, J., DiPersio, R., Karpp, R. and Jameson, R., "A Simplified Shaped Charge Computer Code: BASC," DEA-AF-F/G-7304 Technical Meeting: Physics of Explosives, Vol. II, April-May 1974, Paper 13 presented at the Naval Ordnance Laboratory, Silver Spring, MD.

12. Walters, W. P., "Influence of Material Viscosity on the Theory of Shaped-Charge Jet Formation," Memorandum Report ARBRL-MR-02941, August 1979.
13. Al'tshuler, L. V., Kanel', G. I. and Chekin, B. S., "New Measurements of the Viscosity of Water Behind a Shock Wave Front," Sov. Phys. JETP, 45(2), Feb. 1977.
14. Deribas, A. A. and Zakharenko, I. D., "Surface Effects With Oblique Collisions Between Metallic Plates," Fizika Goreniya i Vzryva, v. 10, no. 3, May-June 1974.
15. Gordopolov, Yu. A., Dremine, A. N. and Mikhailov, A. N., "Theory of Waves on the Interface of Metals Welded by Explosion," Fizika Goreniya i Vzryva, v. 14, no. 4, July-August 1978.
16. Gordopolov, Yu. A., Dremine, A. N. and Mikhailov, A. N., "Experimental Determination of the Dependence of the Wavelength on the Angle of Collision in the Process of the Explosive Welding of Metals," Fizika Goreniya i Vzryva, v. 12, no. 4, July-August 1976.
17. Shushko, L. A., Shekhter, B. I. and Krys'kov, S. L., "Bending of a Metal Strip by a Sliding Detonation Wave," Fizika Goreniya i Vzryva, v. 11, no. 2, March-April 1975.
18. Lobanov, V. F., "Numerical Simulation of Flow During Compression of Cylindrical Samples By a Glancing Detonation Wave," Zh. Prikladnoi Mekhaniki i Tekhnicheskoi Fiziki, no. 5, Sept.-Oct. 1975.
19. Efromov, V. V., "Oblique Impacts of Metallic Plates In an Elastic Formulation," Zh. Prikladnoi Mekhaniki i Tekhnicheskoi Fiziki, no. 5, Sept.-Oct. 1975.
20. Bezhanov, K. A., "Irregular Interaction of a Moving Shock Wave With a Tangential Discontinuity," PMM, v. 41, no. 6, 1977.
21. Pogorelov, A. P., Glushok, B. L., Novikov, S. A., Sinitsyn, V. A., and Chernov, A. V., "Dependence of Recoil Impulse From A Rigid Barrier Under Sliding Conditions of Detonation of an Explosive Layer," Fizika Goreniya i Vzryva, v. 13, no. 5, September-October 1977.
22. Gordopolov, Yu. A., Dremine, A. N. and Mikhailov, A. N., "Wave Formation With the High-Speed Collision of Metallic Bodies," Fizika Goreniya i Vzryva, v. 13, no. 2, March-April 1977.

23. Efremov, V. V., "Investigation of Oblique Collisions of Metal Plates in an Elastic Formulation," Zh. Prikladnoi Mekhaniki i Tekhnicheskoi Fiziki, no. 1, January-February 1975.
24. Sanasaryan, N. S., "Explosive Viscoplastic Deformation of a Tube and its Relationship With the Properties of the Surrounding Medium," Fizika Goreniya i Vzryva, no. 4, October-December 1971.
25. Titov, V. M., "Possible Regimes for Hydrodynamic Cumulation During the Collapse of a Casing," Doklady Akademii Nauk. SSSR, v. 247, no. 5, 1979.
26. Kozin, N. A., Mali, V. I. and Rubtsov, M. V., "Tangential Explosion with Collapse of a Bimetallic Casing," Combustion, Explosion and Shock Waves, v. 13, no. 4, July-August 1977.
27. Shurshalov, L. V., "Calculation of Cumulative Jets," Izvestiya Akademii Nauk. SSSR, Mekhanika Zhidkosti i Gaza, no. 4, July-August 1975.
28. Rubtsov, M. V., "Deformation of Liquid Line With the Collision of Jets," Zh. Prikladnoi Mekhaniki i Tekhnicheskoi Fiziki, no. 6, November-December 1977.
29. Mikhailov, A. N. and Dremin, A. N., "Flight Speed of a Plate Propelled by Products From a Sliding Detonation," Fizika Goreniya i Vzryva, v. 10, no. 6, November-December 1974.
30. Godunov, S. K., Kazhdan, Ya. M. and Simonov, V. A., "Shock Wave Incidence on a V-Shaped Cavity," Zh. Prikladnoi Mekhaniki i Tekhnicheskoi Fiziki, v. 10, no. 6, November-December 1969.
31. Ivanov, V. A., "Disintegration of a Liquid Jet," Zh. Prikladnoi Mekhaniki i Tekhnicheskoi Fiziki, v. 7, no. 4, 1966.
32. Ivanov, A. G., Novikov, S. A. and Kochkin, L. I., "Detonation Wave Collision on Surface of an Inert Material," Fizika Goreniya i Vzryva, v. 13, no. 4, July-August 1977.
33. Rubtsov, M. V., "Measurement of Velocity of a Cumulative Jet," Fizika Goreniya i Vzryva, v. 13, no. 6, November-December 1977.
34. Bichenkov, E. I. and Lobanov, V. A., "Acceleration of Metallic Plates by Explosion," Fizika Goreniya i Vzryva, v. 10, no. 2, March-April 1974.

35. Shekhter, B. I., Shushko, L. A. and Krys'kov, S. L., "Investigation of the Squeezing Process of the Lining of an Elongated Hollow-Charge Pedicle," Fizika Goreniya i Vzryva, v. 13, no. 2, March-April 1977.
36. Laptev, V. I. and Trishin, Yu. A., "Increase of Initial Velocity and Pressure Upon Impact on an Inhomogenous Target," Zh. Prikladnoi Mekhaniki i Tekhnicheskoi Fiziki, no. 6, November-December 1974.
37. Chhabildas, L. C. and Asay, J. R., "Rise-Time Measurements of Shock Transitions in Aluminum, Copper, and Steel," J. Appl. Phys. 50(4), April 1979.
38. Walsh, J. M., Shreffler, R. G. and Willig, F. J., "Limiting Conditions for Jet Formation in High Velocity Collisions," J. of Appl. Phys., v. 24, no. 1, March 1953.
39. Mali, V. I., Pai, V. V. and Skovpin, A. I., "Investigation of the Breakdown of Flat Jets," Fizika Goreniya i Vzryva, v. 10, no. 5, September-October 1974.
40. Chou, P. C., Carleone, J. and Karpp, R. R., "Criteria for Jet Formation From Impinging Shells and Plates," J. Appl. Phys., v. 47, no. 7, July 1976.
41. Chou, P. C. and Carleone, J., "Calculation of Shaped-Charge Jet Strain, Radius and Breakup Time," BRL CR 246, July 1975.
42. Allison, F. E. and Vitali, R., "An Application of the Jet-Formation Theory to a 105-mm Shaped Charge," BRL Report No. 1165, March 1962.
43. Majerus, J. N., "A Model for Studying the Influence of Guidance Packages Upon Shaped Charge Warhead Performance," BRL Report No. 1942, November 1976.
44. Carleone, J., Chou, P. C. and Tanzio, C. A., "DESC, A One-Dimensional Computer Code to Model Shaped Charge Liner Collapse, Jet Formation and Jet Properties," Dyna East Corporation Technical Report Number DE-TR-75-4, December 1975.
45. Bauer, D. P. and Bless, S. J., "Strain Rate Effects on Ultimate Strain of Copper," AFML-TR-79-4021, May 1979.
46. Walters, W. P., BRL Unpublished Data, 1979.
47. Majerus, J. N., BRL Private Communication, 1980.
48. DiPersio, R., Jones, W., Merendino, A. and Simon, J., "Characteristics of Jets From Small Caliber Shaped Charges With Copper and Aluminum Liners," BRL MR 1866, September 1967.

EFFECT OF CASE MATERIAL PROPERTIES ON FRAGMENT VELOCITIES FROM BOMBS

O. E. R. HEIMDAHL
Mathematician

W. J. STRONGE
Mechanical Engineer
Naval Weapons Center
China Lake, California 93555

ABSTRACT

This paper presents a numerical investigation of the effect of case material on fragment velocity from explosively filled bombs. Fragment velocities are found to be sensitive to the properties of the explosive, the case density, and the thickness of the case. The fragment velocities are shown to be insensitive to the elastic modulus, Poisson's ratio, strength coefficient, and work hardening index of the case, and are also only weakly related to fracture radius. The four theories studied predict about the same fragment velocities.

NOMENCLATURE

C	Explosive mass
d_0	Initial wall thickness
E_1	Elastic modulus
E_2	Plastic modulus
G	Gurney energy of explosive
K	Strength coefficient
k	Fracture constant
M	Metal mass
n	Strain hardening mass
P	Explosive pressure
r, θ, z	Cylindrical coordinates
r_a	Radius of case element
t	Time
v_a	Radial velocity of case element
γ	Gas expansion coefficient
ϵ	Strain
ν	Poisson's ratio
ρ	Density
σ	Stress
ϕ	Energy ratio parameter

INTRODUCTION

Analyses of fragment velocities from explosively filled bombs have developed based on improved case fracture characterizations. An early analysis by Gurney [1] assumed the case has zero strength. The Gurney equation for fragment velocity from tubular bombs uses only two parameters: the ratio of case metal mass to total explosive mass, M/C ; and the Gurney energy for the explosive, G . The designer using Gurney's equation with any specified explosive would be concerned only with the density, inner radius, and thickness of the case. The Gurney equation, $v/\sqrt{2G} = 1/\sqrt{(M/C) + .5}$, does not depend on other material parameters that characterize the stiffness or strength of the case.

Models describing bomb dynamics which include material properties of the case have been successively devised by Taylor [2], Hoggatt and Recht [3], and Al-Hassani and Johnson [4]. Each study extended the previous work that began with Gurney. Hoggatt and Recht provided a useful method for predicting the minimum breakup radius based on the assumption that fracture of the case occurs along planes of maximum shear stress. Al-Hassani and Johnson provided detailed insight into the effect of material properties on bomb dynamics and, in particular, derived an equation for calculating the wall acceleration. The present investigation uses these theories of bomb dynamics to study the effect of commonly recognized material properties on fragment velocity.

To study the effects of case material parameters on the fragment velocities, mathematical models are developed for the case material, the explosive pressure, the wall dynamics, and the case failure. These models incorporate the following assumptions: The case is an elastic-plastic material; the detonation gas products expand isentropically; the case expansion is in plane strain; the case failure is a function of the stress state; and case failure terminates the buildup of velocity. For this study the ratio of wall thickness to inner radius is taken to be in the interval [.03, .17].

ANALYTICAL MODELS

CASE MATERIAL

The elastic-plastic stress-strain characterization for the case is given by two equations:

$$\sigma = E_1 \cdot \epsilon \quad (1)$$

for most of the elastic portion; and

$$\sigma = K \cdot \epsilon^n \quad (2)$$

for the non-proportional elastic and plastic portion, where E_1 is the elastic modulus, K is the strength coefficient, and n is the strain hardening exponent. The two curves intersect at the proportional limit point ($\epsilon_{pl}, \sigma_{pl}$).

$$\epsilon_{p1} = (K/E_1)^{1/(1-n)} \quad (3)$$

$$\sigma_{p1} = E_1 \cdot (K/E_1)^{1/(1-n)} \quad (4)$$

If E_2' is defined to be the derivative $d\sigma/d\epsilon$ at ϵ_{p1} , then we find that

$$n = E_2'/E_1 \quad (5)$$

Thus n can be interpreted as the reduction factor for Young's modulus at the proportional limit. Estimates of K and n may be made from the following algebraic manipulation of equations (1) and (2). Defining, as is frequently done, the yield stress, σ_y , to be the stress needed to obtain a 0.2% permanent set, and the plastic modulus, E_2 , to be the slope of the plastic curve at the yield point, we may use the stress-strain equations to obtain:

$$n = (E_2/E_1) + .002 \cdot (E_2/\sigma_y) \quad (6)$$

This results in an expression for K ($= \sigma|_{\epsilon=1}$)

$$K = \sigma_y / (.002 + \sigma_y/E_1)^n \quad (7)$$

Empirical values for K and n were obtained by Martin [5] for steel and aluminum, and show for these materials K ranging from 48 000 psi (3.4×10^9 dynes cm^{-2}) to 170 000 psi (1.2×10^{10} dynes cm^{-2}), and n in an interval from 0.1 to 0.3.

EXPLOSIVE PRESSURE

The internal explosive pressure, P , exerted on the inner surface of the case is related to the cavity volume through the perfect gas law,

$$P = (\gamma - 1) \cdot \rho_g \cdot E \quad (8)$$

where γ is the expansion coefficient, ρ_g the gas density, and E the explosive energy. This pressure is assumed to be uniform throughout the cavity. For adiabatic reversible flow, an isentropic expansion of detonation product gases results in [6],

$$P \cdot \rho_g^{-\gamma} = \text{constant} \quad (9)$$

The equation derived from equations (8) and (9) is

$$P = P_0 \cdot (r_0/r_0(0))^{-2\gamma} \quad (10)$$

where P_0 is the effective detonation pressure, r_0 the internal radius, and $r_0(0)$ the initial internal radius. If $r_e (\leq r_0(0))$ is the radius of a cylindrical explosive, then P_0 is given by

$$P_0 = P_0^i \cdot (r_e/r_0(0))^{2\gamma} \quad (11)$$

where P_0^i is the Chapman-Jouguet coefficient for the explosive. C-J coefficients for particular explosives can be found in [7] and vary from 1.5×10^6 psi to 5.5×10^6 psi (100 to 390 Kbars). For these computations γ has been taken to be 3 throughout the expansion although it varies in an actual expansion, starting near 5 and soon falling to smaller values.

WALL ACCELERATION

Figure 1 shows a case element at radius $r(t)$. The equation of radial motion for the element is

$$\rho \cdot d^2r/dt^2 = \partial\sigma_r/\partial r - (\sigma_\theta - \sigma_r)/r \quad (12)$$

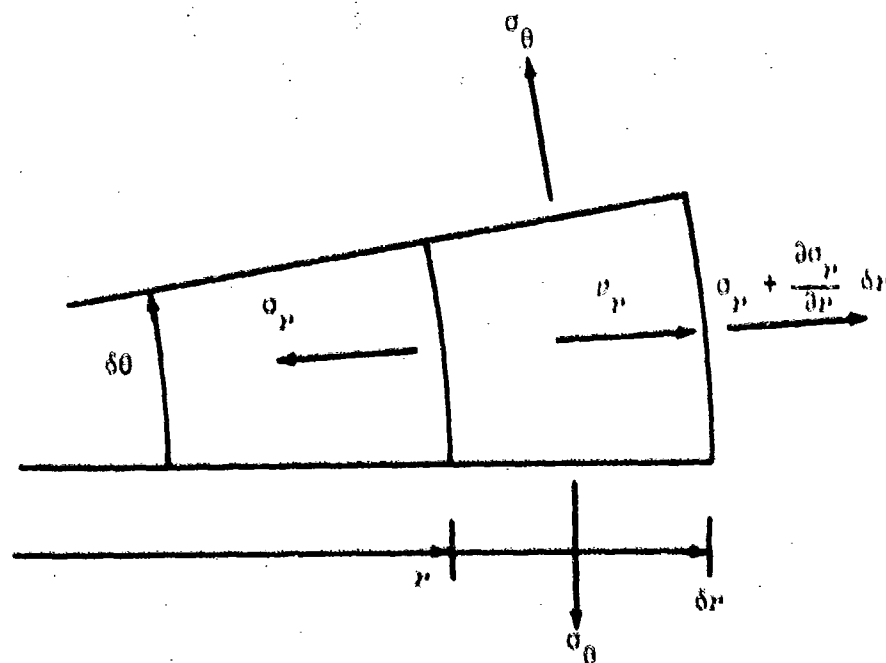


FIGURE 1. Element Within Wall of Case.

Let $r_0(t)$ be the inner case radius, $r_1(t)$ be the outer case radius, and $r_\alpha(t)$, $0 \leq \alpha \leq 1$, be the radius of an arbitrary case element. Define v_α as dr_α/dt . Constancy of volume requires that

$$r^2 - r_\alpha^2 = r^2(0) - r_\alpha^2(0) \quad (13)$$

where α is arbitrary. By twice differentiating (13) and simplifying we obtain

$$dr/dt = (r_\alpha \cdot v_\alpha)/r \quad (14)$$

and

$$d^2r/dt^2 = (v_\alpha^2 + r_\alpha \cdot dv_\alpha/dt)/r - (r_\alpha^2 \cdot v_\alpha^2)/r^3 \quad (15)$$

We will need the following relationships for the strains:

$$\epsilon_r - \epsilon_\theta = \partial(r \cdot \epsilon_\theta)/\partial r - \epsilon_\theta = r \cdot \partial \epsilon_\theta / \partial r \quad (16)$$

From constancy of volume and by assumption of plane strain (using cylindrical coordinates),

$$\epsilon_\theta = -\epsilon_r - \epsilon_z = -\epsilon_r \quad (17)$$

At the inner surface

$$\epsilon_\theta(r_0) = \ln(r_0/r_0(0)) \quad (18)$$

Solving (16), (17), and (18) for ϵ_θ by integration, etc., gives

$$\epsilon_\theta(r) = (r_0(0)^2/r^2) \cdot \ln(r_0/r_0(0)) \quad (19)$$

Define $\bar{\epsilon}$ and $\bar{\sigma}$, the effective stress and strain by

$$\bar{\epsilon} = \sqrt{(2/9) \cdot [(\epsilon_r - \epsilon_\theta)^2 + (\epsilon_\theta - \epsilon_z)^2 + (\epsilon_z - \epsilon_r)^2]} \quad (20)$$

$$\bar{\sigma} = \sqrt{(1/2) \cdot [(\sigma_r - \sigma_\theta)^2 + (\sigma_\theta - \sigma_z)^2 + (\sigma_z - \sigma_r)^2]} \quad (21)$$

Substituting for ϵ_r and ϵ_z in (20) gives

$$\bar{\epsilon} = (2/\sqrt{3}) \cdot \epsilon_\theta \quad (22)$$

Further substitution into the Levy-Mises equations,

$$\epsilon_\theta = [\sigma_\theta - (1/2) \cdot (\sigma_r + \sigma_z)] \cdot \bar{\epsilon}/\bar{\sigma} \quad (23)$$

etc., for ϵ_r , ϵ_z , and $\bar{\epsilon}$ yields

$$\bar{\sigma} = (\sqrt{3}/2) \cdot (\sigma_\theta - \sigma_r) \quad (24)$$

For simplicity assume that strain rate effects are negligible. (Al-Hassani and Johnson have shown how a strain rate index can be successfully included in the solution.) Thus equation (2) says that

$$\bar{\sigma} = K \cdot \bar{\epsilon}^n \quad (25)$$

Manipulating (22), (24), and (25) gives us

$$\sigma_\theta - \sigma_r = (2/\sqrt{3})^{1+n} \cdot K \cdot \epsilon_\theta^n \quad (26)$$

We can now combine (12), (15) (with $\alpha = 1$), (19), and (26) and obtain

$$\begin{aligned} \partial\sigma_r/\partial r = \rho \cdot [(v_1^2 + r_1 \cdot dv_1/dt)/r - r_1^2 \cdot v_1^2/r^3] \\ - (2/\sqrt{3})^{1+n} \cdot K \cdot [r_0(0)^2 \cdot \ln(r_0/r_0(0))]^{n/p} \cdot r^{(2n+1)} \end{aligned} \quad (27)$$

Integrating with respect to r and using the condition

$$\sigma_r(r_0) = -P \quad (28)$$

and equation (14) with $r = r_1$ and $r_0 = r_0$ gives

$$\begin{aligned}\sigma_r = & -P + \rho \cdot [(v_0^2 + r_0 \cdot dv_0/dt) \cdot \ln(r/r_0) + (r_0^2 \cdot v_0^2/2) \\ & \cdot (r^{-2} - r_0^{-2})] - (2/\sqrt{3})^{(1+n)} \cdot (K/2n) \\ & \cdot (r_0^2 \cdot \ln(r_0/r_0(0)))^n \cdot (r^{-2n} - r_0^{-2n})\end{aligned}\quad (29)$$

On the outer surface of the case $\sigma_r(r_1) = 0$, so substituting r_1 for r in (27) and solving for dv_0/dt gives

$$\begin{aligned}dv_0/dt = & (1/(\rho \cdot r_0 \cdot \ln(r_1/r_0))) \cdot [P - \rho \cdot v_0^2 \cdot (\ln(r_1/r_0)) \\ & + (\rho \cdot r_0^2 \cdot v_0^2/2) \cdot (r_0^{-2} - r_1^{-2}) \\ & - (2/\sqrt{3})^{(1+n)} \cdot (K/2n) \cdot (r_0^2 \cdot \ln(r_0/r_0(0)))^n \\ & \cdot (r_0^{-2n} - r_1^{-2n})]\end{aligned}\quad (30)$$

Since

$$r_1^2 = r_0^2 + r_1^2(0) - r_0^2(0) \quad (31)$$

we can use equation (30) to estimate the fragment velocity of the case at the failure radius r_f by numerical integration.

CASE FAILURE

Taylor, Hoggatt and Recht, and Al-Hassani and Johnson have each formulated criteria for case failure. These criteria each involve evaluating the hoop stress at the inner case surface. Combining (19), (26), and (29) and noting that $\sigma_0(r_1) = 0$ results in the inner surface hoop stress,

$$\sigma_0(r_0) = (2/\sqrt{3})^{(1+n)} \cdot K \cdot ((r_0(0)/r_0)^2 \cdot \ln(r_0/r_0(0)))^n - P \quad (32)$$

and the outer surface hoop stress,

$$\sigma_0(r_1) = (2/\sqrt{3})^{(1+n)} \cdot K \cdot ((r_0(0)/r_1)^2 \cdot \ln(r_0/r_0(0)))^n \quad (33)$$

During expansion of the case to failure $\sigma_\theta(r_0)$ is monotonically increasing starting with a value of 0. $\sigma_\theta(r_0)$ is initially negative and eventually increases to a positive value as the hoop strain term increases and the pressure term decreases. (The first term in equation (32) involves the hoop strain, and the second term the applied internal pressure.) Thus during the expansion to failure there is a region of compressive hoop stress extending from the inner radius to a radius of zero hoop stress, and a region of tensile hoop stress between the zero hoop stress radius and the outer radius. The radius of zero hoop stress is initially the outer radius and moves to become the inner radius of the case, after which time failure can occur. Taylor's [2] criterion for failure is that the hoop stress at the inner surface is zero. This radius can be found from equation (32).

Hoggatt and Recht [3] observed that the fracture surfaces of cylinders subject to high order explosions run in planes approximately 45 degrees to the radial direction. These planes parallel planes of principal shear stress. Fractures begin as radial cracks appearing at the outer surface and progress inward as the stress component normal to the shear planes changes from compressive to tensile. This condition is satisfied when the tensile hoop stress becomes equal to the compressive radial stress; therefore, complete failure occurs when the tensile hoop stress at the inner surface is equal to the internal pressure.

Consider a cylindrical differential element at the inner surface of the case. Subject to the internal pressure P of equation (10), it will experience high compressive, radial and hoop stresses, and will expand plastically from a radius r_0 to a radius r_p . The natural strain in the radial direction (assuming $\epsilon_{\theta\theta} = 0$) is given by

$$\epsilon_p = \ln(r_0/r_p) \quad (34)$$

If the stress condition were uniaxial then we would have by equation (2)

$$\epsilon_p = -(P_p/K)^{1/n} \quad (35)$$

where P_p is the compressive uniaxial pressure. If σ_θ and σ_{xx} are the hoop stress and axial stress then

$$P_p = - (1/\sqrt{2}) \cdot \sqrt{(-P-\sigma_\theta)^2 + (\sigma_\theta-\sigma_{xx})^2 + (\sigma_{xx}+P)^2} \quad (36)$$

represents an octahedral shear stress equivalent to the uniaxial stress failure condition [3].

With decreasing P and σ_θ , (σ_θ eventually positive), the differential element at the inner surface expands elastically until case failure at radius r_f and inner pressure P_f . The strains are given by

$$\epsilon_r = -(P_f/E_1) - (\nu/E_1) \cdot (\sigma_\theta + \sigma_z) \quad (37)$$

$$\epsilon_\theta = (\sigma_\theta/E_1) - (\nu/E_1) \cdot (\sigma_z - P_f) = (r_f/r_p) - 1 \quad (38)$$

$$\epsilon_z = (\sigma_z/E_1) - (\nu/E_1) \cdot (\sigma_\theta - P_f) = 0 \quad (39)$$

where ν is Poisson's ratio. We hypothesize that $\sigma_\theta = P_f$ at r_f , so that from (38) and (39) we find

$$r_p = r_f / (1 + (1 + \nu) \cdot (P_f/E_1)) \quad (40)$$

and from equation (36)

$$P_p = P_f \quad (41)$$

Combining (34), (35), (40), and (41) results in

$$r_f/r_0 = [1 + (P_f/E_1) \cdot (1 + \nu)] \cdot \exp(P_f/K)^{1/n} \quad (42)$$

To find the inner radius at failure, r_f , first find by trial and error P_f satisfying

$$(P_0/P_f)^{1/2\gamma} = (1 + (P_f/E_1) \cdot (1 + \nu)) \cdot \exp(P_f/K)^{1/n} \quad (43)$$

since

$$r_f = r_0 \cdot (P_0/P_f)^{1/2\gamma} \quad (44)$$

The criterion for failure suggested by Al-Hassani and Johnson involves a fracture constant, k , equal to the ratio of the hoop stress of the inner radius at failure to the ultimate tensile strength of the material, σ_{uts} . Neglecting strain rate effects, the ultimate tensile strength is calculated from equation (32) as

$$\sigma_{uts} = (2/\sqrt{3})^{1/(1+n)} \cdot K \cdot (\ln(r_f/r_0(0)))^n \quad (45)$$

Radial cracks may propagate only if the hoop stress at their tips are greater than $k \cdot \sigma_{uts}$. Thus the failure radius is found by solving

$$P_0 \cdot (r_f/r_0(0))^{-2\gamma} = (1 - k) \cdot (2/\sqrt{3})^{1+n} \cdot K \cdot (\ln(r_f/r_0(0)))^n \quad (46)$$

for r_f . When $k = 0$ the calculated fracture radius corresponds to that proposed by Taylor; when $k = 1$ the case does not fail. The fracture radius as calculated by Hoggatt and Recht does not correspond to a single value of k .

For consistency in the computations which follow, the radius of failure proposed by Hoggatt and Recht is used. This radius is convenient for a reference since it is not rate dependent, is only slightly greater than Taylor's failure radius, involves the introduction of no new material parameters, and is supported by some experimental observation. We shall, however, want to remark on the equivalent k value obtained for this failure radius and comment on the effect of increasing k on the fragment velocity.

COMPUTATIONS

PROCEDURE

The mathematical models formulated for failure radius and wall acceleration, equations (43) and (30), respectively, in the preceding sections were assembled in a computer program. For given values of $r_0(0)$, $r_1(0)$, P_0 , E_1 , ν , K , n , and ρ , the fracture radius r_f , was calculated according to the formulas developed by Hoggatt and Recht. The equation for the wall acceleration was then used to numerically integrate v_0 from 0 to the velocity at the failure radius. The integration was continued until the inner surface reached a radius of $1.5 r_f$. Values for the fracture constant, k , suggested by Al-Hassani and Johnson which would have resulted in case failure at r_f and $1.5 r_f$ were computed. By repeating the computations over a range of values for the material parameters we were able to see the relative importance of the material parameters on the fragment velocity. The intervals in which the material parameters were taken are: $(r_1(0)-r_0(0))/r_0(0)$ in $[.03, .17]$; P_0 in $[1300000, 4000000]$ psi ($[8 \cdot 10^9, 3 \cdot 10^{10}]$ Pa); E_1 in $[3000000, 90000000]$ psi ($[1.4 \cdot 10^6, 4.3 \cdot 10^7]$ Pa); ν in $[0.0, 0.5]$; K in $[20000, 200000]$ psi ($[9.7 \cdot 10^3, 9.7 \cdot 10^4]$ Pa); n in $[.01, 1.0]$; and ρ in the interval $[.0002, .0015]$ lbm/in³ ($[5.5, 41.5]$ kg/m³).

A dimensional study of the variables used in this study suggests the following scaling parameters for use in describing the results: $r/r_0(0)$, K/P_0 , E_1/P_0 , ν , $\rho \cdot v_0^2/P_0$, and n . Since the mathematical models used are all continuous and dimensionally consistent, it was gratifying, but not surprising, that the results of our computations scaled according to these parameters.

RADIUS OF FRACTURE

Computations using equation (43) show that the elastic modulus, E_1 , and Poisson's ratio, ν , for the case material are not important in determining the radius of failure over a range of E_1 and P_0 likely to occur in practice. This is illustrated in Figures 2 and 3. Examining equation (43) shows that when the ratio of P_0/E_1 is small, as it would be for practical case materials, and with ν in the interval $[0.0, 0.5]$ by definition, the factor $(1 + (P_0/E_1) \cdot (1+\nu))$ varies little from a value of 1.0 and so has little effect on the fracture radius.

The same equation, on the other hand, says that the radius at fracture is a function of K and n , as shown by Figure 4. Higher values for the strength coefficient are paired with lower failure radii. The reason becomes apparent when examining equation (43) which shows that $(P/K)^{(1/n)}$ appears as a power of an exponential factor so that the solution of (43) for P_f is sensitive to both K and n .

The values for the equivalent fracture constant, k , needed to obtain the the calculated fracture radii fell in the interval from $[\.15 \text{ to } .22]$, values which reflect the fact that the calculated radii are slightly larger than the radii that would be calculated by Taylor's method ($k=0$). The equivalent constant needed to obtain fracture radii 1.5 times those calculated fell in the interval $[\.93, .96]$, indicating that the failure radius increases slowly until k reaches values near 1.

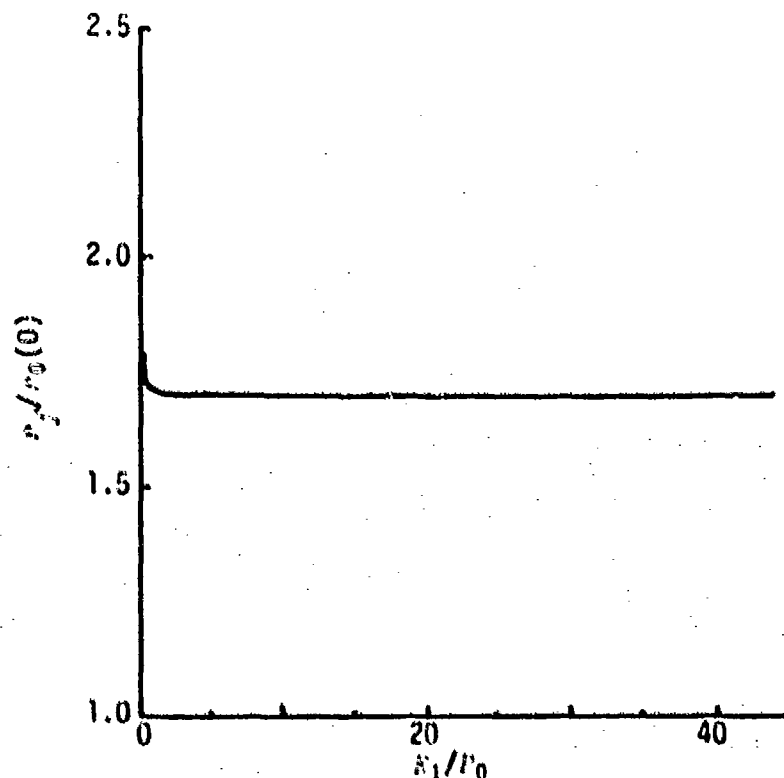


FIGURE 2. Radius at Fracture vs. Elastic Modulus at $n = 2.5$, $\nu = .3$, $K/P_0 = .05$.

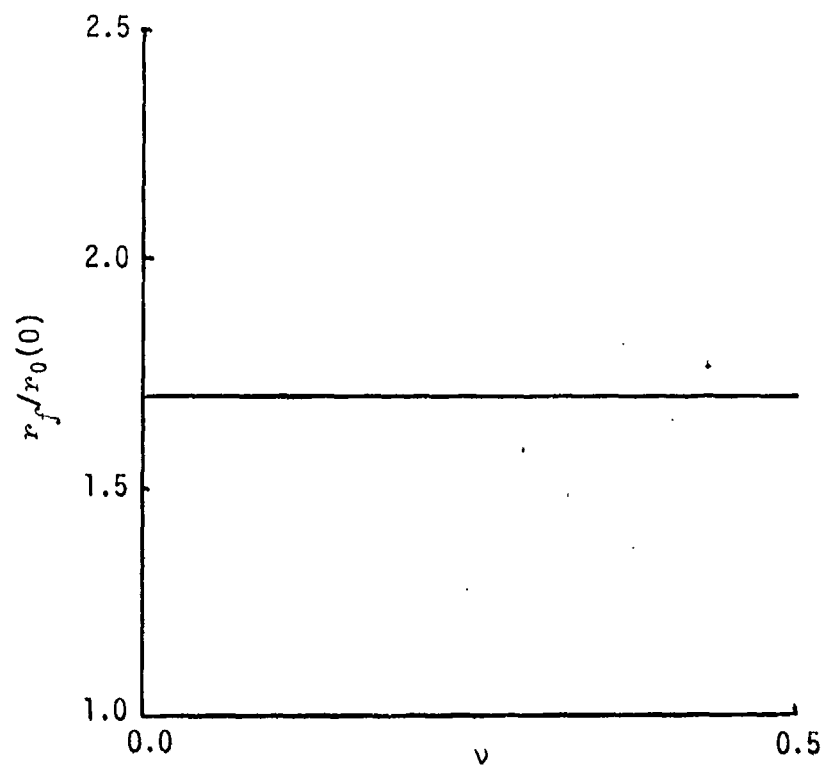


FIGURE 3. Radius at Fracture vs. Poisson's Ratio
at $n = .25$, $E_1 = 30000000$ psi, $K/P_0 = .05$.

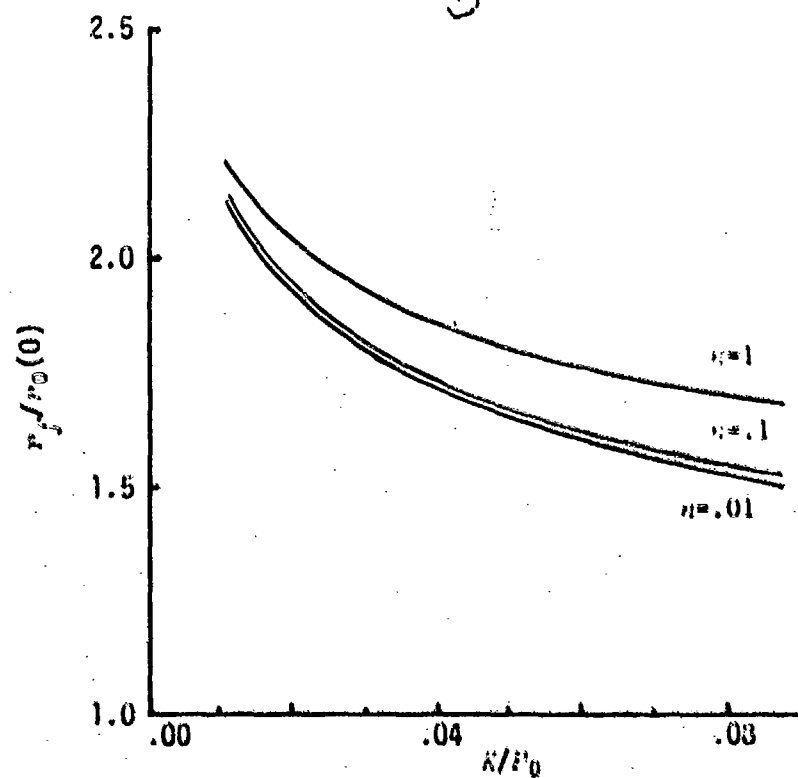


FIGURE 4. Radius at Fracture vs. Strength of Case.

VELOCITY AT FRACTURE

Equation (30) can be used to calculate fragment velocities for a wide range of case parameters. Letting $d_0(0)$ be the initial case thickness ($d_0(0) = r_0(0) - r_1(0)$), it has been found empirically that for fixed values of K/P_0 and n that the ratio of kinetic energy at large deformations to the internal explosive energy, $(\rho \cdot v_0^2/P_0) \cdot (d_0(0)/r_0(0)) \cdot .968$, was a constant in the interval [.45, .50] to within 5% for $d_0(0)/r_0(0)$ in the interval [.03, .17], and that $(d_0(0)/r_0(0)) \cdot .968$ accomplished a better normalizing factor than did a volume term such as $(1 - (r_0(0)/r_1(0))^2)$. Thus, $\phi \triangleq (\rho \cdot v_0^2/P_0) \cdot (d_0(0)/r_0(0)) \cdot .968$ will be used as a descriptive parameter to show the effects of case properties on fragment velocity.

Equation (30) for the wall acceleration can be rewritten showing the terms $\rho \cdot v_0^2/P_0$, K/P_0 , and n as

$$\begin{aligned} d(\rho \cdot v_0^2/P_0)/dt = (v_0/r_0) \cdot & \left[(r_0(0)/r_0)^{2\gamma/\ln(r_1/r_0)} \right. \\ & - (\rho \cdot v_0^2/P_0) \cdot \left(1 - \frac{(1 - (r_0/r_1)^2)}{\ln(r_1/r_0)} \right) - (2/\sqrt{3})^{1+n} \\ & \left. \cdot (K/P_0) \cdot \left(\frac{1 - (r_0/r_1)^{2n}}{2n \cdot \ln(r_0/r_0(0))^{1-n}} \right) \right] \end{aligned} \quad (47)$$

There is only one term on the right-hand side of equation (47) involving K/P_0 and n . This term indicates that increasing K/P_0 yields lower wall accelerations. Coupled with the lower fracture radius for higher K/P_0 as discussed in the previous section this results in lower velocities at fracture. This is, in fact, the result shown in Figure 5. The effect of the third term in (47) is quite small.

Comparing the calculated velocities at r_f and $1.5 \cdot r_f$, or equivalently for fracture constants at about .2 and .9, we found that a 50% increase in fracture radius yielded increases in fragment velocity of less than 1%. It can be concluded that fragment velocity is insensitive to case material properties for values of k between 0 and .96. Consequently, the mode of failure, unless quite different in nature from that of Taylor's or Hoggatt and Recht is not an important factor in determining fragment velocity.

Gurney's equation [1] for calculating fragment velocities is given by

$$v_0 = \sqrt{2G} / \sqrt{(N/C) + .5} \quad (48)$$

where $2G = P_0/\rho_0 \cdot (\gamma - 1)$ and N/C is the ratio of metal mass to total explosive

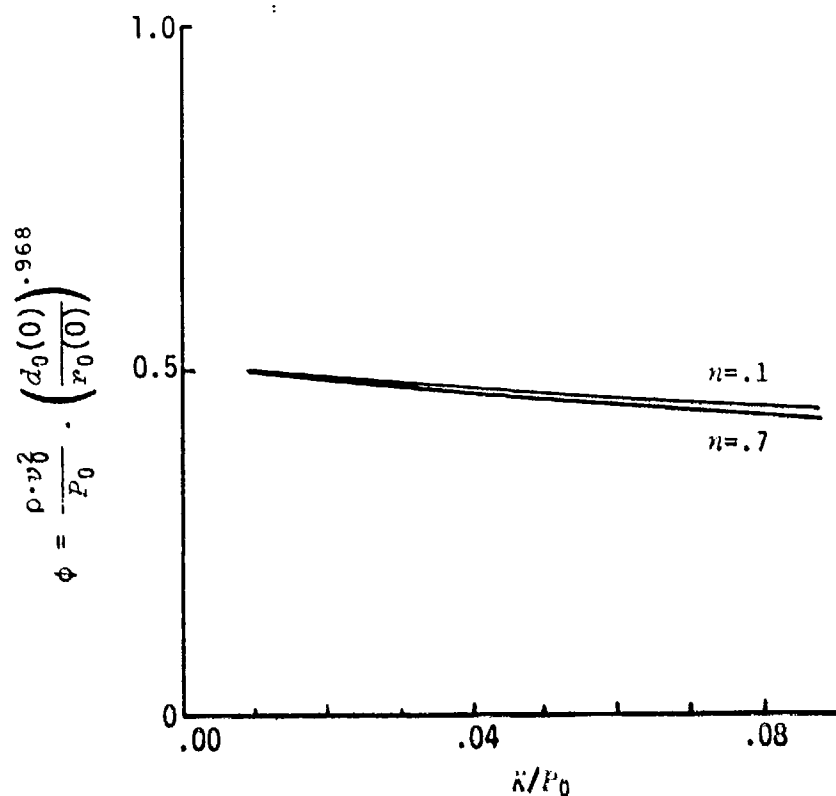


FIGURE 5. Kinetic to Explosive Internal Energy Ratio vs. Strength of Case.

mass. To check the validity of ϕ for filled bombs, substitute v_0 from (48) into the expression for ϕ . This yields

$$\phi = \frac{\rho \cdot v_0^2}{p_0} \cdot \left(\frac{d_0(0)}{r_0(0)} \right)^{.968} = \frac{(d_0(0)/r_0(0))^{.968}}{\left[\left(\frac{d_0(0)}{r_0(0)} \right) \cdot \left(2 + \frac{d_0(0)}{r_0(0)} \right) + .5 \left(\frac{\rho_e}{\rho} \right) \right]} \quad (49)$$

If the explosive mass is zero, equation (49) results in $\phi \approx 0.47$. This is equivalent to velocities at fracture that were found using the equation for wall acceleration (30). A characteristic value of equation (49) for typical tubular bombs is $\phi = 0.3$. Thus, neglecting the kinetic energy of explosive products increases the predicted fragment velocity about 30%.

CONCLUSIONS

A theory for explosively loaded case failure by Hoggatt and Recht and a theory for case acceleration by Al-Hassani and Johnson have been used to investigate the effects of case material properties on fragment velocity. Velocity

calculated using this integrated theory has been compared with that predicted by the Gurney equation. These velocities are very close. Fragment velocity is insensitive to the material properties considered: elastic modulus, Poisson's ratio, strength coefficient, and work hardening index. Fragment velocity is also insensitive to the radius of fracture for values roughly equal to those predicted by Taylor. Consequently, for case materials normally encountered, fragment velocity depends on the properties of the explosive, on the density of the case, and on the bomb geometry. The parameter ϕ , a ratio of expanded case kinetic energy to explosive internal energy, can be used to describe the effects of these parameters. ϕ is approximately equal to 0.5.

REFERENCES

1. Gurney, R. W. "The Initial Velocities of Fragments From Bombs, Shells, and Grenades," Ballistic Research Laboratory, Aberdeen, MD, 1943. (BRL Report 405.)
2. Taylor, G. I., "The Fragmentation of Tubular Bombs," *Scientific Papers of G. I. Taylor*, Vol. III, No. 44. Cambridge University Press, 1963.
3. Hoggatt, Chester R., and Recht, Rodney F., "Fracture Behavior of Tubular Bombs," *J. of Applied Physics*, v. 39, no. 3, 15 February 1968. 1856-61.
4. Al-Hassani, S. T. S., and Johnson, W., "Dynamic Deformation and Fragmentation of Strain-Hardening, Strain-Rate Sensitive Shells Containing High Explosives," *Advances in Machine Tool Design and Research*, S. A. Tobias and F. Koenigsberger, Editors. Pergamon Press, Oxford and New York, 1971. 957-79.
5. Martin, Joseph, *Mechanical Behavior of Engineering Materials*, Prentice-Hall, Inc., Englewood Cliffs, NJ, 1963. 38-41.
6. Kennedy, J. E., "Explosive Output for Driving Metal," in *Behavior and Utilization of Explosives in Engineering Design*, 18th Annual Symposium, Albuquerque, NM, 2-3 March 1972, 109-124. Published by New Mexico Section American Society of Mechanical Engineers.
7. Dobratz, B. M. "Properties of Chemical Explosives and Explosive Simulants," Table 8-4, p. 8-7. Published by University of California-Lawrence Livermore Laboratory, 1974.

IN-BORE MOTION ANALYSIS OF THE 155mm XM712 PROJECTILE
WHEN FIRED IN THE M198 HOWITZER

DR. SZU HSIUNG CHU
Mechanical Engineer
Department of the Army
ARRADCOM
Dover, NJ 07801

ABSTRACT

This paper presents the results of an analysis of the in-bore, transverse motion of the 155mm XM712 projectile when fired in both a new tube and a worn tube of the M198 howitzer. The worn tube condition was taken as one with 1,710 rounds fired in the tube Serial Number 83. The approach taken in this investigation utilized the equations of motion derived previously and reported in several references. An effective rifling angle or twist is introduced, since this projectile uses an obturator instead of a rotating band. The gun tube is considered to be straight and stationary. Effects of projectile bourrelet friction and tube droop have been ignored in the analysis. The center of mass eccentricity of the projectile was assumed to fall in the range of 0 to .287 millimeters or .0113 inches. This is equivalent to maximum imbalance of 176.5 mm-N or 25 in-oz as used in the analysis.

Tabulations are recorded for the peak values of yaw angle and velocity, cross spin, normal accelerations at the c.g., bourrelet center and two axial points, and lateral forces at the c.g., bourrelet and obturator. Time, velocity, acceleration, yaw angle and velocity, normal acceleration, and forces at the bourrelet and the obturator are plotted to show their variations with respect to the travel.

The computation result shows that the lateral bourrelet forces are very small (less than 4,450 newtons or 1,000 lbs) for all cases considered and the effects of the c.g. imbalance, the tube wear and the clearance between the bourrelet and the tube are prominent.

NOMENCLATURE

BRT = Bourrelet
c.g. = Center of gravity or mass
D = Diameter of gun tube bore
E = Young's modulus of bourrelet material
 F_b = Elastic force at bourrelet
 F_x, F_y, F_z = Total force components acting at c.g., in
XYZ directions
h = Distance from c.g. to bourrelet
 h_1, h_2, h_3 = Angular momenta in 1, 2, 3 directions
k = Spring constant at bourrelet
 ℓ = Distance from c.g. to obturator center section

M_1, M_2, M_3 = Total moment components in 1, 2, 3 directions
 m = Mass of projectile
 $1/N$ = Effective twist of rifling
 R = Radius of gun tube bore
 r = Radius of bourrelet
 t = Wall thickness at bourrelet
 V_m = Velocity of projectile at muzzle with same length unit as that of bore diameter
 W = Displacement of obturator in Z direction
 X, Y, Z = Fixed Cartesian coordinates (Figure 1), displacements of c.g. in X, Y, Z directions
 x, y, z = Body-fixed moving Cartesian coordinates (Figure 2)
 γ = Effective twist angle of rifling
 δ = Deflection at bourrelet
 ψ, ϕ, θ = Euler's angles (Figure 3)
 $\pi = 3.141592654$
 Ω = Cross spin of projectile
 Ω_m = Projectile muzzle spin
 $\Omega_1, \Omega_2, \Omega_3$ = Angular velocity components in 1, 2, 3 directions
1, 2, 3 = Moving Cartesian coordinates (Figure 2)
 $\dot{}$ = Dot over a quantity denotes its time derivative
 $\ddot{}$ = Double dots over a quantity denotes its second time derivative

INTRODUCTION

A thorough understanding of the transverse in-bore motion (also called balloting) of a projectile during launch is one of the many challenges of developing modern weapon systems that the designer has to consider seriously. The analysis of this motion can provide estimates of both linear and angular displacements as well as velocities and accelerations, when the projectile is in the gun or at the muzzle. Corresponding forces and moments on the various regions or components of a projectile can also be assessed. In addition, the interface action of the projectile and the gun, as the projectile travels down the bore, can be monitored. The behavior of the system in this environment is important to the designer. Being able to describe the interaction of the projectile and the gun as well as the response of internal projectile components to the anticipated input phenomena can aid greatly in the early evaluation and analysis of the preliminary designs. Furthermore, the motion of the projectile at the muzzle provides the initial condition of the transitional exterior ballistics. It is with these objectives in mind that the investigation of the motion of the XM712 projectile in the M198 howitzer was performed.

PROBLEM FORMULATION

In this analysis the projectile configuration is taken as symmetrical about its longitudinal axis. The base pressure is assumed to be uniformly applied to the projectile and there is no gas leakage around the obturator. Consequently, the point where the cylindrical axis of the projectile intersects

the obturator center plane is assumed to move along the gun tube center line in the analysis. The mass distribution of the projectile may be uniform or non-uniform and may thus be represented by a c.g. eccentricity or static imbalance of a certain value. The exact c.g. eccentricity is usually not known. Consequently, an assumed range of 0 to .0113 in (.287mm) equivalent to 0 to 25 in-oz (176.5mm-N) imbalance is used in the computation.

The gun tube is considered straight and stationary. The influence of gun tube droop is ignored in this analysis, since its effect on the transverse force and accelerations has been shown to be rather small in previous calculations [2, 3]. Past work has shown that the effects of balloting motion will be aggravated if firings are performed in gun tubes having an advanced state of wear. To study this effect, computations were performed with a worn tube (with wear condition after 1,710 rounds) as well as a new tube.

The frictional forces at the bourrelet and the obturator are ignored in the analysis. Their effect on the projectile motion seems to be small as previous computations for projectiles with rotating bands [2] and experimental results obtained at Picatinny Arsenal have shown. Though there is a large slippage between the rifling lands and the obturator, the rifling action on the projectile is not neglected. To account for this action, an effective rifling angle or twist is introduced and expressed as a relationship between the velocity and the spin rate of the projectile at the muzzle. Adequate experimental data is available to substantiate this.

The bourrelet of the projectile is assumed to be elastic. The spring constant may be obtained by a compression test of the bourrelet or approximately computed by using the cylindrical shell deformation equations.

Both fixed and moving coordinate systems are necessary to define the motion of the projectile. In this analysis the fixed or inertial coordinate system XYZ (Figure 1) is located with its origin at the initial position of the obturator center, which is equivalent to the rotating band center of the projectile with a rotating band. The Z-axis coincides with the gun tube center line; X-axis is horizontal and perpendicular to the gun tube axis; and the Y-axis is positive upward in a vertical plane and satisfies the right-hand coordinate system convention. This choice conveniently determines the gun location of the moving position of the obturator center which is the origin of the moving coordinate systems 1 2 3 and xyz.

The moving coordinate system 1 2 3 (Figure 2) has its origin located at the moving obturator center. The 3-axis coincides with the longitudinal axis of the projectile, so that the 1- and 2-axis lie in a plane perpendicular to the projectile axis. The 1-axis is always colinear with the nutation axis determined by the Euler's angles ψ , θ , and ϕ (Figure 3). As a result, this coordinate system is convenient in determining the cocking motion and the bourrelet force of the projectile and the Euler's angles.

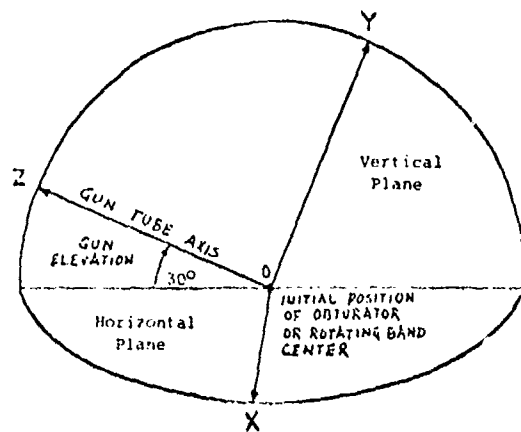


FIGURE 1. Fixed Coordinate System X, Y, Z

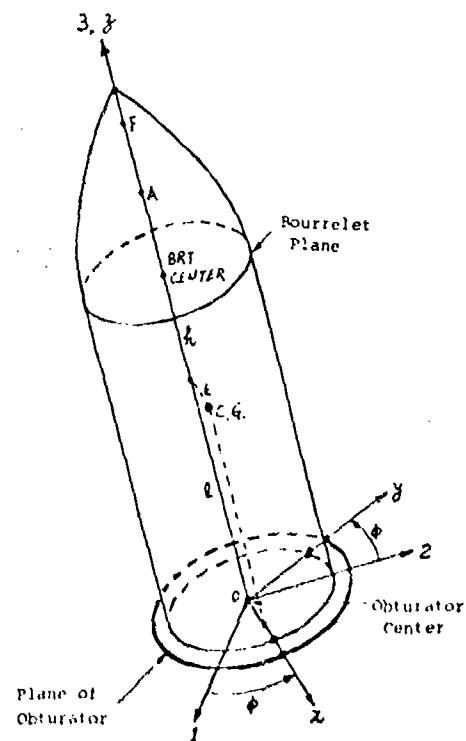


FIGURE 2. Moving Coordinate System 1, 2, 3 and Body-Fixed Coordinate System x, y, z

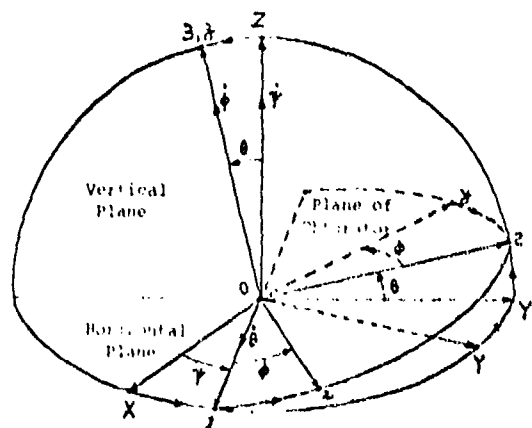


FIGURE 3. Euler's Angles ψ , θ and ϕ

The body-fixed moving coordinate system xyz (Figure 2) is confined on the projectile, with its origin coinciding with that of the 123 coordinate system. In fact, the z -axis coincides with the 3-axis. The x -axis is positioned such that the projection of eccentric c.g. of the projectile on the obturator plane lies on this axis. These two moving coordinate frames are related by the fact that the xyz system (hence the projectile) spins about the 123 system with both the z -axis and the 3-axis as the axis of spin. The angle between the x -axis and the 1-axis (nutation) axis is the Euler's angle ϕ (Figure 3). This coordinate system determines conveniently the positions of c.g. and the other projectile components such as fuze, relative to the projectile.

The orientations of the moving coordinate systems 123 and xyz (hence the projectile) are linked to the fixed system xyz by Euler's angles ψ , θ , and ϕ as shown in Figure 3.

Based on the above-mentioned assumptions and coordinate systems and employing the theory of dynamics of rigid bodies and elasticity principles, Newton's and Euler's equations for the analysis and associated force and moment equations are derived [1, 2, 3, 4]. These equations are too lengthy to be included here. However the simplified main equations are listed in the following Governing Equations Section.

GOVERNING EQUATIONS

The simplified main governing equations in this analysis are as follows. The notations are explained in the Notation Section.

Newton's equations:

$$m\ddot{x} = F_x \quad (1)$$

$$m\ddot{y} = F_y \quad (2)$$

$$m\ddot{z} = F_z \quad (3)$$

Euler's equations:

$$\dot{h}_1 - \Omega_3 h_2 + \Omega_2 h_3 = M_1 \quad (4)$$

$$\dot{h}_2 - \Omega_1 h_3 + \Omega_3 h_1 = M_2 \quad (5)$$

$$\dot{h}_3 - \Omega_2 h_1 + \Omega_1 h_2 = M_3 \quad (6)$$

Bourrelet force and deformation equations:

$$F_b = k\delta \quad (7)$$

$$k = Et^3 / .135r^2 \quad (8)$$

$$\delta = r \cos \theta + (h + \ell) \sin \theta - R \quad (9)$$

Rifling effect equations:

$$1/N = \Omega_m D/V_m \quad (10)$$

$$\gamma = \tan^{-1} (\pi/N) \quad (11)$$

$$\dot{W} \tan \gamma = R (\dot{\psi} + \dot{\phi} \cos \theta) \quad (12)$$

Cross spin rate equation:

$$\Omega = \sqrt{(\dot{\psi} \sin \theta)^2 + \dot{\theta}^2} \quad (13)$$

INPUT DATA FOR ANALYSIS

The gun tube dimensions used in this analysis were obtained from the 155mm M198 howitzer. The projectile travel is 200 inches or 5.08 meters and the land diameter is 6.100 + .002 inches (154.94 + .05mm). The nominal twist is 1/20. The effective twist angle γ is computed from the experimental muzzle velocity and spin data according to Equations (10) and (11). The computed values are: $\gamma = 1.430881$ deg. (0.25 rad) for a muzzle spin of 30 rps and a velocity of 1918 fps (585 mps), and $\gamma = .954031$ deg. (.0167 rad) for a muzzle spin of 20 rps and a velocity of 1918 fps (585 mps).

To investigate the effect of tube wear, the wear condition of the chrome plated gun tube XM199 SN 83 after 1710 rounds was used in the second part of the analysis. This state of wear is shown in Figure 4. This worn tube exhibited large wear only near the muzzle and has slight wear elsewhere.

In the analysis all gun tubes are assumed to be fired at an elevation of 30 degrees (.5236 radian) and they are considered to be straight, rigid and stationary.

The chamber pressure used in the computations is plotted against time in Figure 5.

The simplified dimensions and properties of the projectile XM712 and the M198 howitzer are tabulated in Table 1. As the actual values of c.g. imbalance are not available, values of 0, 5, 10, 15, 20 and 25 in-oz (0, 35.3, 70.6, 105.9, 141.2 and 176.5 mm-N) are used in the analysis. These values are equivalent to c.g. eccentricities of 0, .0023, .0045, .0068, .0091 and .0113 inch (0, .0058, .0115, .0173, .0231 and .0287 cm) respectively.

The actual spring constant of the bourrelet is also not available and was therefore computed from Equation (8). It is calculated to be

$$k = .1306 \times 10^6 \text{ lb/in } (22.86 \times 10^3 \text{ N/mm}),$$

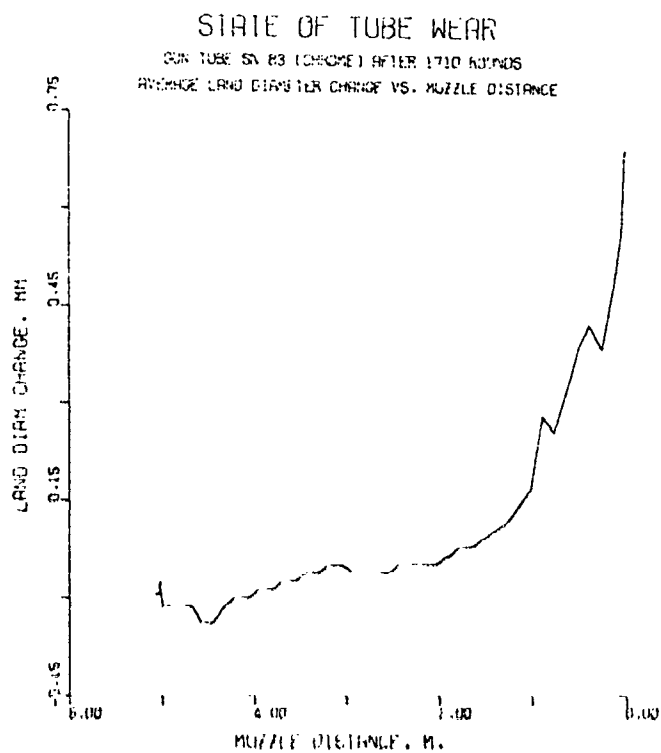


FIGURE 4. State of Tube Wear

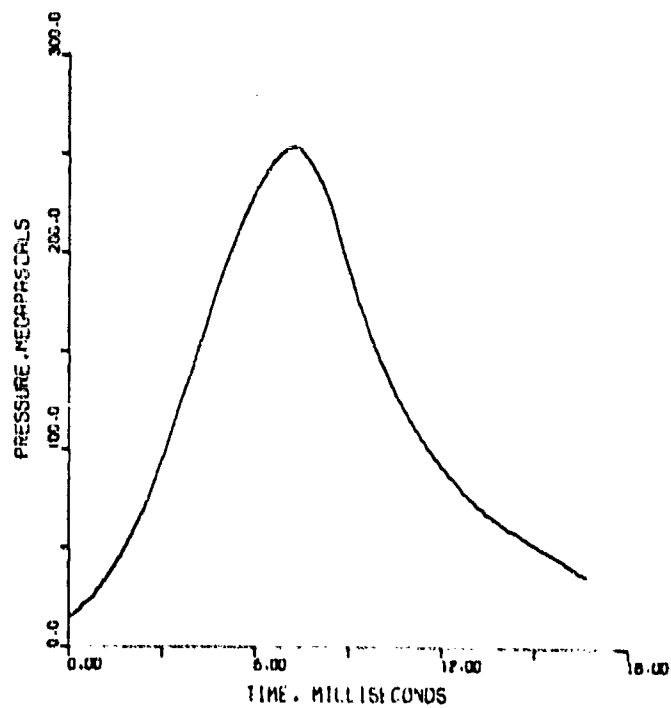


FIGURE 5. Chamber Pressure

using

$$E = 30 \times 10^6 \text{ psi } (206.8 \times 10^3 \text{ N/mm}^2)$$

$$t = .176 \text{ in } (4.47\text{mm})$$

$$r = 3.046 \text{ in } (77.37\text{mm})$$

To aid in visualizing the magnitude of normal accelerations at various points at the projectile axis, axial points A and F in addition to c.g. and the bourrelet center are characterized. The distances from the axial points A and F to the base of the projectile are 44.05 and 51.55 inches (111.89 and 130.94cm) respectively (Figure 2).

TABLE 1

DIMENSIONS AND PHYSICAL PROPERTIES OF PROJECTILE AND GUN TUBE

A. Dimensions and Properties of Projectile

Total length of projectile, cm (in)	137.287	(54.050)
Obturator to base distance, cm (in)	5.055	(1.990)
C.G. to base distance, cm (in)	58.141	(22.890)
Bourrelet to base distance, cm (in)	104.013	(40.950)
Bourrelet diameter, cm (in)	15.474	(6.092)
Bourrelet spring constant computed, 10E6 N/cm (10E6 lb/in)	.229	(.131)
Based on bourrelet wall thickness, cm (in)	.447	(.176)
Axial Point A to base distance, cm (in)	111.887	(44.050)
Axial Point F to base distance, cm (in)	130.937	(51.550)
Weight of projectile, kg (lbs)	62.650	(138.120)
Polar moment of inertia, kg-cm sq (lb-in sq)	53.138	(755.800)
Transverse moment of inertia, kg-cm sq (lb-in sq)	1998.376	(28423.580)

B. Dimensions and Properties of Gun Tube

Bore diameter, mm (in)	154.940	(6.100)
	+.05	(+.002)
Tube inclination, radian (degrees)	.524	(30.000)
Travel, m (in)	5.080	(200.000)
Effective twist angle of rifling, radian (deg) (30 rps spin)	.025	(1.431)
Effective twist angle of rifling, radian (deg) (20 rps spin)	.017	(.954)

RESULTS OF ANALYSIS AND DISCUSSIONS

The computations were performed for the four categories shown in Table 2. In each category, seven cases have been computed. In the first six cases, the parameter varied in the computation is the c.g. imbalance. It is varied from 0 to 25 in-oz (176.5mm-N) in steps of 5 in-oz (35.3mm-N). The first six cases are initialized with the bourrelet contacting the gun tube. In the last or the seventh case the projectile is assumed to be initially parallel to the gun tube axis with the c.g. imbalance taken as 25 in-oz (176.5mm-N). This last case is intended to show the effect of initial projectile position. All other parameters involved are assigned constant magnitudes for the seven cases.

TABLE 2

CATEGORIES OF COMPUTATIONS

Category	1	Gun Tube	1	Land Diameter, mm (in)	1	Spin Rate, rps
1	1	New	1	154.94 (6.100)	1	30
	1		1		1	
2	1	Worn	1	154.94 (6.100)	1	30
	1		1		1	
3	1	New	1	154.99 (6.102)	1	30
	1		1		1	
4	1	New	1	154.99 (6.102)	1	20

The governing and associated equations are solved using a numerical integration method. The computations were performed on a CDC 6600 computer. The peak values of calculated results are tabulated in Tables 3, 4, 5 and 6, and some results of categories 2 and 3 are plotted against travel in Figures 6 to 18 to show their variations. From these tables and figures it is seen that all peak values are very low and the motion has less variations when compared with those of projectiles such as the 155mm M483 [4] and 8 inch XM753 [3]. The peak values, however, are increased as the c.g. eccentricity increases. This, however, is not true for the lateral obturator forces in new and worn tubes or the yaw angles and velocities in the worn tube cases. Peak values for cases with land diameter of 6.100 inches (154.99mm) differ very little from that of the worn tube (nominal land diameter is 6.100 inches or 154.94 millimeters) except for yaw angles and velocities. The differences are large between cases of land diameter of 6.100 inches (154.94mm) and those of land diameter of 6.102 inches (154.99mm).

The obturator slips on the gun tube and thus considerably reduces the centrifugal forces. Consequently the centrifugal force effect is small in this analysis. The reduction of spin rate from 30 rps to 20 rps results in small changes in the peak values. Therefore it seems that the most sensitive factors in this analysis are the c.g. eccentricity, the worn tube, and the

TABLE 3

PEAK VALUES OF BALLOTING MOTION ANALYSIS
155mm Gun M198, XM712 CLGP

Cases of Land Diameter 154.94mm (6.100 in) and Spin 30 rps

Case No.	1	2	3	4	5	6	7
Bourrelet Diameter, cm	15.474	15.474	15.474	15.474	15.474	15.474	15.474
(in)	(6.092)	(6.092)	(6.092)	(6.092)	(6.092)	(6.092)	(6.092)
C.G. Eccentricity, mm	0.0000	.0575	.1149	.1724	.2299	.2873	.2873
(in)	(.0000)	(.0023)	(.0045)	(.0068)	(.0091)	(.0113)	(.0113)
C.G. Imbalance, mm-N	0.00	35.31	70.61	105.92	141.22	176.53	176.53
(in-oz)	(0.00)	(5.00)	(10.00)	(15.00)	(20.00)	(25.00)	(25.00)
Projectile Axis Parallels Tube	NO	NO	NO	NO	NO	NO	YES
Bourrelet-Tube Contact	YES	YES	YES	YES	YES	YES	NO
Bourrelet Force, N	1512	2130	2633	3074	3478	3860	3892
(lbs)	(340)	(479)	(592)	(691)	(782)	(868)	(875)
Lateral C.G. Force, N	1583	1899	2135	2330	2518	2686	2722
(lbs)	(356)	(427)	(480)	(524)	(566)	(604)	(612)
Lateral Obturator Force, N	1401	1210	996	858	1005	1316	1316
(lbs)	(315)	(272)	(224)	(193)	(226)	(296)	(296)
Yaw Angle, radian	.00017	.00020	.00022	.00024	.00026	.00028	.00028
Yaw Velocity, rad/sec	.05	.06	.07	.08	.09	.10	.10
Normal Acceleration at C.G., gees	3.75	4.47	4.99	5.42	5.80	6.16	6.23
Normal Acceleration at Bourrelet Center	6.06	7.23	8.04	8.68	9.24	9.72	9.85
Normal Acceleration at Point A	6.46	7.71	8.57	9.25	9.85	10.37	10.50
Normal Acceleration at Point F	7.43	8.87	9.86	10.65	11.34	11.94	12.09

Initial C.G. o'clock position is at 6 o'clock

Axial point A to base distance is 111.89 cm (44.050 inches)

Axial point F to base distance is 130.94 cm (51.550 inches)

TABLE 4

PEAK VALUES OF BALLOTTING MOTION ANALYSIS
155mm Gun M198, XM712 CLGP

Cases of Land Diameter 154.99mm (6.102 in) and Spin 30 rps

Midpoint A to Base Distance is 111.89cm (44.050 inches)
Nose Point F to Base Distance is 130.94cm (51.550 inches)

Case No.	1	2	3	4	5	6	7
Bourrelet Diameter, cm (in)	15.474 (6.092)	15.474 (6.092)	15.474 (6.092)	15.474 (6.092)	15.474 (6.092)	15.474 (6.092)	15.474 (6.092)
C.G. Eccentricity, mm (in)	.0000 (.0000)	.0575 (.0023)	.1149 (.0045)	.1724 (.0068)	.2299 (.0091)	.2873 (.0113)	.2873 (.0113)
C.G. Imbalance, mm-N (in-oz)	0.00 (0.00)	35.31 (5.00)	70.61 (10.00)	105.92 (15.00)	141.22 (20.00)	176.53 (25.00)	176.53 (25.00)
C.G. O'Clock Position	6	6	6	6	6	6	6
Projectile Axis Parallels Tube	NO	NO	NO	NO	NO	NO	YES
Bourrelet-Tube Contact	YES	YES	YES	YES	YES	YES	NO
Bourrelet Force, N (lbs)	1757 (395)	2460 (553)	3016 (678)	3500 (787)	3940 (886)	4350 (978)	4390 (987)
Lateral C.G. Force, N (lbs)	1855 (417)	2264 (509)	2545 (573)	2784 (626)	2989 (672)	3180 (715)	3220 (724)
Lateral Obturator Force, N (lbs)	1610 (362)	1463 (329)	1259 (283)	1059 (238)	970 (218)	1272 (286)	1272 (286)
Yaw Angle, radian	.00021	.00025	.00027	.00029	.00031	.00033	.00033
Yaw Velocity, rad/sec	.06	.07	.09	.09	.10	.11	.11
Normal Acceleration at C.G., gees	4.47	5.39	6.03	6.53	6.97	7.36	7.45
Normal Acceleration at Bourrelet Center							
Normal Acceleration at Point A	7.18	8.67	9.66	10.44	11.08	11.64	11.79
Normal Acceleration at Point F	7.65	9.23	10.30	11.13	11.81	12.41	12.57
Normal Acceleration at Point F	8.78	10.61	11.84	12.80	13.58	14.28	14.46

TABLE 5

PEAK VALUES OF BALLOTTING MOTION ANALYSIS
155mm Gun M198, XM712 CLGP

Cases of Korn Tube No. 83 and Spin 30 rps

Midpoint A to Base Distance is 111.89cm (44.050 inches)
Nose Point F to Base Distance is 130.94cm (51.550 inches)

Case No.	1	2	3	4	5	6	7
Bourrelet Diameter, cm	15.474	15.474	15.474	15.474	15.474	15.474	15.474
(in)	(6.092)	(6.092)	(6.092)	(6.092)	(6.092)	(6.092)	(6.092)
C.G. Eccentricity, mm	.0000	.0575	.1149	.1724	.2299	.2873	.2873
(in)	(.0000)	(.0023)	(.0045)	(.0068)	(.0091)	(.0113)	(.0113)
C.G. Imbalance, mm-S	0.00	35.31	70.61	105.92	141.22	176.53	176.53
(in-oz)	(0.00)	(5.00)	(10.00)	(15.00)	(20.00)	(25.00)	(25.00)
C.G. O'Clock Position	6	6	6	6	6	6	6
Projectile Axis Parallels Tube	NO	NO	NO	NO	NO	NO	YES
Bourrelet-Tube Contact	YES	YES	YES	YES	YES	YES	NO
Bourrelet Force, N	1481	2068	2602	3060	3474	3860	3892
(lbs)	(333)	(465)	(585)	(688)	(781)	(868)	(875)
Lateral C.G. Force, N	1521	1793	2077	2309	2504	2669	2709
(lbs)	(342)	(403)	(467)	(519)	(563)	(600)	(609)
Lateral Obturator Force, N	1419	1210	1000	800	970	1285	1285
(lbs)	(319)	(272)	(225)	(180)	(218)	(289)	(289)
Yaw Angle, radian	.00019	.00049	.00040	.00038	.00039	.00041	.00041
Yaw Velocity, rad/sec	.05	.11	.08	.08	.10	.11	.11
Normal Acceleration at C.G., gees	3.73	4.37	4.95	5.41	5.82	6.18	6.26
Normal Acceleration at Bourrelet Center	5.96	6.96	7.92	8.64	9.24	9.72	9.85
Normal Acceleration at Point A	6.34	7.41	8.44	9.21	9.85	10.36	10.50
Normal Acceleration at Point F	7.27	8.50	9.69	10.60	11.33	11.92	12.08

TABLE 6

PEAK VALUES OF BALLOTTING MOTION ANALYSIS
155mm Gun M198, XM712 CLGP

Cases of Land Diameter 154.99mm (6.102 in) and Spin 20 rps

Midpoint A to Base Distance is 111.89cm (44.050 inches)

Nose Point F to Base Distance is 130.94cm (51.550 inches)

Case No.	1	2	3	4	5	6	7
Bourrelet Diameter, cm	15.474	15.474	15.474	15.474	15.474	15.474	15.474
(in)	(6.092)	(6.092)	(6.092)	(6.092)	(6.092)	(6.092)	(6.092)
C.G. Eccentricity, mm	.0000	.0575	.1149	.1724	.2299	.2873	.2873
(in)	(.0000)	(.0023)	(.0045)	(.0068)	(.0091)	(.0113)	(.0113)
C.G. Imbalance, mm-N	0.00	35.31	70.61	105.92	141.22	176.53	176.53
(in-oz)	(0.00)	(5.00)	(10.00)	(15.00)	(20.00)	(25.00)	(25.00)
C.G. O'Clock Position	6	6	6	6	6	6	6
Projectile Axis Parallels Tube	NO	NO	NO	NO	NO	NO	YES
Bourrelet-Tube Contact	YES	YES	YES	YES	YES	YES	NO
Bourrelet Force, N	1757	2455	3007	3492	3932	4341	4377
(lbs)	(395)	(552)	(676)	(785)	(884)	(976)	(984)
Lateral C.G. Force, N	1855	2228	2486	2691	2860	3020	3060
(lbs)	(417)	(501)	(559)	(605)	(643)	(679)	(688)
Lateral Obturator Force, N	1610	1437	1214	979	1037	1321	1325
(lbs)	(362)	(323)	(273)	(220)	(233)	(297)	(298)
Yaw Angle, radian	.00021	.00024	.00027	.00029	.00031	.00033	.00033
Yaw Velocity, rad/sec	.06	.07	.09	.09	.10	.11	.11
Normal Acceleration at C.G., gees	4.47	5.34	5.91	6.37	6.75	7.09	7.17
Normal Acceleration at							
Bourrelet Center	7.18	8.60	9.54	10.26	10.85	11.36	11.51
Normal Acceleration at Point A	7.64	9.17	10.17	10.94	11.56	12.11	12.27
Normal Acceleration at Point F	8.78	10.53	11.69	12.58	13.29	13.93	14.11

clearance between the gun tube and the bourrelet. This is also true for projectiles with ordinary rotating bands [1, 2, 3, 4]. The effect of worn tubes on the peak values is small in this analysis compared to the large effect experienced for projectiles with ordinary rotating bands. This minimal effect is due to the reduction in the spin rate resulting from slippage between the gun tube and the obturator. Thus degradation of the spin rate acts to reduce the centrifugal force at the c.g., which in turn reduces the balloting motion. With small balloting motion the effect of a worn tube becomes small. Furthermore, the wear of the worn tube is moderate from the breech to about 70 inches (177.8cm) from the muzzle but severe near the muzzle. The base pressure is high near the breech but low near the muzzle. This combined influence tends to make the worn tube effect on the peak values not so evident as those on projectiles with a rotating band. However the effect of the worn tube on the variations of the various quantities are prominent as seen from a comparison of curves of new and worn tube cases as shown in Figures 7 to 18.

The effect of initial projectile orientation can be seen by comparing the cases having the gun tube in contact with the bourrelet with that of a projectile positioned parallel to the gun tube. This may be seen in cases 6 and 7 of each category. The peak values are not significantly influenced by whether the projectile is initially parallel to the gun tube or contacting the tube.

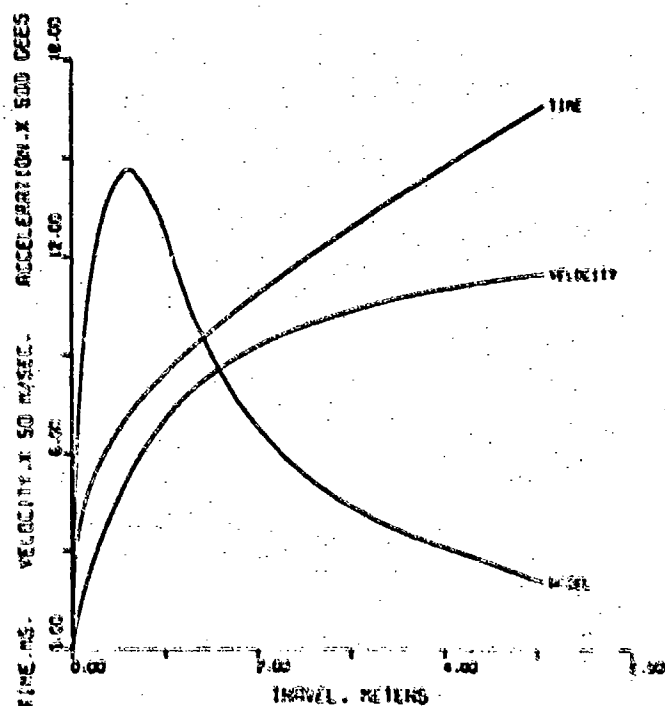
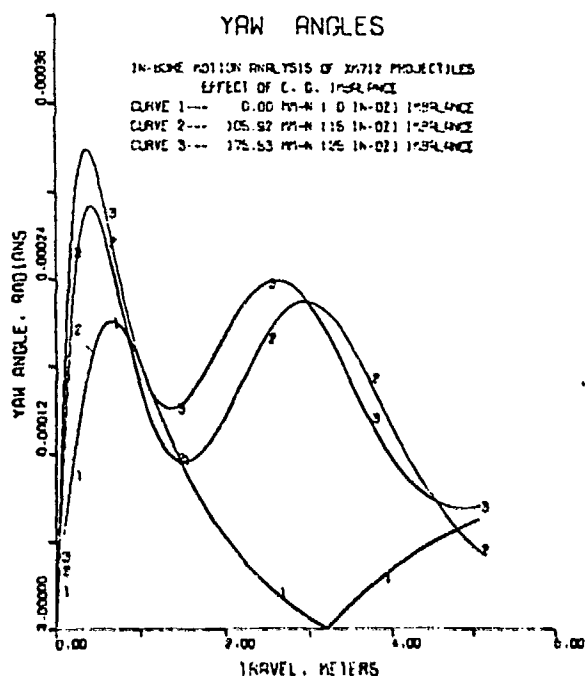
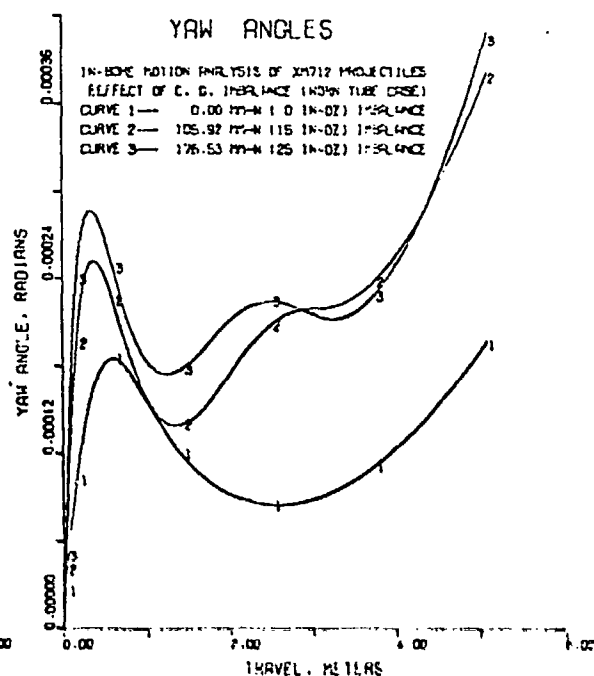


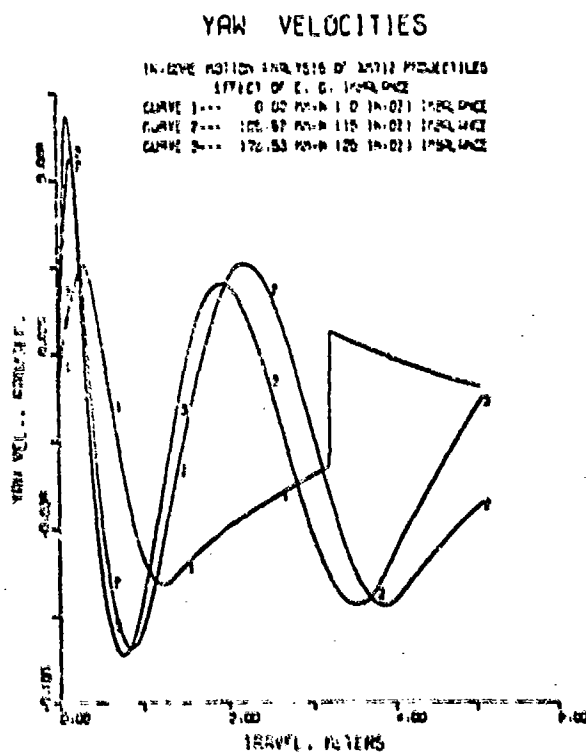
FIGURE 6. Computed Time, Velocity and Acceleration vs. Travel



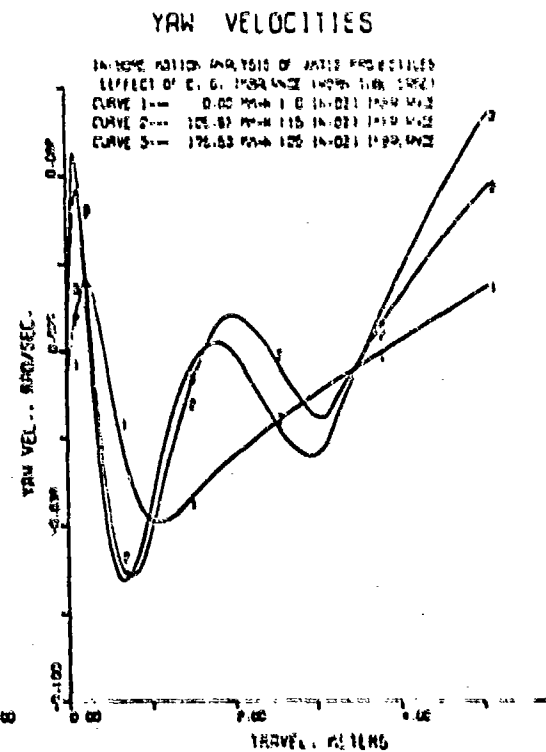
**FIGURE 7. Yaw Angles, New Tube,
Spin 30 rps**



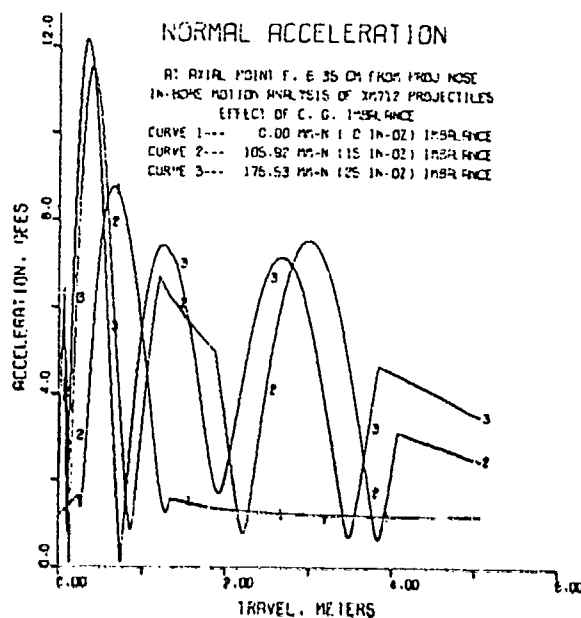
**FIGURE 8. Yaw Angles, Worn Tube,
Spin 30 rps**



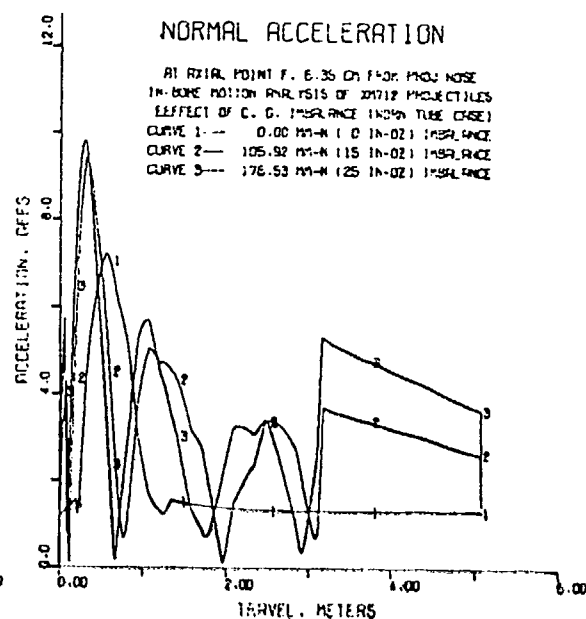
**FIGURE 9. Yaw Velocities, New Tube
Spin 30 rps**



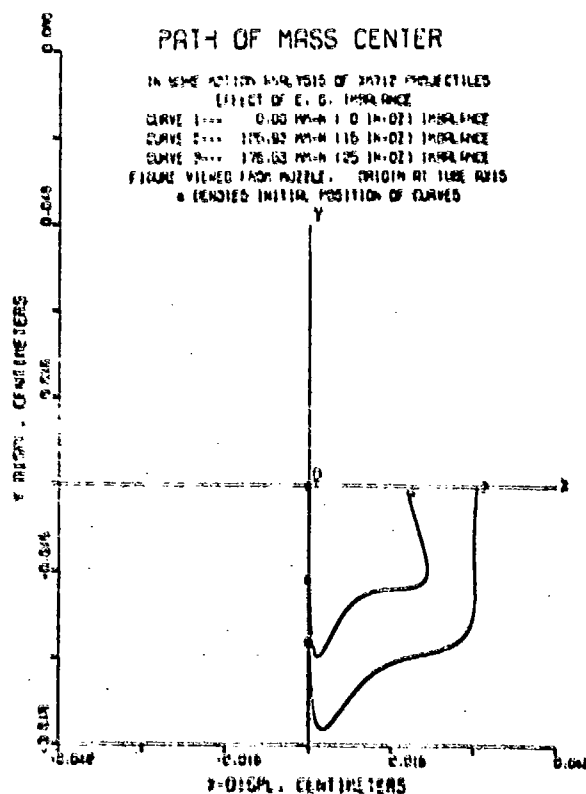
**FIGURE 10. Yaw Velocities, Worn Tube
Spin 30 rps**



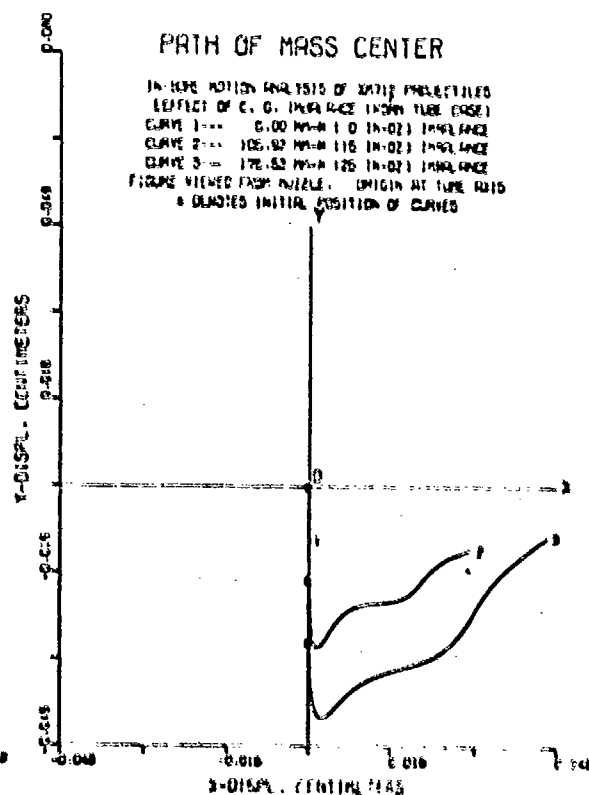
**FIGURE 11. Normal Accelerations
New Tube, Spin 30 rps**



**FIGURE 12. Normal Accelerations
Worn Tube, Spin 30 rps**



**FIGURE 13. Path of Mass Center,
New Tube, Spin 30 rps**



**FIGURE 14. Path of Mass Center,
Worn Tube, Spin 30 rps**

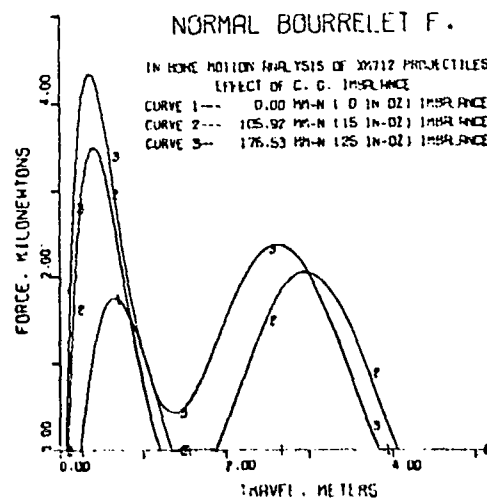


FIGURE 15. Normal Bourrelet Forces,
New Tube, Spin 30 rps

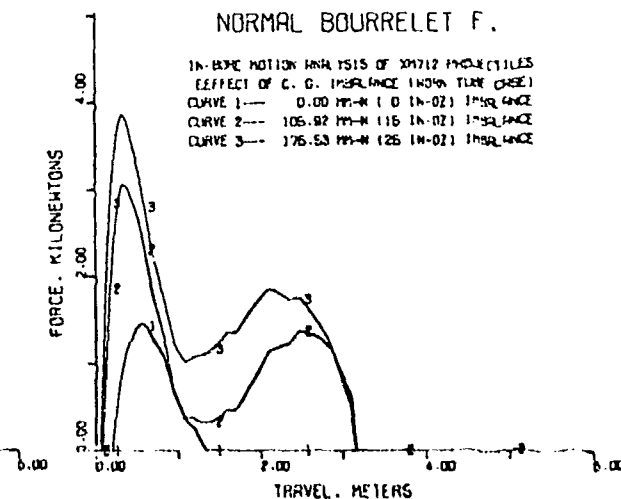


FIGURE 16. Normal Bourrelet Forces,
Worn Tube, Spin 30 rps

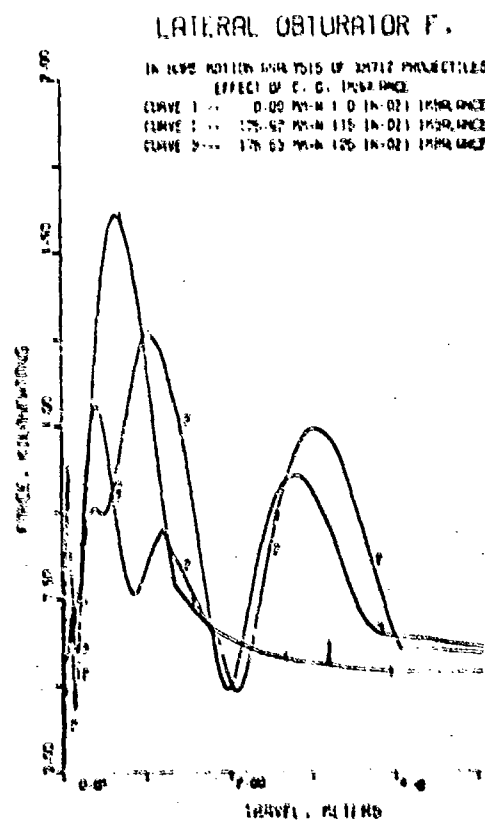


FIGURE 17. Lateral Obstructor Forces,
New Tube, Spin 30 rps

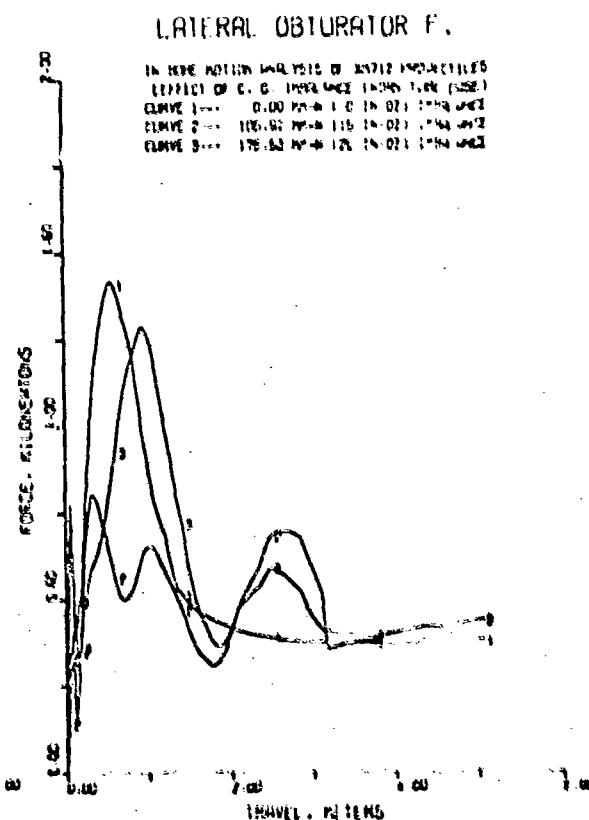


FIGURE 18. Lateral Obstructor Forces,
Worn Tube, Spin 30 rps

CONCLUSIONS

Based on the results of computations and discussions, it is seen that the balloting motion of the XM712 projectile is not severe. The peak values and the variations of motion are much less than those of projectiles having a rotating band. The approximate maximum peak values are as follows.

Bourrelet contact force	990 lbs (4400 N)
C.G. lateral inertial force	720 lbs (3200 N)
Obturator lateral force	300 lbs (1330 N)
C.G. normal acceleration	8 g's
Bourrelet center normal acceleration	12 g's
Axial point A (44.05 in or 111.89 cm to base) normal acceleration	13 g's
Axial point F (51.55 in or 130.94 cm to base) normal acceleration	15 g's
Yaw angle	.0005 rad.
Yaw velocity	.11 rad/sec
Cross spin rate	.11 rad/sec

The effects of increase in the bore diameter and the c.g. eccentricity are prominent. The increase of the c.g. imbalance from 0 to 15 (specifically 10 in some cases) in-oz or 0 to 105.9 (especially 70.6 in some cases) mm-N causes a considerable change in balloting but lesser variations when it is further increased to 25 in-oz or 176.5 mm-N. An increase in the bore diameter causes less variation in the motion pattern but rather large increases in the amplitude or magnitude of the motion.

The effect of the tube wear is such as to produce more fluctuations in the balloting motion as shown by the curves of worn tube cases. The change in the peak values however is small.

The effect of the initial position of the projectile, whether it is parallel to the gun tube or contacting the tube at the bourrelet, is small.

ACKNOWLEDGEMENTS

The author would like to express his special appreciation to Mr. Larry Rosendorf for his helpful suggestions and encouragements, Mr. Robert Salamon for his advice and assistance in manuscript preparation, Messrs. Spero Nicholasides and Carl Gardner for their invaluable experimental work, and Mrs. Barbara Catillo for her patience in typing the manuscript.

REFERENCES

1. Chu, S. H. and Soechting, F. K., "Transverse Motion of an Accelerating Shell," Technical Report 4314, Picatinny Arsenal, Dover, NJ, June 1972.
2. Chu, S. H., "Transverse Motion of 8 Inch Projectile, XM673, Inside XM210, M2A2 Gun Tube, MK-16 and MCLG Gun," Technical Memorandum TM2103, Picatinny Arsenal, Dover, NJ, August 1973.
3. Chu, S. H., "Transverse Motion of Eight Inch Projectile XM753 in Gun Tube XM201," Technical Report 4918, Picatinny Arsenal, Dover, NJ, December 1975.
4. Chu, S. H., "Balloting Motion of an Accelerating Shell," Preprints of papers to be presented at the Fuze/Munitions Environment Characterization Symposium II, pp 648-670, US Army Armament Command, Picatinny Arsenal, Dover, NJ, 7-9 October 1975.

IMPACT OF ROCK PROJECTILES ON A SIMPLY SUPPORTED BEAM

RONALD L. MANN
Consulting Engineer
General Electric Company
Electronic Systems Division
Syracuse, New York 13221

RICHARD W. PERKINS
Professor of Mechanical Engineering
Syracuse University
Syracuse, New York 13210

ABSTRACT

An impact apparatus was developed for firing regular and irregular-shaped rock projectiles. Sedimentary and igneous rock projectiles were fired at the center of a simply supported aluminum beam in a series of impact tests. The experimental investigation was conducted to determine: dynamic response of the beam, localized permanent deformation of the beam in the region of impact, and fracturing behavior of weak and strong sandstone. Strain gages attached to the beam, disclosed that each rock material upon impact exhibits its own mechanical signature. 16-mm high speed films of the impact process, provided valuable projectile and beam displacement data both during and after impact. The experimental data were invaluable to the subsequent development of analytical models which approximate the dynamic behavior of a rock projectile-beam system.

INTRODUCTION

Many of the radars associated with missile defense are "hardened" to withstand nuclear weapon environments. For a nuclear weapon explosion classified as a surface burst, large amounts of soil and rock debris are carried up from the earth's surface into a radioactive cloud [1]. A crater produced in dry soil at ground zero, as a result of the explosion of a 20 megaton weapon is approximately 3000 ft (914 m) in diameter and 300 ft (91.4 m) deep [2]. The crater size will be somewhat less in sandstone and granite. The quantity and size of rock debris which can rain down from the radioactive cloud, on a hardened radar structure in the vicinity of the explosion, can be of major significance in the design of these structures.

During the past decade a new member has been added to the radar family, the phased-array radar. This radar differs from the conventional rotating parabolic dish antenna, in that it is electronically steerable, and does not require moving parts. Phased-array radars are characterized by large numbers of antenna elements mounted to the front face of a flat support structure.

Only a limited amount of debris impact work has been performed during the past several years. The majority of the work has been in the area of failure of antenna element ceramic windows. Presently there is an interest not only in individual antenna elements, but in the response of the array face structure to rock debris impact. Satisfactory radar performance requires that one be concerned with array face vibration, localized indentation, embedding of rock in the array face and total penetration of the structure.

Experimental investigations were performed to study the impact of rock projectiles on a simply supported beam. Projectiles used in the study included sedimentary and igneous rock materials having both regular and irregular shapes. Projectiles had a range of impact velocity sufficiently high to cause severe fracturing to the sedimentary rock group. Projectile initial kinetic energies were limited, so that the beam would only experience localized permanent deformation in the form of an indentation at the point of impact.

High speed film and beam strain gage data provided the crucial measurements necessary to the understanding of this complex impact problem. This data contributed significantly to the development of analytical models, for impact of fracturing and nonfracturing rock with a simply supported beam.

ROCK MATERIALS TESTED

The materials selected for the impact study included both sedimentary and igneous rocks. Two types of fine grained sandstone, and a high strength gabbro, were used for the projectiles. Indiana sandstone which is classified as a weak rock [3] in that it has a uniaxial compressive strength less than $10,000 \text{ lb/in.}^2$ (70.3 MPa), was selected for two reasons. First, it is desirable to include rocks in the study which would experience severe fracturing without inducing plastic deformation of the beam, other than local deformation at the point of contact. Secondly, this sandstone

exhibited good machining qualities which facilitated the grinding of a number of samples into a grouping having the same shape and mass. This made it possible to conduct a series of controlled impact tests where velocity was the only variable.

Indiana sandstone which can be classified as fine grained, quite porous, and not well cemented sandstone bonded with a silica cementing agent. This sandstone is reddish-brown in color. The higher strength sandstone is also a fine grained substance, composed almost entirely of pure quartz. This sandstone is light tan in color. This material is fairly porous. However, it is not as porous as the Indiana sandstone. The quartz grains are also bonded together with a silica cement.

Gabbro is a coarse-grained igneous rock, which is greenish-black in color. This gabbroic material is primarily feldspar and does not contain quartz. Granite is quite similar to gabbro in that it is a coarse-grained igneous rock. However, it contains a minimum of 5% quartz in addition to feldspar [4].

Hardness tests were made on all rock materials using the Rockwell Superficial Hardness Tester. The light areas on a polished surface of the gabbro had a hardness of 96, while the dark areas measured 92. The hardness of the high strength sandstone was found to be 77. It was not possible to obtain a hardness for the Indiana sandstone because the surface would tend to crumble upon application of the load.

Uniaxial compression tests are frequently used to evaluate rock strength [5]. The standard test uses regular shaped specimens, such as cubes, prisms or cylinders. The 1.0 in. (2.54 cm) Sandstone samples were prepared in the shape of a cube in accordance with the procedure of reference [6]. The sandstone specimens upon being subjected to a compressive load were observed to experience axial splitting. The mechanical properties obtained from these tests are given in Table 1.

Table I. Mechanical Properties of Sandstone

Sandstone <u>Type</u>	<u>Compressive Strength</u>		<u>Modulus of Elasticity</u>	
	<u>(lb/in.²)</u>	<u>MPa</u>	<u>(lb/in.²)</u>	<u>MPa</u>
Indiana	4000	28	0.58×10^6	4080
High Strength	11400	80	1.03×10^6	7240

PREPARATION AND CLASSIFICATION OF PROJECTILES

In order to have each projectile consistently impact the beam within 0.250 in. (0.64 cm) of the center position at a desired velocity, it was necessary that it have an almost perfect fit with the 1.0 in. (2.54 cm) inside diameter gun barrel. The normal polyethylene sabot, used for a housing on symmetrical bodies such as cylinders and spheres, could not conveniently be used in this instance. The only feasible way to control rock projectile trajectory, motion and velocity was to encapsulate the projectile in a material having a cylindrical base as shown in Figure 1. Plaster of Paris was found to be most suitable for this application. This potting material is easily prepared, adheres quite well to rock specimens, conforms well with a cylindrical mold, and provides for minimum friction with the gun barrel.

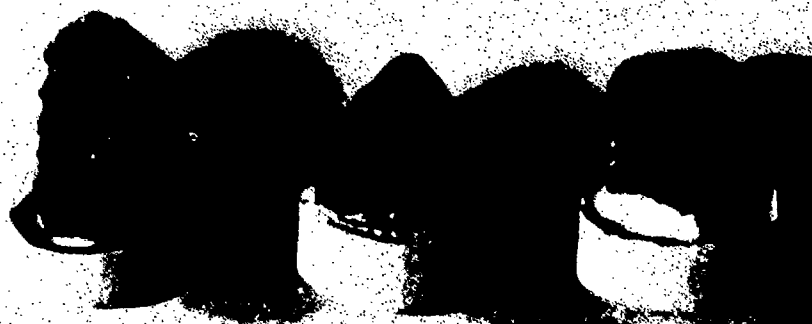


Figure 1. Projectiles Encapsulated in Plaster of Paris

A rock projectile classification has been developed which characterizes irregular 1.0 in. (2.54 cm) rock with regard to shape. This classification is illustrated in Figure 2. The ideal boundary shown in this figure is an outline of the desired projectile profiles. A tolerance zone has been applied to the surface to allow for natural surface irregularity and roughness, which is indeed characteristic of rock.

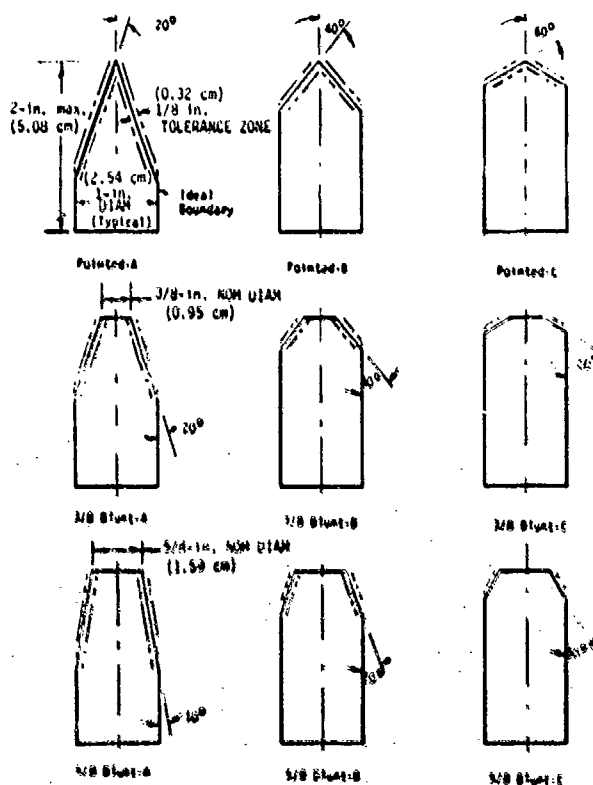


Figure 2. Rock Projectile Classification

IMPACT TEST APPARATUS

Rock projectiles are fired against a simply supported beam using the air gun apparatus shown in Figure 3. The air gun is energized by a 3-in. diameter pressure chamber supplied with air through a fitting at the right and an electrically operated solenoid valve at the other end. This valve separates the pressure vessel from the 25-in. (63.5 cm) gun barrel which has a 1.0 in. (2.54 cm) inside diameter. The switch controlling power to the solenoid valve is mounted at the left end of the apparatus. The simply supported 6061T6 aluminum beam which measures 0.125 in. x 1.00 in. x 18.00 in. (0.32 cm x 2.54 cm x 45.7 cm), is supported with 0.015-in. (0.038-cm)

thick stainless steel column supports. This type of support was used by Goldsmith [7] because the connection approaches that of an ideal simple support.

The horizontal beam projects through both sides of a protective plexiglass housing. This housing serves a number of functions in addition to the most important one being operator protection. It provides a means of capturing all material which may break away from the projectile should severe fracturing occur. In addition, it provides a support for two photocells which are used to measure projectile velocity just prior to impact.

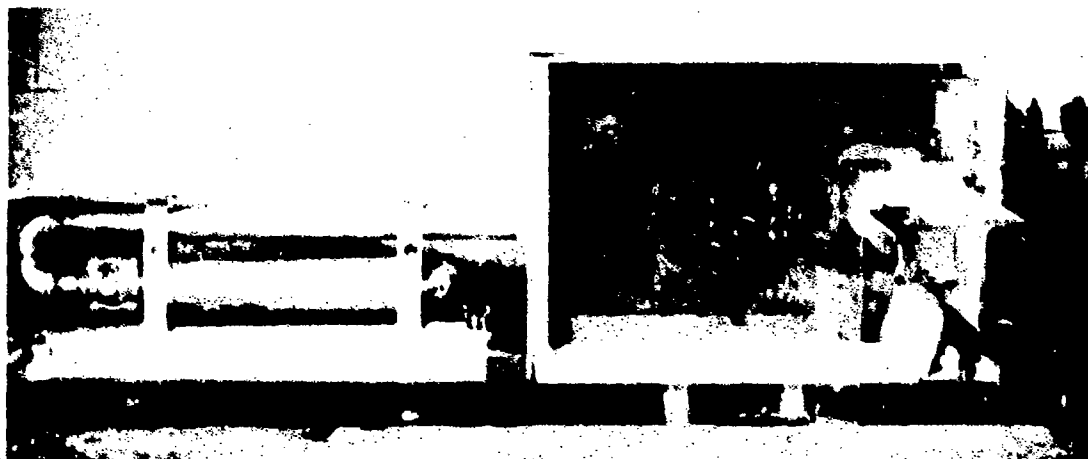


Figure 3. Apparatus Used to Investigate Impact Behavior of Rock Debris with a Simply Supported Beam

Figure 4 shows cross wires connected to terminals positioned above and below one of the photocells. The lower wire located in the projectile path makes contact with the upper wire and triggers the sweep of the oscilloscope. These wires are extremely light and have a negligible effect on projectile trajectory and velocity.

In order to protect the center of the beam in the contact region, 0.250 in. x 1.0 in. x 1.0 in. (0.32 cm x 2.54 cm x 2.54 cm) 6061T6 aluminum contact plates were used. These plates are securely fastened to the beam with four 6-32 flathead screws. After each test, one simply replaces the indented contact plate. This avoids the need for the complete replacement of a beam instrumented with strain gages.

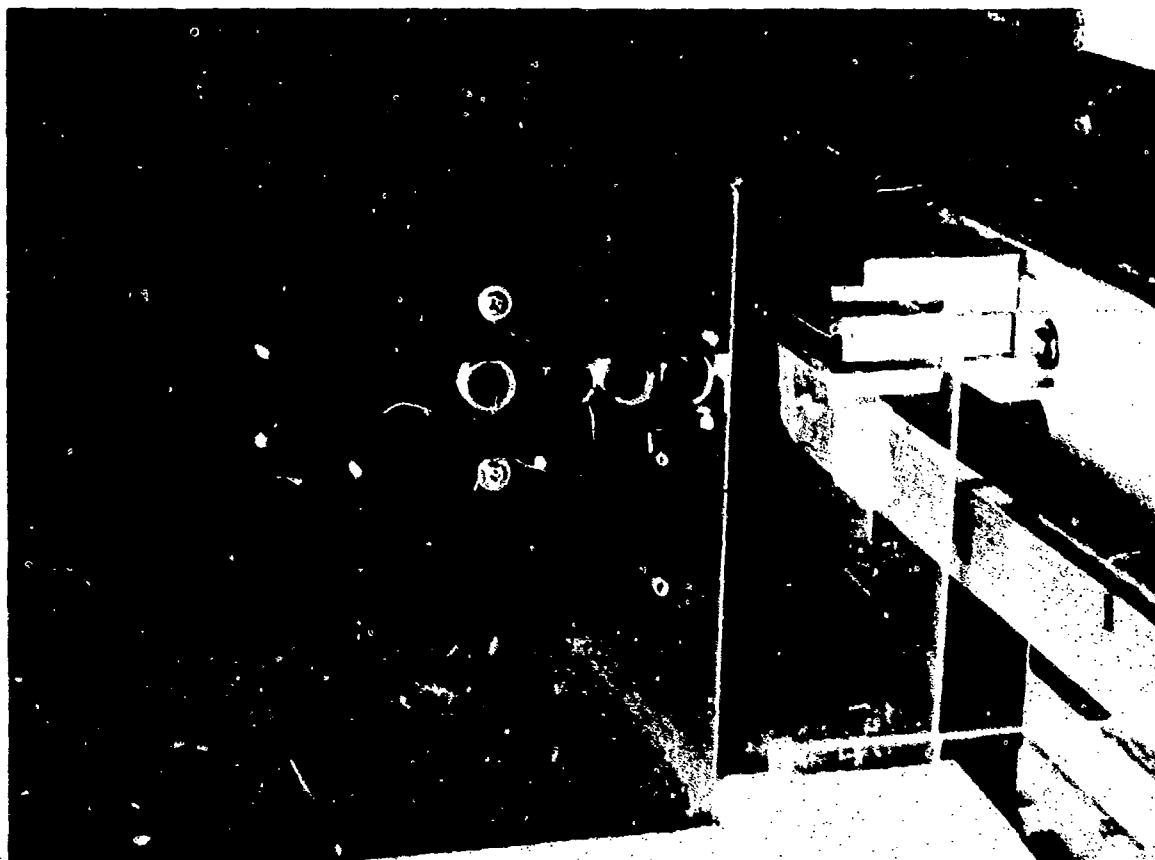


Figure 4. Impact Test Area

IMPACT TEST METHOD

The camera used for the impact studies was a 16-mm Fastax, Type WF3 (see Figure 5). This camera has a maximum speed of 8000 frames/s upon application of 280 V. A control unit is normally used for filming at speeds greater than 4000 frames/s. This equipment contains a time delay circuit which permits the camera to accelerate at low voltage before application of the high voltage required to attain a desired speed [8]. The timing circuits of this control unit were particularly valuable in that, one timer controlled power to the cameras while the other regulated power to the event, the event being firing of the air gun. By setting a suitable time delay between timers, it was possible to achieve desired film speed before firing the gun. The majority of the high speed films were taken at just under 6000 frames/s.

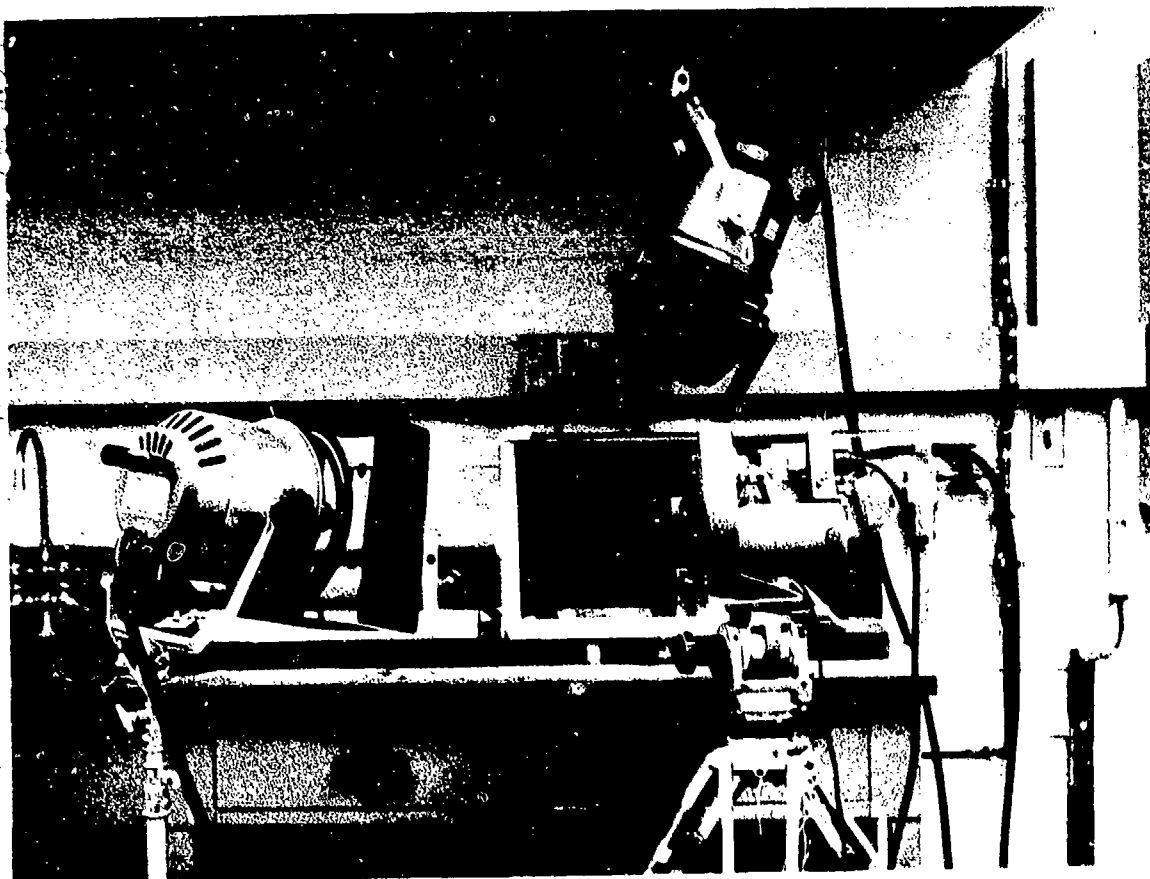


Figure 5. High Speed Camera and Associated High Intensity Lamps

A schematic representation of the impact test apparatus and associated instrumentation is given in Figure 6. A storage oscilloscope was used to record one channel of strain gage data and two channels of photocell data. The oscilloscope was triggered by feeding an 18-V dc signal to the "EXTERNAL TRIGGER IN" connector on the oscilloscope. This trigger was initiated when the projectile caused the cross wire within the test area enclosure to make contact. Strain gage data was also obtained using an oscillograph recorder. This equipment was used to record long-time beam exposure.

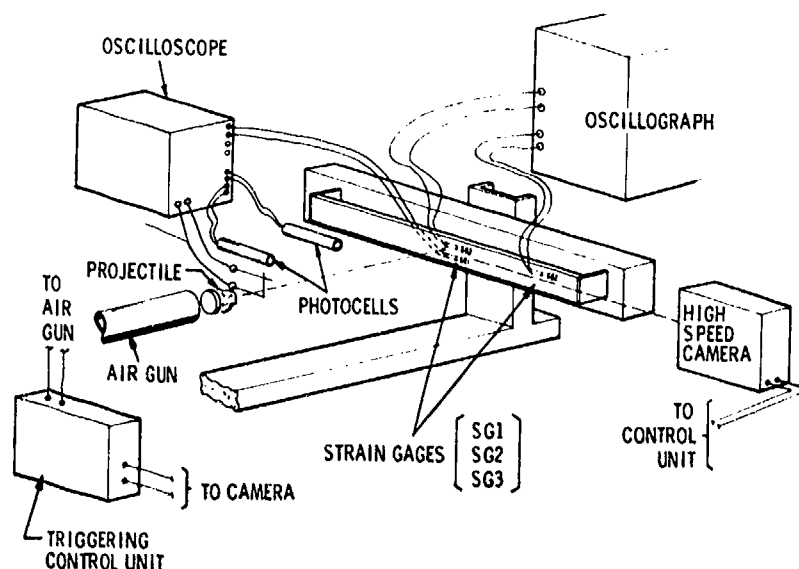


Figure 6. Impact Test Apparatus and Instrumentation

RESULTS OF IMPACT EXPERIMENTS

The experimental studies provided the crucial measurements necessary to the understanding of the rock-beam process. The high speed films were truly invaluable to the understanding of this complex phenomenon. The high-speed film quality was good and it facilitated plotting beam center displacement as a function of time. It was possible to plot 82 frames of beam displacement for one cycle of first-mode beam vibration. For projectiles which did not fracture upon impact, it was possible to track their motion, detect multiple impact and determine time of occurrence and duration of the primary and secondary impacts. For projectiles which fractured it was possible to measure projectile shortening on a frame-by-frame basis, as material spalled away from its contacting surface. The dynamic strain gage data revealed that each rock projectile of a given material exhibits its own unique characteristic shape or mechanical signature.

IMPACT BEHAVIOR OF INDIANA SANDSTONE

Figure 7 shows five 16-mm frames of the impact process for projectile 11. S. For this test the film speed was 5760 frames/s. Frame 1 shows the projectile approaching the beam at a velocity of 1330 in./s (33.8 m/s). Frame 2 shows the projectile making initial contact with the beam impact plate. Frames 3 through 5 are the

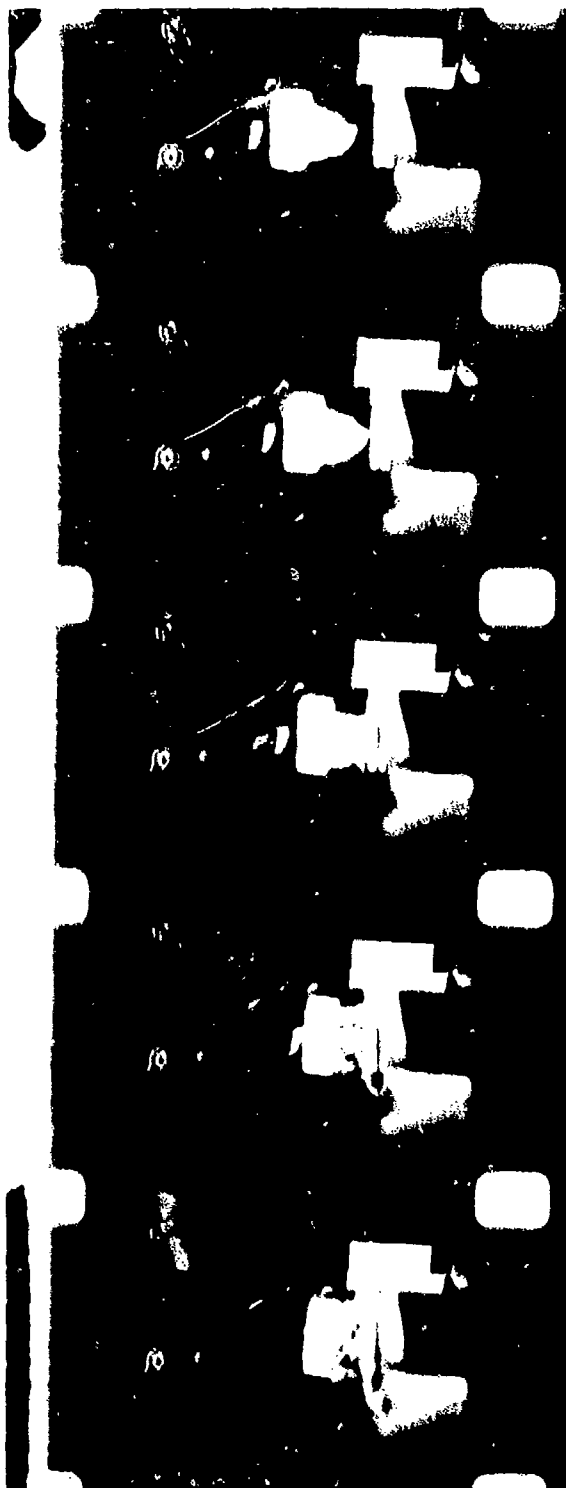


Figure 7. Indiana Sandstone Projectile (11. S.) Impacting Beam (Projectile Velocity 1330 in. /s (33. 8 m/s) Film Speed 5760 Frames/s)

frames of major contact force between the fracturing projectile and the beam. A measurement of projectile shortening, as a result of loss of material at the contact point, shows the following: frame 3 [0.18 in. (0.46 cm)], frame 4 [0.12 in. (0.30 cm)], and frame 5 [0.06 in. (0.15 cm)]. This film indicates the contact time for sample 11.S. is approximately 0.50 ms. This time coupled with negligible contact plate surface damage would indicate that the impulse has a peak contact force of relatively small magnitude and long time duration.

A plot of beam displacement at the contact point vs frame number or time is given in Figure 8. Frames 5, 14, and 22 in this figure show the first few peak values of third mode vibration. The period associated with the 3rd mode contribution to the total vibration is 1.58 ms. Data points between frames 28 and 33 are missing due to the masking of debris passing over the beam. It should also be noted that a second impact took place at frame 45.

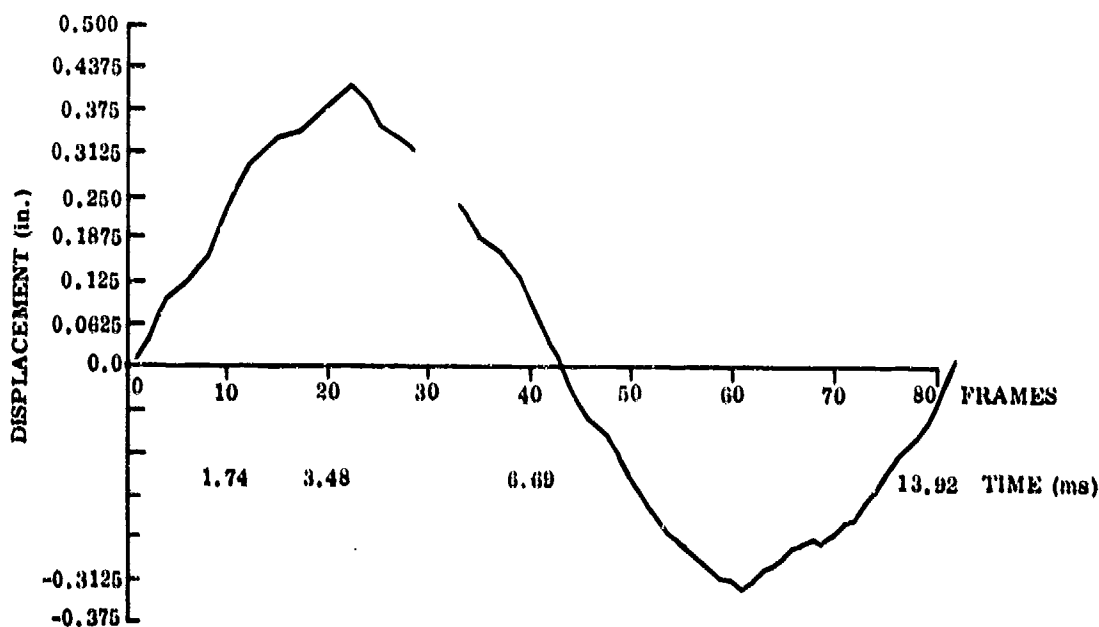


Figure 8. Beam Response to Impact with Indiana Sandstone Projectile (11. S.)

The Indiana sandstone has a fracturing behavior quite different from that of the higher strength sandstones. At velocities as high as 1100 to 1200 in./s (27.9 to 30.5 m/s) the projectile experiences spalling completely around the area of contact. This spalling or flaking away at the surface can be seen in Figure 9 for test samples 8 I. S.

and 10 I.S. It should be noted that these projectiles have been ground to a regular ovigal shape. In addition to the larger flakes of sandstone one can observe a considerable amount of pulverized material. Both contact plates show small amounts of embedded material. This material can easily be wiped away by lightly rubbing the surface.

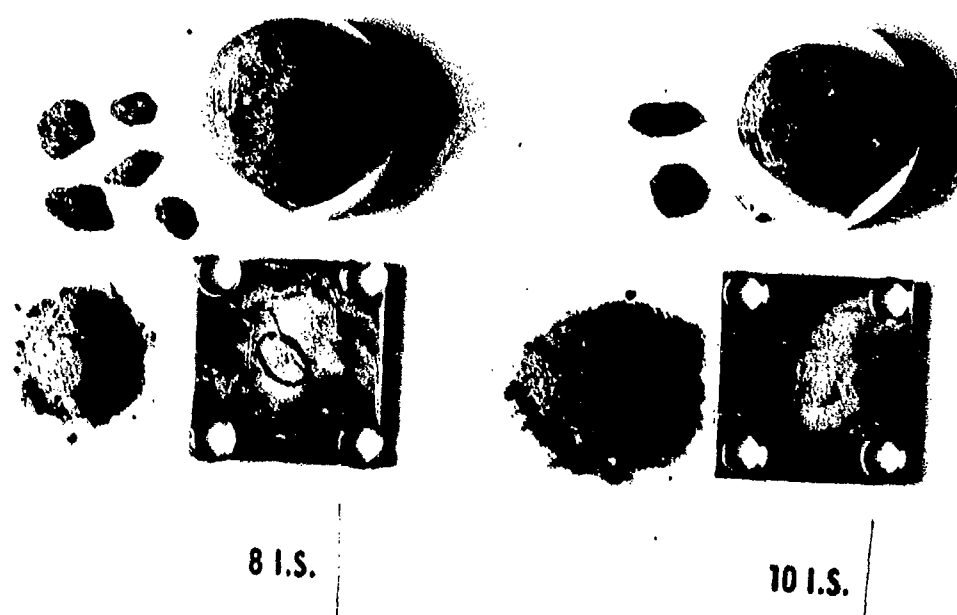


Figure 9. Indiana Sandstone Projectiles Showing Surface Spalling and Pulverized Material

IMPACT BEHAVIOR OF FINE GRAINED, HIGH STRENGTH SANDSTONE

The harder sandstones exhibit a rather interesting behavior upon impact with an aluminum beam. This type of sandstone leaves a permanent indentation in the contact plate. In addition, a conical shaped mound of the rock material remains permanently embedded in the plate. Figure 10 shows rock specimens for 5S and 6S along with the respective contact plates. Sample 5S exhibits the characteristic fracture that occurs for projectile velocities above 1000 in./s (25.4 m/s). One can see the conical shaped cavity both radially and longitudinally through the sample. Figure 10 shows a side view of the contact plate with the embedded conical rock. This contact plate was potted in a hysol epoxy and sectioned. Figure 11 is a 50X photomicrograph that shows a partial

IMPACT BEHAVIOR OF GABBRO

Representative indentations which resulted from the impact of gabbro projectiles with the aluminum beam are shown in Figure 12. The contact plate indentation caused by sample 2G is elliptically shaped and measures 0.18 in. x 0.12 in. (0.46 cm x 0.30 cm) while that associated with 3G is D-shaped, measuring 0.18 in. x 0.15 in. (0.46 cm x 0.38 cm). The maximum crater depths are 0.013 in. (0.033 cm) and 0.016 in. (0.041 cm) respectively for 2G and 3G. The indented surface which resulted from 3G clearly shows a replica of the undulations of the contact surface of the projectile.

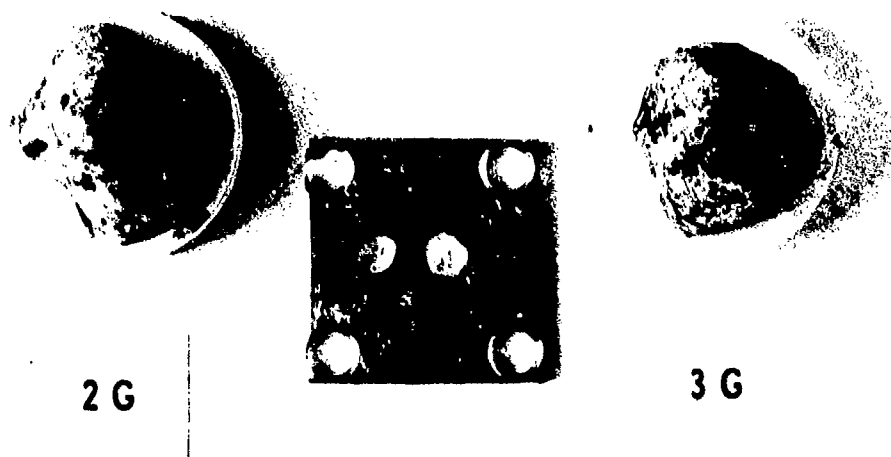


Figure 12. Intact Gabbro Projectiles and Indented Contact Plate [Projectile Velocities for 2G and 3G are 868 in./s (22.0 m/s) and 970 in./s (24.6 m/s)]

Both projectiles experienced a secondary impact upon rebound of the beam. This secondary impact reduces the maximum negative displacement of the beam which occurs at frame number 60 in Figures 13 and 14. Both curves shown significant 3rd mode contribution to the total displacement as well as evidence of 5th mode participation.

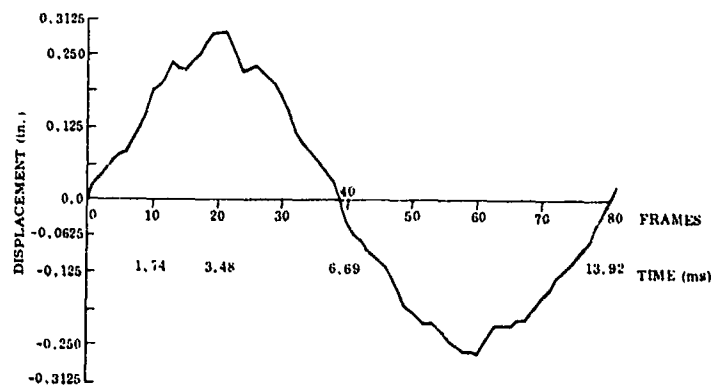


Figure 13. Beam Response to Impact with Gabbro Projectile 2G

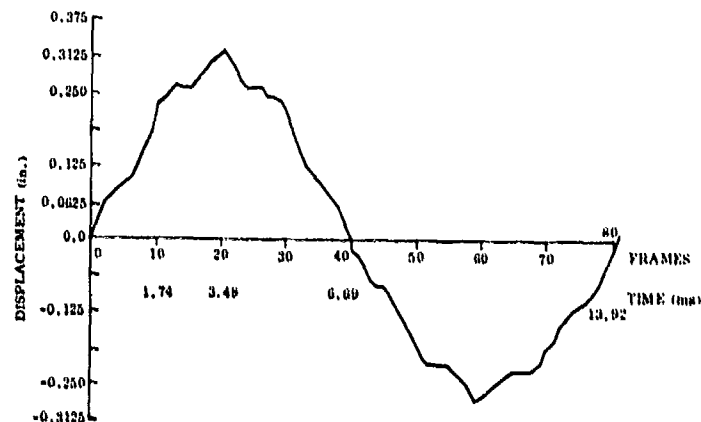


Figure 14. Beam Response to Impact with Gabbro Projectile 3G

COMPARISON OF ROCK-BEAM IMPACT BEHAVIOR

In addition to the extremely valuable 16-mm high speed film data, strain gage data was obtained for each impact experiment. Strain data at the center of the beam is equally as important, since it provides additional information that cannot be deduced from the film data.

After collecting strain data for each material treated in this investigation it became apparent that each material exhibited its own characteristic dynamic strain response, or mechanical signature. A comparison of beam strain response, to each of rock material tested, is presented in Figure 15. The strain response to Indiana sandstone projectile 11.S. is given for approximately 7.0 ms, which is one-half the

section of the permanently deformed surface. The local variations along the profile are due to the deeper penetration of the hard silica grains of the sandstone. Figure 10 also shows a mound of embedded sandstone for 6S. The outline with the plate surface in this case is triangular.

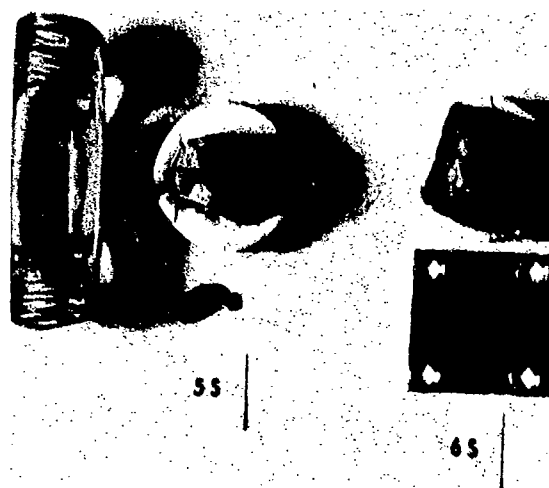
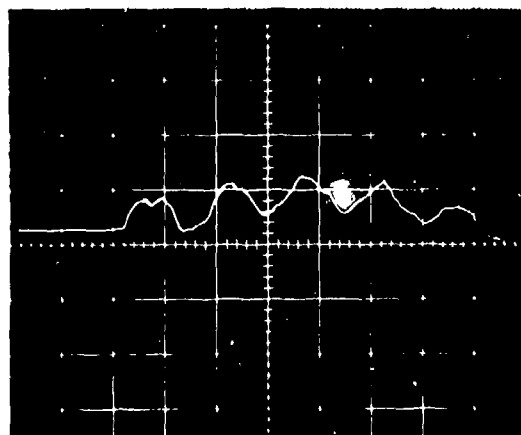


Figure 10. High Strength, Fine Grained Sandstone Projectiles Following Impact (Impact Plate of (5S) Potted and Sectioned)

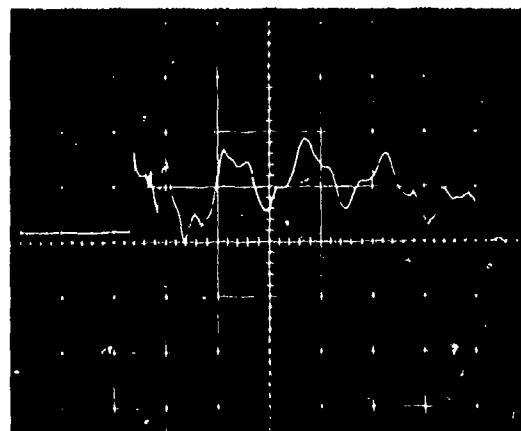


Figure 11. Photomicrograph (50X) Showing Partial Section of Indentation

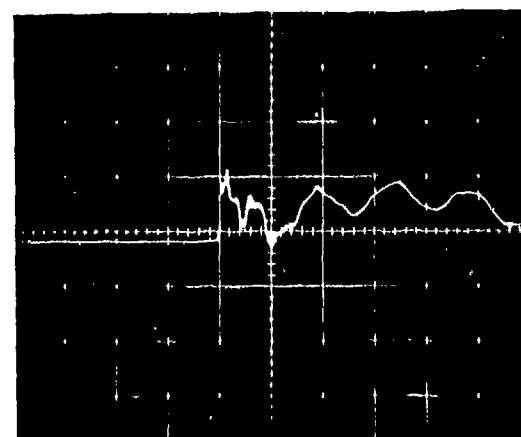
STRAIN



1 I.S.
 STRAIN: 2000 $\mu\text{s}/\text{DIV}$
 TIME: 1.0 ms/DIV
 MASS: 0.000087 $\text{lb} \cdot \text{s}^2/\text{in.}$ (15.23 g)
 VELOCITY: 1330 in./s (33.8 m/s)



1 G
 STRAIN: 1000 $\mu\text{s}/\text{DIV}$
 TIME: 1.0 ms/DIV
 MASS: 0.000108 $\text{lb} \cdot \text{s}^2/\text{in.}$ (18.9 g)
 VELOCITY: 720 in./s (18.3 m/s)



4 S
 STRAIN: 1000 $\mu\text{s}/\text{DIV}$
 TIME: 1.0 ms/DIV
 MASS: 0.000097 $\text{lb} \cdot \text{s}^2/\text{in.}$ (17.0 g)
 VELOCITY: 788 in./s (20.0 m/s)

TIME

Figure 15. Beam Strain Response Due to Impact with Indiana Sandstone (1 I. S.), Gabbro (1 G) and High Strength Sandstone (4 S)

fundamental period of the beam. The periods associated with the 1st, 3rd, 5th and 7th normal modes of vibration of the beam are 14.2, 1.58, 0.56 and 0.289 ms respectively. The first few milliseconds for each response is the zero-strain reference, which commences when the cross wires in the path of the projectile touch, thus triggering the time sweep of the oscilloscope. The strain record for 1I. S. indicates a rather -slow increase in strain during the first 0.4 ms following contact. This behavior is characteristic of all Indiana sandstone projectiles tested. It is the result of an impulse upon impact, which has a small peak contact force and a long-time duration of loading. The response primarily exhibits 1st and 3rd mode participation. Modal participation can be deduced from the strain time response by observing the time interval between major peak values.

The strain response due to impact with gabbro projectile 1G has an entirely different behavior. Within 0.100 ms following contact, the strain at the center of the beam is over 1500 microstrains. In the first millisecond one can observe significant 5th mode participation as well as some evidence of 7th mode. This response, with considerable high frequency content, is due to an impulse with a large peak force having a short time of contact. The maximum strain for 1I. S. is 2000 microstrains, compared with 1700 microstrains for 1G. However, note that the initial kinetic energy of the projectile for 1I. S. was almost 3 times that of 1G.

Figure 15 also gives strain response of the beam upon impact with sandstone projectile 4S. This material exhibits an early time behavior similar to the gabbro. After an initial period of 0.60 ms, the strain behavior appears quite similar to that of the Indiana sandstone. Although this material is not as hard or strong as the gabbro, it has a compressive strength of three times that of the Indiana sandstone. It should therefore be able to develop a fairly high contact force upon impact before fracturing. Secondary impacts occur once fracturing begins. Significant pulverization takes place along the circumferential edges surrounding the embedded mound of sand. These secondary impulses tend to be of longer time duration with a significantly reduced magnitude.

ANALYTICAL MODEL

A method was developed for predicting the dynamic response of the projectile - beam system. The problem was divided into three areas: (1) Prediction of beam motion, (2) Prediction of projectile motion, and (3) Prediction of force interaction between the beam and the projectile including effects of localized plastic deformation of the beam and projectile, and fracture of the projectile.

The motion of the beam can be conveniently studied using the normal mode method [9]. For the case of the simply supported beam which was studied, the characteristic mode shapes are given by

$$\phi_n(x) = \sin \frac{n\pi x}{l} \quad (1)$$

where l represents the length of the beam and $n = 1, 2, \dots, \infty$. For this analysis the mass of the contact plate was neglected, being less than 3 percent of the total mass of the beam. The undamped natural frequencies are given by

$$\omega_n = \frac{n^2 \pi^2}{l^2} \sqrt{\frac{EI}{m}} \quad (2)$$

where EI is the flexural rigidity and m is the mass per unit length. The total deflection of the beam can be written as

$$y(t, x) = \sum_{n=1}^{\infty} A_n(t) \phi_n(x) \quad (3)$$

where $A_n(t)$ is the modal amplitude which is obtained by solving the differential equation

$$\ddot{A}_n(t) + 2\beta \dot{A}_n(t) + \omega_n^2 A_n(t) = \frac{P_n(t)}{M_n} \quad (4)$$

where the generalized mass

$$M_n = \int_0^l m(x) \phi_n^2(x) dx \quad (5)$$

and the generalized force

$$P_n(t) = \int_0^l p(x, t) \phi_n(x) dx \quad (6)$$

and $p(x, t)$ is the load per unit length acting on the beam. Also, $\beta = c/2m$ where c is the beam damping per unit length.

The interaction force between the projectile and the beam was estimated from static load-deflection considerations. In the case of a strong material which does not fracture, the interaction force depends on the elastic deformation of the beam and projectile and on the localized plastic deformation in the vicinity of the impact point.

A number of force deformation laws have been developed to describe the static deflection of two bodies having regular shapes (spheres, cylinders, plane surfaces). The Hertz Law of Contact [10], was one of the first relationships developed to account for local indentations between two contacting elastic bodies. This law is given by

$$F = k_2 \alpha^{3/2} \quad (7)$$

If one considers the compression of a sphere against a flat plate for example, the constant (k_2) is a function of the radius of the sphere and the material properties of both bodies. The (α) term is defined as the approach, and represents the maximum relative compression of the two bodies.

Other laws have been developed to account for plastic contact indentation. One such law is the Meyers Law [10] given by the empirical equation

$$F = \bar{N} A^{\bar{n}} \quad (8)$$

where (A) is the radius of the permanent crater. For the case of a sphere contacting a plane surface, constants (\bar{N}) and (\bar{n}) are a function of material properties of the bodies and the radius of the sphere. For metallic materials \bar{n} has been found to vary between 2.0 and 2.5.

In any particular case, the appropriate form of the relationship can be determined by a static compression test. An example of the form of this relation which was used in this study for nonfracturing impact cases, such as those involving gabbro or glass, is shown in Figure 16.

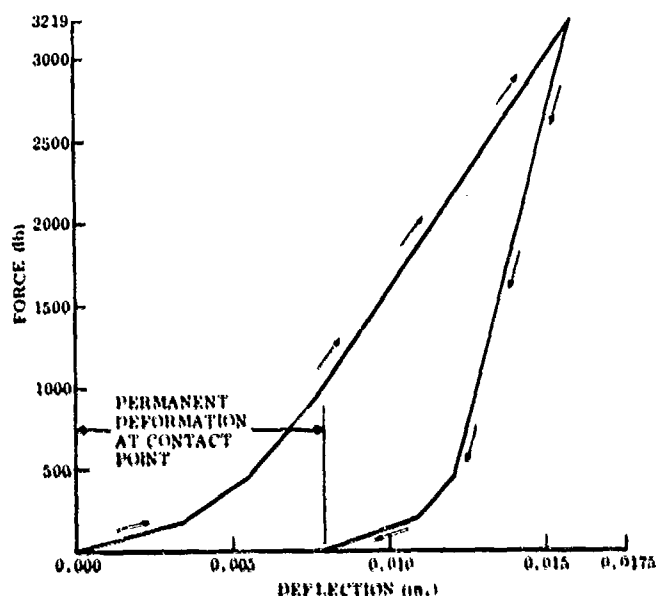


Figure 16. Contact Spring Force Deflection During Loading and Unloading Phase for Computer Model Initial Impact

In those cases involving projectile fracture, a similar procedure can be followed. If an analytical procedure is desired, calculations involving fracture initiation, crack propagation and crack arrest can lead to the development of the appropriate force interaction relation. In the present study, this relation was determined by static compression testing. The type of relation which was used is illustrated by Figure 17 which depicts the essence of the results of the static test for Indiana sandstone. In addition to determining the nature of the force interaction, information must also be obtained concerning the reduction in mass of the projectile which is associated with the fracture process.

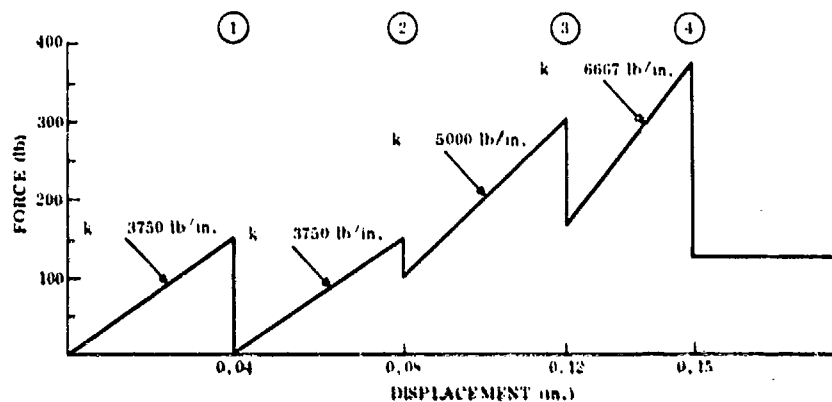
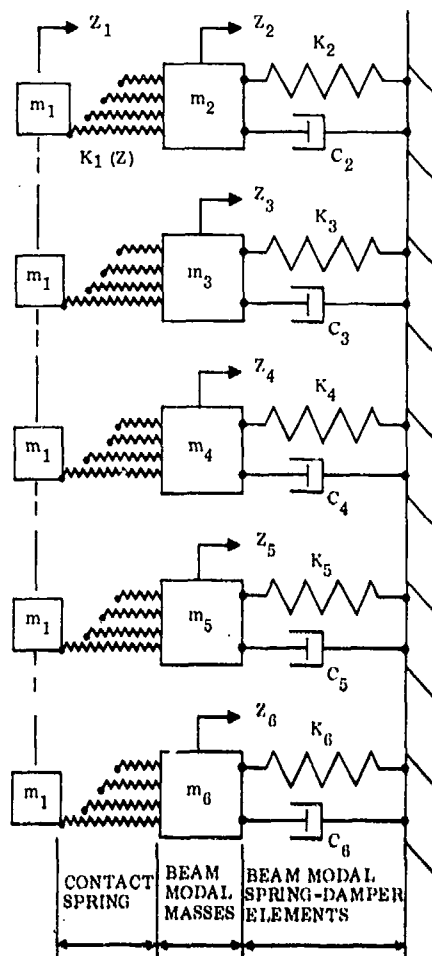


Figure 17. Simplified Resistance Function for Indiana Sandstone Projectile

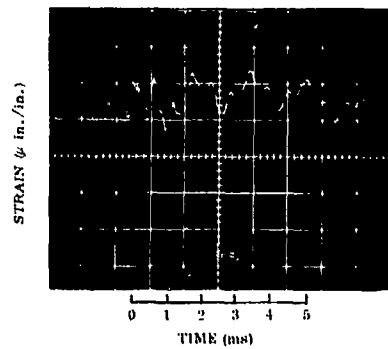
The analytical computations were carried using the component-element method [11]. The component-element method computer model is illustrated in Figure 18. The various elements used to describe the beam response are obtained from the appropriate values of M_n , ω_n , and β . One degree-of-freedom is assigned to the motion of the projectile. The interaction force is modeled using the stop-elements depicted in the figure as a nonlinear contact spring. The entire behavior of the system can be predicted if care is taken to break up the analysis to account for different loading and unloading relations, reduction in mass of the fracturing projectile, rebounding, multiple impacts, etc. A complete discussion of the analytical model and results is given in reference [12].

The degree of success which is achieved in predicting the behavior of the system is illustrated in Figures 19 and 20 which show the experimental and predicted strain response for a nonfracturing and fracturing impact situation. The procedure appears to be capable of describing rather complex behavior with a comparatively simple computational methodology.

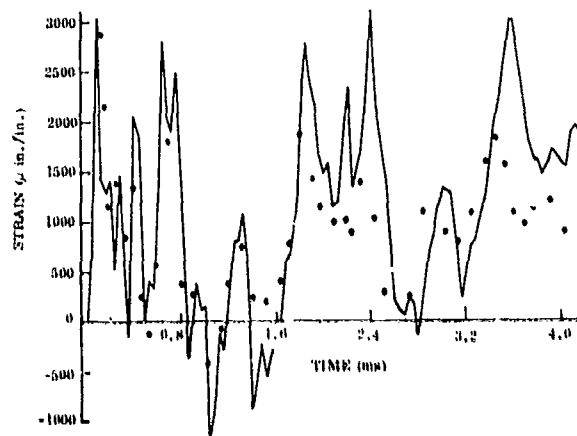


z_1 : GEN DISP OF PROJECTILE
 z_2 : GEN DISP OF 1st MODE OF VIBRATION OF BEAM
 z_3 : GEN DISP OF 3rd MODE OF VIBRATION OF BEAM
 z_4 : GEN DISP OF 5th MODE OF VIBRATION OF BEAM
 z_5 : GEN DISP OF 7th MODE OF VIBRATION OF BEAM
 z_6 : GEN DISP OF 9th MODE OF VIBRATION OF BEAM

Figure 18. Computer Model for Impact of Nonfracturing Projectile with Aluminum Simply Supported Beam

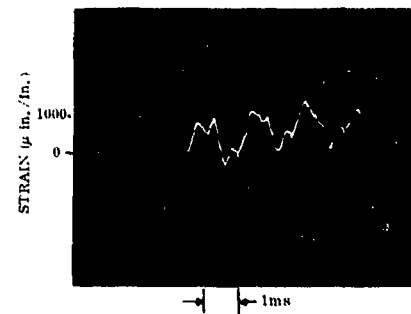


(a) Experimental Strain Response

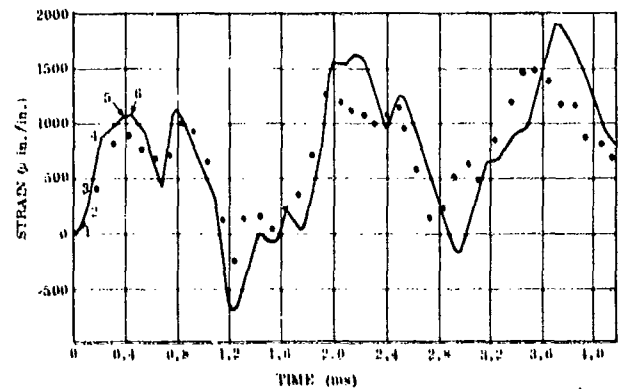


(b) Computer Model (Solid Line)
Experimental (Dotted Line)

Figure 19. Comparison of Experimental and Analytical Beam Strain Response (Glass Sphere Projectile)



(a) Experimental Strain Response



(b) Computer Model (Solid Line)
Experimental (Dotted Line)

Figure 20. Comparison between Experimental and Analytical Strain Response (Indiana Sandstone Projectile)

The analytical results also provided information regarding energy distribution upon impact. For Indiana sandstone, 70% of its energy goes into the fracturing process while only 22% is absorbed by the beam in the form of vibrational energy. The beam indentation is superficial and accounts for only a few percent of the system energy. The higher strength sandstone, having a compressive strength of 11400 lb/in.² (80.1 MPa) produces a significant indentation, in addition to leaving a conical mound of material embedded in the beam. For the igneous rock, approximately 35% of its energy goes into producing permanent localized indentations, for projectile velocities in the range of 800 to 1000 in./s (20.3 to 25.4 m/s).

SUMMARY

Beam strain response is strongly influenced by projectile strength and hardness. Projectile shape appears to have only minor effect on the beam vibration and its associated mechanical signature. Regardless of projectile shape in a given material type, the mechanical signatures are similar over a range of velocity. The mechanical signatures are for the most part a function of the time duration of contact between the projectile and the beam. The major difference is that strain amplitudes naturally will increase with increased projectile velocity. It has been observed that the blunt shaped projectiles of a given mass in Indiana sandstone require greater velocity to fracture than those of equivalent mass having a pointed shape. In any event, regardless of whether or not the projectile completely fractures or remains intact following some material loss, the mechanical signatures of Indiana sandstone are quite similar.

A viable procedure has been developed for predicting dynamic response, impulse and localized permanent deformation of a beam upon impact with both fracturing and nonfracturing rock projectiles. Experimental and analytical results from computer models were compared and found to be in fairly good agreement.

REFERENCES

- [1] Glasstone, S., The Effects of Nuclear Weapons, U.S. Government Printing Office, Washington, D.C., 1977, 29.
- [2] Anderson, F.E., Jr., Hansen, R.J., Murphy, H.L., Newmark, N.M. and White, M.P., "Design of Structures to Resist Nuclear Weapon Effects," ASCE Manual, No. 42, 1964, 11.
- [3] Coates, D.F. and Parsons, R.C., "Experimental Criteria for Classification of Rock Substances," International Journal of Rock Mechanics and Mining Science, V. 3, 1966, 181-89.
- [4] Hurlburt, C.S., Jr., Minerology, John Wiley and Sons, New York, 1966, 515-18.
- [5] Liebowitz, Fracture, Academic Press, New York, 1972, 104-05.
- [6] Protadyakouov, M.M. and Koifman, M.I., Mechanical Properties of Rock, Israel Program for Scientific Translations, Jerusalem, 1968, 78-80.
- [7] Goldsmith, W. and Cunningham, D.M., "An Experimental Investigation of the Oblique Impact of Steel Spheres on Simply Supported Steel Beams," Society of Experimental Stress Analysis Proceedings, V. 15, No. 1, 1955, 171-79.

- [8] Hyzer, W.G., Engineering and Scientific High Speed Photography, MacMillan Company, New York, 1962, 97.
- [9] Hurty, W.C. and Rubinstein, M.F., Dynamics of Structures, Prentice Hall, Englewood Cliffs, New Jersey, 1964, 278.
- [10] Goldsmith, W., Impact, the Theory and Physical Behavior of Colliding Solids, Edward Arnold Ltd., London, 1960, 89-92.
- [11] Levy, S. and Wilkinson, J.P.D., The Component Element Method in Dynamics, McGraw-Hill Book Company, Inc., New York, 1976, 139-47.
- [12] Mann, R.L., "Impact of Rock Debris on a Simply Supported Beam," Ph.D. Dissertation, Syracuse University, New York, 1978, 62-99.

SESSION V: PROJECTILE PHENOMENA-2

Chairman: D. R. Mulville
Program Manager, Aircraft Structures
Naval Air Systems Command

DEFORMATION OF MAR-M200 (A NICKEL BASE SUPERALLOY) UNDER SHOCK LOADING
TO 8.5 GPa AT ROOM TEMPERATURE 317

D. P. Dandekar,
A. G. Martin, and
J. V. Kelley
Army Materials and Mechanics Research Center

A FRACTURE INVESTIGATION OF A LAMELLAR EUTECTIC TWO-PHASE METAL ALLOY
UNDER SHOCK LOADING. 330

G. H. Brawley
Battelle Columbus Laboratories
W. W. Predebon
Michigan Technological University

THE COMPRESSION TEST REVISITED 351

J. F. Mescall,
R. P. Papirno, and
J. McLaughlin
Army Materials and Mechanics Research Center

BEYOND THE TAYLOR TEST TO FRACTURE 367

R. P. Papirno,
J. F. Mescall, and
A. M. Hansen
Army Materials and Mechanics Research Center

DEFORMATION OF MAR-M200 (A NICKEL BASE SUPERALLOY)
UNDER SHOCK LOADING TO 8.5 GPa AT ROOM TEMPERATURE

DATTATRAYA P. DANDEKAR
ANTHONY G. MARTIN
JOHN V. KELLEY

Army Materials and Mechanics Research Center
Watertown, Massachusetts 02172

ABSTRACT

In this work we present the results of shock loading experiments on MAR-M200. MAR-M200 is a vacuum induction melted and vacuum cast nickel base precipitation hardening alloy. Its ambient density is 0.310 lb/cu.in. (8.59 Mg/m³). The values of Young's and Shear moduli, and Poisson's ratio are determined to be 27.7 MSi (191 GPa), 10.4 MSi (72 GPa), and 1/3, respectively. The results of shock loading experiments show that: (a) MAR-M200 deforms in a linear elastic manner to a maximum stress of 0.42 MSi (2.87 GPa) at zero depth, (b) the elastic deformation of MAR-M200 is, however, limited to a stress of 0.13 MSi (0.92 GPa) at a depth of 0.301 in (7.8mm), (c) the deformation of MAR-M200 above the appropriate elastic stress limit does not appear to be like that of an elastic-plastic solid under shock compression, and (d) the spall threshold of MAR-M200 lies between 0.551 and 0.653 MSi (3.8 and 4.5 GPa).

INTRODUCTION

MAR-M200 is a vacuum induction melted and vacuum cast nickel base precipitation hardening alloy. It contains relatively large amounts (12.8% by weight) of tungsten for solid solution strengthening (Table I) and carbide formation. Cobalt is added to increase the solubility temperature, i.e., the solvus temperature of the gamma prime hardening phase, a primary precipitate phase of MAR-M200. This alloy was developed to retain useful strength to 1899 F (1310 K), mainly as a cast turbines and vanes in gas turbine applications. Recently, there has been some interest in determining the response of this material when subjected to both high pressures and elevated temperatures. The above interest is generated primarily because of the low thermal expansion coefficient, high thermal conductivity, high elastic modulus, and moderate density of MAR-M200. There exists a fairly good amount of data pertaining to variation in its physical and metallurgical properties at elevated temperatures at one atmospheric pressure because of its earlier applications in gas turbines, aircraft engine blades, etc. The information with regard to variation in these properties of MAR-M200 at high pressures, however, has not been collected. The present investigation was undertaken to initiate the process of offsetting the said lack of information on MAR-M200. The present work reports the observed response of MAR-M200 to shock loading at room temperature 72 ± 8 F (295 ± 5 K). The maximum stress that MAR-M200 was subjected to in the present investigation was around 1.3×10^6 psi (9.0 GPa). The observed response comprises of Hugoniot of MAR-M200, the nature of deformation, stress wave profile, and spall threshold in MAR-M200.

TABLE I COMPOSITION OF MAR-M200

<u>Element</u>	<u>Weight Percent</u>	<u>Element</u>	<u>Weight Percent</u>	<u>Element</u>	<u>Weight Percent</u>
Al	5.11	Cr	8.82	Ti	2.19
B	0.02	Cu	0.10	W	12.85
C	0.14	Fe	0.20	Zr	0.05
Cb	0.97	Mn	0.02	S	0.01
Co	10.18	Si	0.10	Ni	Balance ~59.2



Figure 1. A Photomicrograph of As-Received MAR-M200
Showing the Heterogeneity of the Grain Size

DESCRIPTION OF MAR-M200

The composition of MAR-M200 used in the present investigation is given in Table I. The presence of the various elements are carefully controlled to provide desirable mechanical property in the range of serviceable temperature. Briefly, nickel, cobalt, tungsten, chromium, and iron make up the face centered-cubic austenite (γ) matrix. The elements aluminum, titanium and niobium, make up the gamma prime (γ') precipitate $Ni_3(Al, Ti, Nb)$. Boron, carbon, and zirconium are the elements which segregate to grain boundaries and are mostly carbides of the type $M_{23}C_6$ and M_6C . The principal thing to note is that desirable high temperature properties of a nickel alloy stems from coherent precipitation of γ' phase with austenite. A detailed discussion of nickel alloy composition and their effect on physical metallurgy and mechanical properties will be found in [1].

The as-cast MAR-M200 used in the present investigation has a density of 0.310 ± 0.001 lb/cu.in. (8.59 ± 0.04 Mg/m³). The material is extremely inhomogeneous with respect to the grain size as shown in Figure 1. This inhomogeneity of MAR-M200 pervades through the bulk of the material. As a consequence it has been difficult to measure velocities of elastic waves in MAR-M200 by means of ultrasonic techniques with a very high precision. The magnitudes of longitudinal and shear elastic wave velocities in MAR-M200 determined by an ultrasonic method, due to Martin [2], were found to be 19.07 ± 0.3 kft/s (5.78 ± 0.09 km/s), and 9.54 ± 0.1 kft/s (2.89 ± 0.04 km/s), respectively. These coupled with the density of MAR-M200 yield a value of 27.7 ± 0.1 MSi (191 ± 10 GPa) for its Young's modulus. The reported value of Young's modulus for MAR-M200 in Ref. [3] is 31.5 MSi (217 GPa). It is not possible to comment on the difference between these two estimates of the Young's modulus of MAR-M200 at least partly because the precision of the magnitude 31.5×10^6 psi (217 GPa) is not reported in Ref. 3. Since the ratio of the longitudinal and shear wave velocities is 2, it implies that Poisson's ratio of MAR-M200 is 1/3 and the values of Young's and bulk moduli are the same.

Mar-M200 was cast by Hitchner Manufacturing Co., Milford, NH, in the form of rectangular plates roughly 11.8 in. x 5.9 in. x 0.16 in. (30cm x 15cm x 0.4cm) in dimensions. The specimens of MAR-M200 fabricated from these plates were square disks with 1.2 in. (3cm) sides and thickness between 0.079 in. (0.2cm) and 0.157 in. (0.04 cm). The specimens were lapped flat to 2×10^{-4} in. (5 μ m) and the opposing faces of the disks were mutually parallel to each other within 2×10^{-4} over the entire faces.

SHOCK EXPERIMENTS

The shock loading experiments were performed on the 4-inch (10.2cm) diameter, 28 ft (8.5m) long light gas gun at AMMRC. The description of the gun and associated recording instruments to determine the response of a material to shock loading are given in Ref. 4. The shock loading response of MAR-M200 was determined by performing six direct impact and two transmission experiments. Brief description of these two types of experiments are given below.

In a direct impact experiment, a specimen of MAR-M200 mounted on a projectile impacted either an x-cut quartz gauge or a thin buffer-quartz gauge composite in a target. The buffer used was either a tungsten carbide or a sapphire or a lucalox disc. These buffer materials deform in an almost linear elastic manner to 1.45 MSi (10 GPa) under shock loading. In either type of direct impact experiment, stress (σ) and particle velocity (u) at the impact surface are obtained from the response of an x-cut quartz gauge and from a knowledge of the Hugoniot of the buffer (in the present case the buffer are linearly elastic), and impact velocity of the projectile. For the range of stress, i.e., a maximum of 1.3 MSi (9.0 GPa) in which these experiments were performed both sapphire and tungsten carbide are very nearly linearly elastic under shock compression and release [5,6]. The final stress in quartz never exceeded 0.6 MSi (4.0 GPa) limit of the gauge operation [7]. The data obtained from the direct impact experiments provided information about the initial shock compression states of MAR-M200 and subsequent release states attained in it when the buffers used were thin disks. The method of extracting these information and a detailed description of these experiments are given in Refs. 8, 9, and 10.

In a transmission experiment, a projectile containing a material whose shock response is known impacted a disk of MAR-M200 behind which an x-cut quartz gauge was bonded. The x-cut quartz gauge provided the stress-time profile which in turn yielded the information about the manner in which shocked states or shock induced deformations were brought about in MAR-M200 of a given thickness. This type of experiment has been routinely performed since the inception of shock wave experiments to determine equation of state of a material and a description of this type of experiment may be found in Ref. 8.

In the present series of experiments the physical entities measured were impact velocity, stress-time profile at the impact surface or the propagated impact stress-time profile at a finite thickness of MAR-M200 and shock wave velocity through MAR-M200 in transmission experiments. X-cut quartz gauges with 1 in. (25.4mm) diameter and 0.126 in. (3.2mm) thickness were used to obtain stress profiles. These gauges were used in shunted mode except in those direct impact experiments where either sapphire or lucalox disks were used as buffer. In these experiments the gauges were used in shorted mode with the ratio of guard ring width and thickness of the gauge exceeding a value of 3. This enabled us to use the calibration coefficient of Graham in reducing the quartz gauge records [7].

The maximum uncertainties in the experimentally determined values of impact velocity, stress, particle velocity, and shock velocity are 0.5, 3, 3, and 4%, respectively. The tilt between the impacting surfaces was less than 0.5 mrad.

RESULTS OF SHOCK EXPERIMENTS

The results of shock experiments are summarized in Tables II and III, and these results are plotted in stress (σ) and particle velocity (u) plane in Figure 2. The results are given in SI units. However, wherever possible,

TABLE II RESULTS OF DIRECT IMPACT EXPERIMENTS

Experiment	Buffer	Compression					Release	
		Impact Velocity km/s	Stress (σ) GPa	Particle Velocity (u) km/s	Shock* Velocity (U) km/s	Density* (ρ) Mg/m ³	Strain %	Stress (σ_r) GPa
								Particle Velocity (u_r) km/s
								Impedance† Gg m ⁻² s ⁻¹
1	None	0.215	2.52	0.049	--	--	--	--
2	Sapphire	0.215	4.78	0.107	4.46	8.77	2.1	2.29
10	Tungsten-Carbide	0.291	8.50	0.205	4.41	8.97	4.2	4.17
12	Lucalox	0.143	3.25	0.068	4.25	8.69	1.2	1.59
14	None	0.183	2.11	0.044	--	--	--	0.036
19	Sapphire	0.341	7.36	0.174	4.51	8.91	3.6	0.127

*The values of shock velocity and density are calculated by applying the conservation relations for momentum and mass with the initial condition of MAR-M200 at HEL, namely: $J = \sigma_e + \rho_e (U-u_e)(u-u_e)$ and $\rho (U-u) = \rho_e (U-u_e)$.

†The release impedance is calculated from the relation $(\sigma-\sigma_r)/(u-u_r)$.

TABLE III RESULTS OF TRANSMISSION EXPERIMENTS

Experiment No.	Thickness of MAR-M200 (mm)	Elastic Compression				Final Compression		
		Impact Velocity km/s	Impact Stress Velocity (σ_e) GPa	Particle Velocity (u_e) km/s	Density (ρ_e) Mg/m ³	Shock Velocity (U) km/s	Stress (σ) GPa	Particle Velocity (u) km/s
								Density (ρ) Mg/m ³
17	3.96	Sapphire	0.308	1.06	0.021	8.62	4.60	0.160
18	7.81	Sapphire	0.308	0.92	0.018	8.61	4.53	0.161
							6.54	8.89
							6.48	8.89

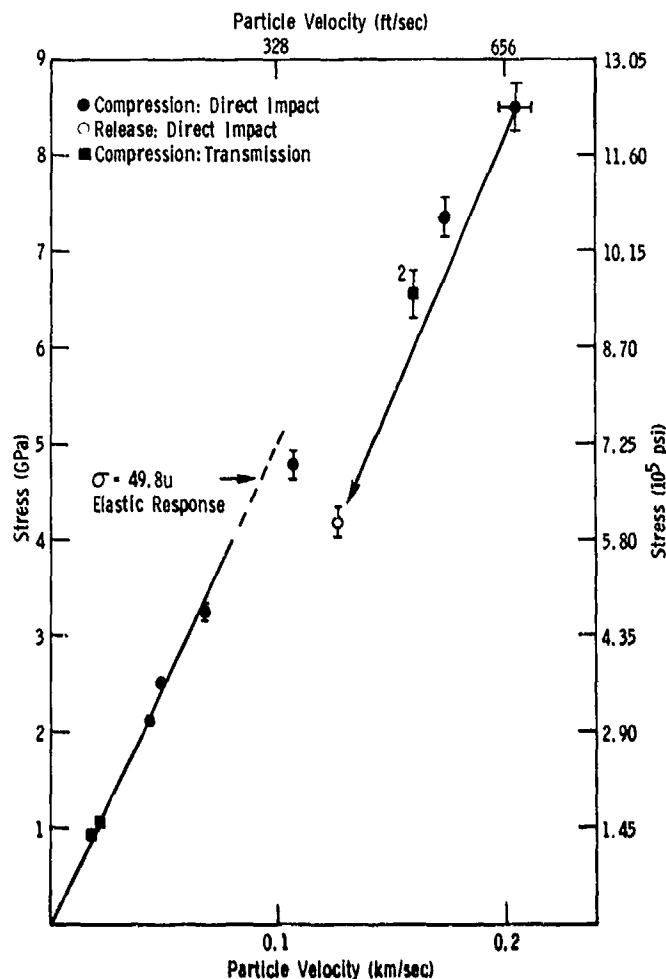


Figure 2. Stress-Particle Velocity Diagram of MAR-M200

graphical representation of the results are given in both SI and English units. A conversion table for the computation of various entities from SI to English units are given in Appendix A.

A. Compression States

The results of six direct impact experiments on MAR-M200 are summarized in Table II. These results show that the response of MAR-M200 when shocked below around 0.435 Msi (3.0 GPa) appears to be elastic and its response above this stress is non-elastic. The response of MAR-M200 below 0.435 Msi (3.0 GPa) is termed elastic because (σ, u) coordinates of experiments 1 and 14 lie on a straight line given by an equation

$$\sigma = 49.8 u \quad \sigma \leq 2.87 \text{ GPa} \quad (1)$$

Where $49.8 \text{ Gg m}^{-2} \text{ s}^{-1}$ is the longitudinal elastic impedance of MAR-M200 derived from the product of measured longitudinal sound speed of 19.07 kft/s (5.8 km/s) and its density 0.310 lb/in.^3 (8.59 Mg/m^3) given earlier in the section

"Description of MAR-M200".

The locus of the compressed state, i.e., (σ, u) coordinates of the remaining four experiments may be represented by the following equation (2)

$$\sigma = 0.6581 + 38.37 u, \quad 2.87 < \sigma \leq 8.56 \text{ GPa} \quad (2)$$

The above equation is the least squared fit to the four points. The standard error of the estimate of stress (σ) is ± 0.1 GPa.

The intersection of equations (1) and (2) is taken to be the limit of linear elastic behavior of MAR-M200 under shock loading, i.e., Hugoniot Elastic Limit (HEL) of MAR-M200. The value of HEL, i.e., $\sigma_e = 0.416$ MSi (2.87 GPa) and the value of associated particle velocity (u) is 189 ft/s (0.0576 km/s). The density of MAR-M200 at the HEL is 0.313 lb/cu in. (8.7 Mg/m³).

B. Release State

The release behavior of MAR-M200 from its compressed states were obtained in three experiments (Table II). The buffers in these experiments were disks of sapphire, or lucalox or tungsten carbide. The results of these experiments indicate that the stress in MAR-M200 is released elastically from its various compressed states. The values of release impedances calculated from the (σ, u) coordinates of the compressed and end release states vary between 10.4 and 11.5 Mlb ft⁻²s⁻¹ (51 and 56 Gg m⁻²s⁻¹). Since the values of impedances are uncertain to $\pm 6\%$, the initial release impedance of MAR-M200 can be represented by the average of these impedances, i.e., 10.8 ± 0.6 Mlb ft⁻²s⁻¹ (53 ± 3 Gg m⁻²s⁻¹).

C. Transmitted Stress Wave Profile

Two experiments were done on specimens of thicknesses 0.156 in. (3.96mm) and 0.307 in. (7.81mm) to induce a peak stress in the neighborhood of 0.87 MSi (6 GPa). The thicker specimen was actually two disks of MAR-M200 bonded together by means of epoxy, because of the limited thickness of the MAR-M200 plates supplied. The purpose of these experiments in addition to determining the transmitted stress wave profile in MAR-M200 was to induce a tension in the neighborhood of 0.435 MSi (3 GPa) and see if it has been spalled.

The quantitative results derived from the observed wave profiles shown in Figure 3 are given in Table III. The observed or calculated values of σ and u are also plotted in Figure 2. These coordinates appear to be consistent with the (σ, u) coordinates derived from the direct impact experiments where stress exceeded the value of HEL. These experiments also show that the deformation or loading of MAR-M200 under shock proceeds in two stages. The initial deformation, represented by the first stress jumps in the profiles, is elastic. However, the stress limits of elastic deformation are only 0.154 MSi (1.06 GPa) and 0.133 MSi (0.92 GPa) for the specimens with thicknesses 0.156 in. (3.96mm) and 0.307 in. (7.81mm), respectively. These values are much smaller than the observed value of HEL at the impact surface of MAR-M200, i.e., 0.416 MSi (2.87

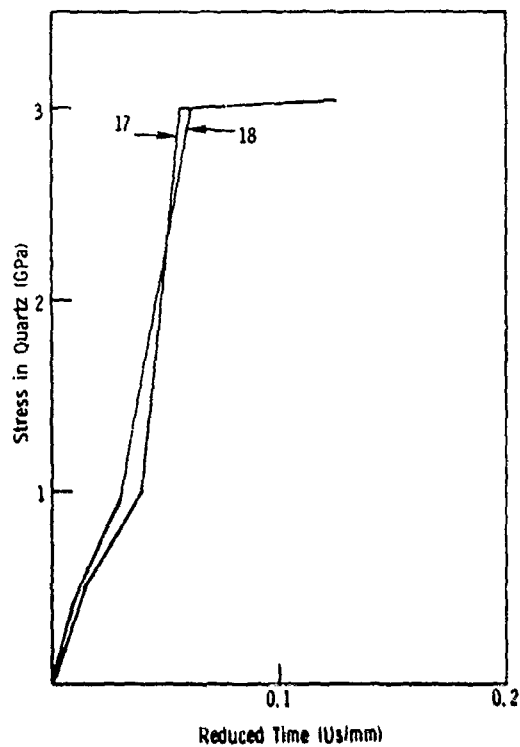


Figure 3. Transmitted Stress Wave Profiles As Recorded By Quartz Gauges

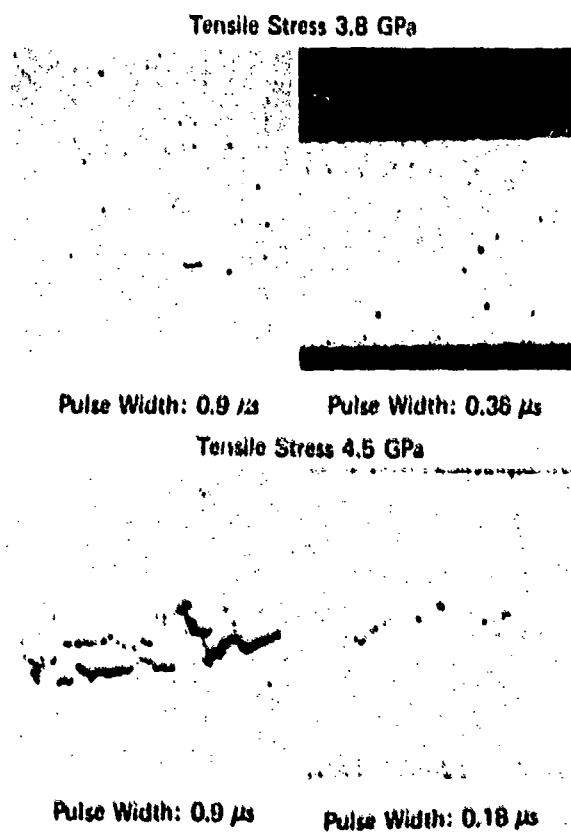


Figure 4. Spall Threshold In MAR-M200 - Shock Propagates From The Bottom To The Top Of Each Photograph, Mag. 50X

GPa) at zero thickness. Such a decay in elastic precursor has been also observed in other alloys like 6061-T6 Al. In other words, the strain rate effect of shock loading on the elastic precursor is significant in MAR-M200 and must be taken into account for wave propagation calculations and their interactions.

The transmitted wave profile also appears to be centered, i.e., the magnitude of final deformation wave velocity following the elastic precursor is invariant with respect to the specimen thickness. The average value of the final deformation or compression wave velocity is 14.96 kft/s (4.56 km/s), and it is this deformation wave which subsequently takes MAR-M200 to its final compressed state of 0.944 MSi (6.5 GPa) in these two experiments.

D. Spall Threshold

It was mentioned earlier that the transmitted wave experiments described previously were designed to induce a tension of approximately 0.435 MSi (3.0 GPa) in MAR-M200. A subsequent calculation based on the results of these two experiments and Hugoniot of sapphire and quartz indicated that MAR-M200 specimens were subjected to a tensile stress of magnitude 0.537 MSi (3.7 GPa). The spall planes in the thinner and thicker specimens were estimated to be located at 0.051 in. (1.3mm) and 0.224 in. (5.7mm) from the respective impact surfaces of these specimens. The tension pulses were approximately of 0.9 μ s durations for both specimens. Examinations of the recovered specimens of MAR-M200 did not indicate any evidence of spall in them. Hence it was decided to do two experiments to determine spall threshold in MAR-M200. The details of these two experiments are given in Table IV. These experiments were done to induce tensile pulses of 0.653 MSi (4.5 GPa) with durations of 0.36 and 0.9 μ s and 0.551 MSi (3.8 GPa) with durations of 0.18 and 0.9 μ s in two specimens of MAR-M200 in each of the two experiments. The results of these two experiments are shown in Figure 4. This figure indicates that for a pulse duration in the range of 0.18 and 0.9 μ s, the spall threshold of MAR-M200 lies between 0.551 and 0.653 MSi (3.8 and 4.5 GPa).

TABLE IV DETAILS OF SPALLATION EXPERIMENTS
IN MAR-M200 (IMPACTEE)

Experiment	Material	Impactor		Impactee		Tension Pulse	
		Thickness (mm)	Velocity (km/s)	Thickness (mm)	Magnitude (GPa)	Duration (μ s)	
20	Lucalox	2	0.195	1.65	4.4	0.30	
21	Sapphire	5	0.195	3.87	4.5	0.94	
22	Sapphire	1	0.161	1.10	3.8	0.18	
23	Sapphire	5	0.161	3.77	3.8	0.92	

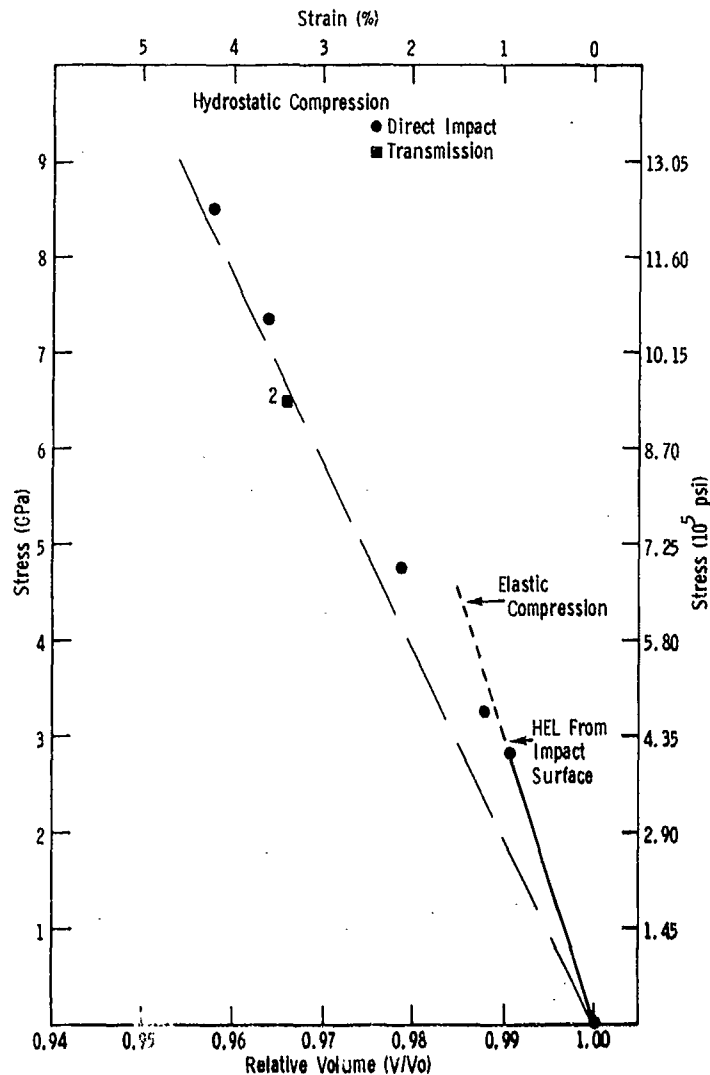


Figure 5. Compression Of MAR-M200. Semi-Continuous Curve Is Estimated From The Ambient Ultrasonic Wave Velocity Measurements On MAR-M200

DISCUSSION

The results of the experiments on MAR-M200 which merit some discussion are the observed low values of compressional wave velocity following the elastic precursor. We will elaborate the above results to understand the observed response of MAR-M200 to shock loading.

It is clear from Table II and III that the velocity of the slow moving stress wave (U) which is responsible for the inelastic deformation of MAR-M200 following the elastic deformation ranges between 13.95 kft/s (4.25 km/s) and 15.09 kft/s (4.60 km/s). If the equation (2) is taken to represent the state of MAR-M200 above the HEL, then the velocity has an invariant value of 14.7 kft/s (4.47 km/s). These values are consistently lower than the bulk sound speed (U_B) of 15.48 kft/s (4.72 km/s). The difference in the values of the bulk sound and inelastic deformation velocities is small but would be of significance if the inequality

$$U < U_B$$

(3)

continues to hold for experiments where peak stress induced in MAR-M200 is just above HEL. This inequality is one of the properties of a solid which deforms like an elastic-isotropic solid under shock loading [5]. The effect of such a deformation is that when shock compression of an elastic-isotropic solid is compared with its hydrostatic compression curve, the coordinates of the former tend to move towards the latter with increasing value of stress. This appears to be the case when one plots the stress-relative volume (V/V_0 or ρ_0/ρ) for MAR-M200 obtained from the shock compression experiments and the hydrostatic compression curve calculated from the bulk sound speed in MAR-M200 (Figure 5). The hydrostatic compression curve in Figure 5 is the limit of maximum compressibility of MAR-M200 since it assumes no increase in its bulk modulus with pressure. The above result suggests that the deformation of MAR-M200 appears to proceed more like an elastic-isotropic solid than an elastic-plastic solid under shock compression. The inability of a metallic material to withstand a decreasing amount of shear stress at high compression is uncommon but is not unknown. Polycrystalline tungsten shows such a behavior [11,12]. However, to put the observed behavior of MAR-M200 on a more sound basis, more transmission experiments must be performed on it at various stress levels. If these experiments tend to confirm the results of the present investigation, an explanation for the deformation behavior of MAR-M200 must be presented or sought in terms of the deformation behavior of its constituents.

SUMMARY

The principal results of shock compression experiments reported here may be summarized as follows:

1. The deformation of MAR-M200 appears to proceed in linear elastic manner provided stress is below 0.416 MSi (2.87 GPa).
2. The value of HEL is dependent on the thickness of MAR-M200. It declines from 2.87 GPa at zero depth to 0.92 GPa at (7.81mm) of MAR-M200.
3. The deformation above the HEL proceeds by the propagation of a shock with a velocity lower than the bulk sound speed in MAR-M200.
4. A two-wave shock structure is developed in MAR-M200 which appears to be centered.
5. The deformation of MAR-M200 under shock loading appears to be akin to the deformation of an elastic-isotropic solid.
6. The spall threshold of MAR-M200 lies between (3.8 GPa) and (4.5 GPa) for a tension of duration between 0.18 and 0.9 μ s.

APPENDIX

TABLE AI CONVERSION TABLE FOR CALCULATING THE MAGNITUDE OF VARIOUS ENTITIES FROM SI TO BRITISH UNITS

Item	Units		Multiply SI Units by the Following to Calculate Values in British Units
	SI	British	
Length	Meter (m)	Feet (ft)	3.280
Weight	Kilogram (kg)	Pound (lb)	2.205
Velocity	km/s	ft/s	3.280
Density	Mg/m ³	lb/in ³	0.03616
Stress	GPa	MSi	0.14504
Impedance	Gg m ⁻² s ⁻¹	M lb ft ⁻² s ⁻¹	0.2048

REFERENCES

1. Decker, R. F. and Sims, C. T., "The Metallurgy of Nickel-Base Alloys", The Superalloys, Ed. C. T. Sims and W. C. Hagel, John Wiley & Sons, New York, 1972, 33-75.
2. Martin, A. G., "Phase Velocity Measurements in Dispersive Materials By Narrow Band Burst Phase Comparison". Army Materials & Mechanics Research Center Report, AMMRC TR 76-22, July 1976.
3. INCO, "High Temperature High Strength Nickel Base Alloys", International Nickel Company, Inc., New York, 1977, 10.
4. Jones, A. H., Rosato, N., and Dignam, J. F., "AMMRC Plate Acceleration Facility," Army Materials & Mechanics Research Center Report, AMMRC SP 73-5, March 1973.
5. Graham, R. A. and Brooks, W. P., "Shock Wave Compression of Sapphire From 15 To 420 Kbar. The Effect of Large Anisotropic Compression," J. Phys. Chem. Solids, V. 32, 1971, 2311-2330.
6. Karnes, C. H. (unpublished).
7. Graham, R. A. and Asay, James R., "Measurement of Wave Profiles in Shock Loaded Solids, High Temp.-High Press.", V. 10, 1978, 355-390.
8. Halpin, W. J., Jones, O. E. and Graham, R. A., "A Submicrosecond Technique For Simultaneous Observation Of Input and Propagated Impact Stresses," Symposium on Dynamics Behavior of Materials Special Technical Publication No. 336, American Society for Testing and Materials, Philadelphia, PA, 1963, 208-218.

9. Lysne, P. C., Boade, R., Percival, C. M. and Jones, O. E., "Determination of Release Adiabats and Recentered Hugoniot Curves by Shock Reverberation Techniques," J. Appl. Phys., Vol. 40, 1969, 3786-3795.
10. Dandekar, D. P. and Lamothe, R. M., "Behavior of Porous Tungsten Under Shock Compression at Room Temperature," J. Appl. Phys., Vol. 48, 1977, 2871-2879.
11. Dandekar, D. P., "Loss of Shear Strength in Polycrystalline Tungsten Under Shock Compression," J. Appl. Phys., Vol. 47, 1976, 4703-4705.
12. Asay, J., Chabildas, L. C. and Dandekar, D. P., "Shear Strength of Shock Loaded Polycrystalline Tungsten," (unpublished).

A FRACTURE INVESTIGATION OF A LAMELLAR EUTECTIC TWO-PHASE METAL ALLOY
UNDER SHOCK LOADING*

Gary H. Brawley
Researcher
Battelle's Columbus Laboratories
Columbus, Ohio 43201

William W. Predebon
Associate Professor of Engineering Mechanics
Michigan Technological University
Dept. of Mechanical Eng. and Eng. Mechanics
Houghton, Michigan 49931

ABSTRACT

A preliminary study of the nature of dynamic fracture in a bi-phase lamellar eutectic metal is made by a finite-difference computer code simulation. Through the simulation, the mode and location of incipient fracture are predicted, and these are compared to experimental results. The case where an initially planar shock pulse traveling parallel to the direction of the lamellae is considered. Incipient fracture is predicted through the use of the cumulative damage spall model, based on a maximum principle stress criterion for the damage threshold.

Results of the simulation show that incipient fracture occurs in the intermetallic CoAl phase, and along the interphase boundary. Dynamic fracture experiments with soft recovery of the lamellar cobalt-aluminum eutectic using a bi-crystal have been performed. The experimental results indicate that incipient dynamic fracture occurs throughout the CoAl phase and along the interphase boundary and at approximately the stress level predicted. Thus good agreement between the experimental results and the simulation was achieved.

INTRODUCTION

Solid mechanics in modern defense system design is frequently concerned with either reducing or maintaining the integrity of structures under impact loading. Traditional structural design analyses typically model structural

* Supported by the National Science Foundation under grants DMR-76-02367101 and DMR 78-05741.

materials with a single phase macroscopic description. The actual microstructure of structural materials is usually neither homogeneous nor single phase. More often it is multiphase in a manner similar to a composite material where there is a matrix and reinforcing second phase, although the characteristic dimensions of such microstructures are generally quite small. Nevertheless, the microstructure of a material is known to influence its response to some loading conditions [1]. For example, it is believed that the interphase boundary in these multiphase materials is responsible for some of the strengthening effect observed in dynamic loading conditions. To exploit the strengthening effect, as well as other effects, it is necessary to understand the effect of the interphase boundary during dynamic loading and the nature of fracture in multiphase materials.

Shock induced fracture has been studied since the early 1900's, but most of the studies have been in single phase materials or multiphase mixtures considered to be single phase and homogeneous. Little work has been done to predict fracture in multiphase materials where the individual phases retain their character. Some investigators have studied various laminated composites in different orientations to the wave front and have found that the primary fracture mode under shock loading conditions was debonding in most cases [2,3]. In these works the materials studied were manufactured from their individual components. It is to be noted, however, that in manufactured composites the bond is usually weaker than either of its constituent phases; debonding is not unusual. With other multiphase materials, this may not be the case.

One interesting class of those multiphase materials which do not necessarily debond are the naturally occurring, "as-formed", in situ metallic eutectics. Compared to the relatively weak interphase bonds in most manufactured composites, the interphase interfaces in eutectics are known to be interfaces of "best fit" and are not necessarily weak [4]. The additional strength at the interphase boundary in the eutectics results from a chemical equilibrium between the phases [5]. To the authors' knowledge there have been no dynamic fracture studies reported in the literature on such materials where properties of constituent phases are considered individually.

OBJECTIVE

In this work, an in situ lamellar eutectic of the cobalt-aluminum system is considered in an analytical and experimental program to predict and verify the mode, location, and conditions of shock-induced incipient fracture. The objective is to further understand the role of the interphase boundary in shock induced fracture of multiphase materials.

Although the cobalt-aluminum eutectic is not a common structural material, it was chosen because of its known ability to form a symmetrical and regular bi-phase structure. Because of the difficulties in describing shock produced fracture in any arbitrary orientation, only one specific case will be considered: an initially planar shock front of known pressure

and duration is to be impinged on the lamellar eutectic such that the shock front is propagating parallel to the lamellae, as shown schematically in Figure 1, with the planar wave front propagating in the x-direction.

Because of typical strain rates of 10^5 seconds⁻¹ or greater and loading and unloading time in the nanosecond-microsecond range, observing the shock induced fracture process is difficult. This difficulty is compensated for by analytical techniques used to simulate the wave motion from fundamental principles through use of a digital computer and appropriate numerical techniques.

The material constitutive equations are required to compute the wave response to some loading condition. Properties for describing dynamic response are different from those used to describe quasi-static response, the most outstanding of these is the dynamic stress-strain relation in compression termed a "Hugoniot". From the data obtained in shock wave experiments and the application of the well known Rankine-Hugoniot jump conditions, the Hugoniot stress-strain relation is defined.

To determine when fracture occurs in the lamellar eutectic, a fracture criterion must be specified. Many dynamic fracture models have been developed and could be used, but one is needed that can accommodate only a small amount of experimental data. In this study it is assumed that if fracture can be predicted in a single phase with its loading history known, then it can be predicted in a bi-phase material, if the fracture properties of each phase, the loading history, and the appropriate interphase boundary conditions are known. In this study four modes of fracture are possible: inter-lamellar fracture where internal separation crosses lamellar boundaries; intra-lamellar fracture where fracture takes place within one of the phases; interphase boundary fracture, where the lamellae separate along the interphase boundary; or any combination of the above modes. The exact mode of fracture is not known a priori for the case considered.

In summary, this study will be presented in the following manner. First, the dynamic material properties will be determined for each phase of the eutectic individually through shock wave experimentation. Second, utilizing a Lagrangian-explicit two-dimensional finite-difference computer code, a computer simulation of a plate-impact experiment will be undertaken. The code is to be applied to the two-dimensional dynamic plane strain case of a two-phase lamellar cobalt-aluminum eutectic under shock pulse loading where the shock pulse will propagate parallel to the lamellae. Third, through the fracture model used and the computer simulation, the location and mode of incipient fracture will be predicted. Lastly, shock loading experiments on the actual lamellar eutectic will be conducted and compared to the computer simulation and predictions.

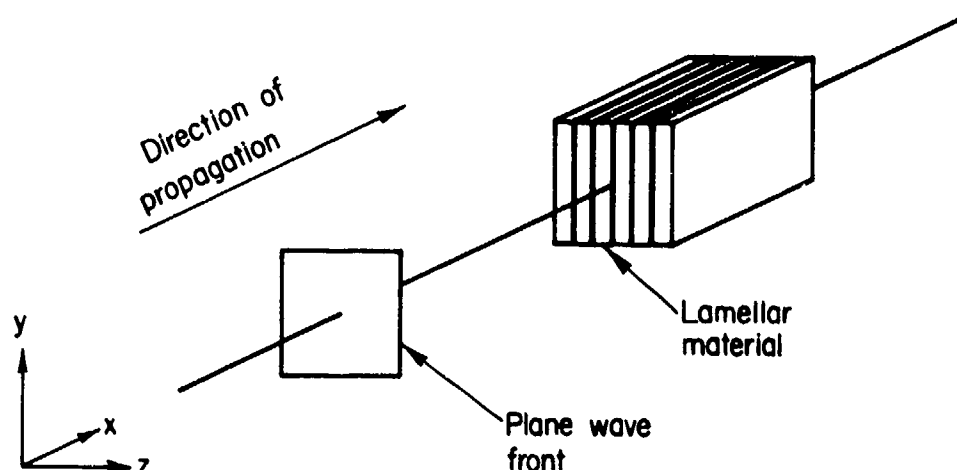


Figure 1. Orientation of Lamellar Eutectic to Wave Front

PROPERTIES FOR Co-Al EUTECTIC CONSTITUENTS

The eutectic composition of the cobalt-aluminum system forms a bi-phase lamellar structure as seen in Figure 2. The lamellar structure is produced by directionally solidifying the proper composition through a steep temperature gradient obtained in a water-cooled chill block. The branching and inclusion visible in Figure 2 are shown for completeness. Such defects are somewhat common but not prevalent and are not considered in this work, instead an ideal bi-phase lamellar geometry is assumed. The interlamellar spacing may be varied by altering the solidification rate; typical spacings are on the order of 10-40 μm . The two constituent phases, when formed in the eutectic, have precise compositions and volume fractions as determined by the phase diagram for the Co-Al system. Stout, et al. [6] have determined the invariant compositions and volume fractions in the eutectic. Besides the composition and volume fractions in the eutectic being invariant, the constituents exist as single crystals and the orientation relationships between phases are well defined [7]. Table 1 summarizes some of the physical characteristics of the eutectic constituents.

Recent work at Michigan Technological University [8,9,10] has yielded static measurements of some properties which will be used in this work. The elastic constants of Co(Al) single crystals have been determined by an acoustic pulse-echo-overlap technique and are given in Table 2 for the alloy nearest the invariant composition (93.1 wt.% Co-Al). Table 3 summarizes useful strength measurements obtained through tensile tests on the eutectic and the Co(Al) phase.

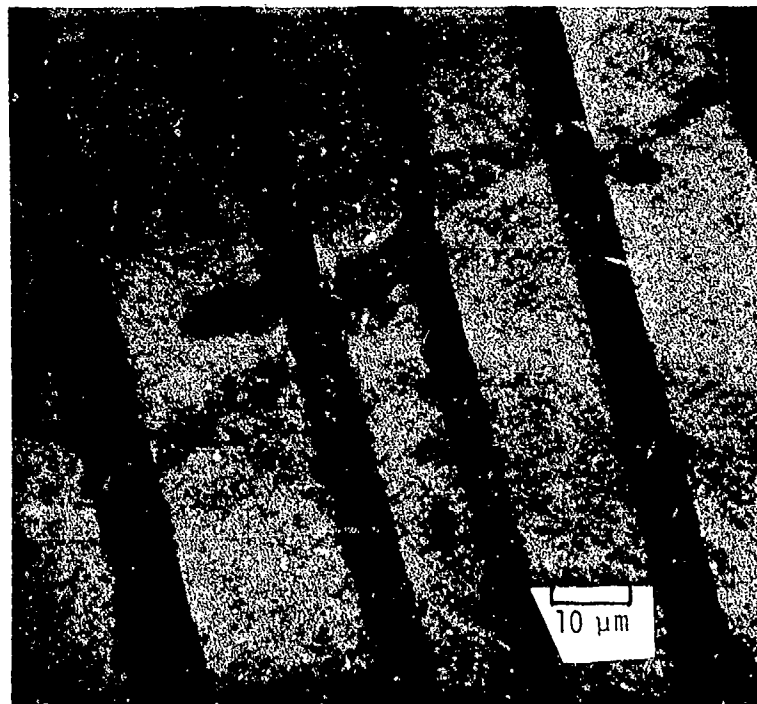


Figure 2. Lamellar Eutectic of Cobalt-Aluminum System

TABLE 1.

Characteristics of Cobalt-Aluminum Eutectic

Alloy Designation	Co(Al)	Eutectic	CoAl
Composition, wt.% Co	93.1	90.5	81.9
Density kg/m ³	7920		6900
Volume Fraction	0.705		0.295
Growth Direction#	$\langle 11\bar{2} \rangle$		$\langle 10\bar{T} \rangle$
Interface Plane#	(111)		(101)
Crystal Structure	FCC		Ordered-BCC#
			(B ₂)

See Reference [7].

The properties and characteristics listed in Tables 1-3 are not enough to fully specify the materials constitutive relations for shock wave problems. In addition, the Hugoniot, or dynamic stress-strain relation, must be specified, as well as fracture properties.

Experimental Hugoniot Data

To determine the Hugoniot properties of the Co-Al system, projectile impact experiments were contracted to Drs. E. R. Lemar and G. E. Duvall at Washington State University. The experiments were conducted at their gas gun facility which is described in [11] and [12]. Six uniaxial strain experiments were carried out on the Co(Al) phase and two on the CoAl phase. Due to the difficulty in producing samples, more experiments were not conducted. It was desired to conduct the experiments on single crystals of the constituent phases so that grain boundary effects would be eliminated. The single crystal would be oriented as it occurs in the eutectic. Although treated as an isotropic material (an assumption in the interpretation of the uniaxial strain experiments), this orientation reflects the generally anisotropic nature of the material.

For the Co(Al) phase, three 6 mm diameter specimens and three 12 mm diameter specimens were prepared. The 6 mm diameter specimens were single crystals obtained in an electron beam zone melting device and oriented in the $\langle 112 \rangle$ direction consistent with the observed direction in the eutectic. The Hugoniot experiments on these samples are numbered: 77-053, 77-059, and 77-060. The 12 mm diameter specimens were not single crystals, but tri-

TABLE 2.
Elastic Constants of Co(Al) Invariant
93.1 wt.% Co-Al.

$$C_1 = 1/2 (C_{11} + C_{12} + 2C_{44}) = 298.0 \text{ GPa} = 2.980 \text{ Mbars}$$

Longitudinal; $\langle 110 \rangle$ direction.

$$C' = 1/2 (C_{11} - C_{12}) = 28.7 \text{ GPa} = 0.287 \text{ Mbars}$$

Shear; $\langle 1\bar{1}0 \rangle$ direction.

$$C_{44} = 116.2 \text{ GPa} = 1.162 \text{ Mbars}$$

Shear; $\langle 001 \rangle$ direction.

$$C_{12} = 153.1 \text{ GPa} = 1.531 \text{ Mbars}$$

$$C_{11} = 210.5 \text{ GPa} = 2.105 \text{ Mbars}$$

$$K = 1/2(2C_{12} + C_{11}) = 172.2 \text{ GPa} = 1.722 \text{ Mbar}$$

Bulk modulus estimate (average stress or strain model).

Table 2 (Cont.)

$$Y_R = \left[\frac{(3C_{11} + C_{12})}{5(C_{11} - C_{12})(C_{11} + 2C_{12})} + \frac{1}{5C_{44}} \right]^{-1}$$

$$= 142.6 \text{ GPa} = 1.426 \text{ Mbars}$$

Young's modulus estimate (Reuss average stress model).

$$Y_V = \frac{(C_{11} + 2C_{12})(C_{11} - C_{12} + 3C_{44})}{(2C_{11} + 3C_{12} + C_{44})}$$

$$= 210.5 \text{ GPa} = 2.105 \text{ Mbars}$$

Young's modulus estimate (Voight average strain model).

$$G_R = \left[\frac{4}{5(C_{11} - C_{12})} + \frac{3}{5C_{44}} \right]^{-1}$$

$$= 52.3 \text{ GPa} = 0.523 \text{ Mbars}$$

Shear modulus estimate (Reuss average stress model).

$$G_V = \frac{C_{11} - C_{12} + 3C_{44}}{5}$$

$$= 81.2 \text{ GPa} = 0.812 \text{ Mbars}$$

Shear modulus estimate (Voight average strain model).

TABLE 3.

Strength Properties of Co-Al Lamellar Eutectic System.

	Co(Al)	Eutectic*	CoAl
Yield Stress, Y_0	0.176 GPa [1.758 kbars]	0.690 GPa [6.895 kbars]	
Fracture Stress, F		0.896 GPa [8.964 kbars]	2.069 GPa# [20.69 kbars]

* Volume fraction CoAl = 0.29
Young's modulus $E \approx 206.9 \text{ GPa}$ [2.069 Mbars]

Estimated by theory of mixtures

crystals, all cut from the same ingot with the largest grain about 90 percent of the cross-sectional area. A vertical Bridgman technique was used to directionally solidify the Co(Al) at 25 cm/hr. The major grain was also oriented in the $\langle 112 \rangle$ direction which was found to be about 5° off the growth axis. The minor grains are assumed to be near the same orientation due to the direction of solidification. The experiments for the 12 mm samples are numbered: 79-018, 79-019, and 79-020.

Obtaining specimens of CoAl was more difficult than the other phase. The vertical Bridgman method yielded the 12 mm specimens used. Although the CoAl specimens were not single crystal, considerable effort was made to obtain even homogeneous polycrystalline specimens without voids or quench cracks. The resulting specimens had about five grains and were cut perpendicular to the growth direction. Two specimens were used in Hugoniot experiments and numbered: 79-021 and 79-022. Each of the specimens were solutionized and properly oriented before the Hugoniot experiments were conducted.

In the gas gun Hugoniot experiments, stress and particle velocity data were obtained; Table 4 summarizes the data collected [12]. On shot 79-018, the stress gage wires were damaged during the experiment and the data was lost. The initial density of the Co(Al) phase was measured to be 8000 kg/m^3 and for the CoAl phase, 6914 kg/m^3 .

Interpretation of Data

The data obtained in the Hugoniot experiments is interpreted by application of the Rankine-Hugoniot jump conditions:

$$\rho_0 U_s = \rho (U_s - u_p) \quad (1)$$

$$\sigma_{xx} - \sigma_{xx_0} = -\rho_0 U_s u_p \quad (2)$$

where the Hugoniot compressive stress data collected is assumed to be $-\sigma_{xx}$. Assuming that yielding has occurred and using the von Mises yield condition,

$$p = -\sigma_{xx} - 2/3 Y_0 \quad (3)$$

where Y_0 is a constant and is the yield stress in simple tension. For the Co(Al) phase, these assumptions are thought to be valid since the yield stress and Hugoniot elastic limit are low compared to the levels of stress encountered. The experimental oscillograph records of stress indicated no elastic stress precursor wave, although it may have been present, but lower than the resolution capabilities of the measurement system. Thus for the Co(Al) phase, the propagating wave is almost entirely plastic, with a very small elastic precursor presumed to exist because of a known tensile yield

TABLE 4.

Experimental Results of Hugoniot Experiments

<u>Shot No.</u>	<u>Material</u>	<u><112> Stress</u>		<u>Particle Velocity</u>
		<u>GPa</u>	<u>kbar</u>	<u>km/sec</u>
77-053	Co(Al)	2.05 Δ	20.5	0.061 Δ
77-059	Co(Al)	3.76 Δ	37.6	0.098 Δ
77-060	Co(Al)	2.93 Δ	29.3	0.079 Δ
79-018	Co(Al)	--	--	--
79-019	Co(Al)	7.36 ∇	73.6	0.179 ○
79-020	Co(Al)	4.26 ∇	42.6	0.099 ○
79-021	CoAl*	9.83 ∇	98.3	0.259 ○
79-022	CoAl*	7.40 ∇	74.0	0.179 ○

Δ ± 3 percent, Quartz Gage

∇ ± 5 percent, Manganin Gage

○ ± 6 percent, Manganin Gage

* Directionally solidified large grained material.
Stress measured in <110> growth direction.

stress.

As previously discussed, only two Hugoniot data points for the CoAl phase have been obtained as of this date; however, future work is planned. Interpretation of the currently available data is that the CoAl phase exhibits only elastic behavior over the pressure range considered. High shock speeds and the brittle nature of this material under quasi-static loading tend to support this interpretation. The lack of extensive experimental data required that some assumption be made; the elastic assumption seems most reasonable.

Co(Al) Phase

The elastic-plastic nature of the Co(Al) phase will be discussed first. The shock velocity U_s is calculated from the experimental data for $-\sigma_{xx}$ together with the conservation of momentum equation expressed in Equation (2).

$$U_s = \frac{-\sigma_{xx}}{\rho_0 U_p} \quad (4)$$

From conservation of mass, Equation (1), the instantaneous density is also calculated.

$$\rho = \frac{\rho_0 U_s}{U_s - u_p} \quad (5)$$

The compression η is found from the definition and Equation (5).

$$\eta = \frac{\rho}{\rho_0} - 1 = \frac{u_p}{U_s - u_p} \quad (6)$$

The results of calculating pressure, shock velocity, density, and compression for the experimental Co(Al) data are shown in Table 5.

TABLE 5.
Reduced Hugoniot Data for Co(Al)

Shot No.	$-\sigma_{xx}$ GPa	p^* GPa	u_p km/s	U_s km/s	η
77-053	2.05	1.93	0.061	4.20	0.015
77-060	2.93	2.81	0.079	4.64	0.017
77-059	3.76	3.64	0.098	4.80	0.021
77-020	4.26	4.14	0.099	5.38	0.019
77-019	7.36	7.24	0.179	5.14	0.036

* $p = -\sigma_{xx} - 2/3 \gamma_0$; $\gamma_0 = 0.176$ GPa.

From the reduced Hugoniot data, it is necessary to get an expression for pressure p in terms of the compression η for the computer simulation. A commonly used form that is compatible with the computer code used is

$$p = p(\eta) = A\eta + B\eta^2 + C\eta^3 \quad (7)$$

A smooth curve was fitted to the experimental points from Table 5 which is shown in Figure 3. The curve in Figure 3 was fit by a cubic equation by the least-squares method where the coefficients from Equation 7 are, in GPa:

$$\begin{aligned} A &= 165 \\ B &= 512 \\ C &= 1074 \end{aligned}$$

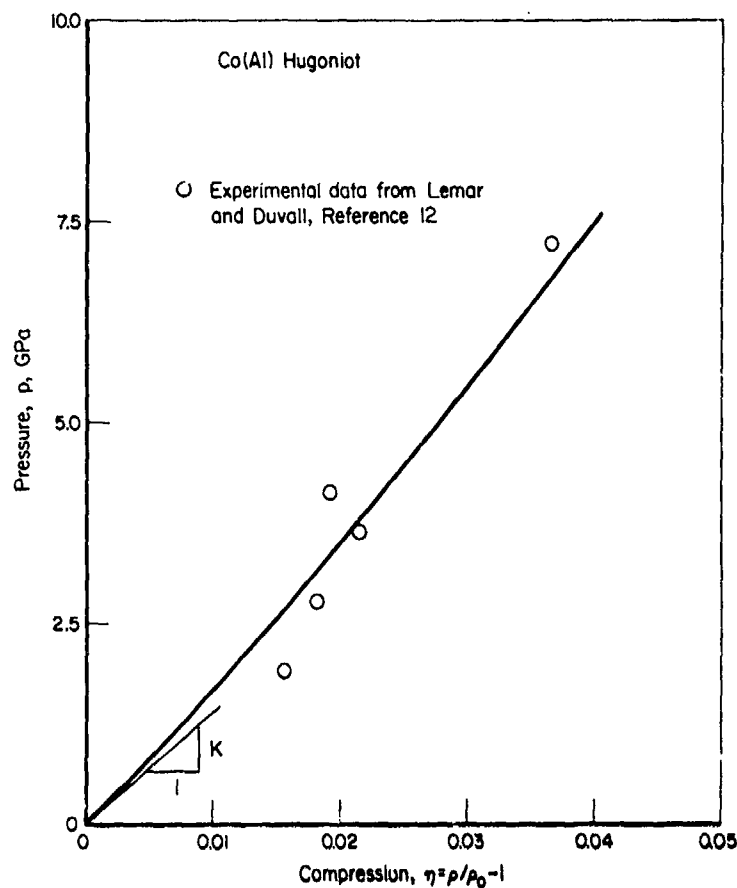


Figure 3. Pressure-Compression Representation of Co(Al) Hugoniot

Note that the first order coefficient A is the bulk modulus. For comparison, the bulk modulus determined by Bennett [8] was $K = 172.2$ GPa (≈ 4 percent difference).

Next, calculation of strength related properties is required. Using measured property values where possible, the following relations are invoked:

$$\text{Elastic Modulus, } E = K + 4/3 G \approx 279.0 \text{ GPa} \quad (8)$$

$$\text{Hugoniot elastic limit, } HEL = Y_0 \left(\frac{K}{2G} + \frac{2}{3} \right) \approx 0.3 \text{ GPa} \quad (9)$$

$$\text{Strain at elastic limit, } \eta_y = \frac{Y_0}{2G} \approx 0.0011 \quad (10)$$

It is also important to note an observation of Lemar and Duvall that the behavior of the Co(Al) is very similar to that of copper [12]. Figure 4 shows the Co(Al) Hugoniot in the compressive stress versus particle velocity plane including strength. Also included in Figure 4 is an accepted copper Hugoniot given by

$$P \text{ (kbar)} = (10) (8.93) (3.94 u_p + 1.489 u_p^2) \quad (11)$$

where the particle velocity u_p is in km/sec. For comparison, the Co(Al) and CoAl experimental points are also shown.

CoAl Phase

Experimentally, the material properties of the CoAl phase are more difficult to determine than the Co(Al) because of its high melting temperature and extremely brittle nature in preparation and handling. Very few investigators have obtained any data for this phase, in static or dynamic experiments. Because the Hugoniot experimental data is limited to two data points, some simplifying assumptions are required. The apparent elastic nature of the material provides a fortunate simplification for the stresses considered. The two Hugoniot data points were at stress levels of 7.40 GPa and 9.83 GPa, with no observed HEL in the stress record. Since the reported average longitudinal wave speed of 6.38 km/sec was relatively constant for the two shots and no definitive HEL was observed, the CoAl phase is assumed to behave elastically for the range of stresses encountered. For this brittle phase, the yield stress is the fracture stress presented in Table 3. This value is approximate and inferred from the eutectic and Co(Al) phase by the theory of mixtures and quasi-static tension tests. An elastic shear modulus G and density ρ_0 was found to be 103.0 GPa and 6914 kg/m³, respectively. The resulting bulk modulus K for CoAl is 144.0 GPa.

Fracture Properties

To date, no separate shock-induced fracture experiments of each individual phase of the eutectic have been completed*. Therefore, the fracture parameters presented and used in this study are necessarily speculative. A detailed discussion of high tensile stress will be left somewhat open-ended here, since it is expected that extensive damage and fracture will occur before the material will build up to very high (greater-than-yield) tensile stresses. The need to accurately describe material behavior after incipient fracture is beyond the scope of this study. Later, more extensive studies will require complete fracture properties. The fracture model used in this study predicts the onset of microfractures (unspecified voids or cracks) through the critical damage threshold stress σ_0 . In reality, the occurrence of new surface formation or micro-fracturing

* These experiments are currently being conducted.

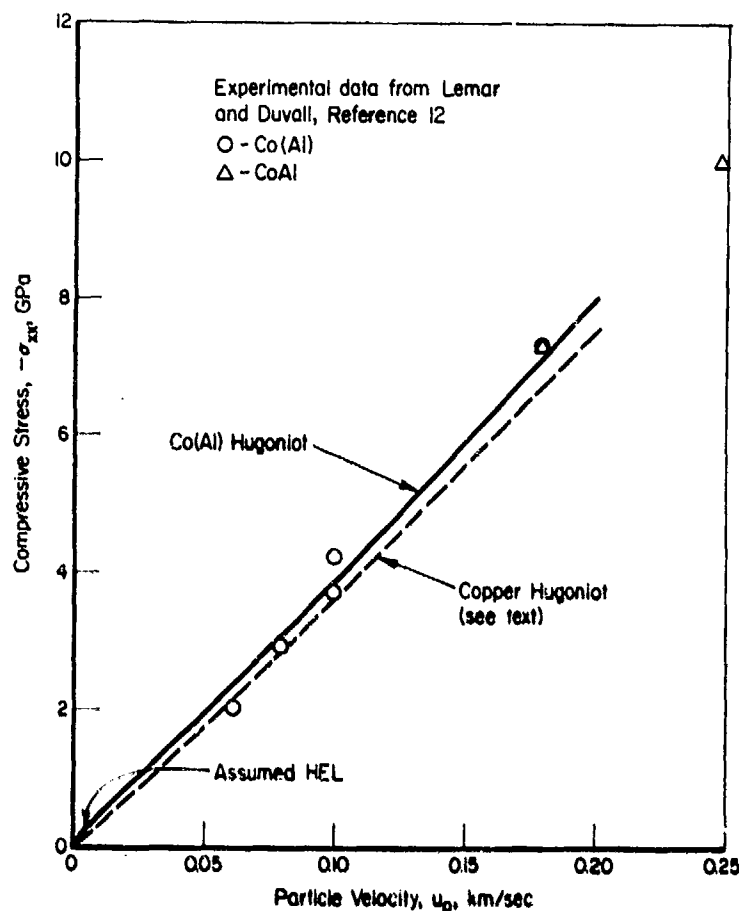


Figure 4. Stress-Particle Velocity Comparison:
Co(Al) - Cu

causes stress relaxation and dissipation of the propagating energy, thus altering the propagating disturbance. This phenomena is not accounted for by the model used. However, in any time-dependent dynamic fracture model there exists a threshold of damage which is determined by correlation with microscopically observed void or crack formation. Thus it is felt that this is reasonable for a preliminary study in incipient fracture. After incipient fracture occurs, the material accumulates damage according to the Tuler-Butcher [14] model

$$D = (\sigma - \sigma_0)^\lambda \Delta t \quad (12)$$

where the damage D increases by the λ power for the length of time Δt that the stress σ is greater than σ_0 . For this two-dimensional problem, the state of stress σ is represented by the maximum principal stress, extending

the Tuler-Butcher fracture model to two dimensions. For convenience, λ is assumed equal to 2.

For the Co(Al) phase, the author is not aware of any fracture data. The low yield stress and very plastic nature of the material would make any prediction of fracture somewhat uncertain, particularly when statically determined values are used in the dynamic case. Since the Co(Al) phase seems to be very similar to copper in structure (FCC), in their Hugoniot, and in their similar ductile behavior under conventional loading, and since dynamic fracture data is available for copper, the damage threshold stress σ_0 for Co(Al) is assumed to be that of copper. This value of σ_0 is reported by Smith [15, Table 2] to be 0.95 GPa for pulse duration of $3/4 \mu\text{sec}$.

From Table 3, the fracture stress F of the CoAl phase was given as 2.069 GPa. It is assumed that this value of stress resulting in fracture in a static tensile test (inferred from eutectic measurements) is also the damage threshold stress σ_0 for the CoAl. Note that this assumed damage threshold stress for CoAl is more than double that assumed for Co(Al).

Error

Because of the lack of material property data and speculative nature of those properties used, an error analysis is not conducted. It is to be emphasized that the results obtained using these properties are highly dependent on the accuracy of the assumed values. It is believed that the values used represent a "best fit" of all data available at this time. It is clear, however, that more experiments are necessary. Within this framework of accuracy, a simulation of dynamic fracture may now be executed.

FRACTURE SIMULATION OF EUTECTIC

With the material properties and the geometry known, the cobalt-aluminum bi-phase eutectic under shock pulse loading can now be simulated on the STEALTH [16] computer code. The STEALTH version used was shortened and modified for this application. From this simulation it is desired to predict the location of incipient fracture and estimate the mode of fracture most likely to occur under experimental conditions. The first step in the simulation is the problem specification. Then the dynamics are described and the simulation is carried out. Later, actual experiments will be discussed and compared to the computational predictions.

Problem Specification

The cobalt-aluminum eutectic has been described as a lamellar bi-phase material. The lamellar nature is not perfect, with lamellar terminations and branching being the most common defects. On a much smaller scale, the nearly ideal character is more apparent as seen in Figure 2. The lamellar nature seen in the plane of the photograph is also observed approximately in a perpendicular section.

For the simulation, a representative region of the eutectic is chosen; Figure 5a shows the problem geometry. The boundary ABC is a specified velocity boundary history representing the shock pulse input. The segments CD and AF are boundaries of symmetry; thus the material is assumed to be infinite and periodic in the y-direction shown. The boundary DEF is a free surface with a vacuum outside the material boundary. The material in the z-direction, the direction perpendicular to the x-y plane shown, is assumed to be infinite in extent such that strain in that direction is constant. Also, shear strains related to that direction are zero, hence the state of two dimensional strain.

The zoning of this geometry for simulation is shown in Figure 5b using a total of 1300 zones; 250 for the CoAl and 1050 for the Co(Al). The CoAl phase is represented by the block of larger zones. The Co(Al) consists of the smaller zones because the plastic behavior expected is likely to produce larger deformations. Finer zoning tends to increase accuracy by reducing deviations from "exact" solution. The physical dimensions chosen were scaled from an interlamellar spacing of $30\text{ }\mu\text{m}$. The volume fraction used is 0.30 CoAl for convenience. The length of the material was chosen to be three times the interlamellar spacing. Although this length is quite small compared to typical specimen lengths, it was chosen to yield approximately square zones and satisfy a maximum number of grid points available in the x-direction.

The interphase boundary is modeled as a perfect bond between the Co(Al) and CoAl phases. This is thought to be a good assumption considering the nature of the in situ boundary. Other models of interphase boundaries were not available in the finite-difference STEALTH code, but their development and use is planned for future work.

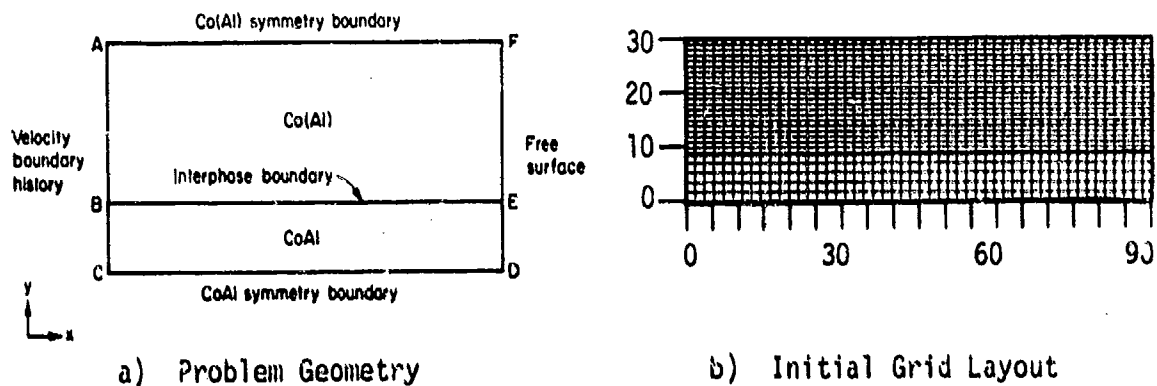


Figure 5. Simulation of Co-Al Eutectic

The constitutive relations and the specific properties of the cobalt-aluminum eutectic constituents were previously given. In addition, both quadratic and linear artificial viscosity are used. The coefficient of quadratic artificial viscosity has a value of 2 and the coefficient of linear artificial viscosity has a value of 0.8.

Dynamic Simulation

The entire grid is assumed to be at rest initially with the transient disturbance introduced at the left hand boundary shown in Figure 5a. The transient disturbance is specified as a particle velocity boundary history. The material particle velocity in the direction of propagation is specified as a constant for some period of time representing a plate impact problem. When the pulse has passed completely into the material, the velocity drops off to a value to which the material has been accelerated. The particle velocity pulse is given as 0.061 km/sec corresponding to a projectile velocity of 0.122 km/sec with the pulse length representing a plate projectile which is approximately one-tenth the thickness of the given impacted target. The velocity that the material has been accelerated to is 0.0015 km/sec as determined by simulations using pressure as the boundary history specification. The stresses produced from the particle velocity input of 0.061 km/sec correspond to about 2.2 GPa in Co(Al) and about 2.7 GPa in CoAl. Although these stresses are compressive, note that they are greater in magnitude than the damage threshold stresses of 0.95 GPa in Co(Al) and 2.07 GPa in CoAl.

The simulation was started on the STEALTH code and allowed to run until some damage had accumulated, indicating the occurrence of micro-fracturing, or incipient fracture. The problem was run long enough for reflection to occur from the free end and a tensile state to build up in the eutectic. Both tabulated and plotted output was produced by the STEALTH program and its companion GRAPHic DISPlay program, GRADIS.

Results and Discussion

The wave propagation was qualitatively monitored through a series of three-dimensional isometric contour plots of the x-particle velocity in the entire grid. Figure 6 shows a sample plot at cycle 100. The cycle is the calculation cycle or number of time steps the grid has been entirely recalculated. The time is in scaled units; the specific conversion does not yield any clarity to this study and will not be discussed. The vertical scale is determined by the maximum and minimum values of velocity at that moment. Reflection of the wave begins later at cycle 130 when the compressive pulse turns to tension.

Before the fracture results are presented, some general features of the wave propagation seen in Figure 6 should be noted. The wave travels faster in the CoAl initially as can be seen at the right-hand side of the grid (CoAl has the larger zones). The Co(Al) is undergoing large deformations and distortions near the interphase boundary as may be inferred from the

large grid distortions. The two-peak appearance of x-particle velocity plots results from x-components in the total particle velocity vector. Intuitively, the compressed region is further ahead in the CoAl phase than the Co(Al) phase. The compressed CoAl tends to spread in the y-direction into the as yet unstressed Co(Al). Lagging behind the CoAl compressed region is the Co(Al) compressed region, spreading into the rarefying CoAl. The result is that the particle velocity vector has y-components not showing up in the x-particle velocity plots. The intuition is backed up by calculated displacements in the tabulated STEALTH outputs. The process just mentioned imparts a rotation to the material near the interphase boundary causing a shear wave to propagate back into the more deformable Co(Al). Shear waves were not discernible in the CoAl. Upon inspection of the STEALTH output, the shear in the zones were generally about one order of magnitude less than the normal stresses, even at the interphase boundary. In the Co(Al) phase, the shear stress is limited by plastic flow.

Fracture in the eutectic did not occur during the first passage of the wave, as modeled in this simulation. Incipient fracture did not occur until the wave reflected from the free surface. The elastic wave traveling through the CoAl phase reaches the free surface and begins to reflect before the elastic-plastic wave in the Co(Al) reaches the free boundary. The occurrence of incipient fracture or damage accumulation first occurs within the CoAl phase just before the 150th cycle nearest the CoAl symmetry boundary and diminishes toward the interphase boundary. This is shown in the isometric contour plot of accumulated damage (DAC), Figure 7a, where the vertical scale is damage in relative units. At a later time, more damage in more zones accumulates toward the interphase boundary as shown in Figure 7b, at cycle 160. Note that the vertical scales are different between Figures 7a and 7b. Note also that there is damage in all of the zones across the width of the CoAl phase, implying incipient fracture throughout the CoAl layer, and that no visible damage exists in the Co(Al) phase. Although part of the Co(Al) phase is hidden in Figure 7, the tabulated output verifies this statement. Thus, it can be concluded, as a result of this simulation, that intraphase CoAl fracture would be the most likely mode of fracture to occur. The specific location where damage occurs first in the CoAl is at the theoretical spall plane which is roughly the distance away from the free surface equal to the thickness of the impacting projectile, if the projectile and target materials are the same.

In this fracture simulation, as in most simulations, the results must be qualified. The first qualification pertains to the material properties used. Many of the elastic properties were estimated from the mixing of anisotropic and isotropic properties, some of which were determined from one experimental data point. The Hugoniot's were defined from limited data and, in the case of the CoAl, from only two data points. The fracture properties of both materials for the simulation were contrived without experimental data. Indeed, the properties of both phases are only rudimentarily defined.

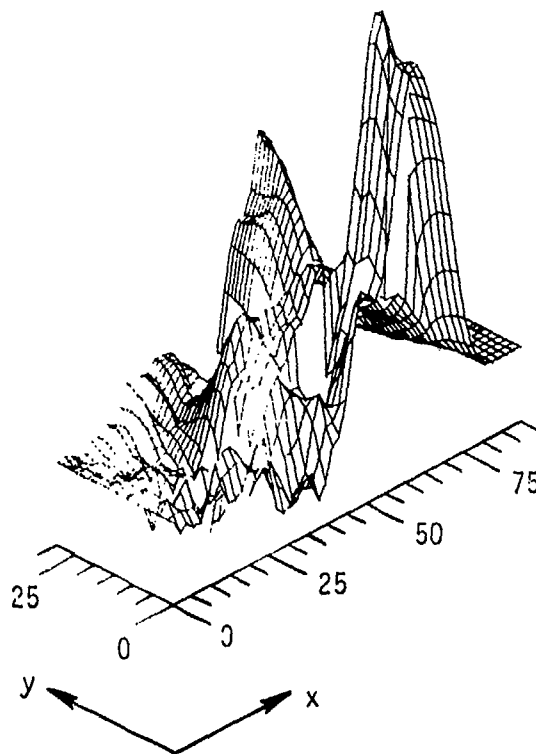


Figure 6. Isometric Contour of XVL Cycle = 100

Secondly, the fracture model used considered a tensile type fracture mode where cracks or voids (unspecified) are assumed to form. The cumulative damage fracture model that was used for this simulation of incipient fracture degenerated to a simple threshold fracture criterion. To refine this investigation, perhaps separate ductile and brittle fracture models should be considered for the two cobalt-aluminum eutectic constituents.

The third qualification involves the simulation itself. The model of the interphase boundary and the method of introducing the shock pulse into the material were very simple. The considerable plastic flow thought to occur along the interphase boundary may result in greater stress relief than simulated by perfect bonding. However, theoretical models of the interphase boundary are not well developed to account for this, nor are their specific properties known for the cobalt-aluminum eutectic interphase boundary.

The pulse shape introduced to the material was approximately a square pulse equal for both phases of the eutectic. In general, if a single phase projectile impacts a bi-phase material, as it does in this study, impedance matching must be considered to determine the input velocity and duration of a simulating pulse in each phase. More sophisticated means of representing

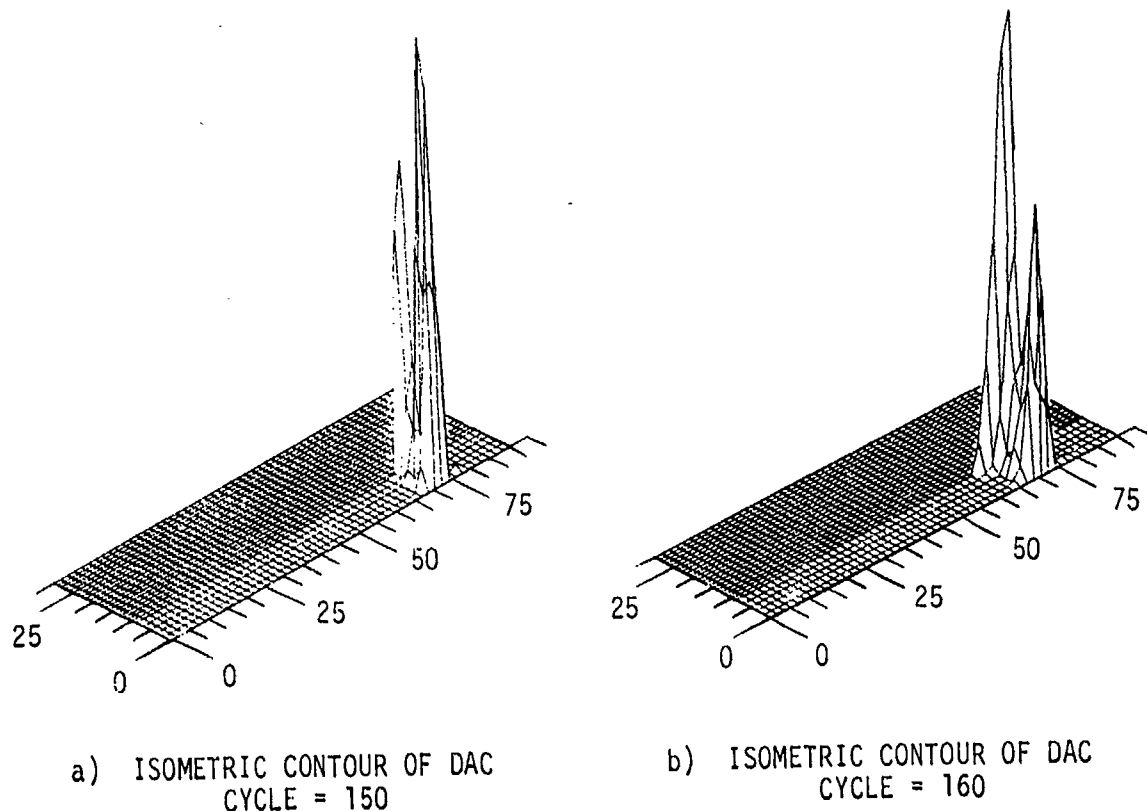


Figure 7. Damage Accumulation After Wave Reflection

the shock pulse input may be in order.

The simulation was not checked by a convergence study due to time and to an extent, computer storage limitations. Finer zoning, however, should provide more accurate results. During the eutectic and other simulations, it was noticed that an unusual amount of oscillation was present in the solution, particularly upon free surface reflection. This oscillation is suspected to be due to the STEALTH treatment of boundary and corner conditions.

COMPARISONS WITH DYNAMIC FRACTURE EXPERIMENTS

To date, three soft recovery plate impact fracture experiments of the eutectic have been conducted using the gas gun facility at Washington State University, Pullman, Wa. Each specimen was a bi-crystal of the eutectic with each grain occupying about 50% of the cross-sectional area. The specimens were nominally 12.7 mm in diameter and 3 mm thick. The flyer

plate material was the Co(Al) phase, and nominally 1 mm thick. The impact velocities in km/sec for the three experiments were 0.23, 0.214, and 0.153.

These experiments have only recently been completed and the data and recovered specimens have not been thoroughly analyzed. Therefore, at this time only qualitative comparisons can be made. Each of the three specimens exhibited internal micro-cracks; with damage decreasing with decreasing impact velocity. The least damage was observed in the 0.153 km/sec impact velocity case. The two lower impact velocity specimens were cut perpendicular to the impact surface, polished, etched and observed using the optical microscope at magnifications of 400x and 800x. Results so far are that all of the observed cracks are in the CoAl phase of the eutectic. Also, in some instances, cracks were observed along interphase boundaries within the eutectic specimen. These results are in good qualitative agreement with the simulation prediction. Further, the simulation was conducted at a corresponding impact velocity of approximately 0.122 km/sec, when damage (unspecified cracks or voids) in the CoAl phase was predicted. At this date, no fracture experiments have been conducted at an impact velocity below the simulation velocity to fully test the simulation predictions. However, since the experimental results for the impact velocities considered all indicated fracture in the CoAl phase, it can be concluded that the simulation and the experimental results are not inconsistent. Additional experiments at other impact velocities nearer the simulation velocity and below are planned. More simulations should also be made with lower impact velocities to predict a lower limit for damage threshold conditions.

With additional theoretical work to develop a better interphase boundary model and more theoretical and experimental work to determine appropriate fracture models of the individual phases, the investigation of more macroscopic spall fracture can be pursued.

ACKNOWLEDGEMENT

The authors wish to acknowledge Drs. G. E. Duvall and E. R. Lemar for their valuable assistance in performing the gas gun experiments, and the National Science Foundation for their support.

REFERENCES

1. Gilman, J. J. and Tuler, F. R., "Dynamic Fracture by Spallation in Metals", Int. J. of Fracture Mechanics 6, 1970, 169-182.
2. Peck, J. C., "Stress Wave Propagation and Fracture in Composites", in Lee, E. H. (editor). Dynamics of Composite Materials, A.S.M.E., New York, 1972, 8-34.

3. Lundergan, C. D. and Drumheller, D. S., "The Propagation of Transient Stress Pulses in an Obliquely Laminated Composite", In Lee, E. H. (editor). Dynamics of Composite Materials, A.S.M.E., New York, 1972, 35-47.
4. Almond, E. A., Embury, J. D., and Wright, E. S., "Fracture in Laminated Material", in Interfaces in Composites, ASTM STP 452, Amer. Soc. Testing and Materials, York PA, 1969, 107-129.
5. Salkino, M. J., "Interfacial Stability of Eutectic Composites", in Interfaces in Composites, ASTM STP 452, Amer. Soc. Testing and Materials, York, PA., 1969, 149-167.
6. Stout, M. G., Courtney, T. H., and Przystupa, M. A., "Redetermination of the Invariant Compositions in the Co-CoAl Eutectic", Met. Trans. A 8A, 1977, 1316-1318.
7. Cline, H. E., "The Mechanical Properties of the CoAl-Co Eutectic", Trans. TMS AIME 239, 1967, 1906-1916.
8. Bennett, B. W., "Single Crystal Elastic Constants of Co(Al) Face Centered Cubic Alloys", M.S. Thesis, Mich. Tech. Univ., 1979.
9. Stout, M. G., Research Notes, Deformation and Fracture of Co(Al)-CoAl. Michigan Technological University, 1978.
10. Przystupa, M. A., Private Communication, 1979.
11. Fowles, G. R., Duvall, G. E., Asay, J., Bellamy, P., Feistmann, F., Grady, D., Michaels, T., and Mitchell, R., "Gas Gun for Impact Studies", Rev. Sci. Instruments 41, 1970, 984-996.
12. Lemar, E. R. and Duvall, G. E., "Hugoniot Measurements and Dynamic Fracture Experiments on the Co-CoAl Eutectic System", Washington State University Report MTU03569, Pullman, Washington, 1979.
13. McQueen, R. G., Marsh, S. P., Taylor, J. W., Fritz, J. N. and Carter, W. J., "The Equation of State of Solids from Shock Wave Studies", In Kinslow, R. (editor). High Velocity Impact Phenomena, Academic Press, New York, 1970, 293-417.
14. Tuler, F. R. and Butcher, B. M., "A Criterion for the Time Dependence of Dynamic Fracture", Int. J. of Fracture Mechanics 4, 1968, 431-437.
15. Smith, J. H., "Three Low-Pressure Spall Thresholds in Copper", in Dynamic Behavior of Materials, American Society for Testing Materials, Philadelphia, PA, 1963, 264-281.
16. Hofman, R., "STEALTH, A Lagrange Explicit Finite-Difference Code for Solids, Structural, and Thermohydraulic Analysis", ERPI NP-260, B7 Science Applications, Inc., for Electric Power Research Institute, Palo Alto, California, 1976.

THE COMPRESSION TEST REVISITED

JOHN MESCALL
Mathematician

RALPH PAPIRNO
Research Mechanical Engineer

JAMES McLAUGHLIN
Mathematician
Army Materials and Mechanics Research Center
Watertown, Massachusetts 02172

ABSTRACT

Theoretical analyses were made of the axial compression test using the HEMP computer code, and the results were compared with experimental observations for 4340 steel. When suitable boundary conditions, including frictional effects, were employed the agreement was excellent. The constitutive relations used were elastic-plastic including work-hardening. Comparisons were made at large strain levels (more than fifty percent reduction in height).

One of the objectives of this study was to obtain theoretical and experimental data for the development of a ductile fracture model involving shear modes and large strains such as are present in ordnance applications. To date fracture has not been observed in the experiments conducted in steel. We have noted fracture in both Aluminum and Titanium specimens. The analytical results are nevertheless of interest in quantifying the large and complex strain fields produced prior to the onset of fracture.

INTRODUCTION

The ultimate objectives we have in mind in the discussions to follow concern the role of material properties in ordnance applications such as armor-projectile interactions, fragmentation munitions and explosively formed devices such as Misznay-Schardin and shaped charge weapons. Computer simulations of such complex events are available using two or three dimensional time-dependent codes such as HEMP, HELP, or EPIC. In general the results of such simulations provide quite credible descriptions of the events transpiring, provided attention is confined to kinematic issues such as momentum transfer or a general picture of particle velocities. When more specific questions are raised concerning issues which depend heavily on material response under such extreme loading conditions, the results are less satisfactory.

As examples of the issues which need clarification, we might cite (a) massive plastic deformation under very brief but very intense pressure fields, (b) spall, which is fracture under a tensile stress field with very little plastic flow and (c) fracture in a shear mode under nominally compres-

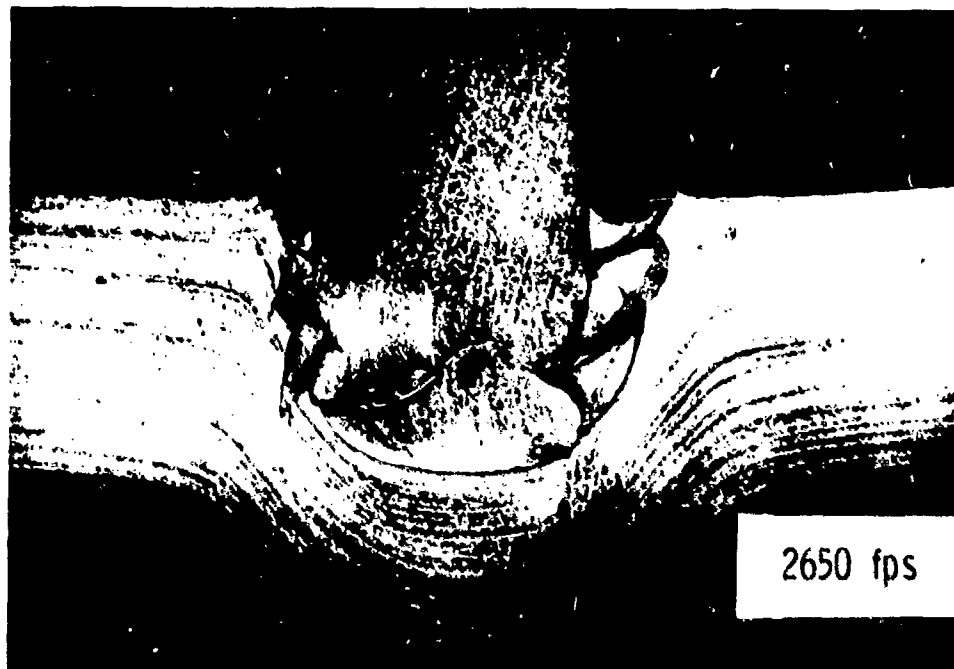
sive loading conditions. This latter situation is probably the most commonly occurring and the most important in ordnance applications, yet it is the least well understood. It is usually preceded by extensive plastic deformation. It may or may not involve an extreme localization of a deformation pattern, sometimes termed adiabatic shear banding. As an example of this, see Figure 1 in which cross sections are shown of targets of the same material (4340) but heat treated to different hardness levels.

Unfortunately, little correlation has been found to date between material behavior in the noted ordnance applications and the mechanical properties of materials as determined by conventional test procedures. Such correlations have been sought for example in terms of yield strength, ultimate strength, reduction in area values from static tensile tests, or in terms of energy absorbed in Charpy tests, as well as fracture toughness parameters such as K_{IC} . While general trends may be observed in such correlations, anomalous behavior is observed frequently and with sufficient magnitude that such correlations are best regarded as qualitative rather than quantitative.

The objection may be raised that, in view of the obvious differences between strain-rates involved in ordnance applications and in those quasi-static mechanical tests mentioned, the observed lack of correlation is not surprising. In the view of the writers, however, differences in stress and deformation states are at least as responsible for the failure of attempts at correlation as are strain-rate effects. As noted earlier, the most commonly occurring mode of failure in ordnance applications is shear, frequently preceded by very extensive plastic deformation. Another dominant feature of the applications of interest is that of a prevailing compression field which is noticeably not present in the conventional mechanical tests.

A parallel situation exists for those interested in fractures which develop in forming operations involving large plastic deformation. As Kuhn [1] observes, tension or torsion test data are of little value in workability evaluations involving surface fractures, largely because of the differences in stress and deformation states which exist between the laboratory test and the forming operation. Kuhn notes that the upset test does provide a useful deformation test which produces a stress state more closely allied to those occurring in forming processes. In the upset test (as distinct from the simple uniaxial compression test) barreling of the cylindrical surface is encouraged, and, in fact, provides flexibility for providing information useful for workability testing. Such data is frequently presented in the form of a locus of strains present at the equatorial surface of the cylindrical specimen when fracture is first observed there during axial compression. See Figure 2 for representative data for mild steel.

An examination of the computer simulations of several ballistic penetration problems as well as several fragmentation problems shows that the strain fields developed in certain critical regions would indeed be approaching the failure locus denoted in Figure 2. It is, therefore, of interest to examine in more detail the utility of upset tests in helping to relate mechanical properties to ordnance performance.



Low Strength 4340 Target



High Strength 4340 Target

Figure 1. Differences In Failure Mode In Steel Targets
(Note Drop In Ballistic Limit As Shear Band
Develops In High Strength Target)

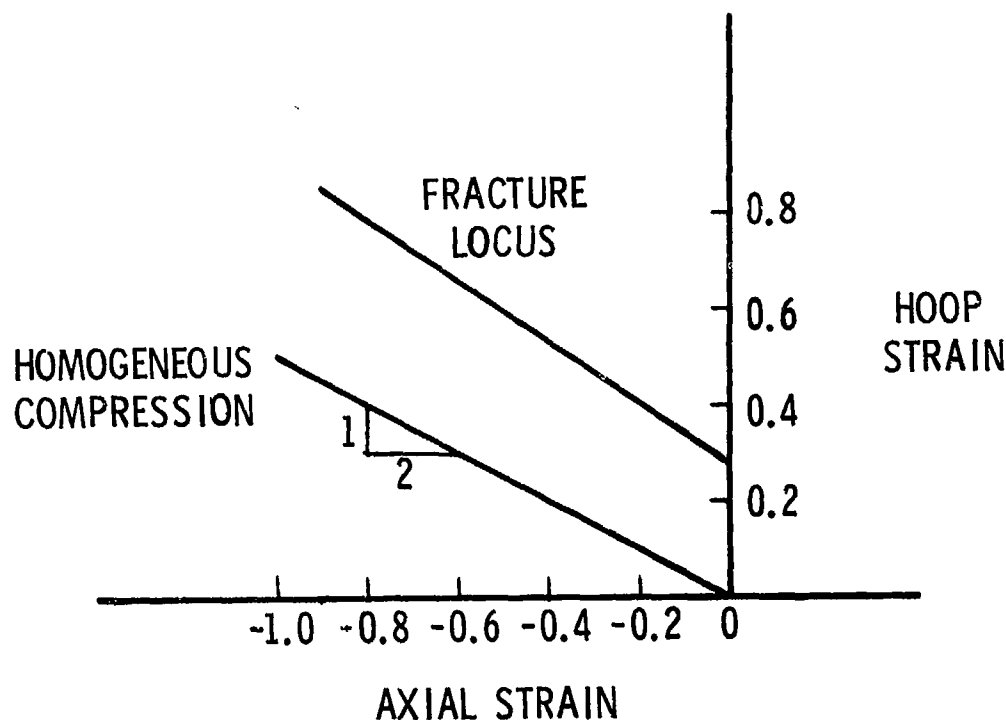


Figure 2. Strains At Fracture At Equatorial Surface In Upset Test On Cold Drawn 1045 Steel Rod

BACKGROUND

In axial compression of a cylinder without friction at the die contact surfaces, the test specimen undergoes uniform axial compression. No barreling of the cylindrical surface occurs and the circumferential and radial strains are tensile and each equal to one-half the axial compressive strain throughout the specimen body. In practice this condition is never realized in static, large strain compression tests. When friction is present at the die contact surfaces, bulging or barreling of the free surface occurs and the stress and strain distributions become highly nonuniform.

Geometric effects are also important. Decreasing the aspect ratio (height to diameter) increases the bulge curvature. The equatorial diameter and associated tensile circumferential strain becomes greater than it would have been for the same height reduction in higher aspect ratio cylinders. L/D ratios commonly employed range from one-half to two. Beyond this one faces a possibility of column buckling.

It is important to note that in an upset test carried out to the onset of fracture we have a competition developing between at least two candidate failure modes. At the equator, tensile circumferential stresses and strains develop due to radial expansion; at the same location there are strong compressive axial stresses and strains, moderate radial strains and, of course, zero radial stress. Under certain conditions failure occurs first in this

general location, but as we shall see later there is another failure mechanism which may prevail. The deformation produced within the specimen is highly nonuniform and very strong shear fields develop in the interior of the specimen which may promote failure along a plane beginning near the outer edge of the specimen-die contact surface and making a shallow angle with the cylinder axis.

The mode of fracture associated with the equatorial plane is somewhat easier to relate to and even very rudimentary analyses give reasonable estimates of the stress fields present at the surface in terms of easy-to-measure gross deformation characteristics such as change in height, change in diameter.

As Murphy's law would have it, the more interesting fracture mode for our purposes is far more difficult to analyze and, because it occurs in the interior of the specimen, it is not possible conveniently to measure experimentally any analogous deformation parameters.

It is, perhaps, this very lack of an adequate analytical model which has inhibited more widespread use of the compression test. The primary purpose of this paper is to demonstrate that the dynamic wave-propagation code HEMP can provide a very detailed analysis of the (static) upset test, including the very large plastic deformations involved prior to fracture. As the reader may have already inferred, our ultimate objective will be to cover the dynamic upset test as well. In this paper, we confine attention to a discussion of some representative cases which were simulated computationally and to a comparison with experimental results obtained to test the validity of the calculations.

It should be pointed out that there do exist in the literature several descriptions of finite element solutions to the problem of upset testing. See, for example, C. Lee and S. Kobayashi [2] and J. Price and J. Alexander [3]. However, the first of these does not reproduce several of the experimentally observed features important to large deformation. The second presents computer printouts of deformed grids, but no information on stress and strain patterns induced. Such solutions are quite useful in certain forming applications concerned with kinematic issues such as velocity fields but provide little insight into the problem we have in mind. Finally, the need to address dynamic tests makes it imperative to consider the problem from the vantage point of the elastic-plastic wave propagation code HEMP, originally developed by Wilkins [4].

The HEMP code couples conservation laws with an appropriate equation of state for dynamic as well as static high pressure conditions. A finite difference formulation is used to integrate the equations of motion step-by-step in time. Problems of two spatial dimensions (plane strain or rotationally symmetric) can be treated and virtually any elastic-plastic constitutive law may be employed.

Input to the code consists of specification of the problem geometry,

appropriate initial velocities or applied stress fields and the dynamic material flow properties. Output consists of a detailed space-time history of all important physical properties such as stress, strain, displacement, and velocity. It is thus a valuable tool for providing a dynamic whole-field analysis required to decipher the sequence of events occurring in complex problems. Numerous comparisons of HEMP code predictions and experimental results indicate excellent agreement when material properties can be adequately specified. The code has been applied by us previously in the analysis of quasi-static problems. For example, we have successfully simulated the details of plastic deformation occurring in the standard uniaxial tension test. The code correctly traces the transition from elastic behavior through the onset of plastic flow, up to and beyond the onset of necking and the development of triaxial stress states beyond necking. The calculated load on the specimen faithfully reproduces the experimentally observed maximum at the appropriate strain level, and the calculated drop in load after the onset of necking is in agreement with the experimental observations of Bluhm and Morrissey [5] up to the onset of fracture. Of course, in its present state, the code is not able to speak to details of void nucleation, growth, and coalescence within the necked region, but it is an extremely valuable aid to develop constitutive models for this purpose.

A related problem area we have addressed with the HEMP code is the tensile deformation of notched cylindrical bars, such as those tested experimentally by Hancock and Mackenzie [6]. Again, good correlation was found with experimental behavior.

EXPERIMENTS

Much of our impact and penetration analytic and experimental research had used 4340 steel for the target material and for some of the projectiles as well. This material is quite versatile for such research since it is possible to obtain a controlled range of stress-strain properties by varying the tempering temperature. Additionally materials property data have been published for the various tempers.

SPECIMENS

We chose to use our standard 4340 steel, test projectiles as compression specimens. These are right circular cylinders, 0.759 cm in diameter, 1.524 cm in length, procured by contract and received with a Rockwell-C hardness (HRC) of approximately 53. This hardness value is a result of tempering at 204°C. The tolerances on uniformity of dimensions, end parallelism and perpendicularity are far more stringent than those required in ASTM standard E9 for compression testing. The specimens were retempered at 482°C in vacuum for two hours and air-cooled resulting in HRC = 40. It should be noted that the specimen ends had been finished in a lathe and circular machining marks were visible using a low power microscope. These marks later could be measured after the test to determine the radial dilation of the specimen end surfaces.

PROCEDURE

Loading was performed in a Wiedemann-Baldwin, screw operated testing machine of 267 kN capacity. The specimens were compressed between tungsten carbide loading blocks which were in turn loaded through massive steel compression fixtures installed on the moveable heads of the testing machine. The loading surfaces of the tungsten carbide blocks were parallel to better than one part in 6000. The machine operates with controllable, constant head closure rate during a test. For these experiments a deflection rate of approximately .03 mm/min was applied for the initial loading up to the yield region and this was increased to 0.1 mm/min thereafter. Test data to be compared with the HEMP code predictions were obtained from tests with no lubrication at the specimen ends. Tests were also performed in which 0.05 mm thick Teflon sheet was used for lubrication (We found no significant effect on large deformation behavior by the lubricant).

A series of tests with maximum loads from 93 kN to 245 kN were performed. Data from tests at 156 kN were used for comparison with the HEMP code results, as will subsequently be described. Longitudinal sections were made of a number of deformed specimens and these were polished and etched (A photomicrograph of one such section appears in Figure 6b).

After the test, measurements were made of the end faces, bulge diameter, and final height using a micrometer caliper and a measuring microscope where appropriate. The results of the measurements are given in the next section.

EXPERIMENTAL AND COMPUTATIONAL RESULTS

In our computer simulation of the experiments described in the preceding section we employed an elastic-plastic constitutive law with work-hardening. Fortunately, a stress-strain curve for the specific material used (4340, HRC 40) was available for strains out to about fifty percent in uniaxial compression. See Chait [7], and Figure 3. This data was used in our computer simulations unless otherwise noted.

To simulate compression of the cylinder, a constant velocity of 0.002 cm/microsecond was imposed on the upper portion of the specimen (Only one-quarter of the specimen need be simulated because of symmetry conditions). This velocity was chosen as a compromise between economy and proper simulation of the quasi-static experiments. Economy requires that as large a velocity be employed as is suitable; a velocity larger than the one chosen would induce plastic deformation rather than elastic on the first wave passage and would result in rapid accumulation of such deformation near the loaded end of the specimen, which, of course, is not in accord with the experiments. We shall be content, for now, to let the comparison between computational results so obtained and the experimental results address the question of the clear differences between theoretical and experimental strain-rates. No explicit description of strain-rate effects was taken into consideration in the analysis.

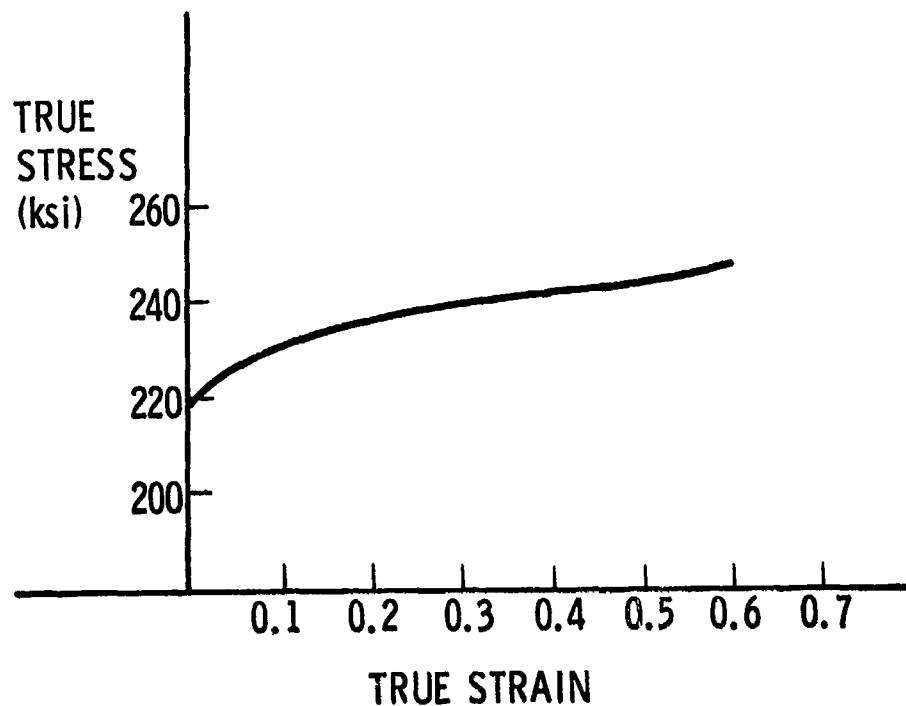


Figure 3. Compression Flow Curve For 4340 Steel, Quenched and Tempered At 800°F (Chait [7])

It is well-known that if friction is absent between the specimen and the loading platens, the result is a uniform compression of the cylinder with uniaxial stress throughout the body and with radial and hoop strains equal to minus one-half of the axial strain. A test case was run to verify that the computer program would reproduce this result and it did with relentless precision.

To simulate the effect of friction between the specimen and end plates, it was assumed that a frictional stress, f , was developed there as the deformation proceeded. The magnitude of this stress was assumed to be given by $f = \mu \cdot \sigma_N$ where σ_N is the normal stress developed at the interface and μ is a coefficient of friction. It was found that the choice of $\mu = 0.3$ gave satisfactory results in the absence of a better guide for such a choice.

It was found that the modeling process described thus far is insufficient to give complete agreement with experiment. With no further conditions imposed as deformation proceeded in our calculations, material from the corners extruded outward and upward into the space physically occupied by the loading platens. See Figure 4. The next step we took was to simulate the platens directly by means of a very rigid block of material all moving with the imposed velocity (Figure 5). These results were also considered unsatisfactory since they produced kinks in the outer surface near the loading platens which were not observed physically.

COMPRESSION TEST RUN1
CYCLE- 8896 TIME-170.006

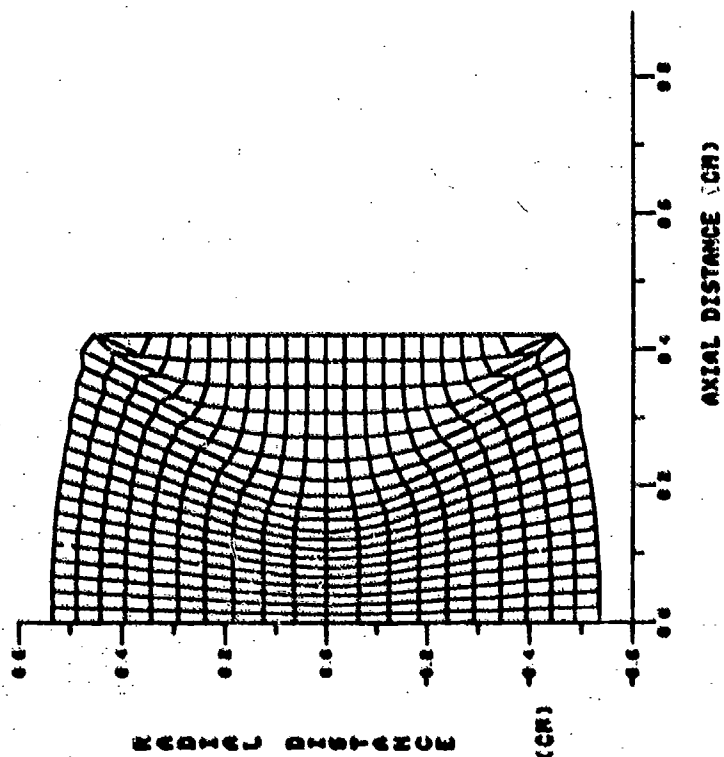


Figure 4. Compression Simulation Without Provision For Roll-Over

COMPRESSION TEST RUN7
CYCLE- 8906 TIME-170.002

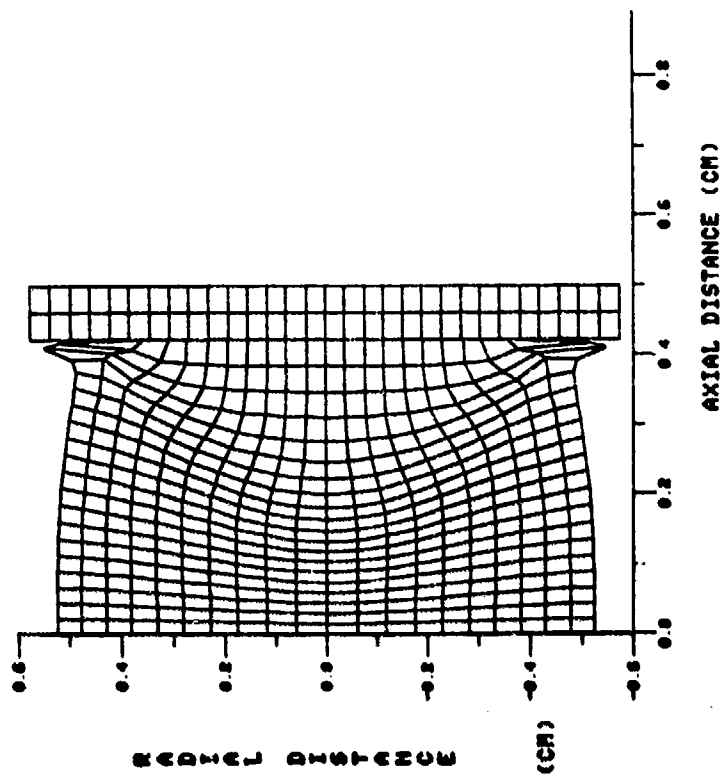


Figure 5. Compression Simulation Including Platen But Without Provision For Roll-Over

The most suitable set of boundary conditions was arrived at by considering the following set of experimental observations. When those experimental specimens which had been shortened in length by approximately fifty to sixty percent were examined closely, it became apparent that the deformation under the loading platens involved the following sequence. The original end diameters (as opposed to the equatorial diameter) increase by only a small amount (say ten percent) while the equatorial diameter is increasing by sixty percent (Small circles due to machining provided fiducial markers in this context). On the other hand, material which is initially on the cylindrical surface "rolls over" and becomes part of the flat end of the specimen under the loading platens, and thereby increasing the observed specimen diameter under the platens. As mentioned, we noticed this process when the end shortening had reached fifty to sixty percent. It had clearly started much earlier in the deformation.

This phenomenon is apparently well-known to workers familiar with forming operations, but it is not as familiar outside such circles. This unfamiliarity persists despite several allusions to the process including quantitative experimental observations by Hsu in 1968 [8].

This phenomenon is clearly an important element in formulating the most suitable boundary conditions. The slide line routine in HEMP was rewritten (a) to permit those edge points on the lateral surface to roll-over and become part of the loaded boundary, and (b) to prescribe the suitable velocity conditions and frictional conditions once they did so. Figure 6a shows the deformed specimen when the simulation considered these issues. The point labeled A designates the location of the point originally at the corner of the unloaded specimen. As can be seen, two points originally located on the lateral surface have rolled over and become part of the loaded surface. This action clearly has a strong influence on the subsequent stress and strain distribution and must be one of the criteria for the acceptance of an analytical solution.

The simulation shown in Figure 6a also shows another essential feature which is observed experimentally viz. the presence of a relatively undeformed conical region under the loading platens. This is bordered by a zone which is heavily deformed in shear. There is a region along the equatorial axis in which one can easily judge (simply by comparing zone sizes with those in the conical region) that there is a strong axial compressive strain but a large tensile hoop strain.

Figure 6b shows the deformation pattern experimentally observed in a cross-section of a 4340 steel cylinder with a stress-strain curve corresponding to the one used in the simulation. The overall amounts of deformation for theory and experiment are quite close in the sense that analytically $L/L_0 \approx 0.46$ and $D/D_0 \approx 1.66$ while experimentally $L/L_0 \approx 0.44$ and $D/D_0 \approx 1.62$.

As can be readily observed, there are many interesting details in terms of which the comparison is excellent. The 4340 rod material used in these experiments has an internal structure (flow lines) which arises as a result

COMPRESSION, FE, RC40, L/D=2
CYCLE- 9883 TIME-199.991

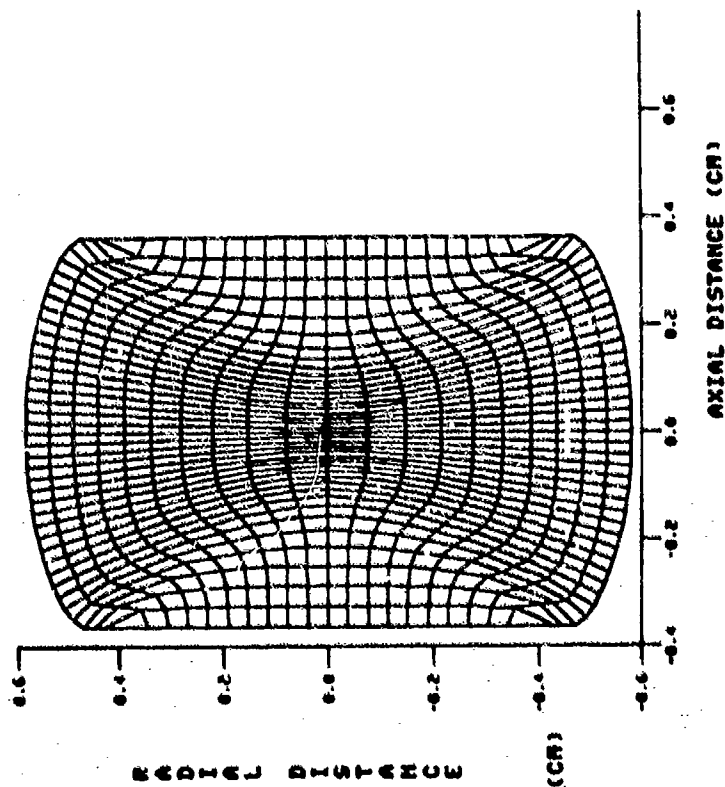


Figure 6a. Compression Simulation Including Roll-Over Effect

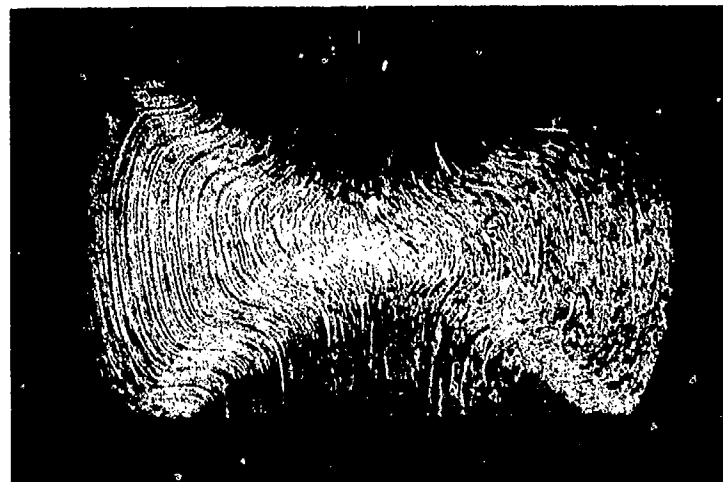


Figure 6b. Experimental Cross Section of RC40 4340 Steel Specimen

of segregation and subsequent rolling. This structure forms a set of fiducial lines which are originally parallel to the axis of the specimen and which delineate the deformation pattern as it occurs (see Figure 6b). If one compares these to the numerical grid lines which were also originally parallel to the specimen axis (Figure 6a), the agreement is clear and indicates we may place a high degree of confidence in both the overall features and in the finer details of the numerical simulation. The highly sheared zones which separate the equatorial regions from the so-called "rigid cones" under the loading platens are also clearly visible in the experiment.

A more quantitative assessment is presented in Figure 7 in which several of the interesting parameters associated with the global deformation are presented as determined analytically and experimentally. The agreement generally is extremely good.

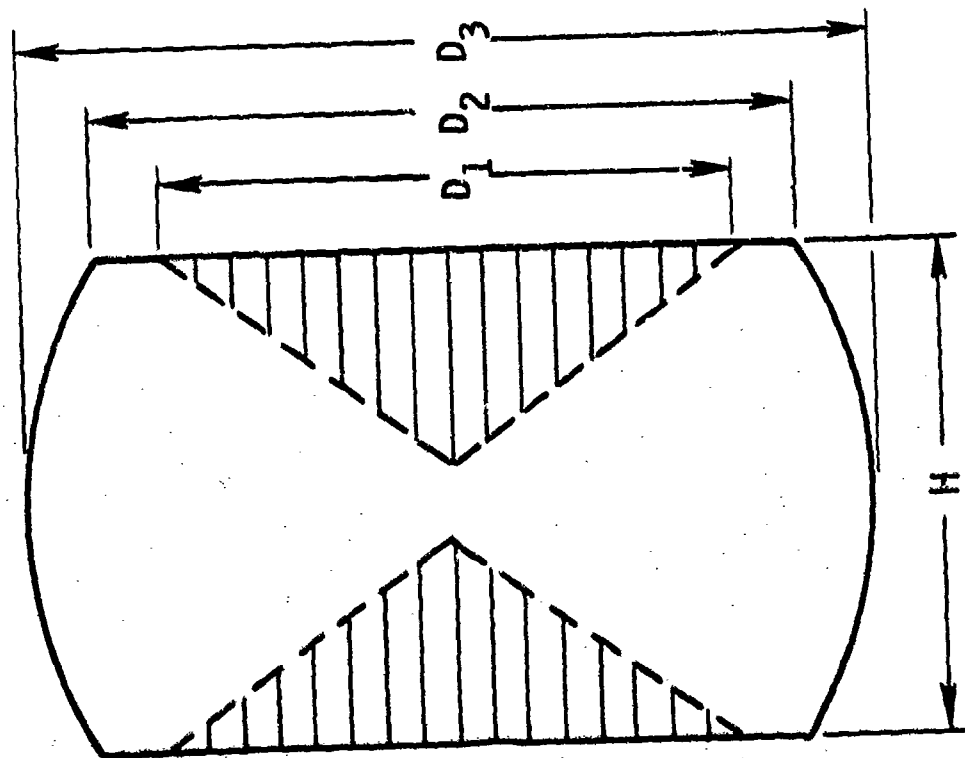
No fracture was observed in the 4340 steel specimens studied up to height reductions of seventy percent, which is at the load limit of our testing machine. This result, therefore, precludes a discussion of the development of a fracture criterion by comparing theoretical and experimental details in this instance. Further testing and computer simulations are required and this paper must be considered a progress report in this respect.

Figure 8 shows some quantitative results in terms of the distribution of plastic strain fields developed in the specimen after a reduction in height of fifty-three percent. The contours plotted are for values of effective plastic strain as conventionally defined. It so happens that these are very close to the values of axial strain for the same locations. Maximum strain values of nearly 1.5 (one hundred and fifty percent) are noted in the geometric center of the specimen.

An interesting feature of the solution presented here deals with the role of hydrostatic pressure (mean normal stress) along the diametral cross-section. Near the specimen axis there is a large compressive value of hydrostatic pressure and all three stress components are negative. This, as shown by Bridgman, permits the development of larger strains before fracture than one might find otherwise. Near the outer surface along the equator the constraint of vanishing normal stress relaxes the level of hydrostatic stress (and, in fact, the hoop stress becomes moderately tensile). This should permit failure to occur at lower strain levels.

Another strain field, slightly less intense than that near the specimen center, but greater than that found elsewhere in the sample is seen to be developing near the specimen corners and proceeding toward the specimen center; these regions are also still located in a compressive stress field, but one less intense than at the specimen center. At the outer ends of the equatorial diameter, the strain fields are roughly fifty percent as intense as those near the center, but a tensile hoop stress is beginning to develop in this region.

The competition between candidate failure modes mentioned earlier is



EXPERIMENT VS THEORY*	
TEST	HEMP
D_1	.79
D_2	1.02
D_3	1.22
H	1.23
* VALUES IN CENTIMETERS	

Figure 7. Quantitative Comparison Between Theory And Experiment

COMPRESSION, FE, RC40, L/D-2
CYCLE- 9883 TIME-199.991

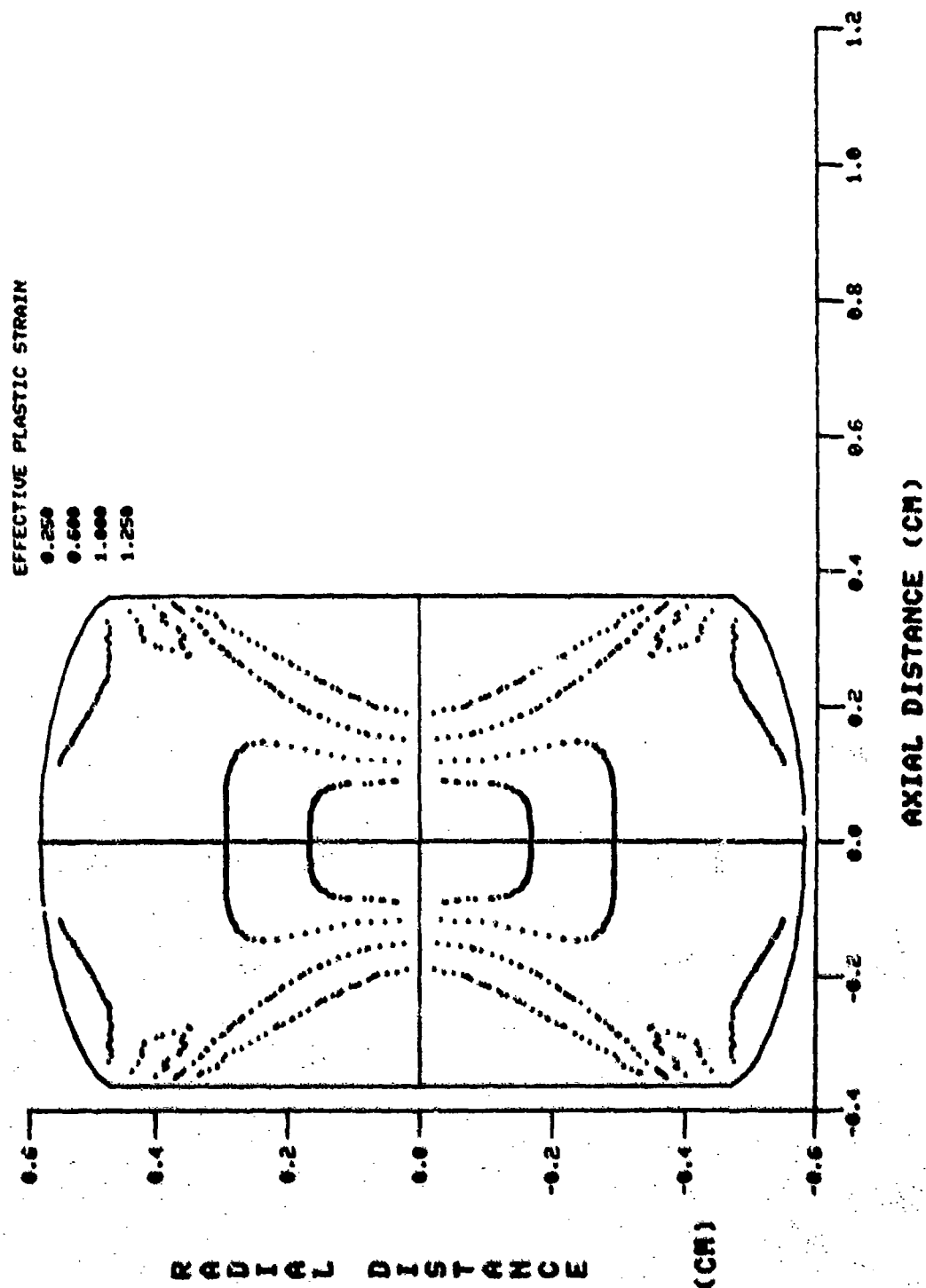


Figure 8. Contours Of Effective Plastic Strain In Compressed RCH40 4340 Steel Cylinder

thus seen to be quite complex and is clearly going to be sensitive to details of geometry and material properties. As such, it needs considerable further study.

SUMMARY AND CONCLUSIONS

A comparison was made between the results of experimental axial-compression tests of 4340 steel and HEMP simulations of those tests. The agreement was sufficiently good to warrant a high level of confidence in those theoretical results which are not amenable to experimental observation, such as stress-strain fields in the interior of the specimen.

It was also demonstrated that when suitable boundary conditions are employed, all essential characteristics of the large deformation processes can be accounted for. In particular, the rolling over of the lateral surface of the specimen is believed to significantly influence further interior deformation and hence must be adequately modeled.

No fracture was observed in the 4340 HRC40 steel specimens we tested so that our original objective of relating the computed stress and deformation fields to the onset of fracture under nominally compressive fields could not be attained in this instance. In this context we should indicate we were limited in our testing machine capacity to 60,000 pounds. We did observe fracture under these conditions in both aluminum and titanium specimens, so there is no inherent flaw in our proposed approach.

Since fracture originates in a localized region where stress, strain and material structure reach a critical mix, the presence, shape and volume fraction of inclusions and other inhomogeneities are expected to have a strong effect (The 4340 steel we used in our experiments was well above average in cleanliness). One of the advantages of the test procedure proposed is that it employs a small specimen size, thereby making it possible to test specimens containing the same microstructural features as the material in an actual component. It also makes it possible to employ samples which are oriented in selective directions with regard to special features produced by fabrication processes.

REFERENCES

- (1) Kuhn, H. A., "Workability in Hot and Cold Deformation Processes," Formability, Analysis Modeling and Experimentation, ed: Hecker, Ghosh and Gogel, published by the Metallurgical Society of the AIME, 1978, pp. 259-280.
- (2) Lee, C. H. and Kobayashi, S., "Analyses of Axisymmetric Upsetting and Plane-Strain Side-Pressing of Solid Cylinders by the Finite Element Method," Journal of Engineering for Industry, May 1971, p. 445.
- (3) Price, J. and Alexander, J., "Specimen Geometries Predicted by Computer Model of High Deformation Forging," Int. J. Mech. Sciences, Vol. 21, 1979, pp. 417-430.

(4) Wilkins, M. L., "Calculation of Elastic-Plastic Flow," Lawrence Livermore Laboratories Report UCRL-7322 Rev. 1. (1969).

(5) Bluhm, J. and Morrissey, R., Proc. 1st Int. Conf. on Fracture, 3, Sendai, Japan (1965), p. 1739.

(6) Hancock, J. and MacKenzie, A., "On the Mechanisms of Ductile Fracture in High Strength Steels Subjected to Multi-Axial Stress States," J. Mech. Physics of Solids, (1976), Vol. 24, pp. 147-169.

(7) Chait, R., "Factors Influencing the Strength Differential of High Strength Steels," Metallurgical Transactions, Vol. 3, February 1972, p. 365.

BEYOND THE TAYLOR TEST TO FRACTURE

RALPH P. PAPIRNO
Research Mechanical Engineer

JOHN F. MESCALL
Chief, Engineering Mechanics Division

ANNA M. HANSEN
Mathematician

Army Materials and Mechanics Research Center
Watertown, Massachusetts 02172

ABSTRACT

Taylor tests were performed for a number of tempers of 4340 steel having a range of hardness from approximately 38 to 55. Theoretical analyses of the test were also performed using the HEMP computer code. The HEMP code correctly predicts the deformed shape of the projectile cylinder and code results suggest that the Taylor formula for dynamic flow stress, when applied to high strength materials, yields results which are nonconservative.

At high impact velocities, where dynamic fracture occurs, two types of behavior were observed. For tempering temperatures of 400 F to 600 F (204 C to 316 C) brittle fracture is observed, with a conical fracture surface at the impact end of the projectile. For the higher tempering temperatures, the projectile remains intact and the impact surface petals. In these cases we have measured a characteristic dynamic fracture strain using a computer-assisted technique.

There is metallographic evidence that, in the case of brittle fracture, narrow bands of adiabatic shear are formed and these serve as the sites where the cracking initiates.

INTRODUCTION

Among the many contributions of G. I. Taylor to ballistics was a suggested method for determining the flow stress of a rigid-pure plastic material at high rates of strain [1]. In the suggested method, a right circular cylinder is ballistically impacted on a thick rigid target at relatively low velocities. The ballistically deformed cylinder is recovered and the deformed length of the test cylinder is measured. Taylor's analysis indicated that the flow stress could be inferred from the relation:

$$Y = \rho u^2 / 2 \ln(L/L_0) \quad (1)$$

where

- Y = flow stress
- ρ = density
- u = striking velocity
- L = deformed length
- L_0 = initial length

The ideal conditions for the test are that the target remains rigid when it is impacted, there shall be no friction at the impact surface, and the cylinder should deform into the shape shown schematically in Figure 1. Implied in the theory is that the same value of Y should result from experiments with cylinders of varying L/D ratio and over a range of velocities.

There is some question of the meaning of the flow stress for many high-strength materials of ballistic interest such as 4340 steel whose dynamic stress-strain curves may exhibit strain hardening. We will show that there are discrepancies between analytic predictions of stress, obtained from a well-established computer code, and those of the Taylor test for such strain-hardening materials. Experimental results also show that the value of Y is not independent of the test cylinder length.

Tests were also performed in which striking velocity was sufficiently increased to cause cracks to form and then further increased to cause complete fracture of test cylinders of 4340 steel of various tempers. Observations and measurements of the recovered specimens showed:

1. There were characteristic fracture modes associated with the various tempering temperatures.
2. There is a characteristic fracture initiation strain for each tempering temperature and this strain is independent of the striking velocity.

In the next section of the report we describe the experimental procedure. This is followed by a section containing a brief description of the analytic procedures. There are then two sections on the results: One on the flow stress studies and one on the fracture investigations. The last section of this paper contains a summary of the work and conclusions.

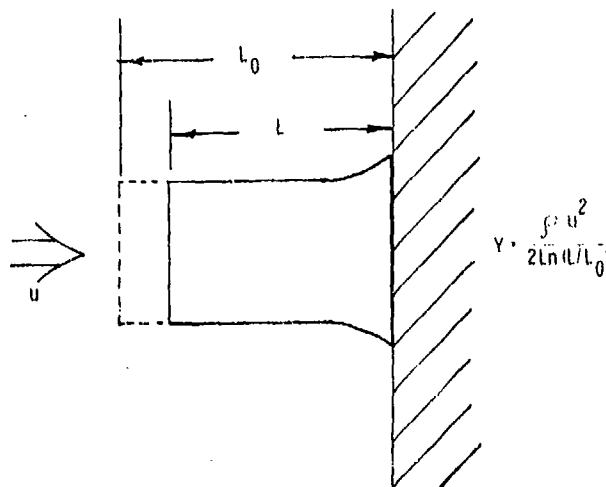


Figure 1 Taylor Test Parameters

EXPERIMENTAL PROCEDURES

In this section we describe the specimen material, the test procedures, and a computer-assisted data reduction method used in the investigation.

Specimen and Target Material

Heat-treated test cylinders of 4340 steel which had been tempered at 400 F were procured by contract. All cylinders were 0.299 in. (7.59 mm) in diameter. The majority of the cylinders were 0.600 in. (15.24 mm) long, having a nominal length to diameter ratio (L/D) of 2. A smaller number were 1.200 in. (30.48 mm) long with a nominal L/D = 4.

A previous investigation using 4340 steel projectiles [2] had indicated that ballistic fracture mode (specifically the occurrence of adiabatic shear) was influenced by factors associated with specimen hardness. We therefore planned to perform tests with specimens of various hardness values. Sets of cylinders were retempered for two hours at the following temperatures: 600 F, 700 F, 800 F, 900 F, and 980 F. The resulting hardness values for the originally received and the retempered material are given in Table I. Each value in the table is the average of eight hardness tests performed on two randomly chosen samples.

Table I Specimen Hardness

Tempering Temperature (Deg F (C))	Rockwell-C Hardness, HRC
400 (204)	53.2
600 (316)	48.7
700 (371)	46.8
800 (427)	44.0
900 (482)	40.7
980 (527)	38.2

All target plates were of the same 4340 material, tempered at 400 F (204 C). The nominal dimensions were: 0.75×6.0×6.0 in. (19×152×152 mm).

Launch Apparatus

The test cylinders were fired from a smooth bore, 20 ft (6.1 m) long, helium propellant gun. The target plates were mounted 19.6 in. (500 mm) from the muzzle. Cylinder velocities were determined using a two-beam laser velocimeter which measured the time of flight over a 6.00-in. (152.4-mm) gage distance. The time measurements were made by a conventional 10-megacycle ballistic chronograph. The major error in velocity arises because of possible differences in the relative positions of the cylinder in the two laser beams when the chronograph trigger signals are generated. We estimate the uncertainty

to be the equivalent to an error in the gage distance. This possible error is equal to the laser beam diameter of 0.09 in. (2.3 mm) resulting in an error of 1.5% in velocity.

Projectile Impact Face Measurements

In experiments where no cracking occurred it was of interest to measure the area or the perimeter of the impact face of the deformed projectile. In cases where the deformation was not symmetric, micrometer measurements of the diameter were inappropriate. In other experiments at higher impact velocities where cracking did occur, measurements of the arc segment lengths between cracks could be used to determine crack initiation strains. We will subsequently describe the formation of such cracks as are shown in Figure 2.

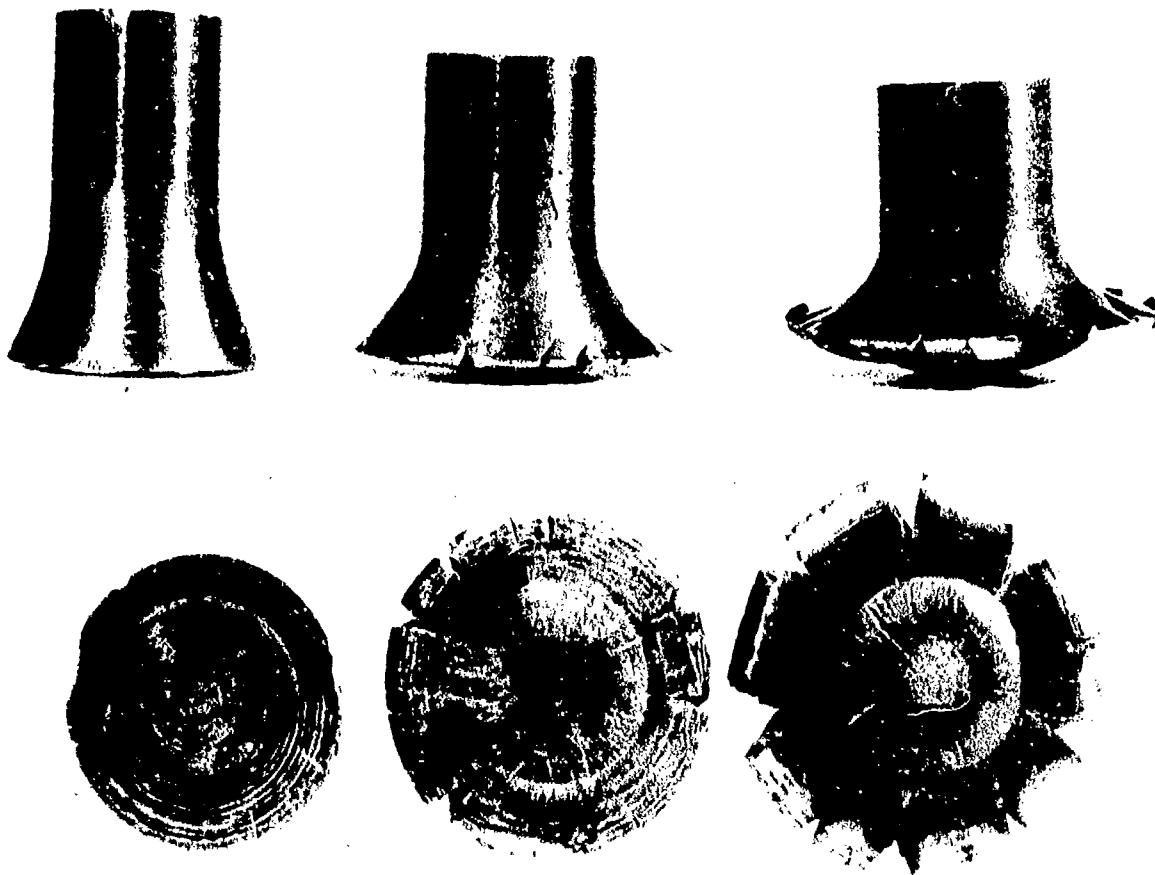


Figure 2 Side views (upper) and impact faces (lower) of three projectile cylinders of 4340 steel tempered at approximately 1000 F (538 C). Impact velocities: left -- 1033 ft/sec (315 m/sec); center -- 1401 ft/sec (427 m/sec); right -- 1736 ft/sec (529 m/sec).

The lower photographs show the impact faces of three projectiles impacted at increasing velocities while the upper photographs are elevation views of the same projectiles.

If the outline of the impact face of such a cracked projectile is traced to a known scale, as shown schematically in Figure 3, the length of one perimeter arc segment L_i , can be approximated by a series of small straight line segments designated as Δ_i in the figure. If a set of coordinate axes is established on the tracing, the lengths of each of the segments can be calculated in the manner illustrated in the figure.

This scheme was the basis of a computer-assisted method for measuring the lengths of the arc segments and for calculating the crack threshold value of the circumference and diameter of the projectile. An enlarged shadowgraph image of the end face was projected on graph paper and hand-traced. A scale length was also marked on the graph. An interactive computer program was written for use with a Tektronix Model 4662-Digital Plotter (operating as a digitizer) and a Tektronix 4014-Graphics Terminal coupled to the AMMRC UNIVAC 1106 computer. With the graph sheet installed on the plotter, the operator digitized the required segments on the tracing and the computer made the appropriate calculations. The results were displayed on the screen of the graphics terminal where they were automatically copied by a hard-copy device. An analogous program, using numerical integration was written to calculate the irregular areas of uncracked end-faces.

We used test tracings of known dimensions to evaluate both the accuracy of the plotter and that of the operator. We found that the average total error in perimeter or in area was less than 2%.

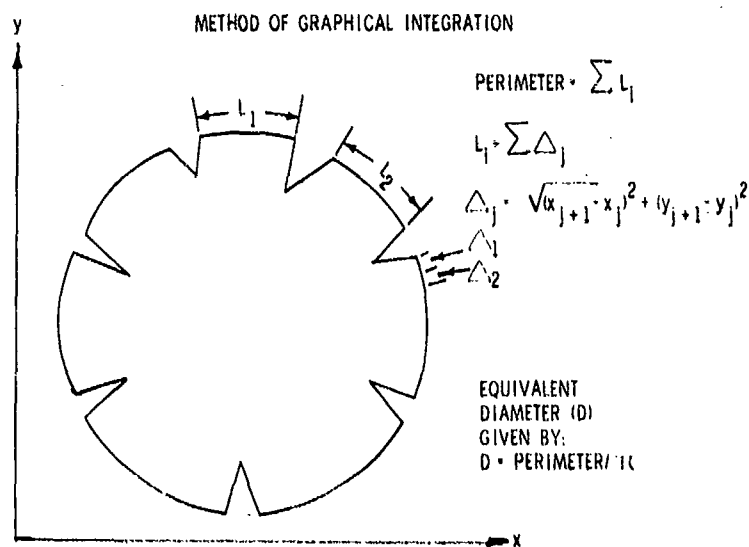


Figure 3 Schematic, enlarged, shadowgraph image of projectile end face illustrating the method of graphical determination of the crack threshold perimeter.

ANALYTICAL PROCEDURE

The stated problem is two-dimensional in character, involving rotational symmetry about the cylinder axis. The HEMP code is suitable for a detailed spatial and temporal analyses of the wave propagation events involved in the experiments; indeed this is the approach used by Wilkins and Guinan [4]. Such a procedure has the advantage of not involving any simplifying hypotheses such as the one-dimensional analysis used by Taylor [1]; it has the disadvantage of a numerical procedure that it does not result in a one-line formula such as Equation 1 for determining useful theoretical parameters.

The HEMP Code

To describe the capabilities of the code as succinctly as possible one might say that it begins with the conservation laws, couples to these an equation of state which is quite realistic for the dynamic high-pressure regimes encountered, casts the entire assembly into a finite-difference formulation and integrates the equations of motion step by step in time.

Code Input

Input to the code consists of a specification of the geometry of the problem, the appropriate initial velocity and the dynamic stress-strain properties of the material involved. Foremost among these are the so-called Hugoniot characteristics describing the dynamic pressure-volume relationship. These are generated in uniaxial-strain shock-wave experiments similar to those in which spall properties are measured. The analytical model incorporates elastic-plastic behavior including strain-hardening effects and employs a Von Mises yield criterion. Details of the flow curve beyond initial yield are obtained, generally, from static tension or compression tests. In the computer simulations performed for this report, only data from compression tests as reported by Chait [3] were used as initial estimates of yield stress to begin the iterative process of comparing theory versus experiment. If agreement was not satisfactory, the initial estimate of yield stress used in the theoretical calculation was modified and the simulation repeated iteratively until agreement was satisfactory.

Code Output

Output from the code consists of a detailed space-time history of all the important physical quantities such as stress, strain, displacement, velocity, etc. Thus it is an extremely valuable tool for providing a dynamic "whole field" analysis required to decipher the complex sequence of events leading up to the final deformation of the recovered projectile. Numerous comparisons between the predictions of HEMP and experimental results tend to show excellent agreement when suitable material properties are employed.

In the computations whose results are reported here, the pressure-volume curve used for the 4340 material was

$$P \approx 1.65 \mu + 1.82 \mu^2$$

where $\mu = (V_0/V - 1)$, V is relative volume, V_0 is the initial value of V and P is pressure in megabars. A constant value of yield stress was used (as discussed in detail in the following) to define the elastic-plastic behavior of the material for most of the comparisons with experiment. The specific value of yield stress chosen corresponds to the value of flow stress at a 50% strain level in the static compression tests on these same materials reported in Reference 3. A few computer simulations were conducted using work-hardening details, but these tended not to greatly illuminate the comparison with experiment. However in this regard, it should be observed that such comparisons only involved what might be termed global features (e.g., overall length of the projectile, circumference of the mushroomed end, etc.) rather than any detailed mapping of the local changes in hardness within the deformed projectile.

TAYLOR TEST DEFORMATIONS

One objective of our Taylor test program was to determine the effect of tempering temperature on the dynamic deformation and fracture behavior of 4340 steel. Another objective was to compare the deformed dimensions of the test cylinders with values predicted by the HEMP-computer code. In this section of the paper we discuss only the deformation studies while the fracture results are described in the next section.

Taylor Flow Stress Errors

It is important to note that small errors in measurement of the impact velocity or of the deformed length of impacted cylinders can lead to larger errors in the value of the Taylor stress as calculated by Equation 1. The value of Y is especially sensitive to length errors and the sensitivity increases as the amount of deformation decreases.

In our experiments, the possible error in velocity measurement is 1.5%. This leads to a possible error of 3% in values of Y calculated by Equation 1.

Length measurement errors are more serious. Let us define the following quantities for a quantitative assessment of the length error in Y . (In the analysis we assume that the initial length of the projectile is determined without error):

- L_0 = original length of the cylinder
- L = true final length
- L_0 = erroneous, measured final length
- e = error in length measurement: $(1 + e) L = L_0$
- Y = true Taylor stress
- Y_e = erroneous Taylor stress (using L_0 in Equation 1)

Now let $\Delta Y = Y_0 - Y$

From Equation 1:

$$Y_0/Y = \ln(L/L_0)/\ln(L_0/L_0) \quad (2)$$

From the definition of e

$$L_e/L_0 = (1 + e) L/L_0 \quad (3)$$

and from the definition of ΔY

$$Y_e/Y = (\Delta Y/Y) + 1 \quad (4)$$

where $\Delta Y/Y$ is the error in Y .

Equations 2 to 4 can be combined and rearranged to

$$\Delta Y/Y = \frac{\ln(L/L_0)}{\ln(1 + e) + \ln(L/L_0)} - 1 \quad (5)$$

Shown in Figure 4 are values of the error in Taylor stress for four values of the length error. It should be noted that for high-strength materials the

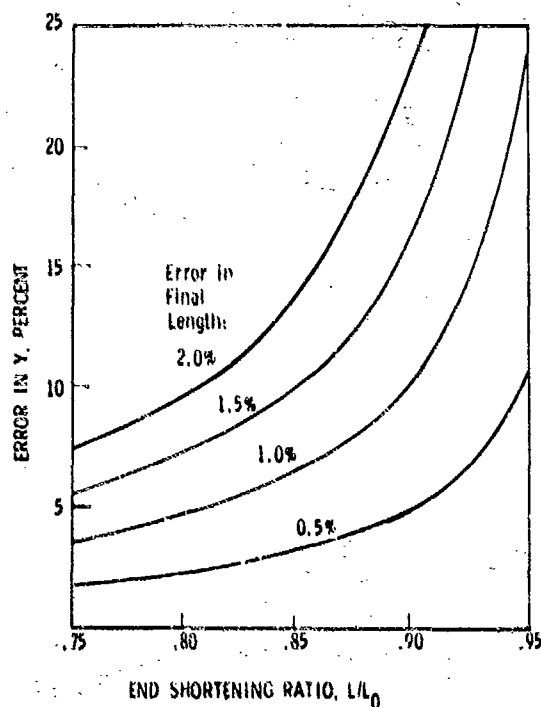


Figure 4 Possible errors in the Taylor stress as a result of errors in measuring the deformed length of the impacted cylinders. For the high-strength 4340 material used in this program the range of L/L_0 values was from about 0.85 to 0.95.

amount of end shortening of the cylinder in a Taylor test is small, hence L/L_0 may be typically greater than 0.85. Here the errors in stress can be very large.

Taylor-Stress Values

Well over 200 specimens were tested in the program. We chose for Taylor stress calculations only specimens which were uncracked and which had impacted with no more than 1° obliquity. The experimental conditions for the selected specimens are shown in Table II.

The mean Taylor-stress values for each temper are shown in Figure 5, separately for $L/D = 2$ and $L/D = 4$. The curves were hand-faired between the data points. The values for $L/D = 4$ are approximately 10% lower than for $L/D = 2$. We have no ready explanation for the difference.

Table II Experimental Conditions for Taylor-Stress Tests for 4340 Steel

Hardness HRC	L/D Ratio	Velocity Range (min - max)		L/L ₀ Range (min - max)	No. of Shots
		ft/sec	m/sec		
53.2	2	435-656	133-200	0.95-0.98	5
53.2	4	520-778	158-237	.93- .97	6
48.7	2	744-1054	227-321	.85- .92	6
46.8	2	858-1015	262-309	.87- .91	5
46.8	4	840-961	256-293	.88- .90	3
44.0	2	818-1063	243-324	.85- .91	4
44.0	4	833-1056	254-322	.84- .89	3
40.7	2	823-974	251-297	.86- .90	3
40.7	4	954-1053	291-321	.82- .86	2
38.2	2	868-1023	265-312	.84- .86	10

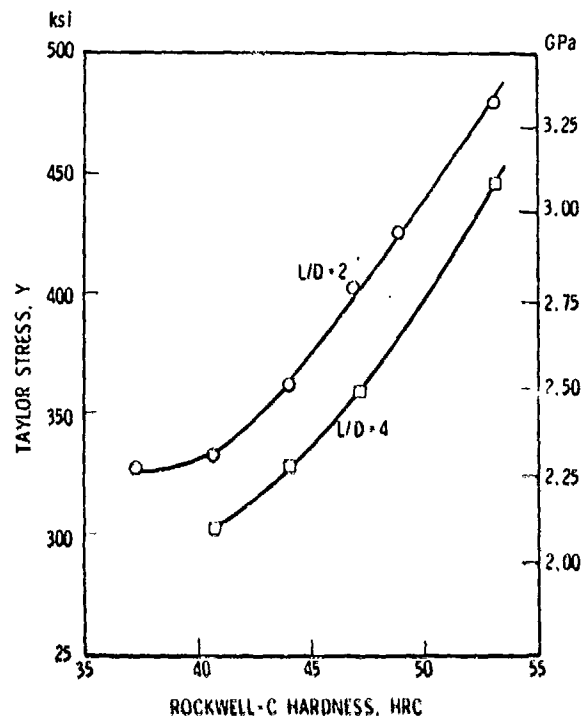


Figure 5 Experimental Taylor-stress values as a function of hardness for tempered 4340 steel.

Static compression data for the same material for the same range of tempering temperatures, reported by Chait [3], are shown in Figure 6 together with the Taylor-stress values for $L/D = 2$. The lower of the two static curves is the 0.2% yield stress; the upper curve is the true stress for a true strain of 0.5. The difference between the two static curves is an indication of the amount of work hardening up to a true strain of 0.5. The elevation of the Taylor-stress values over the static suggests a strain-rate effect. However this is contrary to the findings by Wilkins [4] which indicate that at large strains, flow stress is rate independent for steel above some critical value. The large difference between the Taylor-stress and the static values indicates a large strain-rate effect which also is contrary to the findings of Reference 4. The discrepancy is greater than can be accounted for by experimental error. We tentatively concluded that the Taylor formula is nonconservative when applied to high-strength steel. We will show that HEMP-code analyses lead to the same conclusion.

HEMP-Code Predictions

Computations were made for the two L/D ratios of the experiments: $L/D = 2$ and $L/D = 4$. The input conditions were as follows: impact velocity = 900 ft/sec (274 m/sec) and cylinder diameter = 0.300 in. (7.62 mm). Two sets of HEMP-code runs were made using two different flow stresses but both with

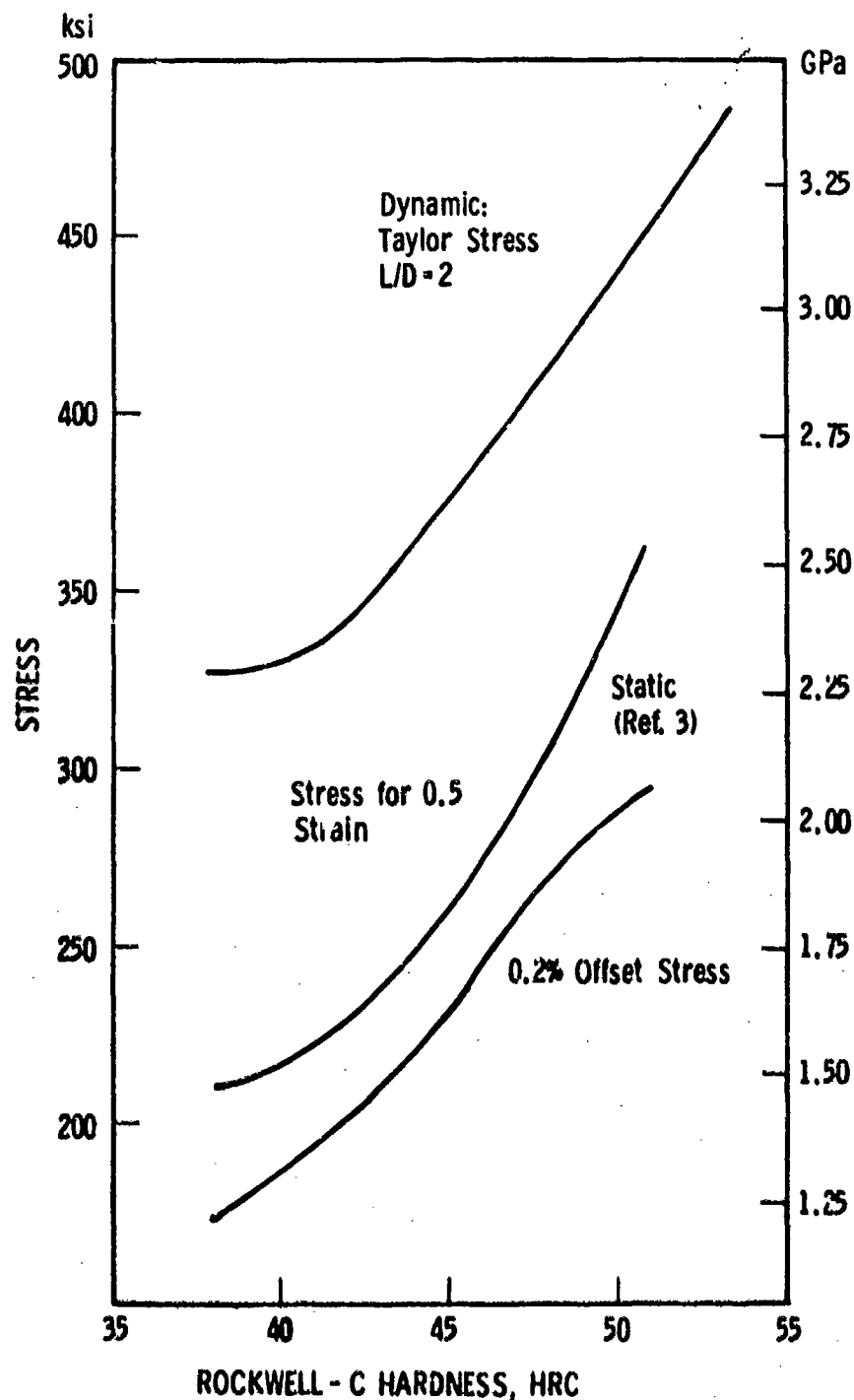


Figure 6 Static compression yield stress data for various hardnesses of 4340 steel (two lower curves) shown with Taylor-stress values for $L/D = 2$. The lower of the two static curves is the 0.2% yield strength. The upper static curve is the stress value for a natural strain of 50%.

stress-strain curves of the elastic-pure plastic type. The flow stresses were 217.6 ksi (1500 MPa) which simulated the material tempered at 900 F (482 C) having HRC = 40.7, and 290.1 ksi (2000 MPa) which simulated the material tempered at 700 F (371 C) having HRC = 46.8. Since there were no data at exactly 900 ft/sec, the experimental values were interpolated from data near this value. The HEMP predictions and experimental values are given in Table III.

Note the remarkable agreement between HEMP values and the experiments which reinforces our confidence in the predictive value of this code.

If we now treat the HEMP data as experimental results, we can compute the Taylor stress for each of the two tempers by substituting the HEMP L/L_0 values in Equation 1 for a velocity of 900 ft/sec (274 m/sec). The results are shown in Table IV.

Table III Comparison of HEMP Predictions and Experimental Values of Final Length and Impact Surface Diameter for Two Tempers of 4340 Steel

Material HRC	L/D Ratio	HEMP		Experimental		Difference (%)	
		L/L_0	D/D_0	L/L_0	D/D_0	L/L_0	D/D_0
40.7	2	0.857	1.42	0.880	1.39	2.6	2.2
40.7	4	.855	1.58	.874	1.56	2.2	1.6
46.8	2	.893	1.32	.900	1.33	0.8	0.8
46.8	4	.892	1.45	.889	1.50	0.3	3.3

Table IV Taylor-Stress Values Computed from HEMP Values of L/L_0

HEMP Input Stress		HEMP L/L_0	Taylor Stress		Diff. %
ksi	MPa		ksi	MPa	
217.6	1500	0.857	273.8	1888	25.8
290.1	2000	0.893	373.4	2575	28.7

Taylor stresses calculated from HEMP L/L_0 values are much elevated above the input flow stress. This behavior is similar to what was shown in Figure 6. We have therefore concluded that the Taylor formula is unreliable for high-strength steel and that a procedure utilizing HEMP and experiments is probably more suitable to obtain dynamic flow stresses of such materials. In such a procedure, deformed lengths of projectile cylinders could be measured with a lower precision than that required for the strictly experimental procedure. Then by an iterative process experimental lengths could be matched with HEMP-

predicted lengths and the appropriate stress would be determined from the HEMP values. The details of such a procedure are now under investigation.

FRACTURE

Dynamic fracture in Taylor test cylinders of 4340 steel occurs in a variety of shear modes which generally fall into two categories. We will apply the term brittle fracture where there is a breakup of the cylinder into large and/or small fragments and the term ductile fracture where the cylinder cracks but remains intact over an extended range of impact velocities. Cylinders tempered below 800 F (427 C), where the HRC is greater than 44, fail by brittle fracture. Cylinders tempered at or above this temperature where the HRC ≤ 44 fail by ductile fracture. In this mode, there is a threshold velocity for cracks to form along the perimeter of the impact face of the projectile. At higher velocities, the cracks propagate in shear, radially inward in the manner shown in Figure 2.

Brittle Fracture in HRC = 53.2

Our most extensive fracture testing was performed with specimens of the hardest of the 4340 steel tempers. The velocity threshold for fragment fracture for this temper is between 740 to 780 ft/sec (226 to 238 m/sec) if the impact is normal. For non-normal impacts, diagonal shear-formed fractures occur with a wedge-shaped fragment at a threshold velocity of approximately 650 ft/sec (198 m/sec). In the $L/D = 4$ cylinders, as the velocity is increased beyond the threshold value, the number of fragments increases and the size of the fragments decreases.

It is in the $L/D = 2$ cylinders that a unique form of fracture occurs which we have not observed in $L/D = 4$, for this temper, or in any cylinder tempered above 400 F (204 C). In this mode a cone-shaped fragment consistently fractures from the impact end. This is shown schematically in Figure 7. The threshold value for cone fracture, when the impact is normal, is in the range from 925 to 1000 ft/sec (282 to 305 m/sec). Shown in Figure 8, on the left

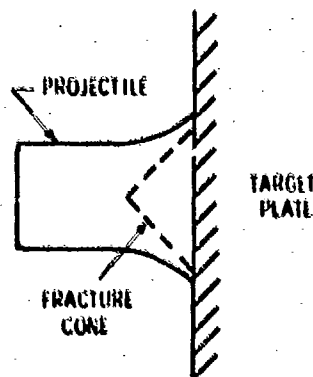


Figure 7 Impact-end fracture cone in $L/D = 2$ projectiles of 4340 steel, tempered at 400 F (204 C) - schematic.

is one such cone. Next to the cone is a typical wedge-shaped fragment. Shown in the figure on the right, for comparison purposes, are an unfractured, but deformed cylinder, and an unfired sample.

We have been able to recover projectile cylinders in which the cone has not yet separated from the body of the cylinder. One such cylinder is shown in several views in Figure 9 from an impact at 1033 ft/sec (315 m/sec).

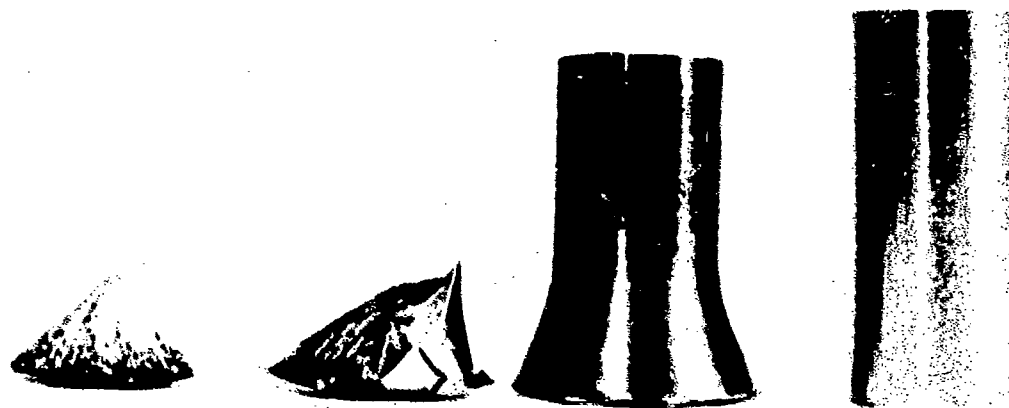


Figure 8 Left: typical cone fragment; second from left: typical wedge fragment; second from right: typical mushroom deformation of softer projectiles; right: undeformed cylinder. The two projectiles on the right are shown for comparison purposes.



Figure 9 Side and end views of an intact, but cracked cylinder of 4340 steel with HRC = 53.2. The cylinder was rotated for the side views to show the distribution of the diagonal cracks. The base of an incipient cone is evident in the end view on the right.

Our interpretation of the chronology of fracture is that cracks initiate at the rim and propagate inward to form the cone surface and diagonally rearward as shown in the two photographs, left and center. The cone base is clearly delineated in the photograph on the right and shows no evidence of the radial cracking typical of the higher temperature temper samples. At higher velocities the cone remains intact and acts as a wedge to cause further fragmentation of the cylinder. The cracks, visible in the left and center photographs of Figure 9, propagate and join together to form individual small fragments many of which contain small concave conical areas.

Fracture cones form and can be recovered over an extended range of velocities. In a series of exploratory penetration experiments using thin, hardened 4340 steel targets which failed by plugging, we recovered cones when the impact velocity was as high as 1729 ft/sec (527 m/sec).

Metallographic Examinations

A number of cone fragments were sectioned, polished, and etched. In each such section we found evidence of the so called white layer which is indicative of adiabatic shear. It was not clear, however, from these examinations whether the effect occurred prior to cracking or was the result of post-cracking events.

An intact, but cracked cylinder, similar to that shown in Figure 9, from an impact experiment at 978 ft/sec (298 m/sec) was sectioned, polished, and etched. Shown in the upper photograph of Figure 10 is a low magnification view of the impact end with a crack which is evidence of an incompletely formed fracture cone. The crack forms a 50° angle with cylinder axis. The lower photograph in the figure is a high magnification view of the crack in an area near the apex of the incipient cone. Note the clear evidence of white layer on the crack surfaces, and also of a thin spike of white layer running diagonally upward into the material near the center of the photograph. We have concluded from this metallographic evidence that adiabatic shear is a precursor to cone cracking and that the crack occurs in the thin adiabatic shear band.

There is yet no adequate theory to account for the formation of this highly localized, thin conical layer of intense shear. We have no ready explanation why conical fragments consistently appear in $L/D = 2$ cylinders of the HRC = 53.2 material and not in $L/D = 4$, and neither can we explain why the adiabatic-shear-cone phenomenon has not been observed in any of the less hard tempers.

We estimate that the shear layer has a thickness of no more than 40 μ in. (1 μ m) when it forms. Since numerical codes like HEMP operate using discrete zones and since it is not feasible to use zone sizes which are even 100 times the shear layer thickness, there appears little possibility at this time that HEMP and other similar computer codes can yield insight into this consistently occurring phenomenon.

Brittle Fracture in HRC = 45.7 and HRC = 46.8

In both of these tempers brittle fracture occurs at higher velocities than for the HRC = 53.2 material. As the impact velocity is increased, there

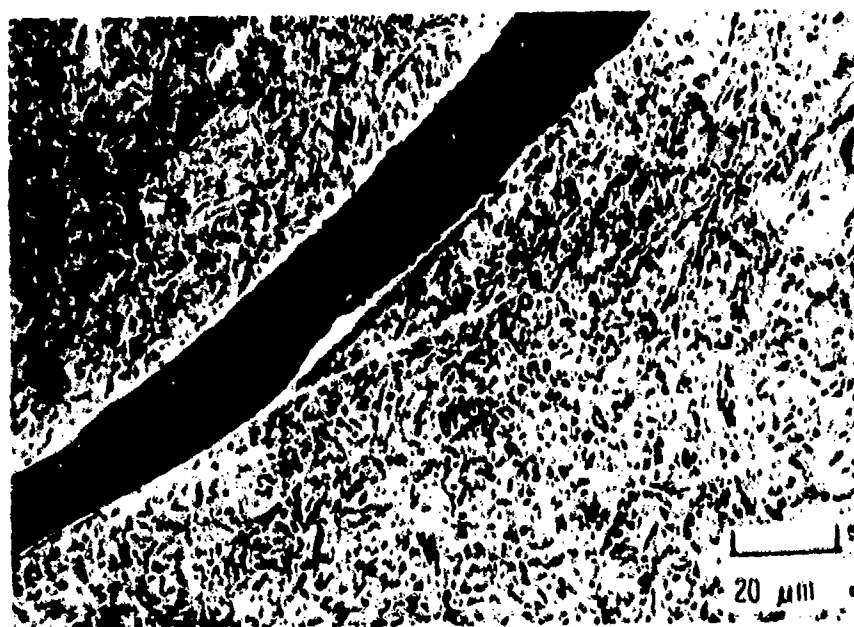
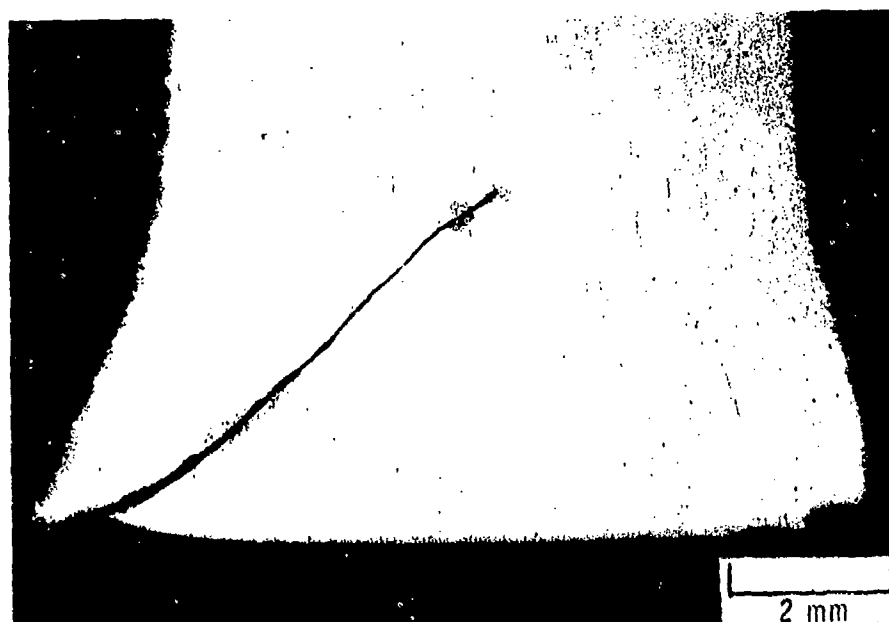


Figure 10 Polished and etched axial section of an HRC = 52.2 which had been impacted at 978 ft/sec (298 m/sec). (Before sectioning this cylinder was similar to that shown in Figure 9.) Upper: crack indicating an incomplete conical fracture surface. Lower: magnified areas near cone apex showing white layer on crack surfaces. Note also a spike of white layer extending left to right from the crack surface near the center of the photomicrograph.

is some ductile deformation, then radial cracking, and finally fragments form. For the HRC = 48.7 material only $L/D = 2$ was tested. Both $L/D = 2$ and $L/D = 4$ were tested for the HRC = 46.8. The velocity thresholds for fracture are approximately 1160 ft/sec (354 m/sec) and 1280 ft/sec (390 m/sec) for the HRC = 48.7 and HRC = 46.8, respectively. In the softer of the two materials threshold values for both L/D values are similar.

In a number of the fractured $L/D = 2$ cylinders for both tempers we found evidence that at least part of the fracture surface was in the shape of an inverse cone as shown schematically in Figure 11. We suspect that adiabatic shear has occurred in these cylinders but scheduled metallographic examinations have not yet been performed.

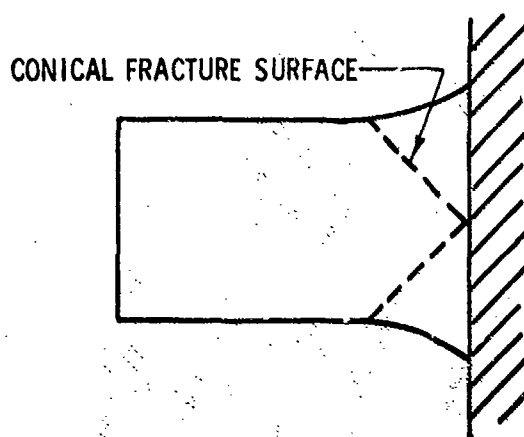


Figure 11 Schematic inverse cone as observed in HRC = 48.7 and HRC = 46.8 cylinders.

Ductile Fracture

Using the computer-assisted technique described previously and illustrated in Figure 3, crack-threshold perimeters were determined and converted to equivalent diameters of the deformed impact faces. The diameter data were then converted to a crack-threshold strain. The strain value can be considered to be an ultimate strain, analogous to a short-gage length elongation in the tensile test. The results are shown in Table V. The data for each condition were obtained by averaging results from the number of tests shown in the last column. The velocity range of the data was over approximately 200 ft/sec (61 m/sec). Note that the standard deviations of the diameter are relatively small and are no more than $\pm 3.5\%$ of the diameter value.

The natural strains are shown graphically in Figure 12. Note that the discrepancy between $L/D = 2$ and $L/D = 4$ increases as the hardness decreases. We have no explanation for the differences in fracture strain but we suspect that the differences in stress-state may exist in the impact-face rim region of the two L/D values and these differences can lead to different fracture strains. Resolution of this problem may be possible when a suitable fracture criterion is developed for the HEMP code. Although such a criterion is not

Table V Cracking Threshold Diameter and Tangential Strain at Impact Face for 4340 Steel*

HRC Value	L/D Ratio	Diam. and Std. Dev.		D/D ₀ Ratio	Strain Ln D/D ₀	No. of Tests
		(in.)	(mm)			
53.2	2	0.339±0.008	8.60±0.20	1.134	0.127	7
53.2	4	.351± .013	8.91± .33	1.174	.160	7
46.8	2	.415± .009	10.54± .22	1.388	.328	7
46.8	4	.464± .012	11.79± .29	1.553	.440	3
44.0	2	.437± .014	11.10± .36	1.462	.380	10
44.0	4	.506± .016	12.84± .40	1.691	.526	4
40.7	2	.451± .016	11.46± .40	1.509	.412	7
40.7	4	.512± .016	13.00± .40	1.712	.538	4
38.2	2	.459± .010	11.67± .25	1.537	.430	5

*There were insufficient data for HRC = 48.7.

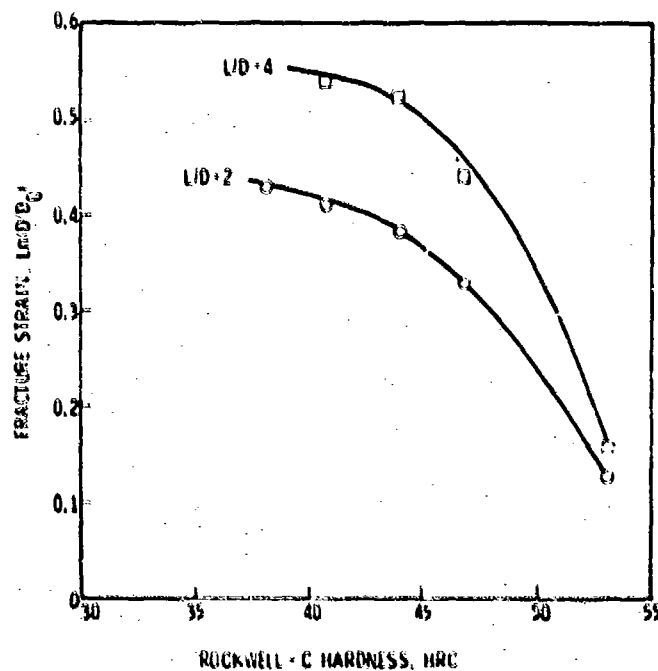


Figure 12 Dynamic fracture strains for 4340 steel of various tempers.

yet available, we are currently studying how the current data may be applied in its development.

An immediate application of the data to two-dimensional code studies of the Taylor test is evident. When the strain at the impact-face rim reaches the experimental value, the two-dimensional problem is completed and further time-steps in the calculation can be aborted. In the case of the 4340 steel, the data of Figure 12 would serve as cut-off criteria.

CONCLUSIONS

The major conclusions from this combined theoretical and experimental study of large deformation and fracture behavior of 4340 steel are as follows:

1. The conventional Taylor test is an unreliable method of obtaining dynamic flow stress data for high-strength materials such as 4340 steel tempered below 800 F (427 C).
2. The HEMP code, using the static value of the compressive stress for 0.5 true strain as the dynamic flow stress, correctly predicts the deformed lengths and the impact-face diameters of Taylor test cylinders of 4340 steel of several tempers.
3. There is a characteristic fracture strain for 4340 steel which can be determined in a Taylor test. There are still unresolved differences in the values obtained from $L/D = 2$ and $L/D = 4$ test cylinders.
4. A more reliable procedure than the use of the Taylor formula for obtaining dynamic flow stresses for high-strength materials would be a combination of Taylor-test-type experiments together with theoretical HEMP-code studies.

ACKNOWLEDGMENTS

Charles Polley and James Dorval performed the experimental firings. Mr. Dorval performed many of the computer-assisted strain analyses. We thank them for their contributions. We especially thank James McLaughlin for his advice and assistance on the HEMP-code studies.

REFERENCES

1. Taylor, G. I., "The Use of Flat-Ended Projectiles for Determining the Dynamic Yield Stress. I: Theoretical Considerations," Proc. Roy. Soc., v. 194A, 1948, 289-299.
2. Mescall, J. and Papirno, R., "Spallation in Cylinder Plate Impact," Experimental Mechanics, v. 14, no. 7, 1974, 257-266.
3. Chait, R., "Factors Influencing the Strength Differential of High Strength Steels," Met. Trans., v. 3, no. 2, 1972, 365-371.
4. Wilkins, M. L. and Guinan, M. W., "Impact of Cylinders on a Rigid Boundary," J. Appl. Phys., v. 44, no. 3, 1973, 1200-1206.

AUTHOR INDEX

Allison, W. D.	Army Ballistic Research Laboratory	Aberdeen, MD	46
Avery, J. G.	Boeing Military Airplane Company	Seattle, WA	159, 187
Bradley, S. J.	Boeing Military Airplane Company	Seattle, WA	159
Brawley, G. H.	Battelle Columbus Laboratories	Columbus, OH	330
Caltagirone, J.	Army Large Caliber Weapon System Laboratory	Dover, NJ	21
Chu, S. H.	Army Large Caliber Weapon System Laboratory	Dover, NJ	270
Curtis, D.	Naval Research Laboratory	Washington, DC	108
Dandekar, D. P.	Army Materials and Mechanics Research Center	Watertown, MA	317
Dharmarajan, S.	San Diego State University	San Diego, CA	204
Dobbs, N.	Ammann & Whitney	New York, NY	21
Dobyns, A. L.	Boeing Military Airplane Company	Seattle, WA	187
Halperson, S.	Naval Research Laboratory	Washington, DC	108
Hansen, A. M.	Army Materials and Mechanics Research Center	Watertown, MA	367
Harrison, J. T.	Army Ballistic Research Laboratory	Aberdeen, MD	239
Heimdahl, O. E. R.	Naval Weapons Center	China Lake, CA	255
Huang, H.	Naval Research Laboratory	Washington, DC	108
Kelley, J. V.	Army Materials and Mechanics Research Center	Watertown, MA	317
King, K. M.	Boeing Military Airplane Company	Seattle, WA	159
Konishi, D. Y.	Rockwell International, North American Aircraft Division	Los Angeles, CA	219
Lee, W. N.	Kaman Avidyne	Burlington, MA	126
Mann, R. L.	General Electric Company	Syracuse, NY	289
Martin, A. G.	Army Materials and Mechanics Research Center	Watertown, MA	317
McLaughlin, J.	Army Materials and Mechanics Research Center	Watertown, MA	351
Mento, L. J.	Kaman Avidyne	Burlington, MA	126
Moscall, J. F.	Army Materials and Mechanics Research Center	Watertown, MA	351, 367
Papirno, R. P.	Army Materials and Mechanics Research Center	Watertown, MA	351, 367
Perkins, R. W.	Syracuse University	Syracuse, NY	289
Predebon, W. W.	Michigan Technological University	Houghton, MI	330
Price, P.	Army Large Caliber Weapon System Laboratory	Dover, NJ	21
San Miguel, A.	Systems, Science and Software	La Jolla, CA	65
Schuman, W. J., Jr.	Harry Diamond Laboratories	Adelphi, MD	46
Shah, K.	Ammann & Whitney	New York, NY	21
Simitses, G. J.	Georgia Institute of Technology	Atlanta, GA	87
Smith, L. M.	General Dynamics Corporation	Fort Worth, TX	3
Sock, F. E.	Ammann & Whitney	New York, NY	21
Stronge, W. J.	Naval Weapons Center	China Lake, CA	255
Stuart, R. J.	San Diego State University	San Diego, CA	204
Walters, W. P.	Army Ballistics Research Laboratory	Aberdeen, MD	239
Yeghiayan, R. P.	Kaman Avidyne	Burlington, MA	46
Zartarian, G.	Kaman Avidyne	Burlington, MA	46